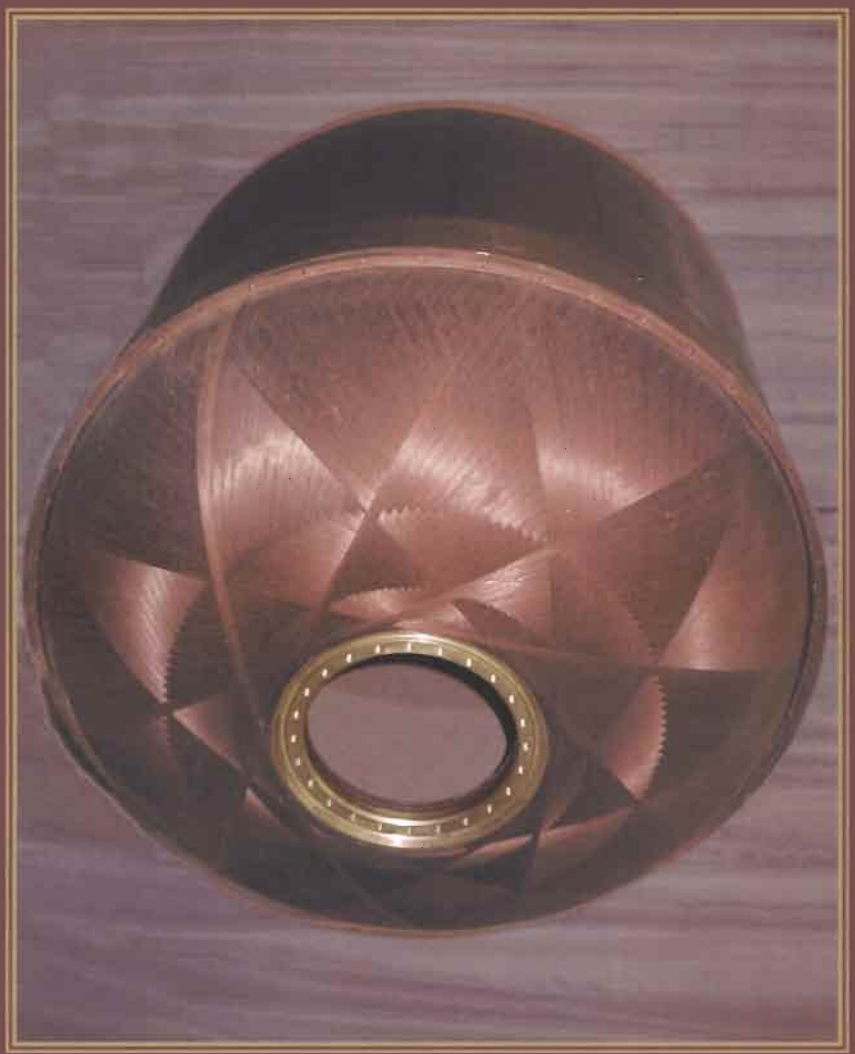

Mechanics and Analysis of Composite Materials

Valery V. Vasiliev & Evgeny V. Morozov

Elsevier

MECHANICS AND ANALYSIS OF COMPOSITE MATERIALS

MECHANICS AND ANALYSIS OF COMPOSITE MATERIALS

Valery V. Vasiliev

Professor of Aerospace Composite Structures
Director of School of Mechanics and Design
Russian State University of Technology, Moscow

Evgeny V. Morozov

Professor of Manufacturing Systems
School of Mechanical Engineering
University of Natal, South Africa

2001

ELSEVIER
AMSTERDAM · LONDON · NEW YORK · OXFORD · PARIS · SHANNON · TOKYO

ELSEVIER SCIENCE Ltd
The Boulevard, Langford Lane
Kidlington, Oxford OX5 1GB, UK

First edition 2001
ISBN: 0-08-042702-2

British Library Cataloguing in Publication Data
Vasiliev, Valery V.
Mechanics and analysis of composite materials
1.Composite materials - Mechanical properties
I.Title II.Morozov, Evgeny V.
620.1'1892

ISBN 0080427022

Library of Congress Cataloging-in-Publication Data
Vasiliev, Valery V.
Mechanics and analysis of composite materials / Valery V. Vasiliev, Evgeny V. Morozov. -- 1st ed.
p. cm.
Includes bibliographical references and index.
ISBN 0-08-042702-2 (hardcover)
1.Composite materials--Mechanical Properties. 2. Fibrous composites--Mechanical properties. I. Morozov, Evgeny V. II. Title.

TA418.9.C6V375 2000
620.1'1892--dc21 00-061765

♾ The paper used in this publication meets the requirements of ANSI/NISO Z39.48-1992 (Permanence of Paper).

Printed in The Netherlands

PREFACE

This book is concerned with the topical problems of mechanics of advanced composite materials whose mechanical properties are controlled by high-strength and high-stiffness continuous fibers embedded in polymeric, metal, or ceramic matrix. Although the idea of combining two or more components to produce materials with controlled properties has been known and used from time immemorial, modern composites have been developed only several decades ago and have found by now intensive application in different fields of engineering, particularly, in aerospace structures for which high strength-to-weight and stiffness-to-weight ratios are required.

Due to wide existing and potential applications, composite technology has been developed very intensively over recent decades, and there exist numerous publications that cover anisotropic elasticity, mechanics of composite materials, design, analysis, fabrication, and application of composite structures. According to the list of books on composites presented in Mechanics of Fibrous Composites by C.T. Herakovich (1998) there were 35 books published in this field before 1995, and this list should be supplemented now with at least five new books.

In connection with this, the authors were challenged with a natural question as to what causes the necessity to publish another book and what is the difference between this book and the existing ones. Concerning this question, we had at least three motivations supporting us in this work.

First, this book is of a more specific nature than the published ones which usually cover not only mechanics of materials but also include analysis of composite beams, plates and shells, joints, and elements of design of composite structures that, being also important, do not strictly belong to mechanics of composite materials. This situation looked quite natural because composite science and technology, having been under intensive development only over several past decades, required the books of a universal type. Nowadays however, application of composite materials has reached the level at which special books can be dedicated to all the aforementioned problems of composite technology and, first of all, to mechanics of composite materials which is discussed in this book in conjunction with analysis of composite materials. As we hope, thus constructed combination of materials science and mechanics of solids has allowed us to cover such specific features of material behavior as nonlinear elasticity, plasticity, creep, structural nonlinearity and discuss in detail the problems of material micro- and macro-mechanics that are only slightly touched in the existing books, e.g., stress diffusion in a unidirectional material with broken fibers, physical and statistical aspects of fiber strength, coupling effects in anisotropic and laminated materials, etc.

Second, this book, being devoted to materials, is written by designers of composite structures who over the last 30 years were involved in practically all main

Soviet and then Russian projects in composite technology. This governs the list of problems covered in the book which can be referred to as material problems challenging designers and determines the third of its specific features – discussion is illustrated with composite parts and structures built within the frameworks of these projects. In connection with this, the authors appreciate the permission of the Russian Composite Center – Central Institute of Special Machinery (CRISM) to use in the book the pictures of structures developed and fabricated in CRISM as part of the joint research and design projects.

The book consists of eight chapters progressively covering all structural levels of composite materials from their components through elementary plies and layers to laminates.

Chapter 1 is an Introduction in which typical reinforcing and matrix materials as well as typical manufacturing processes used in composite technology are described.

Chapter 2 is also a sort of Introduction but dealing with fundamentals of mechanics of solids, i.e., stress, strain, and constitutive theories, governing equations, and principles that are used in the next chapters for analysis of composite materials.

Chapter 3 is devoted to the basic structural element of a composite material – unidirectional composite ply. In addition to traditional description of micromechanical models and experimental results, the physical nature of fiber strength, its statistical characteristics and interaction of damaged fibers through the matrix are discussed, and an attempt is made to show that fibrous composites comprise a special class of man-made materials utilizing natural potentials of material strength and structure.

Chapter 4 contains a description of typical composite layers made of unidirectional, fabric, and spatially reinforced composite materials. Traditional linear elastic models are supplemented in this chapter with nonlinear elastic and elastic–plastic analysis demonstrating specific types of behavior of composites with metal and thermoplastic matrices.

Chapter 5 is concerned with mechanics of laminates and includes traditional description of the laminate stiffness matrix, coupling effects in typical laminates and procedures of stress calculation for in-plane and interlaminar stresses.

Chapter 6 presents a practical approach to evaluation of laminate strength. Three main types of failure criteria, i.e., structural criteria indicating the modes of failure, approximation polynomial criteria treated as formal approximations of experimental data, and tensor-polynomial criteria are analyzed and compared with available experimental results for unidirectional and fabric composites.

Chapter 7 dealing with environmental, and special loading effects includes analysis of thermal conductivity, hydrothermal elasticity, material aging, creep, and durability under long-term loading, fatigue, damping and impact resistance of typical advanced composites. The influence of manufacturing factors on material properties and behavior is demonstrated for filament winding accompanied with nonuniform stress distribution between the fibers and ply waviness and laying-up processing of nonsymmetric laminate exhibiting warping after curing and cooling.

The last Chapter 8 covers a specific for composite materials problem of material optimal design and presents composite laminates of uniform strength providing high weight efficiency of composite structures demonstrated for filament wound pressure vessels.

The book is designed to be used by researchers and specialists in mechanical engineering involved in composite technology, design, and analysis of composite structures. It can be also useful for graduate students in engineering.

Valery V. Vasiliev *Evgeny V. Morozov*

CONTENTS

Chapter 1

INTRODUCTION

1.1. Structural materials

Material is the basic element of all natural and man-made structures. Figuratively speaking it materializes the structural conception. Technological progress is associated with continuous improvement of existing material properties as well as with expansion of structural material classes and types. Usually, new materials emerge due to necessity to improve the structure efficiency and performance, but as a rule, new materials themselves in turn provide new opportunities to develop updated structures and technology, while the latter presents material science with new problems and tasks. One of the best manifestations of this interrelated process in development of materials, structures, and technology is associated with composite materials to which this book is devoted.

Structural materials should possess a great number of physical, chemical and other types of properties, but there exist at least two principal characteristics that are of primary importance. These characteristics are stiffness and strength that provide the structure with the ability to maintain its shape and dimensions under loading or any other external action.

High stiffness means that material exhibits low deformation under loading. However, saying that stiffness is an important property we do not mean that it should be necessarily high. Ability of structure to have controlled deformation (compliance) can be also important for some applications (e.g., springs; shock absorbers; pressure, force, and displacement gauges).

Shortage of material strength results in uncontrolled compliance, i.e., in failure after which a structure does not exist any more. Usually, we need to have as high strength as possible, but there are some exceptions (e.g., controlled failure of explosive bolts is used to separate rocket stages).

Thus, without controlled stiffness and strength the structure cannot exist. Naturally, both properties depend greatly on the structure design but are determined by stiffness and strength of the structural material because a good design is only a proper utilization of material properties.

To evaluate material stiffness and strength, consider the simplest test – a bar with cross-sectional area A loaded with tensile force F as shown in Fig. 1.1. Obviously,

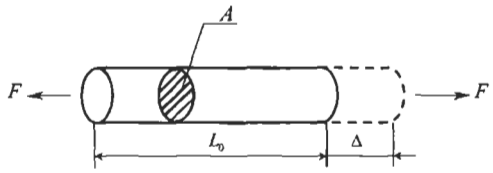

Fig. 1.1. A bar under tension.

the higher is the force causing the bar rupture the higher is the bar strength. However, this strength depends not only on the material properties – it is proportional to the cross-sectional area A. Thus, it is natural to characterize material strength with the ultimate stress

$$\bar{\sigma} = \frac{\bar{F}}{A} \ , \tag{1.1}$$

where $\bar{F}$ is the force causing the bar failure (here and further we use the overbar notation to indicate the ultimate characteristics). As follows from Eq. (1.1), stress is measured in force divided by area, i.e., according to international (SI) units, in pascals (Pa) so that 1 Pa = 1 N/m^2. Because loading of real structures induces relatively high stresses, we also use kilopascals (1 kPa = 10^3 Pa), megapascals (1 MPa = 10^6 Pa), and gigapascals (1 GPa = 10^9 Pa). Conversion of old metric (kilogram per square centimeter) and English (pound per square inch) units to pascals can be done using the following relations: 1 kg/cm^2 = 98 kPa and 1 psi = 6.89 kPa.

For some special (e.g., aerospace or marine) applications, i.e., for which material density, ρ, is also important, a normalized characteristic

$$k_\sigma = \frac{\bar{\sigma}}{\rho} \tag{1.2}$$

is also used to describe the material. This characteristic is called "specific strength" of the material. If we use old metric units, i.e., measure force and mass in kilograms and dimensions in meters, substitution of Eq. (1.1) into Eq. (1.2) yields k_σ in meters. This result has a simple physical sense, namely k_σ is the length of the vertically hanging fiber under which the fiber will be broken by its own weight.

Stiffness of the bar shown in Fig. 1.1 can be characterized with an elongation Δ corresponding to the applied force F or acting stress $\sigma = F/A$. However, Δ is proportional to the bar length L_0. To evaluate material stiffness, we introduce strain

$$\varepsilon = \frac{\Delta}{L_0} \ . \tag{1.3}$$

Since ε is very small for structural materials the ratio in Eq. (1.3) is normally multiplied by 100, and ε is expressed as a percentage.

Naturally, for any material, there should exist some interrelation between stress and strain, i.e.

$$\varepsilon = f(\sigma) \quad \text{or} \quad \sigma = \varphi(\varepsilon). \tag{1.4}$$

These equations specify the so-called constitutive law and are referred to as constitutive equations. They allow us to introduce an important concept of the material model which represents some idealized object possessing only those features of the real material that are essential for the problem under study. The point is that performing design or analysis we always operate with models rather than with real materials. Particularly, for strength and stiffness analysis, this model is described by constitutive equations, Eqs. (1.4), and is specified by the form of function $f(\sigma)$ or $\varphi(\varepsilon)$.

The simplest is the elastic model which implies that $f(0) = 0$, $\varphi(0) = 0$ and that Eqs. (1.4) are the same for the processes of an active loading and an unloading. The corresponding stress–strain diagram (or curve) is presented in Fig 1.2. Elastic model (or elastic material) is characterized with two important features. First, the corresponding constitutive equations, Eqs. (1.4), do not include time as a parameter. This means that the form of the curve shown in Fig. 1.2 does not depend on the rate of loading (naturally, it should be low enough to neglect the inertia and dynamic effects). Second, the work performed by force F is accumulated in the bar as potential energy, which is also referred to as strain energy or elastic energy. Consider some infinitesimal elongation $\mathrm{d}\Delta$ and calculate elementary work performed by the force F in Fig 1.1 as $\mathrm{d}W = F\,\mathrm{d}\Delta$. Then, work corresponding to point 1 of the curve in Fig. 1.2 is

$$W = \int_0^{\Delta_1} F\,\mathrm{d}\Delta \ ,$$

where Δ_1 is the elongation of the bar corresponding to point 1 of the curve. The work W is equal to elastic energy of the bar which is proportional to the bar volume and can be presented as

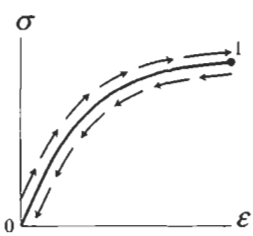

$$E = L_0 A \int_0^{\varepsilon_1} \sigma \, d\varepsilon \ ,$$

where $\sigma = F/A$, $\varepsilon = \Delta/L_0$, and $\varepsilon_1 = \Delta_1/L_0$. Integral

$$U = \int_0^{\varepsilon_1} \sigma \, d\varepsilon = \int_0^{\varepsilon_1} \varphi(\varepsilon) d\varepsilon \tag{1.5}$$

is a specific elastic energy (energy accumulated in the unit volume of the bar) that is referred to as an elastic potential. It is important that U does not depend on the history of loading. This means that irrespective of the way we reach point 1 of the curve in Fig 1.2 (e.g., by means of continuous loading, increasing force F step by step, or using any other loading program), the final value of U will be the same and will depend only on the value of final strain ε_1 for the given material.

A very important particular case of the elastic model is the linear elastic model described by the well-known Hooke's law (see Fig. 1.3)

$$\sigma = E\varepsilon \ . \tag{1.6}$$

Here, E is the modulus of elasticity. As follows from Eqs. (1.3) and (1.6), $E = \sigma$ if $\varepsilon = 1$, i.e. if $\Delta = L_0$. Thus, modulus can be interpreted as the stress causing elongation of the bar in Fig. 1.1 as high as the initial length. Because the majority of structural materials fails before such a high elongation can occur, modulus is usually much higher then the ultimate stress $\bar{\sigma}$.

Similar to specific strength k_σ in Eq. (1.2), we can introduce the corresponding specific modulus

$$k_E = \frac{E}{\rho} \tag{1.7}$$

determining material stiffness with respect to material density.

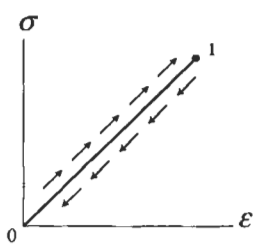

Fig. 1.3. Stress–strain diagram for a linear elastic material.

Absolute and specific values of mechanical characteristics for typical materials discussed in this book are listed in Table 1.1.

After some generalization, modulus can be used to describe nonlinear material behavior of the type shown in Fig. 1.4. For this purpose, the so-called secant, E_s, and tangent, E_t, moduli are introduced as

$$E_s = \frac{\sigma}{\varepsilon} = \frac{\sigma}{f(\sigma)}, \quad E_t = \frac{d\sigma}{d\varepsilon} = \frac{d\varphi(\varepsilon)}{d\varepsilon} \ . \tag{1.8}$$

While the slope α in Fig. 1.4 determines modulus E, the slopes β and γ determine E_s and E_t, respectively. As it can be seen, E_s and E_t, in contrast to E, depend on the level of loading, i.e., on σ or ε. For a linear elastic material (see Fig. 1.3), $E_s = E_t = E$.

Hooke's law, Eq. (1.6), describes rather well the initial part of stress–strain diagram for the majority of structural materials. However, under relatively high level of stress or strain, materials exhibit nonlinear behavior.

One of the existing models is the nonlinear elastic material model introduced above (see Fig. 1.2). This model allows us to describe the behavior of highly deformable rubber-type materials.

Another model developed to describe metals is the so-called elastic–plastic material model. The corresponding stress–strain diagram is shown in Fig. 1.5. In contrast to elastic material (see Fig. 1.2), the processes of active loading and unloading are described with different laws in this case. In addition to elastic strain, ε_e, which disappears after the load is taken off, the residual strain (for the bar shown in Fig. 1.1, it is plastic strain, ε_p) retains in the material. As for an elastic material, stress–strain curve in Fig. 1.5 does not depend on the rate of loading (or time of loading). However, in contrast to an elastic material, the final strain of an elastic–plastic material can depend on the history of loading, i.e., on the law according to which the final value of stress was reached.

Thus, for elastic or elastic–plastic materials, constitutive equations, Eqs. (1.4), do not include time. However, under relatively high temperature practically all the materials demonstrate time-dependent behavior (some of them do it even under room temperature). If we apply to the bar shown in Fig. 1.1 some force F and keep it constant, we can see that for a time-sensitive material the strain increases under constant force. This phenomenon is called the creep of the material.

So, the most general material model that is used in this book can be described with the constitutive equation of the following type:

$$\varepsilon = f(\sigma, t, T) \ , \tag{1.9}$$

where t indicates the time moment, while σ and T are stress and temperature corresponding to this moment. In the general case, constitutive equation, Eq. (1.9), specifies strain that can be decomposed into three constituents corresponding to elastic, plastic and creep deformation, i.e.

$$\varepsilon = \varepsilon_e + \varepsilon_p + \varepsilon_c \ . \tag{1.10}$$

Table 1.1
Mechanical properties of structural materials and fibers.

Material	Ultimate tensile stress, $\bar{\sigma}$ (MPa)	Modulus, E (GPa)	Specific gravity	Maximum specific strength, $k_\sigma \times 10^3$ (m)	Maximum specific modulus, $k_E \times 10^3$ (m)
Metal alloys					
Steel	770–2200	180–210	7.8–7.85	28.8	2750
Aluminum	260–700	69–72	2.7–2.85	26.5	2670
Titanium	1000–1200	110	4.5	26.7	2440
Magnesium	260	40	1.8	14.4	2220
Beryllium	620	320	1.85	33.5	17300
Nickel	400–500	200	8.9	5.6	2250
Metal wires (diameter, μm)					
Steel (20–1500)	1500–4400	180–200	7.8	56.4	2560
Aluminum (150)	290	69	2.7	10.7	2550
Titanium (100–800)	1400–1500	120	4.5	33.3	2670
Beryllium (50–500)	1100–1450	240–310	1.8–1.85	80.5	17200
Tungsten (20–50)	3300–4000	410	19–19.3	21.1	2160
Molybdenum (25–250)	1800–2200	360	10.2	21.5	3500
Thermoset polymeric resins					
Epoxy	60–90	2.4–4.2	1.2–1.3	7.5	350
Polyester	30–70	2.8–3.8	1.2–1.35	5.8	310
Phenol-formaldehyde	40–70	7–11	1.2–1.3	5.8	910
Organosilicone	25–50	6.8–10	1.35–1.4	3.7	740
Polyimide	55–110	3.2	1.3–1.43	8.5	240
Bismaleimide	80	4.2	1.2	6.7	350
Thermoplastic polymers					
Polyethylene	20–45	6–8.5	0.95	4.7	890
Polystyrene	35–45	30	1.05	4.3	2860
Teflon	15–35	3.5	2.3	1.5	150
Nylon	80	2.8	1.14	7.0	240
Polyester (PC)	60	2.5	1.32	4.5	190
Polysulfone (PSU)	70	2.7	1.24	5.6	220
Polyamide–imide (PAI)	90–190	2.8–4.4	1.42	13.4	360
Polyetheretherketone (PEEK)	90–100	3.1–3.8	1.3	7.7	300
Polyphenylenesulfide (PPS)	80	3.5	1.36	5.9	250
Synthetic fibers					
Capron	680–780	4.4	1.1	70	400
Dacron	390–880	4.9–15.7	1.4	60	1430
Teflon	340–440	2.9	2.3	190	130
Nitron	390–880	4.9–8.8	1.2	70	730
Polypropylene	730–930	4.4	0.9	100	480
Viscose	930	20	1.52	60	1300
Fibers for advanced composites (diameter, μm)					
Glass (3–19)	3100–5000	72–95	2.4–2.6	200	3960
Quartz (10)	6000	74	2.2	270	3360
Basalt (9–13)	3000–3500	90	2.7–3.0	130	3300
Aramid (12–15)	3500–5500	140–180	1.4–1.47	390	12800

Table 1.1 (Contd.)

Material	Ultimate tensile stress, $\bar{\sigma}$ (*MPa*)	Modulus E (GPa)	Specific gravity	Maximum specific strength, $k_\sigma \times 10^3$ (m)	Maximum specific modulus, $k_E \times 10^3$ (m)
Polyethylene (20–40)	2600–3300	120–170	0.97	310	17500
Carbon (5–11)					
High-strength	7000	300	1.75	400	17100
High-modulus	2700	850	1.78	150	47700
Boron (100–200)	2500–3700	390–420	2.5–2.6	150	16800
Alumina – Al_2O_3 (20–500)	2400–4100	470–530	3.96	100	13300
Silicon Carbide – SiC (10–15)	2700	185	2.4–2.7	110	7700
Titanium Carbide – TiC (280)	1500	450	4.9	30	9100
Boron Carbide – B_4C (50)	2100–2500	480	2.5	100	10000
Boron Nitride – BN (7)	1400	90	1.9	70	4700

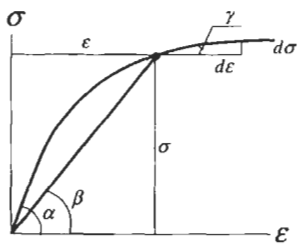

Fig. 1.4. Introduction of secant and tangent moduli.

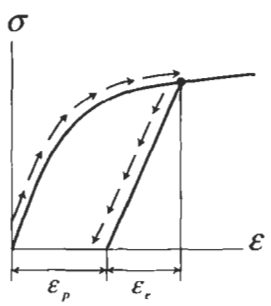

Fig. 1.5. Stress–strain diagram for elastic–plastic material.

However, in application to particular problems, this model can be usually substantially simplified. To show this, consider the bar in Fig. 1.1 and assume that force F is applied at the moment $t=0$ and is taken off at moment $t=t_1$ as shown in Fig. 1.6(a). At the moment $t=0$, elastic and plastic strains that do not depend on time appear, and while time is running, the creep strain is developed. At

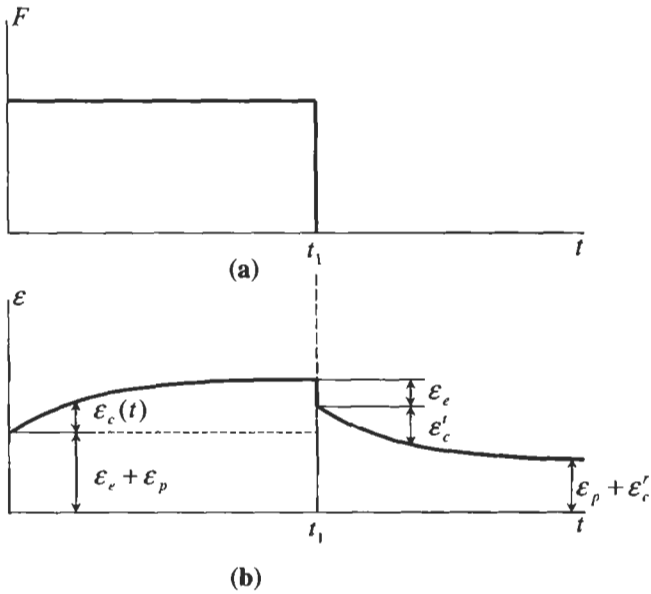

Fig. 1.6. Dependence of force (a) and strain (b) on time.

the moment $t = t_1$ elastic strain disappears, while reversible part of the creep strain, ε_c^l, disappears in time. Residual strain consists of the plastic strain, ε_p, and residual part of the creep strain, ε_c^r.

Now assume that $\varepsilon_p \ll \varepsilon_c$ which means that either material is elastic or the applied load does not induce high stress and, hence, plastic strain. Then we can neglect ε_p in Eq. (1.10) and simplify the model. Furthermore let $\varepsilon_c \ll \varepsilon_e$ which in turn means that either material is not susceptible to creep or the force acts for a short time (t_1 is close to zero). Thus we arrive at the simplest elastic model which is the case for the majority of practical applications. It is important that the proper choice of the material model depends not only on the material nature and properties but also on the operational conditions of the structure. For example, a shell-type structure made of aramid–epoxy composite material, that is susceptible to creep, and designed to withstand the internal gas pressure should be analyzed with due regard to the creep if this structure is a pressure vessel for long term gas storage. At the same time for a solid propellant rocket motor case working for seconds, the creep strain can be ignored.

A very important feature of material models under consideration is their phenomenological nature. This means that these models ignore the actual material microstructure (e.g., crystalline structure of metals or molecular structure of polymers) and represent the material as some uniform continuum possessing some effective properties that are the same irrespective of how small the material volume is. This allows us, first, to determine material properties testing material samples (as in Fig. 1.1). Second, this formally enables us to apply methods of Mechanics of

Solids that deal with equations derived for infinitesimal volumes of material. And third, this allows us to simplify the strength and stiffness evaluation problem and to reduce it to a reasonable practical level not going into analysis of the actual mechanisms of material deformation and fracture.

1.2. Composite materials

This book is devoted to composite materials that emerged in the middle of the 20th century as a promising class of engineering materials providing new prospects for modern technology. Generally speaking any material consisting of two or more components with different properties and distinct boundaries between the components can be referred to as a composite material. Moreover, the idea of combining several components to produce a material with properties that are not attainable with the individual components has been used by man for thousands of years. Correspondingly, the majority of natural materials that have emerged as a result of a prolonged evolution process can be treated as composite materials.

With respect to the problems covered in this book we can classify existing composite materials (composites) into two main groups.

The first group comprises composites that are known as "filled materials". The main feature of these materials is the existence of some basic or matrix material whose properties are improved by filling it with some particles. Usually the matrix volume fraction is more than 50% in such materials, and material properties, being naturally modified by the fillers, are governed mainly by the matrix. As a rule, filled materials can be treated as homogeneous and isotropic, i.e., traditional models of Mechanics of Materials developed for metals and other conventional materials can be used to describe their behavior. This group of composites is not touched on in the book.

The second group of composite materials that is under study here involves composites that are called "reinforced materials". The basic components of these materials (sometimes referred to as "advanced composites") are long and thin fibers possessing high strength and stiffness. The fibers are bound with a matrix material whose volume fraction in a composite is usually less than 50%. The main properties of advanced composites due to which these materials find a wide application in engineering are governed by fibers whose types and characteristics are considered below.

The following sections provide a concise description of typical matrix materials and fiber-matrix compositions. Two comments should be made with respect to the data presented in those sections. First, only a brief information concerning material properties that are essential for the problems covered in this book is presented there, and, second, the given data are of a broad nature and are not expected to be used in design or analysis of particular composite structures. More complete description of composite materials and their components including the history of development and advancement, chemical compositions, physical characteristics, manufacturing, and applications can be found elsewhere (Peters, 1998).

1.2.1. Fibers for advanced composites

Continuous glass fibers (the first type of fibers used in advanced composites) are made by pulling molten glass (at a temperature about 1300°C) through 0.8–3.0 mm diameter dies and further high-speed stretching to a diameter of 3–19 μm. Usually glass fibers have solid circular cross sections. However there exist fibers with rectangular (square or plane), triangular, and hexagonal cross sections, as well as hollow circular fibers. Typical mechanical characteristics and density of glass fibers are listed in Table 1.1, while typical stress–strain diagram is shown in Fig. 1.7.

Important properties of glass fibers as components of advanced composites for engineering applications are their high strength which is maintained in humid environments but degrades under elevated temperatures (see Fig. 1.8), relatively low stiffness (about 40% of the stiffness of steel), high chemical and biological resistance, and low cost. Being actually elements of monolithic glass, the fibers do not absorb water and change their dimensions in water. For the same reason, they are brittle and sensitive to surface damage.

Quartz fibers are similar to glass fibers and are obtained by high-speed stretching of quartz rods made of (under temperature of about 2200°C) fused quartz crystals or sand. Original process developed for manufacturing of glass fibers cannot be used

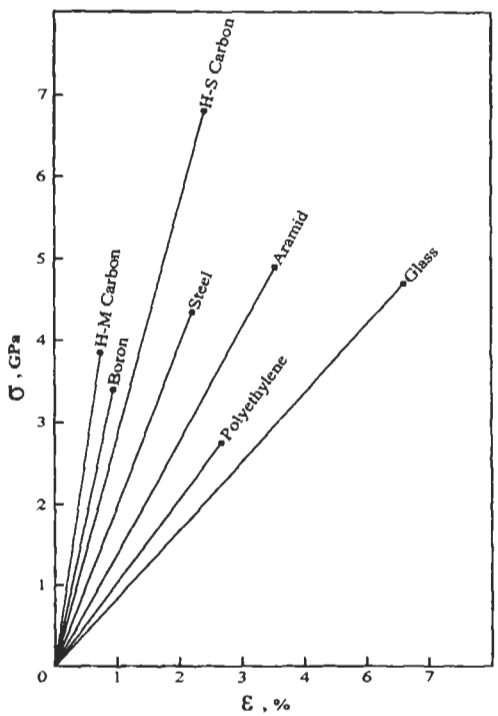

Fig. 1.7. Stress–strain diagrams for typical fibers of advanced composites.

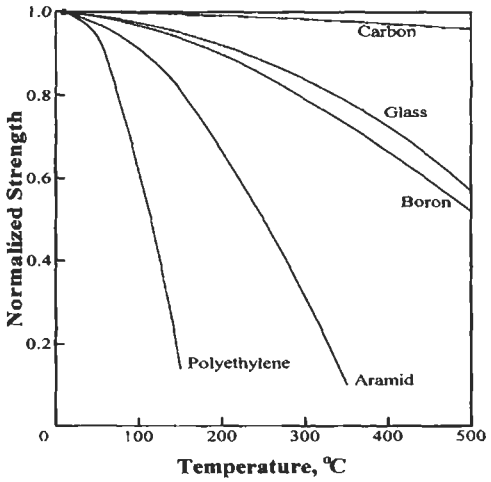

Fig. 1.8. Temperature degradation of fiber strength normalized by the strength at 20°C.

because viscosity of molten quartz is too high to make thin fibers directly. However, more complicated process results in fibers with higher thermal resistance than glass fibers.

The same process that is used for glass fibers can be employed to manufacture mineral fibers, e.g., basalt fibers made of molten basalt rocks. Having relatively low strength and high density (see Table 1.1) basalt fibers are not used for high-performance, e.g. aerospace structures, but are promising reinforcing elements for pre-stressed reinforced concrete structures in civil engineering.

Development of carbon (or graphite) fibers was a natural step aiming at a rise of fiber's stiffness the proper level of which was not exhibited by glass fibers. Modern high-modulus carbon fibers demonstrate modulus that is by the factor of about four higher than the modulus of steel, while the fiber density is by the same factor lower. Though first carbon fibers had lower strength than glass fibers, modern high-strength fibers demonstrate tensile strength that is 40% higher than the strength of the best glass fibers, while the density of carbon fibers is 30% less.

Carbon fibers are made by pyrolysis of organic fibers depending on which there exist two main types of carbon fibers – PAN-based and pitch-based fibers. For PAN-based fibers the process consists of three stages – stabilization, carbonization, and graphitization. In the first step (stabilization) a system of polyacrylonitrile (PAN) filaments is stretched and heated up to about 400°C in the oxidation furnace, while in the subsequent step (carbonization under 900°C in an inert gas media) most elements of the filaments other than carbon are removed or converted into carbon. During the successive heat treatment at temperature reaching 2800°C (graphitization) crystalline carbon structure oriented along the fibers length is formed resulting in PAN-based carbon fibers. The same process is used for rayon organic filaments (instead of PAN), but results in carbon fibers with lower characteristics because rayon contains less carbon than PAN. For pitch-based carbon fibers, initial organic

filaments are made in approximately the same manner as for glass fibers from molten petroleum or coal pitch and pass through carbonization and graphitization processes. Because pyrolysis is accompanied with a loss of material, carbon fibers have a porous structure and their specific gravity (about 1.8) is less than that of graphite (2.26). The properties of carbon fibers are affected with the crystallite size, crystalline orientation, porosity and purity of carbon structure.

Typical stress–strain diagrams for high-modulus (HM) and high-strength (HS) carbon fibers are plotted in Fig. 1.7. As components of advanced composites for engineering applications, carbon fibers are characterized with very high modulus and strength, high chemical and biological resistance, electric conductivity and very low coefficient of thermal expansion. Strength of carbon fibers practically does not decrease under temperature elevated up to 1500°C (in the inert media preventing oxidation of fibers).

The exceptional strength of 7.06 GPa is reached in Toray T-1000 carbon fibers, while the highest modulus of 850 GPa is obtained in Carbonic HM-85 fibers. Carbon fibers are anisotropic, very brittle, and sensitive to damage. They do not absorb water and change their dimensions in humid environments.

There exist more than 50 types of carbon fibers with a broad spectrum of strength, stiffness and cost, and the process of fiber advancement is not over – one may expect fibers with strength up to 10 GPa and modulus up to 1000 GPa within a few years.

Organic fibers commonly encountered in textile applications can be employed as reinforcing elements of advanced composites. Naturally, only high performance fibers, i.e. fibers possessing high stiffness and strength, can be used for this purpose. The most widely used organic fibers that satisfy these requirements are known as aramid (aromatic polyamide) fibers. They are extruded from a liquid crystalline solution of the corresponding polymer in sulfuric acid with subsequent washing in a cold water bath and stretching under heating. Properties of typical aramid fibers are listed in Table 1.1, and the corresponding stress–strain diagram is presented in Fig. 1.7. As components of advanced composites for engineering applications, aramid fibers are characterized with low density providing high specific strength and stiffness, low thermal conductivity resulting in high heat insulation, and negative thermal expansion coefficient allowing us to construct hybrid composite elements that do not change their dimensions under heating. Consisting actually of a system of very thin filaments (fibrils), aramid fibers have very high resistance to damage. Their high strength in longitudinal direction is accompanied with relatively low strength under tension in transverse direction. Aramid fibers are characterized with pronounced temperature (see Fig. 1.8) and time dependence for stiffness and strength. Unlike inorganic fibers discussed above, they absorb water resulting in moisture content up to 7% and degradation of material properties by 15–20%.

The list of organic fibers was supplemented recently with extended chain polyethylene fibers demonstrating outstanding low density (less than that of water) in conjunctions with relatively high stiffness and strength (see Table 1.1 and Fig. 1.7). Polyethylene fibers are extruded from the corresponding polymer melt in

approximately the same way as for glass fibers. They do not absorb water and have high chemical resistance, but demonstrate relatively low temperature and creep resistance (see Fig. 1.8).

Boron fibers were developed to increase the stiffness of composite materials while glass fibers were mainly used to reinforce composites of the day. Being followed by high-modulus carbon fibers with higher stiffness and lower cost, boron fibers have now rather limited application. Boron fibers are manufactured by chemical vapor deposition of boron onto about 12 μm diameter tungsten or carbon fiber (core). Because of this technology, boron fibers have relatively large diameter, 100–200 μm. They are extremely brittle and sensitive to surface damage. Mechanical properties of boron fibers are presented in Table 1.1 and Figs. 1.7 and 1.8. Being mainly used in metal matrix composites, boron fibers degrade under the action of aluminum or titanium matrices at the temperature that is necessary for processing (above 500°C). To prevent this degradation, chemical vapor deposition is used to cover the fiber surface with about 5 μm thick layer of silicon carbide, SiC, (such fibers are called Borsic) or boron carbide, B_4C.

There exists a special class of ceramic fibers for high-temperature applications composed of various combinations of silicon, carbon, nitrogen, aluminum, boron, and titanium. The most commonly encountered are silicon carbide (SiC) and alumina (Al_2O_3) fibers.

Silicon carbide is deposited on a tungsten or carbon core-fibre by the reaction of a gas mixture of silanes and hydrogen. Thin (8–15 μm in diameter) SiC fibers can be made by pyrolysis of polymeric (polycarbosilane) fibers under temperature of about 1400°C in an inert atmosphere. Silicon carbide fibers have high strength and stiffness, moderate density (see Table 1.1) and very high melting temperature (2600°C).

Alumina (Al_2O_3) fibers are fabricated by sintering of fibers extruded from the viscous alumina slurry with rather complicated composition. Alumina fibers, possessing approximately the same mechanical properties as of SiC fibers have relatively large diameter and high density. The melting temperature is about 2000°C.

Silicon carbide and alumina fibers are characterized with relatively low reduction of strength under high temperature (see Fig. 1.9).

Promising ceramic fibers for high-temperature applications are boron carbide (B_4C) fibers that can be obtained either as a result of reaction of a carbon fiber with a mixture of hydrogen and boron chloride under high temperature (around 1800°C) or by pyrolysis of cellulosic fibers soaked with boric acid solution. Possessing high stiffness and strength and moderate density (see Table 1.1) boron carbide fibers have very high thermal resistance (up to 2300°C).

Metal fibers (thin wires) made of steel, beryllium, titanium, tungsten, and molybdenum are used for special, e.g., low-temperature and high-temperature applications. Characteristics of metal fibers are presented in Table 1.1 and Figs. 1.7 and 1.9.

In advanced composites, fibers provide not only high strength and stiffness but also a possibility to tailor the material so that directional dependence of its

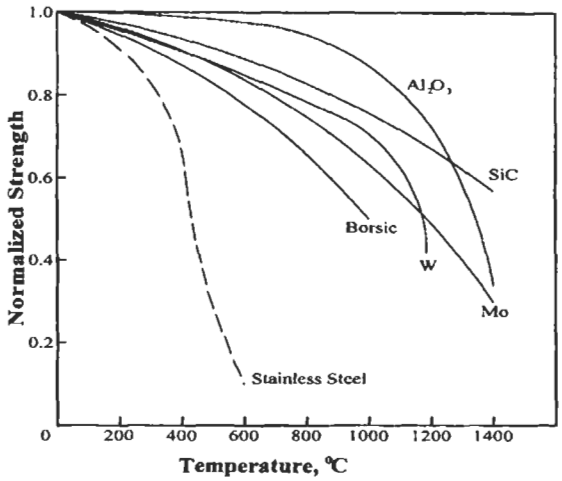

Fig. 1.9. Temperature dependence of high-temperature fibers normalized strength (in comparison with stainless steel).

mechanical properties matches that of the loading environment. The principle of directional properties can be traced in all natural materials that have emerged as a result of a prolonged evolution and, in contrast to man-made metal alloys, are neither isotropic nor homogeneous. Many natural materials have fibrous structures and utilize high strength and stiffness of natural fibers listed in Table 1.2. As can be seen (Tables 1.1 and 1.2), natural fibers, having lower strength and stiffness than man-made fibers, can compete with modern metals and plastics.

Table 1.2
Mechanical properties of natural fibers.

Fiber	Diameter (μm)	Ultimate tensile stress, $\bar{\sigma}$ (MPa)	Modulus, E (GPa)	Specific gravity
Wood	15–20	160	23	1.5
Bamboo	15–30	550	36	0.8
Jute	10–50	580	22	1.5
Cotton	15–40	540	28	1.5
Wool	75	170	5.9	1.32
Coir	10–20	250	5.5	1.5
Bagasse	25	180	9	1.25
Rice	5–15	100	6	1.24
Natural silk	15	400	13	1.35
Spider silk	4	1750	12.7	–
Linen	–	270	–	–
Sisal	–	560	–	–
Asbestos	0.2	1700	160	2.5

Before being used as reinforcing elements of advanced composites, the fibers are subjected to special finish surface treatments undertaken to prevent the fiber damage under contact with processing equipment, to provide surface wetting when fibers are combined with matrix materials, and to improve the interface bond between fibers and matrices. The most commonly encountered surface treatments are chemical sizing performed during the basic fiber formation operation and resulting in a thin layer applied to the surface of the fiber, surface etching by acid, plasma or corona discharge, and coating of fiber surface with thin metal or ceramic layers.

With only a few exceptions (e.g., metal fibers), individual fibers, being very thin and sensitive to damage, are not used in composite manufacturing directly, but in the form of tows (rovings), yarns, and fabrics.

A unidirectional tow (roving) is a loose assemblage of parallel fibers consisting usually of thousands of elementary fibers. Two main designations are used to indicate the size of the tow, namely the *K*-number that gives the number of fibers in the tow (e.g., 3*K* tow contains 3000 fibers) and the tex-number which is the mass in grams of 1000 m of the tow. The tow tex-number depends not only on the number of fibers but also on the fiber diameter and density. For example, AS4-6*K* tow consisting of 6000 AS4 carbon fibers has 430 tex.

A yarn is a fine tow (usually it includes hundreds of fibers) slightly twisted (about 40 turns per meter) to provide the integrity of its structure necessary for textile processing. Yarn size is indicated in tex-numbers or in textile denier-numbers (den) such that 1tex = 9den. Continuous yarns are used to make fabrics with various weave patterns. There exist a wide variety of glass, carbon, aramid, and hybrid fabrics whose nomenclature, structure, and properties are described elsewhere (Peters, 1998; Chou and Ko, 1989; Tarnopol'skii et al., 1992; Bogdanovich and Pastore, 1996).

An important characteristic of fibers is their processability that can be evaluated as the ratio, $K_p = \bar{\sigma}_S/\bar{\sigma}$, of the strength demonstrated by fibers in the composite structure, $\bar{\sigma}_S$, to the strength of fibers before they were processed, $\bar{\sigma}$. This ratio depends on fibers' ultimate elongation, sensitivity to damage, and manufacturing equipment causing the damage of fibers. The most sensitive to operational damage are boron and high-modulus carbon fibers possessing relatively low ultimate elongation $\bar{\varepsilon}$ (less than 1%, see Fig. 1.7). For example, for filament wound pressure vessels, $K_p = 0.96$ for glass fibers, while for carbon fibers, $K_p = 0.86$.

To evaluate fiber processability under real manufacturing conditions, three simple tests are used – tension of a straight dry tow, tension of tows with loops, and tension of a tow with a knot (see Fig. 1.10). Similar tests are used to determine the strength of individual fibers (Fukuda et al., 1997). For carbon tows, normalized strength obtained in these tests is presented in Table 1.3 (for proper comparison, the tows should be of the same size). As follows from the Table, the tow processability depends on the fiber ultimate strain (elongation). The best processability is observed for aramid tows whose fibers have high elongation and low sensitivity to damage (they are not monolithic and consist of thin fibrils).

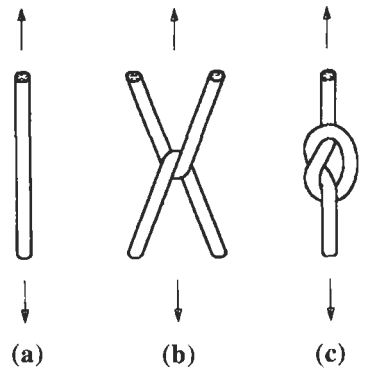

Fig. 1.10. Testing of a straight tow (a), tows with a loop (b), and tow with a knot (c).

Table 1.3
Normalized strength of carbon tows.

Ultimate strain, $\bar{\varepsilon}$ (%)	Normalized strength		
	Straight tow	Tow with a loop	Tow with a knot
0.75	1	0.25	0.15
1.80	1	0.53	0.18

1.2.2. Matrix materials

To utilize high strength and stiffness of fibers in a monolithic composite material suitable for engineering applications, fibers are bound with a matrix material whose strength and stiffness are, naturally, much lower than those of fibers (otherwise, no fibers would be necessary). Matrix materials provide the final shape of the composite structure and govern the parameters of the manufacturing process. Optimal combination of fiber and matrix properties should satisfy a set of operational and manufacturing requirements that sometimes are of a contradictory nature and have not been completely met yet in existing composites.

First of all, the stiffness of the matrix should correspond to the stiffness of the fibers and be sufficient to provide uniform loading of fibers. The fibers are usually characterized with relatively high scatter of strength that could be increasing due to the damage of the fibers caused by the processing equipment. Naturally, fracture of the weakest or damaged fiber should not result in material failure. Instead, the matrix should evenly redistribute the load from the broken fiber to the adjacent ones and then load the broken fiber at a distance from the cross-section at which it failed. The higher is the matrix stiffness, the smaller is this distance, and the less is the influence of damaged fibers on material strength and stiffness (which should be the case). Moreover, the matrix should provide the proper stress diffusion (this is the

term traditionally used for this phenomenon in analysis of stiffened structures (Goodey, 1946)) in the material under given operational temperature. That is why this temperature is limited, as a rule, by the matrix rather than by the fibers. But on the other hand, to provide material integrity up to the failure of the fibers, the matrix material should possess high compliance. Obviously, for a linear elastic material (see Fig. 1.3), combination of high stiffness and high ultimate strain $\bar{\varepsilon}$ results in high strength which is not the case for modern matrix materials. Thus, close to optimal (with respect to the foregoing requirements) and realistic matrix material should have nonlinear stress–strain diagram (of the type shown in Fig. 1.5) and possess high initial modulus of elasticity and high ultimate strain.

However, matrix properties, even being optimal for the corresponding fibers, do not demonstrate themselves in the composite material if the adhesion (the strength of fiber–matrix interface bonding) is not high enough. High adhesion between fibers and matrices providing material integrity up to the failure of the fibers is a necessary condition for high-performance composites. Proper adhesion can be reached for properly selected combinations of fiber and matrix materials under some additional conditions. First, a liquid matrix should have viscosity low enough to allow the matrix to penetrate between the fibers of such dense systems of fibers as tows, yarns, and fabrics. Second, the fiber surface should have good wetability with the matrix. Third, the matrix viscosity should be high enough to retain the liquid matrix in the impregnated tow, yarn or fabric in the process of fabrication of a composite part. And finally, the manufacturing process providing the proper quality of the resulting material should not require high temperature and pressure to make a composite part.

By now, typical matrices are made from polymeric, metal, carbon, and ceramic materials.

Polymeric matrices are divided into two main types, thermoset and thermoplastic. Thermoset polymers which are the most widely used matrix materials for advanced composites include polyester, epoxy, polyimide and other resins (see Table 1.1) cured under elevated or room temperature. A typical stress–strain diagram for a cured epoxy resin is shown in Fig. 1.11. Being cured (polymerized) a thermoset

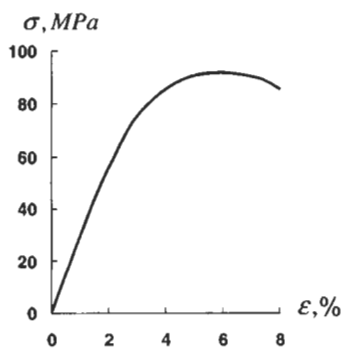

Fig. 1.11. Stress–strain diagram for a typical cured epoxy matrix.

matrix cannot be reset, dissolved or melted. Heating of a thermoset material results first in degradation of its strength and stiffness and then in thermal destruction.

In contrast to thermoset resins, thermoplastic matrices (PSU, PEEK, PPS and others – see Table 1.1) do not require any curing reaction. They melt under heating and convert to a solid state under cooling. Possibility to re-melt and dissolve thermoplastic matrices allows us to reshape composite parts forming them under heating and simplifies their recycling which is a problem for thermoset materials.

Polymeric matrices being combined with glass, carbon, organic, and boron fibers yield a wide class of polymeric composites with high strength and stiffness, low density, high fatigue resistance, and excellent chemical resistance. The main disadvantage of these materials is their relatively low (in comparison with metals) temperature resistance limited by the matrix. The so-called thermo-mechanical curves are plotted to determine this important (for applications) characteristic of the matrix. These curves, presented for typical epoxy resins in Fig. 1.12, show the dependence of some stiffness parameter on the temperature and allow us to find the so-called glass transition temperature, T_g, which indicates dramatic reduction of material stiffness. There exist several methods to obtain material thermo-mechanical diagram. The one used to plot the curves presented in Fig. 1.12 involves compression tests of heated polymeric discs. Naturally, to retain the complete set of properties of polymeric composites, the operating temperature, in general, should not exceed T_g. However, actual material behavior depends on the type of loading. As follows from Fig. 1.13, heating above the glass transition temperature only slightly influences material properties under tension in the fiber direction and dramatically reduces strength in longitudinal compression and transverse bending. Glass transition temperature depends on the processing temperature, T_p, under which material is fabricated, and higher T_p results, as a rule, in higher T_g. Thermoset epoxy matrices cured under 120–160°C have $T_g = 60$–140°C. There also

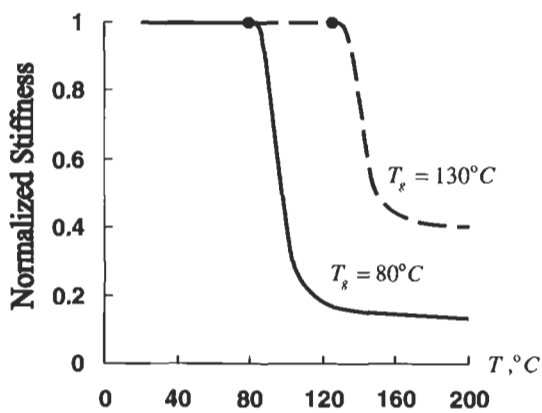

Fig. 1.12. Typical thermo-mechanical diagrams for cured epoxy resins with glass transition temperatures 80°C (———) and 130°C (– – – –).

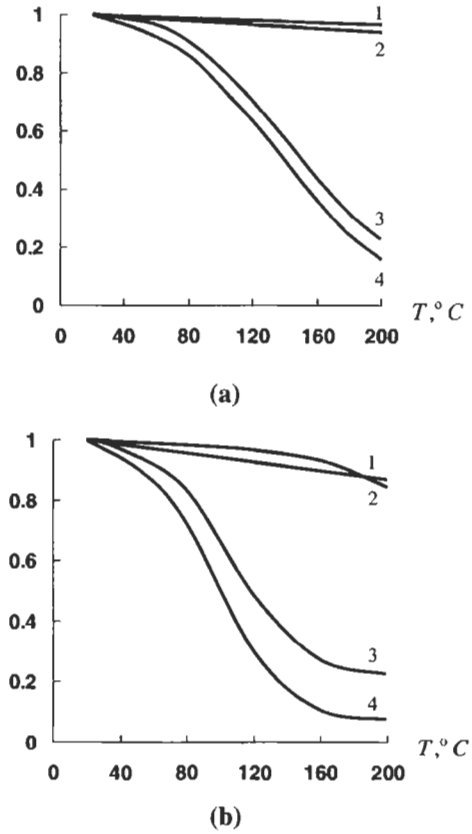

Fig. 1.13. Dependence of normalized longitudinal moduli (1), strength under longitudinal tension (2), bending (3), and compression (4) on temperature for unidirectional carbon composites with epoxy matrices having $T_g = 130°C$ (a) and $T_g = 80°C$ (b).

exist a number of high temperature thermoset matrices (e.g., organosilicone, polyimide, and bismaleimide resins) with $T_g = 250–300°C$ and curing temperatures up to 400°C. Thermoplastic matrices are also characterized with a wide range of glass transition temperatures – from 90°C for PPS and 140°C for PEEK to 190°C for PSU and 270°C for PAI (see Table 1.1 for abbreviations). Processing temperature for different thermoplastic matrices varies from 300°C to 400°C.

Further enhancement in temperature resistance of composite materials is associated with application of metal matrices in combination with high temperature boron, carbon, ceramic fibers and metal wires. The most widespread metal matrices are aluminum, magnesium, and titanium alloys possessing high plasticity (see Fig. 1.14), while for special applications nickel, copper, niobium, cobalt, and lead matrices can be used. Fiber reinforcement essentially improves mechanical properties of metals. For example, carbon fibers increase strength and stiffness of such a soft metal as lead by an order.

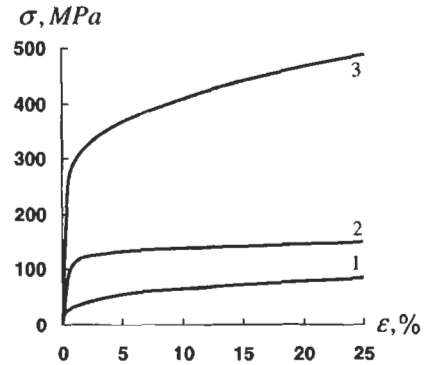

Fig. 1.14. Typical stress–strain curves for aluminum (1), magnesium (2), and titanium (3) matrices.

As noted above, metal matrices allow us to increase operational temperatures for composite structures. Dependencies of longitudinal strength and stiffness of boron-aluminum unidirectional composite material on temperature corresponding to experimental results that can be found in Karpinos (1985) and Vasiliev and Tarnopol'skii (1990) are shown in Fig. 1.15. Naturally, higher temperature resistance requires higher processing temperature, T_p. Indeed, aluminum matrix composite materials are processed under $T_p = 500°C$, while for magnesium, titanium, and nickel matrices this temperature is about 800°C, 1000°C, and 1200°C, respectively. Some processes require also rather high pressure (up to 150 MPa).

In polymeric composites, matrix materials play important but secondary role of holding the fibers in place and providing proper load dispersion in the fibers, while material strength and stiffness are controlled by the reinforcements. By contrast, mechanical properties of metal matrix composites are controlled by the matrix to a considerably larger extent, though fibers still provide the main contribution to strength and stiffness of the material.

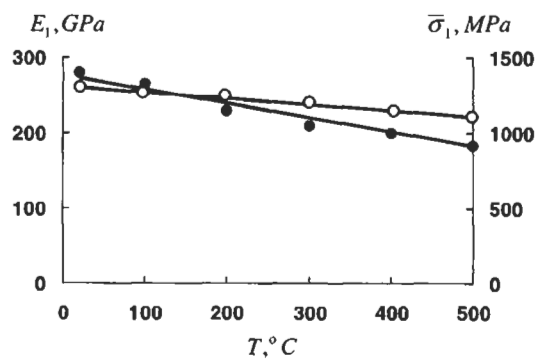

Fig. 1.15. Temperature dependence of tensile strength (•) and stiffness (○) along the fibers for unidirectional boron–aluminum composite.

The next step in the development of composite materials that can be treated as matrix materials reinforced with fibers rather than fibers bonded with matrix (which is the case for polymeric composites) is associated with ceramic matrix composites possessing very high thermal resistance. The stiffnesses of the fibers which are usually metal (steel, tungsten, molybdenum, niobium), carbon, boron, and ceramic (SiC, Al_2O_3) and the ceramic matrices (oxides, carbides, nitrides, borides, and silicides) are not very different, and the fibers do not carry the main fraction of the load in ceramic composites. The function of the fibers is to provide strength and mainly toughness (resistance to cracks) of the composite because non-reinforced ceramics is very brittle. Ceramic composites can operate under very high temperatures depending on the melting temperature of the matrix that varies from 1200°C to 3500°C. Naturally, the higher is this temperature the more complicated is the manufacturing process. The main shortcoming of ceramic composites is associated with a low ultimate tensile elongation of the ceramic matrix resulting in cracks appearing in the matrix under relatively low tensile stress applied to the material.

An outstanding combination of high mechanical characteristics and temperature resistance is demonstrated by carbon–carbon composites in which both components – fibers and matrix are made from one and the same material but with different structure. Carbon matrix is formed as a result of carbonization of an organic resin (phenolic and furfural resin or pitch) with which carbon fibers are impregnated, or of chemical vapor deposition of pyrolytic carbon from a hydrocarbon gas. In an inert atmosphere or in a vacuum, carbon–carbon composites can withstand very high temperatures (more than 3000°C). Moreover, their strength increases under heating up to 2200°C while modulus degrades under temperatures more than 1400°C. However in an oxygen atmosphere, they oxidize and sublime at relatively low temperatures (about 600°C). To use carbon–carbon composite parts in an oxidizing atmosphere, they must have protective coatings made usually from silicon carbide. Manufacturing of carbon–carbon parts is a very energy and time consuming process. To convert initial carbon–phenolic composite into carbon-carbon, it should pass thermal treatment at 250°C for 150 h, carbonization at about 800°C for about 100 h and several cycles of densification (one-stage pyrolysis results in high porosity of the material) each including impregnation with resin, curing, and carbonization. To refine material structure and to provide oxidation resistance, its further high-temperature graphitization at 2700°C and coating (at 1650°C) can be required.

Vapor deposition of pyrolytic carbon is also a time consuming process performed at 900–1200°C under pressure 150–2000 kPa.

1.2.3. Processing

Composite materials do not exist apart from composite structures and are formed while the structure is fabricated. Though a number of methods has been developed by now to manufacture composite structures, two basic processes during which material microstructure and macrostructure are formed are common for all of them.

Being a heterogeneous media, a composite material has two levels of heterogeneity. The first level represents a microheterogeneity induced by at least two phases (fibers and matrix) that form the material microstructure. At the second level the material is characterized with a macroheterogeneity caused by the laminated or more complicated macrostructure of the material which consists usually of a set of layers with different orientations.

The first basic process yielding material microstructure involves the application of a matrix material to fibers. The simplest way to do it used in the technology of composites with thermosetting polymeric matrices is a direct impregnation of tows, yarns, fabrics or more complicated fibrous structures with liquid resins. Thermosetting resin has relatively low viscosity (10–100 Pa s) which can be controlled with solvents or heating and good wetting ability for the majority of fibers. There exist two versions of this process. According to the so-called "wet" process, impregnated fibrous material (tows, fabrics, etc.) is used to fabricate composite parts directly, without any additional treatment or interruption of the process. In contrast to that, in "dry" or "prepreg" processes impregnated fibrous material is dried (not cured) and thus obtained preimpregnated tapes (prepregs) are stored for further utilization (usually under low temperature to prevent uncontrolled polymerization of the resin). Machine making prepregs is shown in Fig. 1.16. Both processes having mutual advantages and shortcomings are widely used for composites with thermosetting matrices.

For thermoplastic matrices, application of the direct impregnation ("wet" processing) is limited by relatively high viscosity (about 10^{12} Pa s) of thermoplastic polymer solutions or melts. For this reason, "prepreg" processes with preliminary fabricated tapes in which fibers are already combined with thermoplastic matrix are used to manufacture composite parts. There also exist other processes that involve application of heating and pressure to hybrid materials including reinforcing fibers and a thermoplastic polymer in the form of powder, films or fibers. A promising process (called fibrous technology) utilizes tows, tapes or fabrics with two types of fibers – reinforcing and thermoplastic. Under heating and pressure thermoplastic fibers melt and form the matrix of the composite material.

Metal and ceramic matrices are applied to fibers by means of casting, diffusion welding, chemical deposition, plasma spraying, processing by compression molding and with the aid of powder metallurgy methods.

The second basic process provides the proper macrostructure of a composite material corresponding to loading and operational conditions of the composite part that is fabricated. There exist three main types of material macrostructure – linear structure which is specific for bars, profiles and beams, plane laminated structure typical for thin-walled plates and shells, and spatial structure which is necessary for thick-walled and solid composite parts.

Linear structure is formed by pultrusion, table rolling or braiding and provides high strength and stiffness in one direction coinciding with the axis of a bar, profile or a beam. Pultrusion results in a unidirectionally reinforced composite profile made by pulling a bundle of fibers impregnated with resin through a heated die to cure the resin and, to provide the proper shape of the profile cross-section. Profiles made by

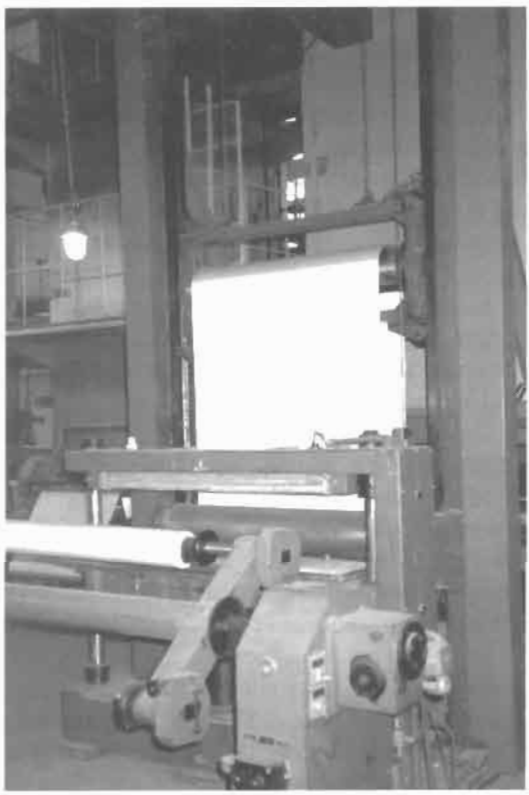

Fig. 1.16. Machine making a prepreg from fiberglass fabric and epoxy resin. Courtesy of CRISM.

pultrusion and braiding are shown in Fig. 1.17. Table rolling is used to fabricate small diameter tapered tubular bars (e.g., ski poles or fishing rods) by rolling preimpregnated fiber tapes in the form of flags around the metal mandrel which is pulled out of the composite bar after the resin is cured. Fibers in the flags are usually oriented along the bar axis or at an angle to the axis thus providing more

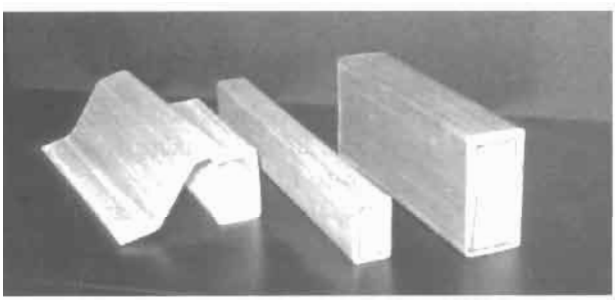

Fig. 1.17. Composite profiles made by pultrusion and braiding. Courtesy of CRISM.

complicated reinforcement than the unidirectional one typical for pultrusion. Even more complicated fiber placement with orientation angle varying from 5° to 85° along the bar axis can be achieved using two-dimensional (2D) braiding which results in a textile material structure consisting of two layers of yarns or tows interlaced with each other while they are wound onto the mandrel.

Plane laminated structure consists of a set of composite layers providing necessary stiffness and strength in at least two orthogonal directions in the plane of the laminate. Plane structure is formed by hand or machine lay-up, fiber placement and filament winding.

Lay-up and fiber placement technology provides fabrication of thin-walled composite parts of practically arbitrary shape by hand or automated placing of preimpregnated unidirectional or fabric tapes onto a mold. Layers with different fiber orientations (and even with different fibers) are combined to result in the laminated composite material exhibiting desirable strength and stiffness in given directions. Lay-up processes are usually accompanied by pressure applied to compact the material and to remove entrapped air. Depending on required quality of the material, as well as on the shape and dimensions of a manufactured composite part compacting pressure can be provided by rolling or vacuum bags, in autoclaves, and by compression molding. A catamaran yacht (length 9.2 m, width 6.8 m, tonnage 2.2 t) made from carbon–epoxy composite by hand lay-up is shown in Fig. 1.18.

Filament winding is an efficient automated process of placing impregnated tows or tapes onto a rotating mandrel (Fig. 1.19) that is removed after curing of the composite material. Varying the winding angle, it is possible to control material strength and stiffness within the layer and through the thickness of the laminate. Winding of a pressure vessel is shown in Fig. 1.20. Preliminary tension applied to the tows in the process of winding induces pressure between the layers providing compaction of the material. Filament winding is the most advantageous in manufacturing thin-walled shells of revolution though it can be used in building composite structures with more complicated shapes (Fig. 1.21).

Spatial macrostructure of the composite material that is specific for thick-walled and solid members requiring fiber reinforcement in at least three directions (not lying in one plane) can be formed by 3D braiding (with three interlaced yarns) or using such textile processes as weaving, knitting or stitching. Spatial (3D, 4D, etc.) structures used in carbon-carbon technology are assembled from thin carbon composite rods fixed in different directions. Such a structure that is prepared for carbonization and deposition of a carbon matrix is shown in Fig. 1.22.

There are two specific manufacturing procedures that have an inverse sequence of the basic processes described above, i.e., first, the macrostructure of the material is formed and then the matrix is applied to fibers.

The first of these procedures is the aforementioned carbon–carbon technology that involves chemical vapor deposition of a pyrolytic carbon matrix on preliminary assembled and sometimes rather complicated structures made from dry carbon fabric. A carbon–carbon shell made by this method is shown in Fig. 1.23.

Fig. 1.18. Catamaran yacht Ivan-30 made from carbon epoxy composite by hand lay-up. Courtesy of CRISM.

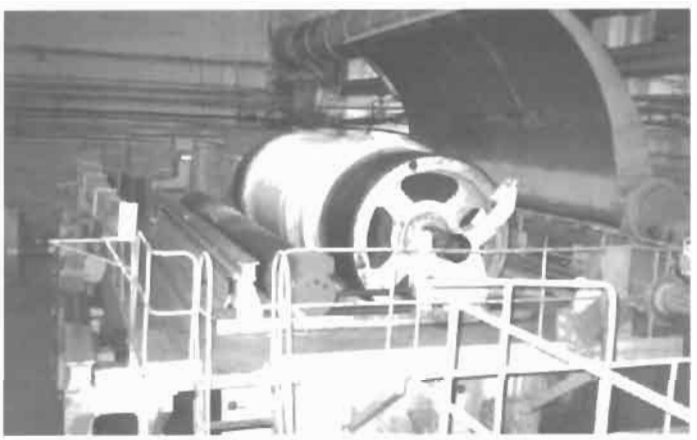

Fig. 1.19. Manufacturing of a pipe by circumferential winding of preimpregnated fiberglass fabric. Courtesy of CRISM.

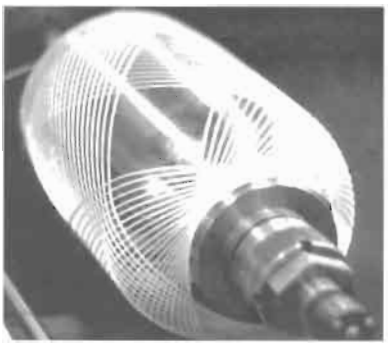

Fig. 1.20. Geodesic winding of a pressure vessel.

Fig. 1.21. A body of a small plane made by filament winding. Courtesy of CRISM.

Fig. 1.22. A 4D spatial structure. Courtesy of CRISM.

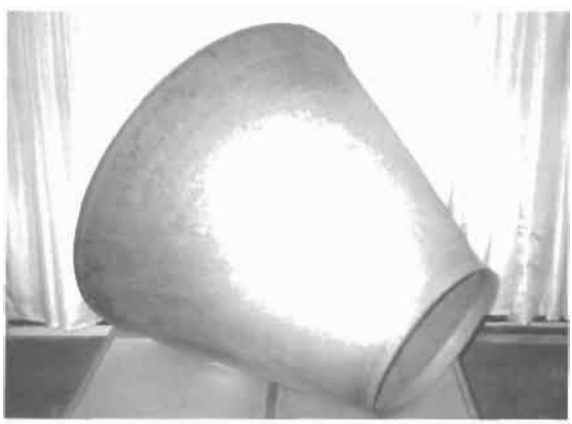

Fig. 1.23. A carbon–carbon conical shell. Courtesy of CRISM.

In more details the fabrication processes are described elsewhere (Peters, 1998).

1.3. References

Bogdanovich, A.E. and Pastore, C.M. (1996). *Mechanics of Textile and Laminated Composites*. Chapman & Hall, London.

Chou, T.W. and Ko, F.K. (1989). *Textile Structural Composites* (T.W. Chou and F.K. Ko eds.). Elsevier, New York.

Fukuda, H., Yakushiji, M. and Wada, A. (1997). Loop test for the strength of monofilaments. In *Proc. 11th Int. Conf. on Comp. Mat. (ICCM-11), Vol. 5: Textile Composites and Characterization* (M.L. Scott ed.). Woodhead Publishing Ltd., Gold Cost, Australia, pp. 886-892.

Goodey, W.J. (1946). *Stress Diffusion Problems. Aircraft Eng.* June, 195–198; July, 227–234; August, 271–276; September, 313–316; October, 343–346; November, 385–389.

Karpinos, D.M. (1985). *Composite Materials. Handbook* (D.M. Karpinos ed.). Naukova Dumka, Kiev (in Russian).

Peters, S.T. (1998). *Handbook of Composites*, 2nd edn. (S.T. Peters ed.). Chapman & Hall, London.

Tarnopol'skii, Yu.M., Zhigun, I.G. and Polyakov, V.A. (1992). *Spatially Reinforced Composites*, Technomic, Pennsylvania.

Vasiliev, V.V. and Tarnopol'skii, Yu.M. (1990). *Composite Materials, Handbook* (V.V. Vasiliev and Yu. M. Tarnopol'skii eds.). Mashinostroenie, Moscow (in Russian).

Chapter 2

FUNDAMENTALS OF MECHANICS OF SOLIDS

Behavior of composite materials whose micro- and macro-structures are much more complicated than those of traditional structural materials such as metals, concrete, and plastics is nevertheless governed by the same general laws and principles of mechanics whose brief description is given below.

2.1. Stresses

Consider a solid body referred to Cartesian coordinates as in Fig. 2.1. The body is fixed at the part S_u of the surface and loaded with body forces q_v having coordinate components q_x, q_y, and q_z, and with surface tractions p_s specified by coordinate components p_x, p_y, and p_z. Surface tractions act on surface S_σ which is determined by its unit normal n with coordinate components l_x, l_y, and l_z that can be referred to as directional cosines of the normal, i.e.,

$$l_x = \cos(n,x), \quad l_y = \cos(n,y), \quad l_z = \cos(n,z) \ . \tag{2.1}$$

Introduce some arbitrary cross-section formally separating the upper part of the body from its lower part. Assume that the interaction of these parts in the vicinity of some point A can be simulated with some internal force per unit area or stress σ distributed over this cross-section according to some unknown yet law. Because the Mechanics of Solids is a phenomenological theory (see the closure of Section 1.1) we do not care about the physical nature of stress, which is only a parameter of our model of the real material (see Section 1.1) and, in contrast to forces F, has never been observed in physical experiments. Stress is referred to the plane on which it acts and is usually decomposed into three components – normal stress (σ_z in Fig. 2.1) and shear stresses (τ_{zx} and τ_{zy} in Fig. 2.1). Subscript of the normal stress and the first subscript of the shear stress indicate the plane on which the stresses act. For stresses shown in Fig. 2.1, this is the plane whose normal is parallel to axis-z. The second subscript of the shear stress shows the axis along which the stress acts. If we single out a cubic element in the vicinity of point A (see Fig. 2.1), we should apply stresses to all its planes as in Fig. 2.2 which also shows notations and positive directions of all the stresses acting inside the body referred to Cartesian coordinates.

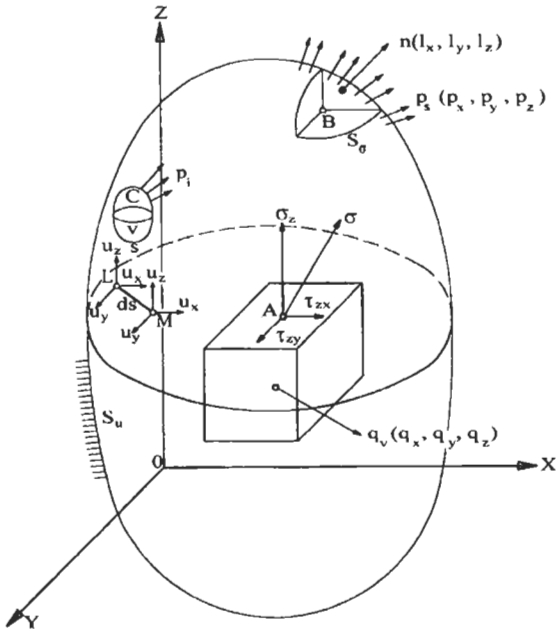

Fig. 2.1. A solid loaded with body and surface forces and referred to Cartesian coordinates.

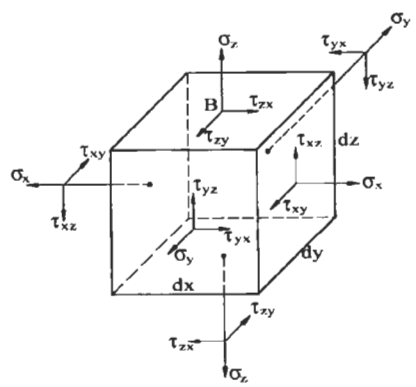

Fig. 2.2. Stresses acting on the planes of the infinitely small cubic element.

2.2. Equilibrium equations

Now assume that the body in Fig. 2.1 is at the state of equilibrium. Then, we can write equilibrium equations for any part of this body. In particular we can do this for an infinitely small tetrahedron singled out in the vicinity of point B (see Fig. 2.1) in such a way that one of its planes coincides with S_σ and the other three planes are

coordinate planes of the Cartesian frame. Internal and external forces acting on this tetrahedron are shown in Fig. 2.3. The equilibrium equation corresponding, e.g., to axis-x can be written as

$$-\sigma_x \, \mathrm{d}S_x - \tau_{yx} \, \mathrm{d}S_y - \tau_{zx} \, \mathrm{d}S_z + p_x \, \mathrm{d}S_\sigma + q_x \, \mathrm{d}V = 0 \ .$$

Here, $\mathrm{d}S_\sigma$ and $\mathrm{d}V$ are the elements of the body surface and volume, while $\mathrm{d}S_x = \mathrm{d}S_\sigma l_x$, $\mathrm{d}S_y = \mathrm{d}S_\sigma l_y$, and $\mathrm{d}S_z = \mathrm{d}S_\sigma l_z$. When the tetrahedron is infinitely diminished, the term including $\mathrm{d}V$ which is of the order of the cube of the linear dimensions can be neglected in comparison with terms containing $\mathrm{d}S$ which is of the order of the square of the linear dimensions. The resulting equation is

$$\sigma_x l_x + \tau_{yx} l_y + \tau_{zx} l_z = p_x \quad (x, y, z) \ . \tag{2.2}$$

Symbol (x, y, z) which is widely used in this chapter denotes permutation with the aid of which we can write two more equations corresponding to the other two axes changing x for y, y for z, and z for x.

Consider now the equilibrium of an arbitrary finite part C of the body (see Fig. 2.1). If we single this part out of the body, we should apply to it body forces q_i and surface tractions p_i whose coordinate components p_x, p_y, and p_z can be expressed, obviously, by Eqs. (2.2) in terms of stresses acting inside the volume C. Because the sum of the components corresponding, e.g., to axis-x must be equal to zero, we have

$$\iiint_v q_x \, \mathrm{d}v + \iint_s p_x \, \mathrm{d}s = 0 \ ,$$

where v and s are the volume and the surface area of the part of the body under consideration. Substituting p_x from Eqs. (2.2) we get

$$\iint_s (\sigma_x l_x + \tau_{yx} l_y + \tau_{zx} l_z) \mathrm{d}s + \iiint_v q_x \, \mathrm{d}v = 0 \quad (x, y, z) \ . \tag{2.3}$$

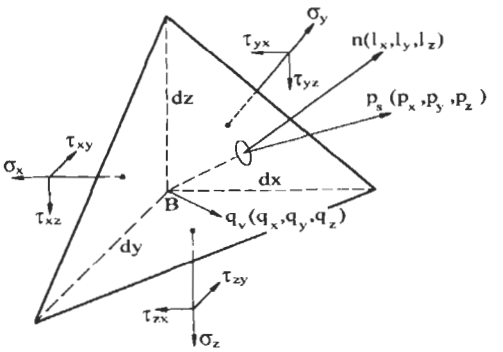

Fig. 2.3. Forces acting on an elementary tetrahedron.

Thus, we have three integral equilibrium equations, Eqs. (2.3), which are valid for any finite part of the body. To convert them into the corresponding differential equations, we use Green's integral transformation

$$\iint_s (f_x l_x + f_y l_y + f_z l_z)\mathrm{d}s = \iiint_v \left(\frac{\partial f_x}{\partial x} + \frac{\partial f_y}{\partial y} + \frac{\partial f_z}{\partial z}\right)\mathrm{d}v \tag{2.4}$$

which is valid for any three continuous, finite, and one-valued functions $f(x,y,z)$ and allows us to transform a surface integral into a volume one. Taking $f_x = \sigma_x$, $f_y = \tau_{yx}$, and $f_z = \tau_{zx}$ we can write Eqs. (2.3) in the following form

$$\iiint_v \left(\frac{\partial \sigma_x}{\partial x} + \frac{\partial \tau_{yx}}{\partial y} + \frac{\partial \tau_{zx}}{\partial z} + q_x\right)\mathrm{d}v = 0 \quad (x,y,z) \ .$$

Because these equations hold whatever the part of the solid may be, provided only that it is within the solid, they yield

$$\frac{\partial \sigma_x}{\partial x} + \frac{\partial \tau_{yx}}{\partial y} + \frac{\partial \tau_{zx}}{\partial z} + q_x = 0 \quad (x,y,z) \ . \tag{2.5}$$

Thus, we have arrived at three differential equilibrium equations that could be also derived from the equilibrium conditions for the infinitesimal element shown in Fig. 2.2.

However, in order to keep part C of the body in Fig. 2.1 in equilibrium the sum of the moments of all the forces applied to this part about any axis must be zero. By taking moments about the z-axis we get the following integral equation

$$\iiint_v (q_x y - q_y x)\mathrm{d}v + \iint_s (p_x y - p_y x)\mathrm{d}s = 0 \ .$$

Using again Eqs. (2.2), (2.4) and taking into account Eqs. (2.5) we finally arrive at the symmetry conditions for shear stresses, i.e.

$$\tau_{xy} = \tau_{yx} \quad (x,y,z) \ . \tag{2.6}$$

So, we have three equilibrium equations, Eqs. (2.5) which include six unknown stresses σ_x, σ_y, σ_z and τ_{xy}, τ_{xz}, τ_{yz}.

Eqs. (2.2) can be treated as force boundary conditions for the stressed state of a solid.

2.3. Stress transformation

Consider the transformation of a stress system from one Cartesian coordinate frame to another. Assume that the elementary tetrahedron shown in Fig. 2.3 is

located inside the body and that point B coincides with the origin 0 of Cartesian coordinates x, y, z in Fig. 2.1. Then, the oblique plane of the tetrahedron can be treated as a coordinate plane $z' = 0$ of a new coordinate frame x', y', z' shown in Fig. 2.4 and such that the normal element to the oblique plane coincides with the z'-axis, while axes x' and y' are located in this plane. Component p_x of the surface traction in Eqs. (2.2) can be treated now as the projection on the x-axis of stress σ acting on plane $z' = 0$. Then, Eqs. (2.2) can be presented in the following explicit form specifying projections of stress σ

$$\begin{aligned} p_x &= \sigma_x l_{z'x} + \tau_{yx} l_{z'y} + \tau_{zx} l_{z'z}, \\ p_y &= \sigma_y l_{z'y} + \tau_{zy} l_{z'z} + \tau_{xy} l_{z'x}, \\ p_z &= \sigma_z l_{z'z} + \tau_{xz} l_{z'x} + \tau_{yz} l_{z'y} \ . \end{aligned} \tag{2.7}$$

Here, l are directional cosines of axis z' with respect to axes x, y, and z (see Fig. 2.4 in which the corresponding cosines of axes x' and y' are also presented). Normal stress $\sigma_{z'}$ can be found now as

$$\begin{aligned} \sigma_{z'} &= p_x l_{z'x} + p_y l_{z'y} + p_z l_{z'z} \\ &= \sigma_x l_{z'x}^2 + \sigma_y l_{z'y}^2 + \sigma_z l_{z'z}^2 + 2\tau_{xy} l_{z'x} l_{z'y} \\ &\quad + 2\tau_{xz} l_{z'x} l_{z'z} + 2\tau_{yz} l_{z'y} l_{z'z} \quad (x', y', z') \ . \end{aligned} \tag{2.8}$$

The final result was obtained with the aid of Eqs. (2.6) and (2.7). Changing x' for y', y' for z', and z' for x', i.e., performing permutation in Eq. (2.8) we can write similar expressions for $\sigma_{x'}$ and $\sigma_{y'}$.

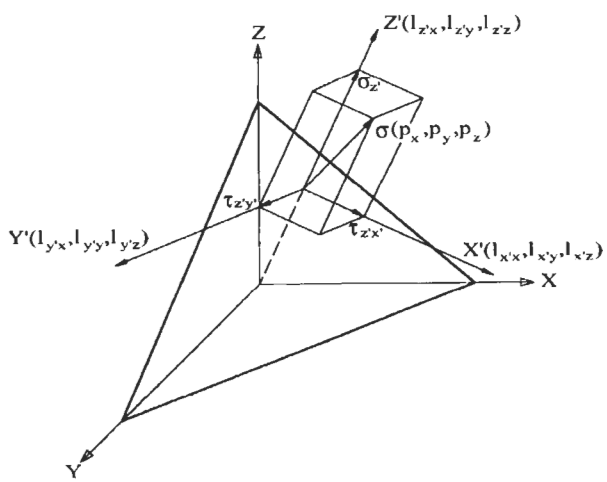

Fig. 2.4. Rotation of the coordinate frame.

Shear stress in new coordinates is

$$\begin{aligned}\tau_{z'x'} &= p_x l_{x'x} + p_y l_{x'y} + p_z l_{x'z} \\ &= \sigma_x l_{x'x} l_{z'x} + \sigma_y l_{x'y} l_{z'y} + \sigma_z l_{x'z} l_{z'z} + \tau_{xy}(l_{x'x} l_{z'y} + l_{x'y} l_{z'x}) \\ &\quad + \tau_{xz}(l_{x'x} l_{z'z} + l_{x'z} l_{z'x}) + \tau_{yz}(l_{x'y} l_{z'z} + l_{x'x} l_{z'y}) \quad (x', y', z') \ . \end{aligned} \tag{2.9}$$

Permutation yields expressions for $\tau_{x'y'}$ and $\tau_{y'z'}$.

2.4. Principal stresses

The foregoing equations, Eqs. (2.8) and (2.9), demonstrate stress transformations under rotation of a coordinate frame. As known, there exists a special position of this frame in which shear stresses acting on coordinate planes vanish. Such coordinate axes are called the principal axes, and normal stresses that act on the corresponding coordinate planes are referred to as the principal stresses.

To determine the principal stresses, assume that coordinates x', y', and z' in Fig. 2.4 are the principal coordinates. Then, according to the aforementioned property of the principal coordinates we should take $\tau_{z'x'} = \tau_{z'y'} = 0$ and $\sigma_{z'} = \sigma$ for the plane $z' = 0$. This means that $p_x = \sigma l_{z'x}$, $p_y = \sigma l_{z'y}$, and $p_z = \sigma l_{z'z}$ in Eqs. (2.7). Introducing new notations for directional cosines of the principal axis, i.e., taking $l_{z'x} = l_{px}$, $l_{z'y} = l_{py}$, $l_{z'z} = l_{pz}$ we have from Eqs. (2.7)

$$\begin{aligned} &(\sigma_x - \sigma) l_{px} + \tau_{xy} l_{py} + \tau_{xz} l_{pz} = 0, \\ &\tau_{xy} l_{px} + (\sigma_y - \sigma) l_{py} + \tau_{yz} l_{pz} = 0, \\ &\tau_{xz} l_{px} + \tau_{yz} l_{py} + (\sigma_z - \sigma) l_{pz} = 0 \ . \end{aligned} \tag{2.10}$$

These equations were transformed with the aid of symmetry conditions for shear stresses, Eqs. (2.6). For some specified point of the body in the vicinity of which the principal stresses are determined in terms of stresses referred to some fixed coordinate frame x, y, z and known, Eqs. (2.10) comprise a homogeneous system of linear algebraic equations. Formally, this system always has the trivial solution, i.e., $l_{px} = l_{py} = l_{pz} = 0$ which we can ignore because directional cosines should satisfy an evident condition following from Eqs. (2.1), i.e.

$$l_{px}^2 + l_{py}^2 + l_{pz}^2 = 1 \ . \tag{2.11}$$

So, we need to find a nonzero solution of Eqs. (2.10) which can exist if the determinant of the set is zero. This condition yields the following cubic equation for σ

$$\sigma^3 - I_1 \sigma^2 - I_2 \sigma - I_3 = 0 \ , \tag{2.12}$$

where

$$I_1 = \sigma_x + \sigma_y + \sigma_z,$$
$$I_2 = -\sigma_x\sigma_y - \sigma_x\sigma_z - \sigma_y\sigma_z + \tau_{xy}^2 + \tau_{xz}^2 + \tau_{yz}^2, \tag{2.13}$$
$$I_3 = \sigma_x\sigma_y\sigma_z + 2\tau_{xy}\tau_{xz}\tau_{yz} - \sigma_x\tau_{yz}^2 - \sigma_y\tau_{xz}^2 - \sigma_z\tau_{xy}^2 \ .$$

are invariant characteristics (invariants) of the stressed state. This means that if we refer the body to any Cartesian coordinate frame with directional cosines specified by Eqs. (2.1), take the origin of this frame at some arbitrary point and change stresses in Eqs. (2.13) with the aid of Eqs. (2.8) and (2.9), the values of I_1, I_2, I_3 at this point will be the same for all such coordinate frames. Eq. (2.12) has three real roots that specify three principal stresses σ_1, σ_2, and σ_3. There is a rule according to which $\sigma_1 \geq \sigma_2 \geq \sigma_3$, i.e., σ_1 is the maximum principal stress and σ_3 is the minimum one. If, for example, the roots of Eq. (2.12) are 100 MPa, −200 MPa, and 0, then $\sigma_1 = 100$ MPa, $\sigma_2 = 0$, and $\sigma_3 = -200$ MPa.

To demonstrate the procedure, consider a particular state of stress, important for applications, namely pure shear in the xy-plane. Let a thin square plate referred to coordinates x, y, z be loaded with shear stresses τ uniformly distributed over the plate thickness and along the edges (see Fig. 2.5).

One principal plane is evident – it is plane $z = 0$, which is free of shear stresses. To find two other planes, we should take in Eqs. (2.13) $\sigma_x = \sigma_y = \sigma_z = 0$, $\tau_{xz} = \tau_{yz} = 0$, and $\tau_{xy} = \tau$. Then, Eq. (2.12) acquires the form

$$\sigma^3 - \tau^2\sigma = 0 \ .$$

The first root of this equation gives $\sigma = 0$ and corresponds to plane $z = 0$. Two other roots are $\sigma = \pm\tau$. Thus, we have three principal stresses, i.e., $\sigma_1 = \tau$, $\sigma_2 = 0$, $\sigma_3 = -\tau$. To find the planes corresponding to σ_1 and σ_3 we should put $I_{pz} = 0$, substitute $\sigma = \pm\tau$ into Eqs. (2.10), write them for the state of stress under study, and

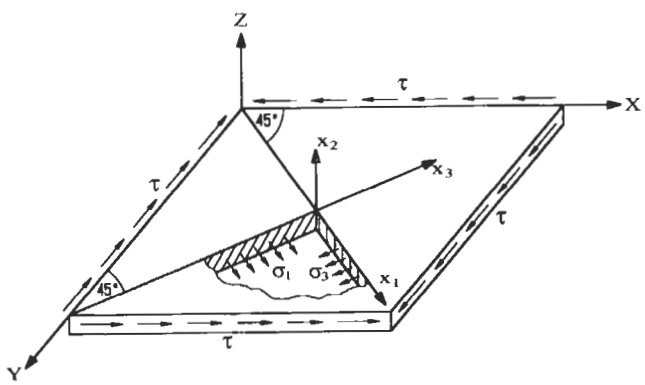

Fig. 2.5. Principal stresses under pure shear.

supplement this set with Eq. (2.11). The final equations allowing us to find l_{px} and l_{py} are

$$\mp\tau\, l_{px} + \tau\, l_{py} = 0, \quad l_{px}^2 + l_{py}^2 = 1 \ .$$

Solution of these equations yields $l_{px} = \pm 1/\sqrt{2}$ and $l_{py} = \mp 1/\sqrt{2}$, and means that principal planes (or principal axes) make 45° angles with axes x and y. Principal stresses and principal coordinates x_1, x_2, x_3 are shown in Fig. 2.5.

2.5. Displacements and strains

For any point of a solid (e.g., L or M in Fig. 2.1) introduce coordinate component displacements u_x, u_y, and u_z specifying the point displacements in the directions of coordinate axes.

Consider an arbitrary infinitely small element LM characterized with its directional cosines

$$l_x = \frac{\mathrm{d}x}{\mathrm{d}s}, \quad l_y = \frac{\mathrm{d}y}{\mathrm{d}s}, \quad l_z = \frac{\mathrm{d}z}{\mathrm{d}s} \ . \tag{2.14}$$

Positions of this element before and after deformation are shown in Fig. 2.6. Assume that displacements of the point L are u_x, u_y, and u_z. Then, displacements of the point M should be

$$u_x^{(1)} = u_x + \mathrm{d}u_x, \quad u_y^{(1)} = u_y + \mathrm{d}u_y, \quad u_z^{(1)} = u_z + \mathrm{d}u_z \ . \tag{2.15}$$

Since u_x, u_y, and u_z are continuous functions of x, y, z

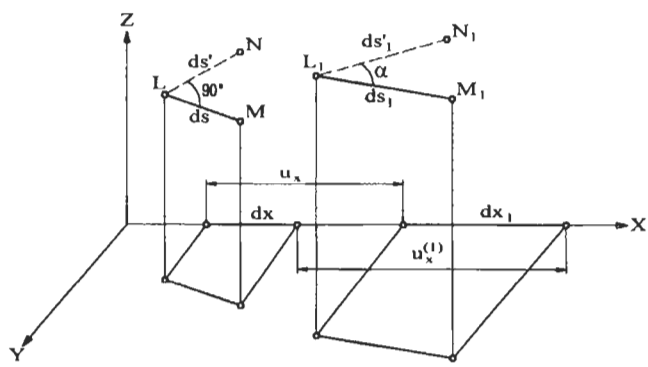

Fig. 2.6. Displacement of an infinitesimal linear element.

$$du_x = \frac{\partial u_x}{\partial x}dx + \frac{\partial u_y}{\partial y}dy + \frac{\partial u_z}{\partial z}dz \quad (x,y,z) \ . \tag{2.16}$$

As follows from Fig. 2.6 and Eqs. (2.15) and (2.16)

$$\begin{aligned} dx_1 &= dx + u_x^{(1)} - u_x = dx + du_x \\ &= \left(1 + \frac{\partial u_x}{\partial x}\right)dx + \frac{\partial u_x}{\partial y}dy + \frac{\partial u_x}{\partial z}dz \quad (x,y,z) \ . \end{aligned} \tag{2.17}$$

Introduce strain of element LM as

$$\varepsilon = \frac{ds_1 - ds}{ds} \ . \tag{2.18}$$

After some rearrangements we arrive at

$$\varepsilon + \frac{1}{2}\varepsilon^2 = \frac{1}{2}\left[\left(\frac{ds_1}{ds}\right)^2 - 1\right] \ ,$$

where

$$ds_1^2 = (dx_1)^2 + (dy_1)^2 + (dz_1)^2 \ .$$

Substituting for dx_1, dy_1, dz_1 their expressions from Eqs. (2.17) and taking into account Eqs. (2.14) we finally get

$$\varepsilon + \tfrac{1}{2}\varepsilon^2 = \varepsilon_{xx}l_x^2 + \varepsilon_{yy}l_y^2 + \varepsilon_{zz}l_z^2 + \varepsilon_{xy}l_xl_y + \varepsilon_{xz}l_xl_z + \varepsilon_{yz}l_yl_z \ , \tag{2.19}$$

where

$$\begin{aligned} \varepsilon_{xx} &= \frac{\partial u_x}{\partial x} + \frac{1}{2}\left[\left(\frac{\partial u_x}{\partial x}\right)^2 + \left(\frac{\partial u_y}{\partial x}\right)^2 + \left(\frac{\partial u_z}{\partial x}\right)^2\right] \quad (x,y,z), \\ \varepsilon_{xy} &= \frac{\partial u_x}{\partial y} + \frac{\partial u_y}{\partial x} + \frac{\partial u_x}{\partial x}\frac{\partial u_x}{\partial y} + \frac{\partial u_y}{\partial x}\frac{\partial u_y}{\partial y} + \frac{\partial u_z}{\partial x}\frac{\partial u_z}{\partial y} \quad (x,y,z) \ . \end{aligned} \tag{2.20}$$

Assuming that the strain is small we can neglect the second term in the left-hand side of Eq. (2.19). Moreover, we further assume that the displacements are continuous functions that change rather slowly with the change of coordinates. This allows us to neglect the products of derivatives in Eqs. (2.20). As a result, we arrive at the following equation

$$\varepsilon = \varepsilon_x l_x^2 + \varepsilon_y l_y^2 + \varepsilon_z l_z^2 + \gamma_{xy}l_xl_y + \gamma_{xz}l_xl_z + \gamma_{yz}l_yl_z \ , \tag{2.21}$$

where

$$\varepsilon_x = \frac{\partial u_x}{\partial x}, \quad \varepsilon_y = \frac{\partial u_y}{\partial y}, \quad \varepsilon_z = \frac{\partial u_z}{\partial z},$$
$$\gamma_{xy} = \frac{\partial u_x}{\partial y} + \frac{\partial u_y}{\partial x}, \quad \gamma_{xz} = \frac{\partial u_x}{\partial z} + \frac{\partial u_z}{\partial x}, \quad \gamma_{yz} = \frac{\partial u_y}{\partial z} + \frac{\partial u_z}{\partial y} \tag{2.22}$$

can be treated as linear strain–displacement equations. Taking $l_x = 1$, $l_y = l_z = 0$ in Eqs. (2.22), i.e., directing element LM in Fig. 2.6 along the x-axis we can readily see that ε_x is the strain along the same x-axis. Similar reasoning shows that ε_y and ε_z in Eqs. (2.22) are strains in the directions of axes y and z. To find out the physical meaning of strains γ in Eqs. (2.22), consider two orthogonal line elements LM and LN and find angle α that they make with each other after deformation (see Fig. 2.6), i.e.,

$$\cos\alpha = \frac{dx_1\,dx_1' + dy_1\,dy_1' + dz_1\,dz_1'}{ds_1\,ds_1'} \ . \tag{2.23}$$

Here, dx_1, dy_1, and dz_1 are specified with Eqs. (2.17), ds_1 can be found from Eq. (2.18) and

$$dx_1' = \left(1 + \frac{\partial u_x}{\partial x}\right)dx' + \frac{\partial u_x}{\partial y}dy' + \frac{\partial u_x}{\partial z}dz' \quad (x, y, z),$$
$$ds_1' = ds'(1 + \varepsilon') \ . \tag{2.24}$$

Introduce directional cosines of element LN as

$$l_x' = \frac{dx'}{ds'}, \quad l_y' = \frac{dy'}{ds'}, \quad l_z' = \frac{dz'}{ds'} \ . \tag{2.25}$$

Because elements LM and LN are orthogonal, we have

$$l_x l_x' + l_y l_y' + l_z l_z' = 0 \ .$$

Using Eqs. (2.14), (2.18), (2.24)–(2.26) and introducing shear strain γ as the difference between angles $M_1L_1N_1$ and MLN, i.e., as

$$\gamma = \frac{\pi}{2} - \alpha$$

we can write Eq. (2.23) in the following form

$$\sin\gamma = \frac{1}{(1+\varepsilon)(1+\varepsilon')}\Big[2(\varepsilon_{xx}l_x l_x' + \varepsilon_{yy}l_y l_y' + \varepsilon_{zz}l_z l_z') + \varepsilon_{xy}(l_x l_y' + l_x' l_y)$$
$$+ \varepsilon_{xz}(l_x l_z' + l_x' l_z) + \varepsilon_{yz}(l_y l_z' + l_y' l_z)\Big] \ . \tag{2.26}$$

Linear approximation of Eq. (2.26) similar to Eq. (2.21) is

$$\gamma = 2(\varepsilon_x l_x l'_x + \varepsilon_y l_y l'_y + \varepsilon_z l_z l'_z) + \gamma_{xy}(l_x l'_y + l'_x l_y) + \gamma_{xz}(l_x l'_z + l'_x l_z) + \gamma_{yz}(l_y l'_z + l'_y l_z) \quad . \tag{2.27}$$

Here, ε_x, ε_y, ε_z and γ_{xy}, γ_{xz}, γ_{yz} components are determined with Eqs. (2.22). If we direct now element LM along the x-axis and element LN along the y-axis putting $l_x = 1$, $l_y = l_z = 0$ and $l'_y = 1$, $l'_x = l'_z = 0$, Eq. (2.27) yields $\gamma = \gamma_{xy}$. Thus, γ_{xy}, γ_{xz}, and γ_{yz} are shear strains that are equal to the changes of angles between axes x and y, x and z, y and z, respectively.

2.6. Transformation of small strains

Consider small strains in Eqs. (2.22) and study their transformation under rotation of the coordinate frame. Assume that x', y', z' in Fig. 2.4 form a new coordinate frame rotated with respect to original frame x, y, z. Because Eqs. (2.22) are valid for any Cartesian coordinate frame, we have

$$\varepsilon_{x'} = \frac{\partial u_{x'}}{\partial x'}, \quad \gamma_{x'y'} = \frac{\partial u_{x'}}{\partial y'} + \frac{\partial u_{y'}}{\partial x'} \quad (x, y, z) \quad . \tag{2.28}$$

Here, $u_{x'}$, $u_{y'}$, and $u_{z'}$ are displacements along the axes x', y', z' which can be linked with displacements u_x, u_y, and u_z of the same point by the following linear relations

$$u_{x'} = u_x l_{x'x} + u_y l_{x'y} + u_z l_{x'z} \quad (x, y, z) \quad . \tag{2.29}$$

Similar relations can be written for derivatives of displacement with respect to variables x', y', z' and x, y, z, i.e.,

$$\frac{\partial u}{\partial x'} = \frac{\partial u}{\partial x} l_{x'x} + \frac{\partial u}{\partial y} l_{x'y} + \frac{\partial u}{\partial z} l_{x'z} \quad (x, y, z) \quad . \tag{2.30}$$

Substituting displacements, Eqs. (2.29), into Eqs. (2.28), passing to variables x, y, z with the aid of Eqs. (2.30), and taking into account Eqs. (2.22) we arrive at

$$\begin{aligned} \varepsilon_{x'} &= \varepsilon_x l^2_{x'x} + \varepsilon_y l^2_{x'y} + \varepsilon_z l^2_{x'z} + \gamma_{xy} l_{x'x} l_{x'y} + \gamma_{xz} l_{x'x} l_{x'z} + \gamma_{yz} l_{x'y} l_{x'z} \quad (x, y, z), \\ \gamma_{x'y'} &= 2\varepsilon_x l_{x'x} l_{y'x} + 2\varepsilon_y l_{x'y} l_{y'y} + 2\varepsilon_z l_{x'z} l_{y'z} + \gamma_{xy}(l_{x'x} l_{y'y} + l_{x'y} l_{y'x}) \\ &\quad + \gamma_{xz}(l_{x'x} l_{y'z} + l_{x'z} l_{y'x}) + \gamma_{yz}(l_{x'y} l_{y'z} + l_{x'z} l_{y'y}) \quad (x, y, z) \quad . \end{aligned} \tag{2.31}$$

These strain transformations are similar to the stress transformations determined with Eqs. (2.8) and (2.9).

2.7. Compatibility equations

Consider strain–displacement equations, Eqs. (2.22), and try to determine displacements u_x, u_y, and u_z in terms of strains ε_x, ε_y, ε_z and γ_{xy}, γ_{xz}, γ_{yz}. As can be seen, there are six equations containing only three unknown displacements. In the general case, such set of equations is not consistent, and some compatibility conditions should be imposed on strains to provide the existence of the solution. To derive these conditions, decompose derivatives of the displacements as follows

$$\frac{\partial u_x}{\partial x} = \varepsilon_x, \quad \frac{\partial u_x}{\partial y} = \frac{1}{2}\gamma_{xy} - \omega_z, \quad \frac{\partial u_x}{\partial z} = \frac{1}{2}\gamma_{xz} + \omega_y \quad (x, y, z) \ . \tag{2.32}$$

Here

$$\omega_z = \frac{1}{2}\left(\frac{\partial u_y}{\partial x} - \frac{\partial u_x}{\partial y}\right) \quad (x, y, z) \tag{2.33}$$

is the angle of rotation of a body element (such as the cubic element shown in Fig. 2.1) around the z-axis. Three Eqs. (2.32) including one and the same displacement u_x allow us to construct three couples of mixed second-order derivatives of u_x with respect to x and y or y and x, x and z or z and x, y and z or z and y. Because the sequence of differentiation does not influence the result and since there are two other groups of equations in Eqs. (2.32), we arrive at nine compatibility conditions that can be presented as

$$\begin{aligned}
&\frac{\partial \omega_x}{\partial x} = \frac{1}{2}\left(\frac{\partial \gamma_{xz}}{\partial y} - \frac{\partial \gamma_{xy}}{\partial z}\right) \quad (x, y, z), \\
&\frac{\partial \omega_x}{\partial y} = \frac{1}{2}\frac{\partial \gamma_{yz}}{\partial y} - \frac{\partial \varepsilon_y}{\partial z} \quad (x, y, z), \\
&\frac{\partial \omega_x}{\partial z} = -\frac{1}{2}\frac{\partial \gamma_{yz}}{\partial z} + \frac{\partial \varepsilon_z}{\partial y} \quad (x, y, z) \ .
\end{aligned} \tag{2.34}$$

These equations are similar to Eqs. (2.32), i.e., they allow us to determine rotation angles only if some compatibility conditions are valid. These conditions compose the set of compatibility equations for strains and have the following final form

$$k_{xy}(\varepsilon, \gamma) = 0, \quad r_x(\varepsilon, \gamma) = 0 \quad (x, y, z) \ , \tag{2.35}$$

where

$$\begin{aligned}
k_{xy}(\varepsilon, \gamma) &= \frac{\partial^2 \varepsilon_x}{\partial y^2} + \frac{\partial^2 \varepsilon_y}{\partial x^2} - \frac{\partial^2 \gamma_{xy}}{\partial x \partial y} \quad (x, y, z), \\
r_x(\varepsilon, \gamma) &= \frac{\partial^2 \varepsilon_x}{\partial y \partial z} - \frac{1}{2}\frac{\partial}{\partial x}\left(\frac{\partial \gamma_{xy}}{\partial z} + \frac{\partial \gamma_{xz}}{\partial y} - \frac{\partial \gamma_{yz}}{\partial x}\right) \quad (x, y, z) \ .
\end{aligned} \tag{2.36}$$

If strains ε_x, ε_y, ε_z and γ_{xy}, γ_{xz}, γ_{yz} satisfy Eqs. (2.35), we can find rotation angles ω_x, ω_y, ω_z integrating Eqs. (2.34) and then determine displacements u_x, u_y, u_z integrating Eqs. (2.32).

Six compatibility equations, Eqs. (2.35), derived formally as compatibility conditions for Eqs. (2.32) have a simple physical meaning. Assume that we have a continuous solid shown in Fig. 2.1 and divide it into a set of pieces that perfectly match each other. Now, apply some strains to each of these pieces. Obviously, for arbitrary strains, the deformed pieces cannot be assembled into a continuous deformed solid. This will happen only under the condition that the strains satisfy Eqs. (2.35). However, even if the strains do not satisfy Eqs. (2.35), we can assume that the solid is continuous but in a more general Riemannian (curved) space rather than in traditional Euclidean space in which the solid existed before the deformation (Vasiliev and Gurdal, 1999). Then, six quantities k and r in Eqs. (2.36), being nonzero, specify curvatures of the Riemannian space caused by small strains ε and γ. Compatibility equations, Eqs. (2.35), require these curvatures to be equal to zero which means that the solid should remain in the Euclidean space under deformation.

2.8. Admissible static and kinematic fields

In solid mechanics we introduce static field variables which are stresses and kinematic field variables which are displacements and strains.

The static field is said to be statically admissible if the stresses satisfy equilibrium equations, Eqs. (2.5), and are in equilibrium with surface tractions on the body surface S_σ where these tractions are given (see Fig. 2.1), i.e., if Eqs. (2.2) are satisfied on S_σ.

The kinematic field is referred to as kinematically admissible if displacements and strains are linked by strain–displacement equations, Eqs. (2.22), and displacements satisfy kinematic boundary conditions on the surface S_u where displacements are prescribed (see Fig. 2.1).

Actual stresses and displacements belong, naturally, to the corresponding admissible fields though actual stresses must in addition provide admissible displacements, while actual displacements should be associated with admissible stresses. Mutual correspondence between static and kinematic variables is established through the so-called constitutive equations that are considered in the next section.

2.9. Constitutive equations for an elastic solid

Consider a solid loaded with body and surface forces as in Fig. 2.1. These forces induce some stresses, displacements, and strains that compose the fields of actual static and kinematic variables. Introduce some infinitesimal additional displacements du_x, du_y, and du_z such that they belong to a kinematically

admissible field. This means that there exist equations that are similar to Eqs. (2.22), i.e.,

$$d\varepsilon_x = \frac{\partial}{\partial x}(du_x), \quad d\gamma_{xy} = \frac{\partial}{\partial y}(du_x) + \frac{\partial}{\partial x}(du_y) \quad (x, y, z) \tag{2.37}$$

and specify additional strains.

Because additional displacements are infinitely small, we can assume that external forces do not change under such variation of the displacements (we do not consider here special cases in which external forces depend on displacements of the points at which these forces are applied). Then we can calculate the work performed by the forces multiplying forces by the corresponding increments of the displacements and write the total work of body forces and surface tractions as

$$dW = \iiint_V (q_x\, du_x + q_y du_y + q_z\, du_z)dV + \iint_S (p_x\, du_x + p_y\, du_y + p_z\, du_z)dS \ . \tag{2.38}$$

Here, V and S are the body volume and external surface of the body in Fig. 2.1. Actually, we must write the surface integral in Eq. (2.38) only for the surface S_σ on which the forces are given. But since the increments of the displacements belong to a kinematically admissible field, they are equal to zero on S_u, and the integral can be written for the whole surface of the body. To proceed, we express p_x, p_y, and p_z in terms of stresses with the aid of Eqs. (2.2) and transform the surface integral into a volume one using Eq. (2.4). For the sake of brevity, consider only x-components of forces and displacement in Eq. (2.38). We have in several steps

$$\begin{aligned}
&\iiint_V q_x\, du_x + \iint_S p_x\, du_x\, ds \\
&\quad = \iiint_V q_x\, du_x + \iint_S (\sigma_x l_x + \tau_{yx} l_y + \tau_{zx} l_z)du_x\, dS \\
&\quad = \iiint_V \left[q_x\, du_x + \frac{\partial}{\partial x}(\sigma_x\, du_x) + \frac{\partial}{\partial y}(\tau_{yx}\, du_x) + \frac{\partial}{\partial z}(\tau_{zx}\, du_x)\right] dV \\
&\quad = \iiint_V \left[\left(q_x + \frac{\partial \sigma_x}{\partial x} + \frac{\partial \tau_{yx}}{\partial y} + \frac{\partial \tau_{zx}}{\partial z}\right) du_x + \sigma_x \frac{\partial}{\partial x}(du_x)\right. \\
&\qquad\qquad \left. + \tau_{yx} \frac{\partial}{\partial y}(du_x) + \tau_{zx} \frac{\partial}{\partial z}(du_x)\right] dV \\
&\quad = \iiint_V \left[\sigma_x\, d\varepsilon_x + \tau_{xy} \frac{\partial}{\partial y}(du_x) + \tau_{xz} \frac{\partial}{\partial z}(du_x)\right] dV \ .
\end{aligned}$$

The last transformation step was performed with due regard to Eqs. (2.5), (2.6), and (2.37). Finally, Eq. (2.38) acquires the form

$$dW = \iiint_V (\sigma_x \, d\varepsilon_x + \sigma_y \, d\varepsilon_y + \sigma_z \, d\varepsilon_z + \tau_{xy} \, d\gamma_{xy} + \tau_{xz} \, d\gamma_{xz} + \tau_{yz} \, d\gamma_{yz}) dV \ . \quad (2.39)$$

Because the right-hand side of this equation includes only internal variables, i.e., stresses and strains, we can conclude that the foregoing formal rearrangement actually allowed us to transform the work of external forces into the work of internal forces or into potential energy accumulated in the body. For further derivation, let us introduce for the sake of brevity new notations for coordinates and use subscripts 1, 2, 3 instead of x, y, z, respectively. We also use the following notations for stresses and strains

$$\sigma_x = \sigma_{11}, \quad \sigma_y = \sigma_{22}, \quad \sigma_z = \sigma_{33},$$
$$\tau_{xy} = \sigma_{12} = \sigma_{21}, \quad \tau_{xz} = \sigma_{13} = \sigma_{31}, \quad \tau_{yz} = \sigma_{23} = \sigma_{32},$$
$$\varepsilon_x = \varepsilon_{11}, \quad \varepsilon_y = \varepsilon_{22}, \quad \varepsilon_z = \varepsilon_{33},$$
$$\gamma_{xy} = 2\varepsilon_{12} = 2\varepsilon_{21}, \quad \gamma_{xz} = 2\varepsilon_{13} = 2\varepsilon_{31}, \quad \gamma_{yz} = 2\varepsilon_{23} = 2\varepsilon_{32} \ .$$

Then, Eq. (2.39) can be written as

$$dW = \iiint_V dU \, dV \ , \quad (2.40)$$

where

$$dU = \sigma_{ij} \, d\varepsilon_{ij} \ . \quad (2.41)$$

This form of equation implies summation over repeated subscripts $i, j = 1, 2, 3$.

It should be emphasized that by now dU is just a symbol, which does not mean that there exists function U and that dU is its differential. This meaning dU acquires if we restrict ourselves to the consideration of an elastic material described in Section 1.1. For this material, the difference between the body potential energy corresponding to some initial state A and the energy corresponding to some other state B does not depend on the way undertaken to transform the body from state A to state B. In other words, the integral

$$\int_A^B \sigma_{ij} \, d\varepsilon_{ij} = U(B) - U(A)$$

does not depend on the path of integration. This means that the element of integration is a complete differential of function U depending on ε_{ij}, i.e., that

$$dU = \frac{\partial U}{\partial \varepsilon_{ij}} d\varepsilon_{ij} \ .$$

Comparing this result with Eq. (2.41) we arrive at Green's formulas

$$\sigma_{ij} = \frac{\partial U}{\partial \varepsilon_{ij}} \tag{2.42}$$

that are valid for any elastic material. Function $U(\varepsilon_{ij})$ can be referred to as specific strain energy (energy accumulated in the unit of body volume) or elastic potential. Potential U can be expanded into the Taylor series with respect to strains, i.e.,

$$U(\varepsilon_{ij}) = s_0 + s_{ij}\varepsilon_{ij} + \tfrac{1}{2} s_{ijkl}\varepsilon_{ij}\varepsilon_{kl} + \cdots \tag{2.43}$$

where

$$s_0 = U(\varepsilon_{ij} = 0), \quad s_{ij} = \left.\frac{\partial U}{\partial \varepsilon_{ij}}\right|_{\varepsilon_{ij}=0.} \quad s_{ijkl} = \left.\frac{\partial^2 U}{\partial \varepsilon_{ij}\partial \varepsilon_{kl}}\right|_{\varepsilon_{ij}=0.\varepsilon_{kl}=0.} \ . \tag{2.44}$$

Assume that in the initial state of the body corresponding to zero external forces we have $\varepsilon_{ij} = 0$, $\sigma_{ij} = 0$, $U = 0$. Then, $s_0 = 0$ and $s_{ij} = 0$ according to Eq. (2.42). For small strains, we can neglect high-order terms in Eq. (2.43) and restrict ourselves to the first system of nonzero terms taking

$$U = \tfrac{1}{2} s_{ijkl}\varepsilon_{ij}\varepsilon_{kl} \ .$$

Then, Eq. (2.42) yields

$$\sigma_{ij} = s_{ijkl}\varepsilon_{kl} \ . \tag{2.45}$$

These linear equations correspond to a linear elastic model of the material (see Section 1.1) and, in general, include $3^4 = 81$ coefficients s. However, because $\sigma_{ij} = \sigma_{ji}$ and $\varepsilon_{ij} = \varepsilon_{ji}$, we have the following equations $s_{ijkl} = s_{jikl} = s_{ijlk}$ which reduce the number of independent coefficients to 36. Then, taking into account the fact that the mixed derivative specifying coefficients s_{ijkl} in Eqs. (2.44) does not depend on the sequence of differentiation we get 15 equations $s_{ijkl} = s_{klij}$ $(ij \neq kl)$. Thus, Eq. (2.45) contains only 21 independent coefficients. Returning to coordinates x, y, z we can write Eq. (2.45) in the following explicit form

$$\{\sigma\} = [S]\{\varepsilon\} \ , \tag{2.46}$$

where

$$\{\sigma\} = \begin{Bmatrix} \sigma_x \\ \sigma_y \\ \sigma_z \\ \tau_{xy} \\ \tau_{xz} \\ \tau_{yz} \end{Bmatrix}, \quad \{\varepsilon\} = \begin{Bmatrix} \varepsilon_x \\ \varepsilon_y \\ \varepsilon_z \\ \gamma_{xy} \\ \gamma_{xz} \\ \gamma_{yz} \end{Bmatrix}, \quad [S] = \begin{bmatrix} S_{11} & S_{12} & S_{13} & S_{14} & S_{15} & S_{16} \\ S_{21} & S_{22} & S_{23} & S_{24} & S_{25} & S_{26} \\ S_{31} & S_{32} & S_{33} & S_{34} & S_{35} & S_{36} \\ S_{41} & S_{42} & S_{43} & S_{44} & S_{45} & S_{46} \\ S_{51} & S_{52} & S_{53} & S_{54} & S_{55} & S_{56} \\ S_{61} & S_{62} & S_{63} & S_{64} & S_{65} & S_{66} \end{bmatrix}. \tag{2.47}$$

Eq. (2.46) are referred to as constitutive equations. They link stresses and strains through 21 stiffness coefficients $S_{ij} = S_{ji}$ that specify material mechanical properties within the framework of a linear elastic model of the material. The inverse form of Eq. (2.46) is

$$\{\varepsilon\} = [C]\{\sigma\} \ . \tag{2.48}$$

Strains are expressed in terms of stresses via the matrix of compliance coefficients that can be written as

$$[C] = \begin{bmatrix} \frac{1}{E_x} & -\frac{\nu_{xy}}{E_y} & -\frac{\nu_{xz}}{E_z} & \frac{\eta_{x,xy}}{G_{xy}} & \frac{\eta_{x,xz}}{G_{xz}} & \frac{\eta_{x,yz}}{G_{yz}} \\ -\frac{\nu_{yx}}{E_x} & \frac{1}{E_y} & -\frac{\nu_{yz}}{E_z} & \frac{\eta_{y,xy}}{G_{xy}} & \frac{\eta_{y,xz}}{G_{xz}} & \frac{\eta_{y,yz}}{G_{yz}} \\ -\frac{\nu_{zx}}{E_x} & -\frac{\nu_{zy}}{E_y} & \frac{1}{E_z} & \frac{\eta_{z,xy}}{G_{xy}} & \frac{\eta_{z,xz}}{G_{xz}} & \frac{\eta_{z,yz}}{G_{yz}} \\ \frac{\eta_{xy,x}}{E_x} & \frac{\eta_{xy,y}}{E_y} & \frac{\eta_{xy,z}}{E_z} & \frac{1}{G_{xy}} & \frac{\lambda_{xy,xz}}{G_{xz}} & \frac{\lambda_{xy,yz}}{G_{yz}} \\ \frac{\eta_{xz,x}}{E_x} & \frac{\eta_{xz,y}}{E_y} & \frac{\eta_{xz,z}}{E_z} & \frac{\lambda_{xz,xy}}{G_{xy}} & \frac{1}{G_{xz}} & \frac{\lambda_{xz,yz}}{G_{yz}} \\ \frac{\eta_{yz,x}}{E_x} & \frac{\eta_{yz,y}}{E_y} & \frac{\eta_{yz,z}}{E_z} & \frac{\lambda_{yz,xy}}{G_{xy}} & \frac{\lambda_{yz,xz}}{G_{xz}} & \frac{1}{G_{yz}} \end{bmatrix}. \tag{2.49}$$

This matrix is symmetric, and the following 15 symmetry conditions are valid

$$\begin{aligned} &\frac{\nu_{xy}}{E_y} = \frac{\nu_{yx}}{E_x}, \quad \frac{\nu_{xz}}{E_z} = \frac{\nu_{zx}}{E_x}, \quad \frac{\nu_{yz}}{E_z} = \frac{\nu_{zy}}{E_y}, \\ &\frac{\eta_{x,xy}}{G_{xy}} = \frac{\eta_{xy,x}}{E_x}, \quad \frac{\eta_{x,xz}}{G_{xz}} = \frac{\eta_{xz,x}}{E_x}, \quad \frac{\eta_{x,yz}}{G_{yz}} = \frac{\eta_{yz,x}}{E_x}, \\ &\frac{\eta_{y,xy}}{G_{xy}} = \frac{\eta_{xy,y}}{E_y}, \quad \frac{\eta_{y,xz}}{G_{xz}} = \frac{\eta_{xz,y}}{E_y}, \quad \frac{\eta_{y,yz}}{G_{yz}} = \frac{\eta_{yz,y}}{E_y}, \\ &\frac{\eta_{z,xy}}{G_{xy}} = \frac{\eta_{xy,z}}{E_z}, \quad \frac{\eta_{z,xz}}{G_{xz}} = \frac{\eta_{xz,z}}{E_y}, \quad \frac{\eta_{z,yz}}{G_{yz}} = \frac{\eta_{yz,z}}{E_z}, \\ &\frac{\lambda_{xy,xz}}{G_{xz}} = \frac{\lambda_{xz,xy}}{G_{xy}}, \quad \frac{\lambda_{xy,yz}}{G_{yz}} = \frac{\lambda_{yz,xy}}{G_{xy}}, \quad \frac{\lambda_{xz,yz}}{G_{yz}} = \frac{\lambda_{yz,xz}}{G_{xz}} \ . \end{aligned} \tag{2.50}$$

Compliance matrix, Eq. (2.49), includes the following engineering constants:

E_x is the modulus of elasticity in the x-direction (x, y, z); ν_{xy} the Poisson's ratio that determines the strain in the x-direction induced by normal stress acting in the orthogonal y-direction (x, y, z); G_{xy} the shear modulus in the xy-plane (x, y, z); $\eta_{x,yz}$ the extension-shear coupling coefficient indicating normal strain in the x-direction induced by shear stress acting in the yz-plane (x, y, z); $\eta_{xy,z}$ the shear-extension coupling coefficient characterizing shear strain in the xy-plane caused by normal stress acting in the z-direction (x, y, z); and $\lambda_{xy,yz}$ the shear–shear coupling coefficient that determines the shear strain taking place in the xy-plane under shear stress acting in the yz-plane (x, y, z).

Having constitutive equations, Eq. (2.46), we can now write the finite expression for elastic potential, U. Substituting stresses into Eq. (2.41) and integrating it with respect to strains we get after some transformation with the aid of Eq. (2.46) the following equation

$$U = \tfrac{1}{2}(\sigma_x\varepsilon_x + \sigma_y\varepsilon_y + \sigma_z\varepsilon_z + \tau_{xy}\gamma_{xy} + \tau_{xz}\gamma_{xz} + \tau_{yz}\gamma_{yz}) \ . \tag{2.51}$$

Potential energy of the body can be found as

$$W = \iiint_V U \, \mathrm{d}V \ . \tag{2.52}$$

Compliance matrix, Eq. (2.49), containing 21 independent elastic constants corresponds to the general case of material anisotropy that practically never appears in real materials. The most common particular case corresponds to an orthotropic (orthogonally anisotropic) material which has three orthogonal orthotropy (coordinate) axes such that normal stresses acting along these axes do not induce shear strains, while shear stresses acting in coordinate planes do not cause normal strains in the direction of these axes. As a result, the stiffness and compliance matrices become uncoupled with respect to normal stresses and strains on one side and shear stresses and strains on the other side. For the case of an orthotropic material, with axes x, y, and z coinciding with the orthotropy axes, Eq. (2.49) acquires the form

$$[C] = \begin{bmatrix} \dfrac{1}{E_x} & -\dfrac{\nu_{xy}}{E_y} & -\dfrac{\nu_{xz}}{E_z} & 0 & 0 & 0 \\ -\dfrac{\nu_{yx}}{E_x} & \dfrac{1}{E_y} & -\dfrac{\nu_{yz}}{E_z} & 0 & 0 & 0 \\ -\dfrac{\nu_{zx}}{E_x} & -\dfrac{\nu_{zy}}{E_y} & \dfrac{1}{E_z} & 0 & 0 & 0 \\ 0 & 0 & 0 & \dfrac{1}{G_{xy}} & 0 & 0 \\ 0 & 0 & 0 & 0 & \dfrac{1}{G_{xz}} & 0 \\ 0 & 0 & 0 & 0 & 0 & \dfrac{1}{G_{yz}} \end{bmatrix} . \tag{2.53}$$

Symmetry conditions, Eqs. (2.50), reduce to

$$\nu_{xy}E_y = \nu_{yx}E_x, \quad \nu_{xz}E_x = \nu_{zx}E_z, \quad \nu_{yz}E_y = \nu_{zy}E_z \ .$$

These equations have a simple physical meaning. The higher the stiffness is, demonstrated by the material in some direction, the less is the strain in this direction under loading in the orthogonal directions. Taking into account the foregoing symmetry conditions we can conclude that an orthotropic material is characterized with nine independent elastic constants.

The simplest material model corresponds to the isotropic material, whose mechanical properties are the same for any direction or plane of loading. As a result, subscripts indicating coordinate directions and planes in Eq. (2.53) disappear, and it reduces to

$$[C] = \begin{bmatrix} \frac{1}{E} & -\frac{\nu}{E} & -\frac{\nu}{E} & 0 & 0 & 0 \\ -\frac{\nu}{E} & \frac{1}{E} & -\frac{\nu}{E} & 0 & 0 & 0 \\ -\frac{\nu}{E} & -\frac{\nu}{E} & \frac{1}{E} & 0 & 0 & 0 \\ 0 & 0 & 0 & \frac{1}{G} & 0 & 0 \\ 0 & 0 & 0 & 0 & \frac{1}{G} & 0 \\ 0 & 0 & 0 & 0 & 0 & \frac{1}{G} \end{bmatrix} . \tag{2.54}$$

Compliance matrix, Eq. (2.54), contains three elastic constants, E, G, and ν. However, only two of them are independent. To show this, consider the problem of pure shear for a plate discussed in Section 2.4 (see Fig. 2.5). For this problem, $\sigma_x = \sigma_y = \sigma_z = \tau_{xz} = \tau_{yz} = 0$, $\tau_{xy} = \tau$ and Eqs. (2.48) and (2.54) yield

$$\gamma_{xy} = \frac{\tau}{G} \ .$$

Specific strain energy in Eq. (2.51) can be written as

$$U = \frac{1}{2}\tau_{xy}\gamma_{xy} = \frac{1}{2G}\tau^2 \ . \tag{2.55}$$

However, as follows from Section 2.4, pure shear can be reduced to tension and compression in the principal directions (see Fig. 2.5). For these directions, Eqs. (2.48) and (2.54) give

$$\varepsilon_1 = \frac{\sigma_1}{E} - \nu\frac{\sigma_3}{E}, \quad \varepsilon_3 = \frac{\sigma_3}{E} - \nu\frac{\sigma_1}{E} \ .$$

Here $\sigma_1 = \tau$, $\sigma_3 = -\tau$ and all the other stresses are equal to zero. The strain energy, Eq. (2.51), can be presented now in the following form

$$U = \frac{1}{2}(\sigma_1 \varepsilon_1 + \sigma_3 \varepsilon_3) = \frac{1+\nu}{E}\tau^2 \quad . \tag{2.56}$$

Because Eqs. (2.55) and (2.56) specify one and the same quantity, we get

$$G = \frac{E}{2(1+\nu)} \quad . \tag{2.57}$$

Thus, an isotropic material is characterized within the linear elastic model by two independent elastic constants – E and ν.

2.10. Formulations of the problem

The problem of Solid Mechanics is reduced, as follows from the foregoing derivation, to a set of 15 equations, i.e., three equilibrium equations, Eqs. (2.5), six strain–displacement equations, Eqs. (2.22), and six constitutive equations, Eq. (2.46) or (2.48). This set of equations is complete, i.e., it contains 15 unknown functions among which there are six stresses, six strains, and three displacements. Solution of a particular problem should satisfy three boundary conditions that can be written at any point of the body surface. Static or force boundary conditions have the form of Eqs. (2.2), while kinematic or displacement boundary conditions are imposed on three displacement functions.

There exist two classical formulations of the problem – displacement formulation and stress formulation.

According to displacement formulation, we first determine displacements u_x, u_y, and u_z from three equilibrium equations, Eqs. (2.5), written in terms of displacements with the aid of constitutive equations, Eq. (2.46), and strain–displacement equations, Eqs. (2.22). Having found displacements we use Eqs. (2.22) and (2.46) to determine strains and stresses.

Stress formulation is much less straightforward than the displacement one. Indeed, we have only three equilibrium equations, Eqs. (2.5), for six stresses which means that the problem of solid mechanics is not, in general, a statically determinate problem. All possible solutions of the equilibrium equations (obviously, there is an infinite number of them because the number of equations is less than the number of unknown stresses) satisfying force boundary conditions (solutions that do not satisfy them, obviously, do not belong to the problem under study) comprise the class of statically admissible stress fields (see Section 2.8). Assume that we have one of these stress fields. Now, we can readily find strains using constitutive equations, Eq. (2.48), but to determine displacements, we need to integrate a set of six strain–displacement equations, Eqs. (2.22) which having only three unknown displacements are, in general, not compatible. As shown in Section 2.7, this set can be

integrated if strains satisfy six compatibility equations, Eqs. (2.35). We can write these equations in terms of stresses using constitutive equations, Eq. (2.48). Thus, the stress formulation of the problem is reduced to a set of nine equations consisting of three equilibrium equations and six compatibility equations in terms of stresses. At first glance it looks like this set is not consistent because it includes only six unknown stresses. However, this is not the case because of special properties of compatibility equations. As was noted in Section 2.7, these equations provide the existence of Euclidean space inside the deformed body. But this space automatically exists if strains can be expressed in terms of three continuous displacements as in Eqs. (2.22). Indeed, substituting strains, Eqs. (2.22), into compatibility equations, Eqs. (2.35), we can readily see that they are identically satisfied for any three functions u_x, u_y, and u_z. This means that the solution of six Eqs. (2.35) including six strains is not unique. The uniqueness is ensured by three equilibrium equations.

2.11. Variational principles

Equations of Solid Mechanics considered in the previous sections can be also derived from variational principles that establish the energy criteria according to which the actual state of the body under loading can be singled out of a system of admissible states (see Section 2.8).

Consider a linear elastic solid and introduce two mutually independent fields of variables: statically admissible stress field σ'_x, σ'_y, σ'_z, τ'_{xy}, τ'_{xz}, τ'_{yz} and kinematically admissible field characterized by displacements u''_x, u''_y, u''_z and corresponding strains ε''_x, ε''_y, ε''_z, γ''_{xy}, γ''_{xz}, γ''_{yz}. To construct the energy criteria allowing us to distinguish the actual variables from admissible ones, consider the following integral similar to the energy integral in Eqs. (2.51) and (2.52)

$$I = \iiint_V (\sigma'_x\varepsilon''_x + \sigma'_y\varepsilon''_y + \sigma'_z\varepsilon''_z + \tau'_{xy}\gamma''_{xy} + \tau'_{xz}\gamma''_{xz} + \tau'_{yz}\gamma''_{yz})\mathrm{d}V \ . \tag{2.58}$$

Here, in accordance with the definition of a kinematically admissible field (see Section 2.8),

$$\varepsilon''_x = \frac{\partial u''_x}{\partial x}, \quad \gamma''_{xy} = \frac{\partial u''_x}{\partial y} + \frac{\partial u''_y}{\partial x} \quad (x,y,z) \ . \tag{2.59}$$

Substituting Eqs. (2.59) into Eq. (2.58) and using the following evident relationships between the derivatives

$$\sigma'_x \frac{\partial u''_x}{\partial x} = \frac{\partial}{\partial x}(\sigma'_x u''_x) - u''_x \frac{\partial \sigma'_x}{\partial x}, \quad \tau'_{xy} \frac{\partial u''_x}{\partial y} = \frac{\partial}{\partial y}(\tau'_{xy} u''_x) - u''_x \frac{\partial \tau'_{xy}}{\partial y} \text{ etc.} \ ,$$

we arrive at

$$I = \iiint_V \left[\frac{\partial}{\partial x}(\sigma'_x u''_x + \tau'_{xy} u''_y + \tau'_{xz} u''_z) + \frac{\partial}{\partial y}(\tau'_{xy} u''_x + \sigma'_y u''_y + \tau'_{yz} u''_z) \right.$$
$$+ \frac{\partial}{\partial z}(\tau'_{xz} u''_x + \tau'_{yz} u''_y + \sigma'_z u''_z) - \left(\frac{\partial \sigma'_x}{\partial x} + \frac{\partial \tau'_{xy}}{\partial y} + \frac{\partial \tau'_{xz}}{\partial z} \right) u''_x$$
$$\left. - \left(\frac{\partial \sigma'_y}{\partial y} + \frac{\partial \tau'_{xy}}{\partial x} + \frac{\partial \tau'_{yz}}{\partial z} \right) u''_y - \left(\frac{\partial \sigma'_z}{\partial z} + \frac{\partial \tau'_{xz}}{\partial x} + \frac{\partial \tau'_{yz}}{\partial y} \right) u''_z \right] \mathrm{d}V \ . \qquad (2.60)$$

Applying now Green's integral transformation, Eq. (2.4), to the first three terms under the integral and taking into account that statically admissible stresses should satisfy equilibrium equations, Eqs. (2.5), (2.6), and force boundary conditions, Eqs. (2.2), we obtain from Eqs. (2.58) and (2.60)

$$\iiint_V (\sigma'_x \varepsilon''_x + \sigma'_y \varepsilon''_y + \sigma'_z \varepsilon''_z + \tau'_{xy} \gamma''_{xy} + \tau'_{xz} \gamma''_{xz} + \tau'_{yz} \gamma''_{yz}) \mathrm{d}V$$
$$= \iint_S (p_x u''_x + p_y u''_y + p_z u''_z) \mathrm{d}S + \iiint_V (q_x u''_x + q_y u''_y + q_z u''_z) \mathrm{d}V \ . \qquad (2.61)$$

For actual stresses, strains and displacements, Eq. (2.61) reduces to the following equation

$$\iiint_V (\sigma_x \varepsilon_x + \sigma_y \varepsilon_y + \sigma_z \varepsilon_z + \tau_{xy} \gamma_{xy} + \tau_{xz} \gamma_{xz} + \tau_{yz} \gamma_{yz}) \mathrm{d}V$$
$$= \iint_S (p_x u_x + p_y u_y + p_z u_z) \mathrm{d}S + \iiint_V (q_x u_x + q_y u_y + q_z u_z) \mathrm{d}V \qquad (2.62)$$

known as Clapeyron's theorem.

2.11.1. Principle of minimum total potential energy

This principle allows us to distinguish the actual displacement field of the body from kinematically admissible fields. To derive it, assume that the stresses in Eq. (2.61) are actual stresses, i.e., $\sigma' = \sigma$, $\tau' = \tau$, while the displacements and the corresponding strains differ from the actual values by small kinematically admissible variations, i.e., $u'' = u + \delta u$, $\varepsilon'' = \varepsilon + \delta\varepsilon$, $\gamma'' = \gamma + \delta\gamma$. Substituting these expressions into Eq. (2.61) and subtracting Eq. (2.62) from the resulting equation we arrive at

$$\iiint_V (\sigma_x \delta\varepsilon_x + \sigma_y \delta\varepsilon_y + \sigma_z \delta\varepsilon_z + \tau_{xy} \delta\gamma_{xy} + \tau_{xz} \delta\gamma_{xz} + \tau_{yz} \delta\gamma_{yz}) \mathrm{d}V$$

$$= \iint_S (p_x \delta u_x + p_y \delta u_y + p_z \delta u_z) \mathrm{d}S + \iiint_V (q_x \delta u_x + q_y \delta u_y + q_z \delta u_z) \mathrm{d}V \ .$$

Assume that under small variation of displacements and strains belonging to the kinematically admissible fields surface tractions and body forces do not change. Then, we can write the foregoing result in the following form

$$\delta W_i - \delta A = 0 \ . \tag{2.63}$$

Here

$$\delta W_i = \iiint_V (\sigma_x \delta\varepsilon_x + \sigma_y \delta\varepsilon_y + \sigma_z \delta\varepsilon_z + \tau_{xy} \delta\gamma_{xy} + \tau_{xz} \delta\gamma_{xz} + \tau_{yz} \delta\gamma_{yz}) \mathrm{d}V \tag{2.64}$$

is the variation of the strain energy (internal potential energy of an elastic solid) associated with small kinematically admissible variations of strains and

$$A = \iint_S (p_x u_x + p_y u_y + p_z u_z) \mathrm{d}S + \iiint_V (q_x u_x + q_y u_y + q_z u_z) \mathrm{d}V \tag{2.65}$$

can be formally treated as work performed by surface tractions and body forces on the actual displacements. Expressing stresses in Eq. (2.64) in terms of strains with the aid of constitutive equations, Eq. (2.46), and integrating, we can determine W_i which is the body strain energy written in terms of strains. Quantity $T = W_i - A$ is referred to as the total potential energy of the body. This name historically came from problems in which external forces had a potential function $F = -A$ so that $T = W_i + F$ was the sum of internal and external potentials, i.e. the total potential function. Then, condition in Eq. (2.63) reduces to

$$\delta T = 0 \tag{2.66}$$

which means that T has a stationary (actually, minimum) value under small admissible variation of displacements in the vicinity of actual displacements. Thus, we arrive at the following variational principle of minimum total potential energy: the actual displacement field, in contrast to all kinematically admissible fields, delivers the minimum value of the body total potential energy. This principle is a variational form of the displacement formulation of the problem discussed in Section 2.10. As can be shown, variational equations ensuring the minimum value of the total potential energy of the body coincide with equilibrium equations written in terms of displacements.

2.11.2. Principle of minimum strain energy

This principle is valid for a linear elastic body and establishes the criterion according to which the actual stress field can be singled out of all statically admissible fields. Assume that displacements and strains in Eq. (2.61) are actual, i.e. $u'' = u$, $\varepsilon'' = \varepsilon$, $\gamma'' = \gamma$, while stresses differ from the actual values by small statically admissible variations, i.e., $\sigma' = \sigma + \delta\sigma$, $\tau' = \tau + \delta\tau$. Substituting these expressions in Eq. (2.61) and subtracting Eq. (2.62) for the actual state we get

$$\delta W_\sigma = 0 \ , \tag{2.67}$$

where

$$\delta W_\sigma = \iiint_V (\varepsilon_x \delta\sigma_x + \varepsilon_y \delta\sigma_y + \varepsilon_z \delta\sigma_z + \gamma_{xy}\delta\tau_{xy} + \gamma_{xz}\delta\tau_{xz} + \gamma_{yz}\delta\tau_{yz})\mathrm{d}V \tag{2.68}$$

is the variation of the strain energy associated with variation of stresses. Expressing strains in terms of stresses with the aid of constitutive equations, Eq. (2.48), and integrating, we can determine W_σ, which is the body strain energy written in terms of stresses. As earlier, Eq. (2.67) indicates that strain energy, W_σ, has a stationary (in fact, minimum) value under admissible variation of stresses. As a result we arrive at the following variational principle of minimum strain energy: the actual stress field, in contrast to all statically admissible fields, delivers the minimum value of the body strain energy. This principle is a variational form of the stress formulation of the problem considered in Section 2.10. As can be shown, variational equations providing the minimum value of the strain energy are compatibility equations written in terms of stresses. It is important that stress variation in Eq. (2.68) should be performed within the statically admissible field, i.e., within stresses that satisfy equilibrium equations and force boundary conditions.

2.11.3. Mixed variational principles

Two variational principles described above imply variations with respect to displacements only or to stresses only. There exist also the so-called mixed variational principles in which variation is performed with respect to both kinematic and static variables. The first principle from this group follows from the principle of minimum total potential energy considered in Section 2.11.1. Let us expand the class of admissible kinematic variables and introduce displacements that are continuous functions satisfying displacement boundary conditions and strains that are not linked with these displacements by strain–displacement equations, Eqs. (2.22). Then we can apply the principle of minimum total potential energy performing a conditional minimization of the total potential energy and introduce Eqs. (2.22) as additional constraints imposed on strains and displacements with the aid of Lagrange's multipliers. Using stresses as these multipliers we can construct the following augmented functional

$$T_L = W_c - A + \iiint_V \left[\sigma_x\left(\frac{\partial u_x}{\partial x} - \varepsilon_x\right) + \sigma_y\left(\frac{\partial u_y}{\partial y} - \varepsilon_y\right) + \sigma_z\left(\frac{\partial u_z}{\partial z} - \varepsilon_z\right)\right.$$
$$+ \tau_{xy}\left(\frac{\partial u_x}{\partial y} + \frac{\partial u_y}{\partial x} - \gamma_{xy}\right) + \tau_{xz}\left(\frac{\partial u_x}{\partial z} + \frac{\partial u_z}{\partial x} - \gamma_{xz}\right)$$
$$\left. + \tau_{yz}\left(\frac{\partial u_y}{\partial z} + \frac{\partial u_z}{\partial y} - \gamma_{yz}\right)\right] dV \ .$$

According to the initial principle, Eq. (2.66), $\delta T_L = 0$. Variation of displacements yields, as earlier equilibrium equations, variation of stresses results in strain–displacement equations, and variation of strains gives constitutive equations (W_c should be expressed in terms of strains).

The second form of the mixed variational principle can be derived from the principle of minimum strain energy discussed in Section 2.11.2. Again expand the class of admissible static fields and introduce stresses that satisfy force boundary conditions but are not linked with equilibrium equations, Eqs. (2.5). Then we can apply the principle of minimum strain energy if we construct an augmented functional adding Eqs. (2.5) as additional constraints. Using displacements as Lagrange's multipliers we obtain

$$W_L = W_\sigma + \iiint_V \left[u_x\left(\frac{\partial \sigma_x}{\partial x} + \frac{\partial \tau_{xy}}{\partial y} + \frac{\partial \tau_{xz}}{\partial z} + q_x\right) + u_y\left(\frac{\partial \sigma_y}{\partial y} + \frac{\partial \tau_{xy}}{\partial x} + \frac{\partial \tau_{yz}}{\partial z} + q_y\right)\right.$$
$$\left. + u_z\left(\frac{\partial \sigma_z}{\partial z} + \frac{\partial \tau_{xz}}{\partial x} + \frac{\partial \tau_{yz}}{\partial y} + q_z\right)\right] dV \ .$$

According to the original principle, Eq. (2.67), $\delta W_L = 0$. Variation with respect to stresses (W_σ should be expressed in terms of stresses) yields constitutive equations in which strains are expressed in terms of displacements via strain–displacement equations, Eqs. (2.22), while variation of displacements gives equilibrium equations.

Equations and principles considered in this chapter will be used in the following chapters of the book for analysis of composite materials.

2.12. References

Vasiliev, V.V. and Gurdal, Z. (1999). Optimal structural design. In *Optimal Design* (V.V. Vasiliev and Z. Gurdal eds.). Technomic, Lancaster, pp. 1–29.

Chapter 3

MECHANICS OF A UNIDIRECTIONAL PLY

Ply or lamina is the simplest element of a composite material, an elementary layer of unidirectional fibers in a matrix (see Fig. 3.1) formed while a unidirectional tape impregnated with resin is placed on the surface of the tool providing the shape of a composite part.

3.1. Ply architecture

As the tape consists of tows (bundles of fibers), the ply thickness (whose minimum value is about 0.1 mm for modern composites) is much higher than the fiber diameter (about 0.01 mm). In an actual ply, the fibers are randomly distributed as in Fig. 3.2. Because the actual distribution is not known and can hardly be predicted, some typical idealized regular distributions, i.e., square (Fig. 3.3), hexagonal (Fig. 3.4), and layer-wise (Fig. 3.5) are used for the analysis.

Composite ply consists of two constituents: fibers and matrix whose quantities in the materials are specified by volume, v, and mass, m, fractions

$$v_f = \frac{V_f}{V_c}, \quad v_m = \frac{V_m}{V_c} \ , \tag{3.1}$$

$$m_f = \frac{M_f}{M_c}, \quad m_m = \frac{M_m}{M_c} \ . \tag{3.2}$$

Here, V and M are volume and mass, while subscripts "f", "m", and "c" correspond to fibers, matrix, and composite material, respectively. Because $V_c = V_f + V_m$ and $M_c = M_f + M_m$, we have

$$v_f + v_m = 1, \quad m_f + m_m = 1 \ . \tag{3.3}$$

There exist the following relationships between volume and mass fractions

$$v_f = \frac{\rho_c}{\rho_f} m_f, \quad v_m = \frac{\rho_c}{\rho_m} m_m \ , \tag{3.4}$$

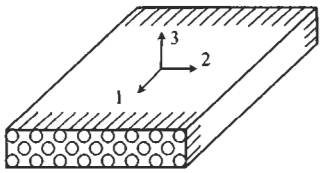

Fig. 3.1. A unidirectional ply.

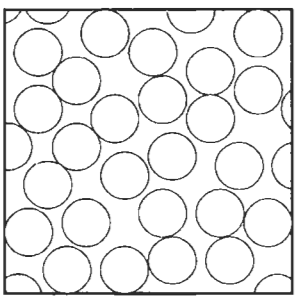

Fig. 3.2. Actual fiber distribution in the cross-section of a ply ($v_f = 0.65$).

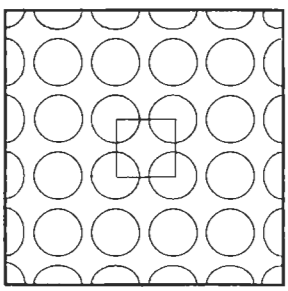

Fig. 3.3. Square fiber distribution in the cross-section of a ply ($v_f = 0.65$).

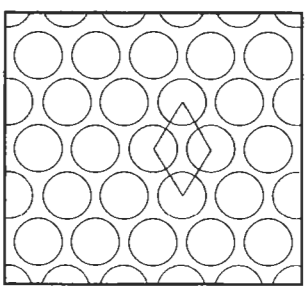

Fig. 3.4. Hexagonal fiber distribution in the cross-section of a ply ($v_f = 0.65$).

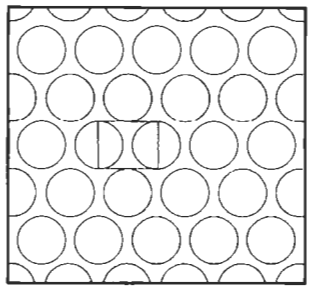

Fig. 3.5. Layer-wise fiber distribution in the cross-section of a ply ($v_f = 0.65$).

where ρ_f, ρ_m, and ρ_c are densities of fibers, matrix, and composite. In analysis, volume fractions are used because they enter the stiffness coefficients for a ply, while mass fractions are usually measured directly during processing or experimental study of the fabricated material.

Two typical situations usually occur. First situation implies that we know the mass of fibers used to fabricate a composite part and the mass of the part itself. The mass of fibers can be found if we weigh the spools with fibers before and after they are used or calculate the total length of tows and multiply it by the tow tex-number that is the mass in grams of 1000 m long tow. So, we know the values of M_f and M_c and can use the first equations of Eqs. (3.2) and (3.4) to calculate v_f.

The second situation takes place if we have a sample of a composite material and know the densities of the fibers and the matrix used for its fabrication. Then, we can find the experimental value of material density, ρ_c^e, and use the following equation for theoretical density

$$\rho_c = \rho_f v_f + \rho_m v_m \quad . \tag{3.5}$$

Putting $\rho_c = \rho_c^e$ and taking into account Eqs. (3.3) we obtain

$$v_f = \frac{\rho_c^e - \rho_m}{\rho_f - \rho_m} \quad . \tag{3.6}$$

Consider for example carbon–epoxy composite material with fibers *AS4* and matrix EPON DPL-862 for which $\rho_f = 1.79$ g/cm^3, $\rho_m = 1.2$ g/cm^3. Let $\rho_c^e = 1.56$ g/cm^3. Then, Eq. (3.6) yields $v_f = 0.61$.

This result is approximate because it ignores possible material porosity. To determine the actual fiber fraction we should remove resin using matrix destruction, solvent extraction, or burning the resin out in an oven. As a result, we get M_f and having M_c can calculate m_f and v_f with the aid of Eqs. (3.2) and (3.4). Then we find ρ_c using Eq. (3.5) and compare it with ρ_c^e. If $\rho_c > \rho_c^e$, material includes voids whose volume fraction (porosity) can be calculated using the following equation

$$v_p = 1 - \frac{\rho_c^e}{\rho_c} \quad . \tag{3.7}$$

For the carbon–epoxy composite material considered above as an example, assume that the foregoing procedure results in $m_f = 0.72$. Then, Eqs. (3.4), (3.5), and (3.7) give $v_f = 0.63$, $\rho_c = 1.58$ g/cm^3, and $v_p = 0.013$.

For real composite materials, we normally have $v_f = 0.50$–0.65. Lower fiber volume content results in lower ply strength and stiffness under tension along the fibers, while higher fiber content, close to the ultimate value, leads to reduction of the ply strength under longitudinal compression and in-plane shear due to poor bonding of the fibers.

Since the fibers have circular cross-sections, there exists the ultimate fiber volume fraction, v_f^u which is less than unity and depends on the fiber arrangement. For typical arrangements shown in Figs. 3.3–3.5, ultimate arrays are presented in Fig. 3.6, and the corresponding ultimate fiber volume fractions are

$$\text{square array} \quad v_f^u = \frac{1}{d^2}\left(\frac{\pi d^2}{4}\right) = \frac{\pi}{4} = 0.785,$$

$$\text{hexagonal array} \quad v_f^u = \frac{2}{d^2\sqrt{3}}\left(\frac{\pi d^2}{4}\right) = \frac{\pi}{2\sqrt{3}} = 0.907,$$

$$\text{layer-wise array} \quad v_f^u = \frac{1}{d^2}\left(\frac{\pi d^2}{4}\right) = \frac{\pi}{4} = 0.785 \ .$$

3.2. Fiber–matrix interaction

3.2.1. *Theoretical and actual strength*

The most important property of advanced composite materials is associated with very high strength of a unidirectional ply accompanied with relatively low density. This advantage of the material is provided mainly by fibers. Correspondingly a natural question arises as to how such traditional lightweight materials like glass or graphite that were never applied as primary load-bearing structural materials can

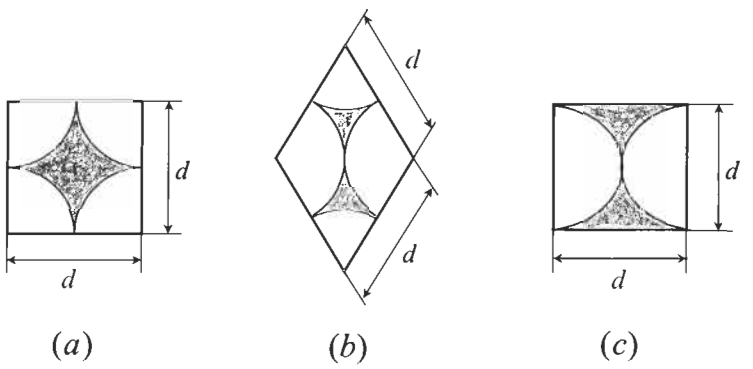

Fig. 3.6. Ultimate fiber arrays for square (a), hexagonal (b), and layer-wise (c) fiber distributions.

be used to make fibers with the strength exceeding the strength of such traditional structural materials as aluminum or steel (see Table 1.1). The general answer is well known: strength of a thin wire is usually much higher than the strength of the corresponding bulk material. This is demonstrated in Fig. 3.7 showing that the wire strength increases while the wire diameter is reduced.

In connection with this, two questions arise. First, what is the upper limit of strength that can be predicted for an infinitely thin wire or fiber? And second, what is the nature of this phenomenon?

The answer for the first question is given in Physics of Solids. Consider an idealized model of a solid, namely a regular system of atoms located as shown in Fig. 3.8 and find the stress, σ, that destroys this system. Dependence of σ on the atomic spacing following from Physics of Solids is presented in Fig. 3.9. Point O of the curve corresponds to the equilibrium of the unloaded system, while point U specifies the ultimate theoretical stress, $\bar{\sigma}_1$. Initial tangent angle, α, characterizes material modulus of elasticity, E. To evaluate $\bar{\sigma}_1$, we can use the following sine approximation (Gilman, 1959) for OU segment of the curve

$$\sigma = \bar{\sigma}_1 \sin 2\pi \frac{a - a_0}{a_0} \quad .$$

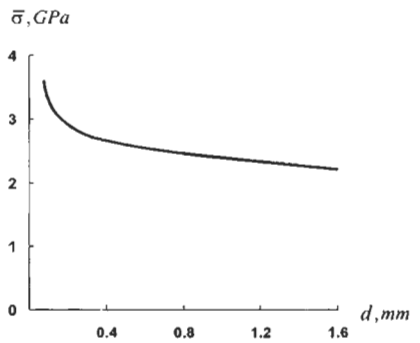

Fig. 3.7. Dependence of high-carbon steel wire strength on the wire diameter.

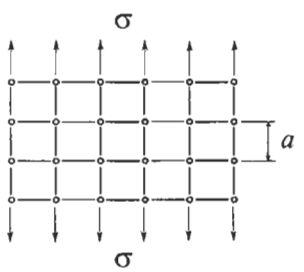

Fig. 3.8. Material model.

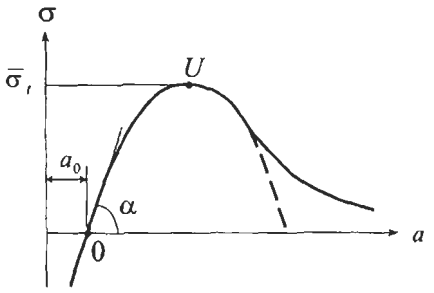

Fig. 3.9. Atoms' interaction curve (———) and its sine approximation (– – – –).

Introducing strain

$$\varepsilon = \frac{a - a_0}{a_0}$$

we arrive at

$$\sigma = \bar{\sigma}_t \sin 2\pi\varepsilon \ .$$

Now, we can calculate modulus as

$$E = \left(\frac{\mathrm{d}\sigma}{\mathrm{d}\varepsilon}\right)\Big|_{\varepsilon=0} = 2\pi\bar{\sigma}_t \ .$$

Thus

$$\bar{\sigma}_t = \frac{E}{2\pi} \ . \tag{3.8}$$

This equation yields a very high value for the theoretical strength. For example, for a steel wire, $\bar{\sigma}_t = 33.4$ GPa. By now the highest strength reached in 2 μm diameter monocrystals of iron (whiskers) is about 12 GPa.

The model under study allows us to introduce another important characteristic of the material. The specific energy that should be spent to destroy the material can be presented in accordance with Fig. 3.9 as

$$2\gamma = \int_{a_0}^{\infty} \sigma(a)\mathrm{d}a \ . \tag{3.9}$$

As material fracture results in formation of two new free surfaces, γ can be referred to as specific surface energy (energy spent to form the surface of unit area).

The answer for the second question (why the fibers are stronger than the corresponding bulk materials) was in fact given by Griffith (1920) whose results have formed the basis of Fracture Mechanics.

Consider a fiber loaded in tension and having a thin circumferential crack as shown in Fig. 3.10. The crack length, l, is much less than the fiber diameter, d.

For a linear elastic fiber, $\sigma = E\varepsilon$, and the elastic potential in Eq. (2.51) can be presented as

$$U = \frac{1}{2}\sigma\varepsilon = \frac{\sigma^2}{2E} \ .$$

When the crack appears, the strain energy is released in a material volume adjacent to the crack. Assume that this volume is comprised by conical ring whose generating lines are shown in Fig. 3.10 by broken lines and heights are proportional to the crack length, l. Then, the total released energy, Eq. (2.52), is

$$W = \frac{1}{2}k\pi\frac{\sigma^2}{E}l^2 d \ , \tag{3.10}$$

where k is some constant coefficient of proportionality. On the other hand, formation of new surfaces consumes the energy

$$S = 2\pi\gamma ld \ , \tag{3.11}$$

where γ is the surface energy, Eq. (3.9). Now assume that the crack length is increased by an infinitesimal increment, dl. Then, if for some value of acting stress, σ

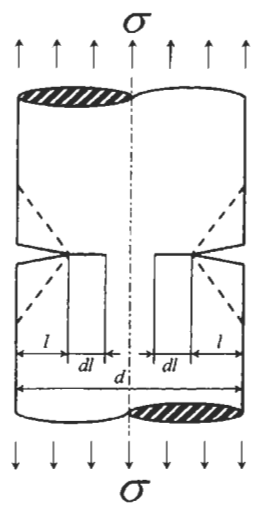

Fig. 3.10. A fiber with a crack.

$$\frac{dW}{dl} > \frac{dS}{dl} \tag{3.12}$$

the crack will propagate, and the fiber will fail. Substituting Eqs. (3.10) and (3.11) into inequality (3.12) we arrive at

$$\sigma > \bar{\sigma}_c = \sqrt{\frac{2\gamma E}{kl}} \,. \tag{3.13}$$

The most important result that follows from this condition specifying some critical stress, σ_c, beyond which the fiber with a crack cannot exist is the fact that $\bar{\sigma}_c$ depends on the absolute value of the crack length (not on the ratio l/d). But for a continuous fiber, $2l < d$ so, the thinner the fiber, the less is the length of the crack that can exist in this fiber and the higher is the critical stress, $\bar{\sigma}_c$. More rigorous analysis shows that reducing l to a in Fig. 3.8 we arrive at $\bar{\sigma}_c = \bar{\sigma}_t$.

Consider for example glass fibers that are widely used as reinforcing elements in composite materials and have been studied experimentally to support the fundamentals of Fracture Mechanics (Griffith, 1920). Theoretical strength of glass, Eq. (3.8), is about 14 GPa, while the actual strength of 1 mm diameter glass fibers is only about 0.2 GPa, and for 5 mm diameter fibers this value is much lower (about 0.05 GPa). The fact that such low actual strength is caused by surface cracks can be readily proved if the fiber surface is smoothed by etching the fiber with acid. Then, the strength of 5 mm diameter fibers can be increased up to 2 GPa. If the fiber diameter is reduced with heating and stretching fibers to a diameter about 0.0025 mm, the strength rises up to 6 GPa. Theoretical extrapolation of the experimental curve, showing dependence of the fiber strength on the fiber diameter for very small fiber diameters, yields $\bar{\sigma} = 11$ GPa, which is close to $\bar{\sigma}_t = 14$ GPa.

Thus, we arrive at the following conclusion clearing out the nature of high performance of advanced composites and their place among the modern structural materials.

Actual strength of advanced structural materials is much lower than their theoretical strength. This difference is caused by defects of material microstructure (e.g., crystalline structure) or microcracks inside the material and on its surface. Using thin fibers we reduce the influence of cracks and thus increase the strength of materials reinforced with these fibers. So, advanced composites comprise a special class of structural materials in which we try to utilize the natural potential properties of the material rather than the possibilities of technology as we do developing high-strength alloys.

3.2.2. Statistical aspects of fiber strength

Fiber strength, being relatively high, is still less than the corresponding theoretical strength which means that fibers of advanced composites have microcracks or other

defects randomly distributed along the fiber length. This is supported by the fact that fiber strength depends on the length of the tested fiber. Dependence of strength on the length for boron fibers (Mikelsons and Gutans, 1984) is shown in Fig. 3.11. The longer the fiber, the higher is the probability of a dangerous defect to exist within this length, and the lower is the fiber strength. Tension of fiber segments with the same length but taken from different parts of a long continuous fiber or from different fibers also demonstrates the strength deviation. Typical strength distribution for boron fibers is presented in Fig. 3.12.

The first important characteristic of the strength deviation is the strength scatter $\Delta\bar{\sigma} = \bar{\sigma}_{\max} - \bar{\sigma}_{\min}$. For the case corresponding to Fig. 3.12, $\bar{\sigma}_{\max} = 4.2$ GPa, $\bar{\sigma}_{\min} = 2$ GPa, and $\Delta\bar{\sigma} = 2.2$ GPa. To plot the diagram presented in Fig. 3.12, $\Delta\bar{\sigma}$ is divided into a set of increments, and a normalized number of fibers $n = N_\sigma/N$ (N_σ is the number of fibers failed under the stress within the increments, and N is the total number of tested fibers) is calculated and shown on the vertical axis. Thus, the so-called frequency histogram can be plotted. This histogram allows us to determine the mean value of the fiber strength as

$$\bar{\sigma}_{\mathrm{m}} = \frac{1}{N}\sum_{i=1}^{N}\bar{\sigma}_i \tag{3.14}$$

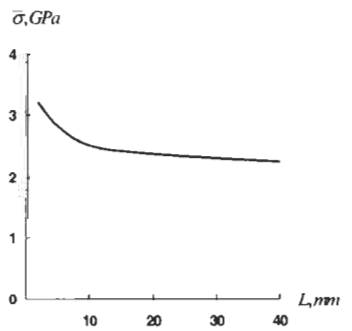

Fig. 3.11. Dependence of strength of boron fibers on the fiber length.

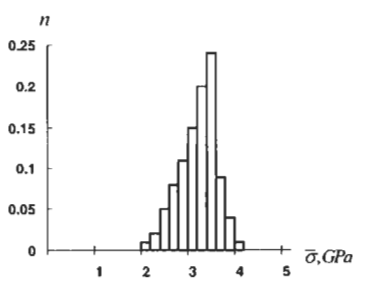

Fig. 3.12. Strength distribution for boron fibers.

and the strength dispersion as

$$d_\sigma = \sqrt{\frac{1}{N-1}\sum_{i=1}^{N}(\bar{\sigma}_m - \sigma_i)^2} \ . \tag{3.15}$$

The deviation of fiber strength is characterized with the coefficient of the strength variation which is presented as follows

$$r_\sigma = \frac{d_\sigma}{\bar{\sigma}_m} 100\% \ . \tag{3.16}$$

For boron fibers under consideration, Eqs. (3.14)–(3.16) yield $\bar{\sigma}_m = 3.2$ GPa, $d_\sigma = 0.4$ GPa, $r_\sigma = 12.5\%$.

To demonstrate the influence of fiber strength deviation on the strength of a unidirectional ply, consider a bundle of fibers, i.e., a system of approximately parallel fibers with different strength and slightly different lengths as in Fig. 3.13. Typical stress–strain diagrams for fibers tested under tension in a bundle are shown in Fig. 3.14 (Vasiliev and Tarnopol'skii, 1990). As can be seen, the diagrams have two nonlinear segments. Nonlinearity in the vicinity of zero stresses is associated with different lengths of fibers in the bundles, while nonlinear behavior of the bundle under stresses close to the ultimate values is caused by fracture of fibers with lower strength.

Useful qualitative results can be obtained if we consider model bundles consisting of five fibers with different strength. Five such bundles are presented in Table 3.1 showing the normalized strength of each fiber. As can be seen, the deviation of fiber strength is such that the mean strength, $\bar{\sigma}_m = 1$, is the same for all the bundles, while the variation coefficient, r_σ, changes from 31.6% for bundle No. 1 to zero for bundle No. 5. The last row in the table shows the effective (observed) ultimate force, $\bar{F}$, for a bundle. Consider, for example, the first bundle. When the force rises up to $F = 3$,

Table 3.1
Strength of bundles consisting of fibers with different strength.

Fiber no.	Bundle no.				
	1	2	3	4	5
1	0.6	0.7	0.85	0.9	1.0
2	0.8	0.9	0.9	0.95	1.0
3	1.0	1.0	1.0	1.0	1.0
4	1.2	1.1	1.1	1.05	1.0
5	1.4	1.3	1.15	1.1	1.0
$\bar{\sigma}_m$	1.0	1.0	1.0	1.0	1.0
r_σ (%)	31.6	22.4	12.8	7.8	0
$\bar{F}$	3.2	3.6	4.25	4.5	5.0

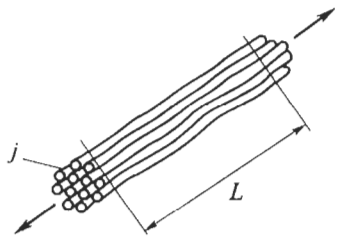

Fig. 3.13. Tension of a bundle of fibers.

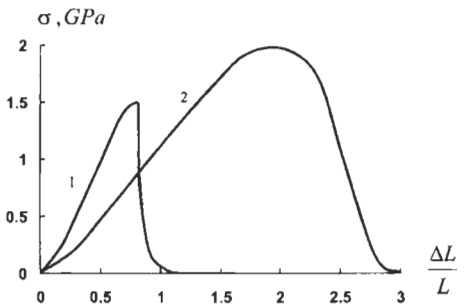

Fig. 3.14. Stress–strain diagrams for bundles of carbon (1) and aramid (2) fibers.

the stresses in all the fibers become $\sigma_j = 0.6$, and fiber No. 1 fails. After this happens, the force, $F = 3$, is taken by four fibers, and $\sigma_j = 0.75$ ($j = 2, 3, 4, 5$). When the force reaches the value $F = 3.2$, the stresses become $\sigma_j = 0.8$, and fiber No. 2 fails. After that, $\sigma_j = 1.07$ ($j = 3, 4, 5$). This means that fiber No. 3 also fails under force $F = 3.2$. Then, for two remaining fibers, $\sigma_4 = \sigma_5 = 1.6$, and they also fail. Thus, $\bar{F} = 3.2$ for bundle No. 1. In a similar way, $\bar{F}$ can be calculated for the other bundles in the table. As can be seen, the lower the fiber strength variation, the higher is $\bar{F}$ which reaches its maximum value, $\bar{F} = 5$, for bundle No. 5 consisting of fibers with the same strength.

Table 3.2 demonstrates that strength variation can be more important than the mean strength. In fact, while the mean strength, $\bar{\sigma}_m$, goes down for bundles No. 1–5, the ultimate force, $\bar{F}$, increases. So, it can be better to have fibers with relatively low strength and low strength variation rather than high strength fibers with high strength variation.

3.2.3. Stress diffusion in fibers interacting through the matrix

The foregoing discussion concerned individual fibers or bundles of fibers that are not joined together. This is not the case for composite materials in which the fibers are embedded in the matrix material. Usually, the stiffness of matrix is much lower than that of fibers (see Table 1.1), and the matrix practically does not take the load applied in the fiber direction. But the fact that the fibers are joined with the matrix even having

Table 3.2
Strength of bundles consisting of fibers with different strength.

Fiber no.	Bundle no.				
	1	2	3	4	5
1	0.6	0.7	0.85	0.9	0.95
2	0.8	0.9	0.9	0.85	0.95
3	1.0	1.2	1.1	1.0	0.95
4	1.6	1.4	1.15	1.05	0.95
5	3.0	1.6	1.4	1.1	0.95
$\bar{\sigma}_m$	1.4	1.16	1.08	1.0	0.95
r_n (%)	95.0	66.0	22.0	7.8	0
$\bar{F}$	3.2	3.6	4.25	4.5	4.75

relatively low stiffness changes the mechanism of fibers interaction and considerably increases their effective strength. To show this, the strength of dry fiber bundles can be compared with the strength of the same bundles after they were impregnated with epoxy resin and cured. The results are listed in Table 3.3. As can be seen, composite bundles in which fibers are joined together with matrix demonstrate significantly higher strength, and the higher the fiber sensitivity to damage, the higher is the difference in strength of dry and composite bundles. The influence of matrix on the variation of strength is even more significant. As follows from Table 3.4, variation coefficients of composite bundles are by an order lower than those of individual fibers.

To clarify the role of matrix in composite materials consider a simple model of a unidirectional ply shown in Fig. 3.15 and apply the method of analysis developed for stringer panels (Goodey, 1946).

Let the ply of thickness δ consist of $2k$ fibers symmetrically distributed on both sides of the central fiber $n = 0$. The fibers are joined with layers of the matrix material, and the fiber volume fraction is

$$v_f = \frac{a_f}{a}, \quad a = a_f + a_m \ . \tag{3.17}$$

Table 3.3
Strength of dry bundles and composite bundles.

Fibers	Sensitivity of fibers to damage	Ultimate tensile load $\bar{F}$ (N)		Strength increase (%)
		Dry bundle	Composite bundle	
Carbon	High	14	26	85.7
Glass	Moderate	21	36	71.4
Aramid	Low	66	84	27.3

Table 3.4
Variation coefficient for fibers and unidirectional composites.

Fibers	Variation coefficient r_x (%)	
	Fibers	Composite
Glass	29	2.0
Carbon	30	4.7
Aramid	24	5.0
Boron	23	3.0

Let the central fiber have a crack induced by the fiber damage or by the shortage of this fiber strength. At a distance from the crack, the fibers are uniformly loaded with stress σ (see Fig. 3.15).

First, derive the set of equations describing the ply under study. Because the stiffness of the matrix is much less than that of fibers, we neglect the stress in the matrix acting in the x-direction and assume that the matrix works only in shear. We also assume that there are no displacements in the y-direction.

Considering equilibrium of the last ($n = k$) fiber, an arbitrary fiber, and the central ($n = 0$) fiber shown in Fig. 3.16 we arrive at the following equilibrium equations

$$\begin{aligned} &a_f\sigma_k' - \tau_k = 0, \\ &a_f\sigma_n' + \tau_{n+1} - \tau_n = 0, \\ &a_f\sigma_0' + 2\tau_1 = 0 \ , \end{aligned} \tag{3.18}$$

where $(\,)' = \mathrm{d}(\,)/\mathrm{d}x$.

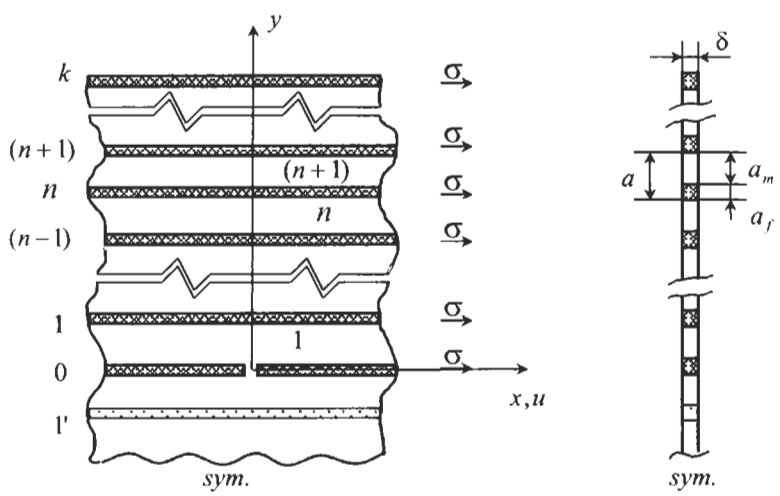

Fig. 3.15. Model of a unidirectional ply with a broken fiber.

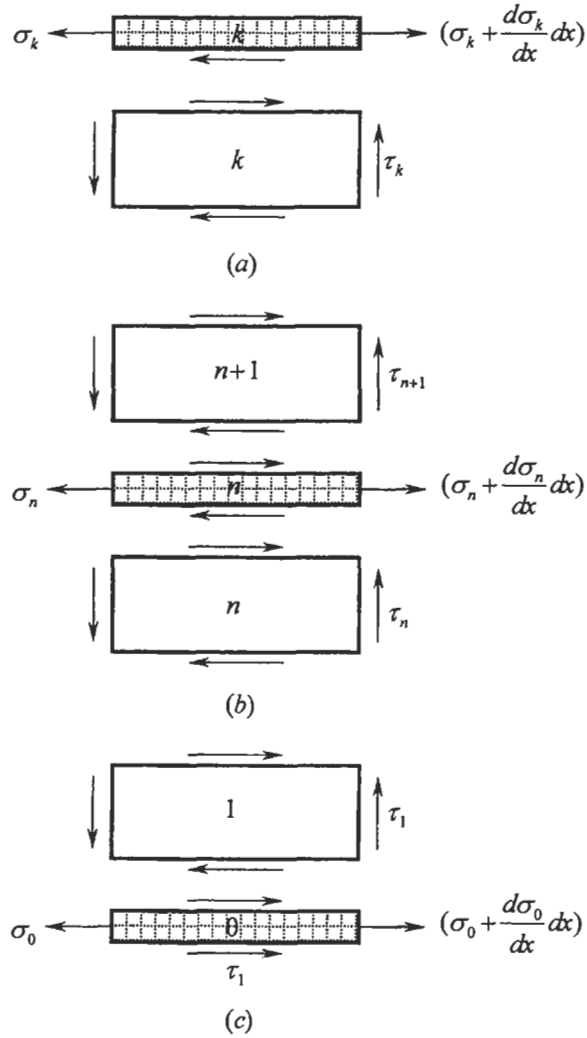

Fig. 3.16. Stresses acting in fibers and matrix layers for the last (a), arbitrary nth fiber (b), and the central $n = 0$ fiber (c).

Constitutive equations for fibers and matrix can be written as

$$\sigma_n = E_f \varepsilon_n, \quad \tau_n = G_m \gamma_n \ . \tag{3.19}$$

Here E_f is the fiber elasticity modulus and G_m is the matrix shear modulus, while

$$\varepsilon_n = u'_n \tag{3.20}$$

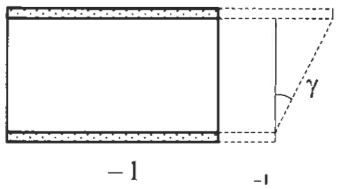

Fig. 3.17. Shear strain in the matrix layer.

is the fiber strain expressed in terms of the displacement in the x-direction. Shear strain in the matrix follows from Fig. 3.17, i.e.,

$$\gamma_n = \frac{1}{a_m}(u_n - u_{n-1}) \ . \tag{3.21}$$

Thus obtained set of equations, Eqs. (3.18)–(3.21) is complete – it includes $10k + 3$ equations and contains the same number of unknown stresses, strains and displacements.

Consider the boundary conditions. If there is no crack in the central fiber, the solution of the problem is evident and has the form $\sigma_n = \sigma$, $\tau_n = 0$. Assuming that the perturbation of the stressed state induced by the crack vanishes at a distance from the crack we arrive at

$$\sigma_n(x \to \infty) = \sigma, \quad \tau_n(x \to \infty) = 0 \ . \tag{3.22}$$

Because of the crack in the central fiber we have

$$\sigma_0(x = 0) = 0 \ . \tag{3.23}$$

For the rest fibers, symmetry conditions yield

$$u_n(x = 0) = 0 \quad (n = 1, 2, 3, \ldots, k) \ . \tag{3.24}$$

To solve the problem, we use the stress formulation and, in accordance with Section 2.10, should consider equilibrium equations in conjunction with compatibility equations expressed in terms of stresses.

First, transform equilibrium equations introducing the stress function, $F(x)$ such that

$$\tau_n = F_n', \quad F_n(x \to \infty) = 0 \ . \tag{3.25}$$

Substituting Eqs. (3.25) into equilibrium equations, Eqs. (3.18), integrating them from x to ∞ and taking into account Eqs. (3.22) and (3.25) we get

$$\sigma_k = \sigma + \frac{1}{a_f} F_k,$$
$$\sigma_n = \sigma - \frac{1}{a_f}(F_{n+1} - F_n), \tag{3.26}$$
$$\sigma_0 = \sigma - \frac{2}{a_f} F_1 \ .$$

Compatibility equations follow from Eqs. (3.20) and (3.21), i.e.,

$$\gamma'_n = \frac{1}{a_m}(\varepsilon_n - \varepsilon_{n-1}) \ .$$

Using constitutive equations, Eqs. (3.19), we can write them in terms of stresses

$$\tau'_n = \frac{G_m}{a_m E_f}(\sigma_n - \sigma_{n-1}) \ .$$

Substituting stresses from Eqs. (3.25), (3.26) and introducing dimensionless coordinate $\bar{x} = x/a$ (see Fig. 3.15) we finally arrive at the following set of governing equations:

$$F''_k - \mu^2(2F_k - F_{k-1}) = 0,$$
$$F''_n + \mu^2(F_{n+1} - 2F_n + F_{n-1}) = 0, \tag{3.27}$$
$$F''_1 + \mu^2(F_2 - 3F_1) = 0 \ ,$$

where in accordance with Eqs. (3.17)

$$\mu^2 = \frac{G_m a^2}{a_f a_m E_f} = \frac{G_m}{v_f(1 - v_f)E_f} \ . \tag{3.28}$$

With due regard to the second equation in Eqs. (3.25) we can take the general solution of Eqs. (3.27) in the form

$$F_n(\bar{x}) = A_n e^{-\lambda \bar{x}} \ . \tag{3.29}$$

Substitution into Eqs. (3.27) yields:

$$A_k\left(2 - \frac{\lambda^2}{\mu^2}\right) - A_{k-1} = 0 \ , \tag{3.30}$$

$$A_{n+1} - A_n\left(2 - \frac{\lambda^2}{\mu^2}\right) + A_{n-1} = 0 \ , \tag{3.31}$$

$$A_2 - A_1\left(3 - \frac{\lambda^2}{\mu^2}\right) = 0 \ . \tag{3.32}$$

Finite-difference equation, (3.31) can be reduced to the following form

$$A_{n+1} - 2A_n \cos\theta + A_{n-1} = 0 \ , \tag{3.33}$$

where

$$\cos\theta = 1 - \frac{\lambda^2}{2\mu^2} \ . \tag{3.34}$$

As can be readily checked the solution for Eq. (3.33) is

$$A_n = B\cos n\theta + C\sin n\theta \tag{3.35}$$

while Eq. (3.34) yields after some transformation

$$\lambda = 2\mu \sin\frac{\theta}{2} \ . \tag{3.36}$$

Substituting the solution, Eq. (3.35), into Eq. (3.30) we obtain after some transformation

$$B = -C\tan(k+1)\theta \ .$$

Thus, Eq. (3.35) can be written as

$$A_n = C[\sin n\theta - \cos n\theta \cdot \tan(k+1)\theta] \ . \tag{3.37}$$

Substituting Eq. (3.37) into Eq. (3.32) and omitting rather cumbersome trigonometric transformations we arrive at the following equation for θ

$$\tan k\theta = -\tan\frac{\theta}{2} \ . \tag{3.38}$$

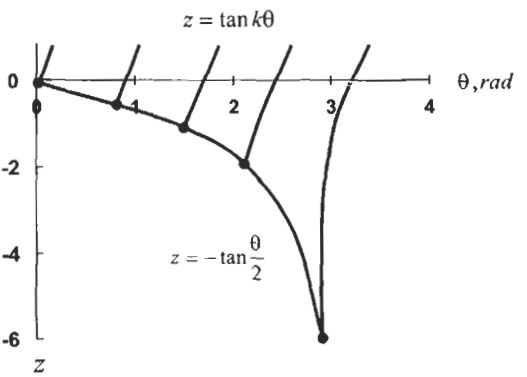

Fig. 3.18. Geometric interpretation of Eq. (3.38) for $k = 4$.

Because of periodic properties of tangent function entering Eq. (3.38), it has $k+1$ different roots corresponding to intersection points of the curves $z = \tan k\theta$ and $z = -\tan\theta/2$. For the case $k = 4$ considered below as an example, these points are shown in Fig. 3.18. Further transformation allows us to reduce Eq. (3.38) to

$$\sin\frac{2k+1}{2}\theta = 0 \ ,$$

from which it follows that

$$\theta_i = \frac{2\pi i}{2k+1} \quad (i = 0, 1, 2, \ldots, k) \ . \tag{3.39}$$

The first root, $\theta_0 = 0$, corresponds to $\lambda = 0$ and $F_n = \text{const}$, i.e., to the ply without a crack in the central fiber. So, Eq. (3.39) specifies k roots ($i = 1, 2, 3, \ldots, k$) for the ply under study, and solution in Eqs. (3.29) and (3.37) can be generalized as

$$F_n(\bar{x}) = \sum_{i=1}^{k} C_i[\sin n\theta_i - \cos n\theta_i \tan(k+1)\theta_i]\, e^{-\lambda_i \bar{x}} \ , \tag{3.40}$$

where, in accordance with Eq. (3.36)

$$\lambda_i = 2\mu \sin\frac{\theta_i}{2} \tag{3.41}$$

and θ_i are determined with Eq. (3.39).

Using Eq. (3.38) we can transform Eq. (3.40) to the following final form

$$F_n(\bar{x}) = \sum_{i=1}^{k} C_i S_n(\theta_i) e^{-\lambda_i \bar{x}} \ , \tag{3.42}$$

where

$$S_n(\theta_i) = \frac{\sin(2n - 1/2)\theta_i}{\cos(\theta_i/2)} \ . \tag{3.43}$$

Applying Eqs. (3.25) and (3.26) we can find shear and normal stresses, i.e.,

$$\tau_n(\bar{x}) = -\frac{1}{a}\sum_{i=1}^{k} \lambda_i C_i S_n(\theta_i) e^{-\lambda_i \bar{x}} \quad (n = 1, 2, 3, \ldots, k) \ , \tag{3.44}$$

$$\sigma_k(\bar{x}) = \sigma + \frac{1}{a_f}\sum_{i=1}^{k} C_i S_k(\theta_i) e^{-\lambda_i \bar{x}} \ , \tag{3.45}$$

$$\sigma_n(\bar{x}) = \sigma - \frac{1}{a_f}\sum_{i=1}^{k} C_i[S_{n+1}(\theta_i) - S_n(\theta_i)] e^{-\lambda_i \bar{x}} \quad (n = 1, 2, 3, \ldots, k-1) \ , \tag{3.46}$$

$$\sigma_0(\bar{x}) = \sigma - \frac{2}{a_f}\sum_{i=1}^{k} C_i S_1(\theta_i)\mathrm{e}^{-\lambda_i \bar{x}} \ . \tag{3.47}$$

Displacements can be determined with the aid of Eqs. (3.19), (3.21) and (3.25). Changing x for $\bar{x} = x/a$ we get

$$u_n(x) = \frac{a_m}{aG_m} F_n'(\bar{x}) + u_{n-1}(\bar{x}) \ .$$

For the first fiber ($n = 1$), we have

$$u_1(\bar{x}) = \frac{a_m}{aG_m} F_1'(\bar{x}) + u_0(\bar{x}) \ .$$

Substituting Eq. (3.42) into these equations we arrive at

$$u_n(\bar{x}) = -\frac{a_m}{aG_m}\sum_{i=1}^{k} C_i \lambda_i S_n(\theta_i)\mathrm{e}^{-\lambda_i \bar{x}} + u_{n-1}(\bar{x}) \quad (n = 2, 3, 4, \ldots, k) \ , \tag{3.48}$$

$$u_1(\bar{x}) = -\frac{a_m}{aG_m}\sum_{i=1}^{k} C_i \lambda_i S_1(\theta_i)\mathrm{e}^{-\lambda_i \bar{x}} + u_0(\bar{x}) \ . \tag{3.49}$$

To determine coefficients C_i, we should apply the boundary conditions and write Eqs. (3.23) and (3.24) in the explicit form using Eqs. (3.47)–(3.49). Substituting S_n from Eq. (3.43) and λ_i from Eq. (3.41) we get

$$\sum_{i=1}^{k} C_i \tan\frac{\theta_i}{2} = \frac{\sigma a_f}{2},$$

$$\sum_{i=1}^{k} C_i \tan\frac{\theta_i}{2}\sin\frac{2n-1}{2}\theta_i = 0 \quad (n = 2, 3, 4, \ldots, k),$$

$$\sum_{i=1}^{k} C_i \tan\frac{\theta_i}{2}\sin\frac{\theta_i}{2} = \frac{aG_m}{2\mu a_m} u_0(0) \ ,$$

Introducing new coefficients

$$D_i = C_i \tan\frac{\theta_i}{2} \ , \tag{3.50}$$

we arrive at the final form of the boundary conditions, i.e.,

$$\sum_{i=1}^{k} D_i = \frac{\sigma a_f}{2} \ , \tag{3.51}$$

$$\sum_{i=1}^{k} D_i \sin\frac{2n-1}{2}\theta_i = 0 \quad (n = 2, 3, 4, \ldots, k) \ , \tag{3.52}$$

$$\sum_{i=1}^{k} D_i \sin\frac{\theta_i}{2} = \frac{aG_m}{2\mu a_m} u_0(0) \ . \tag{3.53}$$

This set contains $k+1$ equations and includes k unknown coefficients D_i and displacement $u_0(0)$.

The foregoing set of equations allows us to obtain the exact analytical solution for any number of fibers, k. To find this solution, perform some transformations. First, multiply Eq. (3.52) by $\sin[(2n-1)\theta_s/2]$ and sum up all the equations from $n=2$ to $n=k$. Adding Eq. (3.53) for $n=1$ multiplied by $\sin(\theta_s/2)$ we obtain

$$\sum_{n=1}^{k}\sum_{i=1}^{k} D_i \sin\frac{2n-1}{2}\theta_i \sin\frac{2n-1}{2}\theta_s = \frac{aG_m}{2\mu a_m} u_0(0)\sin\frac{\theta_s}{2} \ .$$

Now change the sequence of summation, i.e.,

$$\sum_{i=1}^{k} D_i \sum_{n=1}^{k} \sin\frac{2n-1}{2}\theta_i \sin\frac{2n-1}{2}\theta_s = \frac{aG_m}{2\mu a_m} u_0(0)\sin\frac{\theta_s}{2} \ . \tag{3.54}$$

Using the following known series

$$\sum_{n=1}^{k} \cos(2n-1)\theta = \frac{\sin 2k\theta}{2\sin\theta} \ ,$$

we get in several steps

$$\begin{aligned} R_{is} &= \sum_{n=1}^{k} \sin\frac{2n-1}{2}\theta_i \sin\frac{2n-1}{2}\theta_s \\ &= \frac{1}{2}\sum_{n=1}^{k}\left[\cos\frac{2n-1}{2}(\theta_i-\theta_s) - \cos\frac{2n-1}{2}(\theta_i+\theta_s)\right] \\ &= \frac{1}{4}\left[\frac{\sin k(\theta_i-\theta_s)}{\sin\frac{1}{2}(\theta_i-\theta_s)} - \frac{\sin k(\theta_i+\theta_s)}{\sin\frac{1}{2}(\theta_i+\theta_s)}\right] \\ &= \frac{\cos(\theta_i/2)\cos k\theta_i \cos(\theta_s/2)\cos k\theta_s}{\cos\theta_s - \cos\theta_i}\left(\tan k\theta_i \tan\frac{\theta_i}{2} - \tan k\theta_s \tan\frac{\theta_s}{2}\right) \ . \end{aligned}$$

Using Eq. (3.38) we can conclude that $R_{is}=0$ for $i \neq s$. For the case $i=s$, we have

$$R_{ss} = \sum_{n=1}^{k} \sin^2\frac{2n-1}{2}\theta_s = \frac{1}{2}\sum_{n=1}^{k}[1-\cos(2n-1)\theta_s] = \frac{1}{2}\left(k - \frac{\sin 2k\theta_s}{2\sin\theta_s}\right)$$

As a result, Eq. (3.54) yields

$$D_s = \frac{2aG_m u_0(0) \sin(\theta_s/2) \sin\theta_s}{\mu a_m (2k \sin\theta_s - \sin 2k\theta_s)} \quad (s = 1, 2, 3, \ldots, k) \; . \tag{3.55}$$

Substituting these coefficients into Eq. (3.51) we can find $u_0(0)$, i.e.,

$$u_0(0) = \frac{\sigma \mu a_f a_m}{4aG_m} \left(\sum_{i=1}^{k} \frac{\sin(\theta_i/2) \sin\theta_i}{2k \sin\theta_i - \sin 2k\theta_i} \right)^{-1} \; . \tag{3.56}$$

Thus, the solution for the problem under study is specified with Eqs. (3.44)–(3.50), (3.55) and (3.56).

For example, consider a carbon–epoxy ply with the following parameters: $E_f = 250$ GPa, $G_m = 1$ GPa, $v_f = 0.6$, $k = 4$. Distribution of the normalized stresses in the fibers along the ply is shown in Fig. 3.19, while the same distribution of shear stresses in the matrix is presented in Fig. 3.20. As can be seen, in the vicinity of the

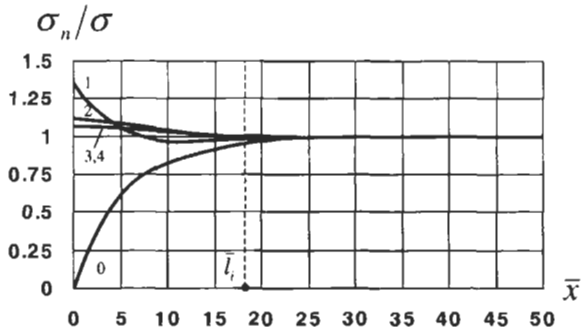

Fig. 3.19. Distribution of normal stresses along the fibers $n = 0, 1, 2, 3, 4$ for $k = 4$ $E_f = 250$ GPa, $G_m = 1$ GPa.

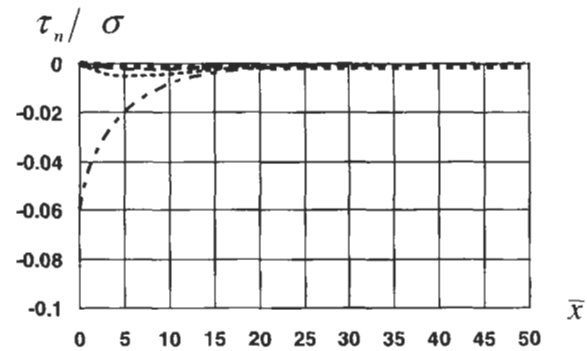

Fig. 3.20. Distribution of shear stresses along the fibers for $k = 4$, $E_f = 250$ GPa, $G_m = 1$ GPa. Numbers of the matrix layers: (– – –) $n = 1$; (·····) $n = 2$; (– – – –) $n = 3$; (▬ ▬ ▬ ▬) $n = 4$.

crack in the central fiber, the load carried by this fiber is transmitted by shear through the matrix to adjacent fibers. At a distance from the end of the fiber more than $\bar{l}_i$, the stress in the broken fiber becomes close to σ, and for $\bar{x} > \bar{l}_i$, the fiber behaves as if there is no crack. A portion of the broken fiber corresponding to $0 \le \bar{x} \le \bar{l}_i$ is not fully effective in resisting the applied load, and $l_i = \bar{l}_i a$ is referred to as the fiber ineffective length. Because the fiber defects are randomly distributed along its length, their influence on the strength of the ply is minimal if there are no other defects in the central and the adjacent fibers within distance l_i from the crack. To minimize the probability of such defects, we should minimize l_i which depends on fiber and matrix stiffnesses and material microstructure.

To evaluate l_i, consider Eq. (3.47) and assume that $\sigma_0(\bar{x})$ becomes close to σ if

$$e^{-\lambda_i l_i} = k \ ,$$

where k is some small parameter indicating how close $\sigma_0(\bar{x})$ should be to σ to neglect the difference between them (as a matter of fact this difference vanishes only for $\bar{x} \to \infty$). Taking approximately $\lambda_i = 2\mu$ in accordance with Eq. (3.41) and using Eq. (3.28) specifying μ we arrive at

$$\bar{l}_i = -\frac{1}{2} \ln k \cdot \sqrt{v_f(1 - v_f)\frac{E_f}{G_m}} \ .$$

For $k = 0.01$ we get

$$l_i = 2.3a \cdot \sqrt{v_f(1 - v_f)\frac{E_f}{G_m}} \ . \tag{3.57}$$

For a typical carbon–epoxy ply (see Fig. 3.19) with $a = 0.016$ mm and $v_f = 0.6$, Eq. (3.57) yields 0.29 mm.

Thus, for real composites, length l_i is very small, and this explains why a unidirectional composite demonstrates much higher strength in longitudinal tension than a dry bundle of fibers (see Table 3.3). Reducing G_m, i.e., the matrix stiffness, we

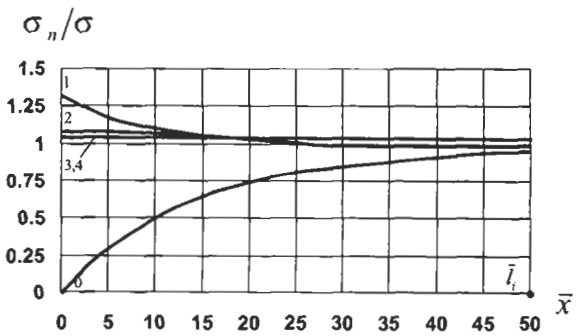

Fig. 3.21. Distribution of normal stresses along the fibers $n = 0, 1, 2, 3, 4$ for $k = 4$, $E_f = 250$ GPa, $G_m = 0.125$ GPa.

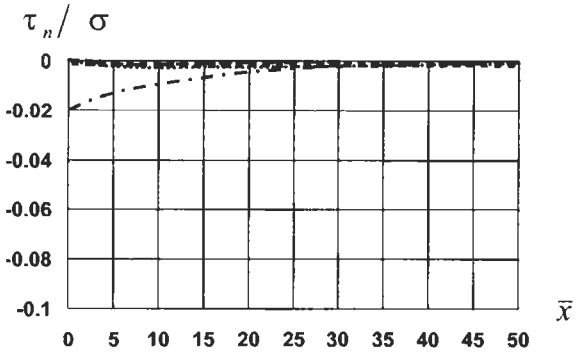

Fig. 3.22. Distribution of shear stresses along the fibers for $k = 4$, $E_f = 250$ GPa, $G_m = 0.125$ GPa. Numbers of the matrix layers: (– – –) $n = 1$; (· · · · · ·) $n = 2$; (– – – –) $n = 3$; (▬ ▬ ▬) $n = 4$.

increase the fiber ineffective length which becomes infinitely large for $G_m \to 0$. This effect is demonstrated in Fig. 3.21 which corresponds to the material whose matrix shear stiffness is much lower than that in the foregoing example (see Fig. 3.19). For this case, $\bar{l}_i = 50$, and Eq. (3.57) yields $l_i = 0.8$ mm. Distribution of shear stresses in this material is shown in Fig. 3.22. Experiments with unidirectional glass–epoxy composites ($E_f = 86.8$ GPa, $v_f = 0.68$, $a = 0.015$) have shown that reduction of the matrix shear modulus from 1.08 GPa ($l_i = 0.14$ mm) to 0.037 GPa ($l_i = 0.78$ mm) results in reduction of longitudinal tensile strength from 2010 to 1290 MPa, i.e., by 35.8% (Chiao, 1979).

Ineffective length of a fiber in a matrix can be found experimentally by the single fiber fragmentation test. For this test, a fiber is embedded in a matrix, and tensile load is applied to the fiber through the matrix until the fiber brakes. Further loading results in fiber fragmentation, and the length of the fiber fragment which no longer brakes is the fiber ineffective length. For a carbon fiber in epoxy matrix, $l_i = 0.3$ mm (Fukuda et al., 1993).

According to the foregoing reasoning, it looks like the stiffness of the matrix should be as high as possible. However, there exists the upper limit of this stiffness. Comparing Figs. 3.20 and 3.22 we can see that the higher the G_m, the higher is the shear stress concentration in the matrix in the vicinity of the crack. If the maximum shear stress, τ_m, acting in the matrix reaches the ultimate value, $\bar{\tau}_m$, delamination will occur between the matrix layer and the fiber, and the matrix will not transfer the load from the broken fiber to the adjacent ones. Maximum shear stress depends on the fiber stiffness – the lower the fiber modulus, the higher is τ_m. This is shown in Figs. 3.23 and 3.24, where shear stress distributions are presented for aramid fibers ($E_f = 150$ GPa) and glass fibers ($E_f = 90$ GPa), respectively.

Finally, it should be emphasized that the plane model of a ply, considered in this section (see Fig. 3.15), provides only qualitative results concerning fibers and matrix interaction. In real materials, a broken fiber is surrounded with more than two fibers (at least 5 or 6 as can be seen in Fig. 3.2), so the stress concentration in these fibers and in the matrix is much lower than would be predicted by the foregoing analysis.

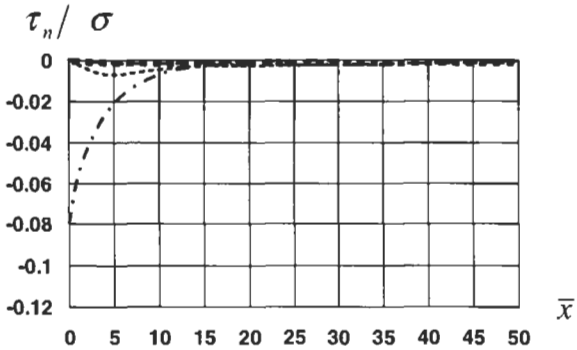

Fig. 3.23. Distribution of shear stresses along the fibres for $k = 4$, $E_f = 150$ GPa, $G_m = 1$ GPa. Numbers of the matrix layers: (– – –) $n = 1$; (· · · · · · ·) $n = 2$; (– – – –) $n = 3$; (▬ ▬ ▬ ▬) $n = 4$.

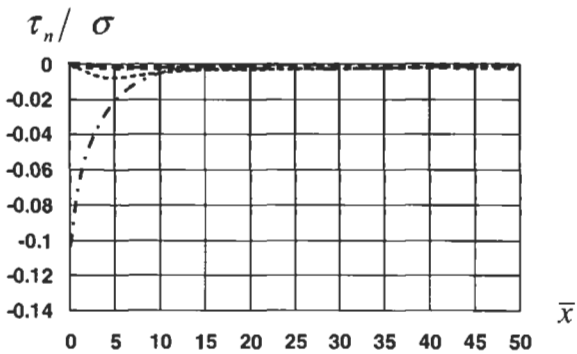

Fig. 3.24. Distribution of shear stresses along the fibres for $k = 4$, $E_f = 90$ GPa, $G_m = 1$ GPa. Numbers of the matrix layers: (– – –) $n = 1$; (· · · · · · ·) $n = 2$; (– – – –) $n = 3$; (▬ ▬ ▬ ▬) $n = 4$.

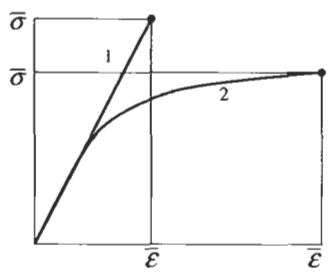

Fig. 3.25. Typical stress–strain diagrams of brittle (1) and ductile (2) metal alloys.

For hexagonal fiber distribution (see Fig. 3.4), stress concentration factor for the fibers does not exceed 1.105 (Tikhomirov and Yushanov, 1980). The effect of fiber breakage on tensile strength of unidirectional composites has been recently studied by Abu-Farsakh et al. (2000).

3.2.4. Fracture toughness

Fracture toughness is a very important characteristic of a structural material indicating resistance of a material to cracks and governed by the work needed to destroy a material (work of fracture). As known, there exist brittle and ductile metal alloys whose typical stress–strain diagrams are shown in Fig. 3.25. Comparing alloys with one and the same basic metal (e.g., steel alloys) we can see that while brittle alloys have higher strength, $\bar{\sigma}$, ductile alloys have higher ultimate elongation, $\bar{\varepsilon}$, and, as a result, higher work of fracture which is proportional to the area under the stress–strain diagram. Though brittle materials have, in general, higher strength, they are sensitive to cracks which propagating can cause material failure under stress that is much lower than the static strength. That is why designers usually prefer ductile materials with lower strength but higher fracture toughness. A typical dependence of fracture toughness on static strength for metals is shown in Fig. 3.26 (line 1). For composites, this dependence is entirely different (line 2) – higher static strength corresponds usually to higher fracture toughness (Mileiko, 1982). This phenomenon is demonstrated for a unidirectional boron–aluminum composite in Fig. 3.27 (Mileiko, 1982). As can be seen, an increase in fiber volume fraction, v_f,

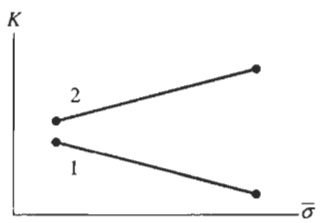

Fig. 3.26. Typical relations between fracture toughness (K) and strength ($\bar{\sigma}$) for metals (1) and composites (2).

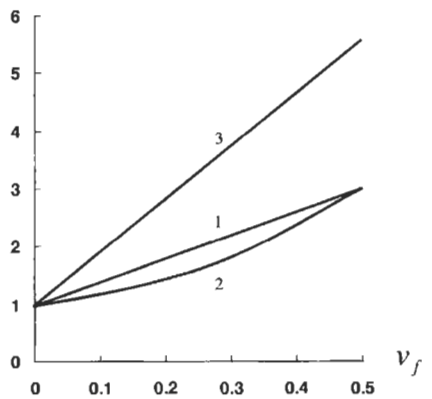

Fig. 3.27. Dependence of static strength (1), work of fracture (2), and fatigue strength (3) on fiber volume fraction for a boron-aluminum composite material.

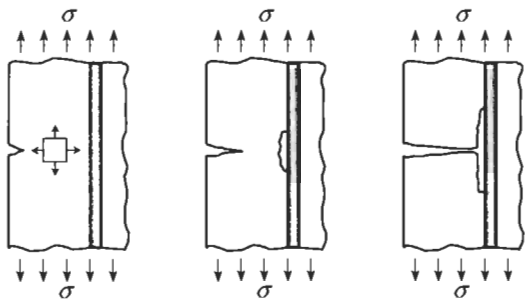

Fig. 3.28. Mechanism of the crack stopping at the fiber–matrix interface.

results not only in higher static strength along the fibers (line 1), which is quite natural. It is also accompanied with elevation of the work of fracture (line 2) and consequently, in the increase of material fatigue strength (bending under 10^6 cycles, line 3), which shows its sensitivity to cracks.

The reason for such a specific behavior of composite materials is associated with their inhomogeneous microstructure, particularly, with fiber–matrix interfaces that restrain free propagation of a crack (see Fig. 3.28). Of some importance are also fiber defects, local delaminations and fiber strength deviation, which reduce the static strength but increase the fracture toughness. As a result, combining brittle fibers and brittle matrix we usually arrive at the composite material whose fracture toughness is higher than that of its components.

Thus, we can conclude that composites comprise a new class of structural materials entirely different from traditional man-made materials for the several reasons. First, using thin fibers we make an attempt to utilize the high strength capacity that is naturally inherent in all the materials. Second, this utilization is provided by the matrix material, which increases the fiber performance and makes it possible to manufacture composite structures. Third, combination of fibers and matrices can result in new qualities of composite materials that are not inherent either in individual fibers or in the matrices and are not described by the laws of mechanical mixtures. For example, as noted above, brittle fiber and matrix materials, both having low fracture toughness, can provide a heterogeneous composite material with high fracture toughness.

3.3. Micromechanics of a ply

Consider a unidirectional composite ply under the action of in-plane normal and shear stresses as in Fig. 3.29. Because normal stresses do not change the right angle between axes 1 and 2, and shear stresses do not cause elongations in the longitudinal and transverse directions 1 and 2, the ply is orthotropic, and the corresponding constitutive equations, Eqs. (2.48) and (2.53) yield for the case under study

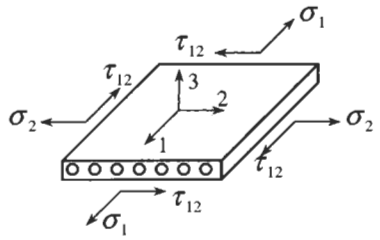

Fig. 3.29. A unidirectional ply under in-plane loading.

$$\begin{aligned}
\varepsilon_1 &= \frac{\sigma_1}{E_1} - \nu_{12}\frac{\sigma_2}{E_2}, \\
\varepsilon_2 &= \frac{\sigma_2}{E_2} - \nu_{21}\frac{\sigma_1}{E_1}, \\
\gamma_{12} &= \frac{1}{G_{12}}\tau_{12} \ .
\end{aligned} \tag{3.58}$$

The inverse form of these equations is

$$\begin{aligned}
\sigma_1 &= \bar{E}_1(\varepsilon_1 + \nu_{12}\varepsilon_2), \\
\sigma_2 &= \bar{E}_2(\varepsilon_2 + \nu_{21}\varepsilon_1), \\
\tau_{12} &= G_{12}\gamma_{12} \ ,
\end{aligned} \tag{3.59}$$

where

$$\bar{E}_{1,2} = \frac{E_{1,2}}{1 - \nu_{12}\nu_{21}}$$

and the following symmetry condition is valid

$$E_1\nu_{12} = E_2\nu_{21} \ . \tag{3.60}$$

Constitutive equations, Eqs. (3.58) and (3.59), include effective or apparent longitudinal, E_1, transverse, E_2, and shear, G_{12}, moduli of a ply and Poisson's ratios ν_{12} and ν_{21} only one of which is independent, while the second one can be found from Eq. (3.60).

Elastic constants, E_1, E_2, G_{12} and ν_{12} or ν_{21}, are governed by fibers and matrix properties and the ply microstructure, i.e., the shape and size of the fibers' cross-sections, fiber volume fraction, distribution of fibers in the ply, etc. The problem of micromechanics is to derive the corresponding governing relationships, i.e., to establish the relation between the properties of a unidirectional ply and those of its constituents.

To do this, we should know first the mechanical characteristics of the fibers and the matrix material of the ply. To determine the matrix modulus, E_m, its Poisson's

Fig. 3.30. Specimens of matrix material.

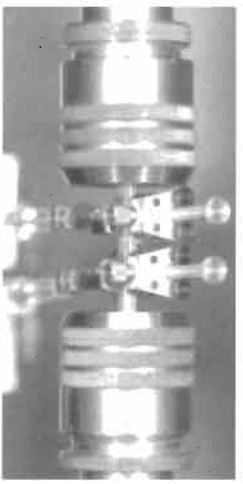

Fig. 3.31. Testing of the matrix specimen.

ratio, ν_m, and strength, $\bar{\sigma}_m$, traditional for material testing specimens and testing procedures can be used (see Figs. 3.30 and 3.31). Shear modulus, G_m, can be calculated with the aid of Eq. (2.57). To find the fibers properties, is a more complicated problem. There exist several methods to test elementary fibers by bending or stretching 10–30 mm long fiber segments. All of them are rather specific because of small (about 0.01 mm) fiber diameter, and, what is more important, fiber properties in a composite material can be different from those of individual fibers (see Section 3.2.3) with pre-assigned lengths provided by these methods.

It is worth to know the fibers actual modulus and strength not only for micromechanics but also to check the fibers quality before they are used to fabricate a composite part. For this purpose, a simple and reliable method has been developed to test the fibers in the actual conditions. According to this method, a fine tow or an assembly of fibers is carefully impregnated with resin, slightly stretched to avoid fiber waviness and cured to provide a specimen of the so-called microcomposite material. The microcomposite strand is overwrapped over two discs as in Fig. 3.32 or fixed in special friction grips as in Fig. 3.33 and tested under tension to determine the ultimate tensile force $\bar{F}$ and strain ε corresponding to some force $F < \bar{F}$. Then, the resin is removed by burning it out, and the mass of fibers being divided by the strand length and fiber density yields the cross-sectional area of fibers in the strand, A_f. Fiber strength and modulus can be calculated as

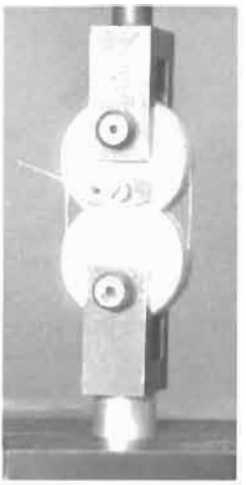

Fig. 3.32. Testing of a microcomposite specimen overwrapped over discs.

$$\bar{\sigma}_f = \frac{\bar{F}}{A_f}, \quad E_f = \frac{F}{A_f \varepsilon} .$$

In addition to fiber and matrix mechanical properties, micromechanical analysis requires the information about the ply microstructure. Depending on the level of this information, there exist micromechanical models of different levels of complexity.

The simplest or zero-order model of a ply is a monotropic model ignoring strength and stiffness of the matrix and assuming that the ply works only in the fiber direction. Taking $E_2 = 0$ and $G_{12} = 0$ in Eqs. (3.59) and putting $\nu_{12} = 0$ in accordance with Eq. (3.60) we arrive at the following equations describing this model

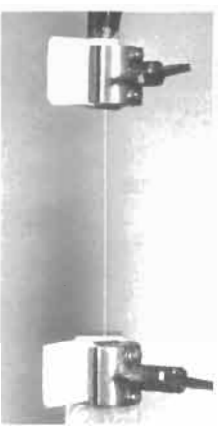

Fig. 3.33. Testing of a microcomposite specimen gripped at the ends.

$$\sigma_1 = E_1\varepsilon_1, \quad \sigma_2 = 0, \quad \tau_{12} = 0 \ , \tag{3.61}$$

where $E_1 = E_f v_f$. Being very simple and too approximate to be used in stress–strain analysis of composite structures, Eqs. (3.61) are extremely efficient for design of optimal composite structures in which the loads are carried mainly by fibers (see Chapter 8).

First-order models allow for the matrix stiffness but require only one structural parameter to be specified – fiber volume fraction, v_f. Because the fiber distribution in the ply is not important for these models, the ply can be presented as a system of strips shown in Fig. 3.34 and simulating fibers (shadowed areas) and matrix (light areas). Structural parameters of the model can be expressed in terms of fiber and matrix volume fractions only, i.e.,

$$\frac{a_f}{a} = v_f, \quad \frac{a_m}{a} = v_m, \quad v_f + v_m = 1 \ . \tag{3.62}$$

Assume that the model ply is under in-plane loading with some effective stresses σ_1, σ_2, and τ_{12} as in Fig. 3.34 and find the corresponding effective elastic constants E_1, E_2, G_{12}, ν_{12}, and ν_{21} entering Eqs. (3.58). Constitutive equations for isotropic fiber and matrix strips can be written as

$$\begin{aligned}
\varepsilon_1^{f,m} &= \frac{1}{E_{f,m}}(\sigma_1^{f,m} - \nu_{f,m}\sigma_2^{f,m}), \\
\varepsilon_2^{f,m} &= \frac{1}{E_{f,m}}(\sigma_2^{f,m} - \nu_{f,m}\sigma_1^{f,m}), \\
\gamma_{12}^{f,m} &= \frac{1}{G_{f,m}}\tau_{12}^{f,m} \ .
\end{aligned} \tag{3.63}$$

Here f and m indices correspond, as earlier, to fibers and matrix, respectively.

Let us make some assumptions concerning the model behavior. First, it is natural to assume that effective stress resultant $\sigma_1 a$ is distributed between fiber and matrix strips and that the longitudinal strains of these strips are the same that the effective (apparent) longitudinal strain of the ply, ε_1, i.e.,

$$\sigma_1 a = \sigma_1^f a_f + \sigma_1^m a_m \ , \tag{3.64}$$

$$\varepsilon_1^f = \varepsilon_1^m = \varepsilon_1 \ . \tag{3.65}$$

Second, as can be seen in Fig. 3.34, under transverse tension the stresses in the strips are the same and are equal to the effective stress σ_2, while the ply elongation in the transverse direction is the sum of the fiber and matrix strips elongations, i.e.,

$$\sigma_2^f = \sigma_2^m = \sigma_2 \ , \tag{3.66}$$

$$\Delta a = \Delta a_f + \Delta a_m \ . \tag{3.67}$$

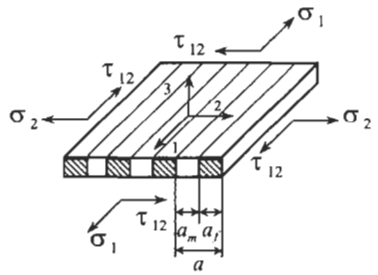

Fig. 3.34. A first-order model of a unidirectional ply.

Introducing transverse strains

$$\varepsilon_2 = \frac{\Delta a}{a}, \quad \varepsilon_2^{\mathrm{f}} = \frac{\Delta a_{\mathrm{f}}}{a_{\mathrm{f}}}, \quad \varepsilon_2^{\mathrm{m}} = \frac{\Delta a_{\mathrm{m}}}{a_{\mathrm{m}}}$$

we can write Eq. (3.67) in the following form

$$\varepsilon_2 a = \varepsilon_2^{\mathrm{f}} a_{\mathrm{f}} + \varepsilon_2^{\mathrm{m}} a_{\mathrm{m}} \ . \tag{3.68}$$

The same assumptions can be made for shear stresses and strains, so that

$$\tau_{12}^{\mathrm{f}} = \tau_{12}^{\mathrm{m}} = \tau_{12} \ , \tag{3.69}$$

$$\gamma_{12} a = \gamma_{12}^{\mathrm{f}} a_{\mathrm{f}} + \gamma_{12}^{\mathrm{m}} a_{\mathrm{m}} \ . \tag{3.70}$$

With due regard to Eqs. (3.65), (3.66), and (3.69) constitutive equations, Eqs. (3.63) can be reduced to

$$\varepsilon_1 = \frac{1}{E_{\mathrm{f}}}(\sigma_1^{\mathrm{f}} - \nu_{\mathrm{f}}\sigma_2), \quad \varepsilon_1 = \frac{1}{E_{\mathrm{m}}}(\sigma_1^{\mathrm{m}} - \nu_{\mathrm{m}}\sigma_2) \ , \tag{3.71}$$

$$\varepsilon_2^{\mathrm{f}} = \frac{1}{E_{\mathrm{f}}}(\sigma_2 - \nu_{\mathrm{f}}\sigma_1^{\mathrm{f}}), \quad \varepsilon_2^{\mathrm{m}} = \frac{1}{E_{\mathrm{m}}}(\sigma_2 - \nu_{\mathrm{m}}\sigma_1^{\mathrm{m}}) \ , \tag{3.72}$$

$$\gamma_{12}^{\mathrm{f}} = \frac{1}{G_{\mathrm{f}}}\tau_{12}, \quad \gamma_{12}^{\mathrm{m}} = \frac{1}{G_{\mathrm{m}}}\tau_{12} \ . \tag{3.73}$$

The first two equations, Eqs. (3.71), allow us to find longitudinal stresses, i.e.,

$$\sigma_1^{\mathrm{f}} = E_{\mathrm{f}}\varepsilon_1 + \nu_{\mathrm{f}}\sigma_2, \quad \sigma_1^{\mathrm{m}} = E_{\mathrm{m}}\varepsilon_1 + \nu_{\mathrm{m}}\sigma_2 \ . \tag{3.74}$$

Equilibrium equation, Eq. (3.64) can be rearranged with the aid of Eqs. (3.62) to the form

$$\sigma_1 = \sigma_1^{\mathrm{f}} v_{\mathrm{f}} + \sigma_1^{\mathrm{m}} v_{\mathrm{m}} \ . \tag{3.75}$$

Substituting Eqs. (3.74) into this equation we can express ε_1 in terms of σ_1 and σ_2. Matching this result to the first constitutive equation in Eqs. (3.58) we arrive at

$$E_1 = E_f v_f + E_m v_m \ , \tag{3.76}$$

$$\frac{\nu_{12}}{E_2} = \frac{\nu_f v_f + \nu_m v_m}{E_f v_f + E_m v_m} \ . \tag{3.77}$$

The first of these equations specifies the apparent longitudinal modulus of the ply and corresponds to the so-called rule of mixtures according to which the property of a composition can be calculated as the sum of its constituent material properties multiplied by the corresponding volume fractions.

Now consider Eq. (3.68) that can be written as

$$\varepsilon_2 = \varepsilon_2^f v_f + \varepsilon_2^m v_m \ .$$

Substituting strains ε_2^f and ε_2^m from Eqs. (3.72), stresses σ_1^f and σ_1^m from Eqs. (3.74) and ε_1 from Eqs. (3.58) with due regard to Eqs. (3.76) and (3.77) we can express ε_2 in terms of σ_1 and σ_2. Comparing this expression with the second constitutive equation in Eqs. (3.58) we get

$$\frac{1}{E_2} = \frac{v_f}{E_f} + \frac{v_m}{E_m} - \frac{v_f v_m (E_f \nu_m - E_m \nu_f)^2}{E_f E_m (E_f v_f + E_m v_m)} \ , \tag{3.78}$$

$$\frac{\nu_{21}}{E_1} = \frac{\nu_f v_f + \nu_m v_m}{E_f v_f + E_m v_m} \ . \tag{3.79}$$

Using Eqs. (3.76) and (3.79) we have

$$\nu_{21} = \nu_f v_f + \nu_m v_m \ . \tag{3.80}$$

This result corresponds to the rule of mixtures. Another Poisson's ratio can be found from Eqs. (3.77) and (3.78). Finally, Eqs. (3.58), (3.70), and (3.73) yield the apparent shear modulus

$$\frac{1}{G_{12}} = \frac{v_f}{G_f} + \frac{v_m}{G_m} \ . \tag{3.81}$$

This expression can be derived from the rule of mixtures if we use compliance coefficients instead of stiffnesses as in Eq. (3.76).

Since the fiber modulus is typically many times greater than the matrix modulus, Eqs. (3.76), (3.78), and (3.81) can be simplified neglecting small terms and presented in the following approximate form

$$E_1 = E_f v_f, \quad E_2 = \frac{E_m}{v_m (1 - \nu_m^2)}, \quad G_{12} = \frac{G_m}{v_m} \ .$$

Only two of the foregoing expressions, namely Eq. (3.76) for E_1 and Eq. (3.80) for ν_{21}, both following from the rule of mixtures, demonstrate good agreement with experimental results. Moreover, expressions analogous to Eqs. (3.76) and (3.80) follow practically from all numerous studies based on different micromechanical models. Comparison of predicted and experimental results is presented in Figs. 3.35–3.37, where theoretical dependencies of normalized moduli on the fiber volume fraction are shown with lines. The circles correspond to the test data for epoxy composites reinforced with different fibers that were obtained by the authors or taken from publications of Tarnopol'skii and Roze (1969), Kondo and Aoki (1982), Lee et al. (1995). As can be seen in Fig. 3.35, not only first-order model, Eq. (3.76), but zero-order model, Eqs. (3.61), as well, provide fair prediction for E_1, while Figs. 3.36 and 3.37 for E_2 and G_{12} call for the improvement of the first-order model (the corresponding results are shown with solid lines).

Second-order models allow for the fiber shape and distribution, but in contrast to higher-order models ignore complicated stressed state of fibers and matrix under the ply loading shown in Fig. 3.29. To demonstrate this approach, consider a layer-wise fiber distribution (see Fig. 3.5) and assume that the fibers are absolutely rigid and the matrix is in the simplest uniaxial stressed state under transverse tension. The typical element of this model is shown in Fig. 3.38 from which we can obtain the following equation

$$v_f = \frac{\pi R^2}{2Ra} = \frac{\pi R}{2a} \quad . \tag{3.82}$$

Because $2R < a$, $v_f < \pi/4 = 0.785$. Equilibrium condition yields

$$2R\sigma_2 = \int_{-R}^{R} \sigma_m \, dx_3 \quad , \tag{3.83}$$

where $x_3 = R\cos\alpha$ and σ_2 is some average transverse stress that induces average strain

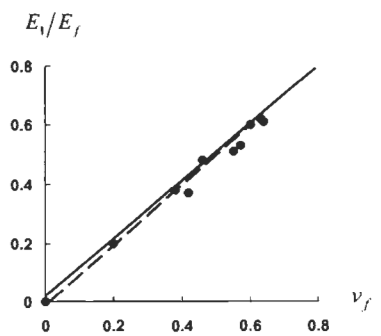

Fig. 3.35. Dependence of the normalized longitudinal modulus on fiber volume fraction: (– – –) zero-order model, Eqs. (3.61); (———) first-order model, Eqs. (3.76); (•) experimental data.

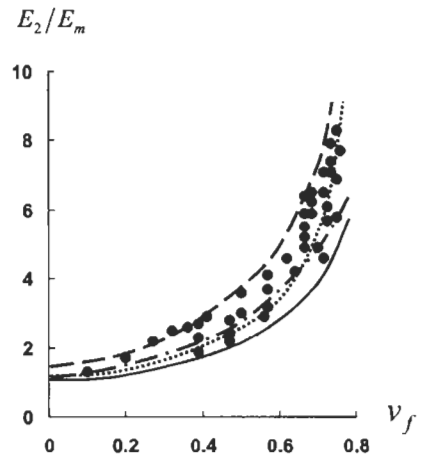

Fig. 3.36. Dependence of the normalized transverse modulus on fiber volume fraction: (———) first-order model, Eq. (3.78); (· · · · · · ·) second-order model, Eq. (3.89); (– – –) higher-order model (elasticity solution) (Van Fo Fy, 1966); (– – – –) the upper bound; (•) experimental data.

$$\varepsilon_2 = \frac{\Delta a}{a} \tag{3.84}$$

such that the effective (apparent) transverse modulus is calculated as

$$E_2 = \frac{\sigma_2}{\varepsilon_2} \quad . \tag{3.85}$$

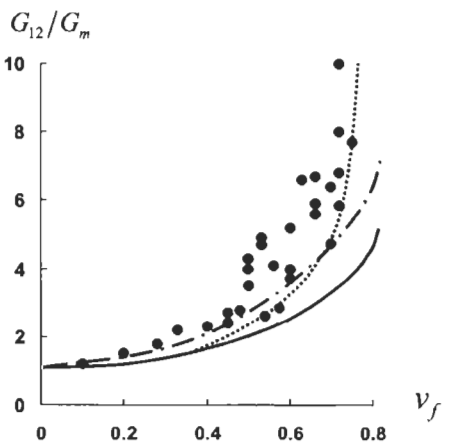

Fig. 3.37. Dependence of the normalized in-plane shear modulus on fiber volume fraction: (———) first-order model, Eq. (3.81); (· · · · · · ·) second-order model, Eq. (3.90); (– – –) higher-order model (elasticity solution) (Van Fo Fy, 1966); (•) experimental data.

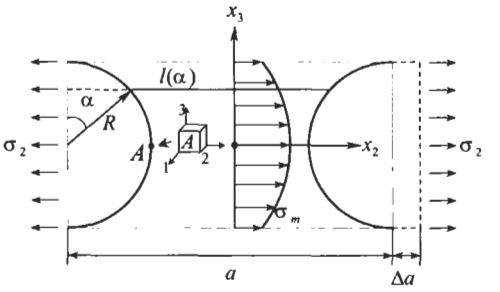

Fig. 3.38. Microstructural model of the second-order.

The strain in the matrix can be determined with the aid of Fig. 3.38 and Eq. (3.84), i.e.,

$$\varepsilon_m = \frac{\Delta a}{l(\alpha)} = \frac{\Delta a}{a - 2R\sin\alpha} = \frac{\varepsilon_2}{1 - \lambda\sqrt{1 - (x_3/R)^2}} \quad , \tag{3.86}$$

where in accordance with Eq. (3.82)

$$\lambda = \frac{2R}{a} = \frac{4v_f}{\pi} \quad . \tag{3.87}$$

Assuming that there is no strain in the matrix in the fiber direction and there is no stress in the matrix in the x_3-direction we have

$$\sigma_m = \frac{E_m \varepsilon_m}{1 - \nu_m^2} \quad . \tag{3.88}$$

Substituting σ_2 from Eq. (3.85) and σ_m, from Eq. (3.88) into Eq. (3.83) and using Eq. (3.86) to express ε_m we arive at

$$E_2 = \frac{E_m}{2R(1 - \nu_m^2)} \int_{-R}^{R} \frac{dx_3}{1 - \lambda\sqrt{1 - x_3^2}} \quad .$$

Calculating the integral and taking into account Eq. (3.87) we finally get

$$E_2 = \frac{\pi E_m r(\lambda)}{2v_f(1 - \nu_m^2)} \quad , \tag{3.89}$$

where

$$r(\lambda) = \frac{1}{\sqrt{1 - \lambda^2}} \tan^{-1} \sqrt{\frac{1 + \lambda}{1 - \lambda}} - \frac{\pi}{4} \quad .$$

Similar derivation for an in-plane shear yields

$$G_{12} = \frac{\pi G_m}{2v_f} r(\lambda) \ . \tag{3.90}$$

Dependencies of E_2 and G_{12} on the fiber volume fraction corresponding to Eqs. (3.89) and (3.90) are shown in Figs. 3.36 and 3.37 (dotted lines). As can be seen, the second-order model of a ply provides better agreement with experimental results than the first-order model. This agreement can be further improved if we take a more realistic microstructure of the material. Consider the actual microstructure shown in Fig. 3.2 and single out a typical square element with size a as in Fig. 3.39. Dimension a should provide the same fiber volume fraction for the element as for the material under study. To calculate E_2, we divide the element into a system of thin ($h \ll a$) strips parallel to axis x_2. The ith strip is shown in Fig. 3.39. For each strip, we measure the lengths, l_{ij}, of the matrix elements the jth of which is shown in Fig. 3.39. Then, equations analogous to Eqs. (3.83), (3.88), and (3.86) acquire the form

$$\sigma_2 a = h \sum_i \sigma_m^{(i)}, \quad \sigma_m^{(i)} = \frac{E_m}{1 - \nu_m^2} \varepsilon_m^{(i)}, \quad \varepsilon_m^{(i)} = \frac{\varepsilon_2 a}{\sum_j l_{ij}}$$

and the final result is

$$E_2 = \frac{E_m \bar{h}}{1 - \nu_m^2} \sum_i \left(\sum_j \bar{l}_{ij} \right)^{-1} ,$$

where $h = h/a$, $\bar{l}_{ij} = l_{ij}/a$. The second-order models considered above can be readily generalized to account for the fiber transverse stiffness and matrix nonlinearity.

Numerous higher-order microstructural models and descriptive approaches have been proposed, including

- analytical solutions in the problems of elasticity for an isotropic matrix having regular inclusions – fibers or periodically spaced groups of fibers,

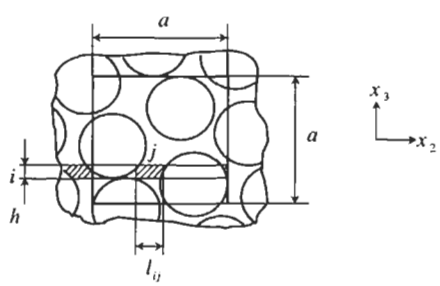

Fig. 3.39. Typical structural element.

- numerical (finite element, finite difference methods) stress analysis of the matrix in the vicinity of fibers,
- averaging of stress and strain fields for a media filled in with regularly or randomly distributed fibers,
- asymptotic solutions of elasticity equations for inhomogeneous solids characterized with a small microstructural parameter (fiber diameter),
- photoelasticity methods.

Exact elasticity solution for a periodical system of fibers embedded in an isotropic matrix (Van Fo Fy (Vanin), 1966) is shown in Figs. 3.36 and 3.37. As can be seen, due to high scatter of experimental data, the higher-order model does not demonstrate significant advantages with respect to elementary models.

Moreover, all the micromechanical models can hardly be used for practical analysis of composite materials and structures. The reason for this is that irrespective of how rigorous the micromechanical model is, it cannot describe quite adequately real material microstructure governed by a particular manufacturing process, take into account voids, microcracks, randomly damaged or misaligned fibers and many other effects that cannot be formally reflected in a mathematical model. Because of this, micromechanical models are mostly used for qualitative analysis providing us with understanding of how material microstructural parameters affect its mechanical properties rather than with quantitative information about these properties. Particularly, the foregoing analysis should result in two main conclusions. First, the ply stiffness along the fibers is governed by the fibers and linearly depends on the fiber volume fraction. Second, the ply stiffness across the fibers and in shear is determined not only by the matrix (which is natural), but by the fibers as well. Though the fibers do not take directly the load applied in the transverse direction, they significantly increase the ply transverse stiffness (in comparison with the stiffness of a pure matrix) acting as rigid inclusions in the matrix. Indeed, as can be seen in Fig. 3.34, the higher the fiber fraction, a_f, the lower is the matrix fraction, a_m, for the same a, and the higher stress σ_2 should be applied to the ply to cause the same transverse strain ε_2 because only matrix strips are deformable in the transverse direction.

Due to the aforementioned limitations of micromechanics, only the basic models were considered above. Historical overview of micromechanical approaches and more detail description of the corresponding results can be found elsewhere (Bogdanovich and Pastore, 1996; Jones, 1999).

To analyze the foregoing micromechanical models we used traditional approach based on direct derivation and solution of the system of equilibrium, constitutive, and strain–displacement equations. As known, the same problems can be solved with the aid of variational principles discussed in Section 2.11. In application to micromechanics, these principles allow us not only to determine apparent stiffnesses of the ply, but also to establish the upper and the lower bounds on them.

Consider for example the problem of transverse tension of a ply under the action of some average stress σ_2 (see Fig. 3.29) and apply the principle of minimum strain energy (see Section 2.11.2). According to this principle, the actual stress field provides the value of the body strain energy, which is equal or less than that of any

statically admissible stress field. Equality takes place only if the admissible stress state coincides with the actual one. Excluding this case, i.e., assuming that the class of admissible fields under study does not contain the actual field we can write the following strict inequality

$$W_\sigma^{\text{adm}} > W_\sigma^{\text{act}} \ . \tag{3.91}$$

For the problem of transverse tension, the fibers can be treated as absolutely rigid, and only the matrix strain energy can be taken into account. We also can neglect the energy of shear strain and consider the energy corresponding to normal strains only. With due regard to these assumptions, we use Eqs. (2.51) and (2.52) to get

$$W = \iiint_{V_m} U \, \mathrm{d}V_m \ , \tag{3.92}$$

where V_m is the volume of the matrix and

$$U = \tfrac{1}{2}(\sigma_1^m \varepsilon_1^m + \sigma_2^m \varepsilon_2^m + \sigma_3^m \varepsilon_3^m) \ . \tag{3.93}$$

To find energy W_σ entering inequality (3.91), we should express strains in terms of stresses with the aid of constitutive equations, i.e.,

$$\begin{aligned}
\varepsilon_1^m &= \frac{1}{E_m}(\sigma_1^m - \nu_m \sigma_2^m - \nu_m \sigma_3^m), \\
\varepsilon_2^m &= \frac{1}{E_m}(\sigma_2^m - \nu_m \sigma_1^m - \nu_m \sigma_3^m), \\
\varepsilon_3^m &= \frac{1}{E_m}(\sigma_3^m - \nu_m \sigma_1^m - \nu_m \sigma_2^m) \ .
\end{aligned} \tag{3.94}$$

Consider first the actual stress state. Let the ply in Fig. 3.29 be loaded with stress σ_2 inducing apparent strain ε_2 such that

$$\varepsilon_2 = \frac{\sigma_2}{E_2^{\text{act}}} \ . \tag{3.95}$$

Here, E_2^{act} is the actual apparent modulus, which is not known. With due regard to Eqs. (3.92) and (3.93) we get

$$W = \frac{1}{2}\sigma_2 \varepsilon_2 V, \quad W_\sigma^{\text{act}} = \frac{\sigma_2^2}{2E_2^{\text{act}}} V \ , \tag{3.96}$$

where V is the volume of the material. As an admissible field, we can take any state of stress that satisfies the equilibrium equations and force boundary conditions. Using the simplest first-order model shown in Fig. 3.34 we assume that

$$\sigma_1^m = \sigma_3^m = 0, \quad \sigma_2^m = \sigma_2 \ .$$

Then, Eqs. (3.92)–(3.94) yield

$$W_\sigma^{\text{adm}} = \frac{\sigma_2^2}{2E_\text{m}} V_\text{m} \ . \tag{3.97}$$

Substituting Eqs. (3.96) and (3.97) into inequality (3.91) we arrive at

$$E_2^{\text{act}} > E_2^{\text{l}} \ ,$$

where in accordance with Eqs. (3.62) and Fig. 3.34

$$E_2^{\text{l}} = \frac{E_\text{m} V}{V_\text{m}} = \frac{E_\text{m}}{v_\text{m}} \ .$$

This result specifying the lower bound on the apparent transverse modulus follows from Eq. (3.78) if we put $E_\text{f} \to \infty$. Thus, the lower (solid) line in Fig. 3.36 represents actually the lower bound on E_2.

To derive the expression for the upper bound, we should use the principle of minimum total potential energy (see Section 2.11.1) according to which (we again assume that the admissible field does not include the actual state)

$$T_{\text{adm}} > T_{\text{act}} \ , \tag{3.98}$$

where $T = W_\varepsilon - A$. Here, W_ε is determined with Eq. (3.92) in which stresses are expressed in terms of strains with the aid of Eqs. (3.94) and A, for the problem under study, is the product of the force acting on the ply by the ply extension induced by this force. Because the force is the resultant of stress σ_2 (see Fig. 3.29) which induces strain ε_2 the same for actual and admissible states, A is also the same for both states, and we can present inequality (3.98) as

$$W_\varepsilon^{\text{adm}} > W_\varepsilon^{\text{act}} \ . \tag{3.99}$$

For the actual state, we can write equations similar to Eqs. (3.96), i.e.,

$$W = \frac{1}{2}\sigma_2 \varepsilon_2 V, \quad W_\varepsilon^{\text{act}} = \frac{1}{2} E_2^{\text{act}} \varepsilon_2^2 V \ , \tag{3.100}$$

where $V = 2Ra$ in accordance with Fig. 3.38. For the admissible state, we use the second-order model (see Fig. 3.38) and assume that

$$\varepsilon_1^\text{m} = 0, \quad \varepsilon_2^\text{m} = \varepsilon_\text{m}, \quad \varepsilon_3^\text{m} = 0 \ ,$$

where ε_m is the matrix strain specified by Eq. (3.86). Then, Eqs. (3.94) yield

$$\sigma_1^\text{m} = \mu_\text{m} \sigma_2^\text{m}, \quad \sigma_3^\text{m} = \mu_\text{m} \sigma_2^\text{m}, \quad \sigma_2^\text{m} = \frac{E_\text{m} \varepsilon_\text{m}}{1 - 2\nu_\text{m} \mu_\text{m}} \ , \tag{3.101}$$

where

$$\mu_m = \frac{\nu_m(1+\nu_m)}{1-\nu_m^2} \quad .$$

Substituting Eqs. (3.101) into Eq. (3.93) and performing integration in accordance with Eq. (3.92) we get

$$W_{\varepsilon}^{adm} = \frac{E_m \varepsilon_2^2}{1-2\nu_m\mu_m} \cdot \int_{-R}^{R} dx_3 \int_0^{(a/2)y} \frac{dx_2}{y^2} = \frac{\pi R a E_m \varepsilon_2^2 r(\lambda)}{2v_f(1-2\nu_m\mu_m)} \quad . \tag{3.102}$$

Here

$$y = 1 - \lambda\sqrt{1-\left(\frac{x_3}{R}\right)^2}$$

and $r(\lambda)$ is given in notation to Eq. (3.89). Applying Eqs. (3.100) and (3.102) in conjunction with inequality (3.99) we arrive at

$$E_2^{act} < E_2^u \quad ,$$

where

$$E_2^u = \frac{\pi E_m}{2v_f(1-2\nu_m\mu_m)}$$

is the upper bound on E_2 shown in Fig. 3.36 with a broken line.

Taking statically and kinematically admissible stress and strain fields that are more close to the actual state of stress and strain one can increase E_2^l and decrease E_2^u making the difference between the bounds smaller (Hashin and Rosen, 1964).

It should be emphasized that thus established bounds are not the bounds on the modulus of a real composite material but on the result of calculation corresponding to the accepted material model. Indeed, return to the first-order model shown in Fig. 3.34 and consider in-plane shear with stress τ_{12}. As can be readily proved, the actual stress–strain state of the matrix in this case is characterized with the following stresses and strains

$$\begin{aligned} &\sigma_1^m = \sigma_2^m = \sigma_3^m = 0, \quad \tau_{12}^m = \tau_{12}, \quad \tau_{13}^m = \tau_{23}^m = 0, \\ &\varepsilon_1^m = \varepsilon_2^m = \varepsilon_3^m = 0, \quad \gamma_{12}^m = \gamma_{12}, \quad \gamma_{13}^m = \gamma_{23}^m = 0 \quad . \end{aligned} \tag{3.103}$$

Assuming that fibers are absolutely rigid and taking stresses and strains in Eqs. (3.103) as statically and kinematically admissible we can readily find that

$$G_{12}^{act} = G_{12}^{l} = G_{12}^{u} = \frac{G_m}{v_m} \quad .$$

Thus, we have found the exact solution, but its agreement with experimental data is rather poor (see Fig. 3.37) because the material model is not quite adequate.

As follows from the foregoing discussion, micromechanical analysis provides only qualitative prediction of the ply stiffness. The same is true for the ply strength. Though micromechanical approach in principle can be used for the strength analysis (Skudra et al., 1989), it provides mainly proper understanding of the failure mechanism rather than the values of the ultimate stresses for typical loading cases. For practical applications, these stresses are determined by experimental methods described in the next section.

3.4. Mechanical properties of a ply under tension, shear, and compression

As shown in Fig. 3.29, a ply can experience five types of elementary loading, i.e.,

- tension along the fibers,
- tension across the fibers,
- in-plane shear,
- compression along the fibers,
- compression across the fibers.

Actual mechanical properties of a ply under these loading cases are determined experimentally by testing specially fabricated specimens. Because the thickness of an elementary ply is very small (0.1–0.2 mm), the specimen consists usually of tens of plies having the same fiber orientations.

Mechanical properties of composite materials depend on the processing type and parameters. So, to obtain the adequate material characteristics that can be used for analysis of structural elements, the specimens should be fabricated with the same processes that are used to manufacture the structural elements. In connection with this, there exist two standard types of specimens – flat ones that are used to test materials made by hand or machine lay-up and cylindrical (tubular or ring) specimens that represent materials made by winding.

Typical mechanical properties of unidirectional advanced composites are presented in Table 3.5 and in Figs. 3.40–3.43.

Consider typical loading cases.

3.4.1. Longitudinal tension

Stiffness and strength of unidirectional composites under longitudinal tension are determined by the fibers. As follows from Fig. 3.35, material stiffness linearly increases with the rise of the fiber volume fraction. The same law following from Eq. (3.75) is valid for the material strength. If the fibers ultimate elongation, $\bar{\varepsilon}_f$, is less than that of the matrix (which is normally the case), longitudinal tensile strength is determined as

Table 3.5
Typical properties of unidirectional composites.

Property	Glass–epoxy	Carbon–epoxy	Carbon–PEEK	Aramid–epoxy	Boron–epoxy	Boron–Al	Carbon–Carbon	Al_2O_3–Al
Fiber volume fraction, v_f	0.65	0.62	0.61	0.6	0.5	0.5	0.6	0.6
Density, ρ (g/cm^3)	2.1	1.55	1.6	1.32	2.1	2.65	1.75	3.45
Longitudinal modulus, E_1 (GPa)	60	140	140	95	210	260	170	260
Transverse modulus, E_2 (GPa)	13	11	10	5.1	19	140	19	150
Shear modulus, G_{12} (GPa)	3.4	5.5	5.1	1.8	4.8	60	9	60
Poisson's ratio, ν_{21}	0.3	0.27	0.3	0.34	0.21	0.3	0.3	0.24
Longitudinal tensile strength, $\bar{\sigma}_1^+$ (MPa)	1800	2000	2100	2500	1300	1300	340	700
Longitudinal compressive strength, $\bar{\sigma}_1^-$ (MPa)	650	1200	1200	300	2000	2000	180	3400
Transverse tensile strength, $\bar{\sigma}_2^+$ (MPa)	40	50	75	30	70	140	7	190
Transverse compressive strength, $\bar{\sigma}_2^-$ (MPa)	90	170	250	130	300	300	50	400
In-plane shear strength, $\bar{\tau}_{12}$ (MPa)	50	70	160	30	80	90	30	120

$$\bar{\sigma}_1^+ = (E_f v_f + E_m v_m)\bar{\varepsilon}_f \ . \tag{3.104}$$

However, in contrast to Eq. (3.76) for E_1, this equation is not valid for very small and very high fiber volume fraction. Dependence of $\bar{\sigma}_1^+$ on v_f is shown in Fig. 3.44. For very low v_f, the fibers do not restrain the matrix deformation. Being stretched by the matrix, the fibers fail because their ultimate elongation is less than that of the matrix and induce stress concentration in the matrix that can reduce material strength below the strength of the matrix (point *B*). Line *BC* in Fig. 3.44 corresponds to Eq. (3.104). At point *C* amount of matrix starts to be less than it is necessary for a monolythic material, and material strength at point *D* approximately corresponds to the strength of a dry bundle of fibers which is less than the strength of a composite bundle of fibers bound with matrix (see Table 3.3).

Strength and stiffness under longitudinal tension are determined using unidirectional strips or rings. The strips are cut out of unidirectionally reinforced plates and their ends are made thicker (usually glass–epoxy tabs are bonded onto the ends) to avoid the specimen failure in the grips of the testing machine (Jones, 1999), (Lagace, 1985). Rings are cut out of a circumferentially wound cylinder or wound individually on a special mandrel shown in Fig. 3.45. The strips are tested using traditional approaches, while the rings should be loaded with internal pressure. There exist several methods to apply the pressure (Tarnopol'skii and Kincis, 1985), the simplest of which involves the use of mechanical fixtures with different

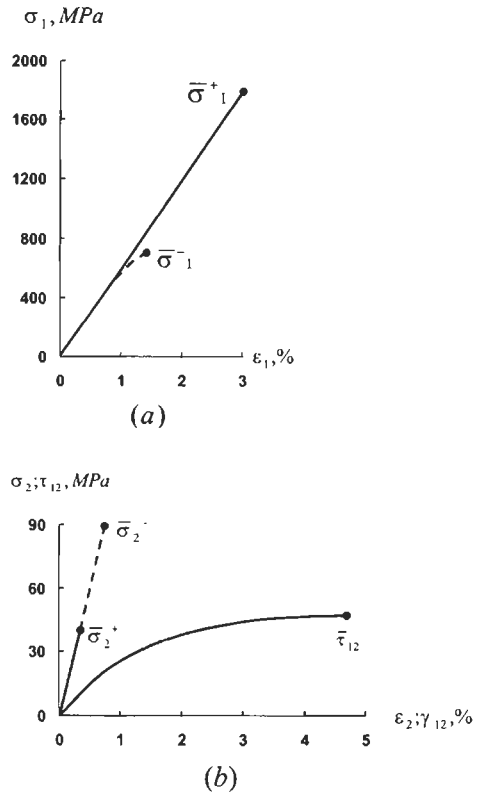

Fig. 3.40. Stress–strain curves for unidirectional glass–epoxy composite material under longitudinal tension and compression (a), transverse tension and compression (b), and in-plane shear (b).

number of sectors as in Figs. 3.46 and 3.47. Failure mode is shown in Fig. 3.48. Longitudinal tension yields the following mechanical properties of the material

- longitudinal modulus, E_1,
- longitudinal tensile strength, $\bar{\sigma}_1^+$,
- Poisson's ratio, ν_{21}.

Typical values of these characteristics for composites with different fibers and matrices are listed in Table 3.5. As follows from Figs. 3.40–3.43, stress–strain diagrams are linear practically up to the failure.

3.4.2. Transverse tension

There are three possible modes of material failure under transverse tension with stress σ_2 shown in Fig. 3.49 – failure of the fiber–matrix interface (adhesion failure), failure of the matrix (cohesion failure), and fiber failure. The last failure mode is specific for composites with aramid fibers which consist of thin filaments (fibrils) that have low transverse strength. As follows from the micromechanical analysis

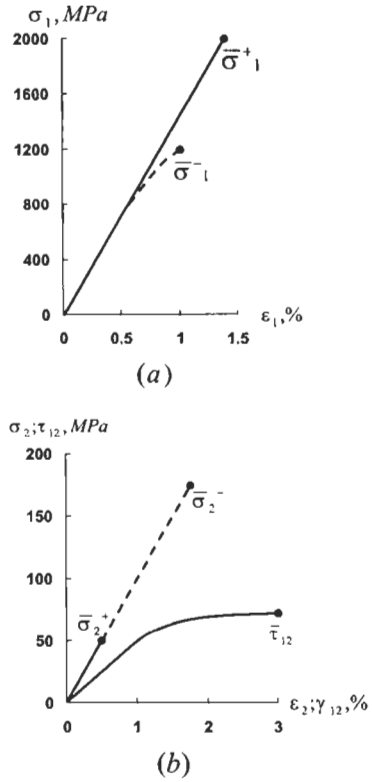

Fig. 3.41. Stress–strain curves for unidirectional carbon–epoxy composite material under longitudinal tension and compression (a), transverse tension and compression (b), and in-plane shear (b).

(Section 3.3), material stiffness under tension across the fibers is higher than that of a pure matrix (see Fig. 3.36).

For qualitative analysis of transverse strength, consider again the second-order model in Fig. 3.38. As can be seen, stress distribution $\sigma_m(x_3)$ is not uniform, and the maximum stress in the matrix corresponds to $\alpha = 90°$. Using Eqs. (3.85), (3.86), and (3.88) we obtain

$$\sigma_m^{max} = \frac{E_m \sigma_2}{(1 - \nu_m^2) E_2 (1 - \lambda)} \ .$$

Taking $\sigma_m^{max} = \bar{\sigma}_m$ and $\sigma_2 = \bar{\sigma}_2^+$, where $\bar{\sigma}_m$ and $\bar{\sigma}_2^+$ are the ultimate stresses for the matrix and for the composite material and substituting for λ and E_2 their expressions in accordance with Eqs. (3.87) and (3.89) we arrive at

$$\bar{\sigma}_2^+ = \bar{\sigma}_m \frac{r(\lambda)}{2v_f} (\pi - 4v_f) \ . \tag{3.105}$$

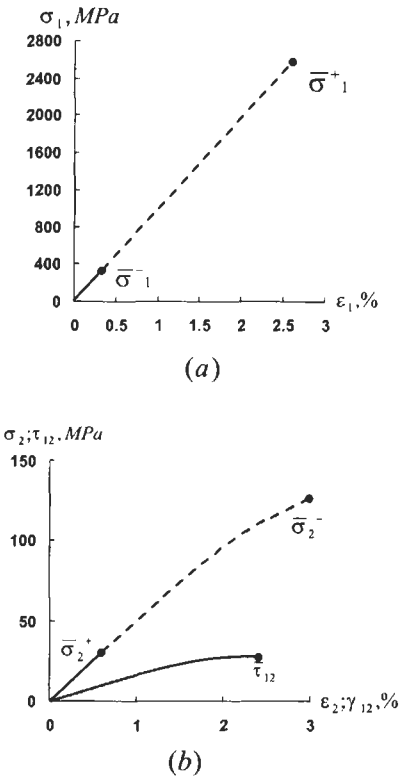

Fig. 3.42. Stress–strain curves for unidirectional aramid–epoxy composite material under longitudinal tension and compression (a), transverse tension and compression (b), and in-plane shear (b).

Dependence of the ratio $\bar{\sigma}_2^+/\bar{\sigma}_m$ for epoxy composite is shown in Fig. 3.50. As can be seen, transverse strength of a unidirectional material is considerably lower than the strength of the matrix. It should be noted that for the first-order model that ignores the shape of the fiber cross-sections (see Fig. 3.34), $\bar{\sigma}_2^+$ is equal to $\bar{\sigma}_m$. Thus, the reduction of $\bar{\sigma}_2^+$ is caused by the stress concentration in the matrix induced by cylindrical fibers.

However, both polymeric and metal matrices exhibit, as follows from Fig. 1.11 and 1.14, elastic–plastic behavior, and plastic deformation reduces, as known, the effect of stress concentration. Nevertheless, stress–strain diagrams $\bar{\sigma}_2^+ - \varepsilon_2$ shown in Figs. 3.40–3.43 are linear up to the failure point. To explain this phenomenon, consider element A of the matrix located in the vicinity of a fiber as in Fig. 3.38. Assuming that the fiber is absolutely rigid we can conclude that the matrix strains in directions 1 and 3 are close to zero. Taking $\varepsilon_1^m = \varepsilon_3^m = 0$ in Eqs. (3.94) we arrive at Eqs. (3.101) for stresses according to which $\sigma_1^m = \sigma_3^m = \mu_m \sigma_2^m$. Dependence of parameter μ_m on the matrix Poisson's ratio is presented in Fig. 3.51. As follows from this figure, in the limiting case $\nu_m = 0.5$ we have $\mu_m = 1$ and $\sigma_1^m = \sigma_2^m = \sigma_3^m$, i.e., the state of stress under which all the materials behave as absolutely brittle. For

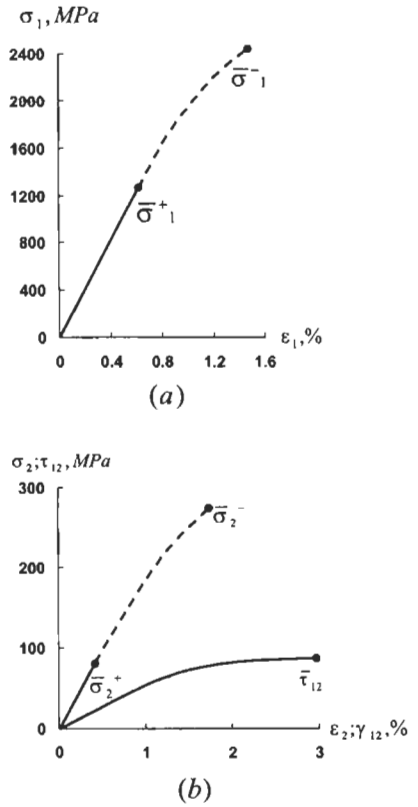

Fig. 3.43. Stress–strain curves for unidirectional boron–epoxy composite material under longitudinal tension and compression (a), transverse tension and compression (b), and in-plane shear (b).

epoxy resin, $\nu_m = 0.35$ and $\mu_m = 0.54$ which, as can be supposed, does not allow the resin to demonstrate its rather limited (see Fig. 1.11) plastic properties.

Strength and stiffness under transverse tension are experimentally determined using flat strips (see Fig. 3.52) or tubular specimens (see Fig. 3.53). These tests allow us to determine

- transverse modulus, E_2,
- transverse tensile strength, $\bar{\sigma}_2^+$.

For typical composite materials, these properties are given in Table 3.5.

3.4.3. In-plane shear

Failure modes of the unidirectional composite under in-plane pure shear with stress τ_{12} shown in Fig. 3.29 are practically the same that ones for a case of transverse tension (see Fig. 3.49). However, there is a principal difference in material behavior. As follows from Figs. 3.40–3.43, stress–strain curves τ_{12}–γ_{12} are

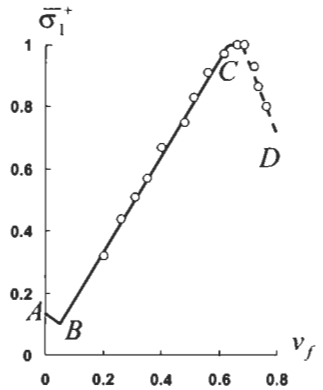

Fig. 3.44. Dependence of normalized longitudinal strength on fiber volume fraction (○ – experimental results).

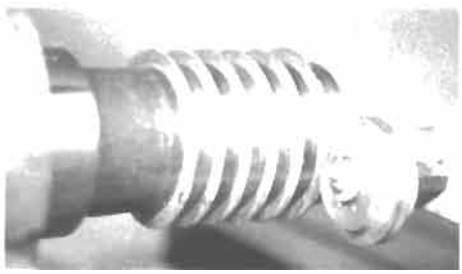

Fig. 3.45. A mandrel for test rings.

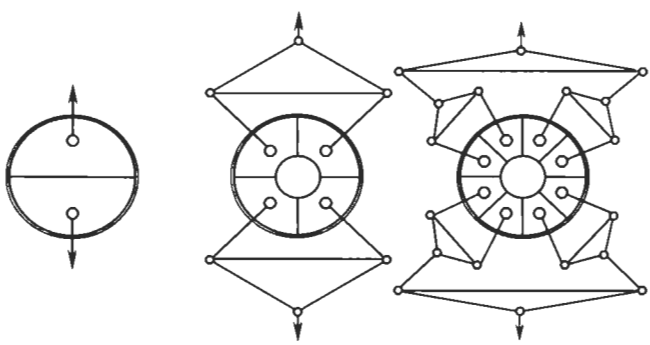

Fig. 3.46. Two-, four-, and eight-sector test fixtures for composite rings.

not linear and $\bar{\tau}_{12}$ exceeds $\bar{\sigma}_2^+$. This means that fibers do not restrict free shear deformation of the matrix, and stress concentration in the vicinity of fibers does not influence significantly material strength because of matrix plastic deformation.

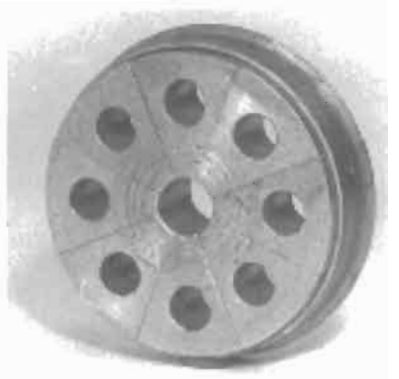

Fig. 3.47. A composite ring on a eight-sector test fixture.

Fig. 3.48. Failure modes of unidirectional rings.

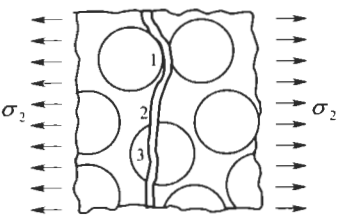

Fig. 3.49. Modes of failure under transverse tension: 1 – adhesion failure; 2 – cohesion failure; 3 – fiber failure.

Strength and stiffness under in-plane shear are determined experimentally by testing plates and thin-walled cylinders. A plate is reinforced at 45° to the loading direction and is fixed in a square frame consisting of four hinged members as in Fig. 3.54. Simple equilibrium consideration and geometric analysis with the aid of Eq. (2.27) yield the following equations

$$\tau_{12} = \frac{P}{\sqrt{2}ah}, \quad \gamma_{12} = \varepsilon_y - \varepsilon_x, \quad G_{12} = \frac{\tau_{12}}{\gamma_{12}},$$

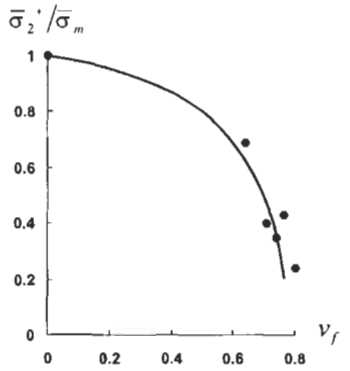

Fig. 3.50. Dependence of material strength under transverse tension on fiber volume fraction: (———) Eq. (3.105); (•) Experimental data.

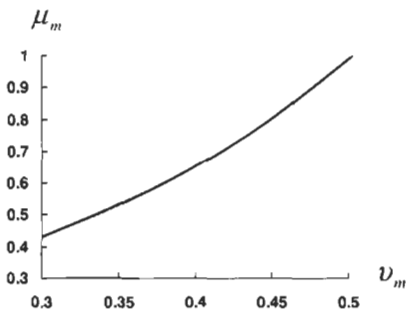

Fig. 3.51. Dependence of parameter μ_m on the matrix Poisson's ratio.

where h is the plate thickness. Thus, knowing P and measuring strains in the x- and y-directions we can determine $\bar{\tau}_{12}$ and G_{12}. More accurate and reliable results can be obtained if we induce pure shear in a twisted tubular specimen reinforced in circumferential direction (Fig. 3.55). Using again simple equilibrium and geometric analysis we get

$$\tau_{12} = \frac{M}{2\pi R^2 h}, \quad \gamma_{12} = \frac{\varphi R}{l}, \quad G_{12} = \frac{\tau_{12}}{\gamma_{12}} .$$

Here, M is the torque, R and h the cylinder radius and thickness, and φ the twist angle between two cross-sections located at some distance l from each other. Thus, having M and measuring φ we can find $\bar{\tau}_{12}$ and G_{12}.

3.4.4. Longitudinal compression

Failure under compression along the fibers can occur in different modes depending on the material microstructural parameters and can hardly be predicted

Fig. 3.52. Test fixture for transverse tension and compression of unidirectional strips.

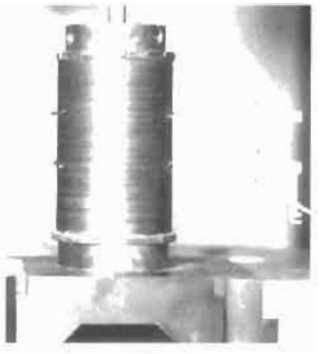

Fig. 3.53. Test fixture for transverse tension or compression of unidirectional tubular specimens.

by micromechanical analysis because of a rather complicated interaction of these modes. Nevertheless, useful qualitative results allowing us to understand material behavior and, hence, to improve its properties, can be obtained with microstructural models.

Consider typical compression failure modes. Traditional failure mode under compression is associated with shear in some oblique plane as in Fig. 3.56. Shear stress can be calculated using Eq. (2.9), i.e.,

$$\tau = \sigma_1 \sin\alpha \cos\alpha$$

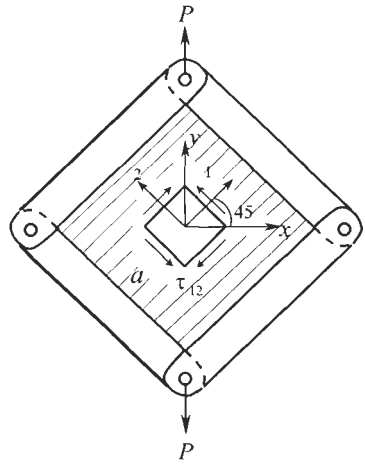

Fig. 3.54. Simulation of pure shear in a square frame.

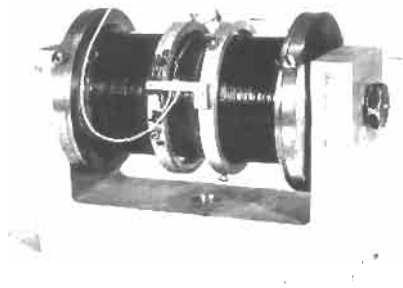

Fig. 3.55. A tubular specimen for shear test.

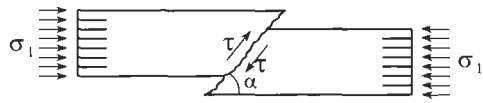

Fig. 3.56. Shear failure under compression.

and reaches the maximum valuc at $\alpha = 45°$. Shear failure under compression is usually typical for unidirectional composites that demonstrate the highest strength under longitudinal compression. On the other hand, materials showing the lowest strength under compression exhibit transverse extension failure mode typical for wood compressed along the fibers and shown in Fig. 3.57. This failure is caused by tensile transverse strain whose absolute value is

$$\varepsilon_2 = \nu_{21}\varepsilon_1 \ , \tag{3.106}$$

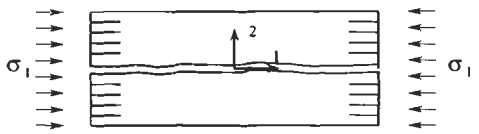

Fig. 3.57. Transverse extension failure mode under longitudinal compression.

where ν_{21} is Poisson's ratio and $\varepsilon_1 = \sigma_1/E_1$ is the longitudinal strain. Consider Table 3.6 showing some data taken from Table 3.5 and results of calculations for epoxy composites. The fourth column displays the experimental ultimate transverse strains $\bar{\varepsilon}_2^+ = \bar{\sigma}_2^+/E_2$ calculated with the aid of data presented in Table 3.5, while the last column shows the results following from Eq. (3.106). As can be seen, the failure mode associated with transverse tension under longitudinal compression is not dangerous for composites under consideration because $\bar{\varepsilon}_2^+ > \bar{\varepsilon}_2$. However, this is true only for fiber volume fraction $v_f = 0.50$–0.65 to which the data presented in Table 3.6 correspond. To see what happens for higher fiber volume fractions, let us use the second-order micromechanical model and the corresponding results in Figs. 3.36 and 3.50. We can plot the strain concentration factor k_ε (which is the ratio of the ultimate matrix elongation, $\bar{\varepsilon}_m$, to $\bar{\varepsilon}_2^+$ for the composite material) versus the fiber volume fraction. As can be seen in Fig. 3.58, this factor, being about 6 for

Table 3.6
Characteristics of epoxy composites.

Material	Characteristic				
	$\bar{\sigma}_1^-$ (MPa)	$\bar{\varepsilon}_1^-$ (%)	ν_{21}	$\bar{\varepsilon}_2^+$ (%)	$\bar{\varepsilon}_2 = \nu_{21}\bar{\varepsilon}_1^-$
Glass–epoxy	600	1.00	0.30	0.31	0.30
Carbon–epoxy	1200	0.86	0.27	0.45	0.23
Aramid–epoxy	300	0.31	0.34	0.59	0.11
Boron–epoxy	2000	0.95	0.21	0.37	0.20

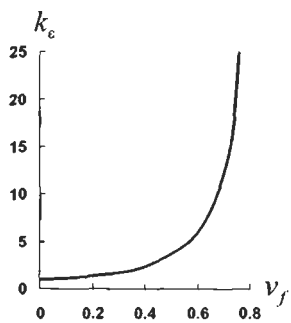

Fig. 3.58. Dependence of strain concentration factor on the fiber volume fraction.

$v_f = 0.6$, becomes as high as 25 for $v_f = 0.75$. This means that $\bar{\varepsilon}_2^+$ dramatically decreases for higher v_f, and the fracture mode shown in Fig. 3.57 becomes quite typical for composites with high fiber volume fractions.

Both fracture modes shown in Figs. 3.56 and 3.57 are accompanied with fibers bending induced by local buckling of fibers. According to N.F. Dow and B.W. Rosen (Jones, 1999), there can exist two modes of fiber buckling shown in Fig. 3.59 – shear mode and transverse extension mode. To study the fibers local buckling (or microbuckling which means that the material specimen is straight, while the fibers inside the material are curved), consider a plane model of a unidirectional ply shown in Figs. 3.15 and 3.60 and take $a_m = a$, $a_f = \delta = d$, where d is the fiber diameter. Then, Eqs. (3.17) yield

$$v_f = \frac{\bar{d}}{1+\bar{d}}, \quad \bar{d} = \frac{d}{a} \ . \tag{3.107}$$

Because of the symmetry conditions, consider two fibers 1 and 2 in Fig. 3.60 and matrix between these fibers. The buckling displacement, v, of the fibers can be

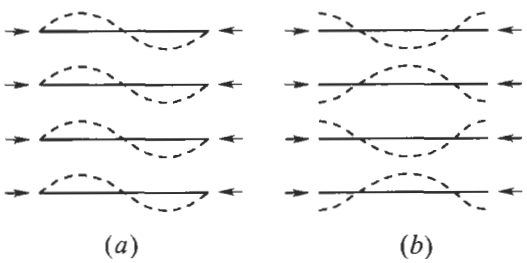

Fig. 3.59. Shear (a) and transverse extension (b) modes of fiber local buckling.

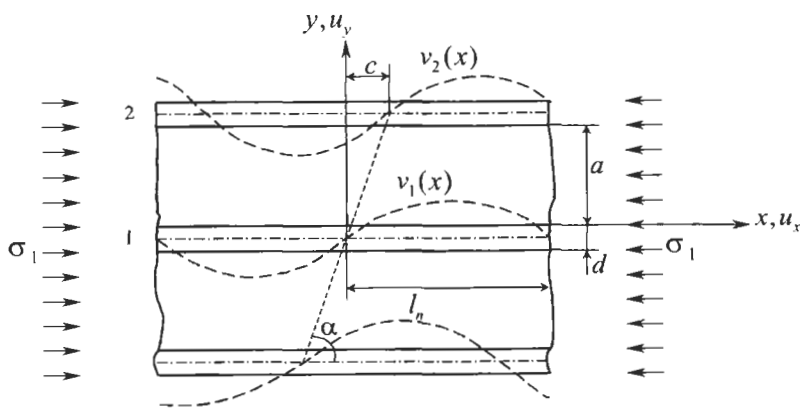

Fig. 3.60. Local buckling of fibers in unidirectional ply.

represented by a sine function as

$$v_1(x) = V \sin \lambda_n x, \quad v_2(x) = V \sin \lambda_n (x - c) \ , \tag{3.108}$$

where V is an unknown amplitude value, the same for all the fibers, $\lambda_n = \pi / l_n$, l_n is a half of a fiber wavelength (see Fig. 3.60), and $c = (a + d) \cot \alpha$ is a phase shift. Taking $c = 0$ we can describe the shear mode of buckling (Fig. 3.59(a)), while $c = l_n$ corresponds to extension mode (Fig. 3.59(b)). To find the critical value of stress σ_1, we use the Timoshenko energy method (Timoshenko and Gere, 1961) yielding the following buckling condition

$$A = W \ . \tag{3.109}$$

Here, A is the work of external forces and W is the strain energy accumulated in the material while the fibers undergo buckling. Work A and energy W are calculated for a typical ply element consisting of two halves of fibers 1 and 2 and matrix between them (see Fig. 3.61). The work, A, can be calculated as

$$A = \sigma_1 (a + d) d \cdot \delta \tag{3.110}$$

with displacement δ following from Fig. 3.62, i.e.,

$$\delta = l_n - \int_0^{l_n - \delta} \sqrt{1 + \left(\frac{\mathrm{d}v_1}{\mathrm{d}x} \right)^2} \, \mathrm{d}x \ .$$

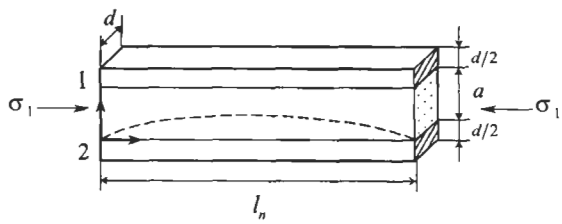

Fig. 3.61. A typical ply element.

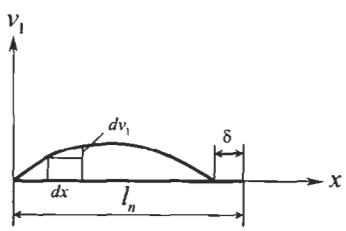

Fig. 3.62. Deformation of a fiber.

Using traditional assumptions, i.e., taking that $(dv_1/dx) \ll 1$ and $\delta \ll l$ and substituting v_1 from Eqs. (3.108) we arrive at

$$\delta = \frac{1}{2}\int_0^{l_n} \left(\frac{dv_1}{dx}\right)^2 dx = \frac{1}{4} V^2 \lambda_n^2 l_n \ .$$

Thus, Eq. (3.110) yields

$$A = \frac{\pi^2}{4 l_n} \sigma_1 V^2 a d (1 + \bar{d}) \ . \tag{3.111}$$

Strain energy consists of three parts, i.e.,

$$W = W_f + W_m^s + W_m^e \ , \tag{3.112}$$

where W_f is the energy of buckled fibers, while W_m^s and W_m^e correspond to shear strain and transverse extension of the matrix which supports the fibers. Strain energy of fibers deformed in accordance with Eqs. (3.108) and shown in Fig. 3.61 has the form

$$W_f = \frac{1}{4} D_f \int_0^{l_n} \left[\left(\frac{d^2 v_1}{dx^2}\right)^2 + \left(\frac{d^2 v_2}{dx^2}\right)^2\right] dx \ ,$$

where D_f is the fiber bending stiffness. Substituting Eqs. (3.108) and calculating the integrals we get

$$W_f = \frac{\pi^4}{4 l_n^3} D_f V^2 \ . \tag{3.113}$$

To determine the strain energy of the matrix, we assume that the matrix element shown in Fig. 3.61 is in the plane state of stress (nonzero stresses are σ_x, σ_y, and τ_{xy}), and equilibrium equations, Eqs. (2.5) can be written as

$$\frac{\partial \sigma_x}{\partial x} + \frac{\partial \tau_{xy}}{\partial y} = 0, \quad \frac{\partial \sigma_y}{\partial y} + \frac{\partial \tau_{xy}}{\partial x} = 0 \ . \tag{3.114}$$

To simplify the solution, we assume that longitudinal stress, σ_x, acting in the matrix can be neglected in comparison with the corresponding stress acting in the fibers. Thus, we can put $\sigma_x = 0$. Then, Eqs. (3.114) can be integrated and yield

$$\tau_{xy} = \tau(x), \quad \sigma_y = \sigma(x) - \tau'(x) y \ . \tag{3.115}$$

Here, $\tau(x)$ and $\sigma(x)$ are arbitrary functions of integration and $(\,)' = d(\,)/dx$. Neglecting also the Poisson effects we can express the strains as follows

$$\gamma_{xy} = \frac{\tau(x)}{G_m}, \quad \varepsilon_y = \frac{1}{E_m}[\sigma(x) - \tau'(x)y] \tag{3.116}$$

which can be in turn expressed in terms of displacements with the aid of Eqs. (2.22), i.e.,

$$\gamma_{xy} = \frac{\partial u_x}{\partial y} + \frac{\partial u_y}{\partial x}, \quad \varepsilon_y = \frac{\partial u_y}{\partial y} \ . \tag{3.117}$$

Substituting Eqs. (3.116) into Eqs. (3.117) and integrating we can determine the displacements as

$$u_x = u(x) + \left[\frac{\tau(x)}{G_m} - v'(x)\right]y - \frac{1}{2E_m}\left[\sigma'(x)y^2 - \frac{1}{3}\tau''(x)y^3\right],$$

$$u_y = v(x) + \frac{1}{E_m}\left[\sigma(x)y - \frac{1}{2}\tau'(x)y^2\right] \ .$$

Here, $u(x)$ and $v(x)$ are functions of integration which, as well as functions $\tau(x)$ and $\sigma(x)$, should be found using compatibility conditions at fiber-matrix interfaces. Using Fig. 3.63 we can write these conditions in the following form:

$$u_x(y = 0) = -\frac{d}{2}v_1'(x), \quad u_x(y = a) = \frac{d}{2}v_2'(x),$$

$$u_y(y = 0) = v_1(x), \quad u_y(y = a) = v_2(x) \ .$$

Satisfying them we can find $u(x)$ and $v(x)$ directly as

$$u(x) = -\frac{d}{2}V\lambda_n \cos\lambda_n x, \quad v(x) = V \sin\lambda_n x$$

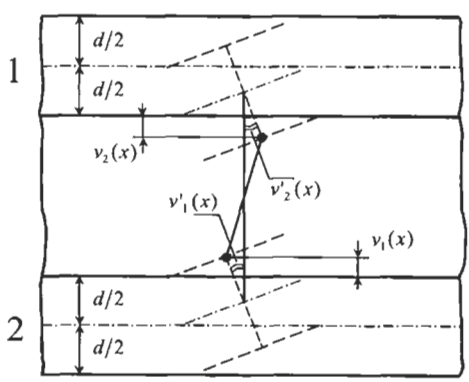

Fig. 3.63. Compatible fiber–matrix deformation.

and derive the following equations for $\sigma(x)$ and $\tau(x)$

$$\sigma(x) = \frac{E_m}{a} V[\sin \lambda_n(x-c) - \sin \lambda_n x] + \frac{1}{2}\tau'(x)a \ , \tag{3.118}$$

$$\frac{a^2}{6E_m}\tau''(x) - \frac{2}{G_m}\tau(x) = -V\lambda_n(1+\bar{d})[\cos \lambda_n(x-c) + \cos \lambda_n x] \ . \tag{3.119}$$

We need a periodic solution of Eq. (3.119) and find it in the following form

$$\tau(x) = C[\cos \lambda_n(x-c) + \cos \lambda_n x] \ . \tag{3.120}$$

Substituting into Eq. (3.119) and taking into account that $\lambda_n = \pi/l_n$ we get

$$C = V\frac{\pi G_m(1+\bar{d})}{2l_n(1+\beta_n)}, \quad \beta_n = \frac{\pi^2 a^2 G_m}{12 l_n^2 E_m} \ . \tag{3.121}$$

Now, using Eqs. (3.115), (3.118), and (3.120) we can write the final expressions for the stresses acting in the matrix

$$\begin{aligned} \tau_{xy} &= C[\cos \lambda_n(x-c) + \cos \lambda_n x], \\ \sigma_y &= -\left[C\lambda_n\left(\frac{a}{2} - y\right) - \frac{E_m}{a}V\right] \sin \lambda_n(x-c) \\ &\quad - \left[C\lambda_n\left(\frac{a}{2} - y\right) + \frac{E_m}{a}V\right] \sin \lambda_n x \ , \end{aligned} \tag{3.122}$$

where C is specified with Eqs. (3.121). The corresponding strain energies of the typical element in Fig. 3.61 are

$$W_m^s = \frac{ad}{2G_m}\int_0^{l_n} \tau_{xy}^2 \, dx, \quad W_m^e = \frac{ad}{2E_m}\int_0^{l_n} \sigma_y^2 \, dx \ .$$

Substituting Eqs. (3.122) and integrating we arrive at

$$\begin{aligned} W_m^s &= \frac{adl_n}{2G_m} C^2(1 + \cos \lambda_n c), \\ W_m^e &= \frac{adl_n}{2E_m}\left[\frac{\pi^2 a^2}{12 l_n^2} C^2(1 + \cos \lambda_n c) + \frac{E_m^2}{a^2} V^2(1 - \cos \lambda_n c)\right] \ . \end{aligned}$$

In conjunction with these results, Eqs.(3.109), (3.111)–(3.113) and (3.121) allow us to determine σ_1 which acquires the following final form

$$\sigma_1 = \frac{\pi^2 D_f}{\bar{l}_n^2 \bar{d}(1+\bar{d})a^4} + \frac{G_m(1+\bar{d})}{2\left(1+(\pi^2 G_m/12\bar{l}_n^2 E_m)\right)}\left(1+\cos\frac{\pi\bar{c}}{\bar{l}_n}\right) + \frac{2E_m\bar{l}_n^2}{\pi^2(1+\bar{d})}\left(1-\cos\frac{\pi\bar{c}}{\bar{l}_n}\right), \tag{3.123}$$

where $\bar{d} = d/a$, $\bar{l}_n = l_n/a$, $\bar{c} = c/a$. The critical value of σ_1 can be found by minimization of the right-hand part of Eq. (3.123) with respect to $\bar{l}_n$ and $\bar{c}$. However, having in mind only qualitative analysis we can omit this cumbersome procedure and use Eq. (3.123) for the qualitative assessments and estimates.

As follows from this equation, the strength of a unidirectional composite under longitudinal compression should increase with the rise of the fiber bending stiffness. This prediction is definitely supported with experimental data presented in Table 3.6. The highest strength is demonstrated by composites reinforced with boron fibers that have relatively high diameter and high modulus providing very high fiber bending stiffness. Carbon fibers also having high modulus but less diameter than boron fibers provide compressive strength which is 40% lower than that of boron composites, but is two times higher than the strength of composite reinforced with glass fibers having the same diameter as that of carbon fibers but lower modulus. The lowest strength in compression is demonstrated by composites with aramid fibers. As was already noted, these fibers having high tensile stiffness consist of a system of poorly bonded thin filaments and possess low bending stiffness. As can be seen in Eq. (3.123), compressive strength also increases with the rise of the matrix stiffness. Available experimental results (Woolstencroft et al., 1982; Crasto and Kim, 1993), show that the strength of carbon composites in compression linearly increases while the matrix shear modulus rises up to $G_m = 1500$ MPa which is the value typical for epoxy resins. For higher values of G_m, compression strength does not change, and we can expect that there exists some maximum value of G_m beyond which the matrix does not allow fibers to buckle, and material strength is controlled by fiber strength in compression. Results listed in Table 3.5 support this conclusion. As can be seen, changing epoxy matrix for aluminum one with higher stiffness we do not increase the compressive strength of boron composites. Moreover, increasing the matrix stiffness we usually reduce its ultimate elongation. As a result, material can fail under relatively low stress because of delamination (see Fig. 3.57). An example of such a material can also be found in Table 3.5. Carbon–carbon unidirectional composites with brittle carbon matrix possessing very high stiffness demonstrate very low strength under longitudinal compression.

Fracture of actual unidirectional composites occurs usually as a result of interaction of fracture modes discussed above. Such fracture is shown in Fig. 3.64. Ultimate stress depends on material structural and manufacturing parameters, has considerable scatter, and can hardly be predicted theoretically. For example, compression strength of composites with the same fibers and matrices having the same stiffness but different nature (thermoset or thermoplastic) can be different (Crasto and Kim, 1993).

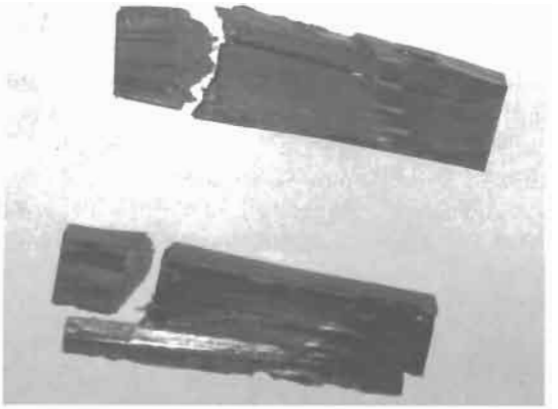

Fig. 3.64. Failure mode of a unidirectional carbon–epoxy composite under longitudinal compression.

Strength of composites under longitudinal compression is determined experimentally using ring or flat specimens and special methods to prevent the specimen buckling (Tarnopol'skii and Kincis, 1985). The most accurate results are provided by compression of sandwich specimens with composite facings made from the material under study (Crasto and Kim, 1993).

3.4.5. Transverse compression

Under compression across the fibers, unidirectional composites exhibit traditional shear mode of fracture of the type shown in Fig. 3.65. Transverse compression strength is higher than in-plane shear strength (see Table 3.5) because of two main reasons. First, the area of the oblique failure plane is larger than the area of the orthogonal longitudinal ply cross-section in which the ply fails under in-plane shear and, second, additional compression across the oblique failure plane (see Fig. 3.65) increases the shear strength. Strength under transverse compression is measured using flat or tubular specimens shown in Figs. 3.52 and 3.53.

3.5. Hybrid composites

The foregoing sections of this chapter concern the properties of unidirectional plies reinforced with fibers of a certain type – glass, carbon, aramid, etc. In

Fig. 3.65. Failure under transverse compression.

hybrid composites, the plies can include fibers of two, or may be more types, e.g., carbon and glass, glass and aramid and so on. Hybrid composites provide wider possibilities to control material stiffness, strength and cost. A promising application of these materials is associated with the so-called thermostable structures that do not change their dimensions under heating or cooling. For some composites, e.g., with glass of boron fibers, longitudinal coefficient of thermal expansion is positive, while for other materials, e.g., with carbon or aramid fibers, it is negative (see Table 7.1 and Section 7.1.2 of Chapter 7). So, the proper combination of fibers with positive and negative coefficients can result in material with zero thermal expansion.

Consider the problem of micromechanics for a unidirectional ply reinforced with two types of fibers. Naturally, the stiffness of these fibers should be different, and we assume that $E_f^{(1)} > E_f^{(2)}$. The first-order model of the ply that generalizes the model in Fig. 3.34 is presented in Fig. 3.66. For tension in the fiber direction, the apparent stress and strain, σ_1 and ε_1, are linked by Hooke's law

$$\sigma_1 = E_1 \varepsilon_1 \tag{3.124}$$

in which the effective modulus is specified by the following equation generalizing Eq. (3.76)

$$E_1 = E_f^{(1)} v_f^{(1)} + E_f^{(2)} v_f^{(2)} + E_m v_m \ . \tag{3.125}$$

Here, $v_f^{(1)}$ and $v_f^{(2)}$ are volume fractions of the fibers of the first and of the second type and v_m is the matrix volume fraction, so that

$$v_f^{(1)} + v_f^{(2)} + v_m = 1 \ .$$

We also introduce the total volume fraction of the fibers

$$v_f = v_f^{(1)} + v_f^{(2)}$$

and normalized volume fractions of fibers as

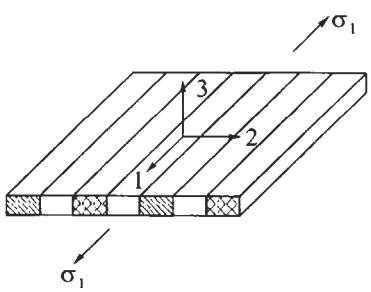

Fig. 3.66. A first-order microstructural model of a hybrid unidirectional ply.

$$w_f^{(1)} = \frac{v_f^{(1)}}{v_f}, \quad w_f^{(2)} = \frac{v_f^{(2)}}{v_f} .$$

Obviously

$$w_f^{(1)} + w_f^{(2)} = 1 .$$

Then, Eq. (3.125) can be written in the form

$$E_1 = v_f[E_f^{(1)} w_f^{(1)} + E_f^{(2)}(1 - w_f^{(1)})] + E_m(1 - v_f) . \tag{3.126}$$

Linear dependence of E_1 on $w_f^{(1)}$ predicted by Eq. (3.126) is in good correlation with experimental data reported by Zabolotskii and Varshavskii (1984) and presented in Fig. 3.67.

Since the fibers of hybrid composites have different stiffness, they are characterized, as a rule, with different ultimate elongations. As follows from Fig. 3.68 plotted with the data listed in Table 3.5, there exists an inverse linear dependence between the ply longitudinal modulus and the ultimate elongation $\bar{\varepsilon}_1$. So, assuming $E_f^{(1)} > E_f^{(2)}$ we should take into account that $\bar{\varepsilon}_f^{(1)} < \bar{\varepsilon}_f^{(2)}$. This means that Eq. (3.124) is valid until $\varepsilon_1 \leqslant \bar{\varepsilon}_f^{(1)}$. Strain $\varepsilon_1 = \bar{\varepsilon}_f^{(1)}$ is accompanied with the failure of fibers of the first type. The corresponding part of a possible stress–strain diagram is shown in Fig. 3.69 with the line OA. The stress at point A is $\sigma_1^{(1)} = E_1 \bar{\varepsilon}_f^{(1)}$. After the fibers of the first type fail, material modulus reduces to

$$E_1^* = E_f^{(2)} v_f (1 - w_f^{(1)}) + E_m(1 - v_f) .$$

This modulus determines the slope of line OC in Fig. 3.69.

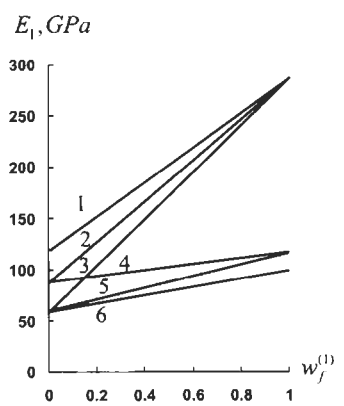

Fig. 3.67. Experimental dependencies of longitudinal modulus on the volume fraction of the higher modulus fibers in hybrid unidirectional composites: 1 – boron–carbon; 2 – boron–aramid; 3 – boron–glass; 4 – carbon–aramid; 5 – carbon–glass; 6 – aramid–glass.

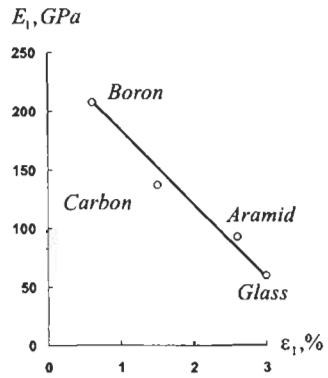

Fig. 3.68. Longitudinal modulus versus ultimate tensile strain for advanced epoxy unidirectional composites.

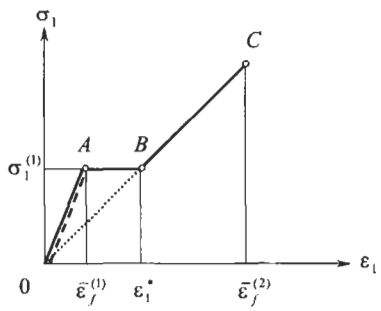

Fig. 3.69. Typical stress–strain diagrams for hybrid unidirectional composites.

As $E_1^* < E_1$, the ply experiences a jump of strain under constant stress $\sigma_1 = \sigma_1^{(1)}$. As follows from Fig. 3.69, the final strain is

$$\varepsilon_1^* = \frac{\sigma_1^{(1)}}{E_1^*} \quad .$$

There are two possible scenarios of the further material behavior depending on the relation of strain ε_1^* and the ultimate strain of the fibers of the second type, $\bar{\varepsilon}_f^{(2)}$. If $\varepsilon_1^* \geqslant \bar{\varepsilon}_f^{(2)}$, these fibers will also fail under stress $\sigma_1^{(1)}$, and the material stress–strain diagram corresponds to the broken line OA in Fig. 3.69. If $\bar{\varepsilon}_f^{(2)} > \varepsilon_1^*$, material will work up to point C in this figure. Experimental diagrams supporting this prediction are shown in Fig. 3.70 (Gunyaev, 1981).

The threshold value of $w_f^{(2)}$ indicating the minimum amount of the second-type fibers that is enough to withstand the load after the failure of the first-type fibers

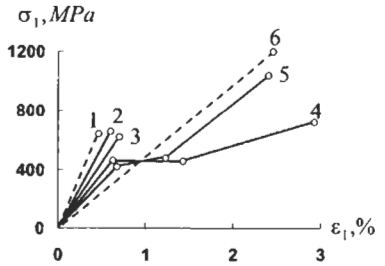

Fig. 3.70. Experimental stress–strain diagrams for hybrid carbon–glass epoxy unidirectional composite with various volume fraction of glass fibers v_g and carbon fibers v_c: 1 – $v_g = 0$; 2 – $v_g = 0.07$; 3 – $v_g = 0.14$; 4 – $v_g = 0.25$; 5 – $v_g = 0.5$; 6 – $v_c = 0$.

can be found from the condition $\bar{\varepsilon}_1^* = \bar{\varepsilon}_f^{(2)}$ (Skudra et al., 1989). The final result is as follows

$$\bar{w}_f^{(2)} = \frac{E_f^{(1)} v_f \bar{\varepsilon}_f^{(1)} - (1 - v_f) E_m (\bar{\varepsilon}_f^{(2)} - \bar{\varepsilon}_f^{(1)})}{v_f [E_f^{(1)} \bar{\varepsilon}_f^{(1)} + E_f^{(2)} (\bar{\varepsilon}_f^{(2)} - \bar{\varepsilon}_f^{(1)})]} .$$

For $w_f^{(2)} < \bar{w}_f^{(2)}$, material strength can be calculated as $\bar{\sigma}_1 = E_1 \bar{\varepsilon}_f^{(1)}$, while for $w_f^{(2)} > \bar{w}_f^{(2)}$, $\bar{\sigma}_1 = E_1^* \bar{\varepsilon}_f^{(2)}$. The corresponding theoretical prediction of the dependence of material strength on $w_f^{(2)}$ are shown in Fig. 3.71 (Skudra et al., 1989).

3.6. Phenomenological homogeneous model of a ply

As follows from the foregoing discussion, micromechanical analysis provides very approximate prediction for the ply stiffness and only qualitative information concerning the ply strength. However, design and analysis of composite structures require rather accurate and reliable information about the properties of the ply

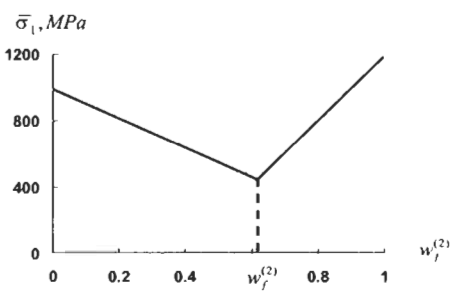

Fig. 3.71. Dependence of the longitudinal strength of unidirectional carbon–glass epoxy composite on the volume fraction of glass fibers.

that is the basic element of composite structures. This information is provided by experimental methods discussed above. As a result, the ply is presented as an orthotropic homogeneous material possessing some apparent (effective) mechanical characteristics determined experimentally. This means that on the ply level we use a phenomenological model of a composite material (see Section 1.1) that ignores its actual microstructure.

It should be emphasized that this model, being quite natural and realistic for the majority of applications, sometimes does not allow us to predict actual material behavior. To demonstrate this, consider a problem of biaxial compression of a unidirectional composite in the 23-plane as in Fig. 3.72. Testing a glass–epoxy composite material described by Koltunov et al. (1977) shows a surprising result – its strength is about $\bar{\sigma} = 1200$ MPa which is quite close to the level of material strength under longitudinal tension, and material failure is accompanied with the fiber breakage typical for longitudinal tension.

Phenomenological model fails to predict this mode of failure. Indeed, the average stress in the longitudinal direction specified by Eq. (3.75) is equal to zero under loading shown in Fig. 3.72, i.e.,

$$\sigma_1 = \sigma_1^{\mathrm{f}} v_{\mathrm{f}} + \sigma_1^{\mathrm{m}} v_{\mathrm{m}} = 0 \ . \tag{3.127}$$

To apply the first-order micromechanical model considered in Section 3.3, we generalize constitutive equations, Eqs. (3.63), for the three-dimensional stress state of the fibers and the matrix as

$$\varepsilon_1^{\mathrm{f,m}} = \frac{1}{E_{\mathrm{f,m}}} [\sigma_1^{\mathrm{f,m}} - \nu_{\mathrm{f,m}} (\sigma_2^{\mathrm{f,m}} + \sigma_3^{\mathrm{f,m}})] \quad (1,2,3) \ . \tag{3.128}$$

Changing 1 for 2, 2 for 3, and 3 for 1 we can write the corresponding equations for ε_2 and ε_3.

Assume that the stresses acting in the fibers and in the matrix in the plane of loading are the same, i.e.,

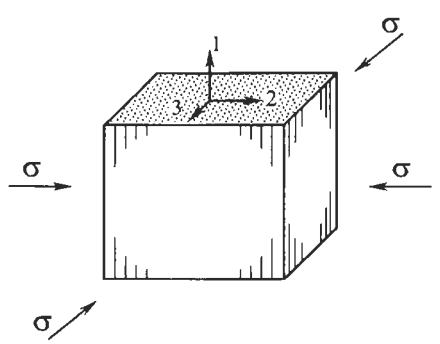

Fig. 3.72. Biaxial compression of a unidirectional composite.

$$\sigma_2^{\mathrm{f}} = \sigma_3^{\mathrm{f}} = \sigma_2^{\mathrm{m}} = \sigma_3^{\mathrm{m}} = -\sigma \tag{3.129}$$

and that $\varepsilon_1^{\mathrm{f}} = \varepsilon_1^{\mathrm{m}}$. Substituting $\varepsilon_1^{\mathrm{f}}$ and $\varepsilon_1^{\mathrm{m}}$ from Eqs. (3.128) we get with due regard to Eqs. (3.129)

$$\frac{1}{E_{\mathrm{f}}}(\sigma_1^{\mathrm{f}} + 2\nu_{\mathrm{f}}\sigma) = \frac{1}{E_{\mathrm{m}}}(\sigma_1^{\mathrm{m}} + 2\nu_{\mathrm{m}}\sigma) \ .$$

In conjunction with Eq. (3.127), this equation allows us to find σ_1^{f} which has the form

$$\sigma_1^{\mathrm{f}} = \frac{2\sigma(E_{\mathrm{f}}\nu_{\mathrm{m}} - E_{\mathrm{m}}\nu_{\mathrm{f}})v_{\mathrm{m}}}{E_{\mathrm{f}}v_{\mathrm{f}} + E_{\mathrm{m}}v_{\mathrm{m}}} \ .$$

Simplifying this result under the condition $E_{\mathrm{f}} \gg E_{\mathrm{m}}$ we arrive at

$$\sigma_1^{\mathrm{f}} = 2\sigma\frac{\nu_{\mathrm{m}}v_{\mathrm{m}}}{v_{\mathrm{f}}} \ .$$

Thus, the loading shown in Fig. 3.72 indeed induces tension of fibers that can be revealed using the micromechanical model. The ultimate stress can be expressed in terms of fibers' strength $\bar{\sigma}_{\mathrm{f}}$ as

$$\bar{\sigma} = \frac{1}{2}\bar{\sigma}_{\mathrm{f}}\frac{v_{\mathrm{f}}}{\nu_{\mathrm{m}}v_{\mathrm{m}}} \ .$$

The actual material strength is not as high as follows from this equation which is derived under the condition that adhesion strength between the fibers and the matrix is infinitely high. Tension of fibers is induced by the matrix that expands in the 1-direction (see Fig. 3.72) due to the Poisson effect and interacts with fibers through shear stresses whose maximum value is limited by the fiber–matrix adhesion strength. Under high shear stress, debonding of fibers can occur reducing the material strength that is, nevertheless, very high. This effect is utilized in composite shell with radial reinforcement designed to withstand high intensity external pressure (Koltunov et al., 1977).

3.7. References

Abu-Farsakh, G.A., Abdel-Jawad, Y.A. and Abu-Laila, Kh.M. (2000). Micromechanical characterization of tensile strength of fiber composite materials. *Mech. Composite Mater. Struct.* 7(1), 105–122.

Bogdanovich, A.E. and Pastore, C.M. (1996). *Mechanics of Textile and Laminated Composites.* Chapman & Hall, London.

Chiao, T.T. (1979). Some interesting mechanical behaviors of fiber composite materials. In *Proc. of 1st USA–USSR Symposium on Fracture of Composite Materials*, Riga, USSR, 4–7 September, 1978 (G.C. Sih and V.P. Tamuzh eds.). Sijthoff and Noordhoff, Alphen aan den Rijn., pp. 385–392.

Crasto, A.S. and Kim, R.Y. (1993). An improved test specimen to determine composite compression strength. In *Proc. 9th Int. Conf. on Composite Materials (ICCM/9)*, Madrid, 12–16 July 1993. *Vol. 6, Composite Properties and Applications.* Woodhead Publishing Ltd, pp. 621–630.

Fukuda, H., Miyazawa, T. and Tomatsu, H. (1993). Strength distribution of monofilaments used for advanced composites. In *Proc. 9th Int. Conf. on Composite Materials (ICCM/9)*, Madrid, 12–16 July 1993 *Vol. 6, Composite Properties and Applications*. University of Zaragoza, Woodhead Publishing Ltd., pp. 687–694.

Gilman, J.J. (1959). *Cleavage, Ductility and Tenacity in Crystals*. In *Fracture*, Wiley, New York.

Griffith, A.A. (1920). The phenomenon of rupture and flow in solids. *Phil. Trans. Roy. Soc.* **A221**, 147–166.

Goodey, W.J. (1946). Stress diffusion problems. *Aircraft Eng.* June 1946, 195–198; July 1946, 227–234; August 1946, 271–276; September 1946, 313–316; October 1946, 343–346; November 1946, 385–389.

Gunyaev, G.M. (1981). *Structure and Properties of Polymeric Fibrous Composites*. Khimia, Moscow (in Russian).

Hashin, Z. and Rosen, B.W. (1964). The elastic moduli of fiber reinforced materials. *J. Appl. Mech.* **31E**, 223–232.

Jones, R.M. (1999). *Mechanics of Composite Materials*, 2nd edn. Taylor & Francis, Philadelphia, PA.

Koltunov, M.A., Pleshkov, L.V., Kanovich, M.Z., Roginskii, S.L. and Natrusov, V.I. (1977). High strength under uniform compression of fiberglass shells with radial reinforcement. *Polym. Mech.* **6**, 1109–1111 (in Russian).

Kondo, K. and Aoki, T. (1982). Longitudinal shear modulus of unidirectional composites. In *Proc. 4th Int. Conf. on Composite Materials (ICCM-IV), Vol.I, Progr. in Sci. and Eng. of Composites* (Hayashi, Kawata and Umeka eds.). Tokyo, 1982, pp. 357–364.

Lagace, P.A. (1985). Nonlinear stress-strain behavior of graphite/epoxy laminates. *AIAA J.* **223**(10), 1583–1589.

Lee, D.J., Jeong, T.H. and Kim, H.G. (1995). Effective longitudinal shear modulus of unidirectional composites. In *Proc. 10th Int. Conf. on Composite Materials (ICCM-10), Vol.4, Characterization and Ceramic Matrix Composites*, Canada, 1995, pp. 171–178.

Mikelsons, M.Ya. and Gutans, Yu.A. (1984). Fracture of boron–aluminum under static and cyclic tension. *Mech. Comp. Mater.* **1**, 52–59.

Mileiko, S.T. (1982). Mechanics of metal–matrix fibrous composites. In *Mechanics of Composites*. (Obraztsov, I.F. and Vasiliev, V.V. eds.). Mir, Moscow, pp. 129–165.

Skudra, A.M., Bulavs, F.Ya., Gurvich, M.R. and Kruklinsh, A.A. (1989). *Elements of Structural Mechanics of Composite Truss Systems*. Riga, Zinatne (in Russian).

Tarnopol'skii, Yu.M. and Roze, A.V. (1969). *Specific Features of Analysis for Structural Elements of Reinforced Plastics*. Riga, Zinatne (in Russian).

Tarnopol'skii, Yu.M. and Kincis, T.Ya. (1985). *Static Test Methods for Composites*. Van Nostrand Reinhold, New York.

Tikhomirov, P.V. and Yushanov, S.P. (1980). Stress distribution after the fracture of fibers in a unidirectional composite. In *Mech. Composite Mater.*, Riga, pp. 28–43 (in Russian).

Timoshenko, S.P. and Gere, J.M. (1961). *Theory of Elastic Stability*, 2nd edn. McGraw-Hill, New York.

Van Fo Fy (Vanin), G.A. (1966). Elastic Constants and state of stress of glass-reinforced strip. *J. Polym Mech.* **2**(4), 368–372.

Vasiliev, V.V. and Tarnopol'skii, Yu.M. (1990). *Composite Materials. Handbook* (Vasiliev, V.V. and Tarnopol'skii, Yu.M. eds.). Mashinostroenie, Moscow (in Russian).

Woolstencroft, D.H., Haresceugh, R.I. and Curtis, A.R. (1982). The compressive behavior of carbon fiber reinforced plastic. In *Proc. 4th Int. Conf. on Composite Materials (ICCM-IV), Vol.I, Progress in Science and Engineering of Composites* (Hayashi, Kawata and Umeka eds.). Tokyo, 1982, pp. 439–446.

Zabolotskii, A.A. and Varshavskii, V.Ya. (1984). Multireinforced (Hybrid) composite materials. In *Science and Technology Reviews*, Composite Materials, Part 2, Moscow.

Chapter 4

MECHANICS OF A COMPOSITE LAYER

A typical composite laminate consists of individual layers (see Fig. 4.1) which are usually made of unidirectional plies with the same or regularly alternating orientation. A layer can be also made from metals, thermosetting or thermoplastic polymers, and fabric or can have a spatial three-dimensionally reinforced structure. In contrast to a ply considered in Chapter 3, a layer is referred to a global coordinate frame x, y, z of the structural element rather than to coordinates 1, 2, 3 associated with the ply orientation. Usually, a layer is much thicker than a ply and has a more complicated structure, but this structure does not change through its thickness, or this change is ignored. Thus, a layer can be defined as a three-dimensional structural element that is uniform in transverse (normal to the layer plane) direction.

4.1. Isotropic layer

The simplest layer that can be observed in composite laminates is an isotropic layer of metal or thermoplastic polymer that is used to protect the composite material (Fig. 4.2) and to provide the tightness. For example, filament wound composite pressure vessels usually have a sealing metal (Fig. 4.3) or thermoplastic (Fig. 4.4) internal liner, that can also be used as a mandrel for winding. Because the layer is isotropic, we need only one coordinate system and let it be the global coordinate frame as in Fig. 4.5.

4.1.1. Linear elastic model

Explicit form of Hooke's law in Eqs. (2.48) and (2.54) can be written as:

$$\begin{aligned}
\varepsilon_x &= \frac{1}{E}(\sigma_x - \nu\sigma_y - \nu\sigma_z), \quad \gamma_{xy} = \frac{\tau_{xy}}{G}, \\
\varepsilon_y &= \frac{1}{E}(\sigma_y - \nu\sigma_x - \nu\sigma_z), \quad \gamma_{xz} = \frac{\tau_{xz}}{G}, \\
\varepsilon_z &= \frac{1}{E}(\sigma_z - \nu\sigma_x - \nu\sigma_y), \quad \gamma_{yz} = \frac{\tau_{yz}}{G} \ ,
\end{aligned} \tag{4.1}$$

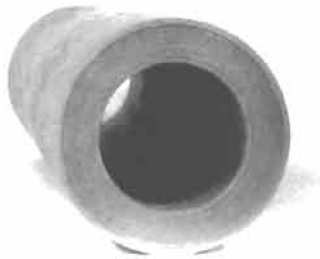

Fig. 4.1. Laminated structure of a composite pipe.

Fig. 4.2. Composite drive shaft with external metal protection layer. Courtesy of CRISM.

Fig. 4.3. Aluminum liner for a composite pressure vessel.

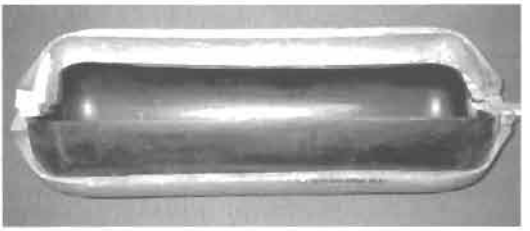

Fig. 4.4. Filament wound composite pressure vessel with a polyethylene liner. Courtesy of CRISM.

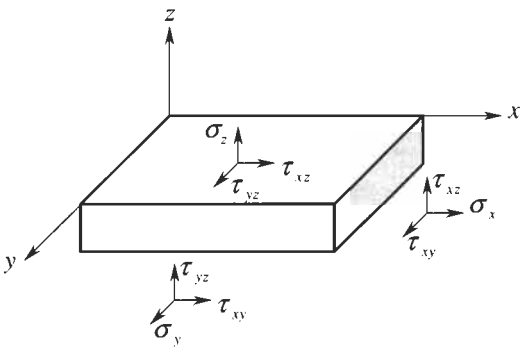

Fig. 4.5. An isotropic layer.

where E is the modulus of elasticity, ν the Poisson's ratio, and G is the shear modulus that can be expressed in terms of E and ν with Eq. (2.57). Adding Eqs. (4.1) for normal strains, we get

$$\varepsilon_0 = \frac{1}{K}\sigma_0 \ , \tag{4.2}$$

where

$$\varepsilon_0 = \varepsilon_x + \varepsilon_y + \varepsilon_z \tag{4.3}$$

is the volume deformation. For small strains, volume dV_1 of an infinitesimal material element after the deformation can be found knowing volume dV before the deformation and ε_0 as

$$dV_1 = (1 + \varepsilon_0)dV \ .$$

Volume deformation is linked with the mean stress

$$\sigma_0 = \tfrac{1}{3}(\sigma_x + \sigma_y + \sigma_z) \tag{4.4}$$

through volume or bulk modulus

$$K = \frac{E}{3(1-2\nu)} \quad . \tag{4.5}$$

For $\nu = 1/2$, $K \to \infty$, $\varepsilon_0 = 0$, and $dV_1 = dV$ for any stresses. Such materials are called incompressible – they do not change their volume under deformation and can change only their shape.

The foregoing equations correspond to the general three-dimensional stressed state of a layer. However, working as a structural element of a thin-walled composite laminate a layer is usually loaded with a system of stresses one of which, namely, transverse normal stress σ_z is much less than the other stresses. Bearing this in mind, we can neglect the terms in Eqs. (4.1) that include σ_z and write these equations in a simplified form:

$$\begin{aligned} &\varepsilon_x = \frac{1}{E}(\sigma_x - \nu\sigma_y), \quad \varepsilon_y = \frac{1}{E}(\sigma_y - \nu\sigma_x), \\ &\gamma_{xy} = \frac{\tau_{xy}}{G}, \quad \gamma_{xz} = \frac{\tau_{xz}}{G}, \quad \gamma_{yz} = \frac{\tau_{yz}}{G} \end{aligned} \tag{4.6}$$

or

$$\begin{aligned} &\sigma_x = \bar{E}(\varepsilon_x + \nu\varepsilon_y), \quad \sigma_y = \bar{E}(\varepsilon_y + \nu\varepsilon_x), \\ &\tau_{xy} = G\gamma_{xy}, \quad \tau_{xz} = G\gamma_{xz}, \quad \tau_{yz} = G\gamma_{yz} \ , \end{aligned} \tag{4.7}$$

where $\bar{E} = E/(1-\nu^2)$.

4.1.2. Nonlinear models

Materials of metal and polymeric layers considered in this section demonstrate linear response only under moderate stresses (see Fig. 1.11 and 1.14). Further loading results in nonlinear behavior to describe which we need to apply one of nonlinear material models discussed in Section 1.1.

A relatively simple nonlinear constitutive theory suitable for polymeric layers can be constructed using nonlinear elastic material model (see Fig. 1.2). In the strict sense, this model can be applied to materials whose stress–strain curves are the same for active loading and unloading. But normally structural analysis is undertaken only for active loading. If unloading is not considered, elastic model can be formally used for materials that are not perfectly elastic.

There exists a number of models developed to describe nonlinear behavior of highly deformable elastomers like rubber (Green and Adkins, 1960). Polymeric materials used to form isotropic layers of composite laminates admitting, in principal, high strains usually do not demonstrate them in composite structures whose deformation is governed by fibers with relatively low ultimate elongation (1–3%). So, creating the model we can restrict ourselves to the case of small strains, i.e., to materials whose typical stress–strain diagram is shown in Fig. 4.6.

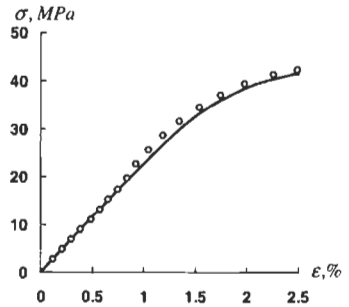

Fig. 4.6. A typical stress–strain diagram (circles) for a polymeric film and its cubic approximation (solid line).

A natural way is to apply Eqs. (2.41) and (2.42), i.e., (we use tensor notations for stresses and strains introduced in Section 2.9 and the rule of summation over repeated subscripts),

$$dU = \sigma_{ij}\, d\varepsilon_{ij}, \quad \sigma_{ij} = \frac{\partial U}{\partial \varepsilon_{ij}} \ . \tag{4.8}$$

Approximation of elastic potential U as a function of ε_{ij} with some unknown parameters allows us to write constitutive equations directly using the second relation in Eqs. (4.8). However, the polynomial approximation similar to Eq. (2.43), which is the most simple and natural results in constitutive equation of the type $\sigma = S\varepsilon^n$, where S is some stiffness coefficient and n is an integer. As can be seen in Fig. 4.7, the resulting stress–strain curve is not typical for materials under study. Better agreement with nonlinear experimental diagrams presented, e.g., in Fig. 4.6, is demonstrated by the curve specified by the equation $\varepsilon = C\sigma^n$, where C is some compliance coefficient. To arrive at this form of a constitutive equation, we need to have a relationship similar to the second one in Eqs. (4.8) but allowing us to express strains in terms of stresses. Such relationships exist and are known as Castigliano's formulas. To derive them, introduce the complementary elastic potential U_c in accordance with the following equation:

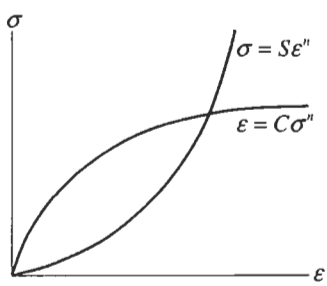

Fig. 4.7. Two forms of approximation of the stress–strain curve.

$$dU_c = \varepsilon_{ij}\, d\sigma_{ij} \ . \tag{4.9}$$

The name "complementary" becomes clear if we consider a bar in Fig. 1.1 and the corresponding stress–strain curve in Fig. 4.8. The area *OBC* below the curve represents U in accordance with the first equation in Eqs. (4.8), while the area *OAB* above the curve is equal to U_c. As was shown in Section 2.9, dU in Eqs. (4.8) is an exact differential. To prove the same for dU_c, consider the following sum:

$$dU + dU_c = \sigma_{ij}\, d\varepsilon_{ij} + \varepsilon_{ij}\, d\sigma_{ij} = d(\sigma_{ij}\varepsilon_{ij}) \ ,$$

which is obviously an exact differential. Since dU in this sum is also an exact differential, dU_c should have the same property and can be expressed as

$$dU_c = \frac{\partial U_c}{\partial \sigma_{ij}} d\sigma_{ij} \ .$$

Comparing this result with Eq. (4.9), we arrive at Castigliano's formulas

$$\varepsilon_{ij} = \frac{\partial U_c}{\partial \sigma_{ij}} \ , \tag{4.10}$$

which are valid for any elastic solid (for a linear elastic solid, $U_c = U$).

Complementary potential, U_c, in general, depends on stresses, but for an isotropic material, Eq. (4.10) should yield invariant constitutive equations that do not depend on the direction of coordinate axes. This means that U_c should depend on stress invariants I_1, I_2, I_3 in Eqs. (2.13). Assuming different approximations for function $U_c(I_1, I_2, I_3)$we can construct different classes of nonlinear elastic models. Existing experimental verification of such models shows that dependence U_c on I_3 can be neglected. Thus, we can present complementary potential in a simplified form $U_c(I_1, I_2)$and expand this function into the Taylor series as

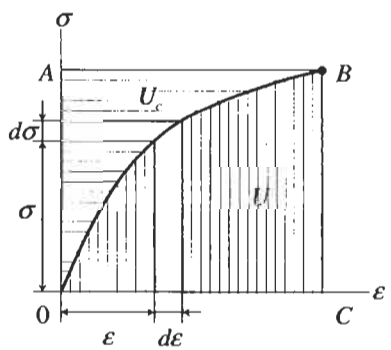

Fig. 4.8. Geometric interpretation of elastic potential, U, and complementary potential, U_c.

$$U_c = c_0 + c_{11}I_1 + \frac{1}{2}c_{12}I_1^2 + \frac{1}{3!}c_{13}I_1^3 + \frac{1}{4!}c_{14}I_1^4 + \cdots$$
$$+ c_{21}I_2 + \frac{1}{2}c_{22}I_2^2 + \frac{1}{3!}c_{23}I_2^3 + \frac{1}{4!}c_{24}I_2^4 + \cdots$$
$$+ \frac{1}{2}c_{1121}I_1I_2 + \frac{1}{3!}c_{1221}I_1^2I_2 + \frac{1}{3!}c_{1122}I_1I_2^2$$
$$+ \frac{1}{4!}c_{1321}I_1^3I_2 + \frac{1}{4!}c_{1222}I_1^2I_2^2 + \frac{1}{4!}c_{1123}I_1I_2^3 + \cdots \quad , \tag{4.11}$$

where

$$c_{in} = \left.\frac{\partial^n U_c}{\partial I_i^n}\right|_{\sigma_{ij}=0}, \quad c_{injm} = \left.\frac{\partial^{n+m} U_c}{\partial I_i^n \partial I_j^m}\right|_{\sigma_{ij}=0} .$$

Constitutive equations follow from Eq. (4.10) and can be written in the form

$$\varepsilon_{ij} = \frac{\partial U_c}{\partial I_1}\frac{\partial I_1}{\partial \sigma_{ij}} + \frac{\partial U_c}{\partial I_2}\frac{\partial I_2}{\partial \sigma_{ij}} \quad . \tag{4.12}$$

Assuming that for zero stresses $U_c = 0$ and $\varepsilon_{ij} = 0$ we should take $c_0 = 0$ and $c_{11} = 0$ in Eq. (4.11).

Consider a plane stressed state with stresses σ_x, σ_y, τ_{xy} shown in Fig. 4.5. Stress invariants in Eqs. (2.13) entering Eq. (4.12) are

$$I_1 = \sigma_x + \sigma_y, \quad I_2 = -\sigma_x\sigma_y + \tau_{xy}^2 \quad . \tag{4.13}$$

Linear elastic material model is described with Eq. (4.11) if we take

$$U_c = \tfrac{1}{2}c_{12}I_1^2 + c_{21}I_2 \quad . \tag{4.14}$$

Using Eqs. (4.12)–(4.14) and engineering notations for stresses and strains, we arrive at

$$\varepsilon_x = c_{12}(\sigma_x + \sigma_y) - c_{21}\sigma_y, \quad \varepsilon_y = c_{12}(\sigma_x + \sigma_y) - c_{21}\sigma_x, \quad \gamma_{xy} = 2c_{21}\tau_{xy} \quad .$$

These equations coincide with the corresponding equations in Eqs. (4.6) if we take

$$c_{12} = \frac{1}{E}, \quad c_{21} = \frac{1+\nu}{E} \quad .$$

To describe nonlinear stress–strain diagram of the type shown in Fig. 4.6, we can generalize Eq. (4.14) as

$$U_c = \frac{1}{2}c_{12}I_1^2 + c_{21}I_2 + \frac{1}{4!}c_{14}I_1^4 + \frac{1}{2}c_{22}I_2^2 \quad .$$

Then, Eqs. (4.12) yield the following cubic constitutive law:

$$\varepsilon_x = c_{12}(\sigma_x + \sigma_y) - c_{21}\sigma_y + \tfrac{1}{6}c_{14}(\sigma_x + \sigma_y)^3 + c_{22}(\sigma_x\sigma_y - \tau_{xy}^2)\sigma_y,$$
$$\varepsilon_y = c_{12}(\sigma_x + \sigma_y) - c_{21}\sigma_x + \tfrac{1}{6}c_{14}(\sigma_x + \sigma_y)^3 + c_{22}(\sigma_x\sigma_y - \tau_{xy}^2)\sigma_x,$$
$$\gamma_{xy} = 2[c_{21} - c_{22}(\sigma_x\sigma_y - \tau_{xy}^2)]\tau_{xy} \ .$$

The corresponding approximation is shown in Fig. 4.6 with a solid line. Retaining more higher-order terms in Eq. (4.11), we can describe nonlinear behavior of any isotropic polymeric material.

To describe nonlinear elastic–plastic behavior of metal layers, we should use constitutive equations of the theory of plasticity. As known, there exist two basic versions of this theory – the deformation theory and the flow theory that are briefly described below.

According to the deformation theory of plasticity, the strains are decomposed into two components – elastic strains (with superscript 'e') and plastic strains (superscript 'p'), i.e.,

$$\varepsilon_{ij} = \varepsilon_{ij}^{e} + \varepsilon_{ij}^{p} \ . \tag{4.15}$$

We again use the tensor notations of strains and stresses (i.e., ε_{ij} and σ_{ij}) introduced in Section 2.9. Elastic strains are linked with stresses by Hooke's law, Eqs. (4.1), which can be written with the aid of Eq. (4.10) in the form

$$\varepsilon_{ij}^{e} = \frac{\partial U_e}{\partial \sigma_{ij}} \ , \tag{4.16}$$

where U_e is the elastic potential that for the linear elastic solid coincides with complementary potential U_c in Eq. (4.10). Explicit expression for U_e can be obtained from Eq. (2.51) if we change strains for stresses with the aid of Hooke's law, i.e.,

$$U_e = \frac{1}{2E}[\sigma_{11}^2 + \sigma_{22}^2 + \sigma_{33}^2 - 2\nu(\sigma_{11}\sigma_{22} + \sigma_{11}\sigma_{33} + \sigma_{22}\sigma_{33})]$$
$$+ \frac{1}{2G}(\sigma_{12}^2 + \sigma_{13}^2 + \sigma_{23}^2) \ . \tag{4.17}$$

Now present plastic strains in Eqs. (4.15) in the form similar to Eq. (4.16):

$$\varepsilon_{ij}^{p} = \frac{\partial U_p}{\partial \sigma_{ij}} \ , \tag{4.18}$$

where U_p is the plastic potential. To approximate dependence of U_p on stresses, a special generalized stress characteristic, i.e., the so-called stress intensity σ, is introduced in classical theory of plasticity as

$$\sigma = \frac{1}{\sqrt{2}}[(\sigma_{11} - \sigma_{22})^2 + (\sigma_{22} - \sigma_{33})^2 + (\sigma_{11} - \sigma_{33})^2 + 6(\sigma_{12}^2 + \sigma_{13}^2 + \sigma_{23}^2)]^{1/2} \ . \tag{4.19}$$

Transforming Eq. (4.19) with the aid of Eqs. (2.13) we can reduce it to the following form:

$$\sigma = \sqrt{I_1^2 + 3I_2} \ .$$

This means that σ is an invariant characteristic of a stress state, i.e., that it does not depend on position of a coordinate frame. For a unidirectional tension as in Fig. 1.1, we have only one nonzero stress, e.g., σ_{11}. Then Eq. (4.19) yields $\sigma = \sigma_{11}$. In a similar way, strain intensity ε can be introduced as

$$\varepsilon = \frac{\sqrt{2}}{3}[(\varepsilon_{11} - \varepsilon_{22})^2 + (\varepsilon_{22} - \varepsilon_{33})^2 + (\varepsilon_{11} - \varepsilon_{33})^2 + 6(\varepsilon_{12}^2 + \varepsilon_{13}^2 + \varepsilon_{23}^2)]^{1/2} \ . \tag{4.20}$$

Strain intensity is also an invariant characteristic. For a uniaxial tension (Fig. 1.1) with stress σ_{11} and strain ε_{11} in the loading direction, we have $\varepsilon_{22} = \varepsilon_{33} = -\nu_p \varepsilon_{11}$, where ν_p is the elastic–plastic Poisson's ratio which, in general, depends on σ_{11}. For this case, Eq. (4.20) yields

$$\varepsilon = \tfrac{2}{3}(1 + \nu_p)\varepsilon_{11} \ . \tag{4.21}$$

For an incompressible material (see Section 4.1.1), $\nu_p = 1/2$ and $\varepsilon = \varepsilon_{11}$. Thus, numerical coefficients in Eqs. (4.19) and (4.20) provide $\sigma = \sigma_{11}$ and $\varepsilon = \varepsilon_{11}$ for uniaxial tension of an incompressible material. Stress and strain intensities in Eqs. (4.19) and (4.20) have an important physical meaning. As known from experiments, metals do not demonstrate plastic properties under loading with stresses $\sigma_x = \sigma_y = \sigma_z = \sigma_0$ resulting only in the change of material volume. Under such loading, materials exhibit only elastic volume deformation specified by Eq. (4.2). Plastic strains occur in metals if we change material shape. For a linear elastic material, elastic potential U in Eq. (2.51) can be reduced after rather cumbersome transformation with the aid of Eqs. (4.3), (4.4) and (4.19), (4.20) to the following form:

$$U = \tfrac{1}{2}\sigma_0 \varepsilon_0 + \tfrac{1}{2}\sigma\varepsilon \ . \tag{4.22}$$

The first term in the right-hand side part of this equation is the strain energy associated with the volume change, while the second term corresponds to the change of material shape. Thus, σ and ε in Eqs. (4.19) and (4.20) are stress and strain

characteristics associated with the change of material shape under which it demonstrates the plastic behavior.

In the theory of plasticity, plastic potential U_p is assumed to be a function of stress intensity σ, and according to Eqs. (4.18), plastic strains are

$$\varepsilon_{ij}^{p} = \frac{dU_p}{d\sigma}\frac{\partial\sigma}{\partial\sigma_{ij}} \quad . \tag{4.23}$$

Consider further a plane stress state with stresses σ_x, σ_y, and τ_{xy} in Fig. 4.5. For this case, Eq. (4.19) acquires the form

$$\sigma = \sqrt{\sigma_x^2 + \sigma_y^2 - \sigma_x\sigma_y + 3\tau_{xy}^2} \tag{4.24}$$

Using Eqs. (4.15)–(4.17) and (4.23), (4.24) we finally arrive at the following constitutive equations:

$$\begin{aligned}
\varepsilon_x &= \frac{1}{E}(\sigma_x - \nu\sigma_y) + \omega(\sigma)\left(\sigma_x - \frac{1}{2}\sigma_y\right), \\
\varepsilon_y &= \frac{1}{E}(\sigma_y - \nu\sigma_x) + \omega(\sigma)\left(\sigma_y - \frac{1}{2}\sigma_x\right), \\
\gamma_{xy} &= \frac{1}{G}\tau_{xy} + 3\omega(\sigma)\tau_{xy} \quad ,
\end{aligned} \tag{4.25}$$

where

$$\omega(\sigma) = \frac{1}{\sigma}\frac{dU_p}{d\sigma} \quad . \tag{4.26}$$

To find $\omega(\sigma)$, we need to specify dependence of U_c on σ. The most simple and suitable for practical applications is the power approximation

$$U_p = C\sigma^n \quad , \tag{4.27}$$

where C and n are some experimental constants. As a result, Eq. (4.26) yields

$$\omega(\sigma) = Cn\sigma^{n-2} \quad . \tag{4.28}$$

To determine coefficients C and n we introduce the basic assumption of the plasticity theory concerning the existence of the universal stress–strain diagram (master curve). According to this assumption, for any particular material there exists the dependence between stress and strain intensities, i.e., $\sigma = \varphi(\varepsilon)$ (or $\varepsilon = f(\sigma)$), that is one and the same for all the loading cases. This fact enables us to find coefficients C and n from the test under uniaxial tension and extend thus obtained results to an arbitrary state of stress.

Indeed, consider a uniaxial tension as in Fig. 1.1 with stress σ_{11}. For this case, $\sigma = \sigma_x$, and Eqs. (4.25) yield

$$\varepsilon_x = \frac{\sigma_x}{E} + \omega(\sigma_x)\sigma_x \ , \tag{4.29}$$

$$\varepsilon_y = -\frac{\nu}{E}\sigma_x - \frac{1}{2}\omega(\sigma_x)\sigma_x \ , \tag{4.30}$$

$$\gamma_{xy} = 0 \ .$$

Solving Eq. (4.29) for $\omega(\sigma_x)$, we get

$$\omega(\sigma_x) = \frac{1}{E_s(\sigma_x)} - \frac{1}{E} \ , \tag{4.31}$$

where $E_s = \sigma_x/\varepsilon_x$ is the secant modulus introduced in Section 1.1 (see Fig. 1.4). Using now the existence of the universal diagram for stress intensity σ and taking into account that $\sigma = \sigma_x$ for a uniaxial tension, we can generalize Eq. (4.31) and write it for an arbitrary state of stress as

$$\omega(\sigma) = \frac{1}{E_s(\sigma)} - \frac{1}{E} \ . \tag{4.32}$$

To determine $E_s(\sigma) = \sigma/\varepsilon$, we need to plot the universal stress–strain curve. For this purpose, we can use an experimental diagram $\sigma_x(\varepsilon_x)$ for the case of uniaxial tension, e.g., the one shown in Fig. 4.9 for an aluminum alloy with a solid line. To plot the universal curve $\sigma(\varepsilon)$, we should put $\sigma = \sigma_x$ and change the scale on the strain axis in

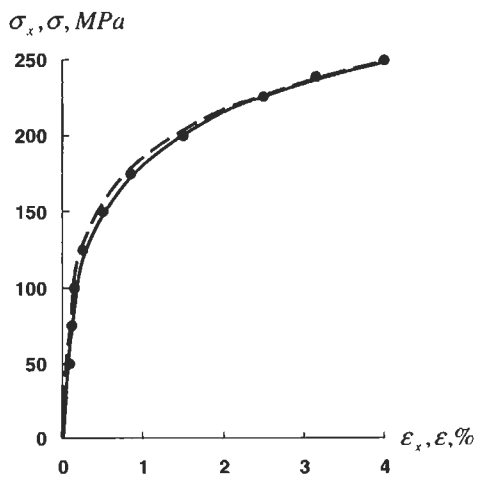

Fig. 4.9. Experimental stress–strain diagram for an aluminum alloy under uniaxial tension (solid line), the universal stress–strain curve (broken line) and its power approximation (circles).

accordance with Eq. (4.21). To do this, we need to know the plastic Poisson's ratio ν_p that can be found as $\nu_p = -\varepsilon_y/\varepsilon_x$. Using Eqs. (4.29) and (4.30) we arrive at

$$\nu_p = \frac{1}{2} - \frac{E_s}{E}\left(\frac{1}{2} - \nu\right) .$$

As follows from this equation $\nu_p = \nu$ if $E_s = E$ and $\nu_p \to 1/2$ for $E_s \to 0$. Dependencies of E_s and ν_p on ε for the aluminum alloy under consideration are presented in Fig. 4.10. With the aid of this figure and Eq. (4.21) in which we should take $\varepsilon_{ll} = \varepsilon_x$, we can calculate ε and plot the universal curve shown in Fig. 4.9 with a broken line. As can be seen, this curve is slightly different from the diagram corresponding to a uniaxial tension. For the power approximation in Eq. (4.27), from Eqs. (4.26) and (4.32) we get

$$\omega(\sigma) = Cn\sigma^{n-2}, \quad \omega(\sigma) = \frac{\varepsilon}{\sigma} - \frac{1}{E} .$$

Matching these results we find

$$\varepsilon = \frac{\sigma}{E} + Cn\sigma^{n-1} . \tag{4.33}$$

This is a traditional approximation for a material with a power hardening law. Now, we can find C and n using Eq. (4.33) to approximate the broken line in Fig. 4.9. The results of approximation are shown in this figure with circles that correspond to $E = 71.4$ GPa, $n = 6$, and $C = 6.23 \times 10^{-15}$ (MPa)$^{-5}$.

Thus, constitutive equations of the deformation theory of plasticity are specified by Eqs. (4.25) and (4.32). These equations are valid only for active loading that can

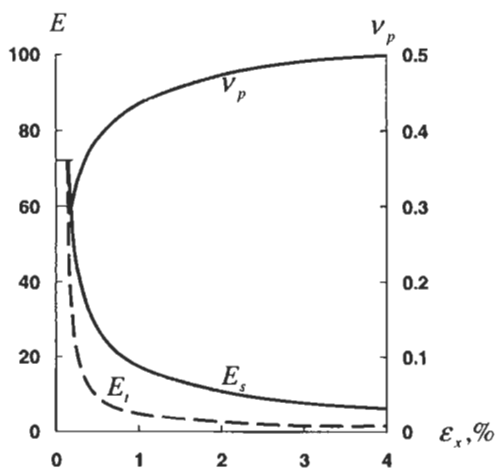

Fig. 4.10. Dependencies of the secant modulus (E_s), tangent modulus (E_t), and the plastic Poisson's ratio (ν_p) on strain for an aluminum alloy.

be identified by the condition $d\sigma > 0$. Being applied for unloading (i.e., for $d\sigma < 0$), Eqs. (4.25) correspond to nonlinear elastic material with stress–strain diagram shown in Fig. 1.2. For elastic–plastic material (see Fig. 1.5), unloading diagram is linear. So, if we reduce the stresses by some increments $\Delta\sigma_x$, $\Delta\sigma_y$, $\Delta\tau_{xy}$, the corresponding increments of strains will be

$$\Delta\varepsilon_x = \frac{1}{E}(\Delta\sigma_x - \nu\Delta\sigma_y), \quad \Delta\varepsilon_y = \frac{1}{E}(\Delta\sigma_y - \nu\Delta\sigma_x), \quad \Delta\gamma_{xy} = \frac{1}{G}\Delta\tau_{xy} \ .$$

Direct application of nonlinear equations (4.25) substantially hinders the problem of stress–strain analysis because these equations include function $\omega(\sigma)$ in Eq. (4.32) which, in turn, contains secant modulus $E_s(\sigma)$. For the power approximation corresponding to Eq. (4.33), E_s can be expressed analytically, i.e.,

$$\frac{1}{E_s} = \frac{1}{E} + Cn\sigma^{n-2} \ .$$

However, in many cases E_s is given graphically as in Fig. 4.10 or numerically in the form of a table. Thus, Eqs. (4.25) sometimes cannot be even written in the explicit analytical form. This implies application of numerical methods in conjunction with iterative linearization of Eqs. (4.25).

There exist several methods of such linearization that will be demonstrated using the first equation in Eqs. (4.25), i.e.,

$$\varepsilon_x = \frac{1}{E}(\sigma_x - \nu\sigma_y) + \omega(\sigma)\left(\sigma_x - \frac{1}{2}\sigma_y\right) \ . \tag{4.34}$$

In the method of elastic solutions (Ilyushin, 1948), Eq. (4.34) is used in the following form:

$$\varepsilon_x^s = \frac{1}{E}(\sigma_x^s - \nu\sigma_y^s) + \eta_{s-1} \ , \tag{4.35}$$

where s is the number of the iteration step and

$$\eta_{s-1} = \omega(\sigma_{s-1})(\sigma_x^{s-1} - \tfrac{1}{2}\sigma_y^{s-1}) \ .$$

For the first step ($s = 1$), we take $\eta_0 = 0$ and solve the problem of linear elasticity with Eq. (4.35) in the form

$$\varepsilon_x^1 = \frac{1}{E}(\sigma_x^1 - \nu\sigma_y^1) \ . \tag{4.36}$$

Finding the stresses, we calculate η_1 and write Eq. (4.35) as

$$\varepsilon_x^2 = \frac{1}{E}(\sigma_x^2 - \nu\sigma_y^2) + \eta_1 \ ,$$

where the first term is linear, while the second term is a known function of coordinates. Thus, we have another linear problem resolving which we find stresses, calculate η_2 and switch to the third step. This process is continued until the strains corresponding to some step become close within the given accuracy to the results found at the previous step.

Thus, the method of elastic solutions reduces the initial nonlinear problem to a sequence of linear problems of the theory of elasticity for the same material but with some initial strains that can be transformed into initial stresses or additional loads. This method readily provides a nonlinear solution for any problem that has a linear solution, analytical or numerical. The main shortcoming of the method is its poor convergence. Graphical interpretation of this process for the case of uniaxial tension with stress σ is presented in Fig. 4.11a. This figure shows a simple way to improve the convergence of the process. If we need to find strain at the point of the curve that is close to point A, it is not necessary to start the process with initial modulus E. Taking $E' < E$ in Eq. (4.36) we can reach the result with much less number of steps.

According to the method of elastic variables (Birger, 1951), we should present Eq. (4.34) as

$$\varepsilon_x^s = \frac{1}{E}(\sigma_x^s - \nu\sigma_y^s) + \omega(\sigma_{s-1})\left(\sigma_x^s - \frac{1}{2}\sigma_y^s\right) . \tag{4.37}$$

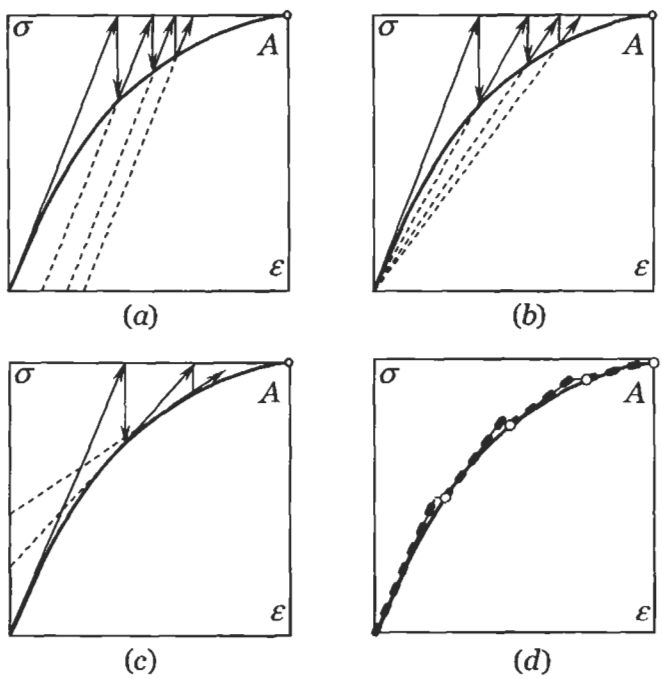

Fig. 4.11. Geometric interpretation of (a) the method of elastic solutions, (b) the method of variable elasticity parameters, (c) Newton's method, and (d) method of successive loading.

In contrast to Eq. (4.35), stresses σ_x^s and σ_y^s in the second term correspond to the current step rather than to the previous one. This enables us to write Eq. (4.37) in the form analogous to Hooke's law, i.e.,

$$\varepsilon_x^s = \frac{1}{E_{s-1}}(\sigma_x^s - \nu_{s-1}\sigma_y^s) \ , \tag{4.38}$$

where

$$E_{s-1} = \left[\frac{1}{E} + \omega(\sigma_{s-1})\right]^{-1} , \quad \nu_{s-1} = E_{s-1}\left[\frac{\nu}{E} + \frac{1}{2}\omega(\sigma_{s-1})\right] \tag{4.39}$$

are elastic variables corresponding to the step with number $s-1$. The iteration procedure is similar to that described above. For the first step we take $E_0 = E$ and $\nu_0 = \nu$ in Eq. (4.38). Find σ_x^1, σ_y^1 and σ_1, determine E_1, ν_1, switch to the second step and so on. Graphical interpretation of the process is presented in Fig. 4.11b. Convergence of this method is by an order higher than that of the method of elastic solutions. However, elastic variables in the linear constitutive equation of the method, Eq. (4.38), depend on stresses and hence, on coordinates whence the method has got its name. This method can be efficiently applied in conjunction with the finite element method according to which the structure is simulated with the system of elements with constant stiffness coefficients. Being calculated for each step with the aid of Eqs. (4.39), these stiffnesses will change only with transition from one element to another, and it practically does not hinder the finite element method calculation procedure.

The iteration process having the best convergence is provided by the classical Newton's method requiring the following form of Eq. (4.34):

$$\varepsilon_x^s = \varepsilon_x^{s-1} + c_{11}^{s-1}(\sigma_x^s - \sigma_x^{s-1}) + c_{12}^{s-1}(\sigma_y^s - \sigma_y^{s-1}) + c_{13}^{s-1}(\tau_{xy}^s - \tau_{xy}^{s-1}) \ , \tag{4.40}$$

where

$$c_{11}^{s-1} = \frac{1}{E} + \omega(\sigma_{s-1}) + \left(\sigma_x^{s-1} - \frac{1}{2}\sigma_y^{s-1}\right)\frac{\partial}{\partial\sigma_x^{s-1}}\omega(\sigma_{s-1}),$$

$$c_{12}^{s-1} = -\frac{\nu}{E} - \frac{1}{2}\omega(\sigma_{s-1}) + \left(\sigma_x^{s-1} - \frac{1}{2}\sigma_y^{s-1}\right)\frac{\partial}{\partial\sigma_y^{s-1}}\omega(\sigma_{s-1}),$$

$$c_{13}^{s-1} = \left(\sigma_x^{s-1} - \frac{1}{2}\sigma_y^{s-1}\right)\frac{\partial}{\partial\tau_{xy}^{s-1}}\omega(\sigma_{s-1}) \ .$$

Because coefficients c are known from the previous step $(s-1)$, Eq. (4.40) is linear with respect to stresses and strains corresponding to step number s. Graphical interpretation of this method is presented in Fig. 4.11c. In contrast to the methods discussed above, Newton's method has no physical interpretation and being characterized with very high convergence, is rather cumbersome for practical applications.

Iteration methods discussed above are used to solve the direct problems of stress analysis, i.e., to find stresses and strains induced by a given load. However, there exists another class of problems requiring us to evaluate the load carrying capacity of the structure. To solve these problems, we need to trace the evolution of stresses while the load increases from zero to some ultimate value. To do this, we can use the method of successive loading. According to this method, the load is applied with some increments, and for each s-step of loading the strain is determined as

$$\varepsilon_x^s = \varepsilon_x^{s-1} + \frac{1}{E_{s-1}}(\Delta\sigma_x^s - \nu_{s-1}\Delta\sigma_y^s) \ , \tag{4.41}$$

where E_{s-1} and ν_{s-1} are specified by Eqs. (4.39) and correspond to the previous loading step. Graphical interpretation of this method is presented in Fig. 4.11d. To obtain reliable results, the load increments should be as small as possible, because the error of calculation is accumulated in this method. To avoid this effect, method of successive loading can be used in conjunction with the method of elastic variables. Being applied after several loading steps (black circles in Fig. 4.11d) the latter method allows us to eliminate the accumulated error and to start again the process of loading from a proper initial state (light circles in Fig. 4.11d).

Returning to constitutive equations of the deformation theory of plasticity, Eq. (4.25), it is important to note that these equations are algebraic. This means that strains corresponding to some combination of loads are determined by the stresses induced by these loads and do not depend on the history of loading, i.e., on what happened to the material before this combination of loads was reached.

However, existing experimental data show that, in general, strains should depend on the history of loading. This means that constitutive equations should be differential rather than algebraic as they are in the deformation theory. Such equations are provided by the flow theory of plasticity. According to this theory, decomposition in Eq. (4.15) is used for infinitesimal increments of stresses, i.e.,

$$\mathrm{d}\varepsilon_{ij} = \mathrm{d}\varepsilon_{ij}^{\mathrm{e}} + \mathrm{d}\varepsilon_{ij}^{\mathrm{p}} \ . \tag{4.42}$$

Here, increments of elastic strains are linked with the increments of stresses by Hooke's law, e.g., for the plane stress state

$$\mathrm{d}\varepsilon_x^{\mathrm{e}} = \frac{1}{E}(\mathrm{d}\sigma_x - \nu\,\mathrm{d}\sigma_y), \quad \mathrm{d}\varepsilon_y^{\mathrm{e}} = \frac{1}{E}(\mathrm{d}\sigma_y - \nu\,\mathrm{d}\sigma_x), \quad \mathrm{d}\gamma_{xy} = \frac{1}{G}\mathrm{d}\tau_{xy} \ , \tag{4.43}$$

while increments of plastic strains

$$\mathrm{d}\varepsilon_{ij}^{\mathrm{p}} = \frac{\partial U_{\mathrm{p}}}{\partial\sigma_{ij}}\mathrm{d}\lambda$$

are expressed in the form of Eqs. (4.18) but include parameter λ which characterizes the loading process.

Assuming that $U_p = U_p(\sigma)$, where σ is the stress intensity specified by Eqs. (4.19) or (4.24), we get

$$d\varepsilon_{ij}^p = \frac{dU_p}{d\sigma}\frac{\partial\sigma}{\partial\sigma_{ij}}d\lambda \ .$$

The explicit form of these equations for the plane stress state is:

$$\begin{aligned} d\varepsilon_x^p &= d\omega(\sigma)\left(\sigma_x - \tfrac{1}{2}\sigma_y\right), \\ d\varepsilon_y^p &= d\omega(\sigma)\left(\sigma_y - \tfrac{1}{2}\sigma_x\right), \\ d\gamma_{xy}^p &= 3\,d\omega(\sigma)\tau_{xy} \ , \end{aligned} \tag{4.44}$$

where

$$d\omega(\sigma) = \frac{1}{\sigma}\frac{dU_p}{d\sigma}d\lambda \ . \tag{4.45}$$

To determine parameter λ, assume that plastic potential U_p being on the one hand a function of σ, can be treated as the work performed by stresses on plastic strains, i.e.,

$$dU_p = \frac{\partial U_p}{\partial\sigma}d\sigma = \sigma_x\,d\varepsilon_x^p + \sigma_y\,d\varepsilon_y^p + \tau_{xy}\,d\gamma_{xy}^p \ .$$

Substituting strain increments from Eqs. (4.44) and taking into account Eq. (4.24) for σ we get

$$\frac{\partial U_p}{\partial\sigma}d\sigma = \sigma^2\,d\omega(\sigma) \ .$$

With due regard to Eq. (4.45) we arrive at the simple and natural relationship $d\lambda = d\sigma/\sigma$. Thus, Eq. (4.45) acquires the form

$$d\omega(\sigma) = \frac{d\sigma}{\sigma^2}\frac{dU_p}{d\sigma} \tag{4.46}$$

and Eqs. (4.42)–(4.44) result in the following constitutive equations of the flow theory:

$$\begin{aligned} d\varepsilon_x &= \frac{1}{E}(d\sigma_x - \nu\,d\sigma_y) + d\omega(\sigma)\left(\sigma_x - \frac{1}{2}\sigma_y\right), \\ d\varepsilon_y &= \frac{1}{E}(d\sigma_y - \nu\,d\sigma_x) + d\omega(\sigma)\left(\sigma_y - \frac{1}{2}\sigma_x\right), \\ d\gamma_{xy} &= \frac{1}{G}d\tau_{xy} + 3\,d\omega(\sigma)\tau_{xy} \ . \end{aligned} \tag{4.47}$$

As can be seen, in contrast to the deformation theory, stresses govern the increments of plastic strains rather than the strains themselves.

In the general case, irrespective of any particular approximation of plastic potential U_p, we can obtain for function $d\omega(\sigma)$ in Eqs. (4.47) the expression similar to Eq. (4.32). Consider a uniaxial tension for which Eqs. (4.47) yield

$$d\varepsilon_x = \frac{d\sigma_x}{E} + d\omega(\sigma_x)\sigma_x \ .$$

Repeating the derivation of Eq. (4.32) we finally get

$$d\omega(\sigma) = \frac{d\sigma}{\sigma}\left(\frac{1}{E_t(\sigma)} - \frac{1}{E}\right) \ , \tag{4.48}$$

where $E_t(\sigma) = d\sigma/d\varepsilon$ is the tangent modulus introduced in Section 1.1 (see Fig. 1.4). Dependence of E_t on strain for an aluminum alloy is shown in Fig. 4.10. For the power approximation of plastic potential

$$U_p = B\sigma^n \ , \tag{4.49}$$

matching Eqs. (4.46) and (4.48) we arrive at the equation

$$\frac{d\varepsilon}{d\sigma} = \frac{1}{E} + Bn\sigma^{n-2} \ .$$

Upon integration we get

$$\varepsilon = \frac{\sigma}{E} + \frac{Bn}{n-1}\sigma^{n-1} \ . \tag{4.50}$$

This result coincides with Eq. (4.33) within the accuracy of coefficients C and B. As in the theory of deformation, Eq. (4.50) can be used to approximate the experimental stress–strain curve and to determine coefficients B and n. Thus, constitutive equations of the flow theory of plasticity are specified with Eqs. (4.47) and (4.48).

For a plane stress state, introduce the stress space shown in Fig. 4.12 and referred to Cartesian coordinate frame with stresses as coordinates. In this space, any loading can be presented as a curve specified by parametric equations $\sigma_x = \sigma_x(p)$, $\sigma_y = \sigma_y(p)$, $\tau_{xy} = \tau_{xy}(p)$, where p is the loading parameter. To find strains corresponding to point A on the curve, we should integrate Eqs. (4.47) along this curve thus taking into account the whole history of loading. In the general case, the obtained result will be different from what follows from Eqs. (4.25) of the deformation theory for point A. However, there exists one loading path (the straight line OA in Fig. 4.12) that is completely determined by the location of its final point A. This is the so-called proportional loading during which the stresses increase in proportion to parameter p, i.e.,

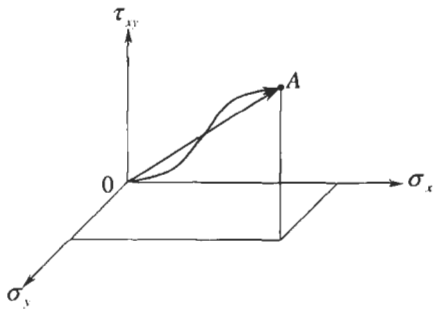

Fig. 4.12. Loading path (0*A*) in the stress space.

$$\sigma_x = \sigma_x^0 p, \quad \sigma_y = \sigma_y^0 p, \quad \tau_{xy} = \tau_{xy}^0 p \ , \tag{4.51}$$

where, stresses with superscript '0' can depend on coordinates only. For such loading, $\sigma = \sigma_0 p$, $d\sigma = \sigma_0 dp$, and Eqs. (4.46) and (4.49) yield

$$d\omega(\sigma) = Bn\sigma^{n-3}\, d\sigma = Bn\sigma_0^{n-2} p^{n-3}\, dp \ . \tag{4.52}$$

Consider, for example, the first equation of Eqs. (4.47). Substituting Eqs. (4.51) and (4.52) we get

$$d\varepsilon_x = \frac{1}{E}\left(\sigma_x^0 - \nu\sigma_y^0\right)dp + Bn\sigma_0^{n-2}\left(\sigma_x^0 - \frac{1}{2}\sigma_y^0\right)p^{n-2}\, dp \ .$$

This equation can be integrated with respect to p. Using again Eqs. (4.51) we arrive at the constitutive equation of the deformation theory

$$\varepsilon_x = \frac{1}{E}(\sigma_x - \nu\sigma_y) + B\frac{n}{n-1}\sigma^{n-2}\left(\sigma_x - \frac{1}{2}\sigma_y\right) \ .$$

Thus, for a proportional loading, the flow theory reduces to the deformation theory of plasticity. Unfortunately, before the problem is solved and the stresses are found we do not know whether the loading is proportional or not and what particular theory of plasticity should be used. There exists a theorem of proportional loading (Ilyushin, 1948) according to which the stresses increase proportionally and the deformation theory can be used if:

(1) external loads increase in proportion to one loading parameter,
(2) material is incompressible and its hardening can be described with the power law $\sigma = S\varepsilon^n$.

In practice, both conditions of this theorem are rarely met. However, existing experience shows that the second condition is not very important and that the deformation theory of plasticity can be reliably (but approximately) applied if all the loads acting on the structure increase in proportion to one parameter.

4.2. Unidirectional orthotropic layer

A composite layer with the simplest structure consists of unidirectional plies whose material coordinates, 1, 2, 3, coincide with coordinates of the layer, x, y, z, as in Fig. 4.13. An example of such a layer is presented in Fig. 4.14 – principal material axes of an outside circumferential unidirectional layer of a pressure vessel coincide with global (axial and circumferential) coordinates of the vessel.

4.2.1. Linear elastic model

For the layer under study, constitutive equations, Eqs. (2.48) and (2.53), yield

$$\begin{aligned}
\varepsilon_1 &= \frac{\sigma_1}{E_1} - \nu_{12}\frac{\sigma_2}{E_2} - \nu_{13}\frac{\sigma_3}{E_3}, \\
\varepsilon_2 &= \frac{\sigma_2}{E_2} - \nu_{21}\frac{\sigma_1}{E_1} - \nu_{23}\frac{\sigma_3}{E_3}, \\
\varepsilon_3 &= \frac{\sigma_3}{E_3} - \nu_{31}\frac{\sigma_1}{E_1} - \nu_{32}\frac{\sigma_2}{E_2}, \\
\gamma_{12} &= \frac{\tau_{12}}{G_{12}}, \quad \gamma_{13} = \frac{\tau_{13}}{G_{13}}, \quad \gamma_{23} = \frac{\tau_{23}}{G_{23}},
\end{aligned} \tag{4.53}$$

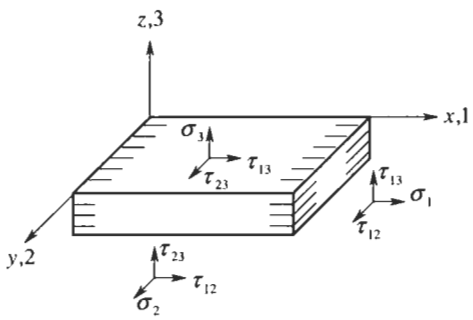

Fig. 4.13. An orthotropic layer.

Fig. 4.14. Filament wound composite pressure vessel.

where

$$\nu_{12}E_1 = \nu_{21}E_2, \quad \nu_{13}E_1 = \nu_{31}E_3, \quad \nu_{23}E_2 = \nu_{32}E_3 \ .$$

The inverse form of Eqs. (4.53) is

$$\begin{aligned}
\sigma_1 &= A_1(\varepsilon_1 + \mu_{12}\varepsilon_2 + \mu_{13}\varepsilon_3), \\
\sigma_2 &= A_2(\varepsilon_2 + \mu_{21}\varepsilon_1 + \mu_{23}\varepsilon_3), \\
\sigma_3 &= A_3(\varepsilon_3 + \mu_{31}\varepsilon_1 + \mu_{32}\varepsilon_2), \\
\tau_{12} &= G_{12}\gamma_{12}, \quad \tau_{13} = G_{13}\gamma_{13}, \quad \tau_{23} = G_{23}\gamma_{23} \ ,
\end{aligned} \tag{4.54}$$

where

$$A_1 = \frac{E_1}{D}(1 - \nu_{23}\nu_{32}), \quad A_2 = \frac{E_2}{D}(1 - \nu_{13}\nu_{31}), \quad A_3 = \frac{E_3}{D}(1 - \nu_{12}\nu_{21}) \ ,$$

$$D = 1 - \nu_{12}\nu_{23}\nu_{31} - \nu_{13}\nu_{21}\nu_{32} - \nu_{13}\nu_{31} - \nu_{12}\nu_{21} - \nu_{23}\nu_{32} \ ,$$

$$\mu_{12} = \frac{\nu_{12} + \nu_{13}\nu_{32}}{1 - \nu_{23}\nu_{32}}, \quad \mu_{21} = \frac{\nu_{21} + \nu_{23}\nu_{31}}{1 - \nu_{13}\nu_{31}},$$

$$\mu_{13} = \frac{\nu_{13} + \nu_{12}\nu_{23}}{1 - \nu_{23}\nu_{32}}, \quad \mu_{31} = \frac{\nu_{31} + \nu_{21}\nu_{32}}{1 - \nu_{12}\nu_{21}},$$

$$\mu_{23} = \frac{\nu_{23} + \nu_{13}\nu_{21}}{1 - \nu_{13}\nu_{31}}, \quad \mu_{32} = \frac{\nu_{32} + \nu_{12}\nu_{31}}{1 - \nu_{12}\nu_{21}} \ .$$

As for an isotropic layer considered in Section 4.1, the terms including transverse normal stress σ_3 can be neglected in Eqs. (4.53) and (4.54) and they can be written in the following simplified forms:

$$\begin{aligned}
\varepsilon_1 &= \frac{\sigma_1}{E_1} - \nu_{12}\frac{\sigma_2}{E_2}, \quad \varepsilon_2 = \frac{\sigma_2}{E_2} - \nu_{21}\frac{\sigma_1}{E_1}, \\
\gamma_{12} &= \frac{\tau_{12}}{G_{12}}, \quad \gamma_{13} = \frac{\tau_{13}}{G_{13}}, \quad \gamma_{23} = \frac{\tau_{23}}{G_{23}}
\end{aligned} \tag{4.55}$$

and

$$\begin{aligned}
\sigma_1 &= \bar{E}_1(\varepsilon_1 + \nu_{12}\varepsilon_2), \quad \sigma_2 = \bar{E}_2(\varepsilon_2 + \nu_{21}\varepsilon_1), \\
\tau_{12} &= G_{12}\gamma_{12}, \quad \tau_{13} = G_{13}\gamma_{13}, \quad \tau_{23} = G_{23}\gamma_{23} \ ,
\end{aligned} \tag{4.56}$$

where

$$\bar{E}_{1,2} = \frac{E_{1,2}}{1 - \nu_{12}\nu_{21}} \ .$$

Constitutive equations presented above include elastic constants of a layer that are determined experimentally. For in-plane characteristics E_1, E_2, G_{12}, and ν_{12}, the corresponding test methods were discussed in Chapter 3. Transverse modulus E_3 is

usually found testing the layer under compression in the z-direction. Transverse shear moduli G_{13} and G_{23} can be obtained by different methods, e.g., by inducing pure shear in two symmetric specimens shown in Fig. 4.15 and calculating shear modulus as $G_{13} = P/(2A\gamma)$, where A is the in-plane area of the specimen.

For unidirectional composites, $G_{13} = G_{12}$ (see Table 3.5) while typical values of G_{23} are listed in Table 4.1 (Herakovich , 1998).

Poisson's ratios ν_{31} and ν_{32} can be determined measuring the change of the layer thickness under in-plane tension in directions 1 and 2.

4.2.2. Nonlinear models

Consider Figs. 3.40–3.43 showing typical stress–strain diagrams for unidirectional advanced composites. As can be seen, materials demonstrate linear behavior only under tension. The curves corresponding to compression are slightly nonlinear, while the shear curves are definitely nonlinear. It should be emphasized that this does not mean that linear constitutive equations presented in Section 4.2.1 are not valid for these materials. First, it should be taken into account that the deformations of properly designed composite materials are controlled by the fibers, and they do not allow the shear strain to reach the values at which the shear stress-strain curve is strongly nonlinear. Second, the shear stiffness is usually very small in comparison with the longitudinal one, and such is its contribution to the apparent material stiffness. Material behavior is usually close to linear even if the shear deformation is nonlinear. Thus, a linear elastic model provides, as a rule, a reasonable approximation to the actual material behavior. However, there exist problems, to solve which we should allow for material nonlinearity and apply one of nonlinear constitutive theories discussed below.

First, note that material behavior under elementary loading (pure tension, compression, and shear) is specified by experimental stress–strain diagrams of the type shown in Figs. 3.40–3.43, and we do not need any theory. The necessity of the

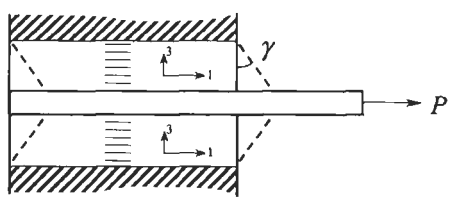

Fig. 4.15. A test to determine transverse shear modulus.

Table 4.1
Transverse shear moduli of unidirectional composites (Herakovich, 1998).

Material	Glass–epoxy	Carbon–epoxy	Aramid–epoxy	Boron–Al
G_{23} (GPa)	4.1	3.2	1.4	49.1

theory appears if we are to study the interaction of simultaneously acting stresses. Because for the layer under study this interaction usually takes place for in-plane stresses σ_1, σ_2, and τ_{12} (see Fig. 4.13), we consider further the plane state of stress.

In the simplest but rather useful for practical analysis engineering approach, the stress interaction is ignored at all, and linear constitutive equations, Eqs. (4.55), are generalized as

$$\varepsilon_1 = \frac{\sigma_1}{E_1^s} - \nu_{12}^s \frac{\sigma_2}{E_2^s}, \quad \varepsilon_2 = \frac{\sigma_2}{E_2^s} - \nu_{21}^s \frac{\sigma_1}{E_1^s}, \quad \gamma_{12} = \frac{\tau_{12}}{G_{12}^s} \ . \tag{4.57}$$

Superscript 's' indicates the corresponding secant characteristics specified by Eqs. (1.8). These characteristics depend on stresses and are determined using experimental diagram similar to those presented in Figs. 3.40–3.43. Particularly, diagrams $\sigma_1(\varepsilon_1)$ and $\varepsilon_2(\varepsilon_1)$ plotted under uniaxial longitudinal loading yield $E_1^s(\sigma_1)$ and $\nu_{21}^s(\sigma_1)$, secant moduli $E_2^s(\sigma_2)$ and $G_{12}^s(\tau_{12})$ are determined from experimental curves $\sigma_2(\varepsilon_2)$ and $\tau_{12}(\gamma_{12})$, respectively, while ν_{12}^s is found from the symmetry condition in Eqs. (4.53). In a more rigorous model (Jones, 1977), the secant characteristics of the material in Eqs. (4.57) are also functions but this time of strain energy U in Eq. (2.51) rather than of individual stresses. Models of this type provide adequate results for unidirectional composites with moderate nonlinearity.

To describe pronounced nonlinear elastic behavior of a unidirectional layer, we can use Eqs. (4.10). Expanding complementary potential U_c into the Taylor series with respect to stresses we have

$$U_c = c_0 + c_{ij}\sigma_{ij} + \frac{1}{2}c_{ijkl}\sigma_{ij}\sigma_{kl} + \frac{1}{3!}c_{ijklmn}\sigma_{ij}\sigma_{kl}\sigma_{mn} + \frac{1}{4!}c_{ijklmnpq}\sigma_{ij}\sigma_{kl}\sigma_{mn}\sigma_{pq}$$
$$+ \frac{1}{5!}c_{ijklmnpqrs}\sigma_{ij}\sigma_{kl}\sigma_{mn}\sigma_{pq}\sigma_{rs} + \frac{1}{6!}c_{ijklmnpqrstw}\sigma_{ij}\sigma_{kl}\sigma_{mn}\sigma_{pq}\sigma_{rs}\sigma_{tw} + \cdots \ , \tag{4.58}$$

where

$$c_0 = U_c(\sigma_{ij} = 0), \quad c_{ij} = \left.\frac{\partial U_c}{\partial \sigma_{ij}}\right|_{\sigma_{ij}=0}, \quad c_{ijkl} = \left.\frac{\partial^2 U_c}{\partial \sigma_{ij}\partial \sigma_{kl}}\right|_{\sigma_{ij}=0,\sigma_{kl}=0}, \text{ etc.}$$

Sixth-order approximation with terms written in Eq. (4.58) (it implies summation over repeated subscripts) allows us to construct constitutive equations including stresses in the fifth power. Coefficients 'c' should be found from experiments with material specimens. Because these coefficients are particular derivatives that do not depend on the sequence of differentiation, the sequence of their subscripts is not important. As a result, the sixth-order polynomial in Eq. (4.58) includes 84 'c'-coefficients. Apparently, this is too many for practical analysis of composite materials. To reduce the number of coefficients, we can first use some general considerations. Namely, assume that $U_c = 0$ and $\varepsilon_{ij} = 0$ if there are no stresses ($\sigma_{ij} = 0$). Then, $c_0 = 0$ and $c_{ij} = 0$. Second, we should take into account that the

material under study is orthotropic. This means that normal stresses do not induce shear strain, while shear stress does not cause normal strains. And third, the direction of shear stresses should influence only shear strains, i.e., shear stresses should have only even powers in constitutive equations for normal strains, while the corresponding equation for shear strain should include only odd powers of shear stresses. As a result, constitutive equations will contain 37 coefficients and acquire the following form (in new notations for coefficients and stresses):

$$
\begin{aligned}
\varepsilon_1 &= a_1\sigma_1 + a_2\sigma_1^2 + a_3\sigma_1^3 + a_4\sigma_1^4 + a_5\sigma_1^5 + d_1\sigma_1 \\
&\quad + 2d_2\sigma_1\sigma_2 + d_3\sigma_2^2 + 3d_4\sigma_1^2\sigma_2 + d_5\sigma_2^3 + d_6\sigma_1\sigma_2^2 + 4d_7\sigma_1^3\sigma_2 + 3d_8\sigma_1^2\sigma_2^2 \\
&\quad + 2d_9\sigma_1\sigma_2^3 + d_{10}\sigma_2^4 + 5d_{11}\sigma_1^4\sigma_2 + 4d_{12}\sigma_1^3\sigma_2^2 + 3d_{13}\sigma_1^2\sigma_2^3 + 2d_{14}\sigma_1\sigma_2^4 \\
&\quad + d_{15}\sigma_2^5 + k_1\sigma_1\tau_{12}^2 + k_2\sigma_2\tau_{12}^2 + 3k_3\sigma_1^2\tau_{12}^2 + 4k_4\sigma_1^3\tau_{12}^2 + 2k_5\sigma_1\tau_{12}^4, \\
\varepsilon_2 &= b_1\sigma_2 + b_2\sigma_2^2 + b_3\sigma_2^3 + b_4\sigma_2^4 + b_5\sigma_2^5 \\
&\quad + d_1\sigma_1 + d_2\sigma_1^2 + 2d_3\sigma_1\sigma_2 + d_4\sigma_1^3 + 3d_5\sigma_1\sigma_2^2 + d_6\sigma_1^2\sigma_2 + d_7\sigma_1^4 \\
&\quad + 2d_8\sigma_1^3\sigma_2 + 3d_9\sigma_1^2\sigma_2^2 + 4d_{10}\sigma_1\sigma_2^3 + d_{11}\sigma_1^5 + 2d_{12}\sigma_1^4\sigma_2 \\
&\quad + 3d_{13}\sigma_1^3\sigma_2^2 + 2d_{14}\sigma_1^2\sigma_2^3 + 5d_{15}\sigma_1\sigma_2^4 + m_1\sigma_2\tau_{12}^2 + k_2\sigma_1\tau_{12}^2 \\
&\quad + 3m_2\sigma_2^2\tau_{12}^2 + 4m_3\sigma_2^3\tau_{12}^2 + 2m_4\sigma_2\tau_{12}^4, \\
\gamma_{12} &= c_1\tau_{12} + c_2\tau_{12}^3 + c_3\tau_{12}^5 + k_1\tau_{12}\sigma_1^2 + m_1\tau_{12}\sigma_2^2 \\
&\quad + 2k_2\tau_{12}\sigma_1\sigma_2 + 2k_3\tau_{12}\sigma_1^3 + 2m_2\tau_{12}\sigma_2^3 \\
&\quad + 2k_4\tau_{12}\sigma_1^4 + 4k_5\tau_{12}^3\sigma_1^2 + 2m_3\tau_{12}\sigma_2^4 + 4m_4\tau_{12}^3\sigma_2^2 \ .
\end{aligned}
\tag{4.59}
$$

For unidirectional composites, dependence $\varepsilon_1(\sigma_1)$ is linear which means that we should put $d_2 = \cdots d_{15} = 0$, $k_1 = \cdots k_5 = 0$. Then, the foregoing equations reduce to

$$
\begin{aligned}
\varepsilon_1 &= a_1\sigma_1 + d_1\sigma_2, \\
\varepsilon_2 &= b_1\sigma_2 + b_2\sigma_2^2 + b_3\sigma_2^3 + b_4\sigma_2^4 + b_5\sigma_2^5 \\
&\quad + d_1\sigma_1 + m_1\sigma_2\tau_{12}^2 + 3m_2\sigma_2^2\tau_{12}^2 + 4m_3\sigma_2^3\tau_{12}^2 + 2m_4\sigma_2\tau_{12}^4, \\
\gamma_{12} &= c_1\tau_{12} + c_2\tau_{12}^3 + c_3\tau_{12}^5 + m_1\tau_{12}\sigma_2^2 \\
&\quad + 2m_2\tau_{12}\sigma_2^3 + 2m_3\tau_{12}\sigma_2^4 + 4m_4\tau_{12}^3\sigma_2^2 \ .
\end{aligned}
\tag{4.60}
$$

As an example, consider a special two-matrix fiberglass unidirectional composite with high in-plane transverse and shear deformation (see Section 4.3 where it is described in details). Stress–strain curves corresponding to transverse tension, compression, and in-plane shear are shown in Fig. 4.16. Solid lines correspond to Eqs. (4.60) used to approximate experimental results (circles in Fig. 4.16). Coefficients a_1 and d_1 in Eqs. (4.60) are found using diagrams $\varepsilon_1(\sigma_1)$ and $\varepsilon_2(\sigma_1)$ which are linear and not shown here. Coefficients $b_1 \cdots b_5$ and c_1, c_2, c_3 are determined using the least-squares method to approximate curves $\sigma_2^+(\varepsilon_2)$, $\sigma_2^-(\varepsilon_2)$, and $\tau_{12}(\gamma_{12})$. The

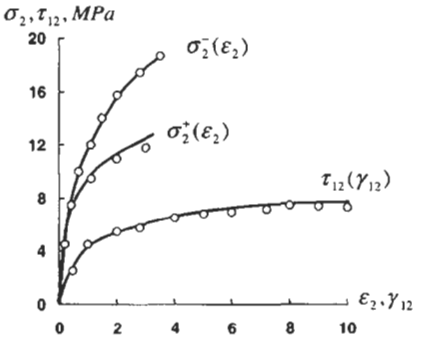

Fig. 4.16. Calculated (solid lines) and experimental (circles) stress–strain diagrams for a two-matrix unidirectional composite under in-plane transverse tension (σ_2^+), compression (σ_2^-) and shear (τ_{12}).

other coefficients, i.e., $m_1 \cdots m_4$, should be determined with the aid of a more complicated experiment involving the loading that induces both stresses σ_2 and τ_{12} acting simultaneously. This experiment is described in Section 4.3.

As follows from Fig. 3.40–3.43, unidirectional composites demonstrate pronounced nonlinearity only under shear. Assuming that dependence $\varepsilon_2(\sigma_2)$ is also linear we can reduce Eqs. (4.60) to

$$\varepsilon_1 = a_1\sigma_1 + d_1\sigma_2, \quad \varepsilon_2 = b_1\sigma_2 + d_1\sigma_1, \quad \gamma_{12} = c_1\tau_{12} + c_2\tau_{12}^3 + c_3\tau_{12}^5 \ .$$

For practical analysis, even more simple form of these equations (with $c_3 = 0$) can be used (Hahn and Tsai, 1973).

Nonlinear behavior of composite materials can be also described with the aid of the theory of plasticity that can be constructed as a direct generalization of the classical plasticity theory developed for metals and described in Section 4.1.2.

To construct such a theory, we decompose strains in accordance with Eq. (4.15) and use Eqs. (4.16) and (4.18) to determine elastic and plastic strains as

$$\varepsilon_{ij}^{e} = \frac{\partial U_e}{\partial \sigma_{ij}}, \quad \varepsilon_{ij}^{p} = \frac{\partial U_p}{\partial \sigma_{ij}} \ , \tag{4.61}$$

where U_e and U_p are elastic and plastic potentials. For elastic potential, elasticity theory yields

$$U = c_{ijkl}\sigma_{ij}\sigma_{kl} \ , \tag{4.62}$$

where c_{ijkl} are compliance coefficients, and summation over repeated subscript is implied. Plastic potential is assumed to be a function of stress intensity, σ, which is constructed for a plane stress state as a direct generalization of Eq. (4.24), i.e.,

$$\sigma = a_{ij}\sigma_{ij} + \sqrt{a_{ijkl}\sigma_{ij}\sigma_{kl}} + \sqrt[3]{a_{ijklmn}\sigma_{ij}\sigma_{kl}\sigma_{mn}} + \cdots \ , \tag{4.63}$$

where coefficients 'a' are material constants characterizing its plastic behavior. And finally, we assume the power law in Eq. (4.27) for the plastic potential.

To write constitutive equations for a plane stress state, we return to engineering notations for stresses and strains and use conditions that should be imposed on an orthotropic material and were discussed above in application to Eqs. (4.59). Finally, Eqs. (4.15), (4.27) and (4.61), (4.62), (4.63) yield

$$\begin{aligned}
\varepsilon_1 &= a_1\sigma_1 + d_1\sigma_2 + n\sigma^{n-1}\left[\frac{1}{R_1}(b_{11}\sigma_1 + c_{12}\sigma_2) + \frac{1}{R_2^2}(d_{11}\sigma_1^2 + 2e_{12}\sigma_1\sigma_2 + e_{21}\sigma_2^2)\right],\\
\varepsilon_2 &= b_1\sigma_2 + d_1\sigma_1 + n\sigma^{n-1}\left[\frac{1}{R_1}(b_{22}\sigma_2 + c_{12}\sigma_1) + \frac{1}{R_2^2}(d_{22}\sigma_2^2 + 2e_{21}\sigma_2\sigma_1 + e_{12}\sigma_1^2)\right],\\
\gamma_{12} &= c_1\tau_{12} + 2n\sigma^{n-1}\frac{b_{12}}{R_1}\tau_{12}\ ,
\end{aligned} \tag{4.64}$$

where

$$\begin{aligned}
&\sigma = R_1 + R_2,\\
&R_1 = \sqrt{b_{11}\sigma_1^2 + b_{22}\sigma_2^2 + b_{12}\tau_{12}^2 + 2c_{12}\sigma_1\sigma_2},\\
&R_2 = \sqrt[3]{d_{11}\sigma_1^3 + d_{22}\sigma_2^3 + 3e_{12}\sigma_1^2\sigma_2 + 3e_{21}\sigma_1\sigma_2^2}\ .
\end{aligned}$$

Deriving Eqs. (4.64) we used new notations for coefficients and restricted ourselves to the three-term approximation for σ as in Eq. (4.63).

For independent uniaxial loading along the fibers, across the fibers, and in pure shear, Eqs. (4.64) reduce to

$$\begin{aligned}
\varepsilon_1 &= a_1\sigma_1 + n\left(\sqrt{b_{11}\sigma_1^2} + \sigma_1\sqrt[3]{d_{11}}\right)^{n-1}\left(\sqrt{b_{11}}\frac{\sigma_1}{\sqrt{\sigma_1^2}} + \sqrt[3]{d_{11}}\right),\\
\varepsilon_2 &= b_1\sigma_2 + n\left(\sqrt{b_{22}\sigma_2^2} + \sigma_2\sqrt[3]{d_{22}}\right)^{n-1}\left(\sqrt{b_{22}}\frac{\sigma_2}{\sqrt{\sigma_2^2}} + \sqrt[3]{d_{22}}\right),\\
\gamma_{12} &= \left[c_1 + 2n\sqrt{b_{12}^n}\left(\sqrt{\tau_{12}^2}\right)^{n-1}\right]\tau_{12}\ .
\end{aligned} \tag{4.65}$$

If nonlinear material behavior does not depend on the sign of normal stresses, then $d_{11} = d_{22} = 0$ in Eqs. (4.65). In the general case, Eqs. (4.65) allow us to describe material with high nonlinearity and different behavior under tension and compression.

As an example, consider a boron–aluminum unidirectional composite whose experimental stress–strain diagrams (Herakovich, 1998) are shown in Fig. 4.17

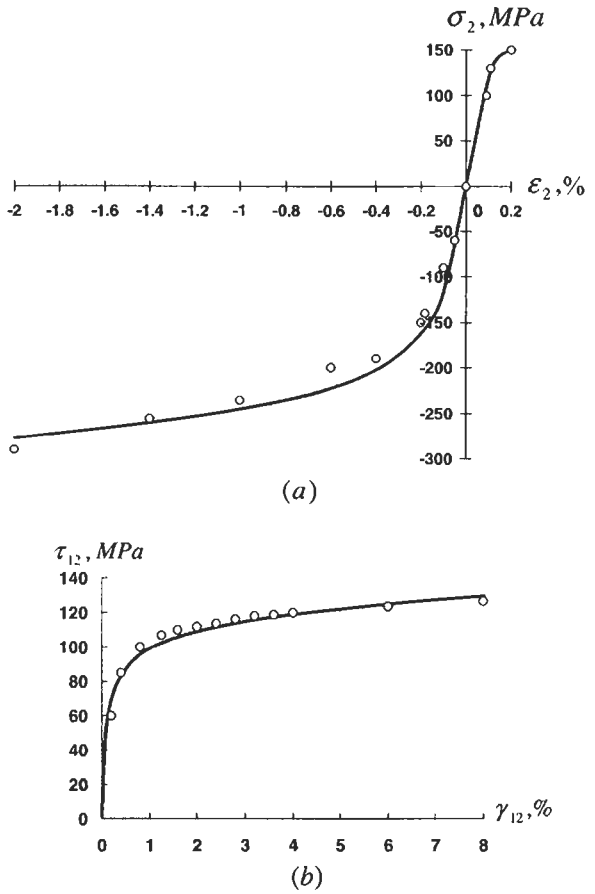

Fig. 4.17. Calculated (solid lines) and experimental (circles) stress–strain diagrams for a boron-aluminum composite under transverse loading (a) and in-plane shear (b).

(circles) along with the corresponding approximations (solid lines) plotted with the aid of Eqs. (4.65).

4.3. Unidirectional anisotropic layer

Consider now a unidirectional layer studied in the previous section and assume that its principal material axis 1 makes some angle ϕ with the x-axis of the global coordinate frame (see Fig. 4.18). An example of such a layer is shown in Fig. 4.19.

4.3.1. Linear elastic model

Constitutive equations of the layer under study referred to the principal material coordinates are given by Eqs. (4.55) and (4.56). We need now to derive such

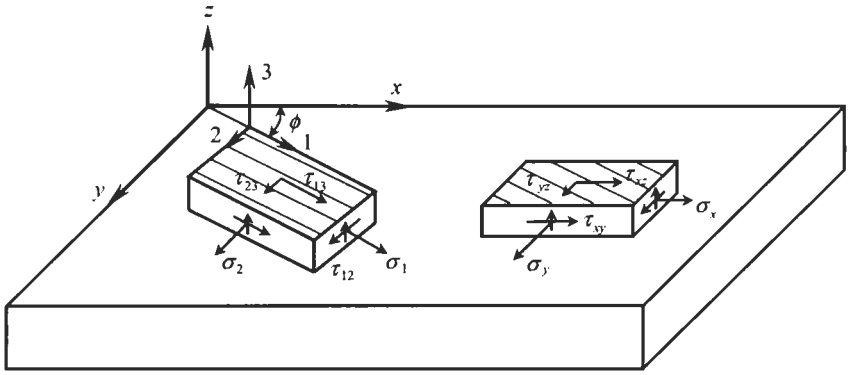

Fig. 4.18. A composite layer consisting of a system of unidirectional plies with the same orientation.

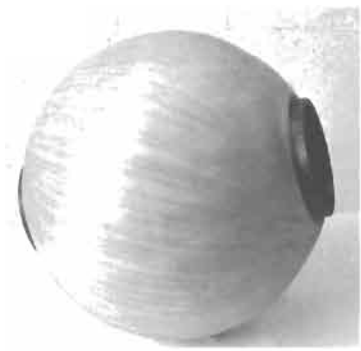

Fig. 4.19. An anisotropic outer layer of a composite pressure vessel. Courtesy of CRISM.

equations for the global coordinate frame x, y, z (see Fig. 4.18). To do this, we should transfer stresses σ_1, σ_2, τ_{12}, τ_{13}, τ_{23} acting in the layer and the corresponding strains ε_1, ε_2, γ_{12}, γ_{13}, γ_{23} into stress and strain components σ_x, σ_y, τ_{xy}, τ_{xz}, τ_{yz} and ε_x, ε_y, γ_{xy}, γ_{xz}, γ_{yz} using Eqs. (2.8), (2.9) and (2.21), (2.27) for coordinate transformation of stresses and strains. According to Fig. 4.18, directional cosines, Eqs. (2.1), of such transformation are (we take $x' = 1$, $y' = 2$, $z' = 3$)

$$\begin{aligned} &l_{x'x} = c, \quad l_{x'y} = s, \quad l_{x'z} = 0, \\ &l_{y'x} = -s, \quad l_{y'y} = c, \quad l_{y'z} = 0, \\ &l_{z'x} = 0, \quad l_{z'y} = 0, \quad l_{z'z} = 1 \ , \end{aligned} \tag{4.66}$$

where $c = \cos\phi$ and $s = \sin\phi$. Using Eqs. (2.8) and (2.9) we get

$$
\begin{aligned}
\sigma_1 &= \sigma_x c^2 + \sigma_y s^2 + 2\tau_{xy} cs, \\
\sigma_2 &= \sigma_x s^2 + \sigma_y c^2 - 2\tau_{xy} cs, \\
\tau_{12} &= (\sigma_y - \sigma_x) cs + \tau_{xy}(c^2 - s^2), \\
\tau_{13} &= \tau_{xz} c + \tau_{yz} s, \\
\tau_{12} &= -\tau_{xz} s + \tau_{yz} c \ .
\end{aligned} \tag{4.67}
$$

The inverse form of these equations is:

$$
\begin{aligned}
\sigma_x &= \sigma_1 c^2 + \sigma_2 s^2 - 2\tau_{12} cs, \\
\sigma_y &= \sigma_1 s^2 + \sigma_2 c^2 + 2\tau_{12} cs, \\
\tau_{xy} &= (\sigma_1 - \sigma_2) cs + \tau_{12}(c^2 - s^2), \\
\tau_{xz} &= \tau_{13} c - \tau_{23} s, \\
\tau_{yz} &= \tau_{13} s + \tau_{23} c \ .
\end{aligned} \tag{4.68}
$$

The corresponding transformation for strains follows from Eqs. (2.21) and (2.27), i.e.,

$$
\begin{aligned}
\varepsilon_1 &= \varepsilon_x c^2 + \varepsilon_y s^2 + \gamma_{xy} cs, \\
\varepsilon_2 &= \varepsilon_x s^2 + \varepsilon_y c^2 - \gamma_{xy} cs, \\
\gamma_{12} &= 2(\varepsilon_y - \varepsilon_x) cs + \gamma_{xy}(c^2 - s^2), \\
\gamma_{13} &= \gamma_{xz} c + \gamma_{yz} s, \\
\gamma_{23} &= -\gamma_{xz} s + \gamma_{yz} c
\end{aligned} \tag{4.69}
$$

or

$$
\begin{aligned}
\varepsilon_x &= \varepsilon_1 c^2 + \varepsilon_2 s^2 - \gamma_{12} cs, \\
\varepsilon_y &= \varepsilon_1 s^2 + \varepsilon_2 c^2 + \gamma_{12} cs, \\
\gamma_{xy} &= 2(\varepsilon_1 - \varepsilon_2) cs + \gamma_{12}(c^2 - s^2), \\
\gamma_{xz} &= \gamma_{13} c - \gamma_{23} s, \\
\gamma_{yz} &= \gamma_{13} s + \gamma_{23} c \ .
\end{aligned} \tag{4.70}
$$

To derive constitutive equations for an anisotropic unidirectional layer, we substitute strains, Eqs. (4.69), into Hooke's law, Eqs. (4.56), and thus obtained stresses – into Eqs. (4.68). The final result is as follows:

$$
\begin{aligned}
\sigma_x &= A_{11}\varepsilon_x + A_{12}\varepsilon_y + A_{14}\gamma_{xy},\\
\sigma_y &= A_{21}\varepsilon_x + A_{22}\varepsilon_y + A_{24}\gamma_{xy},\\
\tau_{xy} &= A_{41}\varepsilon_x + A_{42}\varepsilon_y + A_{44}\gamma_{xy},\\
\tau_{xz} &= A_{55}\gamma_{xz} + A_{56}\gamma_{yz},\\
\tau_{yz} &= A_{65}\gamma_{xz} + A_{66}\gamma_{yz}\ ,
\end{aligned}
\tag{4.71}
$$

where the stiffness coefficients are

$$
\begin{aligned}
A_{11} &= \bar{E}_1 c^4 + \bar{E}_2 s^4 + 2E_{12}c^2s^2,\\
A_{12} &= A_{21} = \bar{E}_1 \nu_{12} + (\bar{E}_1 + \bar{E}_2 - 2E_{12})c^2s^2,\\
A_{14} &= A_{41} = \left[\bar{E}_1 c^2 - \bar{E}_2 s^2 - E_{12}(c^2 - s^2)\right]cs,\\
A_{22} &= \bar{E}_1 s^4 + \bar{E}_2 c^4 + 2E_{12}c^2s^2,\\
A_{24} &= A_{42} = \left[\bar{E}_1 s^2 - \bar{E}_2 c^2 + E_{12}(c^2 - s^2)\right]cs,\\
A_{44} &= (\bar{E}_1 + \bar{E}_2 - 2\bar{E}_1\nu_{12})c^2s^2 + G_{12}(c^2 - s^2)^2,\\
A_{55} &= G_{13}c^2 + G_{23}s^2,\\
A_{56} &= A_{65} = (G_{13} - G_{23})cs,\\
A_{66} &= G_{13}s^2 + G_{23}c^2\ ,
\end{aligned}
\tag{4.72}
$$

where

$$
\bar{E}_{1,2} = \frac{E_{1,2}}{1 - \nu_{12}\nu_{21}}, \quad E_{12} = \bar{E}_1\nu_{12} + 2G_{12}, \quad c = \cos\phi, \quad s = \sin\phi\ .
$$

Dependence of stiffness coefficients A_{mn} in Eqs. (4.72) on ϕ was studied by S.W. Tsai and N.J. Pagano (see, e.g., Tsai, 1987; Verchery, 1999). Changing powers of $\sin\phi$ and $\cos\phi$ in Eqs. (4.72) for multiple-angle trigonometric functions we can reduce these equations to the following form (Verchery, 1999):

$$
\begin{aligned}
A_{11} &= S_1 + S_2 + 2S_3\cos 2\phi + S_4\cos 4\phi,\\
A_{12} &= -S_1 + S_2 - S_4\cos 4\phi,\\
A_{14} &= S_3\sin 2\phi + S_4\sin 4\phi,\\
A_{22} &= S_1 + S_2 - 2S_3\cos 2\phi + S_4\cos 4\phi,\\
A_{24} &= S_3\sin 2\phi - S_4\sin 4\phi,\\
A_{44} &= S_1 - S_4\cos 4\phi,\\
A_{55} &= S_5 + S_6\cos 2\phi,\\
A_{56} &= 4S_6\sin 2\phi,\\
A_{66} &= S_5 - S_6\cos 2\phi\ ,
\end{aligned}
\tag{4.73}
$$

where

$$S_1 = \frac{1}{8}(A_{11}^0 + A_{22}^0 - 2A_{12}^0 + 4A_{44}^0),$$

$$S_2 = \frac{1}{4}(A_{11}^0 + A_{22}^0 + 2A_{12}^0),$$

$$S_3 = \frac{1}{4}(A_{11}^0 - A_{22}^0),$$

$$S_4 = \frac{1}{8}(A_{11}^0 + A_{22}^0 - 2A_{12}^0 - 4A_{44}^0),$$

$$S_5 = \frac{1}{2}(A_{55}^0 + A_{66}^0),$$

$$S_6 = \frac{1}{2}(A_{55}^0 - A_{66}^0) \ ,$$

where, A_n^0 are stiffness coefficients corresponding to $\phi = 0$. As follows from Eqs. (4.72),

$$A_{11}^0 = \bar{E}_1, \quad A_{12}^0 = \bar{E}_1 \nu_{12}, \quad A_{14}^0 = A_{24}^0 = A_{56}^0 = 0,$$
$$A_{22}^0 = \bar{E}_2, \quad A_{44}^0 = G_{12}, \quad A_{55}^0 = G_{13}, \quad A_{66}^0 = G_{23} \ .$$

As can be seen in Eqs. (4.73), there exist the following differential relationships between tensile and coupling stiffnesses (Verchery and Gong, 1999):

$$\frac{dA_{11}}{d\phi} = -4A_{14}, \quad \frac{dA_{22}}{d\phi} = 4A_{24} \ .$$

It can be directly checked that Eqs. (4.73) provide three invariant stiffness characteristics whose forms do not depend on ϕ, i.e.,

$$A_{11}(\phi) + A_{22}(\phi) + 2A_{12}(\phi) = A_{11}^0 + A_{22}^0 + 2A_{12}^0,$$
$$A_{44}(\phi) - A_{12}(\phi) = A_{44}^0 - A_{12}^0, \tag{4.74}$$
$$A_{55}(\phi) + A_{66}(\phi) = A_{55}^0 + A_{66}^0 \ .$$

Any linear combination of these equations is also an invariant combination of stiffness coefficients.

The inverse form of Eqs. (4.71) can be obtained if we substitute stresses, Eqs. (4.67) into Hooke's law, Eqs. (4.55), and thus expressed strains – into Eqs. (4.70). As a result, we arrive at the following particular form of Eqs. (2.48), (2.49):

$$\varepsilon_x = \frac{\sigma_x}{E_x} - \nu_{xy}\frac{\sigma_y}{E_y} + \eta_{x,xy}\frac{\tau_{xy}}{G_{xy}}, \quad \varepsilon_y = \frac{\sigma_y}{E_y} - \nu_{yx}\frac{\sigma_x}{E_x} + \eta_{y,xy}\frac{\tau_{xy}}{G_{xy}},$$
$$\gamma_{xy} = \frac{\tau_{xy}}{G_{xy}} + \eta_{xy,x}\frac{\sigma_x}{E_x} + \eta_{xy,y}\frac{\sigma_y}{E_y}, \tag{4.75}$$
$$\gamma_{xz} = \frac{\tau_{xz}}{G_{xz}} + \lambda_{xz,yz}\frac{\tau_{yz}}{G_{yz}}, \quad \gamma_{yz} = \frac{\tau_{yz}}{G_{yz}} + \lambda_{yz,xz}\frac{\tau_{xz}}{G_{xz}},$$

where compliance coefficients are

$$\frac{1}{E_x} = \frac{c^4}{E_1} + \frac{s^4}{E_2} + \left(\frac{1}{G_{12}} - \frac{2\nu_{21}}{E_1}\right)c^2s^2,$$
$$\frac{\nu_{xy}}{E_y} = \frac{\nu_{yx}}{E_x} = \frac{\nu_{21}}{E_1} - \left(\frac{1}{E_1} + \frac{1}{E_2} + \frac{2\nu_{21}}{E_1} - \frac{1}{G_{12}}\right)c^2s^2,$$
$$\frac{\eta_{x,xy}}{G_{xy}} = \frac{\eta_{xy,x}}{E_x} = 2\left[\frac{c^2}{E_1} - \frac{s^2}{E_2} - \left(\frac{1}{2G_{12}} - \frac{\nu_{21}}{E_1}\right)(c^2 - s^2)\right]cs,$$
$$\frac{1}{E_y} = \frac{s^4}{E_1} + \frac{c^4}{E_2} + \left(\frac{1}{G_{12}} - \frac{2\nu_{21}}{E_1}\right)c^2s^2, \tag{4.76}$$
$$\frac{\eta_{y,xy}}{G_{xy}} = \frac{\eta_{xy,y}}{E_y} = 2\left[\frac{s^2}{E_1} - \frac{c^2}{E_2} + \left(\frac{1}{2G_{12}} - \frac{\nu_{21}}{E_1}\right)(c^2 - s^2)\right]cs,$$
$$\frac{1}{G_{xy}} = 4\left(\frac{1}{E_1} + \frac{1}{E_2} + \frac{2\nu_{21}}{E_1}\right)c^2s^2 + \frac{1}{G_{12}}(c^2 - s^2)^2,$$
$$\frac{1}{G_{xz}} = \frac{c^2}{G_{13}} + \frac{s^2}{G_{23}}, \quad \frac{\lambda_{xz,yz}}{G_{yz}} = \frac{\lambda_{yz,xz}}{G_{xz}} = \left(\frac{1}{G_{13}} - \frac{1}{G_{23}}\right)cs, \quad \frac{1}{G_{yz}} = \frac{s^2}{G_{13}} + \frac{c^2}{G_{23}}.$$

There exist the following dependencies between coefficients of Eqs. (4.71) and (4.75):

$$\frac{1}{E_x} = \frac{1}{D_1}(A_{22}A_{44} - A_{24}^2), \quad \frac{\nu_{xy}}{E_y} = \frac{\nu_{yx}}{E_x} = \frac{1}{D_1}(A_{12}A_{44} - A_{14}A_{24}),$$
$$\frac{\eta_{x,xy}}{G_{xy}} = \frac{\eta_{xy,x}}{E_x} = \frac{1}{D_1}(A_{12}A_{24} - A_{22}A_{14}), \quad \frac{1}{E_y} = \frac{1}{D_1}(A_{11}A_{44} - A_{14}^2),$$
$$\frac{\eta_{y,xy}}{G_{xy}} = \frac{\eta_{xy,y}}{E_y} = \frac{1}{D_1}(A_{12}A_{14} - A_{11}A_{24}), \quad \frac{1}{G_{xy}} = \frac{1}{D_1}(A_{11}A_{22} - A_{12}^2),$$
$$\frac{1}{G_{xz}} = \frac{A_{66}}{D_2}, \quad \frac{1}{G_{yz}} = \frac{A_{55}}{D_2}, \quad \frac{\lambda_{xz,yz}}{G_{yz}} = \frac{\lambda_{yz,xz}}{G_{xz}} = -\frac{A_{56}}{D_2},$$

where

$$D_1 = A_{11}A_{22}A_{44} - A_{11}A_{24}^2 - A_{22}A_{14}^2 - A_{44}A_{12}^2 + 2A_{12}A_{14}A_{24}, \quad D_2 = A_{55}A_{66} - A_{56}^2$$

and

$$A_{11} = \frac{1 - \eta_{y,xy}\eta_{xy,y}}{D_3 E_y G_{xy}}, \quad A_{12} = \frac{\nu_{xy} - \eta_{x,xy}\eta_{xy,y}}{D_3 E_y G_{xy}},$$

$$A_{14} = -\frac{\eta_{x,xy} + \nu_{xy}\eta_{y,xy}}{D_3 E_y G_{xy}}, \quad A_{22} = \frac{1 - \eta_{x,xy}\eta_{xy,y}}{D_3 E_x G_{xy}},$$

$$A_{24} = -\frac{\eta_{y,xy} + \nu_{yx}\eta_{x,xy}}{D_3 E_x G_{xy}}, \quad A_{44} = \frac{1 - \nu_{xy}\nu_{yx}}{D_3 E_x E_y},$$

$$A_{55} = \frac{1}{D_4 G_{yz}}, \quad A_{56} = -\frac{\lambda_{xz,yz}}{D_4 G_{yz}}, \quad A_{66} = \frac{1}{D_4 G_{xz}},$$

where

$$D_3 = \frac{1}{E_x E_y G_{xy}}(1 - \nu_{xy}\nu_{yx} - \eta_{x,xy}\eta_{xy,x} - \eta_{y,xy}\eta_{xy,y} - \nu_{xy}\eta_{y,xy}\eta_{xy,x} - \nu_{yx}\eta_{x,xy}\eta_{xy,y}),$$

$$D_4 = \frac{1}{G_{xz}G_{yz}}(1 - \lambda_{xz,yz}\lambda_{yz,xz}).$$

As can be seen in Eqs. (4.71) and (4.75), the layer under study is anisotropic in plane xy because constitutive equations include shear–extension and shear–shear coupling coefficients η and λ. For $\phi = 0$, the foregoing equations degenerate into Eqs. (4.55) and (4.56) for an orthotropic layer.

Dependencies of stiffness coefficients on the orientation angle for a carbon–epoxy composite with properties listed in Table 3.5 are presented in Figs. 4.20 and 4.21.

Uniaxial tension of the anisotropic layer (the so-called off-axis test of a unidirectional composite) is often used to determine material characteristics that cannot be found in tests with orthotropic specimens or to evaluate constitutive and failure theories. Such a test is shown in Fig. 4.22. To study this loading case, we should take $\sigma_y = \tau_{xy} = 0$ in Eqs. (4.75). Then

$$\varepsilon_x = \frac{\sigma_x}{E_x}, \quad \varepsilon_y = -\nu_{xy}\frac{\sigma_x}{E_x}, \quad \gamma_{xy} = \eta_{xy,x}\frac{\sigma_x}{E_x}. \tag{4.77}$$

As can be seen from these equations, tension in the x-direction is accompanied not only with transverse contraction, as in orthotropic materials, but also with shear. This results in the deformed shape of the sample shown in Fig. 4.23. This shape is natural because material stiffness in the fiber direction is much higher than that across the fibers.

Such an experiment, in case it could be performed, allows us to determine the in-plane shear modulus, G_{12} in principal material coordinates using a simple tensile test rather than much more complicated tests described in Section 3.4.3 and shown in Figs. 3.54 and 3.55. Indeed, if we know E_x from the tensile test in Fig. 4.23 and find E_1, E_2, ν_{21} from tensile tests along and across the fibers (see Sections 3.4.1 and 3.4.2), we can use the first equation of Eqs. (4.76) to determine

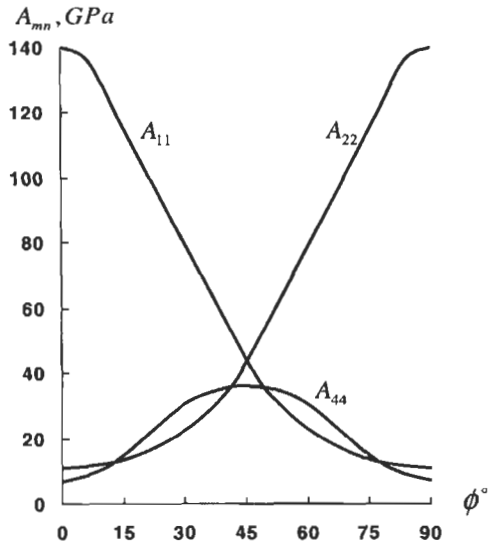

Fig. 4.20. Dependencies of tensile (A_{11}, A_{22}) and shear (A_{44}) stiffnesses of a unidirectional carbon–epoxy layer on the orientation angle.

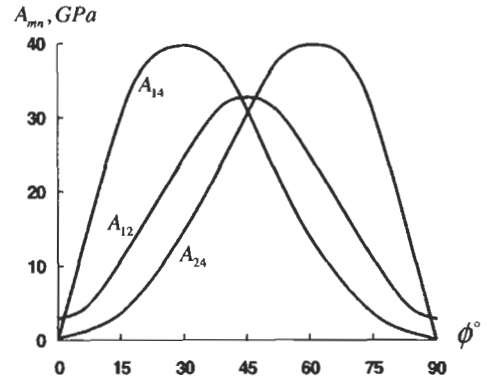

Fig. 4.21. Dependencies of coupling stiffnesses of a unidirectional carbon–epoxy layer on orientation angle.

$$G_{12} = \frac{\sin^2\phi\cos^2\phi}{\frac{1}{E_x} - \frac{\cos^4\phi}{E_1} - \frac{\sin^4\phi}{E_2} + \frac{2\nu_{21}}{E_1}\sin^2\phi\cos^2\phi}.$$

In connection with this, a question arises as to what angle should be substituted into this equation to provide the most accurate result. The answer is given in Fig. 4.24, which displays the strains in principal material coordinates of a carbon–epoxy layer

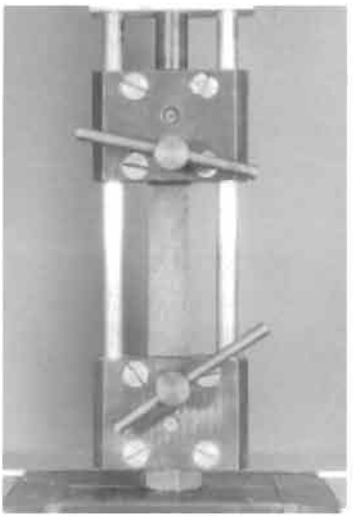

Fig. 4.22. An off-axis test.

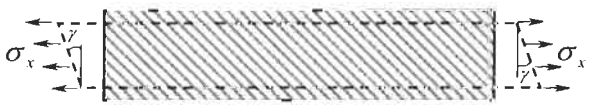

Fig. 4.23. Deformation of a unidirectional layer loaded at an angle to fiber orientation.

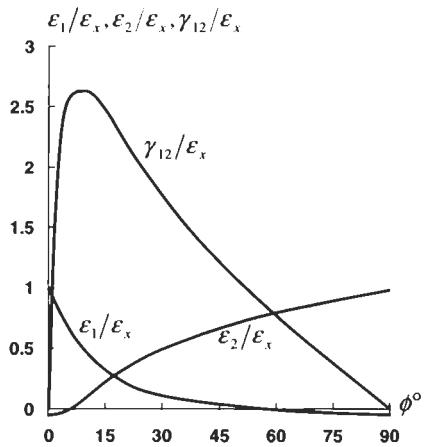

Fig. 4.24. Dependencies of normalized strains in the principle material coordinates on the angle of the off-axis test.

calculated with the aid of Eqs. (4.69) and (4.77). As can be seen in this figure, the best angle is about 10°. At this angle, shear strain γ_{12} is much higher than the normal strains ε_1 and ε_2, so that material deformation is associated mainly with shear. Off-axis test with $\phi = 10°$ can be also used to evaluate material strength in shear $\bar{\tau}_{12}$ (Chamis, 1979). Stresses acting under off-axis tension in the principal material coordinates are statically determinate and can be found directly from Eqs. (4.67) as

$$\sigma_1 = \sigma_x \cos^2\phi, \quad \sigma_2 = \sigma_x \sin^2\phi, \quad \tau_{12} = -\sigma_x \sin\phi\cos\phi \ . \tag{4.78}$$

Thus, applying stress σ_x and changing ϕ we can induce a proportional loading with different combinations of stresses σ_1, σ_2, and τ_{12} to evaluate constitutive or failure theory for a material under study.

However, the test shown in Fig. 4.23 can hardly be performed because the test fixture (see Fig. 4.22) restrains the shear deformation of the specimen. This restraint does not demonstrate itself only if shear is not induced by the off-axis tension, i.e., if $\gamma_{xy} = 0$ in Eqs. (4.77). This means that $\eta_{xy,x} = 0$ or that in accordance with Eqs. (4.76),

$$\left[\frac{\cos^2\phi}{E_1} - \frac{\sin^2\phi}{E_2} - \left(\frac{1}{2G_{12}} - \frac{\nu_{21}}{E_1}\right)\cos 2\phi\right]\sin\phi\cos\phi = 0 \ .$$

This equation has two natural solutions $\phi = 0$ and $\phi = 90°$ corresponding to tension along and across the fibers. However, it can have one more solution, i.e.,

$$\sin^2\phi = \frac{\frac{1+\nu_{21}}{E_1} - \frac{1}{2G_{12}}}{\frac{1+\nu_{21}}{E_1} + \frac{1+\nu_{12}}{E_2} - \frac{1}{G_{12}}} \ . \tag{4.79}$$

Because $0 \leqslant \sin^2\phi \leqslant 1$, solution for this equation exists if

$$\frac{1}{2G_{12}} \leqslant \frac{1+\nu_{12}}{E_2}, \quad \frac{1}{2G_{12}} \leqslant \frac{1+\nu_{21}}{E_1} \ . \tag{4.80}$$

Unfortunately, these conditions cannot be satisfied for unidirectional composites. Indeed, as follows from Eqs. (4.76), there exists the following differential relation between compliance coefficients (Verchery and Gong, 1999):

$$\frac{\mathrm{d}}{\mathrm{d}\phi}\left(\frac{1}{E_x}\right) = -2\frac{\eta_{x,xy}}{G_{xy}} \ .$$

This means that $\eta_{x,xy} = 0$ if E_x reaches its extremum value within the interval $0 < \phi < 90°$. In other words, function $E_x(\phi)$ should be as shown in Fig. 4.25 with a solid line. Then, $\eta_{x,xy} = 0$ at $\phi = \phi_0$. But for unidirectional advanced composites whose properties are listed in Table 3.5, the curve is similar to the broken line in Fig. 4.25, and E_x reaches its extremum values at $\phi = 0$ and $\phi = 90°$ only.

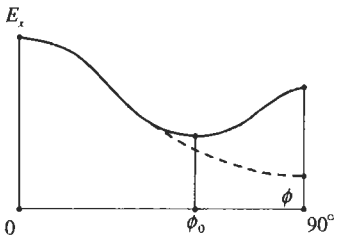

Fig. 4.25. Angle ϕ_0 of an off-axis test without shear–extension coupling.

Thus, to describe a real off-axis test, we need to study the coupled problem for an anisotropic strip in which shear is induced by tension but is restricted at the strip ends by the jaws of a test frame as in Figs. 4.22 and 4.26. As follows from Fig. 4.26, the action of the grip can be simulated if we apply bending moment M and transverse force V such that the rotation of the strip ends (γ in Fig. 4.23) will become zero. As a result, bending normal and shear stresses appear in the strip that can be analysed with the aid of the composite beam theory (Vasiliev, 1993).

To derive the corresponding equations, introduce traditional assumptions of the beam theory according to which axial, u_x, and transverse, u_y, displacements can be presented as

$$u_x = u(x) + y\theta, \quad u_y = v(x) \ ,$$

where u and θ are the axial displacement and the angle of rotation of the strip cross-section x = constant and v is the strip deflection in the xy-plane (see Fig. 4.26). The strains corresponding to these displacements follow from Eqs. (2.22), i.e.,

$$\begin{aligned} \varepsilon_x &= \frac{\partial u_x}{\partial x} = u' + y\theta' = \varepsilon + y\theta', \\ \gamma_{xy} &= \frac{\partial u_x}{\partial y} + \frac{\partial u_y}{\partial x} = \theta + v' \ , \end{aligned} \tag{4.81}$$

where $(\,)' = \mathrm{d}(\,)/\mathrm{d}x$ and ε is the elongation of the strip axis. These strains are linked with stresses by Eqs. (4.75) which reduce to

$$\begin{aligned} \varepsilon_x &= \frac{\sigma_x}{E_x} + \eta_{x,xy}\frac{\tau_{xy}}{G_{xy}}, \\ \gamma_{xy} &= \frac{\tau_{xy}}{G_{xy}} + \eta_{xy,x}\frac{\sigma_x}{E_x} \ . \end{aligned} \tag{4.82}$$

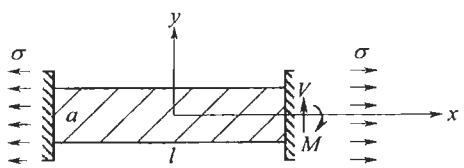

Fig. 4.26. Off-axis tension of a strip fixed at the ends.

The inverse form of these equations is

$$\sigma_x = B_{11}\varepsilon_x + B_{14}\gamma_{xy}, \quad \tau_{xy} = B_{41}\varepsilon_x + B_{44}\gamma_{xy} \ , \tag{4.83}$$

where

$$\begin{aligned} B_{11} &= \frac{E_x}{1 - \eta_{x,xy}\eta_{xy,x}}, \quad B_{44} = \frac{G_{xy}}{1 - \eta_{x,xy}\eta_{xy,x}}, \\ B_{14} = B_{41} &= -\frac{E_x\eta_{x,xy}}{1 - \eta_{x,xy}\eta_{xy,x}} = -\frac{G_{xy}\eta_{xy,x}}{1 - \eta_{x,xy}\eta_{xy,x}} \ . \end{aligned} \tag{4.84}$$

Now, decompose the strip displacements, strains, and stresses into two components corresponding to
(1) free tension (see Figure 4.23), and
(2) bending.
For the free tension we have $\tau_{xy} = 0$ and $v = 0$. So, Eqs. (4.81) and (4.82) yield

$$\varepsilon_x^{(1)} = \varepsilon_1 + y\theta_1', \quad \gamma_{xy}^{(1)} = \theta_1, \quad \varepsilon_x^{(1)} = \frac{\sigma_x^{(1)}}{E_x}, \quad \gamma_{xy}^{(1)} = \eta_{xy,x}\frac{\sigma_x^{(1)}}{E_x} \ , \tag{4.85}$$

where $\varepsilon_1 = u_1'$ and $\sigma_x^{(1)} = \sigma = F/ah$, where F is the axial force applied to the strip, a the strip width and h is its thickness. Because $\sigma_x^{(1)} =$ constant, Eqs. (4.85) give

$$\theta_1 = \eta_{xy,x}\frac{\sigma}{E_x} = \text{constant}, \quad \varepsilon_x^1 = \varepsilon_1 = \frac{\sigma}{E_x} = \frac{F}{ah} \ . \tag{4.86}$$

Adding components corresponding to bending (with index 2) we can write the total displacements and strains as

$$\begin{aligned} u_x &= u_1 + u_2 + y(\theta_1 + \theta_2), \quad u_y = v_2, \\ \varepsilon_x &= \varepsilon_1 + \varepsilon_2 + y\theta_2', \quad \gamma_{xy} = \theta_1 + \theta_2 + v_2' \ . \end{aligned}$$

The total stresses can be expressed with the aid of Eqs. (4.83), i.e.,

$$\begin{aligned} \sigma_x &= B_{11}(\varepsilon_1 + \varepsilon_2 + y\theta_2') + B_{14}(\theta_1 + \theta_2 + v_2'), \\ \tau_{xy} &= B_{41}(\varepsilon_1 + \varepsilon_2 + y\theta_2') + B_{44}(\theta_1 + \theta_2 + v_2') \ . \end{aligned}$$

Transforming these equations with the aid of Eqs. (4.84) and (4.86) we arrive at

$$\begin{aligned} \sigma_x &= \sigma + B_{11}(\varepsilon_2 + y\theta_2') + B_{14}(\theta_2 + v_2'), \\ \tau_{xy} &= B_{41}(\varepsilon_2 + y\theta_2') + B_{44}(\theta_2 + v_2') \ . \end{aligned} \tag{4.87}$$

These stresses are statically equivalent to the axial force P, bending moment M, and transverse force V, which can be introduced as

$$P = h \int_{-a/2}^{a/2} \sigma_x \, dy, \quad M = h \int_{-a/2}^{a/2} \sigma_x y \, dy, \quad V = h \int_{-a/2}^{a/2} \tau_{xy} \, dy \ .$$

Substitution of Eqs. (4.87) and integration yields

$$P = ah[\sigma + B_{11}\varepsilon_2 + B_{14}(\theta_2 + v_2')] \ , \tag{4.88}$$

$$M = B_{11} h \frac{a^3}{12} \theta_2' \ , \tag{4.89}$$

$$V = ah[B_{41}\varepsilon_2 + B_{44}(\theta_2 + v_2')] \ . \tag{4.90}$$

These forces and moment should satisfy the equilibrium equation that follows from Fig. 4.27, i.e.,

$$P' = 0, \quad V' = 0, \quad M' = V \ . \tag{4.91}$$

Solution of the first equation is $P = F = \sigma ah$. Then, Eq. (4.88) gives

$$\varepsilon_2 = -\frac{B_{14}}{B_{11}}(\theta_2 + v_2') \ . \tag{4.92}$$

The second equation of Eqs. (4.91) shows that $V = C_1$, where C_1 is a constant of integration. Then, substituting this result into Eq. (4.90) and eliminating ε_2 with the aid of Eq. (4.92) we get

$$\theta_2 + v_2' = \frac{C_1}{ah\bar{B}_{44}} \ , \tag{4.93}$$

where $\bar{B}_{44} = B_{44} - B_{14}B_{41}$.

Taking in the third equation of Eqs. (4.91) $V = C_1$ and substituting M from Eq. (4.89) we arrive at the following equation for θ_2:

$$\theta_2'' = \frac{12C_1}{a^3 h B_{11}} \ .$$

Integration yields

$$\theta_2 = \frac{6C_1}{a^3 h B_{11}} + C_2 x + C_3 \ .$$

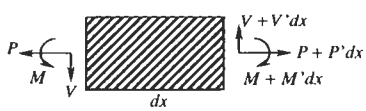

Fig. 4.27. Forces and moments acting on the strip element.

The total angle of rotation $\theta = \theta_1 + \theta_2$, where θ_1 is specified by Eqs. (4.86), should be zero at the ends of the strip, i.e., $\theta(x = \pm l/2) = 0$. Satisfying these conditions we get

$$\theta_2 = \frac{3C_1}{a^3 h B_{11}} \left(2x^2 - \frac{l^2}{2}\right) - \eta_{xy,x} \frac{\sigma}{E_x} \ . \tag{4.94}$$

Substitution into Eq. (4.93) and integration allow us to find the deflection

$$v_2 = \frac{C_1 x}{ah\bar{B}_{44}} - \frac{3C_1 x}{a^3 h B_{11}} \left(\frac{2x^2}{3} - \frac{l^2}{2}\right) + \eta_{xy,x} \frac{\sigma_0 x}{E_x} + C_4 \ . \tag{4.95}$$

This expression includes two constants, C_1 and C_4, which should be determined from the boundary conditions $v_2(x = l/2) = 0$. The final result following from Eqs. (4.86), (4.94), and (4.95) is

$$\begin{aligned} v &= l\eta_{xy,x} \frac{\sigma \bar{x}}{E_x} \left[1 - \frac{B_{11} + \bar{l}^2 \bar{B}_{44}(3/2 - 2\bar{x}^2)}{B_{11} + \bar{l}^2 \bar{B}_{44}}\right], \\ \theta &= \eta_{xy,x} \frac{3\sigma \bar{l}^2}{E_x} \frac{\bar{B}_{44}(2\bar{x}^2 - 1/2)}{B_{11} + \bar{l}^2 \bar{B}_{44}} \ , \end{aligned} \tag{4.96}$$

where $\bar{l} = l/a$ and $\bar{x} = x/l$. Deflection of a carbon–epoxy strip having $\phi = 45°$ and $\bar{l} = 10$ is shown in Fig. 4.28.

Now, we can write the relationship between modulus E_x corresponding to the ideal test shown in Fig. 4.23 and apparent modulus E_x^a that can be found from the real test shown in Figs. 4.22 and 4.26. Using Eqs. (4.84), (4.86), (4.92), and (4.96) we finally get

$$\sigma = E_x^a \varepsilon \ ,$$

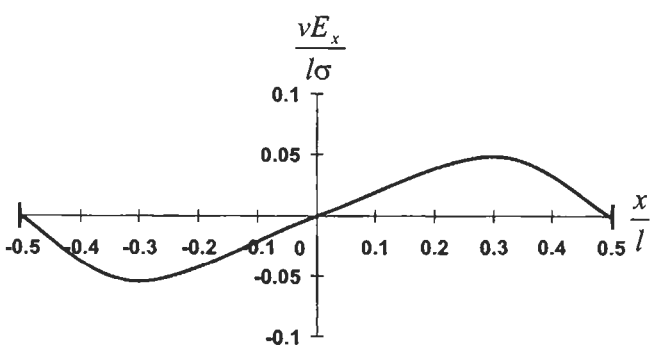

Fig. 4.28. Normalized deflection of a carbon–epoxy strip ($\phi = 45°$, $\bar{l} = 10$).

where

$$E_x^a = \frac{E_x}{1 - \dfrac{E_x \eta_{x,xy} \eta_{xy,x}}{E_x + \bar{l}^2 G_{xy}(1 - \eta_{x,xy}\eta_{xy,x})}} \ .$$

Consider two limiting cases. For an infinitely long strip ($\bar{l} \to \infty$), we have $E_x^a = E_x$. This result corresponds to the case of free shear deformation specified by Eqs. (4.77). For an infinitely short strip ($\bar{l} \to 0$), we get

$$E_x^a = \frac{E_x}{1 - \eta_{x,xy}\eta_{xy,x}} = B_{11} \ .$$

In accordance with Eqs. (4.83), this result corresponds to a restricted shear deformation ($\gamma_{xy} = 0$). For a strip with finite length, $E_x < E_x^a < B_{11}$. Dependence of the normalized modulus on the length-to-width ratio for a 45° carbon–epoxy layer is shown in Fig. 4.29. As can be seen, the difference between E_x^a and E_x becomes less than 5% for $l > 3a$.

4.3.2. Nonlinear models

Nonlinear deformation of an anisotropic unidirectional layer can be rather easily studied because stresses σ_1, σ_2, τ_{12} in the principal material coordinates (see Fig. 4.18) are statically determinate and can be found using Eqs. (4.67). Substituting these stresses into nonlinear constitutive equations, Eqs. (4.60) or Eqs. (4.64), we can express strains ε_1, ε_2, and γ_{12} in terms of stresses σ_x, σ_y, and τ_{xy}. Further substitution into Eqs. (4.70) yields constitutive equations that link strains ε_x, ε_y, and γ_{xy} with stresses σ_x, σ_y, and τ_{xy} thus allowing us to find strains in the global coordinates x, y, z if we know the corresponding stresses.

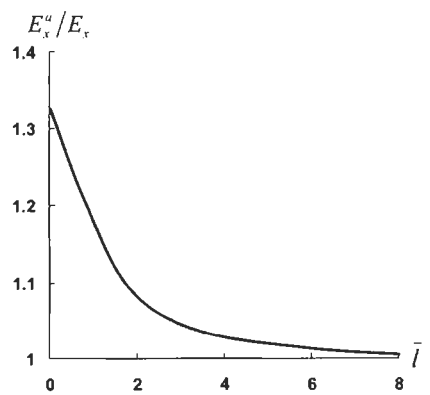

Fig. 4.29. Dependence of the normalized apparent modulus on the strip length-to-width ratio for a 45° carbon–epoxy layer.

As an example of application of a nonlinear elastic material model described by Eqs. (4.60), consider a two-matrix fiberglass composite whose stress–strain curves in the principal material coordinates are presented in Fig. 4.16. These curves allowed us to determine coefficients 'b' and 'c' in Eqs. (4.60). To find coupling coefficients 'm', we use a 45° off-axis test. Experimental results (circles) and the corresponding approximation (solid line) are shown in Fig. 4.30. Thus, constructed material model can be used now to predict its behavior under tension at any other (different from 0°, 45°, and 90°) angle (the corresponding results are given in Fig. 4.31 for 60°) or to study more complicated material structures and loading cases (see Section 4.5).

As an example of application of elastic–plastic material model specified by Eq. (4.64), consider a boron–aluminum composite whose stress–strain diagrams in principal material coordinates are shown in Fig. 4.17. Theoretical and experimental curves (Herakovich, 1998) for 30° and 45° off-axis tension of this material are presented in Fig. 4.32.

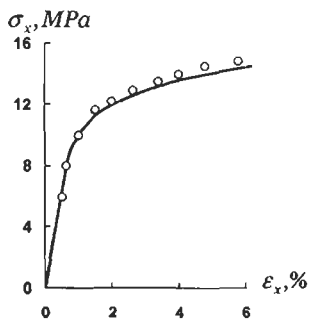

Fig. 4.30. Calculated (solid line) and experimental (circles) stress–strain diagram for 45° off-axis tension of a two-matrix unidirectional composite.

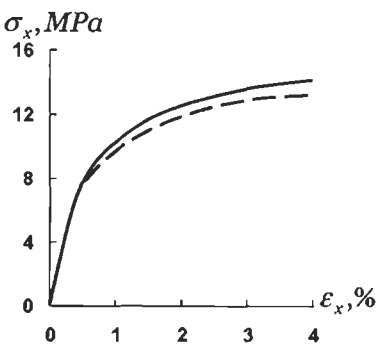

Fig. 4.31. Theoretical (solid line) and experimental (broken line) stress–strain diagrams for 60° off-axis tension of a two matrix unidirectional composite.

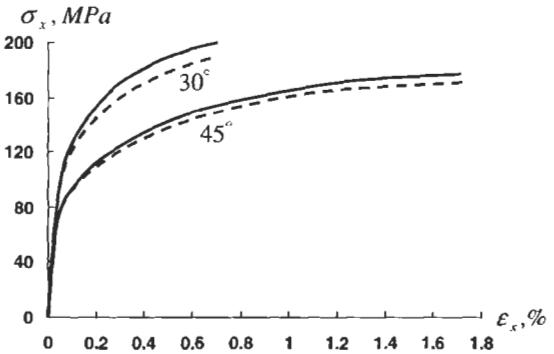

Fig. 4.32. Theoretical (solid lines) and experimental (broken lines) stress–strain diagrams for 30° and 45° off-axis tension of a boron-aluminum composite.

4.4. Orthogonally reinforced orthotropic layer

The simplest layer reinforced in two directions is the so-called cross-ply layer that consists of alternating plies with 0° and 90° orientations with respect to global coordinate frame x, y, z as in Fig. 4.33. Actually, this is a laminated structure, but being formed with a number of plies, it can be treated as a homogeneous orthotropic layer (see Section 5.4.2).

4.4.1. Linear elastic model

Let the layer consist of m longitudinal (0°) plies with thicknesses $h_0^{(i)}$ ($i = 1, 2, 3, \ldots, m$) and n transverse (90°) plies with thicknesses $h_{90}^{(j)}$ ($j = 1, 2, 3, \ldots, n$) made from one and the same composite material. Then, stresses σ_x, σ_y, and τ_{xy} that comprise the plane stress state in the global coordinate frame can be expressed in terms of stresses in the principal material coordinates of the plies as

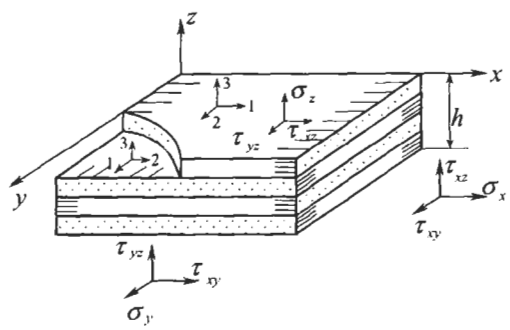

Fig. 4.33. A cross-ply layer.

$$\sigma_x h = \sum_{i=1}^{m} \sigma_1^{(i)} h_0^{(i)} + \sum_{j=1}^{n} \sigma_2^{(j)} h_{90}^{(j)},$$
$$\sigma_y h = \sum_{i=1}^{m} \sigma_2^{(i)} h_0^{(i)} + \sum_{j=1}^{n} \sigma_1^{(j)} h_{90}^{(j)}, \tag{4.97}$$
$$\tau_{xy} h = \sum_{i=1}^{m} \tau_{12}^{(i)} h_0^{(i)} + \sum_{j=1}^{n} \tau_{12}^{(j)} h_{90}^{(j)} \ ,$$

where, h is the total thickness of the layer (see Fig. 4.33), i.e.,

$$h = h_0 + h_{90} \ ,$$

where

$$h_0 = \sum_{i=1}^{m} h_0^{(i)}, \quad h_{90} = \sum_{j=1}^{n} h_{90}^{(j)}$$

are total thickness of longitudinal and transverse plies.

Stresses in the principal material coordinates of the plies are linked with the corresponding strains by Eqs. (3.59) or Eqs. (4.56):

$$\sigma_1^{(i,j)} = \bar{E}_1(\varepsilon_1^{(i,j)} + \nu_{12}\varepsilon_2^{(i,j)}),$$
$$\sigma_2^{(i,j)} = \bar{E}_2(\varepsilon_2^{(i,j)} + \nu_{21}\varepsilon_1^{(i,j)}), \tag{4.98}$$
$$\tau_{12}^{(i,j)} = G_{12}\gamma_{12}^{(i,j)} \ ,$$

where, as earlier $\bar{E}_{1,2} = E_{1,2}/(1 - \nu_{12}\nu_{21})$ and $E_1\nu_{12} = E_2\nu_{21}$. Now assume that deformation of all the plies is the same that the deformation of the whole layer, i.e., that

$$\varepsilon_1^{(i)} = \varepsilon_2^{(j)} = \varepsilon_x, \quad \varepsilon_2^{(i)} = \varepsilon_1^{(j)} = \varepsilon_y, \quad \gamma_{12}^{(i)} = \gamma_{12}^{(j)} = \gamma_{xy} \ .$$

Then, substituting Eqs. (4.98) into Eqs. (4.97) we arrive at the following constitutive equations:

$$\sigma_x = A_{11}\varepsilon_x + A_{12}\varepsilon_y,$$
$$\sigma_y = A_{21}\varepsilon_x + A_{22}\varepsilon_y, \tag{4.99}$$
$$\tau_{xy} = A_{44}\gamma_{xy} \ ,$$

where the stiffness coefficients are

$$A_{11} = \bar{E}_1\bar{h}_0 + \bar{E}_2\bar{h}_{90}, \quad A_{22} = \bar{E}_1\bar{h}_{90} + \bar{E}_2\bar{h}_0,$$
$$A_{12} = A_{21} = \bar{E}_1\nu_{12} = \bar{E}_2\nu_{21}, \quad A_{44} = G_{12} \tag{4.100}$$

and

$$\bar{h}_0 = \frac{h_0}{h}, \quad \bar{h}_{90} = \frac{h_{90}}{h} \ .$$

The inverse form of Eqs. (4.99) is

$$\varepsilon_x = \frac{\sigma_x}{E_x} - \nu_{xy}\frac{\sigma_y}{E_y}, \quad \varepsilon_y = \frac{\sigma_y}{E_y} - \nu_{yx}\frac{\sigma_x}{E_x}, \quad \gamma_{xy} = \frac{\tau_{xy}}{G_{xy}} \ , \tag{4.101}$$

where

$$\begin{aligned} &E_x = A_{11} - \frac{A_{12}^2}{A_{22}}, \quad E_y = A_{22} - \frac{A_{12}^2}{A_{21}}, \quad G_{xy} = A_{44}, \\ &\nu_{xy} = \frac{A_{12}}{A_{11}}, \quad \nu_{yx} = \frac{A_{12}}{A_{22}} \ . \end{aligned} \tag{4.102}$$

To determine transverse shear moduli G_{xz} and G_{yz}, consider, e.g., pure shear in the xz-plane (see Fig. 4.34). As follows from equilibrium conditions for the plies

$$\tau_{13}^{(i)} = \tau_{23}^{(j)} = \tau_{xz}, \quad \tau_{23}^{(i)} = \tau_{13}^{(j)} = \tau_{yz} \ . \tag{4.103}$$

The total shear strains can be found as

$$\begin{aligned} \gamma_{xz} &= \frac{1}{h}\left(\sum_{i=1}^{m} \gamma_{13}^{(i)} h_0 + \sum_{j=1}^{n} \gamma_{23}^{(j)} h_{90}\right), \\ \gamma_{yz} &= \frac{1}{h}\left(\sum_{i=1}^{m} \gamma_{23}^{(i)} h_0 + \sum_{j=1}^{n} \gamma_{13}^{(j)} h_{90}\right) \ , \end{aligned} \tag{4.104}$$

where in accordance with Eqs. (4.56)

$$\gamma_{13}^{(i,j)} = \frac{\tau_{13}^{(i,j)}}{G_{13}}, \quad \gamma_{23}^{(i,j)} = \frac{\tau_{23}^{(i,j)}}{G_{23}} \ . \tag{4.105}$$

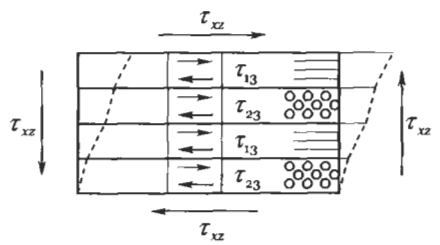

Fig. 4.34. Pure transverse shear of a cross-ply layer.

Substituting Eqs. (4.105) into Eqs. (4.104) and using Eqs. (4.103) we arrive at

$$\gamma_{xz} = \frac{\tau_{xz}}{G_{xz}}, \quad \gamma_{yz} = \frac{\tau_{yz}}{G_{yz}} ,$$

where

$$\frac{1}{G_{xz}} = \frac{\bar{h}_0}{G_{13}} + \frac{\bar{h}_{90}}{G_{23}}, \quad \frac{1}{G_{yz}} = \frac{\bar{h}_0}{G_{23}} + \frac{\bar{h}_{90}}{G_{13}} .$$

4.4.2. *Nonlinear models*

Nonlinear behavior of a cross-ply layer associated with nonlinear material response under loading in the principal material coordinates (see, e.g., Figs. 4.16 and 4.17) can be described using nonlinear constitutive equations, Eqs. (4.60) or Eqs. (4.64) instead of linear equations (4.99).

However, this layer can demonstrate nonlinearity that is entirely different from what was studied in the previous sections. This nonlinearity is observed in the cross-ply layer composed of linear elastic plies and is caused by microcracking of the matrix.

To study this phenomenon, consider a cross-ply laminate consisting of three plies as in Fig. 4.35. Equilibrium conditions yield the following equations:

$$\begin{aligned} 2(\sigma_{x1}\bar{h}_1 + \sigma_{x2}\bar{h}_2) &= \sigma, \\ 2(\sigma_{y1}\bar{h}_1 + \sigma_{y2}\bar{h}_2) &= 0 , \end{aligned} \tag{4.106}$$

where

$$\bar{h}_1 = h_1/h, \quad \bar{h}_2 = h_2/h, \quad h = 2(h_1 + h_2) .$$

Constitutive equations are

$$\begin{aligned} \sigma_{x1,2} &= \bar{E}_{1,2}(\varepsilon_x + \nu_{12,21}\varepsilon_y), \\ \sigma_{y1,2} &= \bar{E}_{2,1}(\varepsilon_y + \nu_{21,12}\varepsilon_x) , \end{aligned} \tag{4.107}$$

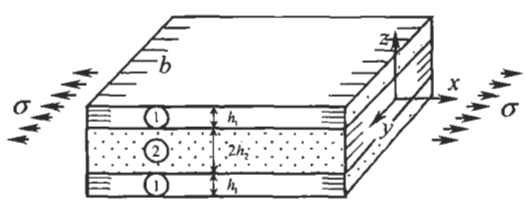

Fig. 4.35. Tension of a cross-ply laminate.

where $\bar{E}_{1,2} = E_{1,2}/(1 - \nu_{12}\nu_{21})$. We assume that strains ε_x and ε_y do not change through the laminate thickness. Substituting Eqs. (4.107) into Eqs. (4.106) we can find strains and then stresses using again Eqs. (4.107). The final result is

$$\sigma_{x1,2} = \frac{\sigma E_{1,2}[E_2\bar{h}_1 + E_1\bar{h}_2 - E_{1,2}\nu_{12,21}^2(\bar{h}_1 + \bar{h}_2)]}{2[(E_1\bar{h}_1 + E_2\bar{h}_2)(E_2\bar{h}_1 + E_1\bar{h}_2) - E_1^2\nu_{12}^2(h_1 + h_2)^2]} .$$

To simplify the analysis, neglect Poisson's effect taking $\nu_{12} = \nu_{21} = 0$. Then

$$\sigma_{x1} = \sigma_1^0 = \frac{\sigma E_1}{2(E_1\bar{h}_1 + E_2\bar{h}_2)}, \quad \sigma_{x2} = \sigma_2^0 = \frac{\sigma E_2}{2(E_1\bar{h}_1 + E_2\bar{h}_2)} . \tag{4.108}$$

Consider, for example, the case $\bar{h}_1 = \bar{h}_2 = 0.5$ and find the ultimate stresses corresponding to the failure of longitudinal plies or to the failure of the transverse ply. Putting $\sigma_1^0 = \bar{\sigma}_1^+$ and $\sigma_2^0 = \bar{\sigma}_2^+$ we get

$$\bar{\sigma}_x^{(1)} = \bar{\sigma}_1^+\left(1 + \frac{E_2}{E_1}\right), \quad \bar{\sigma}_x^{(2)} = \bar{\sigma}_2^+\left(1 + \frac{E_1}{E_2}\right) .$$

The results of calculation for composites listed in Table 3.5 are presented in Table 4.2. As can be seen, $\bar{\sigma}_x^{(1)} \gg \bar{\sigma}_x^{(2)}$. This means that the first failure occurs in the transverse ply under stress

$$\sigma = \bar{\sigma} = 2\bar{\sigma}_2^+\left(\bar{h}_2 + \frac{E_1}{E_2}\bar{h}_1\right) . \tag{4.109}$$

This stress does not cause the failure of the whole laminate because the longitudinal plies can carry the load, but the material behavior becomes nonlinear. Actually, the effect under consideration is the result of the difference between the ultimate elongations of the unidirectional plies along and across the fibers. From the data presented in Table 4.2 we can see that for all the materials listed in the table $\bar{\varepsilon}_1 \gg \bar{\varepsilon}_2$. As a result, transverse plies following under tension longitudinal plies that have

Table 4.2
Ultimate stresses causing the failure of longitudinal ($\bar{\sigma}_x^{(1)}$) or transverse ($\bar{\sigma}_x^{(2)}$) plies and deformation characteristics of typical advanced composites.

σ (MPa); ε (%)	Glass–epoxy	Carbon–epoxy	Carbon–PEEK	Aramid–epoxy	Boron–epoxy	Boron–Al	Carbon–carbon	Al_2O_3–Al
$\bar{\sigma}_x^{(1)}$	2190	2160	2250	2630	1420	2000	890	1100
$\bar{\sigma}_x^{(2)}$	225	690	1125	590	840	400	100	520
$\bar{\varepsilon}_1$	3	1.43	1.5	2.63	0.62	0.50	0.47	0.27
$\bar{\varepsilon}_2$	0.31	0.45	0.75	0.2	0.37	0.1	0.05	0.13
$\bar{\varepsilon}_1/\bar{\varepsilon}_2$	9.7	3.2	2	13.1	1.68	5	9.4	2.1

much higher stiffness and elongation fail because their ultimate elongation is smaller. This failure is accompanied with a system of cracks parallel to fibers which can be observed not only in cross-ply layers but in many other laminates that include unidirectional plies experiencing transverse tension caused by interaction with the adjacent plies (see Fig. 4.36).

Now assume that the acting stress $\sigma \geqslant \bar{\sigma}$, where $\bar{\sigma}$ is specified by Eq. (4.109) and corresponds to the load causing the first crack in the transverse ply as in Fig. 4.37. To study the stress state in the vicinity of the crack, decompose the stresses in three plies shown in Fig. 4.37 as

$$\sigma_{x1} = \sigma_{x3} = \sigma_1^0 + \sigma_1, \quad \sigma_{x2} = \sigma_2^0 - \sigma_2 \ , \tag{4.110}$$

and assume that the crack induces also transverse through-the-thickness shear and normal stresses

$$\tau_{xzi} = \tau_i, \quad \sigma_{zi} = s_i, \quad i = 1, 2, 3 \ . \tag{4.111}$$

Stresses σ_1^0 and σ_2^0 in Eqs. (4.110) are specified by Eqs. (4.108) with $\sigma = \bar{\sigma}$ corresponding to the acting stress under which the first crack appears in the transverse ply. Stresses σ_1 and σ_2 should be self-balanced, i.e.,

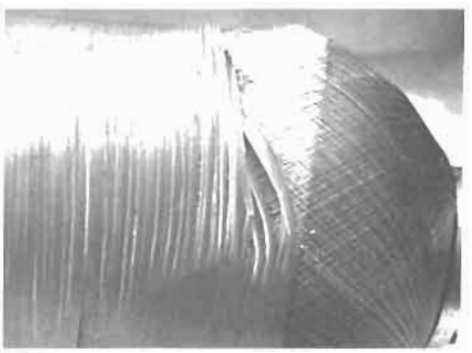

Fig. 4.36. Cracks in the circumferential layer of the failed pressure vessel induced by transverse (for the vessel, axial) tension of the layer.

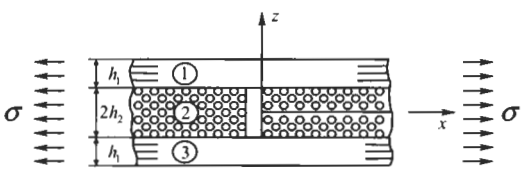

Fig. 4.37. A cross-ply layer with a crack in the transverse ply.

$$\sigma_1 \bar{h}_1 = \sigma_2 \bar{h}_2 \ . \tag{4.112}$$

Total stresses in Eqs. (4.110) and (4.111) should satisfy equilibrium equations, Eqs. (2.5), which yield for the problem under study

$$\frac{\partial \sigma_{xi}}{\partial x} + \frac{\partial \tau_{xzi}}{\partial z} = 0, \quad \frac{\partial \sigma_{zi}}{\partial z} + \frac{\partial \tau_{xzi}}{\partial x} = 0 \ , \tag{4.113}$$

where $i = 1, 2, 3$.

To simplify the problem, assume that the additional stresses σ_1 and σ_2 do not depend on z, i.e., that they are uniformly distributed through the thickness of longitudinal plies. Then, Eqs. (4.113), upon substitution of Eqs. (4.110) and (4.111) can be integrated with respect to z. The resulting stresses should satisfy the following boundary and interface conditions (see Fig. 4.37):

$$\begin{aligned}
&\tau_1(z = h_1 + h_2) = 0, \quad s_1(z = h_1 + h_2) = 0, \\
&\tau_1(z = h_2) = \tau_2(z = h_2), \quad s_1(z = h_2) = s_2(z = h_2), \\
&\tau_2(z = -h_2) = \tau_3(z = -h_2), \quad s_2(z = -h_2) = s_3(z = -h_2), \\
&\tau_3(z = -h_1 - h_2) = 0, \quad s_3(z = -h_1 - h_2) = 0 \ .
\end{aligned}$$

Finally, using Eq. (4.112) to express σ_1 in terms of σ_2 we arrive at the following stress distribution (Vasiliev et al., 1970):

$$\begin{aligned}
&\sigma_{x1} = \sigma_{x3} = \sigma_1^0 + \sigma_2(x)\frac{h_2}{h_1}, \quad \sigma_{x2} = \sigma_2^0 - \sigma_2(x), \\
&\tau_1 = -\frac{h_2}{h_1}\sigma_2'(x)z_1, \quad \tau_2 = \sigma_2'(x)z, \quad \tau_3 = -\frac{h_2}{h_1}\sigma_2'(x)z_2, \\
&s_1 = \frac{h_2}{2h_1}\sigma_2''(x)z_1^2, \quad s_2 = -\frac{1}{2}\sigma_2''(x)(z^2 - h_1 h_2 - h_2^2), \\
&s_3 = \frac{h_2}{2h_1}\sigma_2''(x)z_2^2 \ ,
\end{aligned} \tag{4.114}$$

where

$$z_1 = z - h_1 - h_2, \quad z_2 = z + h_1 + h_2, \quad \text{and} \quad (\,)' = \mathrm{d}(\,)/\mathrm{d}x \ .$$

Thus, we need to find only one unknown function: $\sigma_2(x)$. To do this, we can use the principle of minimum strain energy (see Section 2.11.2) according to which function $\sigma_2(x)$ should deliver the minimum value of

$$W_\sigma = \frac{1}{2}\int_0^l \sum_{i=1}^{3} \int_{h_i} \left(\frac{\sigma_{xi}^2}{E_{xi}} + \frac{\sigma_{zi}^2}{E_{zi}} - 2\frac{\nu_{xzi}}{E_{zi}}\sigma_{xi}\sigma_{zi} + \frac{\tau_{xzi}^2}{G_{xzi}} \right) \mathrm{d}x \ , \tag{4.115}$$

where $E_{x1} = E_{x3} = E_1$, $E_{x2} = E_2$, $E_{zi} = E_2$, $G_{xz1} = G_{xz3} = G_{13}$, $G_{xz2} = G_{23}$, $\nu_{xz1} = \nu_{xz3} = \nu_{13}$, $\nu_{xz2} = \nu_{23}$ and E_1, E_2, G_{13}, G_{23}, ν_{13}, ν_{23} are elastic constants of a unidirectional ply. Substituting stresses, Eqs. (4.114), into the functional in Eq. (4.115), integrating with respect to z, and using traditional procedure of variational calculus providing $\delta W_\sigma = 0$ we arrive at the following equation for $\sigma_2(x)$:

$$\frac{d^4\sigma_2}{dx^4} - 2a^2\frac{d^2\sigma_2}{dx^2} + b^4\sigma_2 = 0 \ ,$$

where

$$a^2 = \frac{1}{d}\left[\frac{h_2}{3G_{23}} + \frac{h_1}{3G_{13}} - \frac{\nu_{23}}{E_2}\left(h_1 + \frac{2}{3}h_2\right) + \frac{h_1\nu_{23}}{3E_2}\right], \quad b^4 = \frac{1}{d}\left(\frac{1}{h_1E_1} + \frac{1}{h_2E_2}\right),$$

$$d = \frac{1}{2E_2}\left[\frac{1}{5}(h_1^3 + h_2^3) - \frac{2}{3}h_2^2(h_1 + h_2) + h_2(h_1 + h_2)^2\right] \ .$$

General solution for this equation is

$$\sigma_2 = e^{-k_1x}(c_1 \sin k_2x + c_2 \cos k_2x) + e^{k_1x}(c_3 \sin k_2x + c_4 \cos k_2x) \ , \tag{4.116}$$

where

$$k_1 = \sqrt{\frac{1}{2}(a^2 + b^2)}, \quad k_2 = \sqrt{\frac{1}{2}(b^2 - a^2)} \ .$$

Assume that the strip shown in Fig. 4.37 is infinitely long in the x-direction. Then, we should have $\sigma_1 \to 0$ and $\sigma_2 \to 0$ for $x \to \infty$ in Eqs. (4.110). This means that we should put $c_3 = c_4 = 0$ in Eq. (4.116). The other two constants, c_1 and c_2, should be determined from the conditions on the crack surface (see Fig. 4.37), i.e.,

$$\sigma_{x2}(x = 0) = 0, \quad \tau_{xz2}(x = 0) = 0 \ .$$

Satisfying these conditions we obtain the following expressions for stresses:

$$\begin{aligned}
\sigma_{x1} &= \sigma_{x3} = \sigma_1^0 + \sigma_2^0\frac{h_2}{h_1}e^{-k_1x}\left(\frac{k_1}{k_2}\sin k_2x + \cos k_2x\right), \\
\sigma_{x2} &= \sigma_2^0\left[1 - e^{-k_1x}\left(\frac{k_1}{k_2}\sin k_2x + \cos k_2x\right)\right], \\
\tau_{xz2} &= -\frac{\sigma_2^0}{k_2}(k_1^2 + k_2^2)z\,e^{-k_1x}\sin k_2x, \\
\sigma_{z2} &= -\frac{\sigma_2^0}{2k_2}(k_1^2 + k_2^2)[z^2 - h_2(h_1 + h_2)]\,e^{-k_1x}(k_1 \sin k_2x - k_2 \cos k_2x) \ .
\end{aligned} \tag{4.117}$$

As an example, consider a glass–epoxy sandwich layer with the following parameters: $h_1 = 0.365$ mm, $h_2 = 0.735$ mm, $E_1 = 56$ GPa, $E_2 = 17$ GPa, $G_{13} =$

5.6 GPa, $G_{23} = 6.4$ GPa, $\nu_{13} = 0.095$, $\nu_{23} = 0.35$, $\bar{\sigma}_2^+ = 25.5$ MPa. Distributions of stresses normalized to the acting stress σ are presented in Fig. 4.38. As can be seen, there is a stress concentration in longitudinal plies in the vicinity of the crack, while the stress in the transverse ply, being zero on the crack surface, practically reaches σ_2^0 at a distance of about 4 mm (or about two thicknesses of the laminate) from the crack. The curves look traditionally for the problem of stress diffusion. However, analysis of the second equation of Eqs. (4.117) allows us to reveal an interesting phenomenon which can be demonstrated if we increase the vertical scale of the graph in the vicinity of points A and B (see Fig. 4.38). As follows from this analysis, stress σ_{x2} becomes equal to σ_2^0 at point A with coordinate

$$x_A = \frac{1}{k_2}\left[\pi - \tan^{-1}\left(\frac{k_2}{k_1}\right)\right]$$

and reaches the maximum value at point B with coordinate $x_B = \pi/k_2$. This maximum value

$$\sigma_{x2}^{\max} = \sigma_2^0\left(1 + e^{-\pi k_1/k_2}\right)$$

is higher than stress σ_2^0 that causes the failure of the transverse ply. This means that a single crack cannot exist. When stress σ_2^0 reaches its ultimate value $\bar{\sigma}_2^+$, a regular system of cracks located at a distance of $l_c = \pi/k_2$ from one another appears in the transverse ply (see Fig. 4.39). For the example considered above, $l_c = 12.8$ mm.

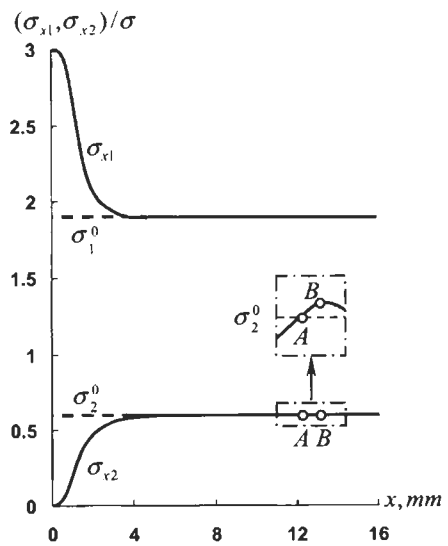

Fig. 4.38. Variation of normalized normal stresses in longitudinal (σ_{x1}) and transverse (σ_{x2}) plies with a distance from the crack.

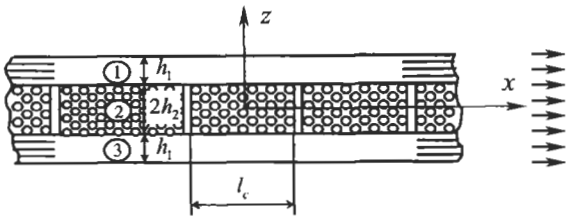

Fig. 4.39. A system of cracks in the transverse ply.

To study the stress state of a layer with cracks shown in Fig. 4.39, we can use solution (4.116) but should write it in a different form, i.e.,

$$\sigma_2 = C_1 \sinh k_1 x \sin k_2 x + C_2 \sinh k_1 x \cos k_2 x + C_3 \cosh k_1 x \sin k_2 x + C_4 \cosh k_1 x \cos k_2 x \ . \tag{4.118}$$

Because the stress state of an element $-l_c/2 \leqslant x \leqslant l_c/2$ is symmetric with respect to coordinate x, we should put $C_2 = C_3 = 0$ and find constants C_1 and C_4 from the following boundary conditions:

$$\sigma_{x2}(x = l_c/2) = 0, \quad \tau_{xz2}(x = l_c/2) = 0 \ . \tag{4.119}$$

The final expressions for stresses are

$$\begin{aligned}
\sigma_{x1} &= \sigma_{x3} = \sigma_1^0 + \sigma_2^0 \frac{h_2}{h_1 c}\left(\frac{k_1}{k_2}\cosh k_1 x \cos k_2 x + \sinh k_1 x \sin k_2 x\right), \\
\sigma_{x2} &= \sigma_2^0\left[1 - \frac{1}{c}\left(\frac{k_1}{k_2}\cosh k_1 x \cos k_2 x + \sinh k_1 x \sin k_2 x\right)\right], \\
\tau_{xz2} &= \frac{\sigma_2^0}{k_2 c}(k_1^2 + k_2^2) z \sinh k_1 x \cos k_2 x, \\
\sigma_{z2} &= -\frac{\sigma_2^0}{2k_2 c}(k_1^2 + k_2^2)\left[z^2 - h_2(h_1 + h_2)\right] \\
&\quad \times (k_1 \cosh k_1 x \cos k_2 x - k_2 \sinh k_1 x \sin k_2 x) \ ,
\end{aligned} \tag{4.120}$$

where $c = \sinh(\pi k_1/2k_2)$.

For the layer considered above as an example, stress distributions corresponding to $\sigma = \bar{\sigma} = 44.7$ MPa are shown in Figs. 4.40 and 4.41. Under further loading ($\sigma > \bar{\sigma}$), two modes of the layer failure are possible. First, formation of another transverse crack separating the block with length l_c in Fig. 4.39 into two pieces. Second, delamination in the vicinity of the crack caused by stresses τ_{xz} and σ_z (see Fig. 4.41). Usually, the first situation takes place because stresses τ_{xz} and σ_z are considerably lower than the corresponding ultimate stresses, while the maximum value of σ_{x2} is close to the ultimate stress $\sigma_2^0 = \bar{\sigma}_2^+$. Indeed, the second equation of Eqs. (4.120) yields

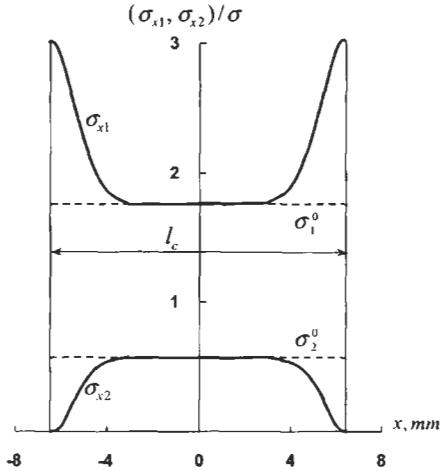

Fig. 4.40. Distribution of normalized stresses in longitudinal (σ_{x1}) and transverse (σ_{x2}) plies between the cracks.

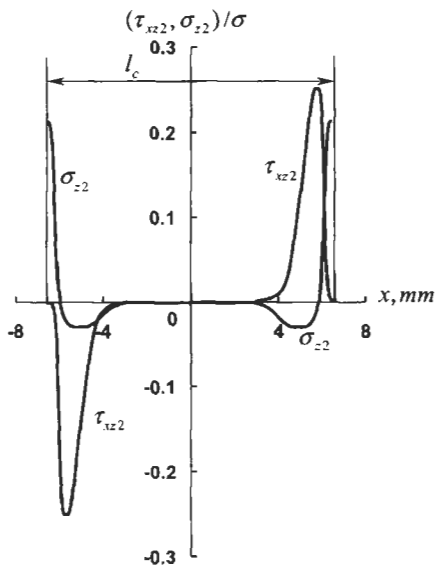

Fig. 4.41. Distribution of normalized shear (τ_{xz2}) and transverse normal stresses (σ_{z2}) at the ply interface ($z = h_2$) between the cracks.

$$\sigma_{x2}^{\max} = \sigma_{x2}(x = 0) = \sigma_2^0(1 - k) \ ,$$

where $k = k_1/(k_2 c)$. For the foregoing example, $k = 3.85 \times 10^{-4}$. So $\sigma_{x2}^{\max}$ is so close to σ_2^0 that we can assume that under practically the same load another crack occurs

in the central cross-section $x = 0$ of the central block in Fig. 4.39 (as well as in all the other blocks). Thus, the distance between the cracks becomes $l_c = \pi/2k_2$ (6.4 mm for the example under study). The corresponding stress distribution can be determined with the aid of Eqs. (4.114) and (4.118) and boundary conditions (4.119) in which we should take $l_c = \pi/2k_2$. The next crack will again appear at the block center and this process will be continued until the failure of longitudinal plies.

To plot the stress–strain diagram of the cross-ply layer with allowance for the cracks in the transverse ply, we introduce the mean longitudinal strain

$$\varepsilon_x = \frac{2}{h_2 l_c} \int_0^{l_c/2} dx \int_0^{h_2} \varepsilon_{x2}\, dz \ ,$$

where

$$\varepsilon_{x2} = \frac{1}{E_2}(\sigma_{x2} - \nu_{23}\sigma_{z2}) \ .$$

For the layer with properties given above, such a diagram is shown in Fig. 4.42 with a solid line and is in good agreement with experimental results (circles). Formation of cracks is accompanied with horizontal jumps and reduction of material stiffness. Stress–strain diagram for the transverse layer that is formally singled out of the diagram in Fig. 4.42 is presented in Fig. 4.43.

To develop a nonlinear phenomenological model of the cross-ply layer, we need to approximate the diagram in Fig. 4.43. As follows from this figure and numerous experiments, the most suitable and simple approximation is that shown by a broken line. It implies that the ply is linear elastic until its transverse stress σ_2 reaches its ultimate value $\bar{\sigma}_2^+$, and after that $\sigma_2 = \bar{\sigma}_2^+$, i.e., σ_2 remains constant up to the failure of longitudinal plies. This means that under transverse tension, unidirectional ply is in the state of permanent failure and takes from the longitudinal plies the necessary load to support this state (Vasiliev and Elpatievskii, 1967). The stress–

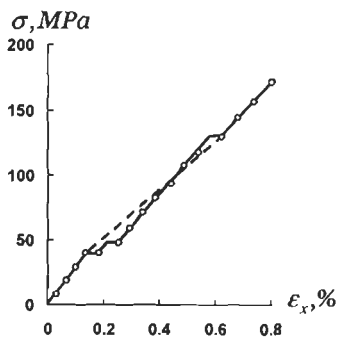

Fig. 4.42. Stress–strain diagram for a glass–epoxy cross-ply layer: o experiment; ——— theoretical prediction; – – – – model.

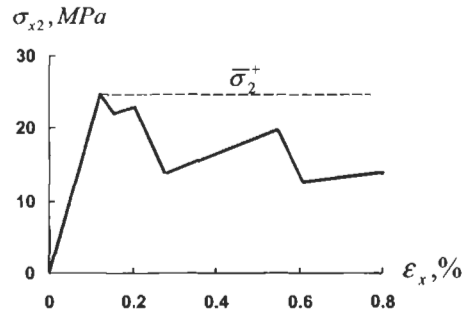

Fig. 4.43. Stress–strain diagram for a transverse ply.

strain diagram of the cross-ply layer corresponding to this model is shown in Fig. 4.42 with a broken line.

Now consider a general plane stress state with stresses σ_x, σ_y, and τ_{xy} as in Fig. 4.44. As can be seen, stress σ_x induces cracks in the inner ply, stress σ_y causes cracks in the outer orthogonal plies, while shear stress τ_{xy} can give rise to cracks in all the plies. The ply model that generalizes the model introduced above for a uniaxial tension is demonstrated in Fig. 4.45. To determine strains corresponding to a given combination of stresses σ_x, σ_y, and τ_{xy}, we can use the following procedure.

1. For the first stage of loading (before the cracks appear), the strains are calculated with the aid of Eqs. (4.100) and (4.101) providing $\varepsilon_x^{(1)}(\sigma)$, $\varepsilon_y^{(1)}(\sigma)$, and $\gamma_{xy}^{(1)}(\sigma)$, where $\sigma = (\sigma_x, \sigma_y, \tau_{xy})$ is the given combination of stresses. Using Eqs. (4.98) we find stresses σ_1, σ_2, τ_{12} in principal material coordinates for all the plies.
2. We determine the combination of stresses σ_{1k}^*, σ_{2k}^*, and τ_{12k}^* which induce the first failure of the matrix in some ply and indicate the number of this ply, say k, applying the proper strength criterion (see Section 6.2). Then, the corresponding stresses $\sigma^* = (\sigma_x^*, \sigma_y^*, \tau_{xy}^*)$ and strains $\varepsilon_x^{(1)}(\sigma^*)$, $\varepsilon_y^{(1)}(\sigma^*)$, and $\gamma_{xy}^{(1)}(\sigma^*)$ are calculated.
3. To proceed, i.e., to study the material behavior for $\sigma > \sigma^*$, we need to consider two possible cases for the layer stiffnesses. For this purpose, we should write Eqs. (4.100) for stiffness coefficients in a more general form, i.e.,

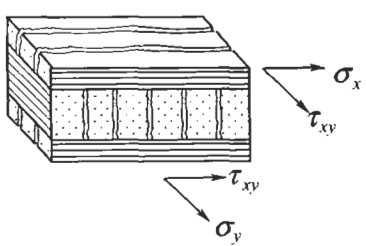

Fig. 4.44. A cross-ply layer in a plane stress state.

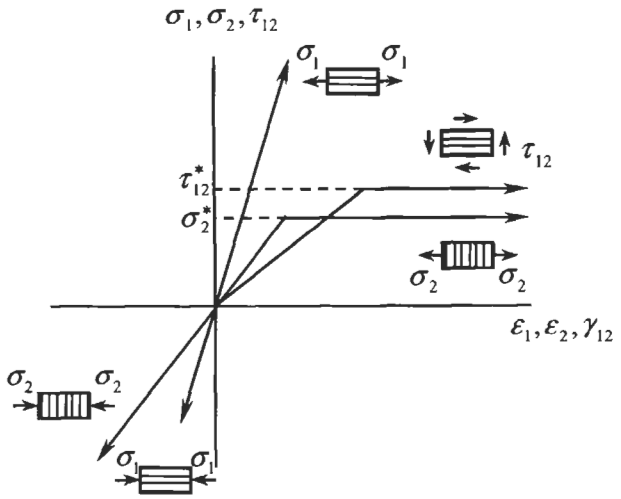

Fig. 4.45. Stress–strain diagrams of a unidirectional ply simulating its behavior in the laminate and allowing for cracks in the matrix.

$$A_{11} = \sum_{i=1}^{m} \bar{E}_1^{(i)} \bar{h}_0^{(i)} + \sum_{j=1}^{n} \bar{E}_2^{(j)} \bar{h}_{90}^{(j)}, \quad A_{22} = \sum_{i=1}^{m} \bar{E}_2^{(i)} \bar{h}_0^{(i)} + \sum_{j=1}^{n} \bar{E}_1^{(j)} \bar{h}_{90}^{(j)},$$
$$A_{12} = \sum_{i=1}^{m} \nu_{12}^{(i)} \bar{E}_1^{(i)} \bar{h}_0^{(i)} + \sum_{j=1}^{n} \nu_{12}^{(j)} \bar{E}_1^{(j)} \bar{h}_{90}^{(j)}, \quad A_{44} = \sum_{i=1}^{m} G_{12}^{(i)} \bar{h}_0^{(i)} + \sum_{j=1}^{n} G_{12}^{(j)} \bar{h}_{90}^{(j)}, \tag{4.121}$$

where $\bar{h}_0^{(i)} = h_0^{(i)}/h$ and $\bar{h}_{90}^{(j)} = h_{90}^{(j)}/h$.

(a) If $\sigma_{2k} > 0$ in the kth ply, it can work only along the fibers, and we should calculate the stiffnesses of the degraded layer taking $E_2^k = 0$, $G_{12}^k = 0$, and $\nu_{12}^k = 0$ in Eqs. (4.121).

(b) If $\sigma_{2k} < 0$ in the kth ply, it cannot work only in shear, so we should take $G_{12}^k = 0$ in Eqs. (4.121).

Thus, we find coefficients $A_{st}^{(2)}$ (st = 11, 12, 22, 44) corresponding to the second stage of loading (with one degraded ply). Using Eqs. (4.102) and (4.101) we can determine $E_x^{(2)}, E_y^{(2)}, G_{xy}^{(2)}, \nu_{xy}^{(2)}, \nu_{yx}^{(2)}$ and express the strains in terms of stresses, i.e., $\varepsilon_x^{(2)}(\sigma)$, $\varepsilon_y^{(2)}(\sigma)$, $\gamma_{xy}^{(2)}(\sigma)$. The final strains corresponding to the second stage of loading are calculated as

$$\varepsilon_x^{\mathrm{f}} = \varepsilon_x^{(1)}(\sigma^*) + \varepsilon_x^{(2)}(\sigma - \sigma^*), \quad \varepsilon_y^{\mathrm{f}} = \varepsilon_y^{(1)}(\sigma^*) + \varepsilon_y^{(2)}(\sigma - \sigma^*),$$
$$\gamma_{xy}^{\mathrm{f}} = \gamma_{xy}^{(1)}(\sigma^*) + \gamma_{xy}^{(2)}(\sigma - \sigma^*) \ .$$

To study the third stage, we should find σ_1, σ_2, τ_{12} in all the plies, except the kth one, identify the next degraded ply and repeat step 3 of the procedure which is continued until the failure of the fibers. The resulting stress–strain curves are multi-segmented

lines with straight segments and kinks corresponding to degradation of particular plies.

The foregoing procedure was described for a cross-ply layer consisting of plies with different properties. For the layer made of one and the same material, there are only three stages of loading – first, before the plies degradation, second, after the degradation of the longitudinal or the transverse ply only, and third, after the degradation of all the plies.

As a numerical example, consider a carbon–epoxy cylindrical pressure vessel consisting of axial plies with total thickness h_0 and circumferential plies with total thickness h_{90}. The vessel has the following parameters: radius $R = 500$ mm, total thickness of the wall $h = 7.5$ mm, $h_0 = 2.5$ mm, $h_{90} = 5$ mm. Mechanical characteristics of a carbon–epoxy unidirectional ply are $E_1 = 140$ GPa, $E_2 = 11$ GPa, $\nu_{12} = 0.0212$, $\nu_{21} = 0.27$, $\bar{\sigma}_1^+ = 2000$ MPa, $\bar{\sigma}_2^+ = 50$ MPa. Axial, σ_x, and circumferential, σ_y, stresses are expressed as (see Fig. 4.46)

$$\sigma_x = \frac{pR}{2h}, \quad \sigma_y = \frac{pR}{h} \ , \tag{4.122}$$

where p is internal pressure.

Using Eqs. (4.100) and (4.102) we calculate first the stiffness coefficients. The result is as follows:

$$\begin{aligned} &A_{11} = 54.1\,\text{GPa}, \quad A_{12} = 3\,\text{GPa}, \quad A_{22} = 97.1\,\text{GPa}, \\ &E_x = 54\,\text{GPa}, \quad E_y = 97\,\text{GPa}, \quad \nu_{xy} = 0.055, \quad \nu_{yx} = 0.031 \ . \end{aligned} \tag{4.123}$$

Substituting stresses, Eqs. (4.122) into constitutive equations (4.101) we obtain

$$\begin{aligned} \varepsilon_x^{(1)}(p) &= \frac{pR}{h}\left(\frac{1}{2E_x} - \frac{\nu_{xy}}{E_y}\right) = 0.58 \times 10^{-3} p, \\ \varepsilon_y^{(1)}(p) &= \frac{pR}{h}\left(\frac{1}{E_y} - \frac{\nu_{yx}}{2E_x}\right) = 0.66 \times 10^{-3} p \ , \end{aligned}$$

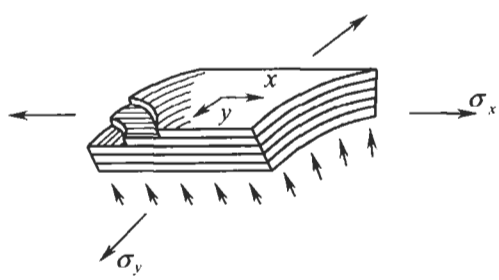

Fig. 4.46. Element of a composite pressure vessel.

where p is measured in MPa. For axial plies, $\varepsilon_x = \varepsilon_{1,0}$ and $\varepsilon_y = \varepsilon_{2,0}$. The corresponding stresses are

$$\sigma_{1,0}^{(1)}(p) = \bar{E}_1(\varepsilon_{1,0} + \nu_{12}\varepsilon_{2,0}) = 83.2p, \quad \sigma_{2,0}^{(1)}(p) = \bar{E}_2(\varepsilon_{2,0} + \nu_{21}\varepsilon_{1,0}) = 9.04p \ .$$

For circumferential plies, $\varepsilon_x = \varepsilon_{2,90}$, $\varepsilon_y = \varepsilon_{1,90}$ and

$$\sigma_{1,90}^{(1)}(p) = \bar{E}_1(\varepsilon_{1,90} + \nu_{12}\varepsilon_{2,90}) = 94.15p, \quad \sigma_{2,90}^{(1)}(p) = \bar{E}_2(\varepsilon_{2,90} + \nu_{21}\varepsilon_{1,90}) = 8.4p \ .$$

As can be seen, $\sigma_{2,0}^{(1)} > \sigma_{2,90}^{(1)}$. This means that the cracks appear first in the axial plies under the pressure p^* that can be found from the equation $\sigma_{2,0}^{(1)}(p^*) = \bar{\sigma}_2^+$. The result is $p^* = 5.53$ MPa.

To study the second stage of loading for $p > p^*$, we should put $E_2 = 0$, and $\nu_{12} = 0$ in Eqs. (4.121) for the axial plies. Then, stiffness coefficients and elastic constants become

$$A_{11} = 54.06\,\text{GPa}, \quad A_{12} = 2\,\text{GPa}, \quad A_{22} = 93.4\,\text{GPa},$$
$$E_x = 54\,\text{GPa}, \quad E_y = 93.3\,\text{GPa}, \quad \nu_{xy} = 0.037, \quad \nu_{yx} = 0.021 \ .$$

Strains and stresses in the plies are

$$\varepsilon_x^{(2)}(p) = 0.59 \times 10^{-3}p, \quad \varepsilon_y^{(2)}(p) = 0.7 \times 10^{-3}p,$$
$$\sigma_{1,0}^{(2)}(p) = 82.6p, \quad \sigma_{1,90}^{(2)}(p) = 99.8p,$$
$$\sigma_{2,90}^{(2)}(p) = 8.62p \ .$$

Total transverse stress in the circumferential plies can be calculated as

$$\sigma_{2,90} = \sigma_{2,90}^{(1)}(p^*) + 8.62(p - p^*) \ .$$

Using condition $\sigma_{2,90}(p^{**}) = \bar{\sigma}_2^+$ we find pressure $p^{**} = 5.95$ MPa at which the cracks appear in the matrix of the circumferential plies.

For $p \geqslant p^{**}$, we should take $E_2 = 0$ and $\nu_{12} = 0$ for all the plies. Then

$$\begin{aligned} &A_{11} = 46.2\,\text{GPa}, \quad A_{12} = 0, \quad A_{22} = 93.4\,\text{GPa}, \\ &E_x = 46.2\,\text{GPa}, \quad E_y = 93.4\,\text{GPa}, \quad \nu_{xy} = \nu_{yx} = 0 \ . \\ &\varepsilon_x^{(3)}(p) = 0.72 \times 10^{-3}p, \quad \varepsilon_y^{(3)}(p) = 0.71 \times 10^{-3}p, \\ &\sigma_{1,0}^{(3)}(p) = 100.8p, \quad \sigma_{1,90}^{(3)}(p) = 99.4p \ . \end{aligned} \tag{4.124}$$

The total stresses acting along the fibers are

$$\sigma_{1.0}(p) = \sigma_{1,0}^{(1)}(p^*) + \sigma_{1,0}^{(2)}(p^{**} - p^*) + \sigma_{1.0}^{(3)}(p - p^{**}) = 100.8p - 105,$$
$$\sigma_{1.90}(p) = \sigma_{1,90}^{(1)}(p^*) + \sigma_{1,90}^{(2)}(p^{**} - p^*) + \sigma_{1.90}^{(3)}(p - p^{**}) = 99.4p - 28.9 \ .$$

To determine the ultimate pressure, we can use two possible strength conditions – for axial fibers and for circumferential fibers. Condition $\sigma_{1.0}(p) = \bar{\sigma}_1^+$ yields $p = 20.9$ MPa, while condition $\sigma_{1.90}(p) = \bar{\sigma}_1^+$ gives $p = 20.4$ MPa. Thus, the burst pressure governed by the failure of the fibers of circumferential plies is $\bar{p} = 20.4$ MPa.

The strains can be calculated for all three stages of loading using the following equations:

- for $p \leqslant p^*$

$$\varepsilon_{x,y}(p) = \varepsilon_{x,y}^{(1)}(p);$$

- for $p^* < p \leqslant p^{**}$

$$\varepsilon_{x,y}(p) = \varepsilon_{x,y}^{(1)}(p^*) + \varepsilon_{x,y}^{(2)}(p - p^*);$$

- for $p^{**} < p \leqslant \bar{p}$

$$\varepsilon_{x,y}(p) = \varepsilon_{x,y}^{(1)}(p^*) + \varepsilon_{x,y}^{(2)}(p^{**} - p^*) + \varepsilon_{x,y}^{(3)}(p - p^{**}) \ .$$

For the pressure vessel under study, dependencies of strains on pressure are shown in Fig. 4.47 (solid lines). Circles correspond to the failure of the matrix and the fibers.

For comparison, consider two limiting cases. First, assume that no cracks occur in the matrix, and the material stiffness is specified by Eqs. (4.123). The corresponding diagrams are shown in Fig. 4.47 with broken lines. Second, assume that the load is taken by the fibers only, i.e., use the monotropic model of a ply introduced in

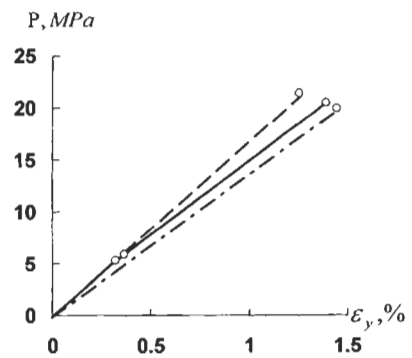

Fig. 4.47. Dependence of the axial and the circumferential strains of the carbon–epoxy pressure vessel on pressure: ——— model allowing for cracks in the matrix; – – – – model ignoring cracks in the matrix; – – – model ignoring the matrix.

Section 3.3. Then, material stiffnesses are given by Eqs. (4.124). The corresponding results are also presented in Fig. 4.47. As follows from this figure, all three models give close results for the burst pressure (which is natural because $\bar{\sigma}_2^+ \ll \bar{\sigma}_1^+$) but different strains.

The problem of analysis of cracked cross-ply composite laminate was studied by Tsai and Azzi (1966), Hahn and Tsai (1974), Vasiliev et al. (1970), Vasiliev and Elpatievskii (1967), Reifsnaider (1977), Hashin (1987) and many other authors. In spite of this, the topic is still receiving repeated attention in the literature (Lungren and Gudmundson, 1999). Taking into account that matrix degradation leads to reduction of material stiffness and fatigue strength, absorption of moisture and many other consequences that can be hardly predicted but are definitely undesirable it is surprising how many efforts were undertaken to study this phenomenon rather than to avoid it. At the first glance, the problem looks simple – all we need is to synthesize unidirectional composite whose ultimate elongations along and across the fibers, i.e., $\bar{\varepsilon}_1$ and $\bar{\varepsilon}_2$, are the same. Actually, the problem is even more simple, because $\bar{\varepsilon}_2$ can be less than $\bar{\varepsilon}_1$ by the factor that is equal to the safety factor of the structure. This means that matrix degradation can occur but at the load that exceeds the operational level (safety factor is the ratio of the failure load to the operational load and can vary from 1.25 up to 3 and more depending on the application of a composite structure). Returning to Table 4.2 in which $\bar{\varepsilon}_1$ and $\bar{\varepsilon}_2$ are given for typical advanced composites we can see that $\bar{\varepsilon}_1 > \bar{\varepsilon}_2$ for all the materials and that for polymeric matrices the problem could be, in principle, solved if we could increase $\bar{\varepsilon}_2$ up to about 1%.

Two main circumstances hinder the direct solution of this problem. The first is that being locked between the fibers, the matrix does not show the high elongation that it has under uniaxial tension and behaves as a brittle material (see Section 3.4.2). To study this effect, epoxy resins were modified to have different ultimate elongations. The corresponding curves are presented in Fig. 4.48 (only the initial part of curve 4 is shown in this figure, the ultimate elongation of this resin is 60%). Fiberglass composites that were fabricated with these resins were tested under transverse tension. As can be seen in Fig. 4.49, the desired value of $\bar{\varepsilon}_2$ (that is about 1%) is reached if the matrix elongation is about 60%. However, the stiffness of this

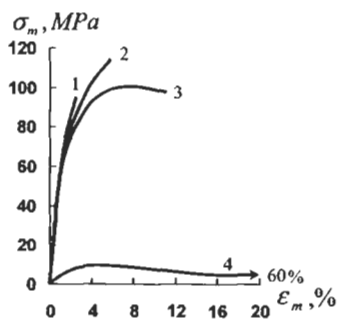

Fig. 4.48. Stress–strain curves for epoxy matrices modified for different ultimate elongations.

matrix is relatively low, and the second circumstance arises – matrix material with low stiffness cannot provide the proper stress diffusion in the vicinity of damaged or broken fibers (see Section 3.2.3). As a result, the main material characteristic – its longitudinal tensile strength – decreases. Experimental results corresponding to composites with resins 1, 2, 3, and 4 are presented in Fig. 4.50. Thus, significant rise in transverse elongation is accompanied with unacceptable drop in longitudinal strength (see also Chiao, 1979).

One of the possible ways for synthesizing composite materials with high transverse elongation and high longitudinal strength is to combine two matrix materials – one with high stiffness to bind the fibers and the other with high elongation to provide the proper transverse deformability (Vasiliev and Salov, 1984). The manufacturing process involves two-stage impregnation. At the first stage a fine tow is impregnated with the high-stiffness epoxy resin (of the type 2 in Fig. 4.48) and cured. The properties of thus fabricated composite fiber are as follows:

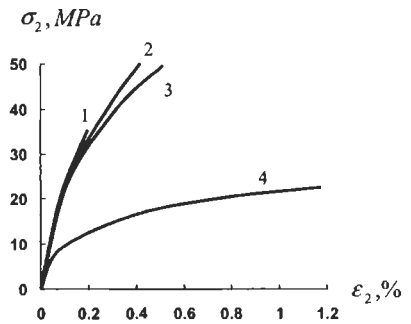

Fig. 4.49. Stress–strain curves for transverse tension of unidirectional fiberglass composites with different epoxy matrices (numbers on the curves correspond to Fig. 4.48).

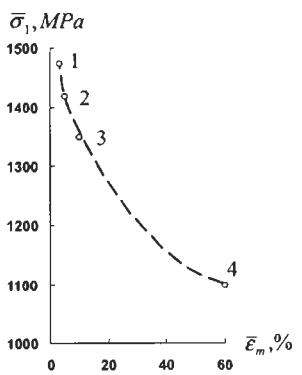

Fig. 4.50. Dependence of the longitudinal strength on the matrix ultimate elongation (numbers on the curve correspond to Figs. 4.48 and 4.49).

- number of elementary glass fibers in the cross-section – 500;
- mean cross-sectional area – 0.15 mm^2;
- fiber volume fraction – 0.75;
- density – 2.2 g/cm^3;
- longitudinal modulus – 53.5 GPa;
- longitudinal strength – 2100 MPa;
- longitudinal elongation – 4.5%;
- transverse modulus – 13.5 GPa,
- transverse strength – 400 MPa;
- transverse elongation – 0.32%.

At the second stage, a tape formed of composite fibers is impregnated with a highly deformable epoxy matrix whose stress–strain diagram is presented in Fig. 4.51. The microstructure of the resulting two-matrix unidirectional composite is shown in Fig. 4.52 (dark areas are cross-sections of composite fibers, magnification is not enough to see elementary glass fibers). Stress–strain diagrams corresponding to transverse tension, compression, and in-plane shear of this material are presented in Fig. 4.16.

The main mechanical characteristics of the two-matrix fiberglass composite are listed in Table 4.3 (material No. 1). As can be seen, two-stage impregnation results in relatively low fiber volume content (about 50%). Material No. 2 that is composed from composite fibers and a traditional epoxy matrix has also low fiber fraction, but its transverse elongation is 10 times less than that of material No. 1. Material No. 3 is a traditional glass–epoxy composite that has the highest longitudinal strength and the lowest transverse strain. Comparing materials No. 1 and No. 3 we can see that though the fiber volume fraction of the two-matrix composite is lower by 24%, its longitudinal strength is less than that of a traditional composite by 3.4% only (because the composite fibers are not damaged in the processing of composite materials), while its specific strength is a bit higher (due to lower density). Material No. 4 demonstrates that direct application of a highly deformable matrix allows us

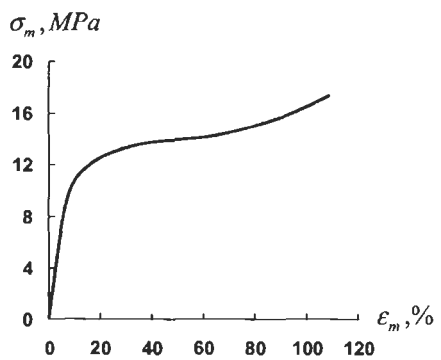

Fig. 4.51. Stress–strain diagram of a deformable epoxy matrix.

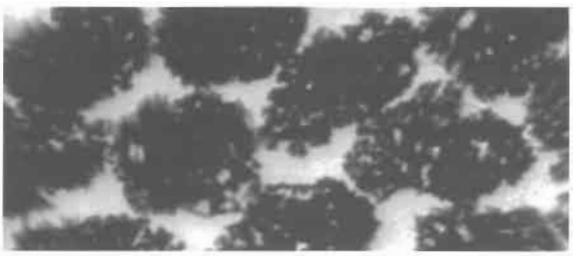

Fig. 4.52. Microstructure of a unidirectional two-matrix composite.

Table 4.3
Properties of glass–epoxy unidirectional composites.

No.	Material components	Fiber volume fraction	Longitudinal strength $\bar{\sigma}_1^+$ (MPa)	Ultimate transverse strain $\bar{\varepsilon}_2^+$ (%)	Density ρ (g/cm^3)	Specific strength $\bar{\sigma}_1^+/\rho \times 10^3$ (m)
1	Composite fibers and deformable matrix	0.51	1420	3.0	1.83	77.6
2	Composite fibers and high-stiffness matrix	0.52	1430	0.3	1.88	76.1
3	Glass fibers and high-stiffness matrix	0.67	1470	0.2	2.07	71.0
4	Glass fibers and deformable matrix	0.65	1100	1.2	2.02	54.4

to increase transverse strains but results in 23% reduction in longitudinal specific strength.

Thus, two-matrix glass-epoxy composites have practically the same longitudinal strength as traditional materials but their transverse elongation is by an order higher.

Comparison of a traditional cross-ply glass–epoxy layer and a two-matrix one is presented in Fig. 4.53. Line 1 corresponds to a traditional material and has a typical for this material kink corresponding to the matrix failure in transverse plies (see also Fig. 4.37). Theoretical diagram was plotted using the procedure described above. Line 2 corresponds to a two-matrix composite and was plotted with the aid of Eqs. (4.60). As can be seen, there is no kink on the stress–strain diagram. To prove that no cracks appear in the matrix of this material under loading, intensity of acoustic emission was recorded during loading. The results are shown in Fig. 4.54.

Composite fibers of two-matrix materials can be also made from fine carbon or aramid tows, while deformable thermosetting resin can be replaced with a thermoplastic matrix (Vasiliev et al., 1998). The resulting hybrid thermoset–thermoplastic unidirectional composite is characterized with high longitudinal strength and transverse strain exceeding 1%. Having high strength composite fibers

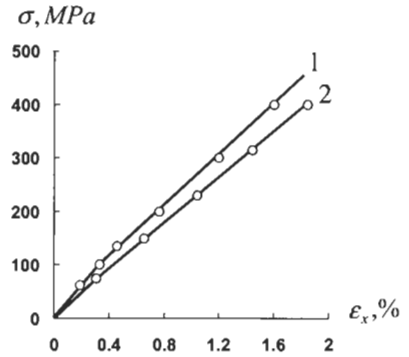

Fig. 4.53. Stress–strain diagrams of a traditional (1) and two-matrix (2) cross-ply glass–epoxy layers under tension: ——— theoretical prediction; ○ experiment.

Fig. 4.54. Intensity of acoustic emission for a cross-ply two-matrix composite (above) and a traditional fiber–glass composite (below).

do not experience any damage during laying-up or winding, and the tapes formed from these fibers are readily impregnated even with high-viscosity thermoplastic polymers.

4.5. Angle-ply orthotropic layer

The angle-ply layer is a combination of an even number of alternating plies with angles $+\phi$ and $-\phi$ as shown in Fig. 4.55. The structure of this layer is typical for the process of filament winding (see Fig. 4.56). As a cross-ply layer considered in the previous section, an angle-ply layer is actually a laminate, but for a large number of plies it can be treated as a homogeneous orthotropic layer (see Section 5.4.3).

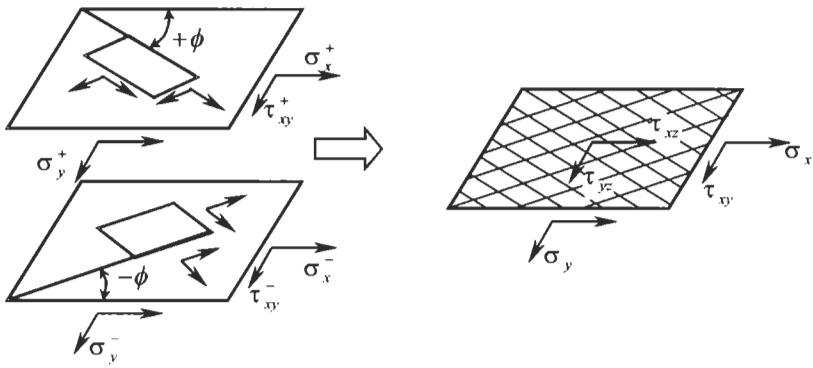

Fig. 4.55. Two symmetric plies forming an angle-ply layer.

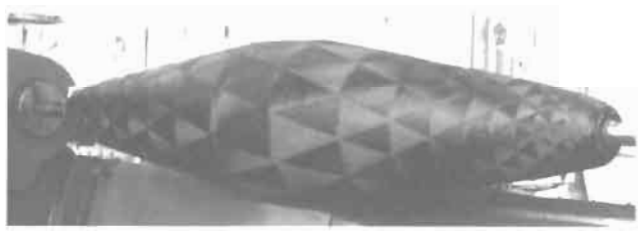

Fig. 4.56. Angle-ply layer of a filament wound shell. Courtesy of CRISM.

4.5.1. Linear elastic model

Consider two symmetric systems of unidirectional anisotropic plies (see Section 4.3) consisting of the same number of plies, made of one and the same material and having alternating angles $+\phi$ and $-\phi$. Then, the total stresses σ_x, σ_y, and τ_{xy} acting on the layer can be expressed in terms of corresponding stresses acting in the $+\phi$ and $-\phi$ plies as

$$\begin{aligned} &\sigma_x h = \sigma_x^+ \frac{h}{2} + \sigma_x^- \frac{h}{2}, \quad \sigma_y h = \sigma_y^+ \frac{h}{2} + \sigma_y^- \frac{h}{2}, \\ &\tau_{xy} h = \tau_{xy}^+ \frac{h}{2} + \tau_{xy}^- \frac{h}{2}, \end{aligned} \tag{4.125}$$

where h is the total thickness of the layer. Stresses with superscripts '+' and '−' are linked with strains ε_x, ε_y, and γ_{xy} which are assumed to be the same for all the plies by Eqs. (4.71), i.e.,

$$\begin{aligned} &\sigma_x^\pm = A_{11}^\pm \varepsilon_x + A_{12}^\pm \varepsilon_y + A_{14}^\pm \gamma_{xy}, \quad \sigma_y^+ = A_{21}^\pm \varepsilon_x + A_{22}^\pm \varepsilon_y + A_{24}^\pm \gamma_{xy}, \\ &\tau_{xy}^\pm = A_{41}^\pm \varepsilon_x + A_{42}^\pm \varepsilon_y + A_{44}^\pm \gamma_{xy}, \end{aligned} \tag{4.126}$$

where $A_{11}^{+} = A_{11}^{-} = A_{11}$, $A_{12}^{+} = A_{12}^{-} = A_{12}$, $A_{22}^{+} = A_{22}^{-} = A_{22}$, $A_{14}^{+} = -A_{14}^{-} = A_{14}$, $A_{24}^{+} = -A_{24}^{-} = A_{24}$, $A_{44}^{+} = A_{44}^{-} = A_{44}$, where A_{mn} ($mn = 11, 12, 22, 14, 24, 44$) are specified by Eqs. (4.72). Substituting Eqs. (4.126) into Eqs. (4.125) we arrive at the following constitutive equations for an angle-ply layer:

$$\begin{aligned} \sigma_x &= A_{11}\varepsilon_x + A_{12}\varepsilon_y, \\ \sigma_y &= A_{21}\varepsilon_x + A_{22}\varepsilon_y, \\ \tau_{xy} &= A_{44}\gamma_{xy} \ . \end{aligned} \tag{4.127}$$

The inverse form of these equations is

$$\varepsilon_x = \frac{\sigma_x}{E_x} - \nu_{xy}\frac{\sigma_y}{E_y}, \quad \varepsilon_y = \frac{\sigma_y}{E_y} - \nu_{yx}\frac{\sigma_x}{E_x}, \quad \gamma_{xy} = \frac{\tau_{xy}}{G_{xy}} \ , \tag{4.128}$$

where

$$\begin{aligned} &E_x = A_{11} - \frac{A_{12}^2}{A_{22}}, \quad E_y = A_{22} - \frac{A_{12}^2}{A_{11}}, \quad G_{xy} = A_{44}, \\ &\nu_{xy} = \frac{A_{12}}{A_{11}}, \quad \nu_{yx} = \frac{A_{12}}{A_{22}} \ . \end{aligned} \tag{4.129}$$

As follows from Eqs. (4.127) and (4.128), the layer under study is orthotropic.

Now derive constitutive equations relating transverse shear stresses τ_{xz} and τ_{yz} and the corresponding shear strains γ_{xz} and γ_{yz}. Let the angle-ply layer be loaded by stress τ_{xz}. Then for all the plies, $\tau_{xz}^{+} = \tau_{xz}^{-} = \tau_{xz}$ and because the layer is orthotropic, $\gamma_{xz}^{+} = \gamma_{xz}^{-} = \gamma_{xz}$, $\gamma_{yz}^{+} = \gamma_{yz}^{-} = \gamma_{yz} = 0$. In a similar way, applying stress τ_{yz} we have $\tau_{yz}^{+} = \tau_{yz}^{-} = \tau_{yz}$, $\gamma_{yz}^{+} = \gamma_{yz}^{-} = \gamma_{yz}$, $\gamma_{xz}^{+} = \gamma_{xz}^{-} = \gamma_{xz} = 0$. Writing two last constitutive equations of Eqs. (4.71) for these two cases we arrive at

$$\tau_{xz} = A_{55}\gamma_{xz}, \quad \tau_{yz} = A_{66}\gamma_{yz} \ , \tag{4.130}$$

where stiffness coefficients A_{55} and A_{66} are specified by Eqs. (4.72).

Dependencies of E_x and G_{xy} on ϕ plotted with the aid of Eqs. (4.129) are shown in Fig. 4.57 with solid lines. Theoretical curve for E_x is in very good agreement with experimental data shown with circles (Lagace, 1985). For comparison, the same moduli are presented for the $+\phi$ anisotropic layer considered in Section 4.3.1. As can be seen, $E_x(\pm\phi) \geqslant E_x^{+}$. To explain this effect, consider a uniaxial tension of both layers in the x-direction. While tension of $+\phi$ ply and of $-\phi$ individual plies shown in Fig. 4.58 is accompanied with shear strain, the system of these plies does not demonstrate shear under tension and, as a result, has higher stiffness. Working as plies of a symmetric angle-ply layer individual anisotropic $+\phi$ and $-\phi$ plies are loaded not only with normal stress σ_x that is applied to the layer, but also with shear stress τ_{xy} that restricts the shear of individual plies (see Fig. 4.58). To find the reactive and balanced between the plies shear stress, we can use Eqs. (4.75). Taking

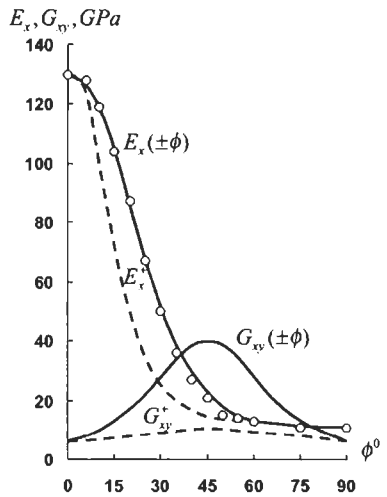

Fig. 4.57. Dependencies of the moduli of a carbon–epoxy layer on the orientation angle: ——— orthotropic angle-ply $\pm\phi$ layer; – – – – anisotropic $+\phi$ layer; o experiment for an angle-ply layer.

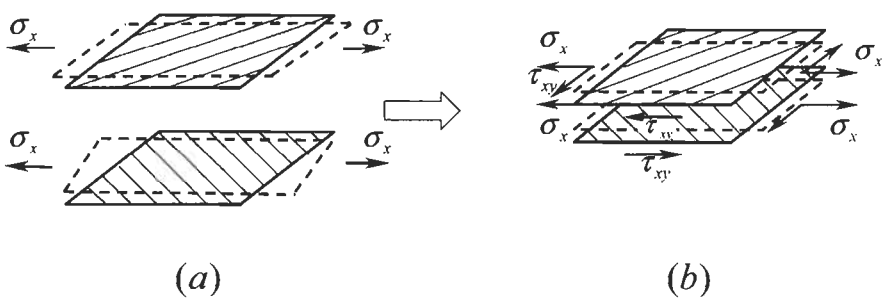

Fig. 4.58. Deformation and stresses induced in individual plies (a) and bonded symmetric plies (b) by uniaxial tension.

$\sigma_y = 0$ we can simulate the stress–strain state of the ply in the $\pm\phi$ angle-ply layer putting $\gamma_{xy} = 0$. Then, the third equation yields

$$\tau_{xy} = -\eta_{xy,x}^{+} \frac{G_{xy}^{+}}{E_x^{+}} \sigma_x \ .$$

Superscript '+' indicates that elastic constants correspond to an individual $+\phi$ ply. Substituting this shear stress into the first equation of Eqs. (4.75) we arrive at $\sigma_x = E_x \varepsilon_x$, where

$$E_x = \frac{E_x^{+}}{1 - \eta_{x,xy}^{+} \eta_{xy,x}^{+}} = \frac{E_x^{+}}{1 - \frac{G_{xy}^{+}}{E_x^{+}} (\eta_{xy,x}^{+})^2} \tag{4.131}$$

is the modulus of the $\pm\phi$ angle-ply layer.

Under pure shear of an angle-ply layer, its plies are loaded with the additional normal stresses. These stresses can be found if we take $\varepsilon_x = 0$ and $\varepsilon_y = 0$ in the first two equations of Eqs. (4.75). The result is

$$\sigma_x = -\tau_{xy}\frac{E_x^+(\eta_{x,xy}^+ - \nu_{xy}^+\eta_{y,xy}^+)}{G_{xy}^+(1-\nu_{xy}^+\nu_{yx}^+)}, \quad \sigma_y = -\tau_{xy}\frac{E_y^+(\eta_{y,xy}^+ + \nu_{yx}^+\eta_{x,xy}^+)}{G_{xy}^+(1-\nu_{xy}^+\nu_{yx}^+)} .$$

Substituting these expressions into the third equation we get $\tau_{xy} = G_{xy}\gamma_{xy}$, where

$$G_{xy} = \frac{G_{xy}^+(1-\nu_{xy}^+\nu_{yx}^+)}{1-\nu_{xy}^+\nu_{yx}^+ - \eta_{x,xy}^+\eta_{xy,x}^+ - \eta_{y,xy}^+\eta_{xy,y}^+ - \nu_{xy}^+\eta_{y,xy}^+\eta_{xy,x}^+ - \nu_{yx}^+\eta_{x,xy}^+\eta_{xy,y}^+}$$

is the shear modulus of an angle-ply layer which is much higher than G_{xy}^+ (see Fig. 4.57).

Tension of ±45° angle-ply specimen provides a simple way to determine in-plane shear modulus of a unidirectional ply, G_{12}. Indeed, for this layer, Eqs. (4.72) and (4.129) yield

$$A_{11}^{45} = A_{22}^{45} = \frac{1}{4}(\bar{E}_1 + \bar{E}_2 + 2\bar{E}_1\nu_{12} + 4G_{12}),$$
$$A_{12}^{45} = \bar{E}_1\nu_{12} + \frac{1}{4}(\bar{E}_1 + \bar{E}_2 - 2\bar{E}_1\nu_{12} - 4G_{12})$$

and

$$E_{45} = \frac{1}{A_{11}^{45}}(A_{11}^{45} + A_{12}^{45})(A_{11}^{45} - A_{12}^{45}), \quad 1 + \nu_{45} = \frac{1}{A_{11}^{45}}(A_{11}^{45} + A_{12}^{45}) .$$

Taking into account that $A_{11}^{45} - A_{12}^{45} = 2G_{12}$ we have

$$G_{12} = \frac{E_{45}}{2(1+\nu_{45})} . \tag{4.132}$$

Thus, to find G_{12}, we can test a ±45° specimen under tension, measure ε_x and ε_y, determine $E_{45} = \sigma_x/\varepsilon_x$, $\nu_{45} = -\varepsilon_y/\varepsilon_x$, and use Eq. (4.132) rather than perform cumbersome tests described in Section 3.

4.5.2. Nonlinear models

To describe nonlinear behavior of an angle-ply layer associated with material nonlinearity of its plies, we can use nonlinear constitutive equations, Eqs. (4.60) or Eqs. (4.64), instead of Hooke's law. Indeed, assuming that the ply behavior is linear under tension or compression along the fibers we can write these equations in the following general form:

$$\varepsilon_1 = c_{11}\sigma_1 + c_{12}\sigma_2, \quad \varepsilon_2 = c_{12}\sigma_1 + c_{22}\sigma_2 + \omega_2(\sigma_2, \tau_{12}),$$
$$\gamma_{12} = c_{44}\tau_{12} + \omega_{12}(\sigma_2, \tau_{12}) \ .$$

Functions ω_2 and ω_{12} include all the nonlinear terms. Inverse form of these equations is

$$\sigma_1 = C_{11}\varepsilon_1 + C_{12}\varepsilon_2 - C_{12}\omega_2, \quad \sigma_2 = C_{12}\varepsilon_1 + C_{22}\varepsilon_2 - C_{22}\omega_2,$$
$$\tau_{12} = C_{44}\gamma_{12} - C_{44}\omega_{12} \ , \tag{4.133}$$

where

$$C_{11} = \frac{c_{22}}{c}, \quad C_{22} = \frac{c_{11}}{c}, \quad C_{44} = \frac{1}{c_{44}}, \quad C_{12} = -\frac{c_{12}}{c}, \quad c = c_{11}c_{22} - c_{12}^2 \ .$$

Repeating the derivation of Eqs. (4.127) but using this time Eqs. (4.133) as constitutive equations for the ply we arrive at

$$\sigma_x = A_{11}\varepsilon_x + A_{12}\varepsilon_y - A_{11}^{\omega}, \quad \sigma_y = A_{21}\varepsilon_x + A_{22}\varepsilon_y - A_{22}^{\omega},$$
$$\tau_{xy} = A_{44}\gamma_{xy} - A_{44}^{\omega} \ ,$$

where ($s = \sin\phi$, $c = \cos\phi$)

$$A_{11}^{\omega} = (C_{22}s^2 + C_{12}c^2)\omega_2 - 2C_{44}cs\omega_{12}, \quad A_{22}^{\omega} = (C_{22}c^2 + C_{12}s^2)\omega_2 + 2C_{44}cs\omega_{12},$$
$$A_{44}^{\omega} = (C_{12} - C_{22})cs\omega_2 + C_{44}(c^2 - s^2)\omega_{12} \ .$$

These equations can be used in conjunction with the method of elastic solutions described in Section 4.1.2.

As an example, consider the two-matrix glass–epoxy composite described in Section 4.4.2 (see also Figs. 4.16, 4.30, and 4.31). Theoretical (solid lines) and experimental (broken lines) stress–strain diagrams for ±30°, ±45°, and ±75° angle-ply layers under tension along the x-axis are shown in Fig. 4.59.

Angle-ply layers demonstrate a specific type of material nonlinearity – structural nonlinearity that can occur in the layers composed of linear elastic plies due to the change of the plies orientations caused by loading. Because this effect manifests itself under high strains, consider a geometrically nonlinear problem of the ply deformation. This deformation can be described with the longitudinal, ε_1, transverse, ε_2, and shear, γ_{12}, strains that follow from Fig. 4.60 and can be expressed as

$$\varepsilon_1 = \frac{1}{ds_1}(ds_1' - ds_1), \quad \varepsilon_2 = \frac{1}{ds_2}(ds_2' - ds_2), \quad \gamma_{12} = \frac{\pi}{2} - \psi \ . \tag{4.134}$$

In addition to this, we introduce strain ε_2'' in the direction normal to the fibers

$$\varepsilon_2'' = \frac{1}{ds_2}(ds_2'' - ds_2) \tag{4.135}$$

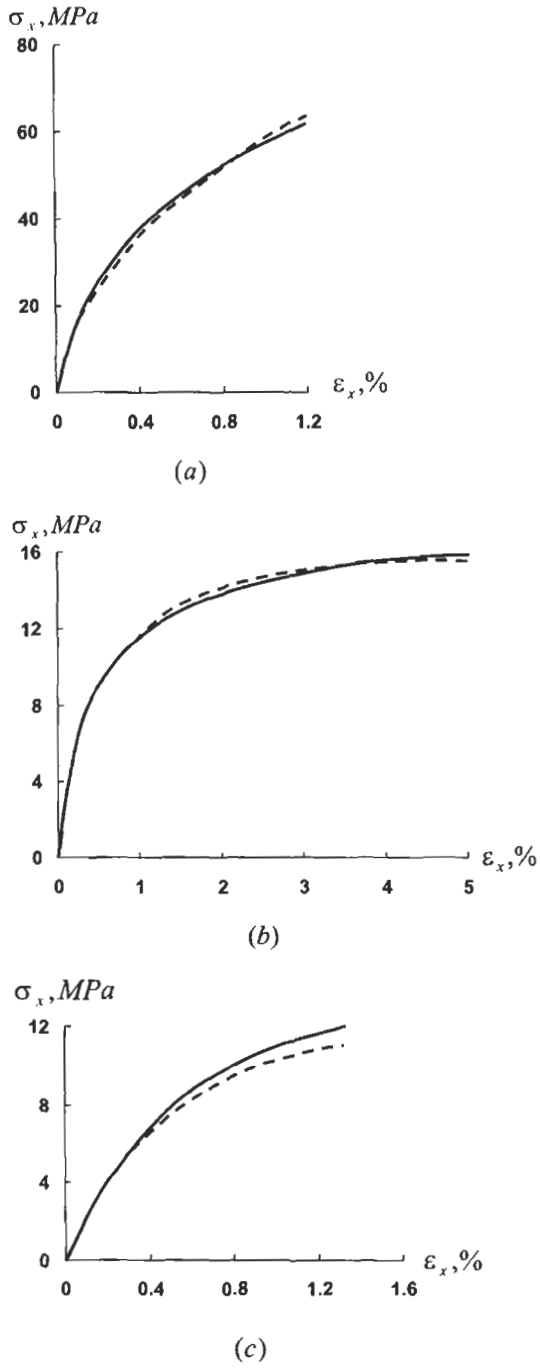

Fig. 4.59. Theoretical (solid lines) and experimental (broken lines) stress–strain diagrams for ±30° (a), ±45° (b) and ±75° (c) angle-ply two-matrix composites under uniaxial tension.

and the angle of rotation of the element as a solid in the 12-plane

$$\omega_{12} = \tfrac{1}{2}(\omega_1 - \omega_2)$$

where

$$\omega_1 = \phi' - \phi, \quad \omega_2 = \frac{\pi}{2} + \phi - (\phi' + \psi)$$

are the angles of rotation of axes 1′ and 2′ (see Fig. 4.60). Thus,

$$\omega_{12} = \phi' - \phi + \frac{\psi}{2} - \frac{\pi}{4} \ . \tag{4.136}$$

Consider some arbitrary element ds_α shown in Fig. 4.61 and introduce its strain

$$\mathrm{d}s_\alpha = \frac{1}{\mathrm{d}s_\alpha}(\mathrm{d}s'_\alpha - \mathrm{d}s_\alpha) \ . \tag{4.137}$$

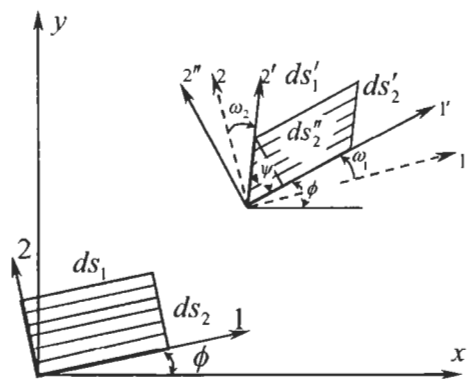

Fig. 4.60. Ply element before and after deformation.

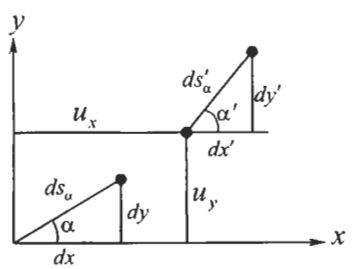

Fig. 4.61. Linear element before and after deformation.

Repeating the derivation described in Section 2.5 we have

$$
\begin{aligned}
&ds_\alpha^2 = dx^2 + dy^2, \\
&(ds'_\alpha)^2 = (dx')^2 + (dy')^2 = (dx + du_x)^2 + (dy + du_y)^2 \\
&\qquad = (1 + \varepsilon_x)^2 dx^2 + (1 + \varepsilon_y)^2 dy^2 + 2\varepsilon_{xy} dx\, dy \ ,
\end{aligned}
$$

where

$$
\begin{aligned}
(1 + \varepsilon_x)^2 &= 1 + 2\left[\frac{\partial u_x}{\partial x} + \frac{1}{2}\left(\frac{\partial u_x}{\partial x}\right)^2 + \frac{1}{2}\left(\frac{\partial u_y}{\partial x}\right)^2\right], \\
(1 + \varepsilon_y)^2 &= 1 + 2\left[\frac{\partial u_y}{\partial y} + \frac{1}{2}\left(\frac{\partial u_x}{\partial y}\right)^2 + \frac{1}{2}\left(\frac{\partial u_y}{\partial y}\right)^2\right], \\
\varepsilon_{xy} &= \frac{\partial u_x}{\partial y} + \frac{\partial u_y}{\partial x} + \frac{\partial u_x}{\partial x}\frac{\partial u_x}{\partial y} + \frac{\partial u_y}{\partial x}\frac{\partial u_y}{\partial y} \ .
\end{aligned}
\tag{4.138}
$$

Using Eq. (4.137) we arrive at

$$
(1 + \varepsilon_\alpha)^2 = (1 + \varepsilon_x)^2 \cos^2\alpha + (1 + \varepsilon_y)^2 \sin^2\alpha + \varepsilon_{xy} \sin 2\alpha \ , \tag{4.139}
$$

where $\cos\alpha = dx/ds_\alpha$ and $\sin\alpha = dy/ds_\alpha$.

In a similar way, we can find the angle α' after the deformation, i.e.,

$$
\begin{aligned}
\sin\alpha' &= \frac{dy'}{ds_\alpha} = \frac{1}{1 + \varepsilon_\alpha}\left[\left(1 + \frac{\partial u_y}{\partial y}\right)\sin\alpha + \frac{\partial u_y}{\partial x}\cos\alpha\right], \\
\cos\alpha' &= \frac{dx'}{ds_\alpha} = \frac{1}{1 + \varepsilon_\alpha}\left[\left(1 + \frac{\partial u_x}{\partial x}\right)\cos\alpha + \frac{\partial u_x}{\partial y}\sin\alpha\right] \ .
\end{aligned}
\tag{4.140}
$$

Now return to the ply element in Fig. 4.60. Taking $\alpha = \phi$ in Eqs. (4.139) and (4.140) we obtain

$$
\begin{aligned}
(1 + \varepsilon_1)^2 &= (1 + \varepsilon_x)^2 \cos^2\phi + (1 + \varepsilon_y)^2 \sin^2\phi + \varepsilon_{xy} \sin 2\phi, \\
\sin\phi' &= \frac{1}{1 + \varepsilon_1}\left[\left(1 + \frac{\partial u_y}{\partial y}\right)\sin\phi + \frac{\partial u_y}{\partial x}\cos\phi\right], \\
\cos\phi' &= \frac{1}{1 + \varepsilon_1}\left[\left(1 + \frac{\partial u_x}{\partial x}\right)\cos\phi + \frac{\partial u_x}{\partial y}\sin\phi\right] \ .
\end{aligned}
\tag{4.141}
$$

Putting $\alpha = \pi/2 + \phi$ we have

$$
\begin{aligned}
(1 + \varepsilon_2)^2 &= (1 + \varepsilon_x)^2 \sin^2\phi + (1 + \varepsilon_y)^2 \cos^2\phi - 2\varepsilon_{xy} \sin 2\phi, \\
\sin(\phi' + \psi) &= \frac{1}{1 + \varepsilon_2}\left[\left(1 + \frac{\partial u_y}{\partial y}\right)\cos\phi - \frac{\partial u_y}{\partial x}\sin\phi\right], \\
\cos(\phi' + \psi) &= \frac{1}{1 + \varepsilon_2}\left[-\left(1 + \frac{\partial u_x}{\partial x}\right)\cos\phi + \frac{\partial u_x}{\partial y}\sin\phi\right] \ .
\end{aligned}
\tag{4.142}
$$

Using the last equation of Eqs. (4.134) we can find the shear strain as $\sin\gamma_{12} = \cos\psi$. After some rearrangements with the aid of Eqs. (4.141) and (4.142) we arrive at

$$\sin\gamma_{12} = \frac{1}{(1+\varepsilon_1)(1+\varepsilon_2)}\left\{[(1+\varepsilon_y)^2 - (1+\varepsilon_x)^2]\sin\phi\cos\phi + \varepsilon_{xy}\cos 2\phi\right\} . \tag{4.143}$$

For $\phi = 0$, axes 1 and 2 coincide, respectively, with axes x and y (see Fig. 4.60), and Eq. (4.143) yields

$$\sin\gamma_{xy} = \frac{\varepsilon_{xy}}{(1+\varepsilon_x)(1+\varepsilon_y)} . \tag{4.144}$$

Using this result to express ε_{xy} we can write Eqs. (4.141)–(4.143) in the following final form:

$$\begin{aligned}
(1+\varepsilon_1)^2 &= (1+\varepsilon_x)^2\cos^2\phi + (1+\varepsilon_y)^2\sin^2\phi + (1+\varepsilon_x)(1+\varepsilon_y)\sin\gamma_{xy}\sin 2\phi,\\
(1+\varepsilon_2)^2 &= (1+\varepsilon_x)^2\sin^2\phi + (1+\varepsilon_y)^2\cos^2\phi - (1+\varepsilon_x)(1+\varepsilon_y)\sin\gamma_{xy}\sin 2\phi,\\
\sin\gamma_{12} &= \frac{1}{(1+\varepsilon_1)(1+\varepsilon_2)}\\
&\quad\times\left\{[(1+\varepsilon_y)^2 - (1+\varepsilon_x)^2]\sin\phi\cos\phi + (1+\varepsilon_x)(1+\varepsilon_y)\sin\gamma_{xy}\cos 2\phi\right\} .
\end{aligned} \tag{4.145}$$

As follows from Fig. 4.60 and the last equation of Eqs. (4.134), $ds_2'' = ds_2'\sin\psi = ds_2'\cos\gamma_{12}$. So in accordance with Eqs. (4.134) and (4.135)

$$1 + \varepsilon_2'' = (1+\varepsilon_2)\cos\gamma_{12} .$$

Using Eqs. (4.145) to transform this equation we get

$$1 + \varepsilon_2'' = \frac{(1+\varepsilon_x)(1+\varepsilon_y)}{1+\varepsilon_1}\cos\gamma_{xy} . \tag{4.146}$$

To express ϕ' in terms of ϕ and strains referred to the global coordinate frame x, y, consider Eq. (4.136). After rather cumbersome transformation with the aid of Eqs. (4.141) and (4.142) we obtain

$$\begin{aligned}
\sin 2\omega_{12} = \frac{1}{(1+\varepsilon_1)(1+\varepsilon_2)}\Bigg\{&\left(\frac{\partial u_y}{\partial x} - \frac{\partial u_x}{\partial y} + \frac{\partial u_y}{\partial x}\frac{\partial u_y}{\partial y} - \frac{\partial u_x}{\partial x}\frac{\partial u_x}{\partial y}\right)\cos^2 2\phi\\
&+ \left(\frac{\partial u_y}{\partial x} - \frac{\partial u_x}{\partial y} + \frac{\partial u_x}{\partial x}\frac{\partial u_y}{\partial x} - \frac{\partial u_x}{\partial y}\frac{\partial u_y}{\partial y}\right)\sin^2 2\phi\\
&+ \frac{1}{4}\left[\left(\frac{\partial u_x}{\partial x} - \frac{\partial u_y}{\partial y}\right)^2 - \left(\frac{\partial u_y}{\partial x} + \frac{\partial u_x}{\partial y}\right)^2\right]\sin 4\phi\Bigg\} .
\end{aligned}$$

Taking $\phi = 0$ we can write rotation angle ω_z around the z-axis of the global coordinate frame, i.e.,

$$\sin 2\omega_z = \frac{1}{(1+\varepsilon_x)(1+\varepsilon_y)}\left(\frac{\partial u_y}{\partial x} - \frac{\partial u_x}{\partial y} + \frac{\partial u_y}{\partial x}\frac{\partial u_y}{\partial y} - \frac{\partial u_x}{\partial x}\frac{\partial u_x}{\partial y}\right) . \tag{4.147}$$

Consider now Eqs. (4.138), (4.144), and (4.147) which form a set of four algebraic equations with respect to the derivatives of displacement. Omitting the solution procedure we can write the final output as

$$\frac{\partial u_x}{\partial x} = (1+\varepsilon_x)\cos\left(\frac{\gamma_{xy}}{2} + \omega_z\right) - 1, \quad \frac{\partial u_x}{\partial y} = (1+\varepsilon_y)\sin\left(\frac{\gamma_{xy}}{2} - \omega_z\right),$$
$$\frac{\partial u_y}{\partial x} = (1+\varepsilon_x)\sin\left(\frac{\gamma_{xy}}{2} + \omega_z\right), \quad \frac{\partial u_y}{\partial y} = (1+\varepsilon_y)\cos\left(\frac{\gamma_{xy}}{2} - \omega_z\right) - 1 .$$

Substituting these expressions into Eqs. (4.141) we get

$$\sin\phi' = \frac{1}{1+\varepsilon_1}\left[(1+\varepsilon_x)\sin\left(\frac{\gamma_{xy}}{2} + \omega_z\right)\cos\phi + (1+\varepsilon_y)\cos\left(\frac{\gamma_{xy}}{2} - \omega_z\right)\sin\phi\right],$$
$$\cos\phi' = \frac{1}{1+\varepsilon_1}\left[(1+\varepsilon_x)\cos\left(\frac{\gamma_{xy}}{2} + \omega_z\right)\cos\phi + (1+\varepsilon_y)\sin\left(\frac{\gamma_{xy}}{2} - \omega_z\right)\sin\phi\right] . \tag{4.148}$$

Thus obtained nonlinear equations, Eqs. (4.145), generalize Eqs. (4.69) for the case of large strains, while Eqs. (4.148) allow us to find the fiber orientation angle after the deformation.

Equilibrium equations, Eqs. (4.68), retain their form but should be written for the deformed state, i.e.,

$$\sigma_x = \sigma_1' \cos^2\phi' + \sigma_2'' \sin^2\phi' - \tau_{12}' \sin 2\phi',$$
$$\sigma_y = \sigma_1' \sin^2\phi' + \sigma_2'' \cos^2\phi' + \tau_{12}' \sin 2\phi', \tag{4.149}$$
$$\tau_{xy} = (\sigma_1' - \sigma_2'')\sin\phi'\cos\phi' + \tau_{12}' \cos 2\phi' ,$$

where σ_1', σ_2'', and τ_{12}' are stresses referred to coordinate frame $1'2''$ (see Fig. 4.60) and to the current thickness of the ply.

Consider a problem of uniaxial tension of a $\pm\phi$ angle-ply layer with stress σ_x. For this case, $\gamma_{xy} = 0$, $\omega_z = 0$, and Eqs. (4.145), (4.146), and (4.148) acquire the form:

$$(1+\varepsilon_1)^2 = (1+\varepsilon_x)^2\cos^2\phi + (1+\varepsilon_y)^2\sin^2\phi,$$
$$(1+\varepsilon_2)^2 = (1+\varepsilon_x)^2\sin^2\phi + (1+\varepsilon_y)^2\cos^2\phi,$$
$$\sin\gamma_{12} = \frac{\sin\phi\cos\phi}{(1+\varepsilon_1)(1+\varepsilon_2)}[(1+\varepsilon_y)^2 - (1+\varepsilon_x)^2],$$

$$1 + \varepsilon_2'' = \frac{(1 + \varepsilon_x)(1 + \varepsilon_y)}{1 + \varepsilon_1},$$

$$\sin\phi' = \frac{1 + \varepsilon_y}{1 + \varepsilon_1}\sin\phi \quad \cos\phi' = \frac{1 + \varepsilon_x}{1 + \varepsilon_1}\cos\phi \ .$$

For composite materials, longitudinal strain ε_1 is usually small, and these equations can be further simplified as follows:

$$\begin{aligned}
&\varepsilon_1 = \varepsilon_x \cos^2\phi + \varepsilon_y \sin^2\phi + \tfrac{1}{2}(\varepsilon_x^2 \cos^2\phi + \varepsilon_y^2 \sin^2\phi),\\
&(1 + \varepsilon_2)^2 = (1 + \varepsilon_x)^2 \sin^2\phi + (1 + \varepsilon_y)^2 \cos^2\phi,\\
&\sin\gamma_{12} = \frac{1}{1 + \varepsilon_2}[(1 + \varepsilon_y)^2 - (1 + \varepsilon_x)^2]\sin\phi\cos\phi,\\
&1 + \varepsilon_2'' = (1 + \varepsilon_x)(1 + \varepsilon_y),\\
&\tan\phi' = \frac{1 + \varepsilon_y}{1 + \varepsilon_x}\tan\phi \ .
\end{aligned} \tag{4.150}$$

As an example, consider a specially synthesized highly deformable composite material made from glass composite fibers and thermoplastic matrix. Neglecting interaction of strains we take constitutive equations for the unidirectional ply as

$$\sigma_1' = \frac{E_1\varepsilon_1}{1 + \varepsilon_2''}, \quad \sigma_2' = \omega_2(\varepsilon_2''), \quad \tau_{12}' = \omega_{12}(\gamma_{12}) \ , \tag{4.151}$$

where E_1 in the first equation is the longitudinal elasticity modulus, while ε_2'' in the denominator takes account of the decrease of the ply stiffness due to increase in the fiber spacing. Constant E_1 and functions ω_2 and ω_{12} are determined from the experimental stress–strain diagrams for 0°, 90°, and ±45° specimens that are shown in Fig. 4.62. Results of calculation with the aid of Eqs. (4.149)–(4.151) are presented together with the corresponding experimental data in Fig. 4.63.

The foregoing equations comprise the analytical background for a promising manufacturing process allowing us to fabricate composite parts with complicated shapes deforming not completely cured preforms of simple shapes made by winding

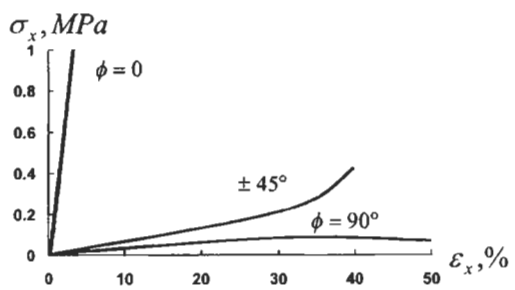

Fig. 4.62. Experimental stress–strain diagrams for 0°, ±45°, and 90° angle-ply layers.

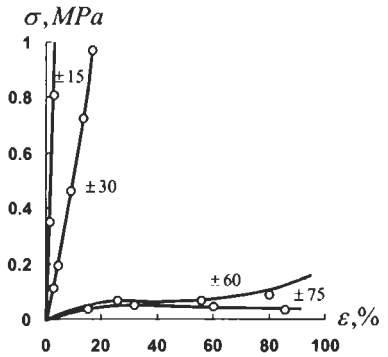

Fig. 4.63. Calculated (circles) and experimental (solid lines) stress–strain diagrams for ±15°, ±30°, ±60°, and ±75° angle-ply layers.

or laying-up (see, e.g., Cherevatsky, 1999). An example of such a part is presented in Fig. 4.64. The curved composite pipe shown in this figure was fabricated from a straight cylinder that was partially cured, loaded with pre-assigned internal pressure and end forces and moments, and cured completely in this state. Desired deformation of the part under loading is provided by the proper change of the fibers orientation angles governed by Eqs. (4.145), (4.148), and (4.149).

Angle-ply layers can also demonstrate nonlinear behavior caused by the matrix cracking described in Section 4.4.2. To illustrate this type of nonlinearity, consider carbon–epoxy ±15°, ±30°, ±45°, ±60°, and ±75° angle-ply specimens studied experimentally by Lagace (1985). Unidirectional ply has the following mechanical properties: $E_1 = 131$ GPa, $E_2 = 11$ GPa, $G_{12} = 6$ GPa, $\nu_{21} = 0.28$, $\bar{\sigma}_1^+ = 1770$ MPa, $\bar{\sigma}_2^+ = 54$ MPa, $\bar{\sigma}_2^- = 230$ MPa, $\bar{\tau}_{12} = 70$ MPa. Dependencies $\sigma_1(\varepsilon_1)$and $\sigma_2(\varepsilon_2)$ are linear, while for the in-plane shear, the stress–strain diagram is not linear and is shown in Fig. 4.65. To take into account material nonlinearity associated with shear, we use constitutive equation derived in Section 4.2.2, i.e.,

Fig. 4.64. A curved angle-ply pipe made by deformation of a filament wound cylinder.

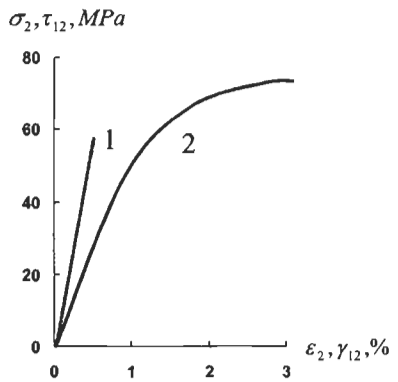

Fig. 4.65. Experimental stress–strain diagrams for transverse tension (1) and in-plane shear (2) of a carbon–epoxy unidirectional ply.

$$\gamma_{12} = c_1\tau_{12} + c_2\tau_{12}^3 \ ,$$

where $c_1 = 1/G_{12}$ and $c_2 = 5.2 \cdot 10^{-8}$ $(\text{MPa})^{-3}$.

The specimens were tested under uniaxial tension in the x-direction. To calculate the applied stress σ_x that causes the failure of the matrix, we use the simplest maximum stress strength criterion (see Chapter 6) that ignores the interaction of stresses, i.e.,

$$-\bar{\sigma}_2^- \leqslant \sigma_2 \leqslant \bar{\sigma}_2^+, \quad |\tau_{12}| \leqslant \bar{\tau}_{12} \ .$$

Nonlinear behavior associated with the ply degradation is predicted applying the procedure described in Section 4.4.2. Stress–strain diagrams are plotted using the method of successive loading (see Section 4.1.2).

Consider a $\pm 15°$ angle-ply layer. Point 1 on the theoretical diagram, shown in Fig. 4.66, corresponds to the cracks in the matrix caused by shear. These cracks do not result in the complete failure of the matrix because transverse normal stress σ_2 is compressive (see Fig. 4.67) and do not reach $\bar{\sigma}_2^-$ before the failure of fibers under tension (point 2 on the diagram). As can be seen, theoretical prediction of material stiffness is rather fair, while predicted material strength (point 2) is much higher than experimental (dark circle on the solid line). The reasons for that are discussed in the next section.

Theoretical diagram corresponding to $\pm 30°$ layer (see Fig. 4.66) also has two specific points. Point 1 again corresponds to the cracks in the matrix induced by shear stress τ_{12}, while point 2 indicates the complete failure of the matrix caused by compressive stress σ_2 which reaches $\bar{\sigma}_2^-$ at this point. After the matrix fails, the fibers of an angle-ply layer cannot take the load. Indeed, putting $E_2 = G_{12} = \nu_{12} = 0$ in Eqs. (4.72) we obtain the following stiffness coefficients:

$$A_{11} = E_1 \cos^4\phi, \quad A_{22} = E_1 \sin^4\phi, \quad A_{12} = E_1 \sin^2\phi \cos^2\phi \ .$$

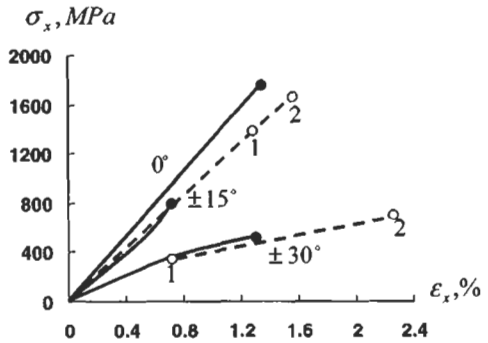

Fig. 4.66. Experimental (solid lines) and calculated (broken lines) stress–strain diagrams for 0°, ±15°, and ±30°) angle-ply carbon–epoxy layers.

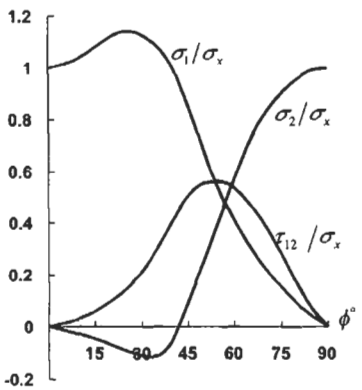

Fig. 4.67. Dependencies of the normalized stresses in the plies on the ply orientation angle.

With these coefficients, the first equation of Eqs. (4.129) yields $E_x = 0$, which means that the system of fibers becomes a mechanism, and the stresses in the fibers, no matter how high they are, cannot balance the load. A typical failure mode of ±30° angle-ply specimen is shown in Fig. 4.68.

Angle-ply layers with fiber orientation angles exceeding 45° demonstrate a different type of behavior. As can be seen in Fig. 4.67, transverse normal stress σ_2 is tensile for $\phi \geqslant 45°$. This means that the cracks induced in the matrix by normal, σ_2, or shear, τ_{12}, stresses cause the failure of the layer. The stress–strain diagrams for ±60° and ±75° layers are shown in Fig. 4.69. As follows from this figure, theoretical diagrams are linear and they are close to the experimental ones, while the predicted ultimate stresses (circles) are again higher than experimental values (dark circles).

Now consider the ±45° angle-ply layer that demonstrates a very specific behavior. For this layer transverse normal stress, σ_2, is tensile but not high (see Fig. 4.67), and the cracks in the matrix are caused by shear stress, τ_{12}. According to the ply model

Fig. 4.68. A failure mode of ±30° angle-ply specimen.

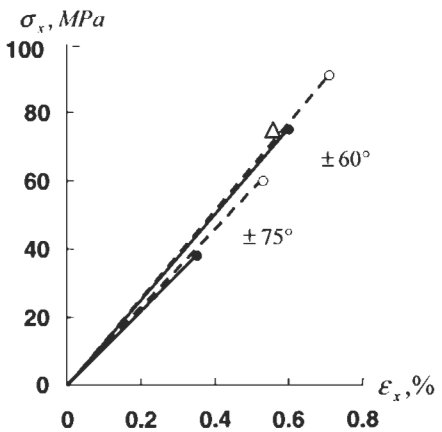

Fig. 4.69. Experimental (solid lines) and calculated (broken lines) stress–strain diagrams for ±60° and ±75° angle-ply carbon–epoxy layers.

we use, to predict material response after the cracks appeared, we should take $G_{12} = 0$ in the stiffness coefficients. Then, Eqs. (4.72) yield

$$A_{11} = A_{12} = A_{22} = \frac{1}{4}(\bar{E}_1 + \bar{E}_2) + \frac{1}{2}\bar{E}_1 \nu_{12} \ ,$$

while Eqs. (4.128) and (4.129) give

$$\varepsilon_x = \frac{A_{22}\sigma_x}{A_{11}A_{22} - A_{12}^2}, \quad \varepsilon_y = -\frac{A_{12}\sigma_x}{A_{11}A_{22} - A_{12}^2} \ .$$

The denominator of both expressions is zero, so it looks like material becomes a mechanism and should fail under the load that causes cracks in the matrix. However, this is not the case. To explain why, consider the last equation of Eqs. (4.150), i.e.,

$$\tan\phi' = \frac{1 + \varepsilon_y}{1 + \varepsilon_x}\tan\phi \ .$$

For the layer under study, $\tan\phi = 1$, $\varepsilon_y < 0$, $\varepsilon_x > 0$, so $\tan\phi' < 1$ and $\phi' < 45°$. But in the plies with $\phi < 45°$ transverse normal stresses, σ_2, become compressive (see Fig. 4.67) and close the cracks. Thus, the load exceeding the level at which the cracks appear due to shear locks the cracks and induces compression across the fibers thus preventing material failure. Because ϕ' is only slightly less than 45°, material stiffness, E_x, is very low and slightly increases with the rise of strains and decrease of ϕ'. For the material under study, the calculated and experimental diagrams are shown in Fig. 4.70. Circle on the theoretical curve indicates the stress σ_x that causes the cracks in the matrix. More pronounced behavior of this type is demonstrated by glass–epoxy composites whose stress–strain curve is presented in Fig. 4.71 (Alfutov and Zinoviev, 1982). A specific plateau on the curve and material hardening at high strain are the result of the angle variation that is also shown in Fig. 4.71.

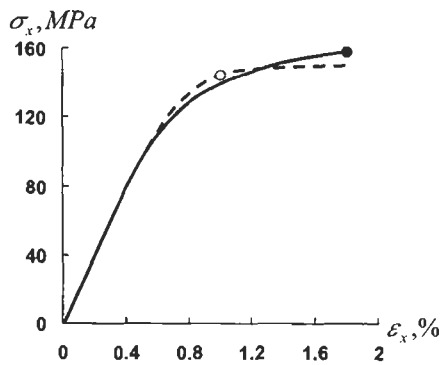

Fig. 4.70. Experimental (solid line) and calculated (broken line) stress–strain diagrams for ±45° angle-ply carbon-epoxy layer.

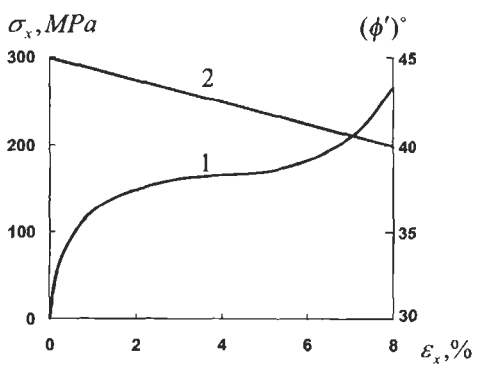

Fig. 4.71. Experimental dependencies of stress (1) and ply orientation angle (2) on strain for ±45° angle-ply glass–epoxy composite.

4.5.3. Free-edge effects

As shown in the previous section, there is a significant difference between predicted and measured strength of an angle-ply specimen loaded in tension. This difference is associated with the stress concentration that takes place in the vicinity of the specimen longitudinal edges and was not taken into account in the analysis.

To study a free-edge effect in an angle-ply specimen, consider a strip whose initial width a is much smaller than the length l. Under tension with longitudinal stress σ, symmetric plies with orientation angles $+\phi$ and $-\phi$ tend to deform as shown in Fig. 4.72. As can be seen, the deformation of the plies in the y-direction is the same, while the deformation in the x-direction tends to be different. This means that symmetric plies forming the angle-ply layer interact through interlaminar shear stress τ_{xz} acting between the plies in the longitudinal direction. To describe the ply interaction, introduce the model shown in Fig. 4.73 according to which the in-plane stresses in the plies are applied to their middle surfaces, while transverse shear stresses act in some hypothetical layers introduced between these surfaces.

To simplify the problem, we further assume that the transverse stress can be neglected, i.e., $\sigma_y = 0$, and that the axial strain in the middle part of the long strip is constant, i.e., $\varepsilon_x = \varepsilon = \text{constant}$. Then, constitutive equations, Eqs. (4.75), for a $+\phi$ ply have a form:

$$\varepsilon_x = \frac{\sigma_x}{E_x^+} + \eta_{x,xy}^+ \frac{\tau_{xy}}{G_{xy}^+} \quad , \tag{4.152}$$

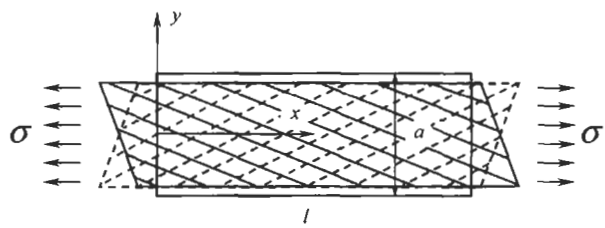

Fig. 4.72. Deformation of symmetric plies under tension.

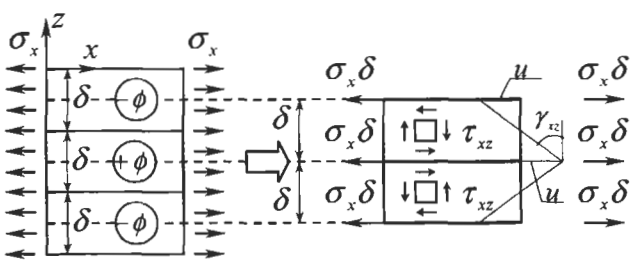

Fig. 4.73. A model simulating the plies interaction.

$$\varepsilon_y = -\nu_{yx}^{+}\frac{\sigma_x}{E_x^{+}} + \eta_{y,xy}^{+}\frac{\tau_{xy}}{G_{xy}^{+}} \ , \tag{4.153}$$

$$\gamma_{xy} = \eta_{xy,x}^{+}\frac{\sigma_x}{E_x^{+}} + \frac{\tau_{xy}}{G_{xy}^{+}} \ , \tag{4.154}$$

where elastic constants of an individual ply are specified by Eqs. (4.76). Strain–displacement equations, Eqs. (2.22), for the problem under study are

$$\varepsilon_x = \varepsilon = \frac{\partial u_x}{\partial x}, \quad \varepsilon_y = \frac{\partial u_y}{\partial y}, \quad \gamma_{xy} = \frac{\partial u_x}{\partial y} + \frac{\partial u_y}{\partial x} \ . \tag{4.155}$$

Integration of the first equation yields for the $+\phi$ and $-\phi$ plies

$$u_x^{+\phi} = \varepsilon \cdot x + u(y), \quad u_x^{-\phi} = \varepsilon \cdot x - u(y) \ , \tag{4.156}$$

where $u(y)$ is the displacement shown in Fig. 4.73. This displacement results in the following transverse shear deformation and transverse shear stress

$$\gamma_{xz} = \frac{2}{\delta}u(y), \quad \tau_{xz} = G_{xz}\gamma_{xz} \ , \tag{4.157}$$

where G_{xz} is the transverse shear modulus of the ply specified by Eqs. (4.76). Consider the equilibrium state of $+\phi$ ply element shown in Fig. 4.74. Equilibrium equations can be written as

$$\delta\frac{\partial \tau_{xy}}{\partial x} = 0, \quad \delta\frac{\partial \tau_{xy}}{\partial y} - 2\tau_{xz} = 0 \ . \tag{4.158}$$

The first of these equations shows that τ_{xy} does not depend on x. Because the axial stress, σ_x, in the middle part of a long specimen also does not depend on x, Eqs. (4.153) and (4.155) allow us to conclude that ε_y and hence u_y do not depend on x. As a result, the last equation of Eqs. (4.155) yields in conjunction with the first equation of Eqs. (4.156):

$$\gamma_{xy} = \frac{\partial u_x}{\partial y} = \frac{du}{dy} \ .$$

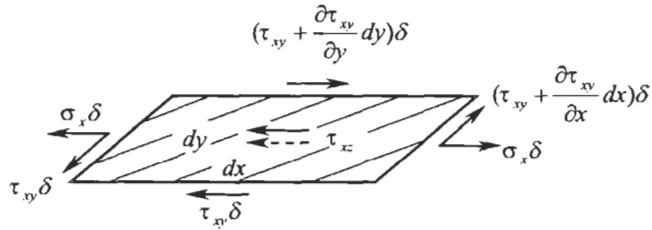

Fig. 4.74. Forces acting on the infinitesimal element of a ply.

Using this expression and substituting ε from Eq. (4.152) into Eq. (4.154) we arrive at

$$\tau_{xy} = \frac{G^+_{xy}}{1-\eta}\left(\frac{du}{dy} - \eta_{xy,x}\varepsilon\right) , \tag{4.159}$$

where $\eta = \eta^+_{x,xy}\eta^+_{xy,x}$.

Substitution of Eqs. (4.157) and (4.159) into the second equation of Eqs. (4.158) provides the following governing equation of the problem under study:

$$\frac{d^2u}{dy^2} - k^2u = 0 , \tag{4.160}$$

where

$$k^2 = \frac{4G_{xz}(1-\eta)}{G^+_{xy}\delta^2} .$$

Using the symmetry conditions we can present the solution of Eq. (4.160) as

$$u = C\sinh ky .$$

Constant C should be found from the boundary conditions for free longitudinal edges of the specimen (see Fig. 4.72) according to which $\tau_{xy}(y = \pm a/2) = 0$. Satisfying these conditions and using Eqs. (4.152), (4.153), (4.157), and (4.159) we finally obtain:

$$\begin{aligned}
\varepsilon_x &= \varepsilon, \\
\varepsilon_y &= \frac{\varepsilon}{1-\eta}\left[\eta^+_{y,xy}\eta^{-1}_{xy,x}\left(\frac{\cosh\lambda\bar{y}}{\cosh\lambda} - 1\right) + \nu^+_{yx}\left(\eta\frac{\cosh\lambda\bar{y}}{\cosh\lambda} - 1\right)\right], \\
\gamma_{xy} &= \varepsilon\eta^+_{xy,x}\frac{\cosh\lambda\bar{y}}{\cosh\lambda}, \\
\sigma_x &= \varepsilon E^+_x\left[1 - \frac{\eta}{1-\eta}\left(\frac{\cosh\lambda\bar{y}}{\cosh\lambda} - 1\right)\right], \\
\tau_{xy} &= \frac{G^+_{xy}\eta^+_{xy,x}}{1-\eta}\left(\frac{\cosh\lambda\bar{y}}{\cosh\lambda} - 1\right), \\
\tau_{xz} &= \frac{2\varepsilon}{k\delta}G_{xz}\eta^+_{xy,x}\frac{\sinh\lambda\bar{y}}{\cosh\lambda} ,
\end{aligned} \tag{4.161}$$

where

$$\lambda = \frac{ka}{2} = \frac{a}{\delta}\sqrt{(1-\eta)\frac{G_{xz}}{G_{xy}^{+}}}, \quad \bar{y} = \frac{2y}{a} \ . \tag{4.162}$$

Axial stress, σ_x, should provide the stress resultant equal to σa (see Fig. 4.72), i.e.,

$$\int_{-a/2}^{a/2} \sigma_x \, dy = \sigma a \ .$$

This condition allows us to determine the axial strain as

$$\varepsilon = \frac{\sigma}{E_x} \ ,$$

where

$$E_x = E_x^{+}\left[1 + \frac{\eta}{1-\eta}\left(1 - \frac{1}{\lambda}\tanh\,\lambda\right)\right] \tag{4.163}$$

is the apparent modulus of an angle-ply specimen.

Consider two limiting cases. First, assume that $G_{xz} = 0$, i.e., that the plies are not bonded. Then, $\lambda = 0$ and because

$$\lim_{\lambda \to 0} \frac{1}{\lambda}\tanh\lambda = 1 \ ,$$

$E_x = E_x^{+}$. Second, assume that $G_{xz} \to \infty$, i.e., that the interlaminar shear stiffness is infinitely high. Then $\lambda \to \infty$ and Eq. (4.163) yields

$$E_x = \frac{E_x^{+}}{1-\eta} \ . \tag{4.164}$$

This result coincides with Eq. (4.131), which specifies the modulus of an angle-ply layer.

For finite values of G_{xz}, parameter λ in Eqs. (4.162) is rather large because it includes the ratio of the specimen width, a, to the ply thickness, δ, which is, usually, a large number. Taking into account that $\tanh\lambda \leqslant 1$ we can neglect the last term in Eq. (4.163) in comparison with unity. Then, this equation reduces to Eq. (4.164). This means that tension of angle-ply specimens allows us to measure material stiffness with proper accuracy despite the fact that the fibers are cut on the longitudinal edges of the specimens.

However, this is not true for strength. Distribution of stresses over the half-width of the carbon–epoxy specimen with properties given above and $a/\delta = 20$, $\phi = 45°$ is

shown in Fig. 4.75. Stresses σ_x, τ_{xy}, and τ_{xz} were calculated with the aid of Eqs. (4.161), while stresses σ_1, σ_2, and τ_{12} in the principal material directions of the plies were found using Eqs. (4.69) for the corresponding strains and Hooke's law for the plies. As can be seen in Fig. 4.75, there exists a significant concentration of stress σ_2 that causes cracks in the matrix. Moreover, interlaminar shear stress τ_{xz} that appears in the vicinity of the specimen edge can induce delamination of the specimen. The maximum value of stress σ_2 is

$$\sigma_2^{\max} = \sigma_2(\bar{y} = 1) = \bar{E}_2\bar{\varepsilon}[(1 - \nu_{21}\nu_{yx}^{+})\sin^2\phi + (\nu_{21} - \nu_{yx})\cos^2\phi - (1 - \nu_{21})\eta_{xy,x}^{+}\sin\phi\cos\phi] \ .$$

Using the modified strength condition, i.e., $\sigma_2^{\max} = \bar{\sigma}_2^{+}$ to evaluate the strength of $\pm 60°$ specimen we arrive at the result shown with a triangular in Fig. 4.69. As can be seen, the allowance for the stress concentration results in a fair agreement with experimental strength (dark circle).

Thus, the strength of angle-ply specimens is reduced by the free-edge effects which causes the dependence of the observed material strength on the width of the specimen. Such dependence is shown in Fig. 4.76 for 105 mm diameter and 2.5 mm thick fiberglass rings made by winding at $\pm 35°$ angles with respect to the axis and loaded with internal pressure by two half-discs as in Fig. 3.46 (Fukui et al., 1966).

It should be emphasized that the free-edge effect occurs in specimens only and does not show itself in composite structures which, being properly designed, should not have free edges of such a type.

4.6. Fabric layers

Textile preforming plays an important role in composite technology providing glass, aramid, carbon (see Fig. 4.77), and hybrid fabrics that are widely used as

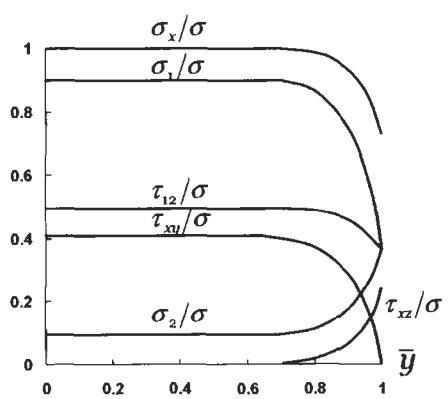

Fig. 4.75. Distribution of normalized stresses over the width of $\pm 45°$ angle-ply carbon–epoxy specimen.

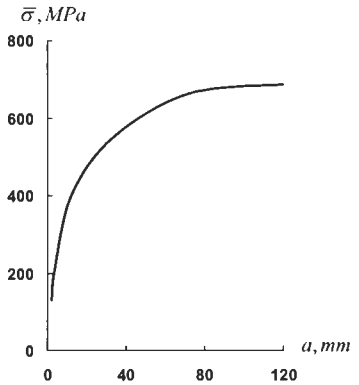

Fig. 4.76. Experimental dependence of strength of a $\pm 35^{\circ}$ angle-ply layer on the width of the specimen.

Fig. 4.77. A carbon fabric tape.

reinforcing materials. The main advantages of woven composites are their cost efficiency and high processability, particularly, in lay-up manufacturing of large-scale structures (see Figs. 4.78 and 4.79). However, on the other hand, processing of fibers and their bending in the process of weaving results in substantial reduction of material strength and stiffness. As can be seen in Fig. 4.80, where a typical woven

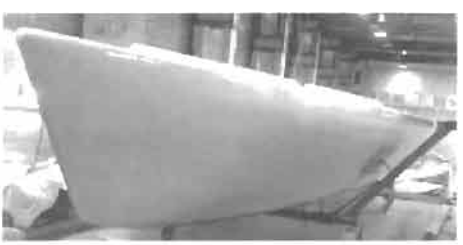

Fig. 4.78. A composite body of a boat made of fiberglass fabric by lay-up method. Courtesy of CRISM.

Fig. 4.79. A composite leading edge of an aeroplane wing made of carbon fabric by lay-up method. Courtesy of CRISM.

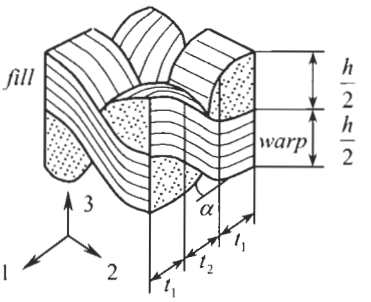

Fig. 4.80. Unit cell of a fabric structure.

structure is shown the warp (lengthwise) and fill (crosswise) yarns forming the fabric make angle $\alpha \geqslant 0$ with the plane of the fabric layer.

To demonstrate how this angle influences material stiffness, consider tension of the structure shown in Fig. 4.80 in the warp direction. Apparent modulus of elasticity can be expressed as

$$E_a A_a = E_f A_f + E_w A_w \ , \tag{4.165}$$

where $A_a = h(2t_1 + t_2)$ is the apparent cross-sectional area and

$$A_f = \frac{h}{2}(2t_1 + t_2), \quad A_w = \frac{h}{4}(4t_1 + t_2)$$

are the areas of the fill and warp yarns in the cross section. Substitution into Eq. (4.165) yields

$$E_a = \frac{1}{2}\left[E_f + \frac{E_w(4t_1 + t_2)}{4(2t_1 + t_2)}\right] \ .$$

Because the fibers of the fill yarns are orthogonal to the loading direction, we can take $E_f = E_2$, where E_2 is the transverse modulus of a unidirectional composite. Compliance of the warp yarn can be decomposed into two parts corresponding to t_1 and t_2 in Fig. 4.80, i.e.,

$$\frac{2t_1 + t_2}{E_w} = \frac{2t_1}{E_1} + \frac{t_2}{E_x} ,$$

where, E_1 is the longitudinal modulus of a unidirectional composite, while E_x can be determined with the aid of the first equation of Eqs. (4.76) if we change ϕ for α, i.e.,

$$\frac{1}{E_x} = \frac{\cos^4\alpha}{E_1} + \frac{\sin^4\alpha}{E_2} + \left(\frac{1}{G_{12}} - \frac{2\nu_{21}}{E_1}\right)\sin^2\alpha\cos^2\alpha . \tag{4.166}$$

The final result is as follows:

$$E_a = \frac{E_2}{2} + \frac{E_1(4t_1 + t_2)}{4\left\{2t_1 + t_2\left[\cos^4\alpha + \frac{E_1}{E_2}\sin^4\alpha + \left(\frac{E_1}{G_{12}} - 2\nu_{21}\right)\sin^2\alpha\cos^2\alpha\right]\right\}} . \tag{4.167}$$

For example, consider a glass fabric with the following parameters: $\alpha = 12°$, $t_2 = 2t_1$. Taking elastic constants of a unidirectional material from Table 3.5 we get for the fabric composite $E_a = 23.5$ GPa. For comparison, a cross-ply $[0°/90°]$ laminate made of the same material has $E = 36.5$ GPa. Thus, the modulus of a woven structure is by 37% less than the modulus of the same material but reinforced with straight fibers. Typical mechanical characteristics of fabric composites are listed in Table 4.4.

Table 4.4
Typical properties of fabric composites.

Property	Glass fabric–epoxy	Aramid fabric–epoxy	Carbon fabric–epoxy
Fiber volume fraction	0.43	0.46	0.45
Density (g/cm^3)	1.85	1.25	1.40
Longitudinal modulus (GPa)	26	34	70
Transverse modulus (GPa)	22	34	70
Shear modulus (GPa)	7.2	5.6	5.8
Poisson's ratio	0.13	0.15	0.09
Longitudinal tensile strength (MPa)	400	600	860
Longitudinal compressive strength (MPa)	350	150	560
Transverse tensile strength (MPa)	380	500	850
Transverse compressive strength (MPa)	280	150	560
In-plane shear strength (MPa)	45	44	150

Stiffness and strength of fabric composites depend not only on the yarns and matrix properties, but on material structural parameters, i.e., on fabric count and weave, as well. The fabric count specifies the number of warp and fill yarns per inch (25.4 mm), while the weave determines how the warp and the fill yarns are interlaced. Typical weave patterns are shown in Fig. 4.81 and include plain, twill, and satin. In the plain weave (see Fig. 4.81a) which is the most common and the oldest, the warp yarn is repeatedly woven over the fill yarn and under the next fill yarn. In the twill weave, the warp yarn passes over and under two (as in Fig. 4.81b) or more fill yarns in a regular way. A structure with one warp yarn passing over four and under one fill yarn is referred to as a five harness satin weave (Fig. 4.81c).

Being formed from one and the same type of yarns plain, twill, and satin weaves provide approximately the same strength and stiffness of the fabric in the warp and the fill directions. Typical stress–strain diagrams for a fiberglass fabric composite of such a type are presented in Fig. 4.82. As can be seen, material demonstrates relatively low stiffness and strength under tension at the angle of 45° with respect to the warp or fill directions. To improve these properties, multiaxial woven fabrics, one of which is shown in Fig. 4.81d, can be used.

Fabric materials whose properties are more close to those of unidirectional composites are made by weaving a great number of larger yarns in longitudinal direction and fewer and smaller yarns in the orthogonal direction. Such weave is called unidirectional. It provides materials with high stiffness and strength in one direction, which is specific for unidirectional composites and high processability typical for fabric composites.

Being fabricated as planar structures, fabrics can be shaped on shallow surfaces using the material high stretching ability under tension at 45° to the yarns'

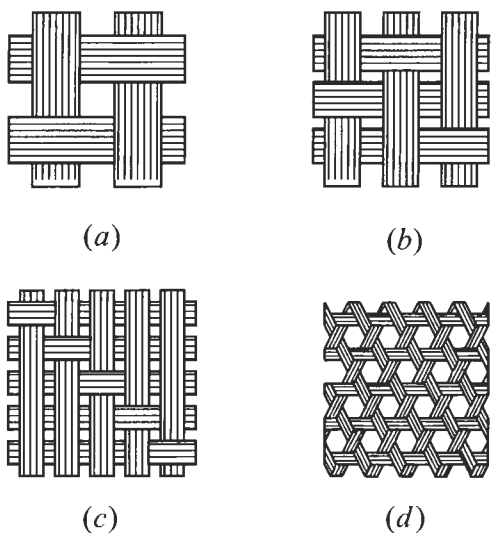

Fig. 4.81. Plain (a), twill (b), satin (c), and triaxial (d) woven fabrics.

directions. Much more possibilities for such shaping are provided by implementation of knitted fabrics whose strain to failure exceeds 100%. Moreover, knitting allows us to shape the fibrous preform in accordance with the shape of the future composite part. There exist different knitting patterns, some of which are shown in Fig. 4.83. Relatively high curvature of the yarns in knitted fabrics and possible fiber breakage in the process of knitting result in materials whose strength and stiffness are less than those of woven fabric composites, but whose processability is higher, and the cost is lower. Typical stress–strain diagrams for composites reinforced by knitted fabrics are presented in Fig. 4.84.

Material properties close to those of woven composites are provided by braided structures which, being usually tubular in form are fabricated by mutual intertwining, or twisting of yarns about each other. Typical braided structures are shown in Fig. 4.85. Biaxial braided fabrics in Fig. 4.85 can incorporate longitudinal yarns forming a triaxial braid whose structure is similar to that shown in Fig. 4.81d. Braided preforms are characterized with very high processability providing near net-shape manufacturing of tubes, and profiles with various cross-sectional shapes.

Although microstructural models of the type shown in Fig. 4.80 and leading to equations similar to Eq. (4.167) have been developed to predict stiffness and even

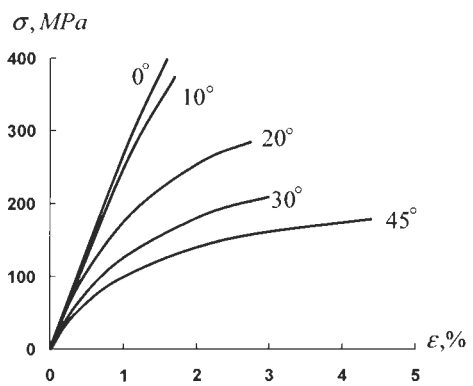

Fig. 4.82. Stress–strain curves for fiber glass fabric composite loaded in tension at different angles with respect to the warp direction.

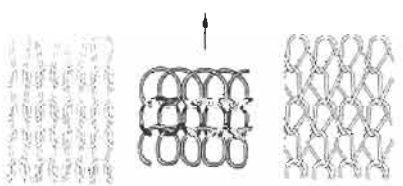

Fig. 4.83. Typical knitted structures.

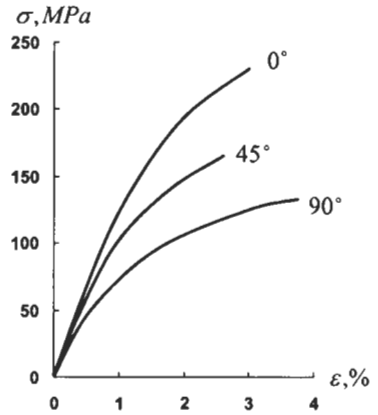

Fig. 4.84. Typical stress–strain curves for fiberglass knitted composites loaded in tension at different angles with respect to direction indicated by the arrow Fig. 4.83.

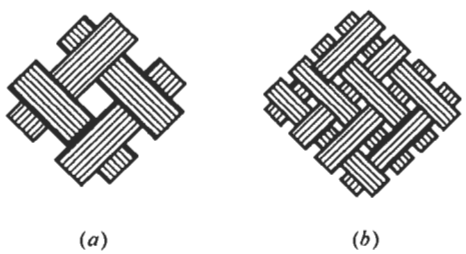

Fig. 4.85. Diamond (a) and regular (b) braided fabric structures.

strength characteristics of fabric composites (e.g., Skudra et al., 1989), for practical design and analysis, these characteristics are usually determined by experimental methods. Elastic constants entering constitutive equations written in the principal material coordinates, e.g., Eqs. (4.55), are found testing strips cut out of fabric composite plates at different angles with respect to the orthotropy axes. The 0° and 90° specimens are used to determine moduli of elasticity E_1, E_2 and Poisson's ratios ν_{12}, ν_{21} (or parameters of nonlinear stress–strain diagrams), while the in-plane shear stiffness can be obtained with the aid of off-axis tension described in Section 4.3.1. For fabric composites, elastic constants usually satisfy conditions in Eqs. (4.80), and there exists the angle ϕ specified by Eq. (4.79) such that off-axis tension under this angle is not accompanied with shear–extension coupling.

Because Eq. (4.79) specifying ϕ includes shear modulus G_{12}, which is not known, transform the results presented in Section 4.3.1. Using Eqs. (4.76) and assuming that there is no shear–extension coupling ($\eta_{x,xy} = 0$) we can write the following equations:

$$\frac{1}{E_x} = \frac{1+\nu_{21}}{E_1}\cos^4\phi + \frac{1+\nu_{12}}{E_2}\sin^4\phi - \frac{\nu_{21}}{E_1} + \frac{1}{G_{12}}\sin^2\phi\cos^2\phi,$$
$$\frac{\nu_{yx}}{E_x} = \frac{\nu_{21}}{E_1} - \left(\frac{1+\nu_{21}}{E_1} + \frac{1+\nu_{12}}{E_2} - \frac{1}{G_{12}}\right)\sin^2\phi\cos^2\phi, \tag{4.168}$$
$$\frac{1+\nu_{21}}{E_1}\cos^2\phi - \frac{1+\nu_{12}}{E_2}\sin^2\phi - \frac{1}{2G_{12}}\cos 2\phi = 0 \ .$$

Summing up the first two of these equations we get

$$\frac{1+\nu_{yx}}{E_x} = \left(\frac{1+\nu_{21}}{E_1}\cos^2\phi - \frac{1+\nu_{12}}{E_2}\sin^2\phi + \frac{2}{G_{12}}\sin^2\phi\cos^2\phi\right) \ .$$

Using the third equation we arrive at the remarkable result

$$G_{12} = \frac{E_x}{2(1+\nu_{yx})} \tag{4.169}$$

similar to the corresponding formula for isotropic materials, Eq. (2.57). It should be emphasized that Eq. (4.169) is valid for off-axis tension in the x-direction making some special angle ϕ with the principal material axis 1. This angle is given by Eq. (4.79). Another form of this expression follows from the last equation of Eqs. (4.168) and (4.169), i.e.,

$$\sin^2\phi = \frac{\dfrac{1+\nu_{yx}}{E_x} - \dfrac{1+\nu_{21}}{E_1}}{2\dfrac{1+\nu_{yx}}{E_x} - \dfrac{1+\nu_{21}}{E_1} - \dfrac{1+\nu_{12}}{E_2}} \ . \tag{4.170}$$

For fabric composites whose stiffness in the warp and the fill directions is the same ($E_1 = E_2$), Eq. (4.170) yields $\phi = 45°$.

4.7. Lattice layer

A layer with a relatively low density and high stiffness can be obtained with a lattice structure which can be made by winding modified in such a way that the tapes are laid onto preceding tapes and not beside them as in conventional filament winding (see Fig. 4.86). Lattice layer can be the single layer of the structure as in Fig. 4.87 or can be combined with a skin as in Fig. 4.88. As a rule, lattice structures have the form of cylindrical or conical shells in which the lattice layer is formed with two systems of ribs – a symmetric system of helical ribs and a system of circumferential ribs (see Fig. 4.87 and 4.88). However, there exist lattice structures with three systems of ribs as in Fig. 4.89.

In general, lattice layer can be assumed to consist of k symmetric systems of ribs making angles $\pm\phi_j$ ($j = 1, 2, 3, \ldots, k$) with the x-axis and having geometric

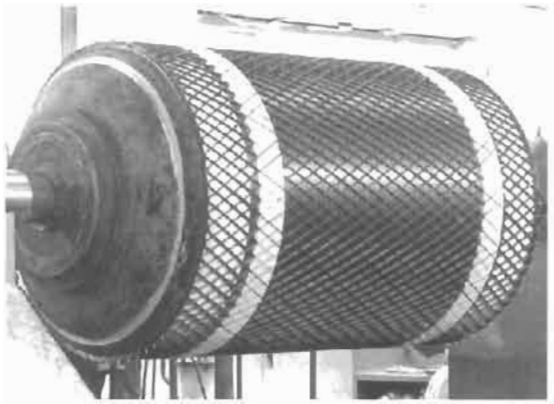

Fig. 4.86. Winding of a lattice layer. Courtesy of CRISM.

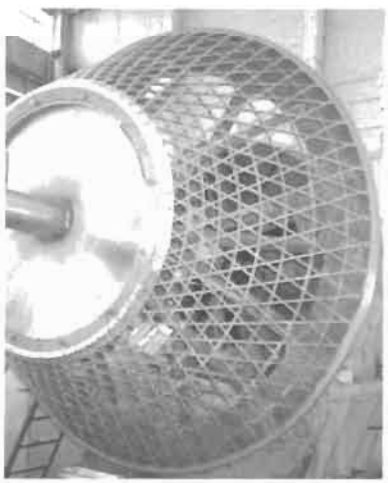

Fig. 4.87. Carbon–epoxy lattice spacecraft fitting in the assemble fixture. Courtesy of CRISM.

parameters shown in Fig. 4.90. Particularly, the lattice layer presented in this figure has $k = 2$, $\phi_1 = \phi$, and $\phi_2 = 90°$.

Because the lattice structure is formed with dense and regular systems of ribs, the ribs can be smeared over the layer surface, which is thus simulated with a continuous layer having some effective (apparent) stiffnesses. Taking into account that the ribs work in their axial directions only, neglecting the ribs torsion and bending in the plane of the lattice layer, and using Eqs. (4.72) we get

$$A_{11} = \sum_{j=1}^{k} B_j \cos^4 \phi_j, \quad A_{22} = \sum_{j=1}^{k} B_j \sin^4 \phi_j \ ,$$

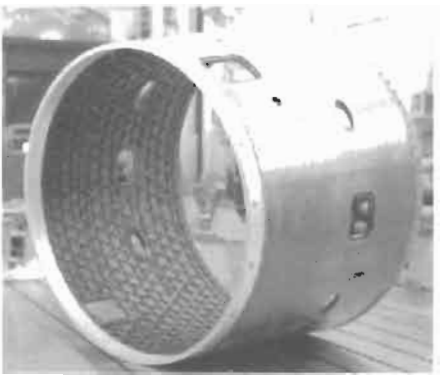

Fig. 4.88. Interstage composite lattice structure. Courtesy of CRISM.

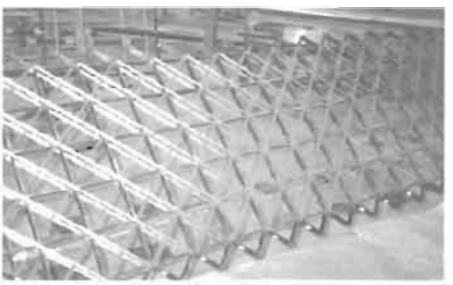

Fig. 4.89. A composite lattice shear web structure.

$$A_{12} = A_{21} = A_{44} = \sum_{j=1}^{k} B_j \sin^2 \phi_j \cos^2 \phi_j,$$

$$A_{44} = \sum_{j=1}^{k} C_j \cos^2 \phi_j, \quad A_{55} = \sum_{j=1}^{k} C_j \sin^2 \phi_j \ ,$$

where $B_j = E_j \delta_j / a_j$ and $C_j = G_j \delta_j / a_j$, where E_j and G_j are the modulus of elasticity and the shear modulus of the ribs materials, δ_j the ribs widths, and a_j are the ribs spacings (see Fig. 4.90).

4.8. Spatially reinforced layers and bulk materials

The layers considered in the previous sections and formed of unidirectionally reinforced plies and tapes (Sections 4.2–4.5 and 4.7) or fabrics reinforced in the layer plane (Section 4.6) suffer from a serious shortcoming – their transverse (normal to

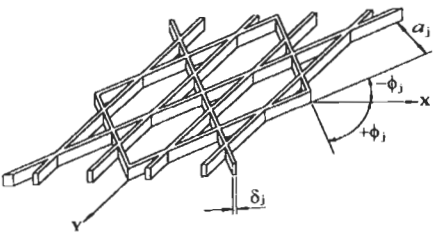

Fig. 4.90. Geometric parameters of a lattice structure.

the layer plane) stiffness and strength are substantially lower than the corresponding in-plane characteristics. To improve material properties under tension or compression in the z-direction and in shear in the xz-and the yz-planes (see, e.g., Fig. 4.18), material should be additionally reinforced with fibers or yarns directed along the z-axis or making some angles (less than the right angle) with this axis.

A simple and natural way of such a triaxial reinforcement is provided by implementation of three-dimensionally woven or braided fabrics. Three-dimensional weaving or braiding is a variant of the corresponding planar process wherein some yarns are going in the thickness direction. Another way involves assembling of elementary fabric layers or unidirectional plies into a three-dimensionally reinforced structure by sewing or stitching. Depending on the size of the additional yarn and frequency of sewing or stitching, transverse mechanical properties of the two-dimensionally reinforced composite can be improved to a greater or lesser extent. The third way is associated with introduction of composite or metal pins parallel to the z-axis that can be inserted in the material before or after it is cured. The close to this effect is reached by the so-called needle punching. The needles puncture the fabric, break the fibers that compose the yarns, and direct the broken fibers through the layer thickness. Short fibers (or whiskers) may also be introduced into the matrix with which the fabrics or the systems of fibers are impregnated.

Another class of spatially reinforced composites used mainly in carbon–carbon technology is formed by bulk materials multi-dimensionally reinforced with fine rectilinear yarns composed of carbon fibers bound with a polymeric or carbon matrix. The basic structural element of these materials is a parallelepiped shown in Fig. 4.91. The simplest spatial structure is the so-called 3D (three-dimensionally reinforced) in which reinforcing elements are directed along the ribs AA_1, AB and AD of the basic parallelepiped in Fig. 4.91. This structure is shown in Fig. 4.92 (Vasiliev and Tarnopol'skii, 1990). More complicated 4D structure with reinforcing elements directed along the diagonals AC_1, A_1C, BD_1 and B_1D (see Fig. 4.91) is shown in Fig. 4.93 (Tarnopol'skii et al., 1987). An example of this structure is presented in Fig. 1.22. Cross-section of a 5D structure reinforced along diagonals AD_1, A_1D and ribs AA_1, AB, AD is shown in Fig. 4.94 (Vasiliev and Tarnopol'skii, 1990). There exist structures with higher numbers of reinforcing directions. For example, combination of a 4D structure (Fig. 4.93) with reinforcements along the ribs AB and AD (see Fig. 4.91) results in a 6D structure; addition of reinforcements in the

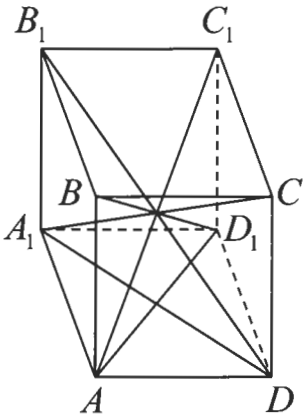

Fig. 4.91. The basic structural element of multi-dimensionally reinforced materials.

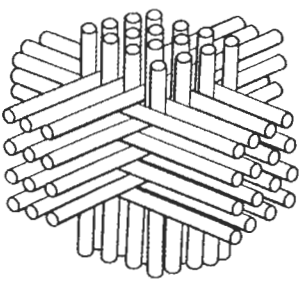

Fig. 4.92. 3D spatially reinforced structure.

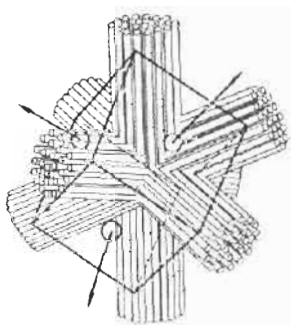

Fig. 4.93. 4D spatially reinforced structure.

direction of the rib AA_1 gives a 7D structure, and so on up to 13D which is the most complicated of the spatial structures under discussion.

Mechanical properties of multi-dimensional composite structures can be qualitatively predicted with microstructural models discussed, e.g., by Tarnopol'skii

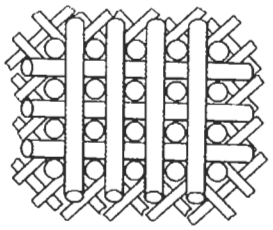

Fig. 4.94. Cross-section of a 5D spatially reinforced structure.

et al. (1992). However, for practical applications these characteristics are usually obtained by experimental methods. Being orthotropic in the global coordinates of the structure x, y, z, spatially reinforced composites are described within the framework of a phenomenological model ignoring their microctructure by three-dimensional constitutive equations analogous to Eqs. (4.53) or Eqs. (4.54) in which 1 should be changed for x, 2 – for y, and 3 – for z. These equations include nine independent elastic constants. Stiffness coefficients in the basic plane, i.e., E_x, E_y, G_{xy}, and ν_{xy}, are determined using traditional tests developed for unidirectional and fabric composites and discussed in Sections 3.4, 4.2, and 4.6. Transverse modulus E_z and the corresponding Poisson's ratios ν_{xz} and ν_{yz} can be found studying material compression in the z-direction. Transverse shear moduli G_{xz} and G_{yz} can be calculated using the results of a three-point beam bending test shown in Fig. 4.95. A specimen cut out of the material is loaded with force P, and the deflection at the central point, w, is measured. According to the theory of composite beams (Vasiliev, 1993)

$$w = \frac{Pl^3}{4bh^3E_x}\left(1 + \frac{h^2E_x}{l^2G_{xz}}\right) .$$

Knowing P, the corresponding w and modulus E_x (or E_y) we can calculate G_{xz} (or G_{yz}). It should be noted that for reliable calculation the beam should be rather short, because of high ratios l/h the second term in parenthesis is small in comparison with unity.

The last spatially reinforced structure that is considered here is formed by a unidirectional composite material whose principal material axes 1, 2, 3 make some

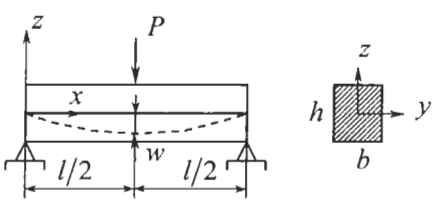

Fig. 4.95. Three-point bending test.

angles with the global structural axes x, y, z (see Fig. 4.96). In the principal material coordinates, constitutive equations have the form of Eqs. (4.53) or Eqs. (4.54). Introducing directional cosines l_{xi}, l_{yi}, l_{zi} which are cosines of the angles that the i-axis ($i = 1, 2, 3$) makes with axes x, y, z, respectively, applying Eqs. (2.8), (2.9) and (2.31) to transform stresses and strains in coordinates 1, 2, 3 to stresses and strains referred to coordinates x, y, z, and using the procedure described in Section 4.3.1 we finally arrive at the following constitutive equations in the global structural coordinate frame

$$\begin{Bmatrix} \sigma_x \\ \sigma_y \\ \sigma_z \\ \tau_{xy} \\ \tau_{xz} \\ \tau_{yz} \end{Bmatrix} = [S] \begin{Bmatrix} \varepsilon_x \\ \varepsilon_y \\ \varepsilon_z \\ \gamma_{xy} \\ \gamma_{xz} \\ \gamma_{yz} \end{Bmatrix}, \tag{4.171}$$

where

$$[S] = \begin{bmatrix} S_{1111} & S_{1122} & S_{1133} & S_{1112} & S_{1113} & S_{1123} \\ & S_{2222} & S_{2233} & S_{2212} & S_{2213} & S_{2223} \\ & & S_{3333} & S_{3312} & S_{3313} & S_{3323} \\ & & & S_{1212} & S_{1213} & S_{1223} \\ & sym & & & S_{1313} & S_{1323} \\ & & & & & S_{2323} \end{bmatrix}$$

is the stiffness matrix in which

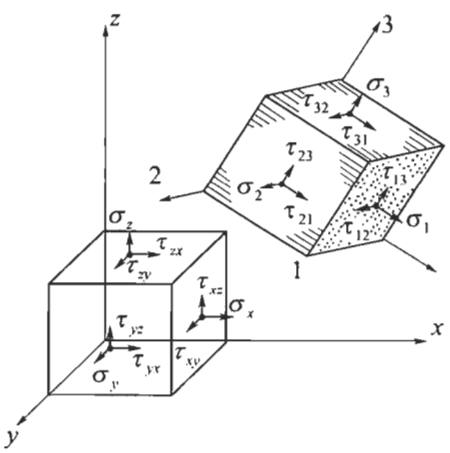

Fig. 4.96. Material elements referred to the global structural coordinate frame x, y, z and to the principal material axes 1, 2, 3.

$$
\begin{aligned}
S_{1111} &= A_1 l_{x1}^4 + A_2 l_{x2}^4 + A_3 l_{x3}^4 + 2A_{112} l_{x1}^2 l_{x2}^2 + 2A_{113} l_{x1}^2 l_{x3}^2 + 2A_{223} l_{x2}^2 l_{x3}^2 \quad (1, 2, 3), \\
S_{1122} &= A_1 l_{x1}^2 l_{y1}^2 + A_2 l_{x2}^2 l_{y2}^2 + A_3 l_{x3}^2 l_{y3}^2 + A_1 \mu_{12} (l_{x1}^2 l_{y2}^2 + l_{x2}^2 l_{y1}^2) \\
&\quad + A_1 \mu_{13} (l_{x1}^2 l_{y3}^2 + l_{x3}^2 l_{y1}^2) + A_2 \mu_{23} (l_{x2}^2 l_{y3}^2 + l_{x3}^2 l_{y3}^2) \\
&\quad + 4(G_{12} l_{x1} l_{x2} l_{y1} l_{y2} + G_{13} l_{x1} l_{x3} l_{y1} l_{y3} + G_{23} l_{x2} l_{x3} l_{y2} l_{y3}) \quad (1, 2, 3), \\
S_{1112} &= A_1 l_{x1}^3 l_{y1} + A_2 l_{x2}^3 l_{y2} + A_3 l_{x3}^3 l_{y3} + A_{112} (l_{x1} l_{y2} + l_{x2} l_{y1}) l_{x1} l_x^2 \\
&\quad + A_{113} (l_{x1} l_{y3} + l_{x3} l_{y1}) l_{x1} l_{x3} + A_{223} (l_{x2} l_{y3} + l_{x3} l_{y2}) l_{x2} l_{x3} \quad (1, 2, 3), \\
S_{1113} &= A_1 l_{x3}^3 l_{z1} + A_2 l_{x2}^3 l_{z2} + A_3 l_{x3}^3 l_{z3} + A_{112} (l_{x1} l_{z2} + l_{x2} l_{z1}) l_{x1} l_{x2} \\
&\quad + A_{113} (l_{x1} l_{z2} + l_{x3} l_{z1}) l_{x1} l_{x3} + A_{223} (l_{x2} l_{z3} + l_{x3} l_{z2}) l_{x2} l_{x3} \quad (1, 2, 3), \\
S_{1123} &= A_1 l_{x1}^2 l_{y1} l_{z1} + A_2 l_{x2}^2 l_{y2} l_{z2} + A_3 l_{x3}^2 l_{y3} l_{z3} \\
&\quad + A_1 \mu_{12} (l_{x1}^2 l_{y2} l_{z2} + l_{x2}^2 l_{y1} l_{z1}) + A_1 \mu_{13} (l_{x1}^2 l_{y3} l_{z3} + l_{x3}^2 l_{y1} l_{z1}) \\
&\quad + A_2 \mu_{23} (l_{x2}^2 l_{y3} l_{z3} + l_{x3}^2 l_{y2} l_{z2}) + 2[G_{12} (l_{y1} l_{z2} + l_{z1} l_{y2}) l_{x1} l_{x2} \\
&\quad + G_{13} (l_{y1} l_{z2} + l_{z1} l_{y2}) l_{x1} l_{x3} + G_{23} (l_{y3} l_{z2} + l_{y2} l_{z3}) l_{x2} l_{x3}] \quad (1, 2, 3), \\
S_{1212} &= A_1 l_{x1}^2 l_{y1}^2 + A_2 l_{x2}^2 l_{y2}^2 + A_3 l_{x3}^2 l_{y3}^2 \\
&\quad + 2(A_1 \mu_{12} l_{x1} l_{x2} l_{y1} l_{y2} + A_1 \mu_{13} l_{x1} l_{x3} l_{y1} l_{y3} + A_2 \mu_{23} l_{x2} l_{x3} l_{y2} l_{y3}) \\
&\quad + G_{12} (l_{x1} l_{y2} + l_{x2} l_{y1})^2 + G_{13} (l_{x1} l_{y3} + l_{x3} l_{y1})^2 \\
&\quad + G_{23} (l_{x2} l_{y3} + l_{x3} l_{y2})^2 \quad (1, 2, 3), \\
S_{1213} &= A_1 l_{x1}^2 l_{y1} l_{z1} + A_2 l_{x2}^2 l_{y2} l_{z2} + A_3 l_{x3}^2 l_{y3} l_{z3} \\
&\quad + A_1 \mu_{12} (l_{y1} l_{z2} + l_{y2} l_{z1}) l_{x1} l_{x2} + A_1 \mu_{13} (l_{y1} l_{z3} + l_{y2} l_{z1}) l_{x1} l_{x3} \\
&\quad + A_2 \mu_{23} (l_{y2} l_{z3} + l_{y3} l_{z2}) l_{x1} l_{x3} + G_{12} (l_{x1} l_{y2} + l_{x2} l_{y1}) (l_{x1} l_{y2} + l_{x2} l_{z1}) \\
&\quad + G_{13} (l_{x1} l_{y3} + l_{x3} l_{y1}) (l_{x1} l_{z3} + l_{x3} l_{z2}) \\
&\quad + G_{23} (l_{x2} l_{y3} + l_{x3} l_{y2}) (l_{x2} l_{z3} + l_{x3} l_{z2}) \quad (1, 2, 3) \ .
\end{aligned}
\tag{4.172}
$$

It should be noted that stiffness coefficients are symmetric with respect to the couples of subscripts ($S_{ijkl} = S_{klij}$) and that notation (1, 2, 3) means that performing permutation, i.e., changing 1 for 2, 2 for 3, and 3 for 1, we can use Eqs. (4.172) to write the expressions for all the stiffness coefficients entering Eq. (4.171). Coefficients A_i and μ_{ij} in Eqs. (4.172) are given in notations to Eqs. (4.54) and

$$
A_{112} = A_1 \mu_{12} + 2G_{12}, \quad A_{113} = A_1 \mu_{13} + 2G_{13}, \quad A_{223} = A_2 \mu_{23} + 2G_{23} \ .
$$

Resolving Eqs. (4.171) for strains we arrive at Eq. (2.48) with the following coefficients of the compliance matrix in Eq. (2.49):

$$
\frac{1}{E_x} = \frac{l_{x1}^4}{E_1} + \frac{l_{y1}^4}{E_2} + \frac{l_{z1}^4}{E_3} + C_{122} l_{x1}^2 l_{y1}^2 + C_{133} l_{x1}^2 l_{z1}^2 + C_{233} l_{y1}^2 l_{z1}^2 \quad (1, 2, 3) \ (x, y, z) \ .
$$

$$\frac{\nu_{xy}}{E_y}=\frac{\nu_{yx}}{E_x}=\frac{\nu_{12}}{E_2}(l_{x1}^2l_{y2}^2+l_{x2}^2l_{y1}^2)+\frac{\nu_{13}}{E_3}(l_{x1}^2l_{z2}^2+l_{x2}^2l_{z1}^2)$$
$$+\frac{\nu_{23}}{E_3}(l_{y1}^2l_{z2}^2+l_{y2}^2l_{z1}^2)-\frac{l_{x1}^2l_{x2}^2}{E_1}-\frac{l_{y1}^2l_{y2}^2}{E_2}-\frac{l_{z1}^2l_{z2}^2}{E_3}$$
$$-\frac{1}{G_{12}}l_{x1}l_{x2}l_{y1}l_{y2}-\frac{1}{G_{13}}l_{x1}l_{x2}l_{z1}l_{z2}-\frac{1}{G_{23}}l_{y1}l_{y2}l_{z1}l_{z2}\quad(1,2,3)\ (x,y,z)\ , \tag{4.173}$$

$$\frac{\eta_{x,xy}}{G_{xy}}=\frac{\eta_{xy,x}}{E_x}=2\left(\frac{l_{x1}^3l_{x2}}{E_1}+\frac{l_{y1}^3l_{y2}}{E_2}+\frac{l_{z1}^3l_{z2}}{E_3}\right)+C_{122}(l_{x1}l_{y2}+l_{x2}l_{y1})l_{x1}l_{y1}$$
$$+C_{133}(l_{x1}l_{z2}+l_{x2}l_{z1})l_{x1}l_{z1}+C_{233}(l_{y1}l_{z2}+l_{y2}l_{z1})l_{y1}l_{z1}\quad(1,2,3)\ (x,y,z)\ ,$$

$$\frac{\eta_{x,xz}}{G_{xz}}=\frac{\eta_{xz,x}}{E_x}$$
$$=2\left(\frac{l_{x1}^3l_{x3}}{E_1}+\frac{l_{y1}^3l_{y3}}{E_2}+\frac{l_{z1}^3l_{z3}}{E_3}\right)+C_{122}(l_{x1}l_{y3}+l_{y1}l_{x3})l_{x1}l_{y1}$$
$$+C_{133}(l_{x1}l_{z3}+l_{x3}l_{z1})l_{x1}l_{z1}+C_{233}(l_{y1}l_{z3}+l_{y3}l_{z1})l_{y1}l_{z1}\quad(1,2,3)\ (x,y,z)\ ,$$

$$\frac{\eta_{x,yz}}{G_{yz}}=\frac{\eta_{yz,x}}{E_x}$$
$$=2\left[\frac{l_{x1}^2l_{x2}l_{x3}}{E_1}+\frac{l_{y1}^2l_{y2}l_{y3}}{E_2}+\frac{l_{z1}^2l_{z2}l_{z3}}{E_3}-\frac{\nu_{12}}{E_2}(l_{x1}^2l_{y2}l_{y3}+l_{y1}^2l_{x2}l_{x3})\right.$$
$$\left.\cdot-\frac{\nu_{13}}{E_3}(l_{x1}^2l_{z2}l_{z3}+l_{z1}^2l_{x2}l_{x3})-\frac{\nu_{23}}{E_3}(l_{y1}^2l_{z2}l_{z3}+l_{z1}^2l_{y2}l_{y3})\right]$$
$$+\frac{l_{x1}l_{y1}}{G_{12}}(l_{x2}l_{y3}+l_{x3}l_{y2})+\frac{l_{x1}l_{z1}}{G_{13}}(l_{x2}l_{z3}+l_{x3}l_{z2})$$
$$+\frac{l_{y1}l_{z1}}{G_{23}}(l_{y2}l_{z3}+l_{y3}l_{z2})\quad(1,2,3)\ (x,y,z)\ ,$$

$$\frac{1}{G_{xy}}=4\left[\frac{l_{x1}^2l_{x2}^2}{E_1}+\frac{l_{y1}^2l_{y2}^2}{E_2}+\frac{l_{z1}^2l_{z2}^2}{E_3}\right.$$
$$\left.-2\left(\frac{\nu_{12}}{E_2}l_{x1}l_{x2}l_{y1}l_{y2}+\frac{\nu_{13}}{E_3}l_{x1}l_{x2}l_{z1}l_{z2}+\frac{\nu_{23}}{E_3}l_{y1}l_{y2}l_{z1}l_{z2}\right)\right]$$
$$+\frac{1}{G_{12}}(l_{x1}l_{y2}+l_{x2}l_{y1})^2+\frac{1}{G_{13}}(l_{x1}l_{z2}+l_{x2}l_{z1})^2$$
$$+\frac{1}{G_{23}}(l_{y1}l_{z2}+l_{y2}l_{z1})^2\quad(1,2,3)\ (x,y,z)\ ,$$

$$\frac{\lambda_{xy,xz}}{G_{xz}} = \frac{\lambda_{xz,xy}}{G_{xy}}$$
$$= 4\left[\frac{l_{x1}^2 l_{x2} l_{x3}}{E_1} + \frac{l_{y1}^2 l_{y2} l_{y3}}{E_2} + \frac{l_{z1}^2 l_{z2} l_{z3}}{E_3} - \frac{\nu_{12}}{E_2}(l_{x3} l_{y2} + l_{x2} l_{y3}) l_{x1} l_{y1}\right.$$
$$\left. - \frac{\nu_{13}}{E_3}(l_{x2} l_{z3} + l_{z2} l_{x3}) l_{x1} l_{z1} - \frac{\nu_{23}}{E_3}(l_{y2} l_{z3} + l_{y3} l_{z2}) l_{y1} l_{z1}\right]$$
$$+ \frac{1}{G_{12}}(l_{x1} l_{y3} + l_{x3} l_{y1})(l_{x1} l_{y2} + l_{x2} l_{y1})$$
$$+ \frac{1}{G_{13}}(l_{x1} l_{z3} + l_{x3} l_{z1})(l_{x1} l_{z2} + l_{x2} l_{z1})$$
$$+ \frac{1}{G_{23}}(l_{y1} l_{z3} + l_{y3} l_{z1})(l_{y1} l_{z2} + l_{y2} l_{z1}) \quad (1, 2, 3)\ (x, y, z)\ ,$$

where

$$C_{122} = \frac{1}{G_{12}} - \frac{2\nu_{12}}{E_2}, \quad C_{133} = \frac{1}{G_{13}} - \frac{2\nu_{13}}{E_3}, \quad C_{233} = \frac{1}{G_{23}} - \frac{2\nu_{23}}{E_3}\ .$$

Consider a special spatial structure (Pagano and Whitford, 1985) formed by the fabric composite in which the plies reinforced at angle ϕ (warp direction) with respect to the x-axis make angles α and β with the x-axis and the y-axis, respectively, as in Fig. 4.97. Directional cosines for this structure are:

$$l_{x1} = \cos\lambda\cos\psi, \quad l_{x2} = -\sin\lambda\cos\psi,$$
$$l_{x3} = -\sin\psi, \quad l_{y1} = \sin\lambda\cos\beta - \cos\lambda\sin\beta\sin\psi,$$
$$l_{y2} = \cos\lambda\cos\beta + \sin\lambda\sin\beta\sin\psi, \quad l_{y3} = -\sin\beta\cos\psi,$$
$$l_{z1} = \sin\lambda\sin\beta + \cos\lambda\cos\beta\sin\psi,$$
$$l_{z2} = \cos\lambda\sin\beta - \sin\lambda\cos\beta\sin\psi, \quad l_{z3} = \cos\beta\cos\psi\ ,$$

where

$$\lambda = \phi + \tan^{-1}(\tan\beta\sin\psi), \quad \psi = \tan^{-1}(\tan\alpha\cos\beta)\ .$$

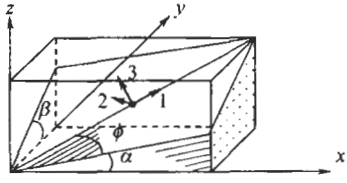

Fig. 4.97. Orientation angles in a spatial composite structure.

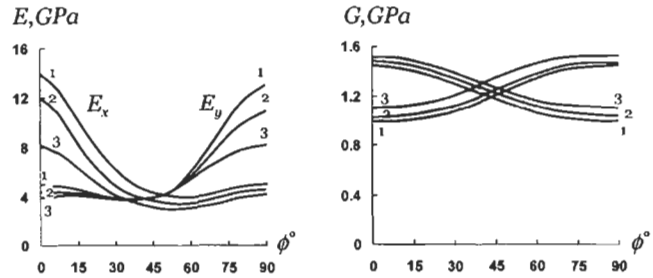

Fig. 4.98. Dependencies of the elastic constants of a spatially reinforced composite on the orientation angles: $1 - \alpha = \beta = 0°$, $2 - \alpha = \beta = 8°$, $3 - \alpha = \beta = 16°$.

Dependencies of elastic constants E_x, E_y, G_{xz} and G_{yz} calculated with the aid of Eqs. (4.173) for the material with $E_1 = 12.9$ GPa, $E_2 = 5.2$ GPa, $E_3 = 3$ GPa, $G_{12} = G_{13} = 1.5$ GPa, $G_{23} = 1$ GPa, $\nu_{21} = 0.15$, $\nu_{31} = 0.2$, $\nu_{32} = 0.2$ are presented in Fig. 4.98 (Vasiliev and Morozov, 1988).

For planar structures ($\alpha = \beta = 0$), Eqs. (4.172) and (4.173) generalize Eqs. (4.72) and (4.76) for a three-dimensional stress state of a layer.

4.9. References

Alfutov, N.A. and Zinoviev, P.A. (1982). Deformation and failure of fibrous composites with brittle polymeric matrix under plane stress. In *Mechanics of Composites* (I.F. Obraztsov and V.V. Vasiliev eds.). Mir, Moscow, pp. 166–185.

Birger, I.A. (1951). General solutions of some problems of the plasticity theory. *Prikl. Mat. Mekh.* **15**(6), 765–770 (in Russian).

Chamis, C.C. (1979). Impetus of composite mechanics on test methods for fiber composites. In *Proc. First USA–USSR Symp. Fracture of Composite Materials*, Riga, USSR 4–7 Sept. 1978 (G.C. Sih and V.P. Tamuzh eds.). Sijthoff & Noordhoff, The Netherlands, pp. 329–348.

Chiao, T.T. (1979). Some interesting mechanical behaviors of fiber composite materials. In *Proc. 1st USA–USSR Symp. Fracture of Composite Materials*, Riga, USSR 4–7 Sept. 1978 (G.C. Sih and V.P. Tamuzh eds.). Sijthoff and Noordhoff, Alphen a/d Rijn, pp. 385–392.

Cherevatsky, A.S. (1999). Manufacturing technology of wound structures by transformation of wound preforms. In *Proc. 12th Int. Conf. on Composite Materials (ICCM-12)*, Paris, France, 5–9 July, 10p (CD-ROM).

Fukui, S., Kawata, K., Kobayashi, R., Takana, N., Hashimoto, S., Otani, N. and Hondo, A. (1966). Some theoretical and experimental studies on the width variation effects for the filament-wound cylinders. In *Proc. 6th Int. Symp. Space Techn. and Sci.*, Tokyo, pp. 467–470.

Green, A.E. and Adkins, J. E. (1960). *Large Elastic Deformations and Nonlinear Continuum Mechanics*. Oxford University Press, London.

Hann, H.T. and Tsai S.W. (1973). Nonlinear elastic behavior of unidirectional composite laminae. *J. Composite Mater.* **7**, 102–118.

Hahn, H.T. and Tsai, S.W. (1974). On the behavior of composite laminates after initial failures. *J. Composite Mater.* **8**, 288–305.

Hashin, Z. (1987). Analysis of orthogonally cracked laminates under tension. *J. Appl. Mech.* **54**, 872–879.

Herakovich, C.T. (1998). *Mechanics of Fibrous Composites*. Wiley, New York.

Ilyushin, A.A. (1948). *Plasticity*. Gostekhizdat, Moscow (in Russian).

Jones, R.M. (1977). A nonsymmetric compliance matrix approach to nonlinear multimodulus orthotropic materials. *AIAA J.* **15**(10), 1436–1443.

Lagace, P.A. (1985). Nonlinear stress-strain behavior of graphite/epoxy laminates. *AIAA J.* **223**(10), 1583–1589.

Lungren, J.-E. and Gudmundson, P. (1999). Influence of matrix cracks and swelling on moisture absorption in cross-ply GFRP laminates. In *Proc. 12th Int. Conf. on Composite Materials (ICCM-12)*, Paris, France, 5–9 July, 9p (CD-ROM).

Pagano, N.J. and Whitford, L.E. (1985). On the solution for the elastic response of involute bodies. *Composite Sci. Technol.* **22**(4), 295–317.

Reifsnaider, K.L. (1977). Some fundamental aspects of the fatigue and fracture responses of composite materials. In *Proc. 14th Annual Meeting of Society of Engineering Science*, Bethlehem, PA, pp. 343–384.

Skudra, A.M., Bulavs, F.Ya., Gurvich, M.R., and Kruklinsh, A.A. (1989). *Elements of Structural Mechanics of Composite Truss Systems*. Riga, Zinatne (in Russian).

Tarnopol'skii, Yu.M., Zhigun, I.G. and Polyakov, V.A. (1987). *Spatially Reinforced Composite Materials – Handbook*. Mashinostroenie, Moscow (in Russian).

Tarnopol'skii, Yu.M., Zhigun, I.G. and Polyakov, V.A. (1992). *Spatially Reinforced Composites*. Technomic, PA.

Tsai, S.W. and Azzi, V.D. (1966). Strength of laminated composite materials, *AIAA J.* **4**(2), 296–301.

Tsai, S.W. (1987). *Composite Design*, 3rd edn., Think Composites, Dayton.

Vasiliev, V.V. and Elpatievskii, A.N. (1967). Deformation of tape-wound cylindrical shells under internal pressure. *J. Polymer Mech.* **3**(5), 604–607.

Vasiliev, V.V., Dudchenko, A.A. and Elpatievskii, A.N. (1970). Analysis of the tensile deformation of glass-reinforced plastics. *J. Polymer Mech.* **6**(1), 127–130.

Vasiliev, V.V. and Salov, V.A. (1984). Development and examination of a two-matrix glass–fiber composite with high transverse strain. *J. Mech. of Composite Mater.* **20**(4), 463–467.

Vasiliev, V.V. and Morozov, E.V. (1988). Applied theory of spatially reinforced composite shells. *J. Mech. of Composite Mater.* **24**(3), 393–400.

Vasiliev, V.V. and Tarnopol'skii, Yu.M. (eds.) (1990). *Composite Materials. Handbook*. Mashinostroenie, Moscow (in Russian).

Vasiliev, V.V. (1993). *Mechanics of Composite Structures*. Taylor & Francis, Washington.

Vasiliev, V.V., Salov, V.A. and Salov, O.V. (1998). *Patent of Russian Federation*, No. 2111120.

Verchery, G. (1999). Designing with anisotropy. Part 1: Methods and general results for laminates. In *Proc. 12th Int. Conf. on Composite Mater. (ICCM-12)*, Paris, France, 5–9 July, 11p (CD-ROM).

Verchery, G. and Gong, X.J. Pure tension with off-axis tests for orthotropic laminates. In *Proc. 12th Int. Conf. on Composite Materials (ICCM-12)*, Paris, France, 5 9 July, 7p (CD-ROM).

Chapter 5

MECHANICS OF LAMINATES

A typical composite structure consists of a system of layers bonded together. The layers can be made of different isotropic or anisotropic materials, and have different structures (see Chapter 4), thicknesses, and mechanical properties. In contrast to typical layers which are described in Chapter 4 and whose basic properties are determined experimentally, the laminate characteristics are usually calculated using the information concerning the number of layers, their stacking sequence, geometric and mechanical properties which should be known. A finite number of layers can be combined to form so many laminates that the idea to study them using experimental methods does not look realistic. While the most complicated typical layer is described with nine stiffness coefficients A_{mn} ($mn = 11, 22, 12, 14, 24, 44, 55, 56, 66$), some of which can be calculated, the laminate is characterized with 21 coefficients and demonstrates coupling effects that can hardly be simulated in experiments.

Thus, the topic of this chapter is to provide equations allowing us to predict the behavior of a laminate as a system of layers with given properties. The only restriction that is imposed on the laminate as an element of a composite structure concerns its total thickness which is assumed to be much smaller than the other dimensions of the structure.

5.1. Stiffness coefficients of a generalized anisotropic layer

For the sake of brevity, consider first a thin homogeneous layer, which is anisotropic in the xy-plane and whose mechanical properties are some functions of the normal coordinate z (see Fig. 5.1). Coordinate axes x and y belong to some plane which is referred to as a reference plane such that $z = 0$ on this plane and $-e \leqslant z \leqslant s$ for the layer under study. There exist some special locations of the reference plane discussed below, but in this section its coordinates e and s are not specified. We introduce two assumptions both based on the fact that thickness $h = e + s$ is small.

First, it is assumed that the layer thickness, h, does not change under the action of stresses shown in Fig. 5.1. Actually, the thickness does change, but because it is

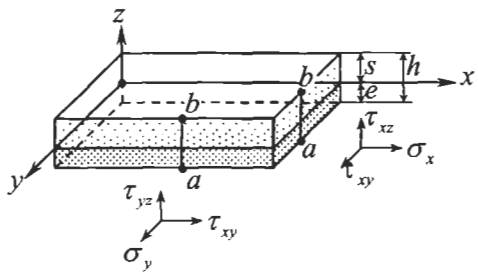

Fig. 5.1. An element of a generalized layer.

small, this change is negligible. This means that there is no strain in the z-direction, and in accordance with Eqs. (2.22),

$$\varepsilon_z = \frac{\partial u_z}{\partial z} = 0, \quad u_z = w(x,y) \ . \tag{5.1}$$

Here, $w(x,y)$ is the so-called normal deflection which is a translational displacement of a normal element a–b (see Fig. 5.1) as a solid in the z-direction.

Second, we assume that in-plane displacements u_x and u_y are linear functions of the thickness coordinate z, i.e.,

$$\begin{aligned} u_x(x,y,z) &= u(x,y) + z\theta_x(x,y), \\ u_y(x,y,z) &= v(x,y) + z\theta_y(x,y) \ , \end{aligned} \tag{5.2}$$

where u and v are the displacements of the points of the reference plane $z = 0$ or, which is the same, the translational displacements of the normal element a–b (see Fig. 5.1) as a solid in the x- and y-directions, while θ_x and θ_y are the angles of rotations (usually referred to as "rotations") of the normal element a–b in the xz- and yz-planes. Geometric interpretation of the first expression in Eqs. (5.2) is presented in Fig. 5.2.

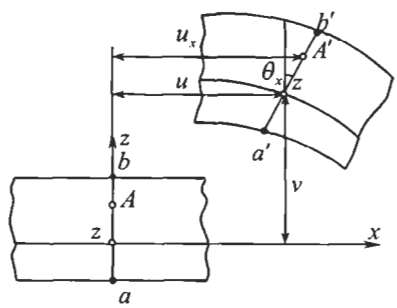

Fig. 5.2. Decomposition of displacement u_x of point A into translational (u) and rotation ($z\theta_x$) components.

In-plane strains of the layer, ε_x, ε_y, and γ_{xy}, can be found using Eqs. (2.22) and (5.1), (5.2) as

$$\begin{aligned}
\varepsilon_x &= \frac{\partial u_x}{\partial x} = \varepsilon_x^0 + z\kappa_x, \\
\varepsilon_y &= \frac{\partial u_y}{\partial y} = \varepsilon_y^0 + z\kappa_y, \\
\gamma_{xy} &= \frac{\partial u_x}{\partial y} + \frac{\partial u_y}{\partial x} = \gamma_{xy}^0 + z\kappa_{xy} \ ,
\end{aligned} \tag{5.3}$$

where

$$\begin{aligned}
&\varepsilon_x^0 = \frac{\partial u}{\partial x}, \quad \varepsilon_y^0 = \frac{\partial v}{\partial y}, \quad \gamma_{xy}^0 = \frac{\partial u}{\partial y} + \frac{\partial v}{\partial x}, \\
&\kappa_x = \frac{\partial \theta_x}{\partial x}, \quad \kappa_y = \frac{\partial \theta_y}{\partial y}, \quad \kappa_{xy} = \frac{\partial \theta_x}{\partial y} + \frac{\partial \theta_y}{\partial x} \ .
\end{aligned}$$

These generalized strains correspond to the following four basic deformations of the layer shown in Fig. 5.3:

- in-plane tension or compression (ε_x^0, ε_y^0),
- in-plane shear (γ_{xy}^0),
- bending in xz- and yz-planes (κ_x, κ_y), and
- twisting (κ_{xy}).

Constitutive equations for an anisotropic layer Eqs. (4.71), upon substitution of Eqs. (5.3) yield

$$\begin{aligned}
\sigma_x &= A_{11}\varepsilon_x^0 + A_{12}\varepsilon_y^0 + A_{14}\gamma_{xy}^0 + z(A_{11}\kappa_x + A_{12}\kappa_y + A_{14}\kappa_{xy}), \\
\sigma_y &= A_{21}\varepsilon_x^0 + A_{22}\varepsilon_y^0 + A_{24}\gamma_{xy}^0 + z(A_{21}\kappa_x + A_{22}\kappa_y + A_{24}\kappa_{xy}), \\
\tau_{xy} &= A_{41}\varepsilon_x^0 + A_{42}\varepsilon_y^0 + A_{44}\gamma_{xy}^0 + z(A_{41}\kappa_x + A_{42}\kappa_y + A_{44}\kappa_{xy}) \ ,
\end{aligned} \tag{5.4}$$

where, $A_{mn} = A_{nm}$ are the stiffness coefficients of the material that can depend, in general, on coordinate z.

As follows from Eqs. (5.4), stresses depend on six generalized strains ε, γ, and κ which are the functions of coordinates x and y only. To fulfil the derivation of constitutive equations for the layer under study, we introduce the corresponding force functions as stress resultants and couples shown in Fig. 5.4 and specified as (see also Fig. 5.1)

$$\begin{aligned}
N_x &= \int_{-e}^{s} \sigma_x \, dz, \quad N_y = \int_{-e}^{s} \sigma_y \, dz, \quad N_{xy} = \int_{-e}^{s} \tau_{xy} \, dz, \\
M_x &= \int_{-e}^{s} \sigma_x z \, dz, \quad M_y = \int_{-e}^{s} \sigma_y z \, dz, \quad M_{xy} = \int_{-e}^{s} \tau_{xy} z \, dz \ .
\end{aligned}$$

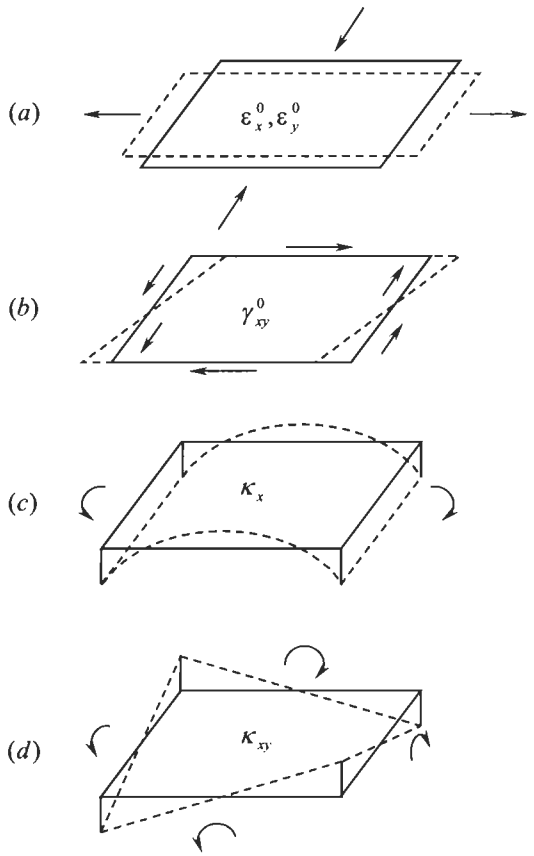

Fig. 5.3. Basic deformations of the layer: (a) in-plane tension and compression $(\varepsilon_x^0, \varepsilon_y^0)$; (b) in-plane shear (γ_{xy}^0); (c) bending (κ_x); (d) twisting (κ_{xy}).

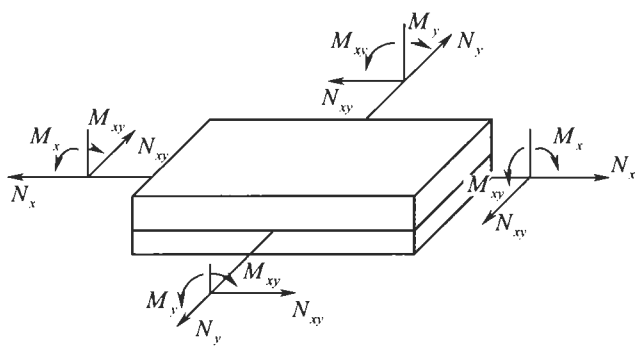

Fig. 5.4. Stress resultants and couples applied to the reference plane of the layer.

Substituting stresses in Eqs. (5.4) into these equations we arrive at constitutive equations that link stress resultants and couples with the corresponding generalized strains, i.e.,

$$\begin{aligned}
N_x &= B_{11}\varepsilon_x^0 + B_{12}\varepsilon_y^0 + B_{14}\gamma_{xy}^0 + C_{11}\kappa_x + C_{12}\kappa_y + C_{14}\kappa_{xy},\\
N_y &= B_{21}\varepsilon_x^0 + B_{22}\varepsilon_y^0 + B_{24}\gamma_{xy}^0 + C_{21}\kappa_x + C_{22}\kappa_y + C_{24}\kappa_{xy},\\
N_{xy} &= B_{41}\varepsilon_x^0 + B_{42}\varepsilon_y^0 + B_{44}\gamma_{xy}^0 + C_{41}\kappa_x + C_{42}\kappa_y + C_{44}\kappa_{xy},\\
M_x &= C_{11}\varepsilon_x^0 + C_{12}\varepsilon_y^0 + C_{14}\gamma_{xy}^0 + D_{11}\kappa_x + D_{12}\kappa_y + D_{14}\kappa_{xy},\\
M_y &= C_{21}\varepsilon_x^0 + C_{22}\varepsilon_y^0 + C_{24}\gamma_{xy}^0 + D_{21}\kappa_x + D_{22}\kappa_y + D_{24}\kappa_{xy},\\
M_{xy} &= C_{41}\varepsilon_x^0 + C_{42}\varepsilon_y^0 + C_{44}\gamma_{xy}^0 + D_{41}\kappa_x + D_{42}\kappa_y + D_{44}\kappa_{xy}\ .
\end{aligned} \tag{5.5}$$

These equations include membrane stiffness coefficients

$$B_{mn} = B_{nm} = \int_{-e}^{s} A_{mn}\,\mathrm{d}z\ , \tag{5.6}$$

which specify the layer stiffness under in-plane deformation (Figs. 5.3a and b), bending stiffness coefficients

$$D_{mn} = D_{nm} = \int_{-e}^{s} A_{mn}z^2\,\mathrm{d}z\ , \tag{5.7}$$

which are associated with the layer bending and twisting (Figs. 5.3c and d), and membrane-bending coupling coefficients

$$C_{mn} = C_{nm} = \int_{-e}^{s} A_{mn}z\,\mathrm{d}z \tag{5.8}$$

through which in-plane stress resultants are linked with bending deformations and stress couples are linked with in-plane strains.

Coefficients with subscripts 11, 12, 22, and 44 compose the basic set of the layer stiffnesses associated with in-plane extension, contraction, and shear (B_{11}, B_{12}, B_{22}, B_{44}), bending and twisting (D_{11}, D_{12}, D_{22}, D_{44}), and coupling effects (C_{11}, C_{12}, C_{22}, C_{44}). For an anisotropic layer there exist also coupling between extension (a) and shear (b) in Fig. 5.3 (coefficients B_{14}, B_{24}), extension (a) and twisting (d) in Fig. 5.3 (coefficients C_{14}, C_{24}), bending (c) and twisting (d) in Fig. 5.3 (coefficients D_{14}, D_{24}).

Forces and moments N and M specified by Eqs. (5.5) are resultants and couples of in-plane stresses σ_x, σ_y, and τ_{xy} (see Fig. 5.1). However, there exist also transverse shear stresses τ_{xz} and τ_{yz} which should be expressed in terms of the corresponding shear strains. Unfortunately, we cannot apply for this purpose the direct approach

that was used above to derive Eqs. (5.5). This approach involves strain–displacement equations, Eqs. (2.22),

$$\gamma_{xz} = \frac{\partial u_x}{\partial z} + \frac{\partial u_z}{\partial x}, \quad \gamma_{yz} = \frac{\partial u_y}{\partial z} + \frac{\partial u_z}{\partial y} \tag{5.9}$$

in conjunction with Hooke's law

$$\tau_{xz} = A_{55}\gamma_{xz} + A_{56}\gamma_{yz}, \quad \tau_{yz} = A_{65}\gamma_{xz} + A_{66}\gamma_{yz} \tag{5.10}$$

or

$$\gamma_{xz} = a_{55}\tau_{xz} + a_{56}\tau_{yz}, \quad \gamma_{yz} = a_{65}\tau_{xz} + a_{66}\tau_{yz}\ , \tag{5.11}$$

where A_{mn} and a_{mn} are stiffness and compliance coefficients, respectively. The problem is associated with Eqs. (5.2) which specify only approximate dependence of displacements u_x and u_y on coordinate z (actual distribution of u_x and u_y through the layer thickness is not known) and must not be differentiated with respect to z. So we cannot substitute Eqs. (5.2) into Eqs. (5.9) which include derivatives of u_x and u_y with respect to z. To see what can happen if we violate this well-known mathematical restriction, consider a sandwich laminate shown in Fig. 5.5. It can be seen that while linear approximation of $u(z)$ looks reasonable, derivatives of the actual and approximate displacements have little in common.

To derive constitutive equations for transverse shear, consider Fig. 5.6. Actual distribution of shear stresses τ_{xz} and τ_{yz} across the layer thickness is not known, but we can suppose that it is not important. Indeed, as follows from Eqs. (5.1), elements a–b along which the shear stresses act are absolutely rigid. This means (in accordance with the corresponding theorem of Statics of Solids) that the displacements of these elements in the z-direction depend only on resultants of the shear stresses, i.e., on transverse shear forces

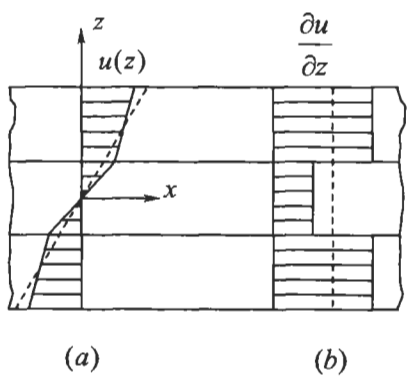

Fig. 5.5. Actual (solid lines) and approximate (broken lines) distributions of a displacement (a) and its derivative (b) through the thickness of a sandwich laminate.

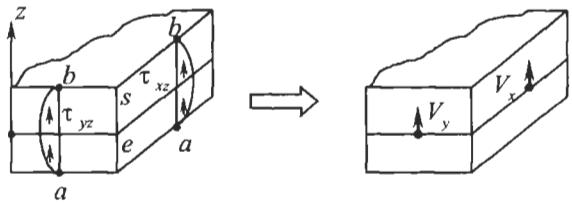

Fig. 5.6. Reduction of transverse shear stresses to stress resultants (transverse shear forces).

$$V_x = \int_{-e}^{s} \tau_{xz}\,dz, \quad V_y = \int_{-e}^{s} \tau_{yz}\,dz \ . \tag{5.12}$$

Because the particular distribution of τ_{xz} and τ_{yz} does not influence the displacements, we can introduce some average stresses having the same resultants as the actual ones, i.e.,

$$\tau_x = \frac{V_x}{h} = \frac{1}{h}\int_{-e}^{s} \tau_{xz}\,dz, \quad \tau_y = \frac{V_y}{h} = \frac{1}{h}\int_{-e}^{s} \tau_{yz}\,dz \ .$$

However, according to Eqs. (5.11), shear strains are linear combinations of shear stresses. So we can use the same law to introduce average shear strains as

$$\gamma_x = \frac{1}{h}\int_{-e}^{s} \gamma_{xz}\,dz, \quad \gamma_y = \frac{1}{h}\int_{-e}^{s} \gamma_{yz}\,dz \ . \tag{5.13}$$

Average shear strains γ_x and γ_y can be readily expressed in terms of displacements if we substitute Eqs. (5.9) into Eqs. (5.13), i.e.,

$$\gamma_x = \frac{1}{h}\left[u_x(s) - u_x(-e) + \int_{-e}^{s} \frac{\partial u_z}{\partial x}\,dz\right],$$

$$\gamma_y = \frac{1}{h}\left[u_y(s) - u_x(-e) + \int_{-e}^{s} \frac{\partial u_z}{\partial y}\,dz\right] \ .$$

These equations, in contrast to Eqs. (5.9), do not include derivatives with respect to z. So we can substitute Eqs. (5.1) and (5.2) to get the final result

$$\gamma_x = \theta_x + \frac{\partial w}{\partial x}, \quad \gamma_y = \theta_y + \frac{\partial w}{\partial y} \ . \tag{5.14}$$

Consider Eqs. (5.10) and (5.11). Integrating them over the layer thickness and using Eqs. (5.12) and (5.13) we get

$$V_x = \int_{-e}^{s} (A_{55}\gamma_{xz} + A_{56}\gamma_{yz})\mathrm{d}z, \quad V_y = \int_{-e}^{s} (A_{65}\gamma_{xz} + A_{66}\gamma_{yz})\mathrm{d}z,$$

$$\gamma_x = \frac{1}{h}\int_{-e}^{s} (a_{55}\tau_{xz} + a_{56}\tau_{yz})\mathrm{d}z, \quad \gamma_y = \frac{1}{h}\int_{-e}^{s} (a_{65}\tau_{xz} + a_{66}\tau_{yz})\mathrm{d}z \ .$$

Because the actual distribution of stresses and strains according to the foregoing reasoning is not significant, we can change them for the corresponding average stresses and strains:

$$V_x = S_{55}\gamma_x + S_{56}\gamma_y, \quad V_y = S_{65}\gamma_x + S_{66}\gamma_y \ , \tag{5.15}$$

$$\gamma_x = s_{55}V_x + s_{56}V_y, \quad \gamma_y = s_{65}V_x + s_{66}V_y \ , \tag{5.16}$$

where

$$S_{mn} = S_{nm} = \int_{-e}^{s} A_{mn}\,\mathrm{d}z \ , \tag{5.17}$$

$$s_{mn} = s_{nm} = \frac{1}{h^2}\int_{-e}^{s} a_{mn}\,\mathrm{d}z \ . \tag{5.18}$$

It should be emphasized that Eqs. (5.16) are not the inverse form of Eqs. (5.15). Indeed, solving Eqs. (5.16), using Eqs. (5.18) and taking into account that

$$a_{55} = \bar{A}_{66}, \quad a_{56} = -\bar{A}_{56}, \quad a_{66} = \bar{A}_{55},$$

$$\bar{A}_{mn} = \frac{A_{mn}}{A_{55}A_{66} - A_{56}^2} \ ,$$

we arrive at Eqs. (5.15) in which

$$S_{mn} = \frac{h^2 \int_{-e}^{s} \bar{A}_{mn}\,\mathrm{d}z}{\left(\int_{-e}^{s} \bar{A}_{55}\,\mathrm{d}z\right)\left(\int_{-e}^{s} \bar{A}_{66}\,\mathrm{d}z\right) - \left(\int_{-e}^{s} \bar{A}_{56}\,\mathrm{d}z\right)^2} \ . \tag{5.19}$$

These expressions, in general, do not coincide with Eqs. (5.17).

Thus, the constitutive equations for transverse shear are specified by Eqs. (5.15), and there exist two, in general different, approximate forms of stiffness coefficients – Eqs. (5.17) and (5.19). The fact that equations obtained in this way are approximate is quite natural because the assumed displacement field, Eqs. (5.1) and (5.2), is also approximate.

To compare two possible forms of constitutive equations for transverse shear, consider for the sake of brevity an orthotropic layer for which

$$A_{56} = 0, \quad a_{56} = 0, \quad A_{55} = G_{xz}, \quad A_{66} = G_{yz},$$
$$a_{55} = \tilde{A}_{66} = \frac{1}{G_{xz}}, \quad a_{66} = \tilde{A}_{55} = \frac{1}{G_{yz}} .$$

For transverse shear in the xz-plane Eqs. (5.15) yield

$$V_x = S_{55}\gamma_x , \tag{5.20}$$

where

$$S_{55} = \int_{-e}^{s} G_{xz}\,\mathrm{d}z \tag{5.21}$$

in accordance with Eq. (5.17), while Eq. (5.19) yields

$$S_{55} = \frac{h^2}{\int_{-e}^{s} \frac{\mathrm{d}z}{G_{xz}}} . \tag{5.22}$$

If the shear modulus does not depend on z, both equations, Eqs. (5.21) and (5.22), give the same result $S_{55} = G_{xz}h$.

Using the energy method applied in Section 3.3 we can show that the Eqs. (5.21) and (5.22) provide the upper and the lower bounds for the actual transverse shear stiffness. Indeed, consider a strip with unit width experiencing transverse shear induced by force V_x as in Fig. 5.7. Assume that Eq. (5.20) links the actual force V_x with the actual angle $\gamma_x = \Delta/l$ through the actual shear stiffness S_{55} which we do not know and which we would like to evaluate. To do this, we can use two variational principles described in Section 2.11. According to the principle of minimum total potential energy

$$T_{\mathrm{act}} \leqslant T_{\mathrm{adm}} , \tag{5.23}$$

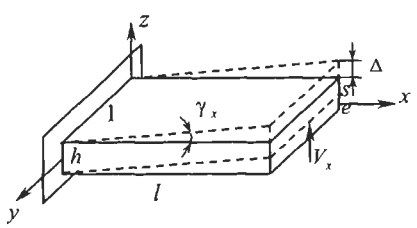

Fig. 5.7. Transverse shear of a strip with unit width.

where

$$T_{\text{act}} = U^{\varepsilon}_{\text{act}} - A_{\text{act}}, \quad T_{\text{adm}} = U^{\varepsilon}_{\text{adm}} - A_{\text{adm}}$$

are the total energies of the actual state and some admissible kinematic state expressed in terms of the strain energy, U, and work A performed by force V_x on displacement Δ (see Fig. 5.7). For both states

$$A_{\text{act}} = A_{\text{adm}} = V_x \Delta$$

and condition (5.23) reduces to

$$U^{\varepsilon}_{\text{act}} \leqslant U^{\varepsilon}_{\text{adm}} \ . \tag{5.24}$$

For the actual state, with due regard to Eq. (5.20) we get

$$U_{\text{act}} = \frac{l}{2} V_x \gamma_x = \frac{l}{2} S_{55} \gamma_x^2 \ . \tag{5.25}$$

For the admissible state, we should use the following general equation:

$$U = \frac{1}{2} \int_0^l \mathrm{d}x \int_{-e}^{s} \tau_{xz} \gamma_{xz} \, \mathrm{d}z = \frac{1}{2} \int_0^l \mathrm{d}x \int_{-e}^{s} G_{xz} \gamma_{xz}^2 \, \mathrm{d}z = U^{\varepsilon}$$

and admit some approximation for γ_{xz}. The simplest one is $\gamma_{xz} = \gamma_x$, so that

$$U^{\varepsilon}_{\text{adm}} = \frac{l}{2} \gamma_x^2 \int_{-e}^{s} G_{xz} \, \mathrm{d}z \ . \tag{5.26}$$

Then, Eqs. (5.24)–(5.26) yield

$$S_{55} \leqslant \int_{-e}^{s} G_{xz} \, \mathrm{d}z \ .$$

Comparing this inequality with Eq. (5.21) we can conclude that this equation specifies the upper bound for S_{55}.

To determine the lower bound, we should apply the principle of minimum strain energy according to which

$$U_{\text{act}} \leqslant U^{\sigma}_{\text{adm}} \ , \tag{5.27}$$

where

$$U_{\text{act}} = \frac{l}{2} V_x \gamma_x = \frac{l}{2} \frac{V_x^2}{S_{55}} \ .$$

For the admissible state we should apply

$$U = \frac{1}{2}\int_0^l \mathrm{d}x \int_{-e}^{s} \tau_{xz}\gamma_{xz}\,\mathrm{d}z = \frac{1}{2}\int_0^l \mathrm{d}x \int_{-e}^{s} \frac{\tau_{xz}^2}{G_{xz}}\,\mathrm{d}z = U^{\sigma}$$

and use some admissible distribution for τ_{xz}. The simplest approximation is $\tau_{xz} = V_x/h$ so that

$$U^{\sigma}_{\mathrm{adm}} = \frac{l}{2h^2} V_x^2 \int_{-e}^{s} \frac{\mathrm{d}z}{G_{xz}} \ .$$

Substitution into condition (5.27) yields

$$S_{55} \geqslant \frac{h^2}{\int_{-e}^{s} \frac{\mathrm{d}z}{G_{xz}}} \ .$$

Thus, Eq. (5.22) provides the lower bound for S_{55}, and the actual stiffness satisfies the following inequality:

$$\frac{h^2}{\int_{-e}^{s} \frac{\mathrm{d}z}{G_{xz}}} \leqslant S_{55} \leqslant \int_{-e}^{s} G_{xz}\,\mathrm{d}z \ .$$

So, constitutive equations for the generalized layer under study are specified with Eqs. (5.5) and (5.15). Stiffness coefficients that are given by Eqs. (5.6)–(5.8), and (5.17) or (5.19) can be written in a form more suitable for calculations. To do this, introduce new coordinate $t = z + e$ such that $0 \leqslant t \leqslant h$ (see Fig. 5.8). Transforming the integrals to this new variable we get

$$B_{mn} = I^{(0)}_{mn}, \quad C_{mn} = I^{(1)}_{mn} - eI^{(0)}_{mn}, \quad D_{mn} = I^{(2)}_{mn} - 2eI^{(1)}_{mn} + e^2 I^{(0)}_{mn} \ , \tag{5.28}$$

where $mn = 11, 12, 22, 14, 24, 44$ and

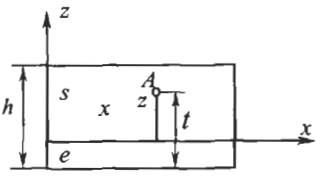

Fig. 5.8. Coordinates of an arbitrary point A.

$$I_{mn}^{(r)} = \int_0^h A_{mn} t^r \, dt, \quad r = 0, 1, 2 \ . \tag{5.29}$$

Transverse shear stiffnesses, Eqs. (5.17) and (5.19), acquire the form

$$S_{mn} = I_{mn}^{(0)} \tag{5.30}$$

and

$$S_{mn} = \frac{h^2 \bar{I}_{mn}^{(0)}}{\bar{I}_{55}^{(0)} \bar{I}_{66}^{(0)} - (\bar{I}_{56}^{(0)})^2} \ , \tag{5.31}$$

where $mn = 55, 56, 66$ and

$$\bar{I}_{mn}^{(0)} = \int_0^h \bar{A}_{mn} \, dt \ . \tag{5.32}$$

5.2. Stiffness coefficients of a homogeneous layer

Consider a layer whose material stiffness coefficients A_{mn} do not depend on coordinate z. Then

$$I_{mn}^{(r)} = \frac{A_{mn}}{r+1} h^{r+1}, \quad \bar{I}_{mn}^{(0)} = \bar{A}_{mn} h \ , \tag{5.33}$$

and Eqs. (5.28), (5.30), and (5.31) yield the following stiffness coefficients of the layer:

$$\begin{aligned} &B_{mn} = A_{mn} h, \quad C_{mn} = A_{mn} \left(\frac{h}{2} - e \right), \\ &D_{mn} = A_{mn} \left(\frac{h^3}{3} - eh + e^2 \right), \quad S_{mn} = A_{mn} h \ . \end{aligned} \tag{5.34}$$

Both Eqs. (5.30) and (5.31) give the same result for S_{mn}. As follows from the second of these equations, membrane-bending coupling coefficients C_{mn} become equal to zero if we take $e = h/2$, i.e., if the reference plane coincides with the middle plane of the layer shown in Fig. 5.9. In this case, Eqs. (5.5) and (5.15) acquire the following de-coupled form:

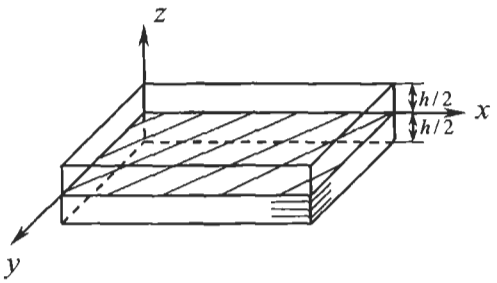

Fig. 5.9. Middle plane of a laminate.

$$
\begin{aligned}
&N_x = B_{11}\varepsilon_x^0 + B_{12}\varepsilon_y^0 + B_{14}\gamma_{xy}^0, \quad N_y = B_{21}\varepsilon_x^0 + B_{22}\varepsilon_y^0 + B_{24}\gamma_{xy}^0,\\
&N_{xy} = B_{41}\varepsilon_x^0 + B_{42}\varepsilon_y^0 + B_{44}\gamma_{xy}^0,\\
&M_x = D_{11}\kappa_x + D_{12}\kappa_y + D_{14}\kappa_{xy}, \quad M_y = D_{21}\kappa_x + D_{22}\kappa_y + D_{24}\kappa_{xy},\\
&M_{xy} = D_{41}\kappa_x + D_{42}\kappa_y + D_{44}\kappa_{xy},\\
&V_x = S_{55}\gamma_x + S_{56}\gamma_y, \quad V_y = S_{65}\gamma_x + S_{66}\gamma_y \ .
\end{aligned}
\tag{5.35}
$$

As can be seen, we have arrived at three independent groups of constitutive equations for in-plane stressed state of the layer, bending and twisting, and transverse shear. Stiffness coefficients, Eqs. (5.34), become

$$
B_{mn} = A_{mn}h, \quad D_{mn} = \frac{A_{mn}}{12}h^3, \quad S_{mn} = A_{mn}h \ . \tag{5.36}
$$

For an orthotropic layer, there are no in-plane stretching-shear coupling ($B_{14} = B_{24} = 0$) and transverse shear coupling ($S_{56} = 0$). Then, Eqs. (5.35) reduce to

$$
\begin{aligned}
&N_x = B_{11}\varepsilon_x^0 + B_{12}\varepsilon_y^0, \quad N_y = B_{21}\varepsilon_x^0 + B_{22}\varepsilon_y^0, \quad N_{xy} = B_{44}\gamma_{xy}^0,\\
&M_x = D_{11}\kappa_x + D_{12}\kappa_y, \quad M_y = D_{21}\kappa_x + D_{22}\kappa_y, \quad M_{xy} = D_{44}\kappa_{xy},\\
&V_x = S_{55}\gamma_x, \quad V_y = S_{66}\gamma_y \ .
\end{aligned}
\tag{5.37}
$$

In terms of engineering elastic constants material stiffness coefficients of an orthotropic layer can be expressed as

$$
\begin{aligned}
&A_{11} = \bar{E}_x, \quad A_{12} = \nu_{xy}\bar{E}_x, \quad A_{22} = \bar{E}_y, \quad A_{44} = G_{xy},\\
&A_{55} = G_{xz}, \quad A_{66} = G_{yz} \ ,
\end{aligned}
\tag{5.38}
$$

where $\bar{E}_{x,y} = E_{x,y}/(1 - \nu_{xy}\nu_{yx})$. Then, Eqs. (5.36) yield

$$
\begin{aligned}
&B_{11} = \bar{E}_x h, \quad B_{12} = \nu_{xy}\bar{E}_x h, \quad B_{22} = \bar{E}_y h, \quad B_{44} = G_{xy} h, \\
&D_{11} = \frac{1}{12}\bar{E}_x h^3, \quad D_{12} = \frac{\nu_{xy}}{12}\bar{E}_x h^3, \quad D_{22} = \frac{1}{12}\bar{E}_y h^3, \quad D_{44} = \frac{1}{12} G_{xy} h^3, \\
&S_{55} = G_{xz} h, \quad S_{66} = G_{yz} h \ .
\end{aligned} \tag{5.39}
$$

Finally, for an isotropic layer, we have

$$
E_x = E_y = E, \quad \nu_{xy} = \nu_{yx} = \nu, \quad G_{xy} = G_{xz} = G_{yz} = G = \frac{E}{2(1+\nu)}
$$

and

$$
\begin{aligned}
&B_{11} = B_{22} = \bar{E}h, \quad B_{12} = \nu\bar{E}h, \quad B_{44} = S_{55} = S_{66} = Gh, \\
&D_{11} = D_{22} = \frac{1}{12}\bar{E}h^3, \quad D_{12} = \frac{\nu}{12}\bar{E}h^3, \quad D_{44} = \frac{1}{12} G h^3 \ ,
\end{aligned} \tag{5.40}
$$

where $\bar{E} = E/(1-\nu^2)$.

5.3. Stiffness coefficients of a laminate

Consider a general case, i.e., a laminate consisting of an arbitrary number of layers with different thicknesses h_i and stiffnesses $A_{mn}^{(i)}$ $(i = 1, 2, 3, \ldots, k)$. Location of an arbitrary ith layer of the laminate is specified by coordinate t_i, which is the distance from the bottom plane of the laminate to the top plane of the ith layer (see Fig. 5.10). Assuming that material stiffness coefficients do not change within the thickness of the layer and using piece-wise integration we can write parameter I_{mn} in Eqs. (5.29) and (5.32) as

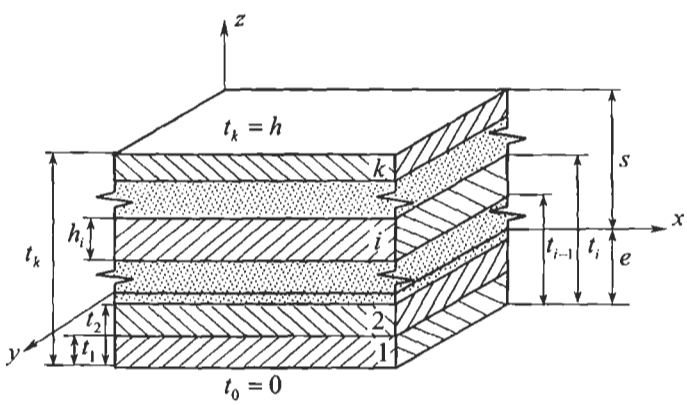

Fig. 5.10. Structure of the laminate.

$$I_{mn}^{(r)} = \frac{1}{r+1}\sum_{i=1}^{k} A_{mn}^{(i)}(t_i^{r+1} - t_{i-1}^{r+1}), \quad \bar{I}_{mn}^{(0)} = \sum_{i=1}^{k} \bar{A}_{mn}^{(i)}(t_i - t_{i-1}) \ , \tag{5.41}$$

where $r = 0, 1, 2$ and $t_0 = 0$, $t_k = h$ (see Fig. 5.10). For thin layers, Eqs. (5.41) can be reduced to the following form, which is more suitable for calculations:

$$\begin{aligned} &I_{mn}^{(0)} = \sum_{i=1}^{k} A_{mn}^{(i)} h_i, \quad \bar{I}_{mn}^{(0)} = \sum_{i=1}^{k} \bar{A}_{mn}^{(i)} h_i, \\ &I_{mn}^{(1)} = \frac{1}{2}\sum_{i=1}^{k} A_{mn}^{(i)} h_i(t_i + t_{i-1}), \quad I_{mn}^{(2)} = \frac{1}{3}\sum_{i=1}^{k} A_{mn}^{(i)} h_i(t_i^2 + t_i t_{i-1} + t_{i-1}^2) \ , \end{aligned} \tag{5.42}$$

where $h_i = t_i - t_{i-1}$ is the thickness of the ith layer.

Thus, membrane, coupling, and bending stiffness coefficients of the laminate are specified with Eqs. (5.28) and (5.42). Consider transverse shear stiffnesses which have two different forms determined by Eqs. (5.30) and (5.31). Because both equations coincide for a homogeneous layer (see Section 5.2), we can expect that the difference shows itself in laminates consisting of layers with different transverse shear stiffnesses. The laminate for which this difference is the most pronounced is a sandwich structure with metal facings (inner and outer layers) and a foam core (middle layer) that has very low shear stiffness. For such a sandwich, experimentally found transverse shear stiffness is $S = 389$ kN/m (Aleksandrov et al., 1960), while Eqs. (5.30) and (5.31) yield, respectively, $S = 37200$ kN/m and $S = 383$ kN/m. Thus, Eq. (5.31) provides much more accurate result for sandwich structures. This conclusion is also valid for composite laminates (Chen and Tsai, 1996).

A particular case, important for applications, is an orthotropic laminate for which Eqs. (5.5) and (5.15) acquire the form:

$$\begin{aligned} N_x &= B_{11}\varepsilon_x^0 + B_{12}\varepsilon_y^0 + C_{11}\kappa_x + C_{12}\kappa_y, \\ N_y &= B_{21}\varepsilon_x^0 + B_{22}\varepsilon_y^0 + C_{12}\kappa_x + C_{22}\kappa_y, \\ N_{xy} &= B_{44}\gamma_{xy}^0 + C_{44}\kappa_{xy}, \\ M_x &= C_{11}\varepsilon_x^0 + C_{12}\varepsilon_y^0 + D_{11}\kappa_x + D_{12}\kappa_y, \\ M_y &= C_{21}\varepsilon_x^0 + C_{22}\varepsilon_y^0 + D_{21}\kappa_x + D_{22}\kappa_y, \\ M_{xy} &= C_{44}\gamma_{xy}^0 + D_{44}\kappa_{xy}, \\ V_x &= S_{55}\gamma_x, \\ V_y &= S_{66}\gamma_y \ , \end{aligned} \tag{5.43}$$

where, membrane, coupling, and bending stiffnesses, B_{mn}, C_{mn}, and D_{mn}, are specified by Eqs. (5.28) and (5.42), while transverse shear stiffnesses are

$$S_{mm} = \frac{h^2}{\sum_{i=1}^{k} \frac{h_i}{A_{mm}^{(i)}}} \quad . \tag{5.44}$$

Laminates composed of unidirectional plies have special stacking-sequence notations. For example, notation $[0_2^\circ/+45^\circ/-45^\circ/90_2^\circ]$ means that the laminate consists of 0° layer having two plies, ±45° angle-ply layer, and 90° layer also having two plies. Notation $[0^\circ/90^\circ]_5$ means that the laminate has five cross-ply layers.

5.4. Quasi-homogeneous laminates

Some typical layers considered in Chapter 4 were actually quasi-homogeneous laminates (see Sections 4.4, and 4.5), but being composed of a number of identical plies, they were treated as homogeneous layers. The accuracy of this assumption is evaluated below.

5.4.1. Laminate composed of identical homogeneous layers

Consider a laminate composed of layers with different thicknesses but the same stiffnesses, i.e., such that $A_{mn}^{(i)} = A_{mn}$ for all $i = 1, 2, 3, \ldots k$. Then, Eqs. (5.29) and (5.32) yield

$$I_{mn}^{(r)} = \frac{A_{mn}}{r+1} h^{r+1}, \quad \bar{I}_{mn}^{(0)} = \bar{A}_{mn} h \quad .$$

This result coincides with Eqs. (5.33), which means that the laminate consisting of the layers with the same mechanical properties is a homogeneous laminate (layer) studied in Section 5.2.

5.4.2. Laminate composed of inhomogeneous orthotropic layers

Let the laminate have the structure $[0^\circ/90^\circ]_p$, where $p = 1, 2, 3, \ldots$ specifies the number of elementary cross-ply couples of 0° and 90° plies. In Section 4.4, this laminate was treated as a homogeneous layer with material stiffness coefficients specified by Eqs. (4.100). Taking $\bar{h}_0 = \bar{h}_{90} = 0.5$ in these equations we get

$$A_{11} = A_{22} = \tfrac{1}{2}(\bar{E}_1 + \bar{E}_2), \quad A_{12} = \bar{E}_1 \nu_{12}, \quad A_{44} = G_{12} \quad . \tag{5.45}$$

In accordance with Eqs. (5.36), stiffness coefficients of this layer should be

$$B_{mn}^0 = A_{mn} h, \quad C_{mn}^0 = 0, \quad D_{mn}^0 = \tfrac{1}{12} A_{mn} h^3 \quad . \tag{5.46}$$

To calculate the actual stiffnesses of the laminate, we should put $h_i = \delta$, $t_i = i\delta$, $k = 2p$, $e = h/2$, and $h = 2p\delta$ (see Fig. 5.10), where δ is the thickness of a unidirectional ply. Then, Eqs. (5.28) and (5.42) yield

$$B_{mn} = I^{(0)}_{mn}, \quad C_{mn} = I^{(1)}_{mn} - p\delta I^{(0)}_{mn}, \quad D_{mn} = I^{(2)}_{mn} - 2p\delta I^{(1)}_{mn} + p^2\delta^2 I^{(0)}_{mn} , \tag{5.47}$$

where

$$\begin{aligned}
&I^{(0)}_{11} = I^{(0)}_{22} = p\delta\bar{E}_1(1+\alpha) = \frac{h}{2}\bar{E}_1(1+\alpha), \quad I^{(0)}_{12} = 2p\delta\,\bar{E}_1\nu_{12} = \bar{E}_1\nu_{12}h,\\
&I^{(0)}_{44} = 2p\delta G_{12} = G_{12}h, \quad I^{(1)}_{11} = \frac{\delta^2}{2}\bar{E}_1\sum_{j=1}^{p}[4j(1+\alpha) - (3+\alpha)],\\
&I^{(1)}_{22} = \frac{\delta^2}{2}\bar{E}_1\sum_{j=1}^{p}[4j(1+\alpha) - (3\alpha+1)], \quad I^{(1)}_{12} = \frac{1}{2}E_1\nu_{12}h^2,\\
&I^{(1)}_{44} = \frac{1}{2}G_{12}h^2,\\
&I^{(2)}_{11} = \frac{\delta^3}{3}\bar{E}_1\sum_{j=1}^{p}[12j^2(1+\alpha) - 6j(3+\alpha) + 7 + \alpha],\\
&I^{(2)}_{22} = \frac{\delta^3}{3}\bar{E}_1\sum_{j=1}^{p}[12j^2(1+\alpha) - 6j(3\alpha+1) + 7\alpha + 1],\\
&I^{(2)}_{12} = \frac{1}{3}\bar{E}_1\nu_{12}h^3, \quad I^{(2)}_{44} = \frac{1}{3}G_{12}h^3 ,
\end{aligned} \tag{5.48}$$

where $\alpha = E_2/E_1$.

Matching Eqs. (5.45), (5.46) and (5.47), (5.48) we can see that $B_{mn} = B^0_{mn}$, i.e., membrane stiffnesses are the same for both models of the laminate. Coupling and bending stiffnesses are also the same for $mn = 12, 44$. There is no difference between the models for $\alpha = 1$ because the laminate reduces in this case to a homogeneous layer.

Summing up the series in Eqs. (5.48) and using Eqs. (5.47) we arrive at

$$\begin{aligned}
&C_{11} = -C_{22} = \tfrac{1}{2}\bar{E}_1\delta^2 p(\alpha - 1), \quad C_{12} = C_{44} = 0,\\
&D_{11} = D_{22} = \tfrac{1}{3}\bar{E}_1\delta^3 p^3(1+\alpha), \quad D_{12} = D^0_{12}, \quad D_{44} = D^0_{44} .
\end{aligned} \tag{5.49}$$

Taking into account that in accordance with Eqs. (5.46) and accepted notations

$$D^0_{11} = D^0_{22} = \tfrac{1}{3}\bar{E}_1\delta^3 p^3(1+\alpha) ,$$

we can conclude that the only difference between the homogeneous and the laminated models is associated with coupling coefficients C_{11} and C_{22} which are

equal to zero for the homogeneous model and are specified by Eqs. (5.49) for the laminated one. Because $p\delta = h/2$, we can write these coefficients in the form

$$C_{11} = -C_{22} = \tfrac{1}{4}\bar{E}_1 h\delta(1+\alpha)$$

showing that $C_{mn} \to 0$ for $\delta \to 0$.

5.4.3. *Laminate composed of angle-ply layers*

Consider a laminate with the structure $[+\phi/-\phi]_p$, where p is the number of layers each consisting of $+\phi$ and $-\phi$ unidirectional plies. Constitutive equations (5.5) for this laminate are

$$\begin{aligned}
N_x &= B_{11}\varepsilon_x^0 + B_{12}\varepsilon_y^0 + C_{14}\kappa_{xy},\\
N_y &= B_{21}\varepsilon_x^0 + B_{22}\varepsilon_y^0 + C_{24}\kappa_{xy},\\
N_{xy} &= B_{44}\gamma_{xy}^0 + C_{41}\kappa_x + C_{42}\kappa_y,\\
M_x &= C_{14}\gamma_{xy}^0 + D_{11}\kappa_x + D_{12}\kappa_y,\\
M_y &= C_{24}\gamma_{xy}^0 + D_{21}\kappa_x + D_{22}\kappa_y,\\
M_{xy} &= C_{41}\varepsilon_x^0 + C_{42}\varepsilon_y^0 + D_{44}\kappa_{xy}\ ,
\end{aligned} \tag{5.50}$$

where

$$B_{mn} = A_{mn}h, \quad C_{mn} = -\frac{1}{2}A_{mn}h\delta, \quad D_{mn} = \frac{1}{12}A_{mn}h^3\ ,$$

where, h is the laminate thickness, δ the ply thickness, and A_{mn} are material stiffness coefficients specified by Eqs. (4.72). As can be seen, the laminate is anisotropic because $+\phi$ and $-\phi$ plies are located in different planes. Homogeneous model of the laminate ignores this fact and yields $C_{14} = C_{24} = 0$. Calculations show that these coefficients, not being actually equal to zero, practically do not influence the laminate behavior for $h/\delta \geqslant 20$.

Laminates in which any ply or layer with orientation angle $+\phi$ is accompanied by the same ply or layer but with angle $-\phi$ are referred to as balanced laminates. Being composed of only angle-ply layers these laminates have no shear-extension coupling ($B_{14} = B_{24} = 0$), bending–stretching and shear-twisting coupling ($C_{11} = C_{12} = C_{22} = C_{44} = 0$). As follows from Eqs. (5.50), only stretching–twisting and bending-shear coupling can exist in balanced laminates. These laminates can include also 0° and 90° layers, but membrane-bending coupling can appear in such laminates.

5.5. Quasi-isotropic laminates

The layers of the laminate can be arranged in such a way that the laminate will behave as an isotropic layer under in-plane loading. Actually, the laminate is not isotropic (that is why it is called a quasi-isotropic laminate) because under transverse (normal to the laminate plane) loading and under interlaminar shear its behavior is different from that of an isotropic (e.g., metal) layer.

To derive the conditions that should be met by the structure of a quasi-isotropic laminate consider in-plane loading with stresses σ_x, σ_y, and τ_{xy} that are shown in Fig. 5.1 and induce only in-plane strains ε_x^0, ε_y^0, and γ_{xy}^0. Taking $\kappa_x = \kappa_y = \kappa_{xy} = 0$ in Eqs. (5.5) and introducing average (through the laminate thickness h) stresses as

$$\sigma_x = N_x/h, \quad \sigma_y = N_y/h, \quad \tau_{xy} = N_{xy}/h \ ,$$

we can write the first three equations of Eqs. (5.5) in the following form:

$$\begin{aligned} \sigma_x &= \bar{B}_{11}\varepsilon_x^0 + \bar{B}_{12}\varepsilon_y^0 + \bar{B}_{14}\gamma_{xy}^0, \\ \sigma_y &= \bar{B}_{21}\varepsilon_x^0 + \bar{B}_{22}\varepsilon_y^0 + \bar{B}_{24}\gamma_{xy}^0, \\ \tau_{xy} &= \bar{B}_{41}\varepsilon_x^0 + \bar{B}_{42}\varepsilon_y^0 + \bar{B}_{44}\gamma_{xy}^0 \ , \end{aligned} \tag{5.51}$$

where in accordance with Eqs. (5.28) and (5.42)

$$\bar{B}_{mn} = \sum_{i=1}^{k} A_{mn}^{(i)} \bar{h}_i, \quad \bar{h}_i = h_i/h \ , \tag{5.52}$$

where, $\bar{h}_i$ is the thickness of the ith layer normalized to the laminate thickness and A_{mn} are the stiffness coefficients specified by Eqs. (4.72). For an isotropic layer, constitutive equations analogous to Eqs. (5.51) are

$$\sigma_x = \bar{E}(\varepsilon_x^0 + \nu\varepsilon_y^0), \quad \sigma_y = \bar{E}(\varepsilon_y^0 + \nu\varepsilon_x^0), \quad \tau_{xy} = G\gamma_{xy}^0 \ , \tag{5.53}$$

where

$$\bar{E} = \frac{E}{1-\nu^2}, \quad G = \frac{E}{2(1+\nu)} = \frac{1}{2}(1-\nu)\bar{E} \ . \tag{5.54}$$

Matching Eqs. (5.51) and (5.53) we can see that shear stretching coefficients of the laminate, i.e., $\bar{B}_{14} = \bar{B}_{41}$ and $\bar{B}_{24} = \bar{B}_{42}$ should be equal to zero. As follows from Eqs. (4.72) and Section 5.4.3, this means that the laminate should be balanced, i.e., it should be composed of 0°, $\pm\phi_i$ (or ϕ_i and $\pi - \phi_i$), and 90°layers only. Because the laminate stiffness in the x- and the y-directions must be the same, we require that $\bar{B}_{11} = \bar{B}_{22}$. Using Eqs. (4.72), taking $\bar{h}_i = \bar{h}$ for all i, and performing some transformation we arrive at the following condition:

$$\sum_{i=1}^{k} \cos 2\phi_i = 0 \ .$$

As can be checked by direct substitutions, for $k = 1$ this equation is satisfied if $\phi_1 = 45°$ and for $k = 2$ if $\phi_1 = 0$ and $\phi_2 = 90°$. Naturally, such one- and two-layered materials cannot be isotropic even in one plane. So consider the case $k \geqslant 3$, for which the solution has the form

$$\phi_i = (i-1)\frac{\pi}{k}, \quad i = 1, 2, 3, \ldots, k \ . \tag{5.55}$$

Using the sums that are valid for angles specified by Eqn. (5.55) i.e.,

$$\sum_{i=1}^{k} \sin^2 \phi_i = \sum_{i=1}^{k} \cos^2 \phi_i = \frac{k}{2},$$
$$\sum_{i=1}^{k} \sin^4 \phi_i = \sum_{i=1}^{k} \cos^4 \phi_i = \frac{3k}{8},$$
$$\sum_{i=1}^{k} \sin^2 \phi_i \cos^2 \phi_i = \frac{k}{8} \ ,$$

and calculating stiffness coefficients in Eqs. (5.52) and (4.72) we get

$$\bar{B}_{11} = \bar{B}_{12} = \tfrac{1}{8}[3(\bar{E}_1 + \bar{E}_2) + 2(\bar{E}_1 \nu_{12} + 2G_{12})],$$
$$\bar{B}_{12} = \tfrac{1}{8}[\bar{E}_1 + \bar{E}_2 + 2(3\bar{E}_1 \nu_{12} - 2G_{12})],$$
$$\bar{B}_{44} = \tfrac{1}{8}[\bar{E}_1 + \bar{E}_2 - 2(\bar{E}_1 \nu_{12} - 2G_{12})] \ .$$

These stiffnesses provide constitutive equations in the form of Eqs. (5.53) and satisfy conditions (5.54) which can be written as

$$\bar{B}_{11} = \bar{B}_{22} = \frac{E}{1-\nu^2}, \quad \bar{B}_{44} = \frac{E}{2(1+\nu)}$$

if

$$E = \frac{(\bar{E}_1 + \bar{E}_2 + 2\bar{E}_1\nu_{12})(\bar{E}_1 + \bar{E}_2 - 2\bar{E}_1\nu_{12} + 4G_{12})}{3(\bar{E}_1 + \bar{E}_2) + 2(\bar{E}_1\nu_{12} + 2G_{12})},$$
$$\nu = \frac{\bar{E}_1 + \bar{E}_2 + 2(3\bar{E}_1\nu_{12} - 2G_{12})}{3(\bar{E}_1 + \bar{E}_2) + 2(\bar{E}_1\nu_{12} + 2G_{12})} \ . \tag{5.56}$$

Possible solutions (5.55) providing quasi-isotropic properties of the laminates with different number of layers are listed in Table 5.1 for $k \leqslant 6$.

All quasi-isotropic laminates having different structures determined by Eqn. (5.55) for a given number of layers, k, possess the same apparent modulus and Poisson's ratio specified by Eqs. (5.56). For typical advanced composites with properties listed in Table 3.5, these characteristics are presented in Table 5.2.

As follows from Tables 5.2 and 1.1, specific stiffness of quasi-isotropic composites with carbon and boron fibers exceeds the corresponding characteristic of traditional isotropic structural materials – steel, aluminum, and titanium.

5.6. Symmetric laminates

Symmetric laminates are composed of layers that are symmetrically arranged with respect to the laminate middle plane shown in Fig. 5.9. To study general properties of symmetric laminates, consider Eqs. (5.28) and (5.29) and apply them to calculate stiffness coefficients with some combination of subscripts, e.g., $m = 1$ and $n = 1$. Because coordinate of the reference plane, e, is an arbitrary parameter, we can find it from the condition $C_{11} = 0$. Then,

$$e = \frac{I_{11}^{(1)}}{I_{11}^{(0)}} \tag{5.57}$$

Table 5.1
Angles providing quasi-isotropic properties of the laminates.

Number of layers, k	Orientation angle of the ith layer					
	ϕ_1°	ϕ_2°	ϕ_3°	ϕ_4°	ϕ_5°	ϕ_6°
3	0	60	120			–
4	0	45	90	135	–	–
5	0	36	72	108	144	–
6	0	30	60	90	120	150

Table 5.2
Modulus of elasticity and Poisson's ratio of quasi-isotropic laminates made of typical advanced composites.

Property	Glass–epoxy	Carbon–epoxy	Aramid–epoxy	Boron–epoxy	Boron–Al
Modulus, E, GPa	27.0	54.8	34.8	80.3	183.1
Poisson's ratio, ν	0.34	0.31	0.33	0.33	0.28
Specific modulus, $k_E \times 10^3$, m	1290	3530	2640	3820	6910

and

$$D_{11} = I_{11}^{(2)} - \left[\frac{(I_{11}^{(1)})^2}{I_{11}^{(0)}}\right] . \tag{5.58}$$

Introduce a new coordinate of an arbitrary point A in Fig. 5.11 as $z = t - (h/2)$. Changing t for z we can present Eq. (5.29) in the form

$$I_{11}^{(r)} = \int_{-h/2}^{h/2} A_{11}\left(\frac{h}{2}+z\right)^r \mathrm{d}z .$$

Substituting these integrals into Eqs. (5.57) and (5.58) we get

$$e = \frac{h}{2} + \frac{J_{11}^{(1)}}{J_{11}^{(0)}} \tag{5.59}$$

and

$$D_{11} = J_{11}^{(2)} - \left[\frac{(J_{11}^{(1)})^2}{J_{11}^{(0)}}\right] , \tag{5.60}$$

where

$$J_{11}^{(r)} = \int_{-h/2}^{h/2} A_{11} z^r \, \mathrm{d}z \tag{5.61}$$

and $r = 0, 1, 2$.

Now decompose A_{11} as a function of z into symmetric and antisymmetric components, i.e.,

$$A_{11}(z) = A_{11}^{\mathrm{s}}(z) + A_{11}^{\mathrm{a}}(z) .$$

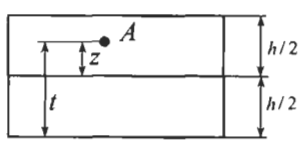

Fig. 5.11. Coordinate of point A referred to the middle plane.

Then, Eq. (5.61) yields

$$J_{11}^{(0)} = \int_{-h/2}^{h/2} A_{11}^{s}\,dz, \quad J_{11}^{(1)} = \int_{-h/2}^{h/2} A_{11}^{a} z\,dz, \quad J_{11}^{(2)} = \int_{-h/2}^{h/2} A_{11}^{s} z^2\,dz\ .$$

As can be seen from Eq. (5.60), D_{11} reaches its maximum value if $J_{11}^{(1)} = 0$ or $A_{11}^{a} = 0$ and $A_{11} = A_{11}^{s}$. In this case, Eq. (5.59) gives $e = h/2$.

Thus, symmetric laminates provide the maximum bending stiffness for a given number and mechanical properties of layers and, being referred to the middle-plane, do not have membrane-bending coupling effects. This essentially simplifies behavior of the laminate under loading and constitutive equations which have the form specified by Eqs. (5.35). For a symmetric laminate with the layer coordinates shown in Fig. 5.12, stiffness coefficients are calculated as

$$B_{mn} = 2\sum_{i-1}^{k/2} A_{mn}^{(i)}(z_i - z_{i-1}) = 2\sum_{i-1}^{k/2} A_{mn}^{(i)} h_i,$$

$$C_{mn} = 0,$$

$$D_{mn} = \frac{2}{3}\sum_{i=1}^{k/2} A_{mn}^{(i)}(z_i^3 - z_{i-1}^3) = \frac{2}{3}\sum_{i-1}^{k/2} A_{mn}^{(i)} h_i (z_i^2 + z_i z_{i-1} + z_{i-1}^2)\ .$$

The transverse shear stiffness coefficients are given by Eq. (5.31) in which

$$\bar{I}_{mn}^{(0)} = 2\sum_{i=1}^{k/2} \bar{A}_{mn}^{(i)} h_i, \quad \bar{A}_{mn}^{(i)} = \frac{A_{mn}^{(i)}}{A_{55}^{(i)} A_{66}^{(i)} - (A_{56}^{(i)})^2}\ .$$

To indicate symmetric laminates, contracted stacking-sequence notation is used, e.g., $[0°/90°/45°]_s$ instead of $[0°/90°/45°/45°/90°/0°]$.

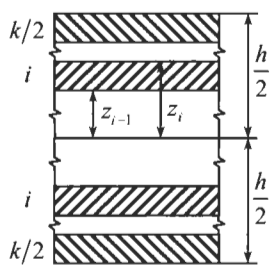

Fig. 5.12. Layer coordinates of a symmetric laminate.

5.7. Antisymmetric laminates

In antisymmetric laminates, symmetrically located layers have mutually reversed orientations. For example, while laminates $[0°/90°/90°/0°]$ and $[+\phi/-\phi/-\phi/+\phi]$ are symmetric, laminates $[0°/90°/0°/90°]$ or $[0°/0°/90°/90°]$ and $[+\phi/-\phi/+\phi/-\phi]$ are antisymmetric. In contrast to symmetric laminates which have maximum bending and zero coupling stiffness coefficients, antisymmetric laminates demonstrate pronounced coupling that can be important for some special applications (e.g., robotic parts undergoing complicated deformation under simple loading, rotor blades that twist under centrifugal forces, airplane wings twisting under bending, etc.).

The simplest antisymmetric laminate is a cross-ply layer consisting of two plies with angles 0° and 90°, and the same thickness $h/2$ (see Fig. 5.13). Taking $e = h/2$ and using Eqs. (5.28) and (5.41) we arrive at the following stiffness coefficients entering Eqs. (5.43):

$$B_{11} = B_{22} = \frac{h}{2}(\bar{E}_1 + \bar{E}_2), \quad B_{12} = \bar{E}_1 \nu_{12} h, \quad B_{44} = G_{12} h,$$

$$C_{11} = -C_{22} = \frac{h^2}{8}(\bar{E}_2 - \bar{E}_1), \quad C_{12} = 0, \quad C_{44} = 0,$$

$$D_{11} = D_{22} = \frac{h^3}{24}(\bar{E}_1 + \bar{E}_2), \quad D_{12} = \frac{h^3}{12} E_1 \nu_{12}, \quad D_{44} = \frac{h^3}{12} G_{12} \ .$$

Comparing these results with Eqs. (5.45) and (5.46) corresponding to a quasi-homogeneous cross-ply laminate we can see that the antisymmetric cross-ply laminate has the same membrane and bending stiffnesses but nonzero coupling coefficients C_{11} and C_{22}. This fact shows, in accordance with Eqs. (5.43), that in-plane tension or compression of this laminate induces bending.

As another typical example of an antisymmetric laminate, consider an angle-ply structure consisting of two plies with the same thickness $h/2$ and orientation angles $+\phi$ and $-\phi$, respectively (see Fig. 5.14). The plies (or layers) are characterized with the following stiffness coefficients:

$$A_{11}^{(1)} = A_{11}^{(2)} = A_{11}, \quad A_{12}^{(1)} = A_{12}^{(2)} = A_{12}, \quad A_{22}^{(1)} = A_{22}^{(2)} = A_{22},$$
$$A_{14}^{(1)} = -A_{14}^{(2)} = A_{14}, \quad A_{24}^{(1)} = -A_{24}^{(2)} = A_{24}, \quad A_{44}^{(1)} = A_{44}^{(2)} = A_{44} \ ,$$

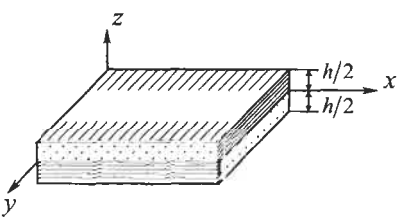

Fig. 5.13. An antisymmetric cross-ply laminate.

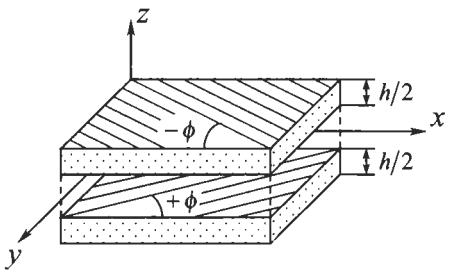

Fig. 5.14. Unbonded view of an antisymmetric angle-ply laminate.

where coefficients A_{mn} are specified by Eqs. (4.72). Taking again $e = h/2$ we arrive at constitutive equations in Eqs. (5.50) in which

$$B_{mn} = A_{mn}h, \quad C_{mn} = -\frac{h^2}{4}A_{mn}, \quad D_{mn} = \frac{h^3}{12}A_{mn} \ .$$

Comparing these coefficients with those entering Eqs. (5.50) and corresponding to a quasi-homogeneous angle-ply laminate we can conclude that the antisymmetric laminate has much more large coupling coefficients C_{14} and C_{24}, and thus much more pronounced extension-twisting coupling effect.

5.8. Sandwich structures

Sandwich structures are three-layered laminates consisting of thin facings and a light-weight honeycomb or foam core as in Figs. 5.15 and 5.16. Because in-plane stiffnesses of the facings are much higher than those of the core, while their transverse shear compliance is much lower than the same parameter of the core, the stiffness coefficients of sandwich structures are usually calculated assuming that in-plane stiffnesses of the core are equal to zero. The transverse shear stiffnesses of

Fig. 5.15. Composite sandwich panel with honeycomb core.

Fig. 5.16. Composite sandwich rings with foam core.

the facings are assumed to be infinitely high. For the laminate shown in Fig. 5.17 this means that

$$A_{mn}^{(2)} = 0, \quad mn = 11, 12, 14, 24, 44,$$
$$A_{mn}^{(1,2)} \to \infty, \quad mn = 55, 56, 66 \ .$$

As a result, coefficients in Eqs. (5.29) become

$$I_{mn}^{(r)} = \frac{1}{r+1}\left[A_{mn}^{(1)} t_1^{r-1} + A_{mn}^{(3)}(t_3^{r+1} - t_2^{r+1})\right] \ , \tag{5.62}$$

where $mn = 11, 12, 22, 14, 24, 44$. Transverse shear stiffnesses, Eqs. (5.31), for an orthotropic core, can be presented in the form

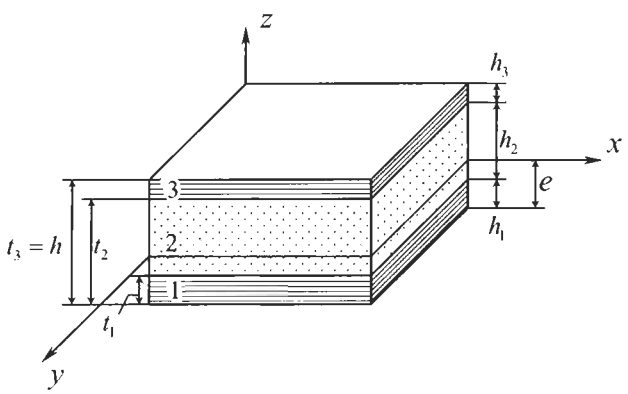

Fig. 5.17. Sandwich laminate with two laminated facings (1 and 3) and foam core (2).

$$S_{55} = \frac{h^2}{h_2} A_{55}^{(2)}, \quad S_{66} = \frac{h^2}{h_2} A_{66}^{(2)} ,$$

where $A_{55}^{(2)} = G_{xz}$ and $A_{66}^{(2)} = G_{yz}$ are shear moduli of the core.

5.9. Coordinate of the reference plane

Stiffness coefficients specified by Eqs. (5.28) include coordinate of the reference plane e (see Fig. 5.1) that, being properly pre-assigned, allows us to simplify constitutive equations for the laminate. As was shown in Sections 5.2 and 5.6, taking the middle plane as the reference plane, i.e., putting $e = h/2$, we sometimes get $C_{mn} = 0$, and constitutive equations acquire the simplest form without membrane-bending coupling terms.

Now, a natural question as to whether it is possible to reduce Eqs. (5.5) to this form in the general case arises. Taking $C_{mn} = 0$ in Eqs. (5.28) we get

$$e = \frac{I_{mn}^{(1)}}{I_{mn}^{(0)}} . \tag{5.63}$$

It is important, that the reference plane should be one and the same for all $mn = 11$, 12, 22, 14, 24, 44, and these six equations should give the same value of e. In the general case, this is not possible, so the universal reference plane providing $C_{mn} = 0$ cannot exist.

However, there are some other (in addition to the homogeneous and symmetric structures) particular laminates for which this condition can be met. For example, consider a laminate composed of isotropic layers (see Sections 4.1 and 5.2). For such laminates

$$A_{11}^{(i)} = A_{22}^{(i)} = \frac{E_i}{1 - \nu_i^2}, \quad A_{12}^{(i)} = \frac{E_i \nu_i}{1 - \nu_i^2}, \quad A_{44}^{(i)} \frac{E_i}{2(1 + \nu_i)} ,$$

and in accordance with Eqs. (5.42)

$$I_{11}^{(0)} = I_{22}^{(0)} = \sum_{i=1}^{k} \frac{E_i h_i}{1 - \nu_i^2}, \quad I_{12}^{(0)} = \sum_{i=1}^{k} \frac{E_i \nu_i h_i}{1 - \nu_i^2}, \quad I_{44}^{(0)} = \sum_{i=1}^{k} \frac{E_i h_i}{2(1 + \nu_i)},$$

$$I_{11}^{(1)} = I_{22}^{(1)} = \frac{1}{2} \sum_{i=1}^{k} \frac{E_i h_i}{1 - \nu_i^2} (t_i + t_{i-1}), \quad I_{12}^{(1)} = \frac{1}{2} \sum_{i=1}^{k} \frac{E_i \nu_i h_i}{1 - \nu_i^2} (t_i + t_{i-1}),$$

$$I_{44}^{(1)} = \frac{1}{2} \sum_{i=1}^{k} \frac{E_i h_i}{2(1 + \nu_i)} (t_i + t_{i-1}) .$$

As can be seen, these parameters, being substituted into Eqs. (5.63) do not provide one and the same value of e. But if Poisson's ratio is the same for all the layers, i.e., $\nu_i = \nu$ $(i = 1, 2, 3, \ldots, k)$ we get

$$e = \frac{\sum_{i=1}^{k} E_i h_i (t_i + t_{i-1})}{2 \sum_{i=1}^{k} E_i h_i} \ .$$

For practical analysis, this result is often used even if Poisson's ratios of the layers are different. In these cases it is approximately assumed that all the layers are characterized with some average value of Poisson's ratio, i.e.,

$$\nu = \frac{1}{h} \sum_{i=1}^{k} \nu_i h_i \ ,$$

As another example, consider a sandwich structure described in Section 5.8. In the general case, we again fail to find the desirable reference plane. However, if we assume that the facings are made of one and the same material (only the thicknesses are different), Eqs. (5.62) and (5.63) yield

$$e = \frac{h_1^2 + h_3(h_3 + 2h_1 + 2h_2)}{2(h_1 + h_3)} \ .$$

Returning to the general case we should emphasize that the reference plane providing $C_{mn} = 0$ for all mn does not exist in this case only if the laminate structure is given. If the stacking sequence of the layers is not pre-assigned and there is a sufficient number of layers, they can be arranged in such a way that $C_{mn} = 0$. Indeed, consider a laminate in Fig. 5.18 and assume that its structure is, in general, not symmetric, i.e., that $z_i' \neq z_i$ and $k' \neq k$. Using plane $z = 0$ as the reference plane we can write the membrane-bending coupling coefficients as

$$C_{mn} = \frac{1}{2} \sum_{i=1}^{k/2} A_{mn}^{(i)} h_i (z_i + z_{i-1}) - \frac{1}{2} \sum_{i'=1}^{k'/2} A_{mn}^{(i')} h_i' (z_i' + z_{i-1}') \ ,$$

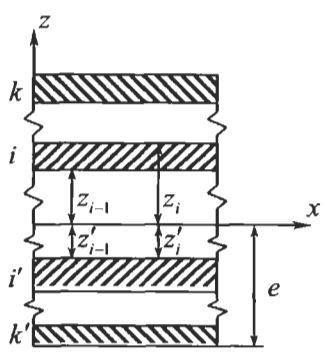

Fig. 5.18. Layer coordinates with respect to the reference plane.

where, $z_i \geqslant 0$ and $z'_i \geqslant 0$. Introduce a new layer coordinate $\bar{z}_i = (z_i + z_{i-1})/2$, which is the distance between the reference plane of the laminate and the middle plane of the i-th layer. Then, condition $C_{mn} = 0$ yields

$$\sum_{i=1}^{k/2} A_{mn}^{(i)} h_i \bar{z}_i = \sum_{i'=1}^{k'/2} A_{mn}^{(i')} h'_i \bar{z}'_i \ .$$

Now assume that we have a group of identical layers or plies with the same stiffness coefficients A_{mn} and thicknesses. For example, the laminate should include a 1.5 mm thick 0° unidirectional layer which consists of 10 plies (the thickness of an elementary ply is 0.15 mm). Arranging these plies above ($\bar{z}_i$) and below ($\bar{z}'_i$) the reference plane in such a way that

$$\sum_{j=1}^{10} (\bar{z}_j - \bar{z}'_j) = 0 \ , \tag{5.64}$$

we have no coupling for this group of plies. Doing the same with the other layers we arrive at the laminate without coupling. Naturally, some additional conditions following from the fact that the laminate is a continuous structure should be satisfied. But even with these conditions, Eqn. (5.64) can be met with several systems of the ply coordinates, and symmetric arrangement of plies ($\bar{z}_j = \bar{z}'_j$) is only one of these systems. General analysis of the problem under discussion is presented by Verchery (1999).

Return to the laminates with pre-assigned stacking sequences of the layers. As follows from Eqs. (5.63), we can always make one of coupling stiffness coefficients equal to zero, e.g., taking $e = e_{st}$ where

$$e_{st} = \frac{I_{st}^{(1)}}{I_{st}^{(0)}} \ , \tag{5.65}$$

we get $C_{st} = 0$ (the rest coupling coefficients are not zero).

Another way to simplify the equations for stiffnesses is to take $e = 0$, i.e., to take the surface of the laminate as the reference plane. In this case, Eqs. (5.28) acquire the form

$$B_{mn} = I_{mn}^{(0)}, \quad C_{mn} = I_{mn}^{(1)}, \quad D_{mn} = I_{mn}^{(2)} \ .$$

In practical analysis, constitutive equations for the laminates with arbitrary structure are often approximately simplified using the method of reduced or minimum bending stiffnesses described, e.g., by Ashton (1969), Karmishin (1974), and Whitney (1987). To introduce this method, consider the corresponding equation of Eqs. (5.28) for bending stiffnesses, i.e.

$$D_{mn} = I_{mn}^{(2)} - 2eI_{mn}^{(1)} + e^2 I_{mn}^{(0)} \tag{5.66}$$

and find coordinate e delivering the minimum value of D_{mn}. Using the minimum conditions

$$\frac{\mathrm{d}}{\mathrm{d}e} D_{mn} = 0, \quad \frac{\mathrm{d}^2}{\mathrm{d}e^2} D_{mn} > 0 \ ,$$

we get

$$e = e_{mn} = \frac{I_{mn}^{(1)}}{I_{mn}^{(0)}} \ . \tag{5.67}$$

This result coincides with Eqn. (5.65) and yields $C_{mn} = 0$. Thus, calculating D_{mn} and C_{mn} we use for each $mn = 11, 12, 22, 14, 24, 44$ the corresponding value e_{mn} specified by Eqn. (5.67). Substitution yields

$$D_{mn}^r = I_{mn}^{(2)} - \frac{(I_{mn}^{(1)})^2}{I_{mn}^{(0)}}, \quad C_{mn}^r = 0 \ , \tag{5.68}$$

and constitutive equations, Eqs. (5.5) become uncoupled. Naturally, this approach is only approximate because the reference plane coordinate should be the same for all stiffnesses, but it is not in the method under discussion. As follows from the foregoing derivation, coefficients D_{mn}^r specified by Eqs. (5.68) do not exceed the actual values of bending stiffnesses, i.e., $D_{mn}^r \leqslant D_{mn}$. So the method of reduced bending stiffnesses leads to underestimation of the laminate bending stiffness. In conclusion, it should be noted that this method is not formally grounded and can yield both good and poor approximation of the laminate behavior.

5.10. Stresses in laminates

Constitutive equations derived in the previous sections of this chapter link forces and moments acting on the laminate with the corresponding generalized strains. For composite structures, forces and moments should satisfy equilibrium equations, while strains are expressed in terms of displacements. As a result, a complete set of equations is formed allowing us to find forces, moments, strains, and displacements corresponding to a given system of loads acting on this structure. Because the problem of structural mechanics is beyond the scope of this book and is discussed elsewhere (Vasiliev, 1993), we assume that this problem has been already solved, i.e., that we know either generalized strains ε, γ, and κ entering Eqs. (5.5) or forces and moments N and M. If this is the case, we can use Eqs. (5.5) to find ε, γ, and κ. Now,

to complete the analysis, we need to determine stress acting in each layer of the laminate.

To do this, we should first find strains in any ith layer using Eqs. (5.3) which yield

$$\varepsilon_x^{(i)} = \varepsilon_x^0 + z_i\kappa_x, \quad \varepsilon_y^{(i)} = \varepsilon_y^0 + z_i\kappa_y, \quad \gamma_{xy}^{(i)} = \gamma_{xy}^0 + z_i\kappa_{xy} \ , \tag{5.69}$$

where z_i is the layer normal coordinate changing over the thickness of the ith layer. If the ith layer is orthotropic with principal material axes coinciding with axes x and y (e.g., made of fabric), Hooke's law provides the stress we need, i.e.,

$$\sigma_x^{(i)} = \bar{E}_x^{(i)}(\varepsilon_x^{(i)} + \nu_{xy}^{(i)}\varepsilon_y^{(i)}), \quad \sigma_y^{(i)} = \bar{E}_y^{(i)}(\varepsilon_y^{(i)} + \nu_{yx}^{(i)}\varepsilon_x^{(i)}), \quad \tau_{xy}^{(i)} = G_{xy}^{(i)}\gamma_{xy}^{(i)} \ , \tag{5.70}$$

where, $\bar{E}_{x,y}^{(i)} = E_{x,y}^{(i)}/(1 - \nu_{xy}^{(i)}\nu_{yx}^{(i)})$ and $E_x^{(i)}$, $E_y^{(i)}$, $G_{xy}^{(i)}$, $\nu_{xy}^{(i)}$, $\nu_{yx}^{(i)}$ are elastic constants of the layer referred to the principal material axes. For an isotropic layer (e.g., metal or polymeric) we should take in Eqs. (5.70) $E_x^{(i)} = E_y^{(i)} = E_i$, $\nu_{xy}^{(i)} = \nu_{yx}^{(i)} = \nu_i$, $G_{xy}^i = G_i = E_i/2(1 + \nu_i)$.

Consider the layer composed of unidirectional plies with orientation angle ϕ_i. Using Eqs. (4.69) we can express strains in the principal material coordinates as

$$\begin{aligned}
\varepsilon_1^{(i)} &= \varepsilon_x^{(i)} \cos^2\phi_i + \varepsilon_y^{(i)} \sin^2\phi_i + \gamma_{xy}^{(i)} \sin\phi_i \cos\phi_i, \\
\varepsilon_2^{(i)} &= \varepsilon_x^{(i)} \sin^2\phi_i + \varepsilon_y^{(i)} \cos^2\phi_i - \gamma_{xy}^{(i)} \sin\phi_i \cos\phi_i, \\
\gamma_{12}^{(i)} &= 2(\varepsilon_y^{(i)} - \varepsilon_x^{(i)}) \sin\phi_i \cos\phi_i + \gamma_{xy}^{(i)} \cos 2\phi_i \ ,
\end{aligned} \tag{5.71}$$

and find the corresponding stresses, i.e.,

$$\sigma_1^{(i)} = \bar{E}_1^{(i)}(\varepsilon_1^{(i)} + \nu_{12}^{(i)}\varepsilon_2^{(i)}), \quad \sigma_2^{(i)} = \bar{E}_2^{(i)}(\varepsilon_2^{(i)} + \nu_{21}^{(i)}\varepsilon_1^{(i)}), \quad \tau_{12}^{(i)} = G_{12}^{(i)}\gamma_{12}^{(i)} \ , \tag{5.72}$$

where $\bar{E}_{1,2}^{(i)} = E_{1,2}^{(i)}/(1 - \nu_{12}^{(i)}\nu_{21}^{(i)})$ and $E_1^{(i)}$, $E_2^{(i)}$, $G_{12}^{(i)}$, $\nu_{12}^{(i)}$, $\nu_{21}^{(i)}$ are elastic constants of a unidirectional ply.

Thus, Eqs. (5.69–5.72) allow us to find in-plane stresses acting in each layer or elementary composite ply.

Compatible deformation of the layers is provided by interlaminar stresses τ_{xz}, τ_{yz}, and σ_z. To find these stresses, we need to attract three-dimensional equilibrium equations, Eqs. (2.5), which yield

$$\frac{\partial\tau_{xz}}{\partial z} = -\left(\frac{\partial\sigma_x}{\partial x} + \frac{\partial\tau_{xy}}{\partial y}\right), \quad \frac{\partial\tau_{yz}}{\partial z} = -\left(\frac{\partial\sigma_y}{\partial y} + \frac{\partial\tau_{xy}}{\partial x}\right), \quad \frac{\partial\sigma_z}{\partial z} = -\left(\frac{\partial\tau_{xz}}{\partial x} + \frac{\partial\tau_{yz}}{\partial y}\right) \ . \tag{5.73}$$

Substituting stresses σ_x, σ_y, and τ_{xy} from Eqs. (5.4) and integrating Eqs. (5.73) with due regard to forces that can act on the laminate surfaces we can calculate transverse shear and normal stresses τ_{xz}, τ_{yz}, and σ_z.

5.11. Example

As an example, consider a two-layered cylinder shown in Fig. 5.19 and consisting of ±36° angle-ply layer with total thickness $h_1 = 0.62$ mm and 90° unidirectional layer with thickness $h_2 = 0.60$ mm. The 200 mm diameter cylinder is made by filament winding from glass–epoxy composite with the following mechanical properties: $E_1 = 44$ GPa, $E_2 = 9.4$ GPa, $G_{12} = 4$ GPa, $\nu_{21} = 0.26$. Consider two loading cases axial – compression with force P and torsion with torque T as in Fig. 5.19.

The cylinder is orthotropic, and to study the problem, we need to apply Eqs. (5.43) with some simplifications specific for this problem. First, we assume that applied loads do not induce interlaminar shear and we can take $\gamma_x = 0$ and $\gamma_y = 0$ in Eqs. (5.43). Hence, $V_x = 0$ and $V_y = 0$. In this case, deformations κ_x, κ_y, and κ_{xy} in Eqs. (5.3) become the changes of curvatures of the laminate. Because the loads shown in Fig. 5.19 deform the cylinder into another cylinder inducing only its axial shortening, change of the radius, and rotation of the cross-sections, there is no bending in the axial direction (see Fig. 5.3c) and out-of-plane twisting (see Fig. 5.3d) of the laminate. So, we can take $\kappa_x = 0$ and $\kappa_{xy} = 0$ and write constitutive equations, Eqs. (5.43), in the following form:

$$
\begin{aligned}
N_x &= B_{11}\varepsilon_y^0 + B_{12}\varepsilon_y^0 + C_{12}\kappa_y, \\
N_y &= B_{21}\varepsilon_x^0 + B_{22}\varepsilon_y^0 + C_{22}\kappa_y, \\
N_{xy} &= B_{44}\gamma_{xy}^0, \\
M_x &= C_{11}\varepsilon_x^0 + C_{12}\varepsilon_y^0 + D_{12}\kappa_y, \\
M_y &= C_{21}\varepsilon_x^0 + C_{22}\varepsilon_y^0 + D_{22}\kappa_y, \\
M_{xy} &= C_{44}\gamma_{xy}^0 \ .
\end{aligned}
\tag{5.74}
$$

To determine the change of the circumferential curvature κ_y, we should take into account that the length of the cross-sectional contour being equal to $2\pi R$ before the deformation becomes equal to $2\pi R(1 + \varepsilon_y^0)$ after the deformation. Thus, the curvature change is

$$
\kappa_y = \frac{1}{R(1+\varepsilon_y^0)} - \frac{1}{R} \approx -\frac{\varepsilon_y^0}{R} \ . \tag{5.75}
$$

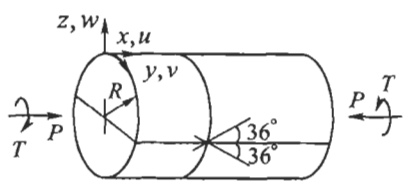

Fig. 5.19. Experimental cylinder.

The final result is obtained under the assumption that the strain is small ($\varepsilon_y^0 << 1$).

Consider the case of axial compression. Free body diagram for the laminate element shown in Fig. 5.20 yields (see Fig. 5.19)

$$N_x = -\frac{P}{2\pi R}, \quad N_y = 0 \ .$$

As a result, the constitutive equations from Eqs. (5.74) that we need to use for the analysis of this case become

$$B_{11}\varepsilon_x^0 + \bar{B}_{12}\varepsilon_y^0 = -\frac{P}{2\pi R}, \quad B_{21}\varepsilon_x^0 + \bar{B}_{22}\varepsilon_y^0 = 0 \ , \tag{5.76}$$

$$M_x = C_{11}\varepsilon_x^0 + \bar{C}_{12}\varepsilon_y^0, \quad M_y = C_{21}\varepsilon_x^0 + \bar{C}_{22}\varepsilon_y^0 \ , \tag{5.77}$$

where

$$\bar{B}_{12} = B_{12} - \frac{C_{12}}{R}, \quad \bar{B}_{22} = B_{22} - \frac{C_{22}}{R}, \quad \bar{C}_{12} = C_{12} - \frac{D_{12}}{R}, \quad \bar{C}_{22} = C_{22} - \frac{D_{22}}{R} \ . \tag{5.78}$$

The first two equations, Eqs. (5.76), allow us to find strains, i.e.,

$$\varepsilon_x^0 = -\frac{P\bar{B}_{22}}{2\pi RB}, \quad \varepsilon_y^0 = \frac{PB_{21}}{2\pi RB} \ , \tag{5.79}$$

where $B = B_{11}\bar{B}_{22} - \bar{B}_{12}B_{21}$ and $B_{21} = B_{12}$.

Bending moments can be determined with the aid of Eqs. (5.77). Axial moment, M_x, has reactive nature in this problem. Nonsymmetric laminate in Fig. 5.20 tends to bend in the xz-plane under axial compression of the cylinder. However, the cylinder meridian remains straight at a distance from its ends. As a result, a reactive axial bending moment appears in the laminate. Circumferential bending moment,

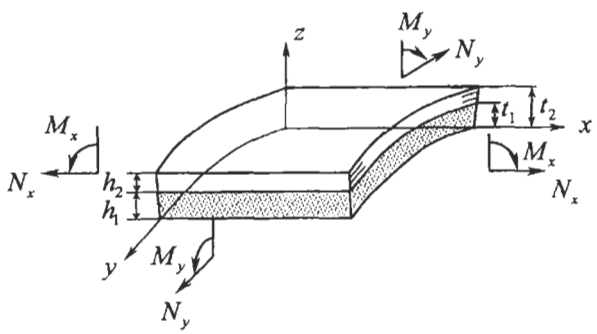

Fig. 5.20. Forces and moments acting on an element of the cylinder under axial compression.

M_y, associated with the change of the curvature of the cross-sectional contour in Eq. (5.75) is very small.

For numerical analysis, we first use Eqs. (4.72) to calculate stiffness coefficients for the angle-ply layer, i.e.,

$$A_{11}^{(1)} = 25 \text{ GPa}, \quad A_{12}^{(1)} = 10 \text{ GPa}, \quad A_{22}^{(1)} = 14.1 \text{ GPa}, \quad A_{44}^{(1)} = 11.5 \text{ GPa} , \tag{5.80}$$

and for the hoop layer

$$A_{11}^{(2)} = 9.5 \text{ GPa}, \quad A_{12}^{(2)} = 2.5 \text{ GPa}, \quad A_{22}^{(2)} = 44.7 \text{ GPa}, \quad A_{44}^{(2)} = 4 \text{ GPa} , \tag{5.81}$$

Then, we apply Eqs. (5.41) to find the I-coefficients that are necessary for the cases (axial compression and torsion) under study:

$$\begin{aligned}
&I_{11}^{(0)} = 21.2 \text{ GPa mm}, \quad I_{12}^{(0)} = 7.7 \text{ GPa mm}, \\
&I_{22}^{(0)} = 35.6 \text{ GPa mm}, \quad I_{44}^{(0)} = 9.5 \text{ GPa mm}, \\
&I_{11}^{(1)} = 10.1 \text{ GPa mm}^2, \quad I_{12}^{(1)} = 3.3 \text{ GPa mm}^2, \\
&I_{22}^{(1)} = 27.4 \text{ GPa mm}^2, \quad I_{44}^{(1)} = 4.4 \text{ GPa mm}^2, \\
&I_{11}^{(2)} = 21.7 \text{ GPa mm}^3, \quad I_{12}^{(2)} = 5.9 \text{ GPa mm}^3, \\
&I_{22}^{(2)} = 94 \text{ GPa mm}^3 .
\end{aligned}$$

To determine stiffness coefficients of the laminate, we should pre-assign the coordinate of the reference plane (a cylindrical surface for the cylinder). Let us put $e = 0$ for simplicity, i.e., we take the inner surface of the cylinder as the reference surface (see Fig. 5.20). Then, Eqs. (5.28) yield

$$\begin{aligned}
&B_{11} = I_{11}^{(0)} = 21.2 \text{ GPa mm}, \quad B_{12} = I_{12}^{(0)} = 7.7 \text{ GPa mm}, \\
&B_{22} = I_{22}^{(0)} = 35.6 \text{ GPa mm}, \\
&C_{11} = I_{11}^{(1)} = 10.1 \text{ GPa mm}^2, \quad C_{12} = I_{12}^{(1)} = 3.3 \text{ GPa mm}^2, \\
&C_{22} = I_{22}^{(1)} = 27.4 \text{ GPa mm}^2, \\
&D_{12} = I_{12}^{(2)} = 5.9 \text{ GPa mm}^3, \quad D_{22} = I_{22}^{(2)} = 94 \text{ GPa mm}^3 ,
\end{aligned}$$

and in accordance with Eqs. (5.78) for $R = 100$ mm,

$$\begin{aligned}
&\bar{B}_{12} = 7.7 \text{ GPa mm}, \quad \bar{B}_{22} = 35.3 \text{ GPa mm}, \\
&\bar{C}_{12} = 3.2 \text{ GPa mm}^2, \quad \bar{C}_{22} = 26.5 \text{ GPa mm}^2 .
\end{aligned}$$

Calculation with the aid of Eqs. (5.79) gives

$$\varepsilon_x^0 = -8.1 \times 10^{-5} P, \quad \varepsilon_y^0 = 1.8 \times 10^{-5} P \ ,$$

where P should be substituted in kN. Comparison of the obtained results with experimental data for the cylinder in Fig. 5.21 is presented in Fig. 5.22.

To determine the stresses, we first use Eqs. (5.69) which, in conjunction with Eq. (5.75) yield

$$\varepsilon_x^{(1)} = \varepsilon_x^{(2)} = \varepsilon_x^0, \quad \varepsilon_y^{(1)} = \varepsilon_y^0\left(1 - \frac{z_1}{R}\right), \quad \varepsilon_y^{(2)} = \varepsilon_y^0\left(1 - \frac{z_2}{R}\right) \ , \tag{5.82}$$

where $0 \leqslant z_1 \leqslant h_1$ and $h_1 \leqslant z_2 \leqslant h_1 + h_2$. Because $(h_1 + h_2)/R = 0.0122$ for the cylinder under study, we can neglect z_1/R and z_2/R in comparison with unity and write

$$\varepsilon_y^{(1)} = \varepsilon_y^{(2)} = \varepsilon_y^0 \ . \tag{5.83}$$

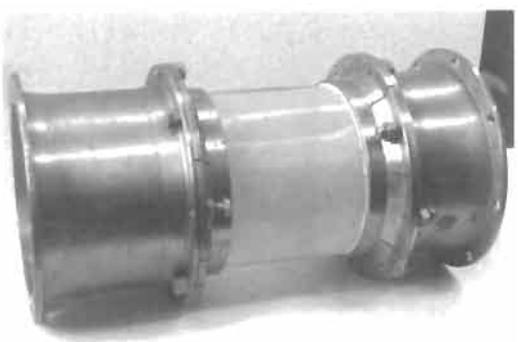

Fig. 5.21. Experimental composite cylinder in test fixtures.

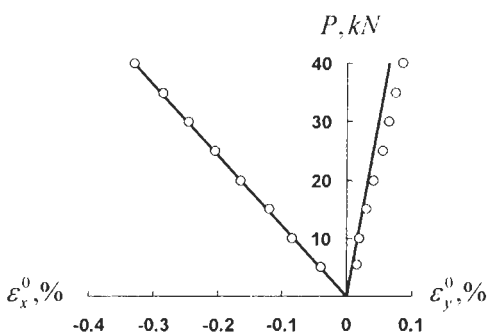

Fig. 5.22. Dependence of axial (ε_x^0) and circumferential (ε_y^0) strains of a composite cylinder on the axial force: (——) analysis; (○) experiment.

Applying Eqs. (5.71) to calculate the strains in the plies principal material coordinates and using Eqs. (5.72) to find the stresses, we get:

- in the angle-ply layer,

$$\sigma_1^{(1)} = -0.26\frac{P}{Rh}, \quad \sigma_2^{(1)} = -0.028\frac{P}{Rh}, \quad \tau_{12}^{(1)} = 0.023\frac{P}{Rh} \ ;$$

- in the hoop layer,

$$\sigma_1^{(2)} = 0.073\frac{P}{Rh}, \quad \sigma_2^{(2)} = -0.089\frac{P}{Rh}, \quad \tau_{12}^{(2)} = 0 \ ,$$

where $h = h_1 + h_2$ is the total thickness of the laminate. To calculate interlaminar stresses acting between the angle-ply and the hoop layers, we apply Eqs. (5.73). Using Eqs. (5.4) and taking Eqs. (5.82) and (5.83) into account, we first find the stresses in the layers referred to the global coordinate frame x, y, z, i.e.,

$$\sigma_x^{(i)} = A_{11}^{(i)}\varepsilon_x^0 + A_{12}^{(i)}\varepsilon_y^0, \quad \sigma_y^{(i)} = A_{21}^{(i)}\varepsilon_x^0 + A_{22}^{(i)}\varepsilon_y^0, \quad \tau_{xy}^{(i)} = 0 \ , \tag{5.84}$$

where, $i = 1, 2$ and $A_{mn}^{(i)}$ are given by Eqs. (5.80) and (5.81). Because these stresses do not depend on x and y, the first two equations in Eqs. (5.73) yield

$$\frac{\partial \tau_{xz}}{\partial z} = 0, \quad \frac{\partial \tau_{yz}}{\partial z} = 0 \ .$$

This means that both interlaminar shear stresses do not depend on z. But on the inner and on the outer surfaces of the cylinder shear stresses are equal to zero. So $\tau_{xz} = 0$ and $\tau_{yz} = 0$. The fact that $\tau_{yz} = 0$ is natural. Both layers are orthotropic and do not tend to twist under axial compression of the cylinder. Concerning $\tau_{xz} = 0$ a question arises as to how compatibility of the axial deformations of the layers with different stiffnesses can be provided without interlaminar shear stresses. The answer follows from the model used above to describe the stress state of the cylinder. According to this model, the transverse shear deformation γ_x is zero. Actually, this condition can be met if the part of the axial force applied to the layer is proportional to the layer stiffness, i.e., as

$$\begin{aligned} P_1 &= -2\pi\sigma_x^{(1)}h_1 = 2\pi h_1(A_{11}^{(1)}\varepsilon_x^0 + A_{12}^{(1)}\varepsilon_y^0), \\ P_2 &= -2\pi\sigma_x^{(2)}h_2 = 2\pi h_2(A_{11}^{(2)}\varepsilon_x^0 + A_{12}^{(2)}\varepsilon_y^0) \ . \end{aligned} \tag{5.85}$$

Substituting strains from Eqs. (5.79) we can conclude that within the accuracy of a small parameter h/R which was neglected in comparison with unity when we calculated stresses $P_1 + P_2 = -P$, and that the axial strains are the same even if the layers are not bonded together. In the middle part of a long cylinder, axial forces are automatically distributed between the layers in accordance with Eqs. (5.85). However, in the vicinity of the cylinder ends this distribution depends on the loading

conditions. The corresponding boundary problem will be discussed further in this section.

The third equation in Eqs. (5.73) formally yields $\sigma_z = 0$. However, this result is not correct because the equation corresponds to the plane laminate and is not valid for the cylinder. In cylindrical coordinates, the corresponding equation has the following form (see, e.g., Vasiliev, 1993):

$$\frac{\partial}{\partial z}\left[\left(1+\frac{z}{R}\right)\sigma_z\right] = -\left[\left(1+\frac{z}{R}\right)\frac{\partial \tau_{xz}}{\partial x} + \frac{\partial \tau_{yz}}{\partial y} - \frac{\sigma_y}{R}\right] .$$

Taking $\tau_{xz} = 0$ and $\tau_{yz} = 0$, substituting σ_y from Eqs. (5.84), and integrating we obtain

$$\sigma_z = \frac{R}{R+z}\left[\frac{1}{R}\int_0^z \left(A_{21}\varepsilon_x^0 + A_{22}\varepsilon_y^0\right)dz + C\right] , \tag{5.86}$$

where, A_{mn} $(mn = 21, 22)$ are the step-wise functions of z, i.e.,

$$A_{mn} = A_{mn}^{(1)} \quad \text{for } 0 \leqslant z \leqslant h_1,$$
$$A_{mn} = A_{mn}^{(2)} \quad \text{for } h_1 \leqslant z \leqslant h = h_1 + h_2 ,$$

and C is the constant of integration. Because no pressure is applied to the inner surface of the cylinder, $\sigma_z(z=0) = 0$ and $C = 0$. Substitution of stiffness coefficients, Eqs. (5.80), (5.81) and strains, Eqs. (5.79) into Eq. (5.86) yields

$$\begin{aligned} \sigma_z^{(1)} &= -0.068\frac{P}{Rh}\cdot\frac{z}{R+z}, \\ \sigma_z^{(2)} &= \sigma_z^{(1)}(z=h_1) + 0.07\frac{P}{Rh}\cdot\frac{z-h_1}{R+z} . \end{aligned} \tag{5.87}$$

On the outer surface of the cylinder, $z = h$ and $\sigma_z^{(2)} = 0$ which is natural because this surface is free of loads. Distribution of σ_z over the laminate thickness is shown in

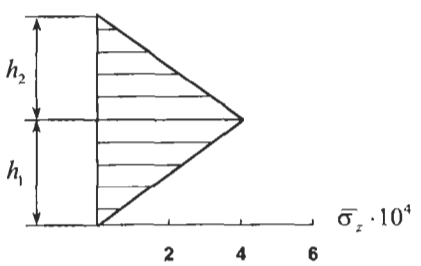

Fig. 5.23. Distribution of the normalized radial stress $\bar{\sigma}_z = \sigma_z Rh/P$ over the laminate thickness.

Fig. 5.23. As can be seen interaction of the layers under axial compression of the cylinder results in radial compression that occurs between the layers.

We now return to transverse shear stress τ_{xz} and try to determine the transverse stresses taking into account transverse shear deformation of the laminate. To do this, we should first specify the character of loading, e.g., assume that axial force T in Fig. 5.19 is uniformly distributed over the cross-sectional contour of the angle-ply layer middle surface as in Fig. 5.24. As a result we can take $T = 2\pi RN$ (because the cylinder is very thin, we neglect the radius change over its thickness).

To study the problem, we should supplement constitutive equations, Eqs. (5.74), with the missing equation for transverse shear, Eqs. (5.20) and add the terms including the change of the meridian curvature κ_x, which is not zero any more. As a result, we arrive at the following constitutive equations:

$$N_x = B_{11}\varepsilon_x^0 + \bar{B}_{12}\varepsilon_y^0 + C_{11}\kappa_x \ , \tag{5.88}$$

$$N_y = B_{21}\varepsilon_x^0 + \bar{B}_{22}\varepsilon_y^0 + C_{21}\kappa_x \ , \tag{5.89}$$

$$M_x = C_{11}\varepsilon_x^0 + C_{12}\varepsilon_y^0 + D_{11}\kappa_x \ , \tag{5.90}$$

$$M_y = C_{21}\varepsilon_x^0 + \bar{C}_{22}\varepsilon_y^0 + D_{21}\kappa_x \ , \tag{5.91}$$

$$V_x = S_{55}\gamma_x \ . \tag{5.92}$$

Forces and moments in the left-hand sides of these equations are linked by equilibrium equations that can be written as (see Fig. 5.25)

$$N_x' = 0, \quad M_x' - V_x = 0, \quad V_x' - \frac{N_y}{R} = 0 \ , \tag{5.93}$$

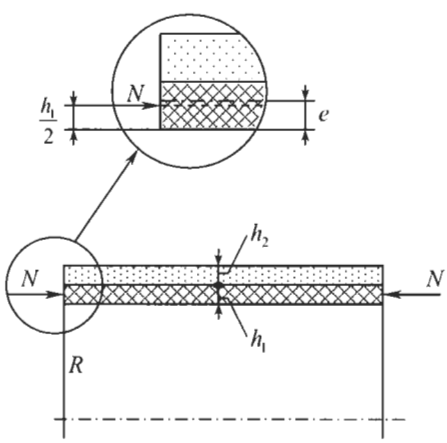

Fig. 5.24. Application of the axial forces.

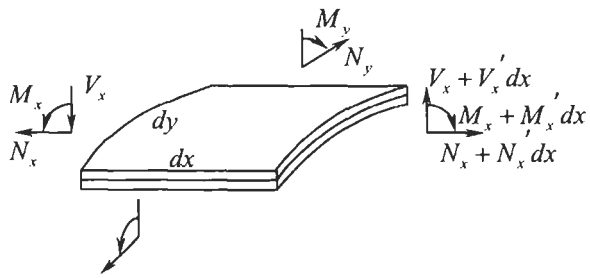

Fig. 5.25. Forces and moments acting on the cylinder element.

where $(\,)' = \mathrm{d}(\,)/\mathrm{d}x$. On the other hand, generalized strains entering Eqs. (5.88)–(5.92) are related to displacements by formulas given as notations to Eqs. (5.3) and (5.14), i.e.,

$$\varepsilon_x^0 = u', \quad \kappa_x = \theta_x', \quad \theta_x = \gamma_x - w' \ , \tag{5.94}$$

where u is the axial displacement and w is the radial displacement (deflection) of the points belonging to the reference surface (see Fig. 5.19), while θ_x is the angle of rotation of the normal to this surface in the xz-plane and γ_x is the transverse shear deformation in this plane. The foregoing strain–displacement equations are the same that for flat laminates. Cylindrical shape of the structure under study shows itself in the expression for circumferential strain ε_y^0. Because the radius of the cylinder after the deformation becomes equal to $(R + w)$, we get

$$\varepsilon_y^0 = \frac{2\pi(R + w) - 2\pi R}{2\pi R} = \frac{w}{R} \ . \tag{5.95}$$

To proceed with the derivation, we introduce coordinate of the laminate reference surface, e, providing $C_{11} = 0$, i.e., in accordance with Eq. (5.65) $e = I_{11}^{(1)}/I_{11}^{(0)}$. For the laminate under study, $e = 0.48$ mm, i.e., the reference surface is located within the internal angle-ply layer. Then, Eqs. (5.88)–(5.90), and (5.92), upon substitution of strains from Eqs. (5.94) and (5.95) can be written as

$$N_x = B_{11}u' + \bar{B}_{12}\frac{w}{R} \ , \tag{5.96}$$

$$N_y = B_{21}u + \bar{B}_{22}\frac{w}{R} + C_{21}\theta_x' \ , \tag{5.97}$$

$$M_x = \bar{C}_{12}\frac{w}{R} + D_{11}\theta_x' \ , \tag{5.98}$$

$$V_x = S_{55}(\theta_x + w') \ , \tag{5.99}$$

where stiffness coefficients B_{11}, $\bar{B}_{12}$, $B_{21} = B_{12}$, $C_{21} = C_{12}$, $\bar{C}_{12}$ were calculated above and

$$D_{11} = I_{11}^{(2)} - \frac{(I_{11}^{(1)})^2}{I_{11}^{(0)}}, \quad S_{55} = \frac{h^2}{\frac{h_1}{A_{55}^{(1)}} + \frac{h_2}{A_{55}^{(2)}}} \ . \tag{5.100}$$

For the unidirectional ply, we take transverse shear moduli $G_{13} = G_{12} = 4\,\text{GPa}$ and $G_{23} = 3\,\text{GPa}$. Using Eqs. (4.72) we get

$$A_{55}^{(1)} = G_{13}\cos^2\phi + G_{23}\sin^2\phi = 3.7\,\text{GPa} \quad \text{and} \quad A_{55}^{(2)} = 3\,\text{GPa} \ .$$

Now, calculation in Eqs. (5.100) yields $D_{11} = 16.9\,\text{GPa mm}^3$ and $S_{55} = 4.05\,\text{GPa mm}$.

Equilibrium equations, Eqs. (5.93), in conjunction with constitutive equations, Eqs. (5.96)–(5.99) compose a set of seven ordinary differential equations including the same number of unknown functions – N_x, N_y, M_x, V_x, u, w, and θ_x. Thus, the set is complete and can be reduced to one governing equation for deflection w.

To do this, we integrate the first equilibrium equation in Eqs. (5.93) which shows that $N_x = \text{constant}$. Because at the cylinder ends $N_x = -N$, this result is valid for the whole cylinder. Using Eqs. (5.94) and (5.96) we obtain

$$\varepsilon_x^0 = u' = -\frac{1}{B_{11}}\left(N + \bar{B}_{12}\frac{w}{R}\right) \ . \tag{5.101}$$

Substitution into Eq. (5.97) yields

$$N_y = \frac{B}{B_{11}R}w - \frac{B_{21}}{B_{11}}N + C_{21}\theta_x' \ , \tag{5.102}$$

where $B = B_{11}\bar{B}_{22} - \bar{B}_{11}B_{21}$. We can express θ_x from Eq. (5.99) and, after differentiation, change V_x' for N_y with the aid of the last equilibrium equation in Eqs. (5.93). Substituting N_y from Eq. (5.102) we arrive at

$$\theta_x' = \frac{1}{C}\left[\frac{1}{S_{55}R}\left(\frac{B}{B_{11}R}w - \frac{B_{21}}{B_{11}}N\right) - w''\right] \ , \tag{5.103}$$

where $C = 1 - (C_{21}/(S_{55}R))$. Using Eqs. (5.98) and (5.103) we can express the bending moment in terms of deflection, i.e.,

$$M_x = \frac{D_{11}}{C}\left[\frac{1}{S_{55}R}\left(\frac{B}{B_{11}R}w - \frac{B_{21}}{B_{11}}N\right) - w''\right] + \bar{C}_{12}\frac{w}{R} \ . \tag{5.104}$$

The governing equation follows now from the second equilibrium equation in Eqs. (5.93) if we differentiate it, substitute M_x'' from Eq. (5.104), express V_x in terms of θ_x' and w'' using Eq. (5.99) and substitute θ_x' from Eq. (5.103). The final equation is as follows:

$$w^{IV} - 2\alpha^2 w'' + \beta^4 w = p \ , \tag{5.105}$$

where

$$\alpha^2 = \frac{1}{2R}\left(\frac{C_{21}}{D_{11}} + \frac{B}{B_{11}S_{55}R}\right), \quad \beta^4 = \frac{B}{D_{11}B_{11}R^2}, \quad p = \frac{B_{21}N}{D_{11}B_{11}R} = \frac{B_{21}P}{2\pi R^2 D_{11}B_{11}} \ .$$

For the cylinder under study, $\alpha^2 = 14/R^2$ and $\beta^2 = 139/R^2$. Because $\beta > \alpha$, the solution of Eq. (5.105) can be written in the following form:

$$w = \sum_{n=1}^{4} C_n F_n(x) + w_p \ , \tag{5.106}$$

where C_n are constants of integration, and

$$F_1 = e^{-rx}\cos tx, \quad F_2 = e^{-rx}\sin tx, \quad F_3 = e^{rx}\cos tx, \quad F_4 = e^{rx}\sin tx,$$
$$r = \sqrt{\frac{1}{2}(\beta^2 - \alpha^2)}, \quad t = \sqrt{\frac{1}{2}(\beta^2 + \alpha^2)}, \quad w_p = \frac{B_{21}P}{2\pi B} \ .$$

To analyze the local effects in the vicinity of the cylinder end, e.g., $x = 0$ (the stress state of the cylinder at a distance from its ends is presented above), we should take $C_3 = 0$ and $C_4 = 0$ in Eq. (5.106) which reduces to

$$w = C_1 F_1(x) + C_2 F_2(x) + w_p \ . \tag{5.107}$$

To differentiate the functions entering this solution, the following relationships can be used:

$$F_1' = -(tF_2 + rF_1), \quad F_2' = tF_1 - rF_2,$$
$$F_1'' = (r^2 - t^2)F_1 + 2rtF_2, \quad F_2'' = (r^2 - t^2)F_2 - 2rtF_1,$$
$$F_1''' = -r(r^2 - 3t^2)F_1 + t(t^2 - 3r^2)F_2,$$
$$F_2''' = -r(r^2 - 3t^2)F_2 - t(t^2 - 3r^2)F_1 \ .$$

Constants of integration C_1 and C_2 entering Eq. (5.107) should be found from the boundary conditions at $x = 0$. As follows from Figs. 5.24 and 5.25,

$$M_x(x = 0) = N\left(e - \frac{h_1}{2}\right), \quad V_x(x = 0) = 0 \ ,$$

where M_x is specified by Eqs. (5.104) and (5.107), while V_x can be found from the second equilibrium equation in Eqs. (5.93).

For the cylinder under study, the final expressions for strains and rotation angle are

$$\varepsilon_x^0 = -\frac{P\bar{B}_{22}}{2\pi RB}[1 + e^{-rx}(0.11\sin tx - 0.052\cos tx)],$$
$$\varepsilon_y^0 = \frac{PB_{21}}{2\pi RB}[1 + e^{-rx}(0.51\sin tx - 0.24\cos tx)], \qquad (5.108)$$
$$\theta_x = \frac{PB_{21}}{2\pi RB}e^{-rx}(6.3\cos tx - 2.3\sin tx) \ ,$$

where $r = 7.9/R$ and $t = 8.75/R$. As can be seen, solution in Eqs. (5.79) is supplemented with a boundary-layer solution that vanishes with a distance from the cylinder end.

To determine transverse shear stress τ_{xz}, we integrate the first equation in Eqs. (5.73) under the condition $\tau_{xz}(z = 0) = 0$. As a result, the shear stress acting in the angle-ply layer is specified by the following expression:

$$\tau_{xz}^{(1)} = -\int_0^z \frac{d\sigma_x^{(1)}}{dx}dz \ ,$$

where

$$\sigma_x^{(1)} = A_{11}^{(1)}\varepsilon_x^{(1)} + A_{12}^{(1)}\varepsilon_y^{(1)},$$
$$\varepsilon_x^{(1)} = \varepsilon_x^0 + z\kappa_x, \quad \varepsilon_y^{(1)} = \varepsilon_y^0 + z\kappa_y,$$
$$\kappa_x = \theta_x', \quad \kappa_y = -\frac{\varepsilon_y^0}{R} \ .$$

Substitution of Eqs. (5.108) and calculation yield

$$\tau_{xz}^{(1)} = \frac{P\bar{B}_{22}}{2\pi R^2 B}e^{-rx}\left[(23.75\cos tx - 9.75\sin tx)z + (6.3\cos tx + 24.9\sin tx)z^2\right] \ . \qquad (5.109)$$

Transverse normal stress can be found from the following equation similar to Eq. (5.86):

$$\sigma_z = \frac{R}{R+z}\int_0^z \left[\frac{1}{R}(A_{21}\varepsilon_x^0 + A_{22}\varepsilon_y^0) - \left(1 + \frac{z}{R}\right)\frac{\partial\tau_{xz}}{\partial x}\right]dz \ .$$

For a thin cylinder, we can neglect z/R in comparison with unity. Using Eqs. (5.108) and (5.109) for the angle-ply layer, we get

$$\sigma_z^{(1)} = -0.068\frac{P}{R^2 h}\{z + e^{-rx}[(0.18\cos tx - 0.0725\sin tx)z$$
$$-(0.12\cos tx + 0.059\sin tx)z^2 + (0.05\cos tx - 0.076\sin tx)z^3]\} \ .$$

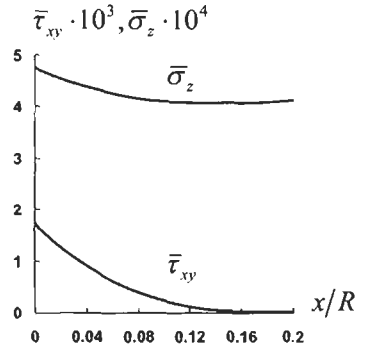

Fig. 5.26. Distribution of normalized transverse shear stress $\bar{\tau}_{xz} = \tau_{xz}^{(1)} Rh/P$ and normal stress $\bar{\sigma}_z = \sigma_z^{(1)} Rh/P$ acting on the layers interface ($z = h_1$) along the cylinder axis.

As can be seen, the first equation in Eqs. (5.87) follows from this solution if $x \to \infty$. Distribution of shear stress $\tau_{xz}^{(1)}$ ($z = h_1$) and normal stress $\sigma_z^{(1)}$ ($z = h_1$) acting at the interface between the angle-ply and the hoop layer of the cylinder along its length is shown in Fig. 5.26.

Consider now the problem of torsion (see Fig. 5.19). Constitutive equations in Eqs. (5.74) that we need to use for this problem are

$$N_{xy} = B_{44}\gamma_{xy}^0, \quad M_{xy} = C_{44}\gamma_{xy} \ . \tag{5.110}$$

Taking coordinate of the reference surface in accordance with Eq. (5.65), i.e.,

$$e = \frac{I_{44}^{(1)}}{I_{44}^{(0)}} \ , \tag{5.111}$$

we get $C_{44} = 0$ and $M_{44} = 0$. For the cylinder under study, $e = 0.46$ mm, i.e., the reference surface is within the angle-ply layer. Free-body diagram for the cylinder loaded with torque T, (see Figs. 5.19 and 5.27) yields

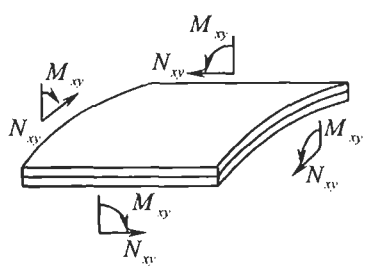

Fig. 5.27. Forces and moments acting on an element of the cylinder under torsion.

$$N_{xy} = \frac{T}{2\pi R^2} \ .$$

Thus,

$$\gamma_{xy}^0 = \frac{T}{2\pi R^2 B_{44}} \ . \tag{5.112}$$

For the experimental cylinder, shown in Fig. 5.21, normal strains were measured in the directions making ±45° angles with the cylinder meridian. To find these strains, we can use Eqs. (5.71) with $\phi_i = \pm 45°$, i.e.,

$$\varepsilon_{45}^{\pm} = \pm \tfrac{1}{2} \gamma_{xy}^0 \ .$$

For the cylinder under study with $B_{44} = I_{44}^{(0)} = 9.5$ GPa mm and $R = 100$ mm, we get

$$\varepsilon_{45}^{\pm} = \pm \frac{T}{4\pi R^2 B_{44}} = \pm 0.84 \times 10^{-6} T \ ,$$

where, T is measured in N m. Comparison of thus obtained result with experimental data is shown in Fig. 5.28.

To find the stresses acting in the plies, we should first use Eqs. (5.69) which for the case under study yield

$$\varepsilon_x^{(i)} = \varepsilon_y^{(i)} = 0, \quad \gamma_{xy}^{(i)} = \gamma_{xy}^0 \quad (i = 1, 2) \ .$$

Then, Eqs. (5.71) allow us to determine the strains:

- in $\pm\phi$ plies of the angle-ply layer,

$$\varepsilon_1^{\pm} = \pm \gamma_{xy}^0 \sin\phi \cos\phi, \quad \varepsilon_2^{\pm} = \mp \gamma_{xy}^0 \sin\phi \cos\phi, \quad \gamma_{12}^{\pm} = \gamma_{xy}^0 \cos 2\phi \ ;$$

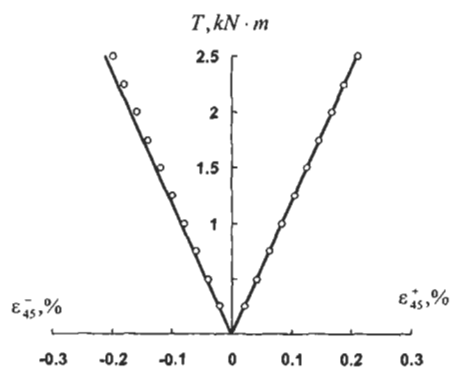

Fig. 5.28. Dependence of $\varepsilon_{45}^{\pm}$ on the torque T for a composite cylinder: (——) analysis; (o) experiment.

- in unidirectional plies of a hoop layer ($\phi = 90^{\circ}$),

$$\varepsilon_1^{90} = \varepsilon_2^{90} = 0, \quad \gamma_{12}^{90} = \gamma_{xy}^{0} \ .$$

Finally, the stresses can be obtained with the aid of Eqs. (5.72). For the cylinder under study, we get:

- in the angle-ply layer,

$$\sigma_1^{\pm} = \pm 0.41 \frac{T}{R^2 h}, \quad \sigma_2^{\pm} = \mp 0.068 \frac{T}{R^2 h}, \quad \tau_{12}^{\pm} = 0.025 \frac{T}{R^2 h} \ ;$$

- in the hoop layer,

$$\sigma_1^{90} = \sigma_2^{90} = 0, \quad \tau_{12}^{90} = 0.082 \frac{T}{R^2 h} \ ,$$

where $h = 1.22$ mm is the total thickness of the laminate.

5.12. References

Aleksandrov, A.Ya., Brukker, L.E., Kurshin, L.M. and Prusakov, A.P. (1960). *Analysis of Sandwich Plates*. Mashinostroenie, Moscow (in Russian).

Ashton, J.E. (1969). Approximate solutions for unsymmetrically laminated plates. *J. Composite Mater.* 189–191.

Chen, H.-J. and Tsai, S.W. (1996). Three-dimensional effective moduli of symmetric laminates. *J. Composite Mater.* **30**(8).

Karmishin, A.V. (1974). Equations for nonhomogeneous thin-walled elements based on minimum stiffnesses. *App. Mech.* (*Prikladnaya Mekhanika*), **10**(6), 34–42 (in Russian).

Vasiliev, V.V. (1993). *Mechanics of Composite Structures*. Taylor & Francis, Washington.

Verchery, G. (1999). Designing with anisotropy. Part 1: Methods and general results for laminates. In *Proc. 12th International Conference on Composite Materials (ICCM-12)*, Paris, France, 5–9 July 1999, ICCM12/TCA (CD-ROM), 11p.

Whitney, J.M. (1987). *Structural Analysis of Laminated Anisotropic Plates*. Technomic Publishing Co., Inc., Lancaster, PA, USA.

Chapter 6

FAILURE CRITERIA AND STRENGTH OF LAMINATES

Consider a laminate consisting of orthotropic layers or plies whose principal material axes 1, 2, 3, in general, do not coincide with global coordinates of the laminate (x, y, z) and assume that this layer or ply is in the plane stressed state as in Fig. 6.1. It should be emphasized that, in contrast to the laminate that can be anisotropic and demonstrate coupling effects, the layer under consideration is orthotropic and is referred to its principal material axes. Using the procedure that is described in Section 5.10 we can find stresses σ_1, σ_2, and τ_{12} corresponding to a given system of loads acting on the laminate. The problem that we approach now is to evaluate the laminate load-carrying capacity, i.e., to calculate the loads that cause the failure of the individual layers and the laminate as a whole. For the layer, this problem can be readily solved if we have a failure or strength criterion

$$F(\sigma_1, \sigma_2, \tau_{12}) = 1 \ , \tag{6.1}$$

specifying the combination of stresses that causes the layer fracture. In other words, the layer works while $F < 1$, fails if $F = 1$, and does not exist as a load-carrying structural element if $F > 1$. In the space of stresses σ_1, σ_2, τ_{12}, Eq. (6.1) specifies the so-called failure surface (or failure envelope) shown in Fig. 6.2. Each point of the space corresponds to a particular stress state, and if the point is inside the surface, the layer resists the corresponding combination of stresses without failure.

Thus, the problem of strength analysis is reduced to a construction of a failure criterion in its analytical, Eq. (6.1), or graphical (Fig. 6.2) form. By now, numerous variants of these forms have been proposed for traditional and composite structural materials (Gol'denblat and Kopnov, 1968; Wu, 1974; Tsai and Hahn, 1975; Rowlands, 1975; Vicario and Toland, 1975; etc.) and described by the authors of many text-books in Composite Materials. Omitting the history and comparative analysis of particular criteria that can be found elsewhere we discuss here mainly the practical aspects of the problem.

6.1. Failure criteria for an elementary composite layer or ply

There exist, in general, two approaches to construct the failure surface, the first of which can be referred to as the microphenomenological approach. The term

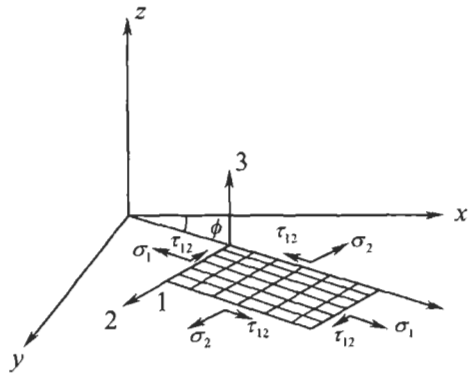

Fig. 6.1. An orthotropic layer or ply in a plane stressed state.

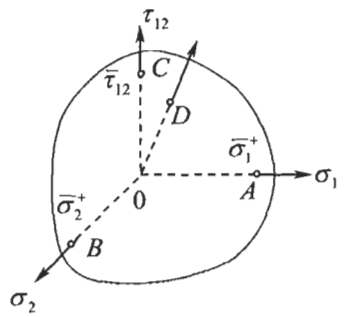

Fig. 6.2. Failure surface in the stress space.

"phenomenological" means that the actual physical mechanisms of failure at the microscopic material level are not touched on and that we deal with stresses and strains, i.e., with conventional and not actually observed state variables introduced in Mechanics of Solids. In the micro-approach, we evaluate the layer strength using microstresses acting in the fibers and in the matrix and failure criteria proposed for homogeneous materials. Being developed up to a certain extent (see, e.g., Skudra et al., 1989), this approach requires the minimum number of experimental material characteristics, i.e., only those determining the strength of fibers and matrices. As a result, coordinates of all the points of the failure surface in Fig. 6.2 including points A, B, and C corresponding to uniaxial and pure shear loading are found by calculation. To do this, we should simulate the layer or the ply with a suitable microstructural model (see, e.g., Section 3.3), apply a pre-assigned system of average stresses σ_1, σ_2, τ_{12} (e.g., corresponding to vector OD in Fig. 6.2), find the stresses acting in material components, specify the failure mode that can be associated with the fibers or with the matrix, and determine the ultimate combination of average stresses corresponding, e.g., to point D in Fig. 6.2. Thus, the whole failure surface

can be constructed. However, uncertainty and approximate character of the existing micromechanical models discussed in Section 3.3 result in relatively poor accuracy of this method which, being in principle rather promising, has not found by now wide practical application.

The second basic approach that can be referred to as macrophenomenological one deals with the average stresses σ_1, σ_2, and τ_{12} shown in Fig. 6.1 and ignores the ply microstructure. For a plane stress state of an orthotropic ply, this approach requires at least five experimental results specifying material strength under:

- longitudinal tension, $\bar{\sigma}_1^+$ (point A in Fig. 6.2),
- longitudinal compression, $\bar{\sigma}_1^-$,
- transverse tension, $\bar{\sigma}_2^+$ (point B in Fig. 6.2),
- transverse compression, $\bar{\sigma}_2^-$,
- in-plane shear, $\bar{\tau}_{12}$ (point C in Fig. 6.2).

Obviously, these data are not enough to construct the complete failure surface, and two possible ways leading to two types of failure criteria can be used.

The first type referred to as structural failure criteria involves some assumptions concerning the possible failure modes that can help us to specify the shape of the failure surface. According to the second way providing failure criteria of approximation type, experiments simulating a set of complicated stress states (such that two or all three stresses σ_1, σ_2, and τ_{12} are induced simultaneously) are undertaken. As a result, a system of points like point D in Fig. 6.2 is determined and approximated with some suitable surface.

Experimental data that are necessary to construct the failure surface are usually obtained testing thin-walled tubular specimens like shown in Figs. 6.3 and 6.4. These specimens are loaded with internal or external pressure p, tensile or compressive axial forces P, and end torques T, providing the given combination of

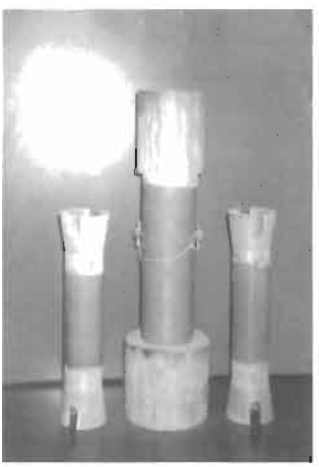

Fig. 6.3. Glass fabric–epoxy test tubular specimens.

Fig. 6.4. Carbon epoxy test tubular specimens made by circumferential winding (the central cylinder failed under axial compression and the right one – under torsion).

the axial stress, σ_x, circumferential stress, σ_y, and shear stress τ_{xy} that can be calculated as

$$\sigma_x = \frac{P}{2\pi Rh}, \quad \sigma_y = \frac{pR}{h}, \quad \tau_{xy} = \frac{T}{2\pi R^2 h} \ .$$

Here, R is the cylinder radius and h is its thickness. For tubular specimens shown in Fig. 6.4 and made from unidirectional carbon–epoxy composite by circumferential winding, $\sigma_x = \sigma_2$, $\sigma_y = \sigma_1$, and $\tau_{xy} = \tau_{12}$ (see Fig. 6.1).

Consider typical structural and approximation strength criteria developed for typical composite layers and plies.

6.1.1. Maximum stress and strain criteria

These criteria belong to a structural type and are based on the assumption that there can exist three possible modes of failure caused by stresses σ_1, σ_2, τ_{12} or strains ε_1, ε_2, γ_{12} when they reach the corresponding ultimate values.

Maximum stress criterion can be presented in the form of the following inequalities:

$$\begin{aligned} &\sigma_1 \leqslant \bar{\sigma}_1^+, \ \sigma_2 \leqslant \bar{\sigma}_2^+ \quad \text{if} \quad \sigma_1 > 0, \ \sigma_2 > 0, \\ &|\sigma_1| \leqslant \bar{\sigma}_1^-, \ |\sigma_2| \leqslant \bar{\sigma}_2 \quad \text{if} \quad \sigma_1 < 0, \ \sigma_2 < 0, \\ &|\tau_{12}| \leqslant \tau_{12} \ . \end{aligned} \tag{6.2}$$

It should be noted that here and further all the ultimate stresses $\bar{\sigma}$ and τ including compressive strength values are taken as positive quantities. The failure surface corresponding to the criterion in Eqs. (6.2) is shown in Fig. 6.5. As can be seen, according to this criterion the failure is associated with independently acting stresses, and the possible stress interaction is ignored.

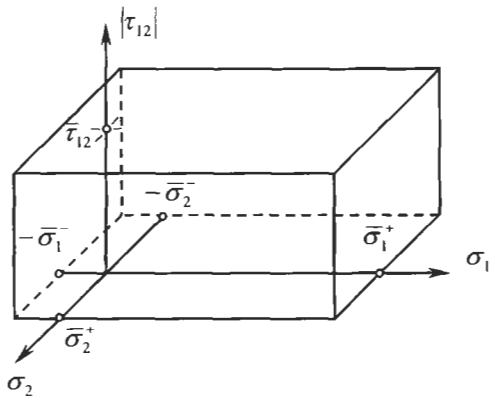

Fig. 6.5. Failure surface corresponding to maximum stress criterion.

It can be expected that the maximum stress criterion describes adequately the behavior of the materials in which stresses σ_1, σ_2, and τ_{12} are taken by different structural elements. A typical example of such a material is a fabric composite layer discussed in Section 4.6. Indeed, warp and filling yarns (see Fig. 4.80) working independently provide material strength under tension and compression in two orthogonal directions (1 and 2), while the polymeric matrix controls the layer strength under in-plane shear. A typical failure envelope in plane (σ_1, σ_2) for a glass–epoxy fabric composite is shown in Fig. 6.6 (experimental data from G. Prokhorov and N. Volkov). The corresponding results in plane (σ_1, τ_{12}), but for a different glass fabric experimentally studied by Annin and Baev (1979) are presented in Fig. 6.7. As follows from Figs. 6.6 and 6.7, the maximum stress criterion provides a satisfactory prediction of strength for fabric composites within

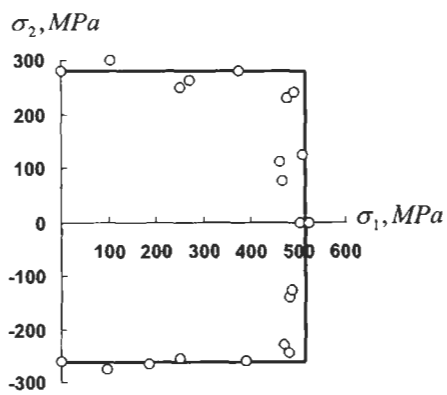

Fig. 6.6. Failure envelope for glass–epoxy fabric composite in plane (σ_1, σ_2). (———) maximum stress criterion, Eqs. (6.2); (o) experimental data.

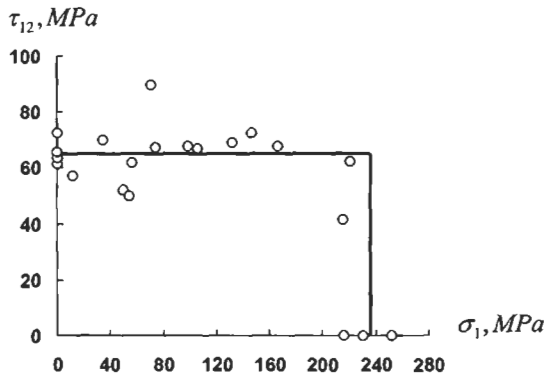

Fig. 6.7. Failure envelope for glass–epoxy fabric composite in plane (σ_1, τ_{12}). (———) maximum stress criterion, Eqs. (6.2); (o) experimental data.

the accuracy determined by the scatter of experimental results. As was already noted, this criterion ignores the interaction of stresses. However, this interaction takes place in fabric composites which are loaded with compression in two orthogonal directions, because compression of the filling yarns increases the strength in the warp direction and vice versa. The corresponding experimental results from Belyankin et al. (1971) are shown in Fig. 6.8. As can be seen, there is a considerable deviation of experimental data from the maximum stress criterion shown with solid lines. However, even in such cases this criterion is sometimes used to design composite structures, because it is simple and conservative, i.e., it underestimates material strength increasing the safety factor for the structure under design. There exist fabric composites for which the interaction of normal stresses shows itself under tension as well. An example of such a material is presented in

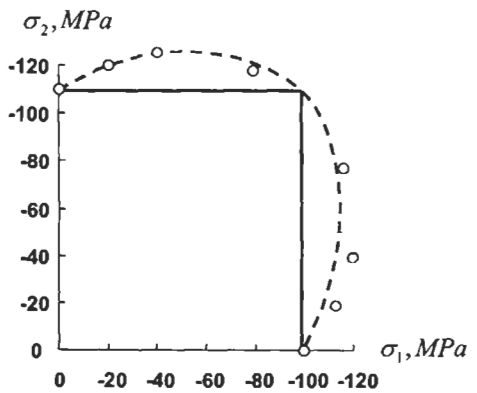

Fig. 6.8. Failure envelope for glass–phenolic fabric composite loaded with compression in plane (σ_1, σ_2). (———) maximum stress criterion, Eqs. (6.2); (– – – –) polynomial criterion, Eqs. (6.15); (o) experimental data.

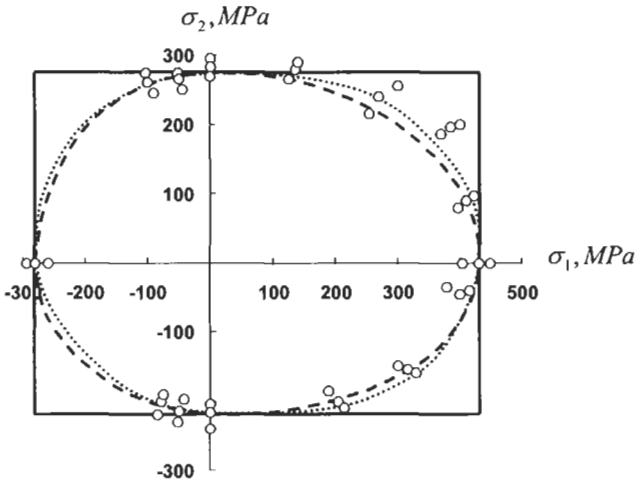

Fig. 6.9. Failure envelope for glass–epoxy fabric composite in plane (σ_1, σ_2). (———) maximum stress criterion, Eqs. (6.2); (– – – –) approximation criterion, Eqs. (6.11), (6.12); (· · · · · ·) approximation criterion, Eqs. (6.14); (o) experimental data.

Fig. 6.9 (experimental data from Gol'denblat and Kopnov, 1968). Naturally, the maximum stress criterion (solid lines in Fig. 6.9) should not be used in this case because it overestimates material strength, and the structure can fail under loads that are lower than those predicted with this criterion.

The foregoing discussion concerns fabric composites. Consider a unidirectional ply and try to apply to it the maximum stress criterion. First of all, because the longitudinal strength of the ply is controlled by the fibers whose strength is much higher than that of the matrix, it is natural to neglect the interaction of stress σ_1 on one side and stresses σ_2 and τ_{12}, on the other side. In other words, we can apply the maximum stress criterion to predict material strength under tension or compression in the fiber direction and, hence, use the first part of Eqs. (6.2), i.e.

$$\begin{aligned} &\sigma_1 \leqslant \bar{\sigma}_1^+ \quad \text{if} \quad \sigma_1 > 0, \\ &|\sigma_1| \leqslant \bar{\sigma}_1^- \quad \text{if} \quad \sigma_1 < 0 \ . \end{aligned} \tag{6.3}$$

Actually, there exist unidirectional composites with very brittle matrix (carbon or ceramic) for which the other conditions in Eqs. (6.2) can be also applied. As an example, Fig. 6.10 displays the failure envelope for a carbon–carbon unidirectional material (experimental data from Vorobey et al., 1992). However, for the majority of unidirectional composites, the interaction of transverse normal and shear stresses is essential and should be taken into account. This means that we should apply Eq. (6.1) but can simplify it as follows:

$$F(\sigma_2, \tau_{12}) = 1 \ . \tag{6.4}$$

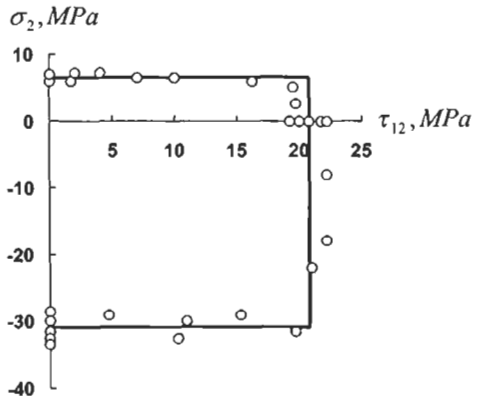

Fig. 6.10. Failure envelope for carbon–carbon unidirectional composite in plane (σ_2, τ_{12}). (———) maximum stress criterion, Eqs. (6.2); (○) experimental data.

The simplest way to induce a combined stress state for the unidirectional ply is to use the off-axis tension or compression discussed in Section 4.3.1. Applying stress σ_x as in Figs. 4.22 and 4.23 we have stresses σ_1, σ_2 and τ_{12} specified by Eqs. (4.78). Then, Eqs. (6.2) yield the following ultimate stresses:
For $\sigma_x > 0$

$$\bar{\sigma}_x = \frac{\bar{\sigma}_1^+}{\cos^2\phi}, \quad \bar{\sigma}_x = \frac{\bar{\sigma}_2^+}{\sin^2\phi}, \quad \bar{\sigma}_x = \frac{\bar{\tau}_{12}}{\sin\phi\cos\phi} \quad . \tag{6.5}$$

For $\sigma_x < 0$

$$\bar{\sigma}_x = \frac{\bar{\sigma}_1^-}{\cos^2\phi}, \quad \bar{\sigma}_x = \frac{\bar{\sigma}_2^-}{\sin^2\phi}, \quad \bar{\sigma}_x = \frac{\bar{\tau}_{12}}{\sin\phi\cos\phi} \quad . \tag{6.6}$$

Actual ultimate stress is the minimum $\bar{\sigma}_x$ value of three values provided by Eqs. (6.5) for tension or Eqs. (6.6) for compression. Experimental data of S.W. Tsai taken from Jones (1999) and corresponding to a glass–epoxy unidirectional composite are presented in Fig. 6.11. As can be seen, the maximum stress criterion (solid lines) demonstrates fair agreement with experimental results for angles close to 0° and 90° only. An important feature of this criterion belonging to a structural type is its ability to predict the failure mode. Curves 1, 2, and 3 in Fig. 6.11 correspond to the first, the second and the third equations of Eqs. (6.5) and (6.6). As follows from Fig. 6.11(a), the fiber failure occurs only for $\phi = 0°$. For $0° < \phi < 30°$, material failure is associated with in-plane shear, while for $30° < \phi \leqslant 90°$ it is caused by transverse normal stress σ_2.

Maximum strain failure criterion is similar to the maximum stress criterion discussed above, but is formulated in terms of strains, i.e.

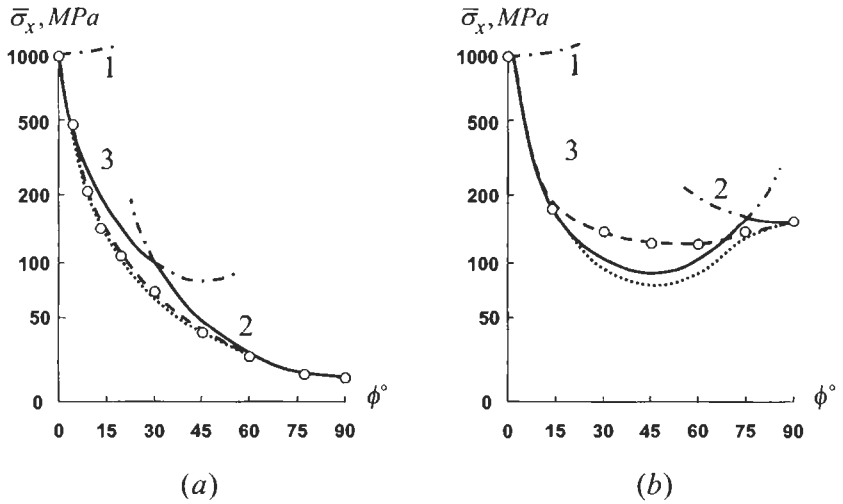

Fig. 6.11. Dependence of the stress on the fiber orientation angle for off-axes tension (a) and compression (b) of glass–epoxy unidirectional composite. (———, – · – · –) maximum stress criterion, Eqs. (6.2); (· · · · · · ·) approximation criterion, Eqs. (6.3) and (6.16); (– – – –) approximation criterion, Eqs. (6.3) and (6.17).

$$\begin{aligned} &\varepsilon \leqslant \bar{\varepsilon}_1^+, \ \varepsilon_2 \leqslant \bar{\varepsilon}_2^+ \quad \text{if} \quad \varepsilon_1 > 0 \ \ \varepsilon_2 > 0, \\ &|\varepsilon_1| \leqslant \bar{\varepsilon}_1^-, \ |\varepsilon_2| \leqslant \bar{\varepsilon}_2^- \quad \text{if} \quad \varepsilon_1 < 0 \ \ \varepsilon_2 < 0, \\ &|\gamma_{12}| \leqslant \bar{\gamma}_{12} \ , \end{aligned} \tag{6.7}$$

where

$$\varepsilon_1 = \frac{\sigma_1}{E_1} - \nu_{12}\frac{\sigma_2}{E_2}, \quad \varepsilon_2 = \frac{\sigma_2}{E_2} - \nu_{21}\frac{\sigma_1}{E_1}, \quad \gamma_{12} = \frac{\tau_{12}}{G_{12}} \ . \tag{6.8}$$

Maximum strain criterion ignores the strain interaction but allows for the stress interaction due to Poisson's effect. This criterion provides the results that are rather close to those following from the maximum stress criterion and has not found wide practical implementation.

However, there exists a unique stress state to study which only the maximum strain criterion can be used. This is longitudinal compression of a unidirectional ply discussed earlier in Section 3.4.4. Under this type of loading only longitudinal stress σ_1 is induced, while $\sigma_2 = 0$ and $\tau_{12} = 0$. Nevertheless, the fracture is accompanied with cracks parallel to fibers (see Fig. 6.12 showing tests performed by Katarzhnov, 1982). These cracks are caused by transverse tensile strain ε_2 induced by Poisson's effect. The corresponding strength condition follows from Eqs. (6.7) and (6.8) and can be written as

$$|\sigma_1| \leqslant \bar{\varepsilon}_2^+ \frac{E_1}{\nu_{21}} \ .$$

Fig. 6.12. Failure modes of a unidirectional glass epoxy composite under longitudinal compression.

It should be emphasized that the test shown in Fig. 6.12 can be misleading because transverse deformation of the ply is not restricted in this test, while it is normally restricted in actual laminated composite structural elements. Indeed, the long cylinder with material structure $[0^\circ_{11}]$ being tested under compression yields material strength $\bar{\sigma}_1 = 300$ MPa, while the same cylinder with material structure $[0^\circ_{10}/90^\circ]$ gives $\bar{\sigma}_1 = 505$ MPa (Katarzhnov, 1982). Thus, if we change one longitudinal ply for a circumferential ply that practically does not work in compression along the cylinder axis but restricts its circumferential deformation, we increase material strength in compression by 68.3%. Correspondingly, the failure mode becomes quite different (see Fig. 6.13).

(a) **(b)**

Fig. 6.13. Failure mode of a glass epoxy tubular specimen with 10 longitudinal plies and one outside circumferential ply: (a) inside view; (b) outside view.

6.1.2. Approximation strength criteria

In contrast to structural strength criteria, approximation criteria do not indicate the mode of failure and are constructed by approximation of available experimental results with some proper function depending on stresses σ_1, σ_2 and τ_{12}. The simplest and the most widely used criterion is a second-order polynomial approximation typical forms of which are presented in Fig. 6.14. In the stress space shown in Fig. 6.2, the polynomial criterion corresponding to Fig. 6.14(a) can be written as

$$F(\sigma_1, \sigma_2, \tau_{12}) = R_{11}\sigma_1^2 + R_{22}\sigma_2^2 + S_{12}\tau_{12}^2 = 1 \ . \tag{6.9}$$

To determine coefficients R and S, we need to perform three tests providing material strength under uniaxial loading in 1 and 2 directions and in shear. Then, applying the following conditions:

$$\begin{aligned} &F(\sigma_1 = \bar{\sigma}_1, \sigma_2 = 0, \tau_{12} = 0) = 1, \\ &F(\sigma_1 = 0, \sigma_2 = \bar{\sigma}_2, \tau_{12} = 0) = 1, \\ &F(\sigma_1 = 0, \sigma_2 = 0, \tau_{12} = \bar{\tau}_{12}) = 1 \ , \end{aligned} \tag{6.10}$$

we can find R and S and write Eq. (6.9) in its final form

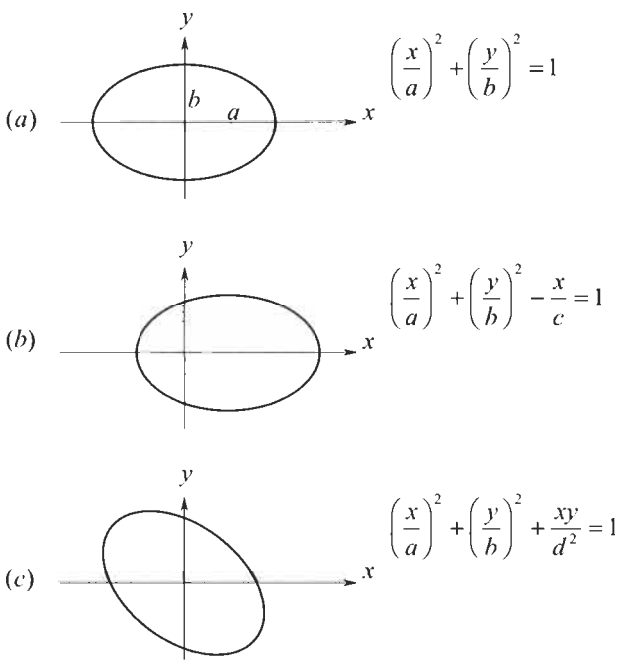

Fig. 6.14. Typical shapes of the curves corresponding to the second-order polynomials.

$$\left(\frac{\sigma_1}{\bar{\sigma}_1}\right)^2+\left(\frac{\sigma_2}{\bar{\sigma}_2}\right)^2+\left(\frac{\tau_{12}}{\bar{\tau}_{12}}\right)^2=1 \ . \tag{6.11}$$

It looks like this criterion yields the same result for tension and compression. However, it can be readily specified for tension or compression. It is important to realize that evaluating material strength we usually know the stresses acting in this material. Thus, we can take in Eq. (6.10)

$$\begin{aligned} &\bar{\sigma}_1=\bar{\sigma}_1^+ \ \text{ if } \ \sigma_1>0 \quad \text{and} \quad \bar{\sigma}_1=\bar{\sigma}_1^- \ \text{ if } \ \sigma_1<0, \\ &\bar{\sigma}_2=\bar{\sigma}_2^+ \ \text{ if } \ \sigma_2>0 \quad \text{and} \quad \bar{\sigma}_2=\bar{\sigma}_2^- \ \text{ if } \ \sigma_2<0 \ , \end{aligned} \tag{6.12}$$

thus describing the cases of tension and compression. Failure criterion in Eqs. (6.11) and (6.12) is demonstrated in Fig. 6.9 in application to a fabric composite loaded with stresses σ_1 and $\sigma_2(\tau_{12}=0)$. Naturally, this criterion is specified by different equations for different quadrants in Fig. 6.9.

For some problems, e.g., for the problem of design, for which we usually do not know the signs of stresses, we may need to use a universal form of the polynomial criterion valid both for tension and compression. In this case, we should apply the approximation of the type shown in Fig. 6.14(b) and generalize Eq. (6.9) as

$$F(\sigma_1,\ \sigma_2,\ \tau_{12})=R_1\sigma_1+R_2\sigma_2+R_{11}\sigma_1^2+R_{22}\sigma_2^2+S_{12}\tau_{12}^2=1 \ .$$

Using conditions similar to Eqs. (6.10), i.e.

$$\begin{aligned} &F(\sigma_1=\bar{\sigma}_1^+,\ \sigma_2=0,\ \tau_{12}=0)=1 \quad \text{if} \quad \sigma_1>0, \\ &F(\sigma_1=-\bar{\sigma}_1^-,\ \sigma_2=0,\ \tau_{12}=0)=1 \quad \text{if} \quad \sigma_1<0, \\ &F(\sigma_1=0,\ \sigma_2=\bar{\sigma}_2^+,\ \tau_{12}=0)=1 \quad \text{if} \quad \sigma_2>0, \\ &F(\sigma_1=0,\ \sigma_2=-\bar{\sigma}_2^-,\ \tau_{12}=0)=1 \quad \text{if} \quad \sigma_2<0, \\ &F(\sigma_1=0,\ \sigma_2=0,\ \tau_{12}=\bar{\tau}_{12})=1 \ , \end{aligned} \tag{6.13}$$

we arrive at

$$\sigma_1\left(\frac{1}{\bar{\sigma}_1^+}-\frac{1}{\bar{\sigma}_1^-}\right)+\sigma_2\left(\frac{1}{\bar{\sigma}_2^+}-\frac{1}{\bar{\sigma}_2^-}\right)+\frac{\sigma_1^2}{\bar{\sigma}_1^+\bar{\sigma}_1^-}+\frac{\sigma_2^2}{\bar{\sigma}_2^+\bar{\sigma}_2^-}+\left(\frac{\tau_{12}}{\bar{\tau}_{12}}\right)^2=1 \ . \tag{6.14}$$

Comparison of this criterion with the criteria discussed above and with experimental results is presented in Fig. 6.9. As can be seen, criteria specified by Eqs. (6.11), (6.12) and (6.14) provide close results which are in fair agreement with experimental data for all the stress states except, may be, biaxial compression for which there are practically no experimental results shown in Fig. 6.9. Such results are presented in Fig. 6.8 and allow us to conclude that the failure envelope can be approximated in this case by the polynomial of the type shown in Fig. 6.14(c), i.e.

$$F(\sigma_1, \sigma_2, \tau_{12}) = R_{11}\sigma_1^2 + R_{12}\sigma_1\sigma_2 + R_{22}\sigma_2^2 + S_{12}\tau_{12}^2 = 1 \ .$$

Coefficients R_{11}, R_{22} and S_{12} can be found as earlier from Eqs. (6.10), and we need to use an additional strength condition to determine the coupling coefficient, R_{12}. A reasonable form of this condition is $F(\sigma_1 = -\bar{\sigma}_1^-, \sigma_2 = -\bar{\sigma}_2^-, \tau_{12} = 0) = 1$. This means that while for $|\sigma_1| < \bar{\sigma}_1^-$ and $|\sigma_2| < \bar{\sigma}_2^-$ the interaction of stresses increases material strength under compression the combination of compressive failure stresses $|\sigma_1| = \sigma_1^-$ and $|\sigma_2| = \sigma_2^-$ results in material failure. Then

$$\left(\frac{\sigma_1}{\bar{\sigma}_1^-}\right)^2 - \frac{\sigma_1\sigma_2}{\bar{\sigma}_1^-\bar{\sigma}_2^-} + \left(\frac{\sigma_2}{\bar{\sigma}_2^-}\right)^2 + \left(\frac{\tau_{12}}{\bar{\tau}_{12}}\right)^2 = 1 \ . \tag{6.15}$$

Comparison of this criterion with experimental data is presented in Fig. 6.8.

Now consider unidirectional composites and return to Fig. 6.11. As can be seen, the maximum stress criterion, (solid lines), ignoring the interaction of stresses σ_2 and τ_{12} demonstrates rather poor agreement with experimental data. The simplest approximation criterion, Eqs. (6.11) and (6.12), acquires, for the case under study, the form

$$F(\sigma_2, \tau_{12}) = \left(\frac{\sigma_2}{\bar{\sigma}_2}\right)^2 + \left(\frac{\tau_{12}}{\bar{\tau}_{12}}\right)^2 = 1 \tag{6.16}$$

and the corresponding failure envelope is shown in Fig. 6.11 with dotted lines. Providing fair agreement with experimental results for tension (Fig. 6.11(a)) this criterion fails to predict material strength under compression (Fig. 6.11(b)). Moreover, for this case, the approximation criterion yields worse results than are demonstrated by the maximum stress criterion. There are simple physical reasons for this discrepancy. In contrast to the maximum stress criterion, Eq. (6.16) allows for stress interaction, but in such a way that transverse stress σ_2 reduces material strength under shear. However, this is true only if transverse stress is tensile. As can be seen in Fig. 6.15, where experimental results taken from Barbero's book (1998) are presented, compressive stress σ_2 increases the ultimate value of shear stress τ_{12}. As a result, the simplest polynomial criterion in Eq. (6.16), being, as it was already noted, quite adequate for $\sigma_2 > 0$, significantly underestimates material strength for $\sigma_2 < 0$ (solid line in Fig. 6.15). As also follows from Fig. 6.15, the proper approximation of experimental results can be achieved if we use the curve of the type shown in Fig. 6.14(b) (but moved to the left with respect to the y-axis), i.e., if we apply for this case the criterion presented with Eq. (6.14) which can be written as

$$F(\sigma_2, \tau_{12}) = \sigma_2\left(\frac{1}{\bar{\sigma}_2^+} - \frac{1}{\bar{\sigma}_2^-}\right) + \frac{\sigma_2^2}{\bar{\sigma}_2^+\bar{\sigma}_2^-} + \left(\frac{\tau_{12}}{\bar{\tau}_{12}}\right)^2 = 1 \ . \tag{6.17}$$

The corresponding approximations are shown in Figs. 6.11 and 6.15 with broken lines.

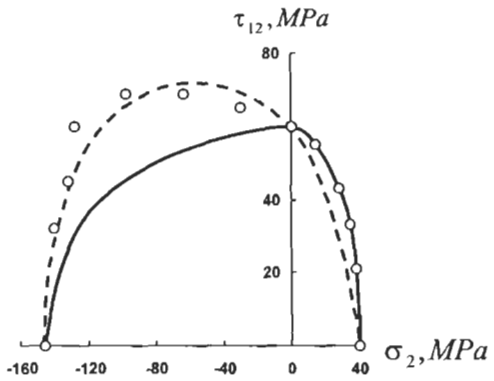

Fig. 6.15. Failure envelope for glass–epoxy unidirectional composite in plane (σ_2, τ_{12}). (———) approximation criterion, Eqs. (6.12) and (6.16); (– – – –) approximation criterion, Eqs. (6.17); (○) experimental data.

In conclusion it should be noted that there exist more complicated polynomial strength criteria than considered above, e.g., the fourth-order criterion of Ashkenazi (1966) and cubic criterion proposed by Tennyson et al. (1980).

6.1.3. Interlaminar strength

The failure of composite laminates can be also associated with interlaminar fracture caused by transverse normal and shear stresses σ_3 and τ_{13}, τ_{23} or σ_z and τ_{xz}, τ_{yz} (see Fig. 4.18). Because $\sigma_3 = \sigma_z$ and shear stresses in coordinates (1, 2, 3) are linked with stresses in coordinates (x, y, z) by simple relationships in Eqs. (4.67) and (4.68), the strength criterion is formulated here in terms of stresses σ_z, τ_{xz}, τ_{yz} which can be found directly from Eqs. (5.73). Since the laminate strength in tension and compression across the layers is different, we can use the polynomial criterion similar to Eq. (6.14). For the stress state under study, we get

$$\sigma_z\left(\frac{1}{\bar{\sigma}_3^+} - \frac{1}{\bar{\sigma}_3^-}\right) + \left(\frac{\tau_r}{\bar{\tau}_i}\right)^2 = 1 \ , \tag{6.18}$$

where

$$\tau_r = \sqrt{\tau_{13}^2 + \tau_{23}^2} = \sqrt{\tau_{xz}^2 + \tau_{yz}^2}$$

is the resultant transverse shear stress and $\bar{\tau}_i$ determines the interlaminar shear strength of the material.

In thin-walled structures, transverse normal stress is usually small and can be neglected in comparison with shear stress. Then, Eq. (6.18) can be simplified and written as

$$\tau_r = \bar{\tau}_i \ . \tag{6.19}$$

As an example, Fig. 6.16 displays the dependence of the normalized maximum deflection w/R on the force P for the fiberglass–epoxy cross-ply cylindrical shell of radius R loaded with a radial concentrated force P (Vasiliev, 1970). The shell failure was caused by delamination. The shadowed interval shows the possible values of the ultimate force calculated with the aid of Eq. (6.19) (this value is not unique because of the scatter of interlaminar shear strength).

6.2. Practical recommendations and discussion

As follows from the foregoing analysis, for practical strength evaluation of fabric composites, we can use either maximum stress criterion, Eqs. (6.2) or second-order polynomial criterion in Eq. (6.14) in conjunction with Eq. (6.15) for the case of biaxial compression. For unidirectional composites with polymeric matrices, we can apply Eqs. (6.3) and (6.4) in which function F is specified by Eq. (6.17). It should be emphasized that experimental data have usually rather high scatter, and the accuracy of more complicated and rigorous strength criteria can be more apparent than real. It should be also noted that the simplicity of the recommended polynomial criteria is associated with the fact that from the very beginning they were introduced in this chapter as formal approximations of experimental data in the principal material coordinates. In the literature, these criteria are sometimes formulated in a tensor–polynomial form as linear combinations of mixed invariants of the stress tensor σ_{ij} and the strength tensors of different ranks S_{ij}, S_{ijkl}, etc., i.e.

$$\sum_{i,k} S_{ik}\sigma_{ik} + \sum_{i,k,m,n} S_{ikmn}\sigma_{ik}\sigma_{mn} + \cdots = 1 \ . \tag{6.20}$$

Using the standard transformation for tensor components we can readily write this equation for an arbitrary coordinate frame. However, the fact that the strength

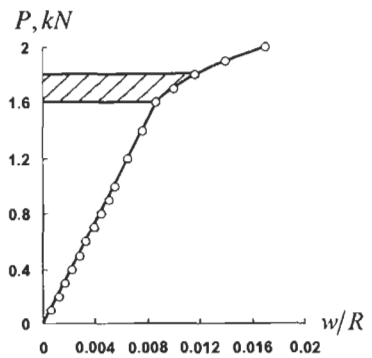

Fig. 6.16. Experimental dependence of the normalized maximum deflection of a fiberglass–epoxy cylindrical shell on the radial concentrated force.

components form a tensor induces some conditions that should be imposed on these components and not necessarily correlate with experimental data.

To be specific, consider a second-order tensor criterion. Introducing contracted notations for tensor components and restricting ourselves to the consideration of orthotropic materials referred to the principal material coordinates 1, 2, 3 (see Fig. 6.1) we can present Eq. (6.20) as

$$F(\sigma_1, \sigma_2, \tau_{12}) = R_1^0\sigma_1 + R_2^0\sigma_2 + R_{11}^0\sigma_1^2 + 2R_{12}^0\sigma_1\sigma_2 + R_{22}^0\sigma_2^2 + 4S_{12}^0\tau_{12}^2 = 1 \ , \tag{6.21}$$

which corresponds to Eq. (6.20) if we put

$$\sigma_{11} = \sigma_1, \ \sigma_{12} = \tau_{12}, \ \sigma_{22} = \sigma_2 \quad \text{and} \quad S_{11} = R_1, \ S_{22} = R_2, \ S_{1111} = R_{11}^0,$$
$$S_{1122} = S_{2211} = R_{12}^0, \ S_{2222} = R_{22}^0, \ S_{1212} = S_{2121} = S_{1221} = S_{2112} = S_{12}^0 \ .$$

Superscript "0" indicates that the components of the strength tensors are referred to the principal material coordinates. Applying strength conditions in Eqs. (6.13) we can reduce Eq. (6.21) to the following form:

$$F(\sigma_1, \sigma_2, \tau_{12}) = \sigma_1\left(\frac{1}{\bar{\sigma}_1^+} - \frac{1}{\bar{\sigma}_1^-}\right) + \sigma_2\left(\frac{1}{\bar{\sigma}_2^+} - \frac{1}{\bar{\sigma}_2^-}\right)$$
$$+ \frac{\sigma_1^2}{\bar{\sigma}_1^+\bar{\sigma}_1^-} + 2R_{12}^0\sigma_1\sigma_2 + \frac{\sigma_2^2}{\bar{\sigma}_2^+\bar{\sigma}_2^-} + \left(\frac{\tau_{12}}{\bar{\tau}_{12}}\right)^2 = 1 \ . \tag{6.22}$$

This equation looks similar to Eq. (6.14), but there is a principal difference between them. While Eq. (6.14) is only an approximation of experimental results, and we can take any suitable value of coefficient R_{12}^0 (in particular, we put $R_{12} = 0$), criterion in Eq. (6.22) has an invariant tensor form, and coefficient R_{12} should be determined using this property of the criterion.

Following Gol'denblat and Kopnov (1968) consider two cases of pure shear in coordinates 1′, 2′ shown in Fig. 6.17 and assume that $\tau_{45}^+ = \bar{\tau}_{45}^+$ and $\tau_{45}^- = \bar{\tau}_{45}^-$, where

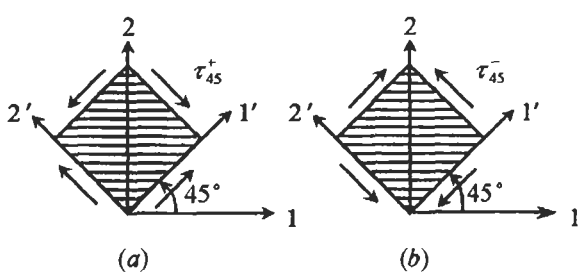

Fig. 6.17. Pure shear in coordinates (1′, 2′) rotated by 45° with respect to the principal material coordinates (1, 2).

the overbar denotes, as earlier, the ultimate value of the corresponding stress. In the general case, $\bar{\tau}_{45}^{+} \neq \bar{\tau}_{45}^{-}$. Indeed, for a unidirectional composite, stress τ_{45}^{+} induces tension of the fibers, while τ_{45}^{-} causes compression of the fibers, and the corresponding ultimate values can be different. Using results presented in Section 2.4 we can conclude that for the loading case shown in Fig. 6.17(a), $\sigma_1 = \tau_{45}^{+}$, $\sigma_2 = -\tau_{45}^{+}$ and $\tau_{12} = 0$, while for the case in Fig. 6.17(b), $\sigma_1 = -\tau_{45}^{-}$, $\sigma_2 = \tau_{45}$ and $\tau_{12} = 0$. Applying strength criterion in Eq. (6.22) for these loading cases we arrive at

$$F(\sigma_1 = \bar{\tau}_{45}^{+}, \sigma_2 = -\bar{\tau}_{45}^{+}, \tau_{12} = 0)$$
$$= \bar{\tau}_{45}^{+}\left(\frac{1}{\bar{\sigma}_1^{+}} - \frac{1}{\bar{\sigma}_1^{-}} - \frac{1}{\bar{\sigma}_2^{+}} + \frac{1}{\bar{\sigma}_2^{-}}\right) + (\bar{\tau}_{45}^{+})^2\left(\frac{1}{\bar{\sigma}_1^{+}\bar{\sigma}_1^{-}} + \frac{1}{\bar{\sigma}_2^{+}\bar{\sigma}_2^{-}} - 2R_{12}^{0}\right) = 1,$$
$$F(\sigma_1 = -\bar{\tau}_{45}, \sigma_2 = \bar{\tau}_{45}^{-}, \tau_{12} = 0)$$
$$= \bar{\tau}_{45}^{-}\left(\frac{1}{\bar{\sigma}_1^{-}} - \frac{1}{\bar{\sigma}_1^{+}} + \frac{1}{\bar{\sigma}_2^{+}} - \frac{1}{\bar{\sigma}_2^{-}}\right) + (\bar{\tau}_{45}^{-})^2\left(\frac{1}{\bar{\sigma}_1^{+}\bar{\sigma}_1^{-}} + \frac{1}{\bar{\sigma}_2^{+}\bar{\sigma}_2^{-}} - 2R_{12}^{0}\right) = 1 .$$

In general, these two equations give different solutions for R_{12}^{0}. The unique solution exists if the following compatibility condition is valid:

$$\frac{1}{\bar{\sigma}_1^{+}} - \frac{1}{\bar{\sigma}_1^{-}} - \frac{1}{\bar{\sigma}_2^{+}} + \frac{1}{\bar{\sigma}_2^{-}} = \frac{1}{\bar{\tau}_{45}^{+}} - \frac{1}{\bar{\tau}_{45}^{-}} \quad . \tag{6.23}$$

If the actual material strength characteristics do not satisfy this equation, then the strength criteria in Eq. (6.22) cannot be applied to this material. If they do, then coefficient R_{12}^{0} can be found as

$$R_{12}^{0} = \frac{1}{2}\left(\frac{1}{\bar{\sigma}_1^{+}\bar{\sigma}_1^{-}} + \frac{1}{\bar{\sigma}_2^{+}\bar{\sigma}_2^{-}} - \frac{1}{\bar{\tau}_{45}^{+}\bar{\tau}_{45}^{-}}\right) \quad . \tag{6.24}$$

For further analysis, consider for the sake of brevity a special orthotropic material shown in Fig. 6.18 for which $\bar{\sigma}_1^{+} = \bar{\sigma}_1^{-} = \bar{\sigma}_2^{+} = \bar{\sigma}_2^{-} = \bar{\sigma}_0$, $\bar{\tau}_{45}^{+} = \bar{\tau}_{45}^{-} = \bar{\tau}_{45}$ and $\bar{\tau}_{12} = \bar{\tau}_0$. As can be seen, Eq. (6.23) is satisfied in this case, and the strength criterion, Eq. (6.22), referred to the principal material coordinates (1, 2) in Fig. 6.18 acquires the form

$$\frac{1}{\bar{\sigma}_0^2}(\sigma_1^2 + \sigma_2^2) + 2R_{12}^{0}\sigma_1\sigma_2 + \left(\frac{\tau_{12}}{\bar{\tau}_0}\right)^2 = 1 \quad , \tag{6.25}$$

where in accordance with Eq. (6.24)

$$R_{12}^{0} = \frac{1}{\bar{\sigma}_0^2} - \frac{1}{2\bar{\tau}_{45}^2} \quad . \tag{6.26}$$

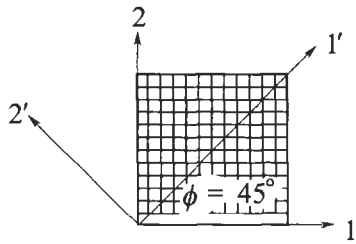

Fig. 6.18. A special orthotropic material with equal strength in directions 1 and 2 referred to coordinates (1, 2) and (1', 2').

Now, present Eq. (6.25) in the following matrix form:

$$\{\sigma\}^{\mathrm{T}}[R^0]\{\sigma\} = 1 \ , \tag{6.27}$$

where

$$\{\sigma\} = \begin{Bmatrix} \sigma_1 \\ \sigma_2 \\ \tau_{12} \end{Bmatrix}, \quad [R^0] = \begin{bmatrix} R^0_{11} & R^0_{12} & 0 \\ R^0_{12} & R^0_{11} & 0 \\ 0 & 0 & 4S^0_{12} \end{bmatrix}, \tag{6.28}$$

$$R^0_{11} = \frac{1}{\bar{\sigma}^2_0}, \quad R^0_{12} = \frac{1}{\bar{\sigma}^2_0} - \frac{1}{2\bar{\tau}^2_{45}}, \quad S^0_{12} = \frac{1}{4\bar{\tau}^2_0} \ .$$

Superscript "T" means transposition converting the column vector $\{\sigma\}$ into the row vector $\{\sigma\}^{\mathrm{T}}$. Let us transform stresses referred to axes (1, 2) into stresses corresponding to axes (1', 2') shown in Fig. 6.18. Such transformation can be performed with the aid of Eqs. (4.68) if we put $\sigma_x = \sigma_1$, $\sigma_y = \sigma_2$, $\tau_{xy} = \tau_{12}$, $\sigma_1 = \sigma^{45}_1$, $\sigma_2 = \sigma^{45}_2$, $\tau_{12} = \tau^{45}_{12}$ and take $\phi = 45°$. The matrix form of this transformation is

$$\{\sigma\} = [T]\{\sigma^{45}\} \ , \tag{6.29}$$

where

$$[T] = \begin{bmatrix} 1/2 & 1/2 & -1 \\ 1/2 & 1/2 & 1 \\ 1/2 & -1/2 & 0 \end{bmatrix} .$$

Substitution of stresses in Eq. (6.29) into Eq. (6.27) yields

$$\{\sigma^{45}\}^{\mathrm{T}}[T]^{\mathrm{T}}[R^0][T]\{\sigma^{45}\} = 1 \ .$$

This equation being rewritten as

$$\{\sigma^{45}\}^{\mathrm{T}}[R^{45}]\{\sigma^{45}\} = 1 \tag{6.30}$$

specifies the strength criterion for the same material but referred to coordinates $(1', 2')$. The strength matrix has the following form:

$$[R^{45}] = [T]^{\mathrm{T}}[R^{0}][T] = \begin{bmatrix} R_{11}^{45} & R_{12}^{45} & 0 \\ R_{12}^{45} & R_{11}^{45} & 0 \\ 0 & 0 & 4S_{12}^{45} \end{bmatrix},$$

where

$$\begin{aligned} R_{11}^{45} &= \frac{1}{\bar{\sigma}_0^2} + \frac{1}{4}\left(\frac{1}{\bar{\tau}_0^2} - \frac{1}{\bar{\tau}_{45}^2}\right), \\ R_{12}^{45} &= \frac{1}{\bar{\sigma}_0^2} - \frac{1}{4}\left(\frac{1}{\bar{\tau}_0^2} + \frac{1}{\bar{\tau}_{45}^2}\right), \\ S_{12}^{45} &= \frac{1}{4\bar{\tau}_{45}^2} \ . \end{aligned} \tag{6.31}$$

The explicit form of Eq. (6.30) is

$$\begin{aligned} &\left[\frac{1}{\bar{\sigma}_0^2} + \frac{1}{4}\left(\frac{1}{\bar{\tau}_0^2} - \frac{1}{\bar{\tau}_{45}^2}\right)\right]\left[(\sigma_1^{45})^2 + (\sigma_2^{45})^2\right] \\ &\quad + \left[\frac{1}{\bar{\sigma}_0^2} - \frac{1}{4}\left(\frac{1}{\bar{\tau}_0^2} + \frac{1}{\bar{\tau}_{45}^2}\right)\right]\sigma_1^{45}\sigma_2^{45} + \left(\frac{\tau_{12}^{45}}{\bar{\tau}_{45}}\right)^2 = 1 \ . \end{aligned} \tag{6.32}$$

However, since criterion in Eq. (6.25) is a tensor relationship, it can be written in coordinates $(1', 2')$ if we change σ_1, σ_2, τ_{12} for σ_1^{45}, σ_2^{45}, τ_{12}^{45}, $\bar{\sigma}_0$ for $\bar{\sigma}_{45}$, and $\bar{\tau}_0$ for $\bar{\tau}_{45}$. The result is as follows:

$$\frac{1}{\bar{\sigma}_{45}^2}\left[(\sigma_1^{45})^2 + (\sigma_2^{45})^2\right] + \left(\frac{1}{\bar{\sigma}_{45}^2} - \frac{1}{2\bar{\tau}_0^2}\right)\sigma_1^{45}\sigma_2^{45} + \left(\frac{\tau_{12}^{45}}{\bar{\tau}_{45}}\right)^2 = 1 \ . \tag{6.33}$$

Because Eqs. (6.32) and (6.33) are the two equivalent forms of one and the same criterion, we arrive at the following equations:

$$\frac{1}{\bar{\sigma}_{45}^2} = \frac{1}{\bar{\sigma}_0^2} + \frac{1}{4}\left(\frac{1}{\bar{\tau}_0^2} - \frac{1}{\bar{\tau}_{45}^2}\right), \quad \frac{1}{\bar{\sigma}_{45}^2} - \frac{1}{2\bar{\tau}_0^2} = \frac{1}{\bar{\sigma}_0^2} - \frac{1}{4}\left(\frac{1}{\bar{\tau}_0^2} + \frac{1}{\bar{\tau}_{45}^2}\right) \ .$$

The second of these equations can be easily reduced to the first one. So, there is only one condition showing that the combination of strength characteristics

$$I_s = \frac{1}{\bar{\sigma}_{45}^2} + \frac{1}{4\bar{\tau}_{45}^2} = \frac{1}{\bar{\sigma}_0^2} + \frac{1}{4\bar{\tau}_0^2} \quad , \tag{6.34}$$

is actually an invariant of the strength tensor. With due regard to Eqs. (6.28) and (6.31) this invariant can be also written as

$$I_s = R_{11}^0 + S_{12}^0 = R_{11}^{45} + S_{12}^{45}$$

If the actual material characteristics do not satisfy Eq. (6.34), then the tensor strength criterion cannot be applied to this material. However, if this equation is consistent with experimental data, then the tensor criterion offers considerable possibilities to study material strength. Indeed, restricting ourselves to two terms presented in Eq. (6.20) let us write this equation in coordinates (1′, 2′) shown in Fig. 6.18 and assume that $\phi \neq 45°$. Then

$$\sum_{i,k} S_{ik}^{\phi} \sigma_{ik}^{\phi} + \sum_{i,k,m,n} S_{ikmn}^{\phi} \sigma_{ik}^{\phi} \sigma_{mn}^{\phi} = 1 \quad . \tag{6.35}$$

Here, S_{ik}^{ϕ} and S_{ikmn}^{ϕ} are the components of the second and the fourth rank strength tensors which are transformed in accordance with tensor calculus as

$$\begin{aligned} S_{ik}^{\phi} &= \sum_{p,q} l_{ip} l_{kq} S_{pq}^0, \\ S_{ikmn}^{\phi} &= \sum_{p,q,r,s} l_{ip} l_{kq} l_{mr} l_{ns} S_{pqrs}^0 \quad . \end{aligned} \tag{6.36}$$

Here, l are directional cosines of axes 1′ and 2′ on the plane referred to coordinates 1 and 2 (see Fig. 6.18), i.e. $l_{11} = \cos\phi$, $l_{12} = \sin\phi$, $l_{21} = -\sin\phi$, $l_{22} = \cos\phi$. Substitution of Eqs. (6.36) into Eq. (6.35) yields the strength criterion in coordinates (1′, 2′) but written in terms of strength components corresponding to coordinates (1, 2), i.e.

$$\sum_{i,k} \sum_{p,q} l_{ip} l_{kq} S_{pq}^0 \sigma_{ik}^{\phi} + \sum_{i,k,m,n} \sum_{p,q,r,s} l_{ip} l_{kq} l_{mr} l_{ns} S_{pqrs}^0 \sigma_{ik}^{\phi} \sigma_{mn}^{\phi} = 1 \quad . \tag{6.37}$$

Apply Eq. (6.37) for the special orthotropic material that was studied above (see Fig. 6.18) and for which

$$\begin{aligned} &S_{pq} = 0, \quad S_{1111} = S_{2222} = R_{11}^0 = R_{22}^0 = \frac{1}{\bar{\sigma}_0^2}, \\ &S_{1122} = S_{2211} = R_{12}^0 = \frac{1}{\bar{\sigma}_0^2} - \frac{1}{2\bar{\tau}_{45}^2}, \\ &S_{1212} = S_{2121} = S_{1221} = S_{2112} = S_{12}^0 = \frac{1}{4\bar{\tau}_0^2} \quad . \end{aligned} \tag{6.38}$$

Following Gol'denblat and Kopnov (1968) consider material strength under tension in the 1′-direction and in shear in plane (1′, 2′). Taking first $\sigma_{11}^{\phi} = \bar{\sigma}_{\phi}$, $\sigma_{22}^{\phi} = 0$, $\tau_{12}^{\phi} = 0$ and then $\tau_{12}^{\phi} = \bar{\tau}_{\phi}$, $\sigma_{11}^{\phi} = 0$, $\sigma_{22}^{\phi} = 0$ we get from Eq. (6.37)

$$\bar{\sigma}_{\phi}^{2} = \frac{1}{\sum_{p,q,r,s} l_{1p} l_{1q} l_{1r} l_{1s} S_{pqrs}^{0}}, \quad \bar{\tau}_{\phi}^{2} = \frac{1}{\sum_{p,q,r,s} l_{1p} l_{2q} l_{1r} l_{2s} S_{pqrs}^{0}},$$

or in the explicit form

$$\begin{aligned} \bar{\sigma}_{\phi}^{2} &= [R_{11}^{0}(\cos^4\phi + \sin^4\phi) + 2(S_{12}^{0} + 2R_{12}^{0})\sin^2\phi\cos^2\phi]^{-1}, \\ \bar{\tau}_{\phi}^{2} &= 4[2(R_{11}^{0} - R_{12}^{0})\sin^2\phi\cos^2\phi + S_{12}^{0}\cos^2 2\phi]^{-1}. \end{aligned} \tag{6.39}$$

These equations allow us to calculate material strength in any coordinate frame whose axes make angle ϕ with the corresponding principal material axes. Taking into account Eqs. (6.34) and (6.38) we can derive the following relationship from Eqs. (6.39):

$$\frac{1}{\bar{\sigma}_{\phi}^{2}} + \frac{1}{4\bar{\tau}_{\phi}^{2}} = \frac{1}{\bar{\sigma}_{0}^{2}} + \frac{1}{4\bar{\tau}_{0}^{2}} = I_{S}. \tag{6.40}$$

So, I_S is indeed the invariant of the strength tensor whose value for a given material does not depend on ϕ.

Thus, tensor–polynomial strength criteria provide universal equations that can be readily written in any coordinate frame, but on the other hand, material mechanical characteristics, particularly material strength in different directions, should follow the rules of tensor transformation, i.e., compose invariants (like I_S) that are the same for all coordinate frames.

To demonstrate the difference between the tensor–polynomial and approximation polynomial criteria, consider again Eq. (6.15) and write it for the special orthotropic material described above (see Fig. 6.18). Then, Eq. (6.15) formally reduces to Eqs. (6.25) or Eq. (6.27) in which

$$R_{11}^{0} = \frac{1}{\bar{\sigma}_{0}^{2}}, \quad R_{12}^{0} = -\frac{1}{2\bar{\sigma}_{0}^{2}}, \quad S_{12}^{0} = \frac{1}{4\bar{\tau}_{0}^{2}}. \tag{6.41}$$

Matching these results with Eqs. (6.28), we can see that coefficient R_{12}^{0} is different here. Moreover, because this coefficient was selected to provide the proper approximation of experimental results (see, e.g., Fig. 6.8), we can hardly expect that Eqs. (6.41) specify the components of a strength tensor. To show that this is really not the case, apply to the approximation criterion under study transformation resulting in Eq. (6.30). The coefficients of thus constructed approximation criterion in coordinates (1′, 2′) become

$$R_{11}^{45} = \frac{1}{4}\left(\frac{1}{\bar{\sigma}_0^2} + \frac{1}{\bar{\tau}_0^2}\right), \quad R_{12}^{45} = \frac{1}{4}\left(\frac{1}{\bar{\sigma}_0^2} - \frac{1}{\bar{\tau}_0^2}\right), \quad S_{12}^{45} = \frac{3}{4\bar{\sigma}_0^2} \ . \tag{6.42}$$

Now assume (and this is what should not be done for approximation criteria) that criterion in Eqs. (6.15) is valid in coordinates (1′, 2′) (see Fig. 6.18) as well. Because material is orthotropic in these coordinates, we have the following equation similar to Eq. (6.33):

$$\frac{1}{\bar{\sigma}_{45}^2}[(\sigma_1^{45})^2 + (\sigma_2^{45})^2] - \frac{\sigma_1^{45}\sigma_2^{45}}{\bar{\sigma}_{45}^2} + \left(\frac{\tau_{45}}{\bar{\tau}_{45}}\right)^2 = 1 \ . \tag{6.43}$$

Matching this result with Eq. (6.30) in which coefficients R are specified by Eqs. (6.42) we arrive at the following conditions:

$$\frac{1}{\bar{\sigma}_{45}^2} = \frac{1}{4}\left(\frac{1}{\bar{\sigma}_0^2} + \frac{1}{\bar{\tau}_0^2}\right),$$
$$-\frac{1}{2\bar{\sigma}_{45}^2} = \frac{1}{4}\left(\frac{1}{\bar{\sigma}_0^2} - \frac{1}{\bar{\tau}_0^2}\right),$$
$$\frac{1}{\bar{\tau}_{45}^2} = \frac{3}{\bar{\sigma}_0^2} \ ,$$

which can be reduced to

$$\bar{\tau}_0^2 = \bar{\tau}_{45} = \frac{\bar{\sigma}_0^2}{3}, \quad \bar{\sigma}_{45} = \bar{\sigma}_0 \ . \tag{6.44}$$

These conditions can hardly be met for cross-ply or fabric composites as in Fig. 6.18.

For an isotropic material, Eqs. (6.25) for the tensor–polynomial criterion and Eq. (6.43) for the approximation criterion yield, with due regard to Eqs. (6.44) one and the same strength criterion that can be written as

$$\sigma_1^2 - \sigma_1\sigma_2 + \sigma_2^2 + 3\tau_{12}^2 = \bar{\sigma}^2 \ , \tag{6.45}$$

where $\bar{\sigma} = \bar{\sigma}_0 = \bar{\sigma}_{45}$. Introducing stress intensity σ specified by Eqs. (4.19) or Eq. (4.24) we arrive at the following result:

$$\sigma = \bar{\sigma} \tag{6.46}$$

known in the theory of plasticity as Huber–Mises plasticity criterion. It should be emphasized that stress intensity, σ, is the invariant characteristic of the stress state (see Section 4.1.2), so for an isotropic material, the approximation criterion in Eq. (6.45) or Eq. (6.46) is also a tensor–polynomial criterion. In this latter form it was

first time proposed by M.T. Huber in 1904. However, this fact became widely known only in 1924 at the International Congress on Applied Mechanics in Delft, The Netherlands. Before this Congress, this criterion was associated with R. Mises' paper published in 1913 in which it was introduced as an approximation criterion. The original plasticity criterion of maximum shear stress being widely recognized but having not an easy-to-use hexagon form on the plane of principal stresses $(\sigma, \sigma_2, \tau_{12} = 0)$ was approximated by R. Mises with Eq. (6.45) as shown in Fig. 6.19.

Thus, for isotropic materials, the quadratic approximation strength criterion under discussion has an invariant form. However, this is not true for orthotropic materials. Using transformation in Eq. (6.37) for $\phi \neq 45°$ we arrive at constraints similar to Eq. (6.40) that do not coincide, in contrast to the tensor criterion, with Eqs. (6.44) for $\phi = 45°$. From this it follows that approximation polynomial criteria can be used only in coordinates in which they approximate experimental results.

In general, comparing tensor–polynomial and approximation strength criteria we can conclude the following. Tensor criteria should be used if our purpose is to develop a theory of material strength, because a consistent physical theory must be covariant, i.e., constraints that are imposed on material properties within the framework of this theory should not depend on a particular coordinate frame. For practical applications, approximation criteria are more suitable, but in the forms they are presented here they should be used only for orthotropic unidirectional plies or fabric layers in coordinates whose axes coincide with the fibers' directions.

To evaluate the laminate strength, we should first determine the stresses acting in the plies or layers (see Section 5.10), identify the layer that is expected to fail first and apply one of the foregoing strength criteria. The fracture of the first ply or layer may not necessarily result in the failure of the whole laminate. Then, simulating the failed element with a proper model (see, e.g., Section 4.4.2) the strength analysis is repeated and continued up to the failure of the last ply or layer.

In principle, failure criteria can be constructed for the whole laminate as a quasi-homogeneous material. Being not realistic for design problems, to solve which we

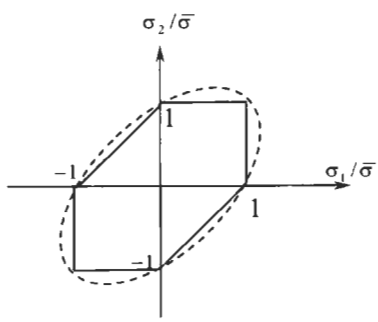

Fig. 6.19. Maximum shear stress criterion (———) and its elliptic approximation with Eq. (6.45) (– – – –) on the plane of principal stresses.

should compare numerous laminate structures and can hardly test all of them, this approach can be successfully used for structures that are under stable and mass production. For example, the segments of two structures of composite drive shafts – one made of fabric and the other of unidirectional composite, are shown in Fig. 6.20. Testing these segments in tension, compression, and torsion we can plot the strength envelope on the plane (M, T), where M is the bending moment and T is the torque, and evaluate the shaft strength for different combinations of M and T with high accuracy and reliability.

6.3. Examples

As the first example, consider a problem of torsion of a thin-walled cylindrical drive shaft (see Fig. 6.21) made by winding of a glass epoxy fabric tape at angles $\pm 45^\circ$. Material properties are $E_1 = 23.5$ GPa, $E_2 = 18.5$ GPa, $G_{12} = 7.2$ GPa, $\nu_{12} = 0.16$, $\nu_{21} = 0.2$, $\bar{\sigma}_1^+ = 510$ MPa, $\sigma_1 = 460$ MPa, $\bar{\sigma}_2^- = 280$ MPa, $\bar{\sigma}_2 = 260$ MPa, $\tau_{12} = 85$ MPa. Shear strain induced by torque T is (Vasiliev, 1993)

$$\gamma_{xy} = \frac{T}{2\pi R^2 B_{44}} \ .$$

Here T is the torque, $R = 0.05$ m is the shaft radius, and B_{44} is the shear stiffness of the wall. According to Eqs. (5.39), $B_{44} = A_{44} h$, where $h = 5$ mm is the wall thickness, while A_{44} is specified by Eqs. (4.72) and can be presented as $(\phi = 45^\circ)$

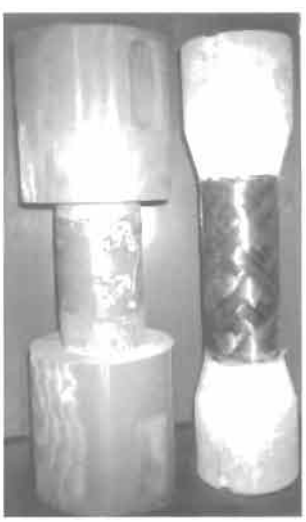

Fig. 6.20. Segments of composite drive shafts with test fixtures. Courtesy of CRISM.

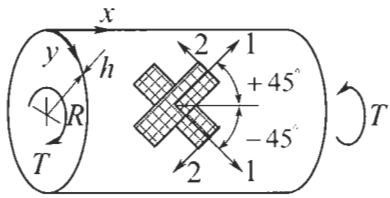

Fig. 6.21. Torsion of a drive shaft.

$$A_{44} = \frac{1}{4(1 - \nu_{12}\nu_{21})}(E_1 + E_2 - 2E_1\nu_{12})$$

Using Eqs. (5.71) we can determine strains in the principal material coordinates 1, 2 of $\pm 45^\circ$ layers (see Fig. 6.21)

$$\varepsilon_1^{\pm} = \pm\tfrac{1}{2}\gamma_{xy}, \quad \varepsilon_2^{\pm} = \mp\tfrac{1}{2}\gamma_{xy}, \quad \gamma_{12}^{\pm} = 0 \ .$$

Applying Eqs. (5.72) and the foregoing results we can express stresses in terms of T as

$$\sigma_1^{\pm} = \pm\frac{TE_1(1 - \nu_{12})}{\pi R^2 h(E_1 + E_2 - 2E_1\nu_{12})},$$

$$\sigma_2^{\pm} = \mp\frac{TE_2(1 - \nu_{21})}{\pi R^2 h(E_1 + E_2 - 2E_1\nu_{12})},$$

$$\tau_{12}^{\pm} = 0 \ .$$

The problem is to determine the ultimate torque, T_u.

First, use the maximum stress criterion, Eqs. (6.2) which gives the following four values of the ultimate torque corresponding to tensile or compressive failure of $\pm 45^\circ$ layers:

$$\sigma_1^{+} = \bar{\sigma}_1^{+}, \quad T_u = 34 \text{ kNm},$$

$$\sigma_1^{-} = \bar{\sigma}_1^{-}, \quad T_u = 30.7 \text{ kNm},$$

$$\sigma_2^{+} = \bar{\sigma}_2^{+}, \quad T_u = 25.5 \text{ kNm},$$

$$\sigma_2^{-} = \bar{\sigma}_2^{-}, \quad T_u = 23.7 \text{ kNm} \ .$$

The actual ultimate torque is the lowest of these values, i.e., $T_u = 23.7$ kNm.

Now apply the polynomial criterion in Eq. (6.14), which acquires the form

$$\sigma_1^{\pm}\left(\frac{1}{\bar{\sigma}_1^{+}} - \frac{1}{\bar{\sigma}_1^{-}}\right) + \sigma_2^{\pm}\left(\frac{1}{\bar{\sigma}_2^{+}} - \frac{1}{\bar{\sigma}_2^{-}}\right) + \frac{(\sigma_1^{\pm})^2}{\bar{\sigma}_1^{+}\bar{\sigma}_1^{-}} + \frac{(\sigma_2^{\pm})^2}{\bar{\sigma}_2^{+}\bar{\sigma}_2^{-}} = 1 \ .$$

For +45° and −45° layers, we get, respectively, $T_u = 21.7$ kNm and $T_u = 17.6$ kNm. Thus, $T_u = 17.6$ kNm.

As the second example, consider the cylindrical shell described in Section 5.11 (see Fig. 5.19) and loaded with internal pressure p. Axial, N_x, and circumferential, N_y, stress resultants can be found as

$$N_x = \tfrac{1}{2}pR, \quad N_y = pR \ ,$$

where $R = 100$ mm is the shell radius. Applying constitutive equations, Eqs. (5.74), and neglecting the change of the cylinder curvature ($\kappa_y = 0$) we arrive at the following equations for strains:

$$B_{11}\varepsilon_x^0 + B_{12}\varepsilon_y^0 = \tfrac{1}{2}pR, \quad B_{12}\varepsilon_x^0 + B_{22}\varepsilon_y^0 = pR \ . \tag{6.47}$$

Using Eqs. (5.71) and (5.72) to determine strains and stresses in the principal material coordinates of the plies, we get

$$\begin{aligned}
\sigma_1^{(i)} &= \frac{pR}{2B}\bar{E}_1\left[(B_{22} - 2B_{12})(\cos^2\phi_i + \nu_{12}\sin^2\phi_i)\right. \\
&\quad \left. + (2B_{11} - B_{12})(\sin^2\phi_i + \nu_{12}\cos^2\phi_i)\right], \\
\sigma_2^{(i)} &= \frac{pR}{2B}\bar{E}_2\left[(B_{22} - 2B_{12})(\sin^2\phi_i + \nu_{21}\cos^2\phi_i)\right. \\
&\quad \left. + (2B_{11} - B_{12})(\cos^2\phi_i + \nu_{21}\sin^2\phi_i)\right], \\
\tau_{12}^{(i)} &= \frac{pR}{2B}G_{12}(2B_{11} + B_{12} - B_{22})\sin 2\phi_i \ .
\end{aligned} \tag{6.48}$$

Here, $B = B_{11}B_{22} - B_{12}^2$, and membrane stiffnesses B_{mn} for the shell under study are presented in Section 5.11. Subscript "i" in Eqs. (6.48) indicates the helical plies for which $i = 1$, $\phi_1 = \phi = 36°$ and circumferential plies for which $i = 2$ and $\phi_2 = 90°$.

The problem that we consider is to find the ultimate pressure $\bar{p}_u$. For this purpose, we use strength criteria in Eqs. (6.3), (6.4) and (6.16), and the following material properties $\bar{\sigma}_1^+ = 1300$ MPa, $\bar{\sigma}_2^+ = 27$ MPa, $\bar{\tau}_{12} = 45$ MPa.

Calculation with the aid of Eqs. (6.48) yields

$$\begin{aligned}
&\sigma_1^{(1)} = 83.9p, \quad \sigma_2^{(1)} = 24.2p, \quad \tau_{12}^{(1)} = 1.9p, \\
&\sigma_1^{(2)} = 112p, \quad \sigma_2^{(2)} = 19.5p, \quad \tau_{12}^{(2)} = 0 \ .
\end{aligned}$$

Applying Eqs. (6.3) to evaluate the plies' strength along the fibers, we get

$$\begin{aligned}
&\sigma_1^{(1)} = \bar{\sigma}_1^+, \quad p_u = 14.9 \text{ MPa}, \\
&\sigma_1^{(2)} = \bar{\sigma}_1^+, \quad p_u = 11.2 \text{ MPa} \ .
\end{aligned}$$

The failure of the matrix can be identified using Eq. (6.16), i.e.

$$\left(\frac{\sigma_2^{(1)}}{\bar{\sigma}_2^+}\right)^2 + \left(\frac{\tau_{12}^{(1)}}{\bar{\tau}_{12}}\right)^2 = 1, \quad p_u = 1.1 \text{ MPa} ,$$

$$\left(\frac{\sigma_2^{(2)}}{\bar{\sigma}_2^+}\right)^2 + \left(\frac{\tau_{12}^{(2)}}{\bar{\tau}_{12}}\right)^2 = 1, \quad p_u = 1.4 \text{ MPa} ,$$

Thus, we can conclude that the failure first occurs in the matrix of helical plies and takes place under pressure $p_u^{(1)} = 1.1$ MPa. This pressure destroys only the matrix of helical plies, while the fibers are not damaged and continue to work. According to the model of the unidirectional layer with failed matrix discussed in Section 4.4.2, we should take $E_2 = 0$, $G_{12} = 0$, and $\nu_{12} = 0$ in the helical layer. Then, the stiffness coefficients, Eqs. (4.72) for this layer, become

$$A_{11}^{(1)} = E_1 \cos^4 \phi, \quad A_{12}^{(1)} = E_1 \sin^2 \phi \cos^2 \phi, \quad A_{22}^{(1)} = E_1 \sin^4 \phi \ . \tag{6.49}$$

Calculating again membrane stiffnesses B_{mn} (see Section 5.11) and using Eqs. (6.47) we get for $p \geqslant p_u^{(1)}$:

$$\sigma_1^{(1)} = 92.1p, \quad \sigma_2^{(1)} = 24.2p_u^{(1)} = 26.6 \text{ MPa},$$
$$\tau_{12}^{(1)} = 1.9p_u^{(1)} = 2.1 \text{ MPa}, \quad \sigma_1^{(2)} = 134.6p, \quad \sigma_2^{(2)} = 22.6p, \quad \tau_{12}^{(2)} = 0 \ .$$

Under $p \geqslant p_u^{(1)}$, three modes of failure are possible. The pressure causing the failure of helical plies under longitudinal stress $\sigma_1^{(1)}$ can be calculated from the following equation:

$$\sigma_1^{(1)} = 83.9p_u^{(1)} + 92.1(p_u - p_u^{(1)}) = \bar{\sigma}_1^+$$

which yields $p_u = 14.2$ MPa. Analogous value for the circumferential ply is determined by the following condition:

$$\sigma_1^{(2)} = 112p_u^{(1)} + 134.6(p_u - p_u^{(1)}) = \bar{\sigma}_1^+$$

which gives $p_u = 9.84$ MPa. And finally, the matrix of the circumferential layer can fail under tension across the fibers. Because $\tau_{12}^{(2)} = 0$, we put

$$\sigma_2^{(2)} = 19.5p_u^{(1)} + 22.6(p_u - p_u^{(1)}) = \bar{\sigma}_2^+$$

and find $p_u = 1.4$ MPa.

Thus, the second failure takes place at $p_u^{(2)} = 1.4$ MPa and is accompanied with cracks in the matrix of the cicumferential layer (see Fig. 4.36).

For $p \geqslant p_u^{(2)}$, we should put $E_2 = 0, G_{12} = 0$ and $\nu_{12} = 0$ in the circumferential layer whose stiffness coefficients become

$$A_{11}^{(2)} = 0, \quad A_{12}^{(2)} = 0, \quad A_{22}^{(2)} = E_1 \ . \tag{6.50}$$

Membrane stiffnesses of the structure now correspond to the monotropic model of a composite unidirectional ply (see Section (3.3)) and can be calculated as

$$B_{mn} = A_{mn}^{(1)} h_1 + A_{mn}^{(2)} h_2 \ ,$$

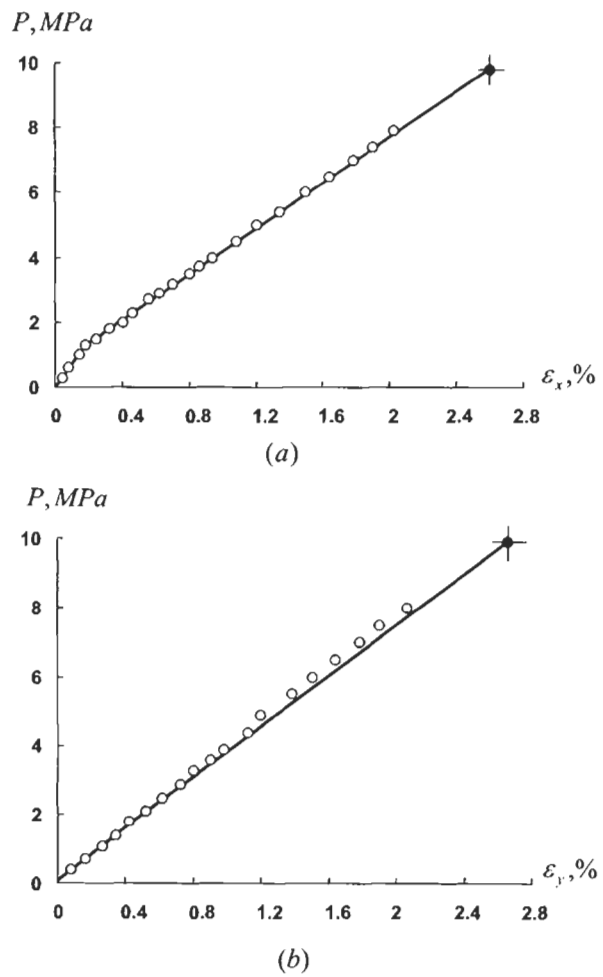

Fig. 6.22. Dependence of the axial (a) and the circumferential (b) strains on internal pressure. (———) analysis; (o) experimental data.

where A_{mn} are specified by Eqs. (6.49) and (6.50), and $h_1 = 0.62$ mm, $h_2 = 0.6$ mm are the thicknesses of the helical and circumferential layers. Using again Eqs. (6.48) we get for $p \geqslant p_u^{(2)}$:

$$\sigma_1^{(1)} = 137.7p, \quad \sigma_1^{(2)} = 122.7p \ .$$

The cylinder failure can now be caused by the fracture of either helical fibers or circumferential fibers. The corresponding values of the ultimate pressure can be found from the following equations:

$$\sigma_1^{(1)} = 83.9p_u^{(1)} + 92.1(p_u^{(2)} - p_u^{(1)}) + 137.7(p_u - p_u^{(2)}) = \bar{\sigma}_1^- ,$$
$$\sigma_1^{(2)} = 112p_u^{(1)} + 134.6(p_u^{(2)} - p_u^{(1)}) + 122.7(p_u - p_u^{(2)}) = \sigma_1^- \ ,$$

where $p_u^{(1)} = 1.1$ MPa and $p_u^{(2)} = 1.4$ MPa.

The first of these equations yields $p_u = 10$ MPa, while the second $p_u = 10.7$ MPa.

Thus, the failure of the structure under study occurs at $\bar{p}_u = 10$ MPa as a result of fiber fracture in the helical layer.

Dependencies of strains that can be calculated using Eqs. (6.47) and the appropriate values of B_{mn} are shown in Fig. 6.22 (solid lines). As can be seen, the

Table 6.1
Burst pressure for filament wound fiberglass pressure vessels.

Diameter of the vessel (mm)	Layer thickness (mm)		Calculated burst pressure (MPa)	Number of tested vessels	Experimental burst pressure	
	h_1	h_2			Mean value (MPa)	Variation coefficient (%)
200	0.62	0.60	10	5	9.9	6.8
200	0.92	0.93	15	5	13.9	3.3

Fig. 6.23. The failure mode of a composite pressure vessel.

theoretical prediction is in fair agreement with experimental results. The same conclusion can be made for the burst pressure that is listed in Table 6.1 for two types of filament wound fiberglass pressure vessels. Typical failure mode for the vessels presented in Table 6.1 is shown in Fig. 6.23.

6.4. References

Annin, B.D. and Baev, L.V. (1979). Criteria of composite material strength. In *Proc First USA–USSR Symposium on Fracture of Composite Materials*, Riga, USSR, Sept. 1978 (G.C. Sih and V.P. Tamuzh eds.). Sijthoff & Noordhoff, The Netherlands, pp. 241–254.

Ashkenazi, E.K. (1966). *Strength of Anisotropic and Synthetic Materials.* Lesnaya Promyshlennost. Moscow (in Russian).

Barbero, E.J. (1998). *Introduction to Composite Materials Design.* West Virginia University, USA.

Belyankin, F.P., Yatsenko, V.F. and Margolin, G.G. (1971). *Strength and Deformability of Fiberglass Plastics Under Biaxial Compression.* Naukova Dumka, Kiev (in Russian).

Gol'denblat, I.I. and Kopnov, V.A. (1968). Criteria of Strength and Plasticity for Structural Materials. Mashinostroenie, Moscow.

Jones, R.M. (1999). *Mechanics of Composite Materials*, 2nd edn. Taylor and Francis, Philadelphia, PA.

Katarzhnov, Yu.I. (1982). Experimental study of load carrying capacity of hollow circular and box composite beams under compression and torsion. Dissertation. Riga (in Russian).

Rowlands, R.E. (1975). Flow and failure of biaxially loaded composites: experimental–theoretical correlation. In *AMD – Vol. 13, Inelastic Behavior of Composite Materials.* ASME Winter Annual Meeting, Houston, TX (C.T. Herakovich ed.). ASME, New York, 1975, pp. 97–125.

Skudra, A.M., Bulavs, F.Ya., Gurvich, M.R. and Kruklinsh, A.A. (1989). *Elements of Structural Mechanics of Composite Truss Systems.* Riga, Zinatne (in Russian).

Tennyson, R.C., Nanyaro, A.P. and Wharram, G.E. (1980). Application of the cubic polynomial strength criterion to the failure analysis of composite materials. *J. Composite Mater.* **14** (suppl) 28–41.

Tsai, S.W. and Hahn, H.T. (1975). Failure analysis of composite materials. In *AMD – Vol. 13, Inelastic Behavior of Composite Materials.* ASME Winter Annual Meeting, Houston, TX (C.T. Herakovich ed.). ASME, New York, pp. 73–96.

Vasiliev, V.V. (1970). Effect of a local load on an orthotropic glass-reinforced plastic shell. *J. Polymer Mech.* **6**(1), 80–85.

Vasiliev, V.V. (1993). *Mechanics of Composite Structures.* Taylor & Francis, Washington.

Vicario, A.A. Jr. and Toland, R.H. (1975). Failure criteria and failure analysis of composite structural components. In *Composite Materials* (L.J. Broutman and R.H. Krock eds.), *Vol. 7, Structural Design and Analysis, Part I* (C.C. Chamis ed.). Academic Press, New York, pp. 51–97.

Vorobey, V.V., Morozov, E.V. and Tatarnikov, O.V. (1992). *Analysis of Thermostressed Composite Structures.* Moscow, Mashinostroenie (in Russian).

Wu, E.M. (1974). Phenomenological anisotropic failure criterion. In *Composite Materials* (L.J. Broutman and R.H. Krock eds.), *Vol. 2, Mechanics of Composite Materials* (G.P. Sendeckyj ed.). Academic Press, New York, pp. 353–431.

Chapter 7

ENVIRONMENTAL, SPECIAL LOADING, AND MANUFACTURING EFFECTS

Properties of composite materials, as well as properties of all structural materials are affected by environmental and operational conditions. Moreover, for polymeric composites this influence is more pronounced than for conventional metal alloys because polymers are more sensitive to temperature, moisture, and time than metals. There exists also a specific feature of composites associated with the fact that they do not exist apart from composite structures and are formed while these structures are fabricated. As a result, material characteristics depend on the type and parameters of the manufacturing process, e.g., unidirectional composites made by pultrusion, hand lay-up, and filament winding can demonstrate different properties.

This section of the book is concerned with the effect of environmental, loading, and manufacturing factors on mechanical properties and behavior of composites.

7.1. Temperature effects

Temperature is the most important of environmental factors affecting the behavior of composite materials. First, because polymeric composites are rather sensitive to temperature and have relatively low thermal conductivity. This combination of properties allows us, on one hand, to use these materials in structures subjected to short-term heating, and on the other hand, requires us to perform analysis of these structures with due regard to temperature effects. Second, there exist composite materials, e.g., carbon–carbon and ceramic composites, that are specifically developed for the operation under intense heating and materials like mineral–fiber composites that are used to form heatproof layers and coatings. And third, fabrication of composite structures is usually accompanied with more or less intensive heating (e.g., for curing or carbonization), and the further cooling induces thermal stresses and strains to calculate which we need to attract equations of thermal conductivity and thermoelasticity that are discussed below.

7.1.1. Thermal conductivity

Heat flow through the unit area of the surface with normal n is linked with the temperature gradient in the n-direction by Fourier's law as

$$q = -\lambda \frac{\partial T}{\partial n} \ , \tag{7.1}$$

where λ is the thermal conductivity of the material. Temperature distribution along the n-axis is governed by the following equation:

$$\frac{\partial}{\partial n}\left(\lambda \frac{\partial T}{\partial n}\right) = c\rho \frac{\partial T}{\partial t} \tag{7.2}$$

in which c and ρ are specific heat and density of the material and t is time. For a steady (time-independent) temperature distribution, $\partial T/\partial t = 0$ and Eq. (7.2) yields

$$T = C_1 \int \frac{\mathrm{d}n}{\lambda} + C_2 \ . \tag{7.3}$$

Consider a laminated structure referred to coordinates x, z and shown in Fig. 7.1. To determine the temperature distribution along the x-axis only we should take into account that λ does not depend on x, and assume that T does not depend on z. Using conditions $T(x = 0) = T_0$ and $T(x = l) = T_l$ to find constants C_1 and C_2 in Eq. (7.3), where $n = x$, we get

$$T = T_0 + \frac{x}{l}(T_l - T_0)$$

Introduce the apparent thermal conductivity of the laminate in the x-direction, λ_x, and write Eq. (7.1) for the laminate as

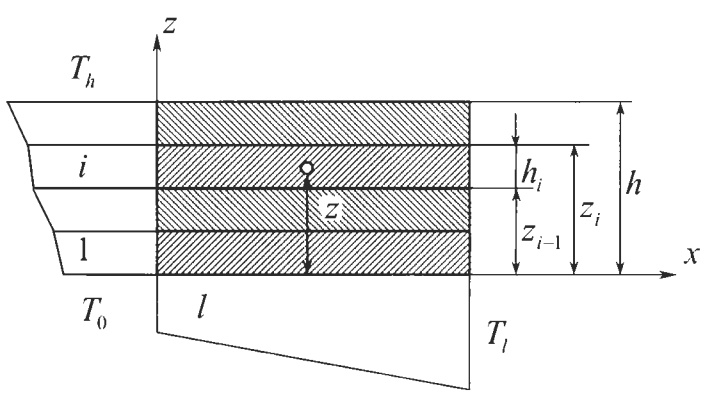

Fig. 7.1. Temperature distribution in a laminate.

$$q_x = -\lambda_x \frac{T_l - T_0}{l} \ .$$

The same equation can be written for the ith layer, i.e.

$$q_i = -\lambda_i \frac{T_l - T_0}{l} \ .$$

The total heat flow through the laminate in the x-direction is

$$q_x h = \sum_{i=1}^{k} q_i h_i \ .$$

Substituting the foregoing results we arrive at

$$\lambda_x = \sum_{i=1}^{k} \lambda_i \bar{h}_i \ , \tag{7.4}$$

where $\bar{h}_i = h_i/h$.

Now consider the heat transfer in the z-direction and introduce the apparent thermal conductivity λ_z in accordance with the following form of Eq. (7.1):

$$q_z = -\lambda_z \frac{T_h - T_0}{h} \ . \tag{7.5}$$

Taking $n = z$ and $\lambda = \lambda_i$ for $z_{i-1} \leqslant z \leqslant z_i$ in Eq. (7.3), using step-wise integration and conditions $T(z = 0) = T_0$, $T(z = h) = T_h$ to find constants C_1 and C_2 we get for the ith layer

$$T_i = T_0 + \frac{T_h - T_0}{\sum_{i=1}^{k} \frac{h_i}{\lambda_i}} \left(\frac{z - z_{i-1}}{\lambda_i} + \sum_{j=1}^{i-1} \frac{h_j}{\lambda_j} \right) \ . \tag{7.6}$$

The heat flow through the ith layer follows from Eqs. (7.1) and (7.6), i.e.

$$q_i = -\lambda_i \frac{\partial T_i}{\partial z} = -\frac{T_h - T_0}{\sum_{i=1}^{k} \frac{h_i}{\lambda_i}} \ .$$

Obviously, $q_i = q_z$ (see Fig. 7.1), and with due regard to Eq. (7.5)

$$\frac{1}{\lambda_z} = \sum_{i=1}^{k} \frac{\bar{h}_i}{\lambda_i} \ , \tag{7.7}$$

where as earlier, $\bar{h}_i = h_i/h$.

Thus obtained results, Eqs. (7.4) and (7.7), can be used to determine the thermal conductivity of a unidirectional composite ply. Indeed, comparing Fig. 7.1 with

Fig. 3.34 showing the structure of the first-order ply model, we can write the following equations specifying thermal conductivity of a unidirectional ply along and across the fibers:

$$\lambda_1 = \lambda_{1f} v_f + \lambda_m v_m,$$
$$\frac{1}{\lambda_2} = \frac{v_f}{\lambda_{2f}} + \frac{v_m}{\lambda_m} \quad . \tag{7.8}$$

Here λ_{1f} and λ_{2f} are thermal conductivities of the fiber in longitudinal and transverse directions (for some fibers they are different), λ_m is the corresponding characteristic of the matrix, and v_f, $v_m = 1 - v_f$ are fibers and matrix volume fractions. Conductivity coefficients in Eqs. (7.8) are analogous to elastic constants specified by Eqs. (3.76) and (3.78), and the discussion presented in Section 3.3 is valid for Eqs. (7.8) as well. Particularly, it should be noted that application of higher-order microstructural models practically does not change λ_1 but substantially improves λ_2 determined by Eqs. (7.8). Typical properties of unidirectional and fabric composites are listed in Table 7.1.

Consider heat transfer in an orthotropic ply or layer in coordinate frame x, y whose axes x and y make angle ϕ with the principal material coordinates x_1 and x_2 as in Fig. 7.2. Heat flows in coordinates x, y and x_1, x_2 are linked by the following equations:

$$q_x = q_1 \cos\phi - q_2 \sin\phi, \quad q_y = q_1 \sin\phi + q_2 \cos\phi \quad . \tag{7.9}$$

Here, in accordance with Eq. (7.1)

$$q_1 = -\lambda_1 \frac{\partial T}{\partial x_1}, \quad q_2 = -\lambda_2 \frac{\partial T}{\partial x_2} \quad .$$

Table 7.1
Typical thermal conductivity and expansion coefficients of composite materials.

Property	Glass–epoxy	Carbon–epoxy	Aramid–epoxy	Boron–epoxy	Glass fabric–epoxy	Aramid fabric–epoxy
Longitudinal conductivity λ_1 (W/m K)	0.6	1	0.17	0.5	0.35	0.13
Transverse conductivity λ_2 (W/m K)	0.4	0.6	0.1	0.3	0.35	0.13
Longitudinal CTE 10^6 α_1 (1/°C)	7.4	−0.3	−3.6	4.1	8	0.8
Transverse CTE 10^6 α_2 (1/°C)	22.4	34	60	19.2	8	0.8

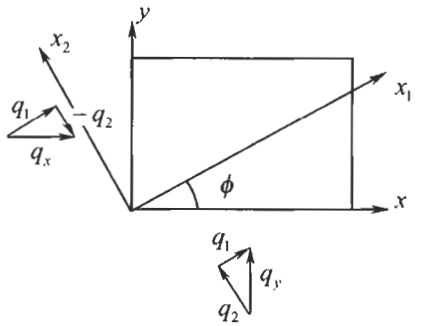

Fig. 7.2. Heat flows in coordinates x, y and x_1, x_2.

Changing variables x_1, x_2 for x, y with the aid of the following transformation relationships:

$$x = x_1 \cos\phi - x_2 \sin\phi, \quad y = x_1 \sin\phi + x_2 \cos\phi$$

and substituting q_1 and q_2 into Eqs. (7.9) we arrive at

$$q_x = -\lambda_x \frac{\partial T}{\partial x} - \lambda_{xy} \frac{\partial T}{\partial y}, \quad q_y = -\lambda_y \frac{\partial T}{\partial y} + \lambda_{xy} \frac{\partial T}{\partial x} \ ,$$

where

$$\begin{aligned} \lambda_x &= \lambda_1 \cos^2\phi + \lambda_2 \sin^2\phi, \\ \lambda_y &= \lambda_1 \sin^2\phi + \lambda_2 \cos^2\phi, \\ \lambda_{xy} &= (\lambda_2 - \lambda_1) \sin\phi \cos\phi \ . \end{aligned} \tag{7.10}$$

can be treated as the ply thermal conductivities in coordinates x, y. Because the ply is anisotropic in these coordinates, the heat flow in the, e.g. x-direction induces the temperature gradient not only in the x-direction, but in the y-direction as well. Using Eq. (7.4) we can now determine the in-plane thermal conductivities of the laminate as

$$\Lambda_x = \sum_{i=1}^{k} \lambda_x^{(i)} \bar{h}_i, \quad \Lambda_y = \sum_{i=1}^{k} \lambda_y^{(i)} \bar{h}_i, \quad \Lambda_{xy} = \sum_{i=1}^{k} \lambda_{xy}^{(i)} \bar{h}_i \ , \tag{7.11}$$

where $\lambda_{x,y}^{(i)}$ are specified by Eqs. (7.10) in which $\lambda_{1,2} = \lambda_{1,2}^{(i)}$ and $\phi = \phi_i$. For $\pm\phi$ angle-ply laminates which are orthotropic, $\Lambda_{xy} = 0$.

As an example, consider the composite body of a space telescope the section of which is shown in Fig. 7.3. The cylinder having diameter $D = 1$ m and total thickness $h = 13.52$ mm consists of four layers, i.e.

Fig. 7.3. A composite section of a space telescope. Courtesy of CRISM.

- $\pm\phi_s$ angle-ply carbon–epoxy external skin with the following parameters:
  $\phi_s = 20^\circ$, $h_s^e = 3.5$ mm, $E_1^e = 120$ GPa,
  $E_2^e = 11$ GPa, $G_{12}^e = 5.5$ GPa, $\nu_{21}^e = 0.27$,
  $\lambda_1^e = 1$ W/m K, $\lambda_2^e = 0.6$ W/m K,
  $\alpha_1^e = -0.3 \times 10^{-6}\ 1/^\circ\text{C}$, $\alpha_2^e = 34 \times 10^{-6}\ 1/^\circ\text{C}$,
- carbon–epoxy lattice layer (see Fig. 4.90) formed by a system of $\pm\phi_r$ helical ribs with
  $\phi_r = 26^\circ$, $h_r = 9$ mm, $\delta_r = 4$ mm, $a_r = 52$ mm, $E_r = 80$ GPa,
  $\lambda_r = 0.9$ W/m K, $\alpha_r = -1 \times 10^{-6}\ 1/^\circ\text{C}$,
- internal skin made of aramid fabric with
  $h_s^i = 1$ mm, $E_x^i = E_y^i = 34$ GPa, $G_{xy}^i = 5.6$ GPa,
  $\nu_{xy}^i = \nu_{yx}^i = 0.15$, $\lambda_x^i = \lambda_y^i = 0.13$ W/m K,
  $\alpha_x^i = \alpha_y^i = 0.8 \times 10^{-6}\ 1/^\circ\text{C}$ (x and y are the axial and the circumferential coordinates of the cylinder),
- internal layer of aluminum foil with
  $h_f = 0.02$ mm, $E_f = 70$ GPa, $\nu_f = 0.3$,
  $\lambda_f = 210$ W/m K, $\alpha_f = 22.3 \times 10^{-6}\ 1/^\circ\text{C}$.

Apparent thermal conductivity of the cylinder wall can be found with the aid of Eqs. (7.10), (7.11) and the continuum model of the lattice layer described in Section 4.7 as

$$\Lambda_x = \frac{1}{h}\left[(\lambda_1^e \cos^2\phi_e + \lambda_2^e \sin^2\phi_e)h_s^e + \frac{2}{a_r} h_r \delta_r \lambda_r \cos^2\phi_r + \lambda_x^i h_s^i + \lambda_f h_f\right]$$

Calculating yields $\Lambda_x = 0.64$ W/m K. Thermal resistance of a unit length of this structure is

$$r_x = \frac{1}{\Lambda_x \pi D h} = 36.8 \frac{\text{K}}{\text{W m}} \quad .$$

7.1.2. Thermoelasticity

As known, heating gives rise to thermal strains which, being restricted, induce thermal stresses. Assume that the temperature distribution in a composite structure is known and consider the problem of thermoelasticity.

Consider first a thermoelastic behavior of a unidirectional composite ply studied in Section 3.3 and shown in Fig. 3.29. The generalized Hooke's law, Eqs. (3.58) allowing for the temperature effects can be written as:

$$\varepsilon_{1T} = \varepsilon_1 + \varepsilon_1^T, \quad \varepsilon_{2T} = \varepsilon_2 + \varepsilon_2^T, \quad \gamma_{12T} = \gamma_{12} \ . \tag{7.12}$$

Here and further subscript "T" shows the strains that belong to the problem of thermoelasticity, while superscript "T" indicates temperature terms. Elastic strains $\varepsilon_1, \varepsilon_2$ and γ_{12} in Eqs. (7.12) are linked with stresses by Eqs. (3.58). Temperature strains, in the first approximation, can be taken as linear functions of the temperature change, i.e.

$$\varepsilon_1^T = \alpha_1 \Delta T, \quad \varepsilon_2^T = \alpha_2 \Delta T \ , \tag{7.13}$$

where α_1 and α_2 are coefficients of thermal expansion (CTE) along and across the fibers and $\Delta T = T - T_0$ is the difference between the current temperature T and some initial temperature T_0 at which thermal strains are zero. Inverse form of Eqs. (7.12) is:

$$\begin{aligned} \sigma_1 &= \bar{E}_1(\varepsilon_{1T} + \nu_{12}\varepsilon_{2T}) - \bar{E}_1(\varepsilon_1^T + \nu_{12}\varepsilon_2^T), \\ \sigma_2 &= \bar{E}_2(\varepsilon_{2T} + \nu_{21}\varepsilon_{1T}) - \bar{E}_2(\varepsilon_2^T + \nu_{21}\varepsilon_1^T), \\ \tau_{12} &= G_{12}\gamma_{12T} \ , \end{aligned} \tag{7.14}$$

where $\bar{E}_{1,2} = E_{1,2}/(1 - \nu_{12}\nu_{21})$.

To describe thermoelastic behavior of a ply, apply the first-order micromechanical model shown in Fig. 3.34. Because CTE (and elastic constants) of some fibers can be different in longitudinal and transverse directions generalize the first two equations of Eqs. (3.63) as:

$$\begin{aligned} \varepsilon_{1T}^{f,m} &= \frac{1}{E_{f1,m}}(\sigma_1^{f,m} - \nu_{f2,m}\sigma_2^{f,m}) + \alpha_{f1,m}\Delta T, \\ \varepsilon_{2T}^{f,m} &= \frac{1}{E_{f2,m}}(\sigma_2^{f,m} - \nu_{f1,m}\sigma_1^{f,m}) + \alpha_{f2,m}\Delta T \ . \end{aligned} \tag{7.15}$$

Repeating the derivation of Eqs. (3.76)–(3.79) we arrive at

$$E_1 = E_{f1}v_f + E_m v_m, \quad \nu_{21} = \nu_{f2}v_f + \nu_m v_m,$$

$$\frac{1}{E_2} = (1 - \nu_{f1}\nu_{f2})\frac{v_f}{E_{f2}} + (1 - \nu_m^2)\frac{v_m}{E_m} + \frac{\nu_{21}^2}{E_1}$$

$$\alpha_1 = \frac{1}{E_1}(E_{f1}\alpha_{f1}v_f + E_m\alpha_m v_m),$$
$$\alpha_2 = (\alpha_{f2} + \nu_{f2}\alpha_{f1})v_f + (1 + \nu_m)\alpha_m v_m - \nu_{21}\alpha_1 \ . \tag{7.16}$$

These equations generalize Eqs. (3.76)–(3.79) for the case of anisotropic fibers and specify apparent CTE of a unidirectional ply.

As an example, consider a high-modulus carbon–epoxy composite tested by Rogers et al. (1977). Microstructural parameters of the material are as follows ($T = 27°C$):
$E_{f1} = 411$ GPa, $E_{f2} = 6.6$ GPa, $\nu_{f1} = 0.06$,
$\nu_{f2} = 0.35$, $\alpha_{f1} = -1.2 \times 10^{-6}$ 1/°C, $\alpha_{f2} = 27.3 \times 10^{-6}$ 1/°C,
$E_m = 5.7$ GPa, $\nu_m = 0.316$, $\alpha_m = 45 \times 10^{-6}$ 1/°C, $v_f = v_m = 0.5$.
For these properties, Eqs. (7.16) yield
$E_1 = 208.3$ GPa, $E_2 = 6.5$ GPa, $\nu_{21} = 0.33$,
$\alpha_1 = -0.57 \times 10^{-6}$ 1/°C, $\alpha_2 = 43.4 \times 10^{-6}$ 1/°C,
while experimental results are
$E_1 = 208.6$ GPa, $E_2 = 6.3$ GPa, $\nu_{21} = 0.33$
$\alpha_1 = -0.5 \times 10^{-6}$ 1/°C, $\alpha_2 = 29.3 \times 10^{-6}$ 1/°C.
Thus, it can be concluded that the first-order microstructural model providing proper results for longitudinal material characteristics fails to predict α_2 with required accuracy. Discussion and conclusions concerning this problem and presented in Section 3.3 for elastic constants are valid for thermal expansion coefficients as well. For practical applications α_1 and α_2 are normally determined by experimental methods. However, in contrast to the elasticity problem, for which the knowledge of experimental elastic constants and material strength excludes the micromechanical models from consideration, for the thermoelasticity problems, these models provide us with useful information even if we know experimental thermal expansion coefficients. Indeed, consider a unidirectional ply that is subjected to uniform heating which induces only thermal strains, i.e., $\varepsilon_{1T} = \varepsilon_1^T$, $\varepsilon_{2T} = \varepsilon_2^T$, $\gamma_{12T} = 0$. Then, Eqs. (7.14) yield $\sigma_1 = 0$, $\sigma_2 = 0$, $\tau_{12} = 0$. For homogeneous materials, this means, that no stresses occur under uniform heating. However, this is not the case for a composite ply. Generalizing Eqs. (3.74) that specify longitudinal stresses in the fibers and in the matrix we get

$$\sigma_1^f = E_{f1}(\alpha_1 - \alpha_{f1})\Delta T, \quad \sigma_1^m = E_m(\alpha_1 - \alpha_m)\Delta T \ ,$$

where α_1 and α_2 are specified by Eqs. (7.16). Thus, because thermal expansion coefficients of the fibers and the matrix are different from those of the material, there exist microstructural thermal stresses in the composite structural elements. These stresses are self-balanced. Indeed

$$\sigma_1 = \sigma_1^f v_f + \sigma_1^m v_m = 0 \ .$$

Consider an orthotropic layer referred to coordinate axes x, y making angle ϕ with the principal material coordinate axes (see Fig. 7.2). Using Eqs. (7.14) instead of Eqs. (4.56) and repeating the derivation of Eqs. (4.71) we arrive at

$$\begin{aligned}
\sigma_x &= A_{11}\varepsilon_{x\mathrm{T}} + A_{12}\varepsilon_{y\mathrm{T}} + A_{14}\gamma_{xy\mathrm{T}} - A_{11}^{\mathrm{T}}, \\
\sigma_y &= A_{21}\varepsilon_{x\mathrm{T}} + A_{22}\varepsilon_{y\mathrm{T}} + A_{24}\gamma_{xy\mathrm{T}} - A_{22}^{\mathrm{T}}, \\
\tau_{xy} &= A_{41}\varepsilon_{x\mathrm{T}} + A_{42}\varepsilon_{y\mathrm{T}} + A_{44}\gamma_{xy\mathrm{T}} - A_{12}^{\mathrm{T}} \ ,
\end{aligned} \tag{7.17}$$

where A_{mn} are specified by Eqs. (4.72) and the thermal terms are

$$\begin{aligned}
A_{11}^{\mathrm{T}} &= \bar{E}_1\varepsilon_{12}^{\mathrm{T}}\cos^2\phi + \bar{E}_2\varepsilon_{21}^{\mathrm{T}}\sin^2\phi, \\
A_{22}^{\mathrm{T}} &= \bar{E}_1\varepsilon_{12}^{\mathrm{T}}\sin^2\phi + \bar{E}_2\varepsilon_{21}^{\mathrm{T}}\cos^2\phi, \\
A_{12}^{\mathrm{T}} &= (\bar{E}_1\varepsilon_{12}^{\mathrm{T}} - \bar{E}_2\varepsilon_{21}^{\mathrm{T}})\sin\phi\cos\phi \ .
\end{aligned} \tag{7.18}$$

Here

$$\varepsilon_{12}^{\mathrm{T}} = \varepsilon_1^{\mathrm{T}} + \nu_{12}\varepsilon_2^{\mathrm{T}}, \quad \varepsilon_{21}^{\mathrm{T}} = \varepsilon_2^{\mathrm{T}} + \nu_{21}\varepsilon_1^{\mathrm{T}}$$

and $\varepsilon_1^{\mathrm{T}}$, $\varepsilon_2^{\mathrm{T}}$ are determined by Eqs. (7.13). The inverse form of Eqs. (7.17) is

$$\varepsilon_{x\mathrm{T}} = \varepsilon_x + \varepsilon_x^{\mathrm{T}}, \quad \varepsilon_{y\mathrm{T}} = \varepsilon_y + \varepsilon_y^{\mathrm{T}}, \quad \gamma_{xy\mathrm{T}} = \gamma_{xy} + \gamma_{xy}^{\mathrm{T}} \ . \tag{7.19}$$

Here, $\varepsilon_x, \varepsilon_y$, and γ_{xy} are expressed in terms of stresses σ_x, σ_y, and τ_{xy} with Eqs. (4.75), while the thermal strains are

$$\begin{aligned}
\varepsilon_x^{\mathrm{T}} &= \varepsilon_1^{\mathrm{T}}\cos^2\phi + \varepsilon_2^{\mathrm{T}}\sin^2\phi, \\
\varepsilon_y^{\mathrm{T}} &= \varepsilon_1^{\mathrm{T}}\sin^2\phi + \varepsilon_2^{\mathrm{T}}\cos^2\phi, \\
\gamma_{xy}^{\mathrm{T}} &= (\varepsilon_1^{\mathrm{T}} - \varepsilon_2^{\mathrm{T}})\sin 2\phi \ .
\end{aligned}$$

Introducing thermal expansion coefficients in xy coordinate frame with the following equations:

$$\varepsilon_x^{\mathrm{T}} = \alpha_x\Delta T, \quad \varepsilon_y^{\mathrm{T}} = \alpha_y\Delta T, \quad \gamma_{xy}^{\mathrm{T}} = \alpha_{xy}\Delta T \tag{7.20}$$

and using Eqs. (7.13) we get

$$\begin{aligned}
\alpha_x &= \alpha_1\cos^2\phi + \alpha_2\sin^2\phi, \\
\alpha_y &= \alpha_1\sin^2\phi + \alpha_2\cos^2\phi, \\
\alpha_{xy} &= (\alpha_1 - \alpha_2)\sin 2\phi \ .
\end{aligned} \tag{7.21}$$

As follows from Eqs. (7.19), in an anisotropic layer, uniform heating induces not only normal strains, but also the shear thermal strain. As can be seen in Fig. 7.4,

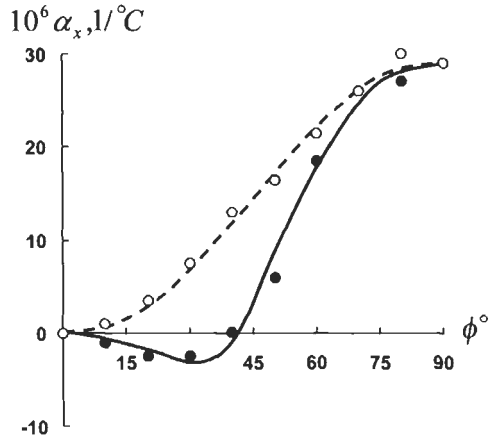

Fig. 7.4. Calculated (lines) and experimental (circles) dependencies of thermal expansion coefficients on the ply orientation angle for unidirectional thermoplastic carbon composite (– – – –, ○) and a $\pm\phi$ angle-ply layer (———, •).

Eqs. (7.21) provide fair agreement with experimental results of Barnes et al. (1989) for composites with carbon fibers and thermoplastic matrix (broken line and light circles).

Consider a symmetric $\pm\phi$ angle-ply layer (see Section 4.5.1). This layer is orthotropic, and the corresponding constitutive equations of thermoelastisity have the form of Eqs. (7.17) in which $A_{14} = A_{41} = 0$, $A_{24} = A_{42} = 0$, and $A_{12}^{\mathrm{T}} = 0$. The inverse form of these equations is

$$\varepsilon_{x\mathrm{T}} = \varepsilon_x + \varepsilon_x^{\mathrm{T}}, \quad \varepsilon_{y\mathrm{T}} = \varepsilon_y + \varepsilon_y^{\mathrm{T}}, \quad \gamma_{xy\mathrm{T}} = \gamma_{xy} \ ,$$

where $\varepsilon_x, \varepsilon_y$, and γ_{xy} are expressed in terms of stresses by Eqs. (4.128), while thermal strains are

$$\varepsilon_x^{\mathrm{T}} = \frac{A_{11}^{\mathrm{T}}A_{22} - A_{22}^{\mathrm{T}}A_{12}}{A_{11}A_{22} - A_{12}^2} \quad \varepsilon_y^{\mathrm{T}} = \frac{A_{22}^{\mathrm{T}}A_{11} - A_{11}^{\mathrm{T}}A_{12}}{A_{11}A_{22} - A_{12}^2} \ .$$

Using Eqs. (4.129), (7.13), (7.18) and (7.20), we arrive at the following expressions for apparent thermal expansion coefficients

$$\alpha_x = \frac{1}{E_y}(a_{11}^{\mathrm{T}} - \nu_{yx}a_{22}^{\mathrm{T}}), \quad \alpha_y = \frac{1}{E_x}(a_{22}^{\mathrm{T}} - \nu_{xy}a_{11}^{\mathrm{T}}) \ , \tag{7.22}$$

where

$$a_{11}^{\mathrm{T}} = \bar{E}_1(\alpha_1 + \nu_{12}\alpha_2)\cos^2\phi + \bar{E}_2(\alpha_2 + \nu_{21}\alpha_1)\sin^2\phi,$$
$$a_{22}^{\mathrm{T}} = \bar{E}_1(\alpha_1 + \nu_{12}\alpha_2)\sin^2\phi + \bar{E}_2(\alpha_2 + \nu_{21}\alpha_1)\cos^2\phi \ .$$

Comparison of α_x with experimental results of Barnes et al. (1989) for a thermoplastic carbon composite is presented in Fig. 7.4 (solid line and dark circles). As can be seen in this figure, there exists an interval ($0 \leqslant \phi \leqslant 40°$) within which the coefficient α_x of the angle-ply layer is negative. The same type of behavior is demonstrated by aramid epoxy angle-ply composites. Comparison of calculation with the aid of Eqs. (7.22) with experimental results of Strife and Prevo (1979) is presented in Fig. 7.5. Looking at Figs. 7.4 and 7.5 we can suppose that supplementing an angle-ply laminate with plies having small thermal elongations in the x-direction we can synthesize composite materials with zero thermal expansion in this direction. Such materials are important for space telescopes (Fig. 7.3), antennas, measuring instruments and other high precision, thermally stable structures (Hamilton and Patterson, 1993).

Consider laminates with arbitrary structural parameters (see Chapter 5). Repeating the derivation of Eqs. (5.5) but using the thermoelasticity constitutive equations, Eqs. (7.17), instead of Eqs. (4.71) we arrive at

$$\begin{aligned}
N_x &= B_{11}\varepsilon^0_{x\mathrm{T}} + B_{12}\varepsilon^0_{y\mathrm{T}} + B_{14}\gamma^0_{xy\mathrm{T}} + C_{11}\kappa_{x\mathrm{T}} + C_{12}\kappa_{y\mathrm{T}} + C_{14}\kappa_{xy\mathrm{T}} - N^{\mathrm{T}}_{11},\\
N_y &= B_{21}\varepsilon^0_{x\mathrm{T}} + B_{22}\varepsilon^0_{y\mathrm{T}} + B_{24}\gamma^0_{xy\mathrm{T}} + C_{21}\kappa_{x\mathrm{T}} + C_{22}\kappa_{y\mathrm{T}} + C_{24}\kappa_{xy\mathrm{T}} - N^{\mathrm{T}}_{22},\\
N_{xy} &= B_{41}\varepsilon^0_{x\mathrm{T}} + B_{42}\varepsilon^0_{y\mathrm{T}} + B_{44}\gamma^0_{xy\mathrm{T}} + C_{41}\kappa_{x\mathrm{T}} + C_{42}\kappa_{y\mathrm{T}} + C_{44}\kappa_{xy\mathrm{T}} - N^{\mathrm{T}}_{12},\\
M_x &= C_{11}\varepsilon^0_{x\mathrm{T}} + C_{12}\varepsilon^0_{y\mathrm{T}} + C_{14}\gamma^0_{xy\mathrm{T}} + D_{11}\kappa_{x\mathrm{T}} + D_{12}\kappa_{y\mathrm{T}} + D_{14}\kappa_{xy\mathrm{T}} - M^{\mathrm{T}}_{11},\\
M_y &= C_{21}\varepsilon^0_{x\mathrm{T}} + C_{22}\varepsilon^0_{y\mathrm{T}} + C_{24}\gamma^0_{xy\mathrm{T}} + D_{21}\kappa_{x\mathrm{T}} + D_{22}\kappa_{y\mathrm{T}} + D_{24}\kappa_{xy\mathrm{T}} - M^{\mathrm{T}}_{22},\\
M_{xy} &= C_{41}\varepsilon^0_{x\mathrm{T}} + C_{42}\varepsilon^0_{y\mathrm{T}} + C_{44}\gamma^0_{xy\mathrm{T}} + D_{41}\kappa_{x\mathrm{T}} + D_{42}\kappa_{y\mathrm{T}} + D_{44}\kappa_{xy\mathrm{T}} - M^{\mathrm{T}}_{12}.
\end{aligned} \tag{7.23}$$

These equations should be supplemented with Eqs. (5.15) for transverse shear forces, i.e.

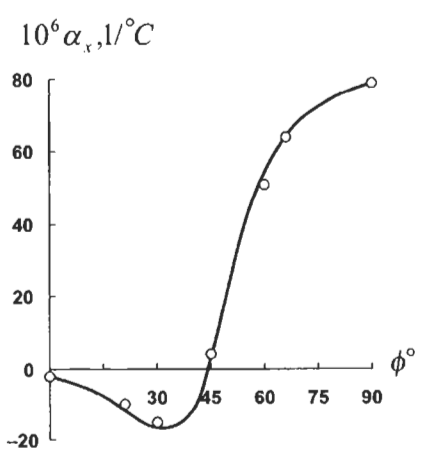

Fig. 7.5. Calculated (line) and experimental (circles) dependencies of thermal expansion coefficient on the ply orientation angle for an aramid–epoxy $\pm\phi$ angle-ply layer.

$$V_x = S_{55}\gamma_{xT} + S_{56}\gamma_{yT}, \quad V_y = S_{65}\gamma_{xT} + S_{66}\gamma_{yT} \ . \tag{7.24}$$

Temperature terms entering Eqs. (7.23) have the following form

$$N_{mn}^{T} = \int_{-e}^{s} A_{mn}^{T}\,\mathrm{d}z \quad M_{mn}^{T} = \int_{-e}^{s} A_{mn}^{T} z\,\mathrm{d}z$$

where A_{mn}^{T} are specified by Eqs. (7.18). Performing transformation that was used in Section 5.1 to reduce Eqs. (5.6), (5.7), and (5.8) to Eqs. (5.28) and (5.29) we get

$$N_{mn}^{T} = J_{mn}^{(0)}, \quad M_{mn}^{T} = J_{mn}^{(1)} - eJ_{mn}^{(0)} \ , \tag{7.25}$$

where (see Fig. 5.8)

$$J_{mn}^{(r)} = \int_{0}^{h} A_{mn}^{T} t^{r}\,\mathrm{d}t \ , \tag{7.26}$$

where $r = 0, 1$ and $mn = 11, 12, 22$.

For a laminate, the temperature governed by Eq. (7.6) is linearly distributed through the layers thicknesses (see Fig. 7.1). The same law can be, obviously, assumed for the temperature coefficients in Eqs. (7.18), i.e., for the ith layer in Fig. 5.10

$$A_{mn}^{Ti} = (A_{mn}^{T})_{i-1} + \frac{1}{h_i}\left[(A_{mn}^{T})_i - (A_{mn}^{T})_{i-1}\right](t - t_{i-1})$$

where $(A_{mn}^{T})_{i-1} = A_{mn}^{T}(t = t_{i-1})$ and $(A_{mn}^{T})_i = A_{mn}^{T}(t = t_i)$. Then, Eq. (7.26) acquires the form

$$J_{mn}^{(r)} = \sum_{i=1}^{k} \frac{1}{h_i}\left\{ \left[(A_{mn}^{T})_{i-1} t_i - (A_{mn}^{T})_i t_{i-1}\right] \frac{t_i^{r+1} - t_{i-1}^{r+1}}{r+1} \right.$$
$$\left. + \left[(A_{mn}^{T})_i - (A_{mn}^{T})_{i-1}\right] \frac{t_i^{r+2} - t_{i-1}^{r+2}}{r+2} \right\} \ .$$

If the temperature variation over the thickness of the ith layer can be neglected, we can introduce some average value

$$(\bar{A}_{mn}^{T})_i = \tfrac{1}{2}\left[(A_{mn}^{T})_{i-1} + (A_{mn}^{T})_i\right]$$

and present Eq. (7.26) as

$$J_{mn}^{(r)} = \frac{1}{r+1} \sum_{i=1}^{k} (\bar{A}_{mn}^{T})_i (t_i^{r+1} - t_{i-1}^{r+1}) \ . \tag{7.27}$$

Total (elastic and temperature) generalized strains ε_T, γ_T and κ_T entering Eqs. (7.23) and (7.24) can be expressed in terms of displacements and rotation angles of the laminate element with the aid of Eqs. (5.3) and (5.14), i.e.

$$\varepsilon_{xT}^0 = \frac{\partial u}{\partial x}, \quad \varepsilon_{yT}^0 = \frac{\partial v}{\partial y}, \quad \gamma_{xyT}^0 = \frac{\partial u}{\partial y} + \frac{\partial v}{\partial x} \ , \tag{7.28}$$

$$\kappa_{xT} = \frac{\partial \theta_x}{\partial x}, \quad \kappa_{yT} = \frac{\partial \theta_y}{\partial y}, \quad \kappa_{xyT} = \frac{\partial \theta_x}{\partial y} + \frac{\partial \theta_y}{\partial x} \ , \tag{7.29}$$

$$\gamma_{xT} = \theta_x + \frac{\partial w}{\partial x}, \quad \gamma_{yT} = \theta_y + \frac{\partial w}{\partial y} \ . \tag{7.30}$$

As follows from Eqs. (7.23), in the general case, uniform heating of laminates induces in contrast to homogeneous materials, not only in-plane strains but also the changes of laminate curvatures and twist. Indeed, assume that the laminate is free from the edge and surface loads so that forces and moments in the left-hand sides of Eqs. (7.23) are equal to zero. Because CTE of the layers, in the general case, are different, thermal terms N^T and M^T in the right-hand sides of Eqs. (7.23) are not zero even for the uniform temperature field, and these equations allow us to find ε_T, γ_T and κ_T specifying the laminate in-plane and out-of-plane deformation. Moreover, using the approach described in Section 5.10 we can conclude that uniform heating of the laminate is accompanied, in the general case, by stresses acting in the layers and between the layers.

As an example, consider the four-layered structure of the space telescope described in Section 7.1.1.

First, we calculate the stiffness coefficients of the layers, i.e.:

- for the internal layer of aluminum foil:

$$A_{11}^{(1)} = A_{22}^{(1)} = \bar{E}_f = 76.92, \quad A_{12}^{(1)} = \nu_f E_f = 23.08 \text{ GPa} \ ,$$

- for the inner skin:

$$A_{11}^{(2)} = A_{22}^{(2)} = \bar{E}_x^i = 34.87, \quad A_{12}^{(2)} = \nu_{xy}^i \bar{E}_x^i = 5.23 \text{ GPa} \ ,$$

- for the lattice layer:

$$A_{11}^{(3)} = 2E_r \frac{\delta_r}{a_r} \cos^4 \phi_r = 14.4 \text{ GPa},$$

$$A_{22}^{(3)} = 2E_r \frac{\delta_r}{a_r} \sin^4 \phi_r = 0.25 \text{ GPa},$$

$$A_{12}^{(3)} = 2E_r \frac{\delta_r}{a_r} \sin^2 \phi \cos^2 \phi = 1.91 \text{ GPa} \ ,$$

- for the external skin:

$$A_{11}^{(4)} = \bar{E}_1^e \cos^4 \phi_e + \bar{E}_2^e \sin^4 \phi_e + 2(\bar{E}_1^e \nu_{12}^e + 2G_{12}^e)\sin^2 \phi_e \cos^2 \phi_e = 99.05 \text{ GPa},$$
$$A_{22}^{(4)} = \bar{E}_1^e \sin^4 \phi_e + \bar{E}_2^e \cos^4 \phi_e + 2(\bar{E}_1^e \nu_{12}^e + 2G_{12}^e)\sin^2 \phi_e \cos^2 \phi_e = 13.39 \text{ GPa},$$
$$A_{12}^{(4)} = \bar{E}_1^e \nu_{12}^e + [\bar{E}_1^e + \bar{E}_2^e - 2(\bar{E}_1^e \nu_{12}^e + 2G_{12}^e)] \sin^2 \phi_e \cos^2 \phi_e = 13.96 \text{ GPa} .$$

Using Eqs. (7.18) we find the thermal coefficients of the layers (the temperature is uniformly distributed through the laminate thickness):

$$(A_{11}^T)_1 = (A_{22}^T)_1 = \bar{E}_f \alpha_f \Delta T = 1715 \times 10^{-6} \Delta T \text{ GPa/°C},$$
$$(A_{11}^T)_2 = (A_{22}^T)_2 = \bar{E}_x^i (1 + \nu_{xy}^i)\alpha_x^i \Delta T = 32.08 \times 10^{-6} \Delta T \text{ GPa/°C},$$
$$(A_{11}^T)_3 = 2E_r \frac{\delta_r}{a_r} \alpha_r \cos^2 \phi_r \Delta T = 4.46 \times 10^{-6} \Delta T \text{ GPa/°C},$$
$$(A_{22}^T)_3 = 2E_r \frac{\delta_r}{a_r} \alpha_r \sin^2 \phi_r \Delta T = 1.06 \times 10^{-6} \Delta T \text{ GPa/°C},$$
$$(A_{11}^T)_4 = [\bar{E}_1^c(\alpha_1^c + \nu_{12}^e \alpha_2^e)\cos^2 \phi + \bar{E}_2^c(\alpha_2^e + \nu_{21}^e \alpha_1^e)\sin^2 \phi]\Delta T$$
$$= 132.43 \times 10^{-6} \Delta T \text{ GPa/°C},$$
$$(A_{22}^T)_4 = [\bar{E}_1^c(\alpha_1^c + \nu_{12}^e \alpha_2^e)\sin^2 \phi + \bar{E}_2^c(\alpha_2^c + \nu_{21}^e \alpha_1^e)\cos^2 \phi]\Delta T$$
$$= 317.61 \times 10^{-6} \Delta T \text{ GPa/°C} .$$

Because the layers are orthotropic, $A_{12}^T = 0$ for all of them. Specifying coordinates of the layers (see Fig. 5.10), i.e.

$$t_0 = 0, \quad t_1 = 0.02, \quad t_2 = 1.02, \quad t_3 = 10.02, \quad t_4 = 13.52 \text{ (mm)}$$

and applying Eq. (7.27) we calculate parameters $J_{mn}^{(r)}$ for the laminate

$$J_{11}^{(0)} = (A_{11}^T)_1(t_1 - t_0) + (A_{11}^T)_2(t_2 - t_1) + (A_{11}^T)_3(t_3 - t_2)$$
$$+ (A_{11}^T)_4(t_4 - t_3) = 570 \times 10^{-6} \Delta T \text{ GPa mm/°C},$$
$$J_{22}^{(0)} = 1190 \times 10^{-6} \Delta T \text{ GPa mm/°C},$$
$$J_{11}^{(1)} = \frac{1}{2}[(A_{11}^T)_1(t_1^2 - t_0^2) + (A_{11}^T)_2(t_2^2 - t_1^2) + (A_{11}^T)_3(t_3^2 - t_2^2) + (A_{11}^T)_4(t_4^2 - t_3^2)]$$
$$= 5690 \times 10^{-6} \Delta T \text{ GPa mm}^2/\text{°C},$$
$$J_{22}^{(1)} = 13150 \times 10^{-6} \Delta T \text{ GPa mm}^2/\text{°C} .$$

To determine M_{mn}^T, we need to specify the reference surface of the laminate. Assume that this surface coincides with the middle surface, i.e., that $e = h/2 = 6.76$ mm. Then, Eqs. (7.25) yield

$$N_{11}^T = J_{11}^{(0)} = 570 \times 10^{-6} \Delta T \text{ GPa mm/°C},$$
$$N_{22}^T = J_{22}^{(0)} = 1190 \times 10^{-6} \Delta T \text{ GPa mm/°C},$$

$$M_{11}^{T} = J_{11}^{(1)} - eJ_{11}^{(0)} = 1840 \times 10^{-6}\,\Delta T \text{ GPa mm}^2/^{\circ}\text{C},$$
$$M_{22}^{T} = 5100 \times 10^{-6}\,\Delta T \text{ GPa mm}^2/^{\circ}\text{C} .$$

Thus, the thermal terms entering costitutive equations of thermoplasticity, Eqs. (7.23), are specified. Apply the obtained results to determine the apparent coefficients of thermal expansion for the space telescope section under study (see Fig. 7.3). We can assume that under uniform heating the curvatures do not change in the middle part of the cylinder so that $\kappa_{xT} = 0$ and $\kappa_{yT} = 0$. Because there are no external loads, free body diagram allows us to conclude that $N_x = 0$ and $N_y = 0$. As a result, the first two equations of Eqs. (7.23) for the structure under study become:

$$B_{11}\varepsilon_{xT}^{0} + B_{12}\varepsilon_{yT}^{0} = N_{11}^{T},$$
$$B_{21}\varepsilon_{xT}^{0} + B_{22}\varepsilon_{yT}^{0} = N_{22}^{T} .$$

Solving these equations for thermal strains and taking into account Eqs. (7.20) we get

$$\varepsilon_{xT}^{0} = \frac{1}{B}(B_{22}N_{11}^{T} - B_{12}N_{22}^{T}) = \alpha_x \Delta T,$$
$$\varepsilon_{yT}^{0} = \frac{1}{B}(B_{11}N_{22}^{T} - B_{12}N_{11}^{T}) = \alpha_y \Delta T .$$

where $B = B_{11}B_{22} - B_{12}^2$. For the laminate under study, calculation yields

$$\alpha_x = -0.94 \times 10^{-6}\ 1/^{\circ}\text{C}, \quad \alpha_y = 14.7 \times 10^{-6}\ 1/^{\circ}\text{C} .$$

Return to Eqs. (7.13) and (7.20) based on the assumption that coefficients of thermal expansion do not depend on temperature. For moderate temperatures, this is a reasonable approximation. This conclusion follows from Fig. 7.6 in which experimental results of Sukhanov et al. (1990) (shown with solid lines) are compared with Eqs. (7.20), where $\Delta T = T - 20^{\circ}\text{C}$ (broken lines) for carbon–epoxy angle-ply laminates. However, for relatively high temperatures, some deviation from the linear behavior can be seen. In this case, Eqs. (7.13) and (7.20) for thermal strains can be generalized as

$$\varepsilon^{T} = \int_{T_0}^{T} \alpha(T)\mathrm{d}T .$$

Temperature action can result also in the change of material mechanical properties. As follows from Fig. 7.7 in which circles correspond to experimental data of Ha and Springer (1987), elevated temperature causes higher or lower reduction of material strength and stiffness characteristics depending on whether the corresponding material characteristic is controlled mainly by the fibers or by the matrix. The curves

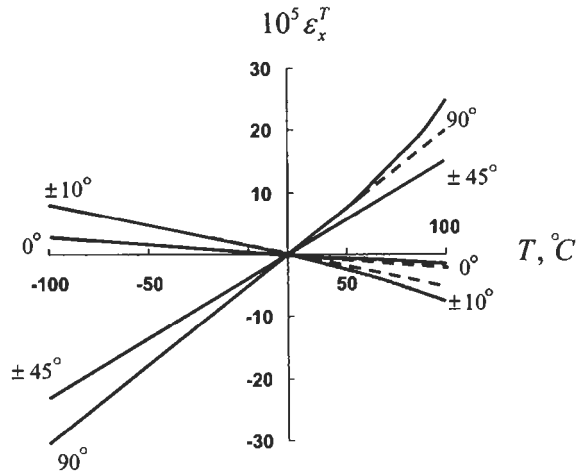

Fig. 7.6. Experimental dependencies of thermal strains on temperature (solid lines) for $\pm\phi$ angle-ply carbon–epoxy composite and the corresponding linear approximations (broken lines).

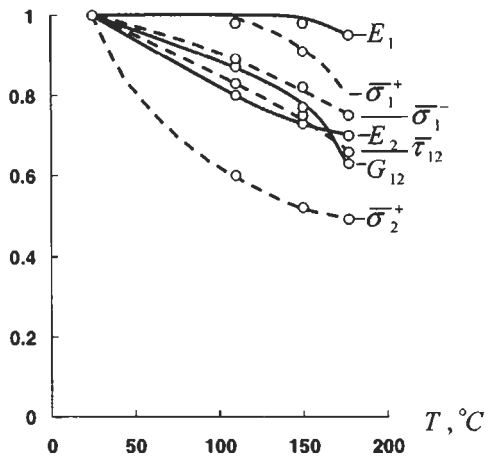

Fig. 7.7. Experimental dependencies of normalized stiffness (solid lines) and strength (broken lines) characteristics of unidirectional carbon–epoxy composite on temperature.

presented in Fig. 7.7 correspond to a carbon–epoxy composite, but they are typical for polymeric unidirectional composites. Longitudinal modulus and tensile strength, being controlled by the fibers, are less sensitive to temperature than longitudinal compressive strength, transverse and shear characteristics. Analogous results for a more temperature sensitive thermoplastic composite studied by Soutis and Turkmen (1993) are presented in Fig. 7.8. Metal matrix composites demonstrate much higher thermal resistance, while ceramic and carbon–carbon composites are specially developed to withstand high temperatures. For example, carbon–carbon fabric

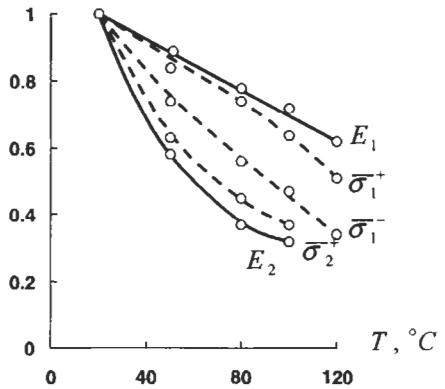

Fig. 7.8. Experimental dependencies of normalized stiffness (solid lines) and strength (broken lines) characteristics of unidirectional glass–polypropylene composite on temperature.

composite under heating up to 2500°C demonstrates only 7% reduction of tensile strength and about 30% reduction of compressive strength without significant change of stiffness.

Analysis of thermoelastic deformation for materials whose stiffness characteristics depend on temperature presents substantial difficulties because thermal strains are caused not only by material thermal expansion, but also by external forces. Consider, for example, a structural element under temperature T_0 loaded with some external force P_0 and assume that the temperature is increased up to the level T_1. Then, the temperature change will cause the thermal strain associated with material expansion, and the force P_0, being constant, also induces additional strain because material stiffness at temperature T_1 is less than stiffness at temperature T_0. To determine the final stress and strain state of the structure, we should describe the process of loading and heating using, e.g., the method of successive loading (and heating) presented in Section 4.1.2.

7.2. Hygrothermal effects and aging

Effects that are similar to temperature action, i.e., expansion and degradation of properties are also exerted by moisture. Moisture absorption is governed by equation analogous to Eq. (7.2) in which T should be changed for moisture concentration W and λ – for moisture diffusion coefficient μ. The principal difference that exists between temperature and moisture diffusion processes is associated with high difference between λ and μ, the first being much higher than the second one. As shown by Shen and Springer (1976), the temperature increasing in time inside the surface-heated shell approaches the steady state temperature about 10^6 times faster than the moisture content approaches the stable state under the same conditions. Moisture content in the material depends on environmental conditions, temperature, pressure, fiber and matrix materials, levels of porosity, and

material damage. Because the stable moisture content is rarely reached in real composite structures, its current distribution through the laminate depends on the laminate structure and thickness. Among the polymeric composites, the highest capacity for water absorption under room temperature is demonstrated by aramid composites ($7 \pm 0.25\%$ by weight) in which both polymeric matrix and fibers are sensitive to moisture. Glass and carbon polymeric composites are characterized by moisture content $3.5 \pm 0.2\%$ and $2 \pm 0.75\%$, respectively. In real aramid–epoxy and carbon–epoxy composite structures moisture content is usually about 2% and 1%, respectively. The lowest sensitivity to moisture is demonstrated by boron composites. Metal matrix, ceramic, and carbon–carbon composites are not affected by moisture.

As follows from Fig. 7.9 in which experimental data of Milyutin et al. (1989) and Perov and Kruzhkova (1991) are approximated, water absorption is dramatically influenced by temperature. While material absorbs water, it expands demonstrating the effects that are analogous to thermal effects and can be modeled using equations presented in Section 7.1.2 if we treat α_1, α_2 and α_x, α_y as coefficients of moisture expansion and change ΔT for ΔW. Just as temperature, moisture reduces material strength and stiffness. For carbon–epoxy composites this reduction is about 12%, for aramid–epoxy composites – about 25%, and glass–epoxy materials – about 35%. After drying up, the effect of moisture usually disappears.

Cyclic action of temperature, moisture, and sun radiation results in material aging, i.e., in degradation of material properties in the process of material or structure storage. For some polymeric composites, exposure to elevated temperature which can reach 70°C and radiation whose intensity can be as high as 1 kW/m^2 can cause more complete curing of the resin and some increase of material strength in compression, shear, or bending. However, under long-term action of the aforementioned factors, material strength and stiffness decrease. To evaluate the

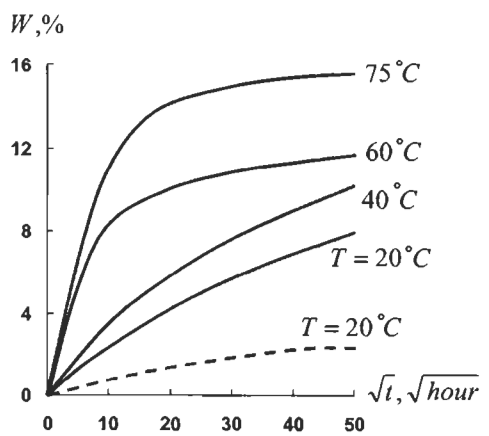

Fig. 7.9. Moisture content as a function of the root of the immersion time and temperature for aramid–epoxy (solid lines) and carbon–epoxy (broken line) composites.

effect of aging, test under transverse bending (see Fig. 4.95) is usually performed. Thus found flexural strength

$$\bar{\sigma}_f = \frac{3\bar{P}l}{2bh^2}$$

allows for both fiber and matrix material degradation in the process of aging. Experimental results of G.M. Gunyaev et al. showing dependence of the normalized flexural strength on time for advanced composites are presented in Fig. 7.10.

7.3. Time and time-dependent loading effects

7.3.1. Viscoelastisity

Polymeric matrices are characterized with pronounced viscoelastic properties resulting in time-dependent behavior of polymeric composites that manifests itself in creep (see Section 1.1), stress relaxation, and dependence of the stress–strain diagram on the rate of loading. It should be emphasized that in composite materials, viscoelastic deformation of the polymeric matrix is restricted by fibers that usually are linear elastic and do not demonstrate time-dependent behavior. The one exception to existing fibers is represented by aramid fibers that are actually polymeric themselves by their nature. Properties of metal matrix, ceramic, and carbon–carbon composites under normal conditions do not depend on time. Rheologic (time-dependent) characteristics of structural materials are revealed in creep tests allowing us to plot the dependence of strain on time under constant stress. Such diagrams are shown in Fig. 7.11 for aramid–epoxy composite described

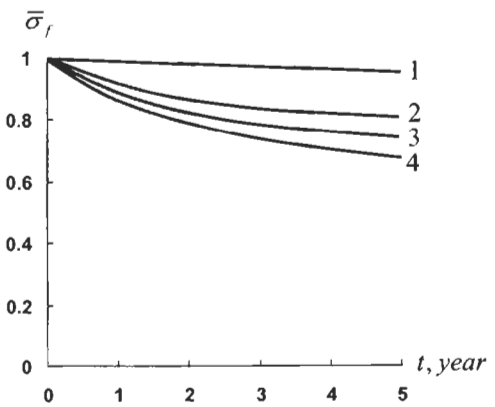

Fig. 7.10. Dependence of the normalized flexural strength on the time of aging for boron (1), carbon (2), aramid (3), and glass (4) epoxy composites.

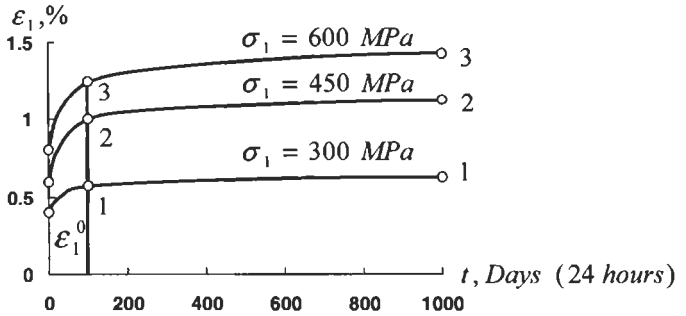

Fig. 7.11. Creep strain response of unidirectional aramid–epoxy composite under tension in longitudinal direction with three constant stresses.

by Skudra et al. (1989). An important characteristic of the material can be established if we plot the so-called isochrone stress-strain diagrams shown in Fig. 7.12. Three curves in this Figure are plotted for $t = 0$, $t = 100$, and $t = 1000$ days, and the points on these curves correspond to points 1, 2, 3 in Fig. 7.11. As can be seen, the initial parts of the isochrone diagrams are linear which means that under moderate stress, material under study can be classified as linear-viscoelastic material. To characterize such a material, we need to have only one creep diagram, while the other curves can be plotted increasing strains in proportion to stress. For example, the creep curve corresponding to $\sigma_1 = 450$ MPa in Fig. 7.11 can be obtained if we multiply strains corresponding to $\sigma_1 = 300$ MPa by 1.5.

Linear-viscoelastic material behavior is described with reasonable accuracy by the hereditary theory according to which the dependence of strain on time is expressed as

$$\varepsilon(t) = \frac{1}{E}\left[\sigma(t) + \int_0^t C(t-\tau)\sigma(\tau)\mathrm{d}\tau\right] . \tag{7.31}$$

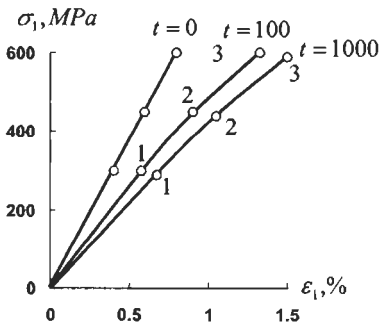

Fig. 7.12. Isochrone stress–strain diagrams corresponding to creep curves in Fig. 7.11.

Here, t is the current time, τ is some moment of time in the past ($0 \leqslant \tau \leqslant t$) at which stress $\sigma(\tau)$ acts and $C(t-\tau)$ is the creep compliance (or creep kernel) depending on time passing from the moment τ to the moment t. Constitutive equation of the hereditary theory, Eq. (7.31), is illustrated in Fig. 7.13 from which it follows that the total strain $\varepsilon(t)$ is composed of the elastic strain ε_e governed by the current stress $\sigma(t)$ and the viscous strain ε_v depending on the loading process as if the material "remembers" this process. Within the frame work of this interpretation, the creep compliance $C(\theta)$, where $\theta = t - \tau$ can be treated as some "memory function" which should, naturally, be infinitely high at $\theta = 0$ and tend to zero while $\theta \to \infty$ as in Fig. 7.14.

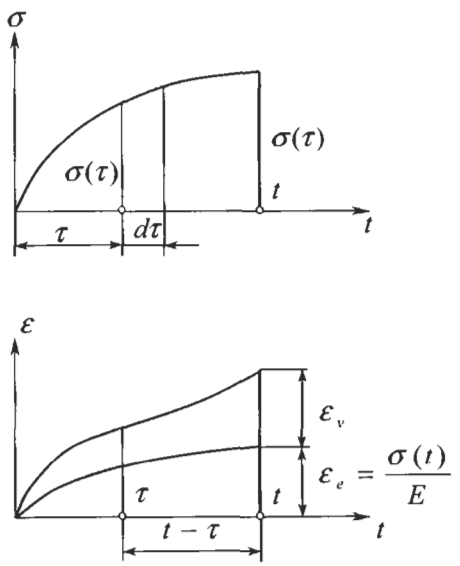

Fig. 7.13. Geometric interpretation of the hereditary constitutive theory.

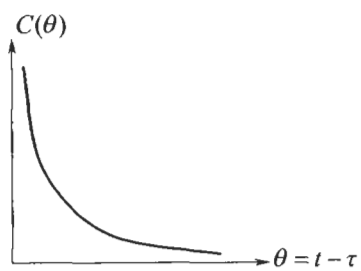

Fig. 7.14. Typical form of the creep compliance function.

The inverse form of Eq. (7.31) is

$$\sigma(t) = E\left[\varepsilon(t) - \int_0^t R(t-\tau)\varepsilon(\tau)\mathrm{d}\tau\right] . \tag{7.32}$$

Here, $R(t-\tau)$ is the relaxation modulus or the relaxation kernel that can be expressed, as shown below, in terms of $C(t-\tau)$.

The creep compliance is determined using experimental creep diagrams. Passing to a new variable $\theta = t - \tau$ we can write Eq. (7.31) in the following form:

$$\varepsilon(t) = \frac{1}{E}\left[\sigma(t) + \int_0^t C(\theta)\sigma(\theta - t)\mathrm{d}\theta\right] . \tag{7.33}$$

For the creep test, stress is constant, so $\sigma = \sigma^0$, and Eq. (7.32) yields

$$\varepsilon(t) = \varepsilon^0\left[1 + \int_0^t C(\theta)\mathrm{d}\theta\right] , \tag{7.34}$$

where $\varepsilon^0 = \sigma^0/E = \varepsilon(t=0)$ is the instant elastic strain (see Fig. 7.11). Differentiating this equation with respect to t we get

$$C(t) = \frac{1}{\varepsilon^0}\frac{\mathrm{d}\varepsilon(t)}{\mathrm{d}t} .$$

This expression allows us to determine the creep compliance differentiating the given experimental creep diagram or its analytical approximation. However, for practical analysis, $C(\theta)$ is usually determined directly from Eq. (7.34) introducing some approximation for $C(\theta)$ and matching thus obtained function $\varepsilon(t)$ with the experimental creep diagram. For this purpose, Eq. (7.34) is written in the form

$$\frac{\varepsilon(t)}{\varepsilon^0} = 1 + \int_0^t C(\theta)\mathrm{d}\theta . \tag{7.35}$$

Experimental creep diagrams for unidirectional glass-epoxy composite are presented in this form in Fig. 7.15 (solid lines).

The simplest is the exponential approximation of the type

$$C(\theta) = \sum_{n=1}^{N} A_n \mathrm{e}^{-\alpha_n\theta} . \tag{7.36}$$

Substituting Eq. (7.36) into Eq. (7.35) we obtain

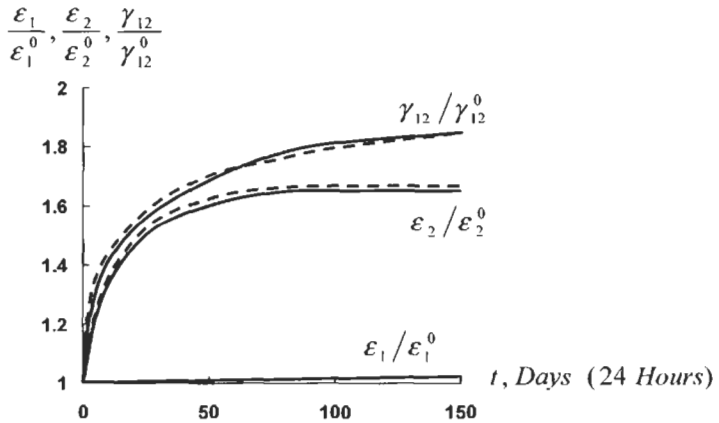

Fig. 7.15. Creep strain diagrams for unidirectional glass–epoxy composite (solid lines) under tension in longitudinal direction ($\varepsilon_1/\varepsilon_1^0$), transverse direction ($\varepsilon_2/\varepsilon_2^0$), and under in-plane shear ($\gamma_{12}/\gamma_{12}^0$) and the corresponding exponential approximations (broken lines).

$$\frac{\varepsilon(t)}{\varepsilon^0} = 1 + \sum_{n=1}^{N} \frac{A_n}{\alpha_n}(1 - e^{-\alpha_n t}) \ .$$

For the curves presented in Fig. 7.15, calculation yields
- longitudinal tension: $N = 1$, $A_1 = 0$;
- transverse tension: $N = 1$, $A_1 = 0.04$, $\alpha_1 = 0.06$ 1/day;
- in-plane shear: $N = 2$, $A_1 = 0.033$, $\alpha_1 = 0.04$ 1/day, $A_2 = 0.06$, $\alpha_2 = 0.4$ 1/day.

The corresponding approximations are shown in Fig. 7.15 with broken lines. The main shortcoming of the exponential approximation in Eq. (7.36) is associated with the fact that, in contrast to Fig. 7.14, $C(\theta)$ has no singularity at $\theta = 0$ which means that it cannot describe properly material behavior in the vicinity of $t = 0$.

It should be emphasized that one-term exponential approximation corresponds to a simple rheological mechanical model shown in Fig. 7.16. The model consists of two linear springs simulating material elastic behavior in accordance with Hooke's law

$$\sigma_1 = E_1 \varepsilon_1, \quad \sigma_2 = E_2 \varepsilon_2 \tag{7.37}$$

and one dash-pot simulating material viscous behavior obeying the Newton flow law

$$\sigma_v = \eta \frac{d\varepsilon_v}{dt} \ . \tag{7.38}$$

Equilibrium and compatibility conditions for the model in Fig. 7.16 are

$$\sigma = \sigma_2 + \sigma_v, \quad \sigma_1 = \sigma, \quad \varepsilon_v = \varepsilon_2, \quad \varepsilon_1 + \varepsilon_2 = \varepsilon \ .$$

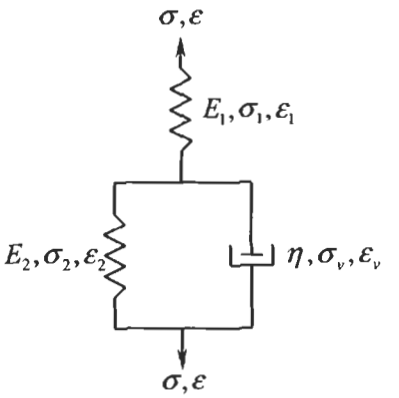

Fig. 7.16. Three-element mechanical model.

Using the first of these equations and Eqs. (7.37) and (7.38) we get

$$\sigma = E_2\varepsilon_2 + \eta\frac{\mathrm{d}\varepsilon_v}{\mathrm{d}t} \ .$$

Taking into account that

$$\varepsilon_2 = \varepsilon_v = \varepsilon - \frac{\sigma}{E} \ ,$$

we finally arrive at the following constitutive equation linking apparent stress σ and apparent strain ε

$$\sigma\left(1 + \frac{E_2}{E_1}\right) + \frac{\eta}{E_1}\frac{\mathrm{d}\sigma}{\mathrm{d}t} = E_2\varepsilon + \eta\frac{\mathrm{d}\varepsilon}{\mathrm{d}t} \ . \tag{7.39}$$

This equation allows us to introduce some useful material characteristics. Indeed, consider a very fast loading, i.e., such that stress σ and strain ε can be neglected in comparison with their rates. Then, integration yields $\sigma = E_i\varepsilon$, where $E_i = E_1$ is the instantaneous modulus of the material. Now assume that the loading is so slow that stress and strain rates can be neglected. Then, Eq. (7.39) yields $\sigma = E_l\varepsilon$, where

$$E_l = \frac{E_1E_2}{E_1 + E_2} \tag{7.40}$$

is the long-time modulus.

Apply the model under study to describe material creep. Taking $\sigma = \sigma_0$ and integrating Eq. (7.39) with initial condition $\varepsilon_0(0) = \sigma_0/E$ we get

$$\varepsilon = \frac{\sigma_0}{E_1}\left[1 + \frac{E_1}{E_2}\left(1 - \mathrm{e}^{(E_2/\eta)t}\right)\right] \ .$$

The corresponding creep diagram is shown in Fig. 7.17. As follows from this figure, $\varepsilon(t \to \infty) = \sigma_0/E_1$, where E_1 is specified by Eq. (7.40). This means that there exists some limit for the creep strain, and materials that can be described with this model should possess the so-called limited creep.

Now assume that the model is loaded in such a way that the apparent strain is constant, i.e., that $\varepsilon = \varepsilon_0$. Then, the solution of Eq. (7.39) that satisfies condition $\sigma(0) = E_1\varepsilon_0$ is

$$\sigma = \frac{E_1\varepsilon_0}{E_1 + E_2}\left(E_2 + E_1 e^{-t/t_r}\right), \quad t_r = \frac{\eta}{E_1 + E_2} \ .$$

The corresponding dependence is presented in Fig. 7.18 and illustrates the process of stress relaxation. Parameter t_r is called the time of relaxation. During this time the stress drops by the factor of e.

Consider again Eq. (7.39) and express E_1, E_2, and η in terms of E_i, E_1, and t_r. The resulting equation is as follows

$$\sigma + t_r\frac{d\sigma}{dt} = E_1\varepsilon + E_i t_r\frac{d\varepsilon}{dt} \ . \tag{7.41}$$

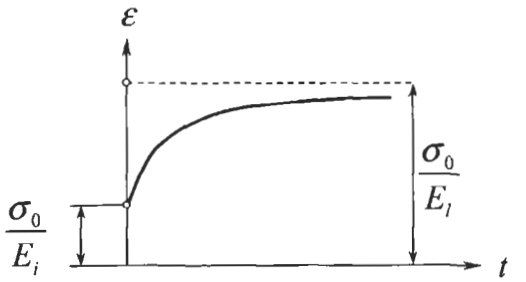

Fig. 7.17. Creep diagram corresponding to mechanical model in Fig. 7.16.

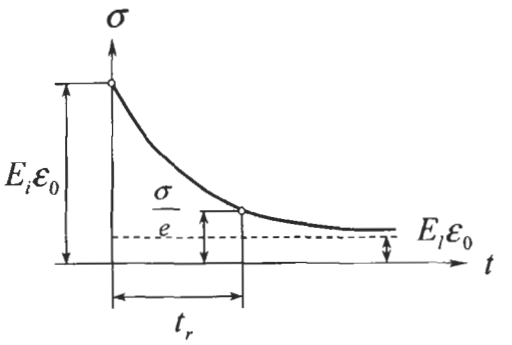

Fig. 7.18. Relaxation diagram corresponding to mechanical model in Fig. 7.16.

This first-order differential equation can be solved for ε in the general case. Omitting rather cumbersome transformations we arrive at the following solution:

$$\varepsilon(t) = \frac{1}{E_i}\left[\sigma(t) + \frac{1}{t_r}\left(1 - \frac{E_l}{E_i}\right)\int_0^t \exp\left(-\frac{E_l}{E_i t_r}(t-\tau)\right)\sigma(\tau)\mathrm{d}\tau\right] .$$

This result corresponds to Eq. (7.33) of the hereditary theory with one-term exponential approximation of the creep compliance in Eq. (7.36), where $N = 1$. Taking more terms in Eq. (7.36) we get more flexibility in approximation of experimental results with exponential functions. However, the main features of material behavior are, in principal the same that for the one-term approximation (see Figs. 7.16 and 7.17). Particularly, there exists the long-time modulus that follows from Eq. (7.34) if we pass to the limit for $t \to \infty$, i.e.

$$\varepsilon(t) \to \frac{\sigma_0}{E_l}, \quad E_l = \frac{E}{1 + \int_0^\infty C(\theta)\mathrm{d}\theta} .$$

For the exponential approximation in Eq. (7.36),

$$I = \int_0^\infty C(\theta)\mathrm{d}\theta = \sum_{n=1}^{N} \frac{A_n}{\alpha_n} .$$

Because integral I has a finite value, the exponential approximation of the creep compliance can be used only for materials with limited creep. There exist more complicated singular approximations, e.g.

$$C(\theta) = \frac{A}{\theta^\alpha}, \quad C(\theta) = \frac{A}{\theta^\alpha}\mathrm{e}^{-\beta\theta}$$

for which $I \to \infty$ and $E_l = 0$. This means that for such materials, creep strain can be infinitely high.

Useful interpretation of the hereditary theory constitutive equations can be constructed with the aid of the integral Laplace transformation according to which function $f(t)$ is associated with its Laplace transform $f^*(p)$ as

$$f^*(p) = \int_0^\infty f(t)\mathrm{e}^{-pt}\,\mathrm{d}t .$$

For some functions that we need to use for the examples presented below, we have

$$f(t) = 1, \quad f^*(p) = \frac{1}{p}, \quad f(t) = \mathrm{e}^{-\alpha t}, \quad f^*(p) = \frac{1}{\alpha + p} . \tag{7.42}$$

Importance of the Laplace transformation for the hereditary theory is associated with the existence of the so-called convolution theorem according to which

$$\left[\int_0^t f_1(\theta) f_2(\theta - t)\mathrm{d}\theta\right]^* = f_1^*(p) f_2^*(p) \ .$$

Using this theorem and applying Laplace transformation to Eq. (7.33) we get

$$\varepsilon^*(p) = \frac{1}{E}[\sigma^*(p) + C^*(p)\sigma^*(p)] \ .$$

This result can be presented in the form analogous to Hooke's law, i.e.

$$\sigma^*(p) = E^*(p)\varepsilon^*(p) \ . \tag{7.43}$$

where

$$E^* = \frac{E}{1 + C^*(p)} \ .$$

Applying Laplace transformation to Eq. (7.32) we arrive at Eq. (7.43) in which

$$E^* = E[1 - R^*(p)] \ . \tag{7.44}$$

Matching Eqs. (7.43) and (7.44) we can link together Laplace transforms of the creep compliance and the relaxation modulus, i.e.

$$\frac{1}{1 + C^*(p)} = 1 - R^*(p) \ .$$

With due regard to Eq. (7.43) we can formulate the elastic–viscoelastic analogy or the correspondence principle, according to which the solution of the linear viscoelasticity problem can be obtained in terms of the corresponding Laplace transforms from the solution of the linear elasticity problem if E is replaced with E^* and all the stresses, strains, displacements, and external loads are replaced with their Laplace transforms.

For an orthotropic material in the plane stress state, e.g., for a unidirectional composite ply or layer referred to the principal material axes, Eqs. (4.55) and (7.31) can be generalized as

$$\varepsilon_1(t) = \frac{1}{E_1}\left[\sigma_1(t) + \int_0^t C_{11}(t - \tau)\sigma_1(\tau)\mathrm{d}\tau\right] - \frac{\nu_{12}}{E_2}\left[\sigma_2(t) + \int_0^t C_{12}(t - \tau)\sigma_2(\tau)\mathrm{d}\tau\right]$$

$$\varepsilon_2(t) = \frac{1}{E_2}\left[\sigma_2(t) + \int_0^t C_{22}(t - \tau)\sigma_2(\tau)\mathrm{d}\tau\right] - \frac{\nu_{21}}{E_1}\left[\sigma_1(t) + \int_0^t C_{21}(t - \tau)\sigma_1(\tau)\mathrm{d}\tau\right]$$

$$\gamma_{12}(t) = \frac{1}{G_{12}} \left[\tau_{12}(t) + \int_0^t K_{12}(t-\tau)\tau_{12}(\tau)\mathrm{d}\tau \right] .$$

Applying Laplace transformation to these equations we can reduce them to the form analogous to Hooke's law, Eqs. (4.55), i.e.

$$\begin{aligned} \varepsilon_1^*(p) &= \frac{\sigma_1^*(p)}{E_1^*(p)} - \frac{\nu_{12}^*(p)}{E_2^*(p)}\sigma_2^*(p), \\ \varepsilon_2^*(p) &= \frac{\sigma_2^*(p)}{E_2^*(p)} - \frac{\nu_{21}^*(p)}{E_1^*(p)}\sigma_1^*(p), \\ \gamma_{12}^*(p) &= \frac{\tau_{12}^*(p)}{G_{12}^*(p)} , \end{aligned} \tag{7.45}$$

where

$$\begin{aligned} &E_1^*(p) = \frac{E_1}{1 + C_{11}^*(p)}, \quad E_2^*(p) = \frac{E_2}{1 + C_{22}^*(p)}, \quad G_{12}^*(p) = \frac{G_{12}}{1 + K_{12}^*(p)}, \\ &\nu_{12}^*(p) = \frac{1 + C_{12}^*(p)}{1 + C_{22}^*(p)}\nu_{12}, \quad \nu_{21}^*(p) = \frac{1 + C_{21}^*(p)}{1 + C_{11}^*(p)}\nu_{21} . \end{aligned} \tag{7.46}$$

For the unidirectional composite ply whose typical creep diagrams are shown in Fig. 7.15, the foregoing equations can be simplified neglecting material creep in the longitudinal direction ($C_{11} = 0$) and assuming that Poisson's effect is linear elastic and symmetric, i.e. that

$$\frac{\nu_{12}^*}{E_2^*} = \frac{\nu_{12}}{E_2}, \quad \frac{\nu_{21}^*}{E_1^*} = \frac{\nu_{21}}{E_1} .$$

Then, Eqs. (7.45) acquire the form:

$$\begin{aligned} \varepsilon_1^*(p) &= \frac{\sigma_1^*(p)}{E_1} - \frac{\nu_{12}}{E_2}\sigma_2^*(p), \\ \varepsilon_2^*(p) &= \frac{\sigma_2^*(p)}{E_2^*} - \frac{\nu_{21}}{E_1}\sigma_1^*(p), \\ \gamma_{12}^*(p) &= \frac{\tau_{12}^*(p)}{G_{12}^*(p)} . \end{aligned} \tag{7.47}$$

Supplementing constitutive equations, Eqs. (7.45) or (7.47), with strain–displacement and equilibrium equations written in terms of Laplace transforms of stresses, strains, displacements, and external loads, and solving the problem of elasticity we can find Laplace transforms of all the variables. To write thus obtained solution in terms of time t, we need to take the inverse Laplace transformation, and this is the

most difficult stage of the problem solution. There exist exact and approximate analytical and numerical methods for performing inverse Laplace transformation discussed, e.g., by Schapery (1974). The most commonly used approach is based on approximation of the solution written in terms of transformation parameter p with some functions for which the inverse Laplace transformation is known.

As an example, consider the problem of torsion for an orthotropic cylindrical shell similar to shown in Figs. 5.19 and 5.21. The shear strain induced by torque T is specified by Eq. (5.112). Using the elastic–viscoelastic analogy we can write the corresponding equation for the creep problem as

$$\gamma_{xy}^{*}(p) = \frac{T^{*}(p)}{2\pi R^2 B_{44}^{*}(p)} \quad . \tag{7.48}$$

Here, $B_{44}^{*}(p) = A_{44}^{*}(p)h$, where h is the shell thickness.

Let the shell be made of glass–epoxy composite whose mechanical properties are listed in Table 3.5 and creep diagrams are shown in Fig. 7.15. To simplify the analysis, we assume that for the unidirectional composite under study $E_2/E_1 = 0.22$, $G_{12}/E_1 = 0.06$, $\nu_{12} = \nu_{21} = 0$ and introduce the normalized shear strain

$$\bar{\gamma} = \gamma_{xy}\left(\frac{T}{R^2 h E_1}\right)^{-1} \quad .$$

Consider first a $\pm 45°$ angle-ply material discussed in Section 4.5 for which, with due regard to Eqs. (4.72), and (7.46) we can write

$$A_{44}^{*}(p) = \frac{1}{4}(E_1 + E_2^{*}) - \frac{1}{4}\left[E_1 + \frac{E_2}{1 + C_{22}^{*}(p)}\right] \quad .$$

Exponential approximation, Eq. (7.36), of the corresponding creep curve in Fig. 7.15 (the lower broken line) is

$$C_{22} = A_1 e^{-\alpha_1 \theta} \quad ,$$

where $A_1 = 0.04$ and $\alpha_1 = 0.06$ 1/day. Using Eqs. (7.42), we arrive at the following Laplace transforms of the creep compliance and the torque which is constant

$$C_{22}^{*}(p) = \frac{A_1}{\alpha_1 + p}, \quad T^{*}(p) = \frac{T}{p} \quad .$$

The final expression for the Laplace transform of the normalized shear strain is

$$\bar{\gamma}^{*}(p) = \frac{2E(\alpha_1 + A_1 + p)}{\pi p(\alpha_1 + A_1 E + p)} \quad , \tag{7.49}$$

where $E = E_1/(E_1 + E_2)$.

To use Eqs. (7.42) for the inverse Laplace transformation, we should decompose the right-hand part of Eq. (7.49) as

$$\bar{\gamma}^*(p) = \frac{2E}{\pi(\alpha_1 + A_1 E)}\left[\frac{\alpha_1 + A_1}{p} - \frac{A_1(1-E)}{\alpha_1 + A_1 E + p}\right] .$$

Applying Eqs. (7.42) we get

$$\bar{\gamma}(t) = \frac{2E}{\pi(\alpha_1 + A_1 E)}\left[\alpha_1 + A_1 - A_1(1-E)e^{-(\alpha_1 + A_1 E)t}\right] .$$

This result is demonstrated in Fig. 7.19. As can be seen, there is practically no creep because the cylinder deformation is controlled mainly by fibers.

Quite different behavior is demonstrated by the cylinder made of 0°/90° cross-ply composite material discussed in Section 4.4. In accordance with Eqs. (4.100) and (7.46), we have

$$A_{44}^*(p) = G_{12}^*(p) = \frac{G_{12}}{1 + K_{12}^*(p)} .$$

Exponential approximation, Eq. (7.36), of the shear curve in Fig. 7.15 (the upper broken line) results in the following equation for the creep compliance

$$K_{12} = A_1 e^{-\alpha_1 t} + A_2 e^{-\alpha_2 t} ,$$

where $A_1 = 0.033$, $\alpha_1 = 0.04\ 1/\text{day}$, $A_2 = 0.06$, $\alpha_2 = 0.4\ 1/\text{day}$. Omitting simple transformations we finally get

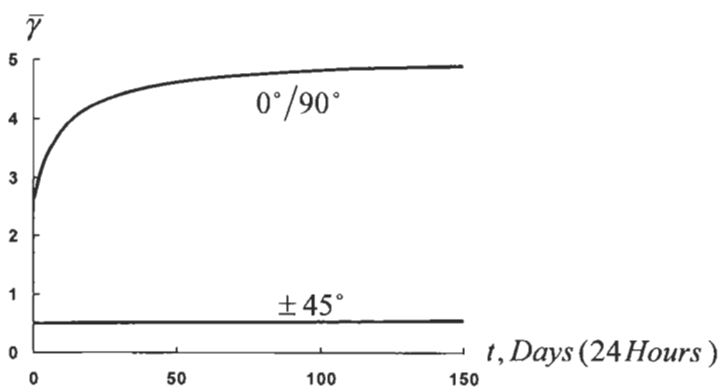

Fig. 7.19. Dependencies of the normalized shear strain on time for 0°/90° cross-ply and ±45° angle-ply glass–epoxy composite cylinders under torsion.

$$\bar{\gamma} = \frac{E_1}{2\pi G_{12}} \left[1 + \frac{A_1}{\alpha_1}(1 - e^{-\alpha_1 t}) + \frac{A_2}{\alpha_2}(1 - e^{-\alpha_2 t}) \right] .$$

The corresponding creep diagram is shown in Fig. 7.19.

Under relatively high stresses, polymeric composites demonstrate nonlinear viscoelastic behavior. The simplest approach to study nonlinear creep problems is based on experimental isochrone stress–strain diagrams of the type shown in Fig. 7.12. Using the curves corresponding to time moments $t_1 < t_2 < t_3$ etc. we can solve a sequence of nonlinear elasticity problems for these time moments and thus determine the change of strains and stresses in time. This approach sometimes referred to as the aging theory is approximate and can be used to study the structures loaded with forces that do not change in time or change very slowly.

There exist also several variants of nonlinear hereditary theory described, e.g. by Rabotnov (1980). According to the most common versions, Eq. (7.31) is generalized as

$$\varepsilon(t) = \frac{1}{E} \left[\sigma(t) + \int_0^t C_1(t-\tau)\sigma(\tau)\mathrm{d}\tau + \int_0^t \int_0^t C_2(t-\tau_1, t-\tau_2)\sigma(\tau_1)\sigma(\tau_2)\mathrm{d}\tau_1\,\mathrm{d}\tau_2 + \cdots \right],$$

$$\varepsilon(t) = \sum_k A_k \left[\sigma(t) + \int_0^t C(t-\tau)\sigma(\tau)\mathrm{d}\tau \right]^k$$

$$f[\varepsilon(t)] = \frac{1}{E} \left[\sigma(t) + \int_0^t C(t-\tau)\sigma(\tau)\mathrm{d}\tau \right],$$

$$\varepsilon(t) = \phi[\sigma(t)] + \int_0^t C(t-\tau)\psi[\sigma(\tau)]\mathrm{d}\tau .$$

In conclusion, it should be noted that properly designed composite structures (see the next chapter) in which material behavior is controlled by fibers usually do not exhibit pronounced time-dependent behavior. For example, consider a filament wound glass–epoxy pressure vessel studied in Section 6.3 (see Fig. 6.23 and the second row in Table 6.1 for parameters of the vessel). The vessel consists of $\pm 36^\circ$ helical plies and circumferential plies, and has structural parameters that are close to optimal (see Section 8.1). Experimental dependence of circumferential strain on time for step-wise loading with internal pressure p presented in Fig. 7.20 does not indicate any significant creep deformation. It should be emphasized that this conclusion is valid for normal conditions only – under elevated temperature composite structures can exhibit significant creep deformation.

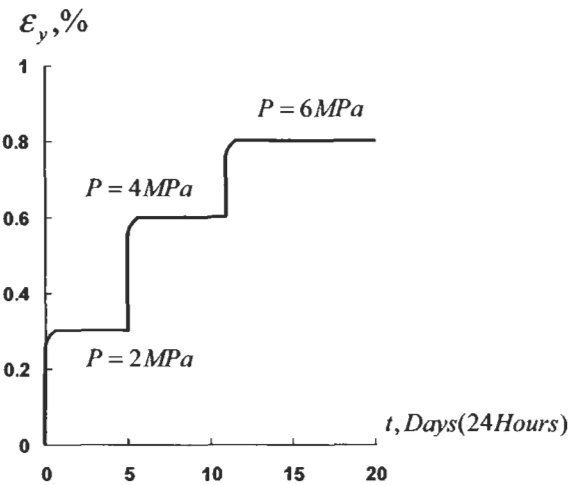

Fig. 7.20. Dependence of the circumferential strain on time for a glass–epoxy cylindrical pressure vessel loaded in steps with internal pressure p.

7.3.2. *Durability*

Composite materials, to be applied to structures with long service life, need to be guaranteed for the corresponding period of time from failure that is usually a result of an evolutionary process of material degradation in the service environment. To provide proper durability of the material, we need, in turn, to study its long-term behavior under load and its endurance limits. The most widely used durability criteria establishing the dependence of material strength on the time of loading are based on the concept of the accumulation of material damage induced by acting stresses and intensified by degrading influence of service conditions such as temperature, moisture etc. Particular criteria depend on the accepted models simulating the material damage accumulation. Though there exist a microstructural approach to the durability evaluation of composite materials (see, e.g. (Skudra et al., 1989)), for practical purposes, experimental dependencies of the ultimate stresses on the time of their action are usually attracted. Particularly, these experiments allow us to conclude that fibers that are the main load-carrying elements of composite materials possess some residual strength $\bar{\sigma}_\infty = \bar{\sigma}(t \to \infty)$ which makes from 50% to 70% of the corresponding static strength $\bar{\sigma}_0 = \bar{\sigma}(t = 0)$ depending on the fiber type. Typical dependencies of the long-term strength of composite materials on the time are presented in Fig. 7.21. As can be seen, time of loading dramatically affects material strength. However, being unloaded at any moment of time t composite materials demonstrate practically the same static strength that they had before long-term loading.

Approximation of the curves shown in Fig. 7.21 can be performed using exponential functions as follows:

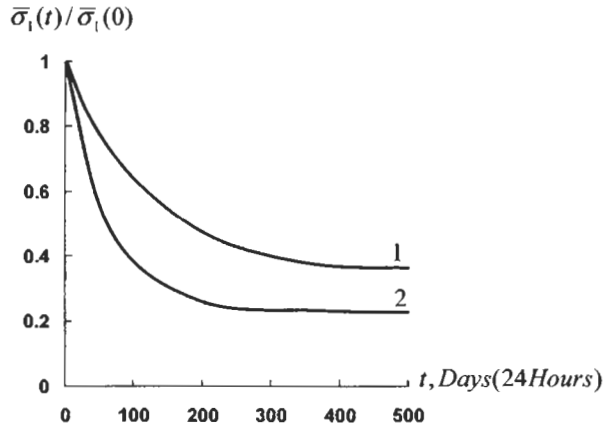

Fig. 7.21. Normalized long-term longitudinal strength of aramid–epoxy (1) and glass–epoxy (2) unidirectional composites.

$$\bar{\sigma}(t) = \bar{\sigma}_\infty + \sum_n A_n e^{-\lambda_n t} \ , \tag{7.50}$$

where $\bar{\sigma}_\infty, A_n$ and λ_n are coefficients providing the proper approximation. Initial static strength is

$$\bar{\sigma}(0) = \bar{\sigma}_0 = \bar{\sigma}_\infty + \sum_n A_n \ .$$

The simplest is one-term approximation

$$\bar{\sigma}(t) = \bar{\sigma}_\infty + (\bar{\sigma}_0 - \bar{\sigma}_\infty)e^{-\lambda t} \ . \tag{7.51}$$

To approximate the initial part of the curve, we can put $\bar{\sigma}_\infty = 0$ and arrive at the following simple equation:

$$\bar{\sigma}(t) = \bar{\sigma}_0 e^{-\lambda t} \ . \tag{7.52}$$

Now assume that we can solve Eqs. (7.50), (7.51), or (7.52) for t and find material durability $t_d(\sigma)$, i.e., the time during which material can stand under stress σ. Present the process of loading as a system of k stages such that the duration of each stage is t_i and the stress acting at this stage is σ_i $(i = 1, 2, 3, \ldots, k)$. Then, the whole period of time during which material can stand under such step-wise loading can be calculated with the aid of the following equation

$$\sum_{i=1}^{k} \frac{t_i}{t_d(\sigma_i)} = 1 \ ,$$

where $t_d(\sigma_i)$ is material durability corresponding to stress σ_i.

Strength criteria discussed in Chapter 6 can be generalized for the case of long-term loading if we change the static ultimate stresses entering these criteria for the corresponding long-term strength characteristics.

7.3.3. Cyclic loading

Consider the behavior of composite materials under the action of loads periodically changing in time. For qualitative analysis, consider first the material that can be simulated with the simple mechanical model shown in Fig. 7.16. Applying stress acting according to the following law:

$$\sigma(t) = \sigma_0 \sin \omega t \ , \tag{7.53}$$

where σ_0 is the amplitude of stress and ω is the frequency we can solve Eq. (7.41) that describes the model under study for strain $\varepsilon(t)$. The result is

$$\varepsilon(t) = \varepsilon_0 \sin(\omega t + \theta) \ , \tag{7.54}$$

where

$$\varepsilon_0 = \sigma_0 \sqrt{\frac{1 + t_r^2 \omega^2}{E_l^2 + E_i^2 t_r^2 \omega^2}}, \quad \tan \theta = -\frac{t_r \omega (E_i - E_l)}{E_l + E_i t_r^2 \omega^2} \ . \tag{7.55}$$

As follows from these equations, viscoelastic material is characterized with a phase shift of strain with respect to stress. Eliminating time variable from Eqs. (7.53) and (7.54) we arrive at the following relationship between stress and strain

$$\left(\frac{\sigma}{\sigma_0}\right)^2 + \left(\frac{\varepsilon}{\varepsilon_0}\right)^2 - 2 \cos \theta \frac{\sigma \varepsilon}{\sigma_0 \varepsilon_0} = \sin^2 \theta \ .$$

This is the equation of an ellipse shown in Fig. 7.22(a). The absolute value of the area A, inside this ellipse (its sign depends on the direction of integration along the contour) determines the energy dissipation per one cycle of vibration, i.e.

$$\Delta W = |A| = \pi \sigma_0 \varepsilon_0 |\sin \theta| \ . \tag{7.56}$$

Folowing Zinoviev and Ermakov (1994) we can introduce the dissipation factor as the ratio of energy loss in a loading cycle, ΔW, to the amplitude value of the elastic potential energy in a cycle, W, as

$$\psi = \frac{\Delta W}{W} \ ,$$

where, in acccordance with Fig. 7.22(b), $W = (1/2)\sigma_0 \varepsilon_0$. Transforming Eq. (7.56) with the aid of Eqs. (7.55) we arrive at

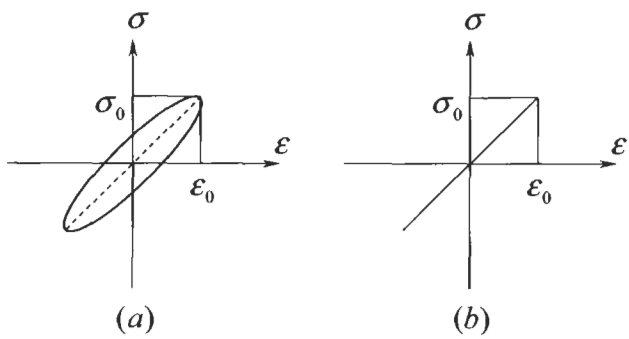

Fig. 7.22. Stress–strain diagrams for viscoelastic (a) and elastic (b) materials.

$$\psi = \frac{2\pi t_r \omega}{1 + t_r^2 \omega^2}\left(1 - \frac{E_l}{E_i}\right) .$$

As follows from this equation, ψ depends on the number of oscillations accomplished during the period of time equal to the material relaxation time, t_r, and reaches the maximum value for $t_r\omega = 1$.

As shown by Zinoviev and Ermakov (1994), for anisotropic materials, the dissipation factor depends also on the direction of loading. Particularly, for a unidirectional composite ply, referred to axes x and y making angle ϕ with the principal material axes 1 and 2 as in Fig. 4.18, the dissipation factors are

$$\psi_x = E_x\left[\left(\frac{\psi_1}{E_1}\cos^2\phi - \frac{\psi_2}{E_2}\sin^2\phi\right)\cos 2\phi + \psi_{45}\mu_{12}\sin^2\phi\cos^2\phi\right],$$

$$\psi_y = E_y\left[\left(\frac{\psi_2}{E_2}\cos^2\phi - \frac{\psi_1}{E_1}\sin^2\phi\right)\cos 2\phi + \psi_{45}\mu_{12}\sin^2\phi\cos^2\phi\right],$$

$$\psi_{xy} = G_{xy}\left[\left(\frac{2\psi_1}{E_1} + \frac{2\psi_2}{E_2} - \psi_{45}\mu_{12}\right)\sin^2\phi\cos^2\phi + \frac{\psi_{12}}{G_{12}}\cos^2 2\phi\right] ,$$

where

$$\mu_{12} = \frac{1 - \nu_{12}}{E_1} + \frac{1 - \nu_{21}}{E_2} + \frac{1}{G_{12}} ,$$

E_x, E_y and G_{xy} are specified by Eqs. (4.76) and ψ_1, ψ_2, ψ_{12}, and ψ_{45} are the ply dissipation factors corresponding to loading along the fibers, across the fibers, under in-plane shear and at 45° with respect to principal material axes 1 and 2. As follows from Fig. 7.23, calculation based on the foregoing equations provides fair agreement with experimental results of Ni and Adams (1984).

Energy dissipation in conjunction with relatively low heat conductivity of composite materials induces self-heating of them during the cyclic loading.

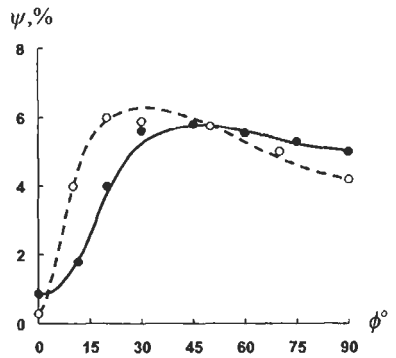

Fig. 7.23. Calculated (lines) and experimental (circles) dependencies of dissipation factor on the ply orientation for glass–epoxy (——— •) and carbon–epoxy (– – – – o) unidirectional composites.

Dependence of an aramid-epoxy composite material temperature on the number of cycles under tensile and compressive loading with frequency 10^3 cycles per minute is shown in Fig. 7.24 (Tamuzh and Protasov, 1986).

Under cyclic loading, structural materials experience a fatigue fracture caused by material damage accumulation. As was already noted in Section 3.2.4, heterogeneous structure of composite materials provides relatively high resistance of these materials to crack propagation resulting in their specific behavior under cyclic loading. As follows from Fig. 7.25 showing experimental results obtained by V.F. Kutinov, stress concentration in aluminum specimens practically does not affect material static strength due to plasticity of aluminum but dramatically reduces its fatigue strength. Conversely, static strength of carbon–epoxy composites that

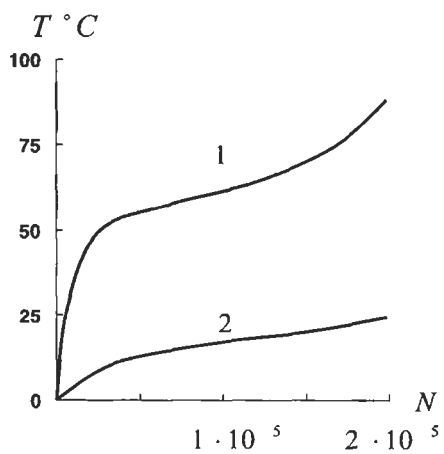

Fig. 7.24. Temperature of an aramid–epoxy composite as a function of the number of cycles under tension (1) and compression (2).

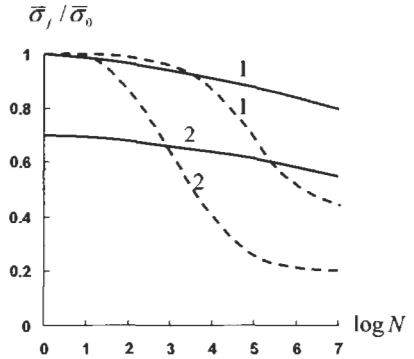

Fig. 7.25. Typical fatigue diagrams for carbon–epoxy composite (solid lines) and aluminum alloy (broken lines) specimens without (1) and with (2) stress concentration (fatigue strength is normalized to static strength of specimens without stress concentration).

belong to brittle materials is reduced by stress concentration that practically does not affect the slope of the fatigue curve. On average, residual strength of carbon composites after 10^6 loading cycles makes 70–80% of material static strength in comparison with 30–40% for aluminum alloys. Qualitatively, this comparative evaluation is true for all fibrous composites that are widely used in structural elements subjected to intensive vibrations such as helicopter rotor blades, airplane propellers, drive shafts, automobile leaf-springs, etc.

A typical for composite materials fatigue diagram constructed with experimental results of Apinis et al. (1991) is shown in Fig. 7.26. Standard fatigue diagrams usually determine material strength for $10^3 \leqslant N \leqslant 10^6$ and are approximated as

$$\sigma_R = a - b \log N \ . \tag{7.57}$$

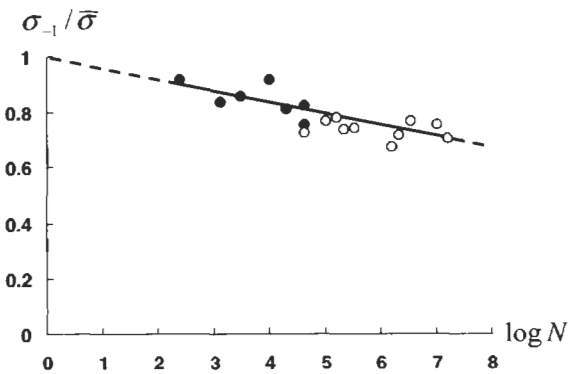

Fig. 7.26. Normalized fatigue diagram for fabric carbon–carbon composite material ($\bar{\sigma}$-static strength), • —·· o experimental part of the diagram (loading frequency 6 Hz (•) and 330 Hz (o)), – – – extrapolation.

Here, N is the number of cycles to failure under stress σ_R, a and b are experimental constants depending on frequency of cyclic loading, temperature and other environmental factors, and on the stress ratio $R = \sigma_{\min}/\sigma_{\max}$, where $\sigma_{\max}$ and $\sigma_{\min}$ are the maximum and minimum stresses. It should be taken into account that results of fatigue tests are characterized, as a rule with high scatter.

Factor R specifies the cycle type. The most common bending fatigue test provides the symmetric cycle for which $\sigma_{\min} = -\sigma$, $\sigma_{\max} = \sigma$, and $R = -1$. Tensile load cycle ($\sigma_{\min} = 0, \sigma_{\max} = \sigma$) has $R = 0$, while compressive cycle ($\sigma_{\min} = -\sigma, \sigma_{\max} = 0$) has $R \to -\infty$. Cyclic tension with $\sigma_{\max} > \sigma_{\min} > 0$ corresponds to $0 < R < 1$, while cyclic compression with $0 > \sigma_{\max} > \sigma_{\min}$ corresponds to $1 < R < \infty$. Fatigue diagrams for unidirectional aramid–epoxy composite studied by Limonov and Anderson (1991) corresponding to various R-values are presented in Fig. 7.27. Analogous results (Anderson et al., 1991) for carbon–epoxy composites are shown in Fig. 7.28.

Because only σ_{-1} is usually available from standard test under cyclic bending, fatigue strength for other load cycles is approximated as

$$\sigma_R = \sigma_{-1} + \sigma_m\left(1 - \frac{\sigma_{-1}}{\bar{\sigma}_t}\right),$$

where $\sigma_m = (\sigma_{\min} + \sigma_{\max})/2$ is the mean stress of the load cycle and $\bar{\sigma}_t$ is the material long-term strength (see Section 7.3.2) for the period of time equal to that of the cyclic loading.

Fabric composites are more sensitive to cyclic loading than materials reinforced with straight fibers. This fact is illustrated in Fig. 7.29 showing experimental results of Schulte et al. (1987). The foregoing discussion deals with the high-cycle fatigue. Initial interval $1 \leqslant N \leqslant 10^3$ corresponding to the so-called low-cycle fatigue is usually studied separately, because the slope of the approximation in Eq. (7.57) can

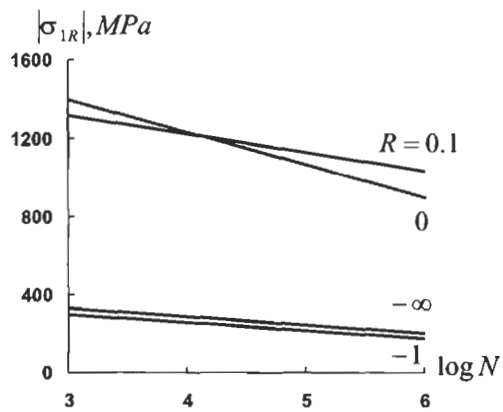

Fig. 7.27. Fatigue diagrams for unidirectional aramid–epoxy composite loaded along the fibers with various stress ratios.

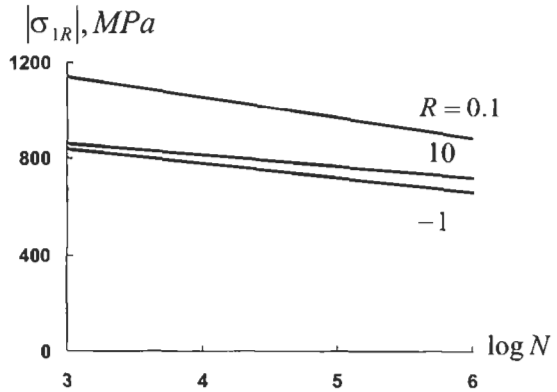

Fig. 7.28. Fatigue diagrams for a unidirectional carbon–epoxy composite loaded along the fibers with various stress ratios.

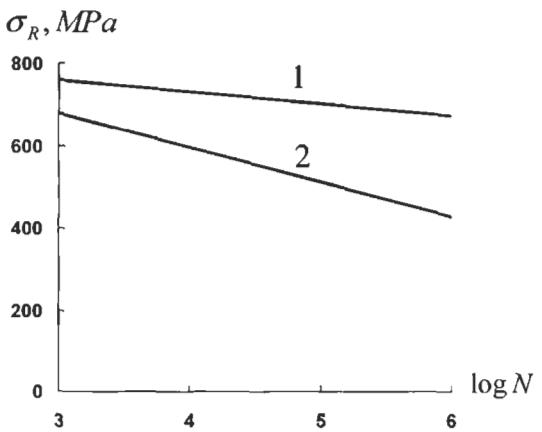

Fig. 7.29. Tensile fatigue diagrams for a cross-ply (1) and fabric (2) carbon–epoxy composites.

be different for high stresses. Typical fatigue diagram for this case is shown in Fig. 7.30 (Tamuzh and Protasov, 1986).

Fatigue has also some effect on the stiffness of composite materials. This can be seen in Fig. 7.31 demonstrating reduction of the elastic modulus for a glass fabric–epoxy–phenolic composite under low-cycle loading (Tamuzh and Protasov, 1986). This effect should be accounted for in application of composites to the design of structural members such as automobile leaf-springs which, being subjected to cyclic loading, are designed under stiffness constraints.

Stiffness degradation can be used as an indication of material damage to predict its fatigue failure. The most sensitive characteristic of the stiffness change is the tangent modulus E_t specified by the second equation in Eqs. (1.8). Dependence of E_t on the number of cycles, $\bar{N}$, normalized to the number of cycles that cause material

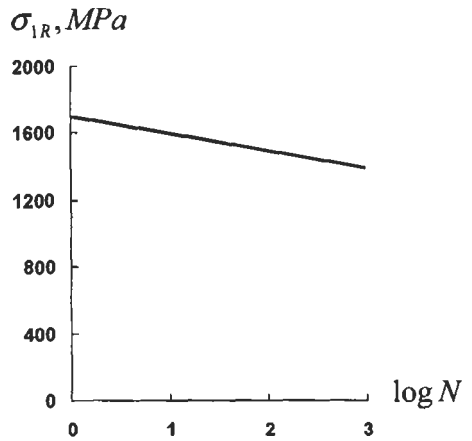

Fig. 7.30. Low-cycle fatigue diagram for unidirectional aramid–epoxy composite loaded along the fibers with $R = 0.1$.

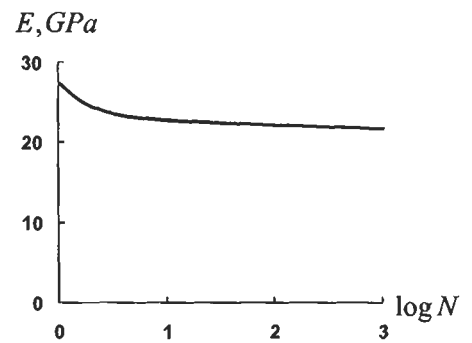

Fig. 7.31. Dependence of elastic modulus of glass fabric–epoxy phenolic composite on the number of cycles at stress $\sigma = 0.5\bar{\sigma}$ ($\bar{\sigma}$ is the static ultimate stress).

fatigue fracture under the pre-assigned stress is presented in Fig. 7.32 corresponding to ±45° angle-ply carbon–epoxy laminate studied by Murakami et al. (1991).

7.3.4. Impact loading

Thin-walled composite laminates possessing high in-plane strength and stiffness are rather sensitive to damage initiated by transverse impact loads that can cause fiber breakage, cracks in the matrix, delamination, and even material penetration by the impactor. Depending on the impact energy determined by the impactor mass and velocity and the properties of laminate impact loading can result in considerable reduction in material strength under tension, compression, and shear. One of the most dangerous consequences of the impact loading is an internal delamination of

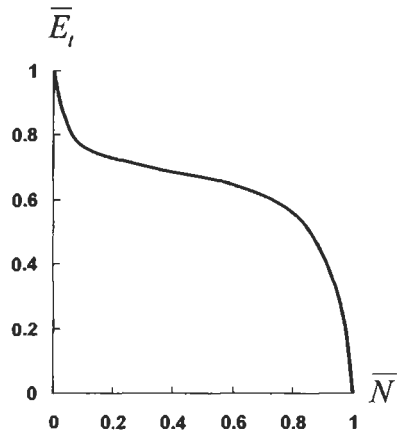

Fig. 7.32. Dependence of the tangent modulus normalized to its initial value on the number of cycles related to the ultimate number corresponding to fatigue failure under stress $\sigma_{max} = 120$ MPa and $R = -1$ for ±45° angle-ply carbon–epoxy laminate.

laminates that sometimes can be hardly identified by visual examination. This type of the defect causes a dramatic reduction in the laminate compressive strength and results in unexpected failure of the thin-walled composite structure due to microbuckling of fibers or local buckling of plies. As follows from Fig. 7.33 showing experimental results of Verpoest et al. (1989) for unidirectional and fabric composite plates, impact can reduce material strength in compression by the factor of 5 and more.

To study the mechanism of material interlaminar delamination, consider a problem of wave propagation through the thickness of the laminate shown in Fig. 7.34. The motion equation has the following well-known form

$$\frac{\partial}{\partial z}\left(E_z \frac{\partial u_z}{\partial z}\right) = \rho \frac{\partial^2 u_z}{\partial t^2} \quad . \tag{7.58}$$

Here, u_z is the displacement in the z-direction, E_z is material modulus in the same direction depending, in the general case on z, and ρ is the material density. For the laminate in Fig. 7.34, the solution of Eq. (7.58) should satisfy the following boundary and initial conditions

$$\sigma_z(z = 0, t) = -p(t), \quad \sigma_z(z = h, t) = 0 \ , \tag{7.59}$$

$$u_z(z,\ t = 0) = 0, \quad \frac{\partial u_z}{\partial t}(z > 0, t = 0) = 0 \tag{7.60}$$

in which

$$\sigma_z = E_z \frac{\partial u_z}{\partial z} \tag{7.61}$$

is the interlaminar normal stress.

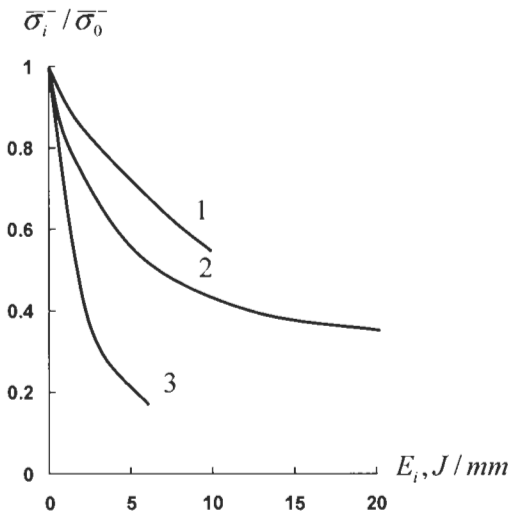

Fig. 7.33. Dependence of compression strength after impact normalized to the initial compressive strength on the impact energy related to the plate thickness for glass fabric–epoxy (1), and unidirectional glass–epoxy (2) and carbon–epoxy (3) composite plates.

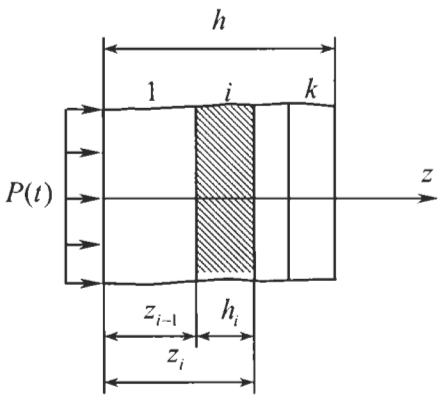

Fig. 7.34. Laminate under impact load.

Consider first a homogeneous layer such that E_z and ρ do not depend on z. Then, Eq. (7.58) acquires the form

$$c^2 \frac{\partial^2 u_z}{\partial z^2} = \frac{\partial^2 u_z}{\partial t^2} \quad ,$$

where $c^2 = E_z/\rho$. Transform this equation introducing new variables, i.e., $x_1 = z + ct$ and $x_2 = z - ct$. Performing traditional transformation we arrive at

$$\frac{\partial^2 u_z}{\partial x_1 \partial x_2} = 0 \ .$$

The solution for this equation can be readily found and presented as

$$u_z = \phi_1(x_1) + \phi_2(x_2) = \phi_1(z + ct) + \phi_2(z - ct) \ ,$$

where ϕ_1 and ϕ_2 are some arbitrary functions. Using Eq. (7.61) we get

$$\sigma_z = E_z[f_1(x + ct) + f_2(x - ct)] \ ,$$

where

$$f_1 = \frac{\partial \phi_1}{\partial z}, \quad f_2 = \frac{\partial \phi_2}{\partial z} \ .$$

Applying boundary and initial conditions, Eqs. (7.59) and (7.60), we arrive at the following final result:

$$\sigma_z = E[f(x + ct) - f(x - ct)] \ , \tag{7.62}$$

in which the form of function f is governed by the shape of the acting pulse. As can be seen, the stress wave is composed of two components having the opposite signs and moving in the opposite directions with one and the same speed c which is the speed of sound in the material. The first term in Eq. (7.62) corresponds to the acting pulse that propagates to the free surface $z = h$ (see Fig. 7.35 demonstrating the propagation of the rectangular pulse), while the second term corresponds to the pulse reflected from the free surface $z = h$. It is important that for the compressive direct pulse (which is usually the case), the reflected pulse is tensile and can cause material delamination since the strength of laminated composites under tension across the layers is very low.

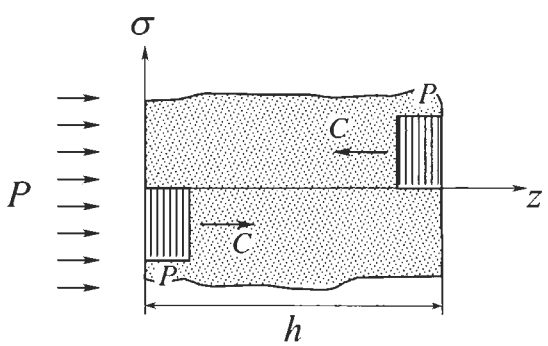

Fig. 7.35. Propagation of direct and reflected pulses through the layer thickness.

For laminates, such as in Fig. 7.34, the boundary conditions, Eqs. (7.59) should be supplemented with the interlaminar conditions $u_z^{(i)} = u_z^{(i-1)}$ and $\sigma_z^{(i)} = \sigma_z^{(i-1)}$. Omitting rather cumbersome solution that can be found elsewhere (Vasiliev and Sibiryakov, 1985) present some numerical results.

Consider the two-layered structure the first layer of which has thickness 15 mm and is made of aramid–epoxy composite material with $E_z^{(1)} = 4.2$ GPa, $\rho_1 = 1.4$ g/cm^3 and the second layer is made of boron–epoxy composite material and has $E_z^{(2)} = 4.55$ GPa, $\rho_2 = 2$ g/cm^3, $h_2 = 12$ mm. The duration of a rectangular pulse of external pressure p acting on the surface of the first layer is $t_p = 5 \times 10^{-6}$ s. Dependence of the interlaminar ($z = 15$ mm) stress on time is shown in Fig. 7.36. As can be seen, at $t \approx 3t_p$ the tensile interface stress exceeds the intensity of the pulse of pressure by the factor of 1.27. This stress is a result of interaction of the direct stress wave with the waves reflected from the laminate's inner, outer, and interface surfaces. Thus, in a laminate, each interface surface generates elastic waves.

For laminates consisting of more than two layers, the wave interaction becomes more complicated and, what is more important, can be controlled by the proper stacking sequence of layers. As an example, consider a sandwich structure shown in Fig. 7.37(a). The first (loaded) layer is made of aluminum and has $h_1 = 1$ mm, $E_z^{(1)} = 72$ GPa, $\rho_1 = 2.7$ g/cm^3, the second layer is a foam core with $h_2 = 10$ mm, $E_z^{(2)} = 0.28$ GPa, $\rho_2 = 0.25$ g/cm^3, and the third (load-carrying) aramid–epoxy composite layer has $h_3 = 12$ mm, $E_z^{(3)} = 10$ GPa, $\rho_3 = 1.4$ g/cm^3. The duration of a rectangular pulse of external pressure is 10^{-6} s. Maximum tensile stress occurs in the middle plane of the load-carrying layer (plane $a - a$ in Fig. 7.37). Normal stress induced in this plane is presented in Fig. 7.38(a). As can be seen, at the moment of time t equal to about 1.75×10^{-5} s this stress is tensile and can cause delamination of the structure.

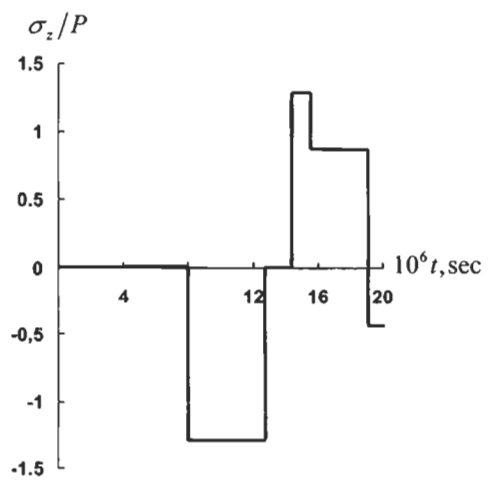

Fig. 7.36. Dependence of the interlaminar stress referred to the acting pressure on time.

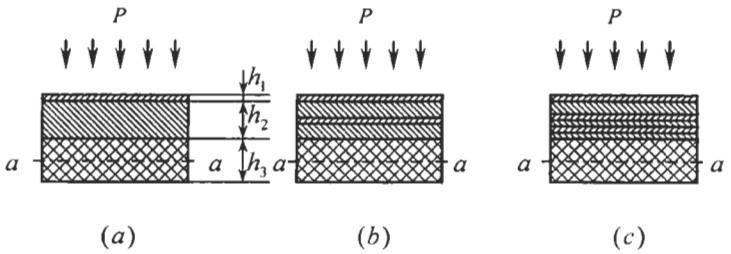

Fig. 7.37. Structure of the laminates under study.

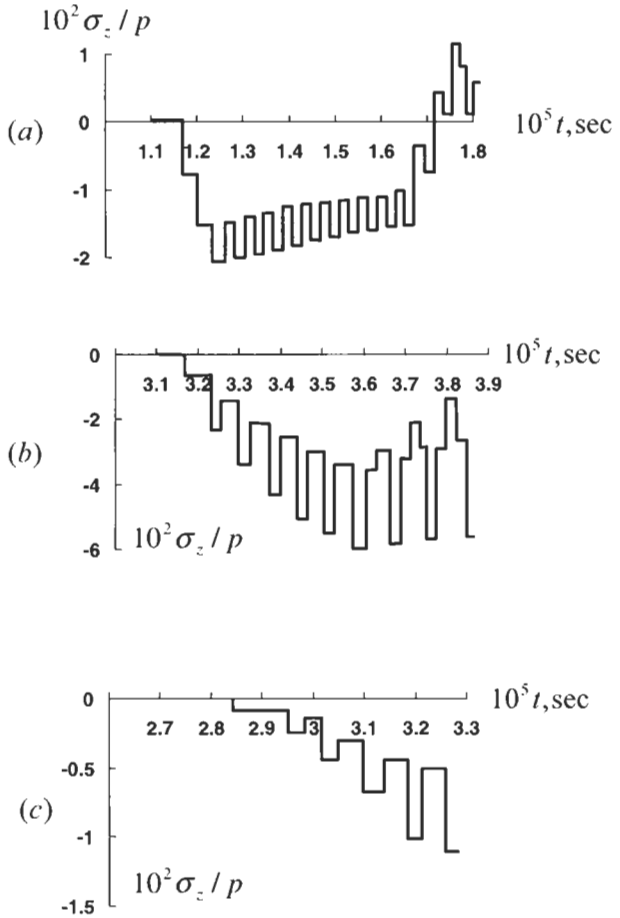

Fig. 7.38. Normal stress related to external pressure acting in section *a a* of the laminates in Fig. 7.37(a)–(c), respectively.

Now introduce an additional aluminum layer in the foam core as shown in Fig. 7.37(b). As follows from Fig. 7.38(b) this layer suppresses tensile stress in section $a - a$. Two intermediate aluminum layers (Fig. 7.37(c)) working as generators of the compression stress waves eliminate the appearance of tensile stress in this section. Naturally, the effect under discussion can be achieved for a limited period of time. But actually, impact tensile stress is dangerous right after the pulse action. Damping capacity of real structural materials (it was not taken into account in the foregoing analysis) dramatically reduces the stress amplitude in time.

A flying projectile with relatively high kinetic energy can penetrate through the laminate. As known, composite materials, particularly, high-strength aramid fabrics are widely used for protection against flying objects. To demonstrate the mechanism of this protection, consider a square composite plate clamped in the steel frame shown in Fig. 7.39 and subjected to impact of a rectangular plane projectile (see Fig. 7.39) simulating the blade of the turbojet engine compressor. The plate consists of the layers of thin aramid fabric impregnated with epoxy resin at a distance from the window in the frame (see Fig. 7.39) and co-cured together as shown in Fig. 7.40. The front (loaded) surface of the plate has a 1 mm thick cover sheet made of glass fabric–epoxy composite. Results of ballistic tests are presented in Table 7.2. Front and back views of plate No. 2 are shown in Fig. 7.39, and the back view of plate No. 3 can be seen in Fig. 7.40. Because mechanical properties of the aramid fabric used to make the plates are different in the warp and in the fill directions (see Section 4.6), the plates consist of couples of mutually orthogonal layers of fabric that are

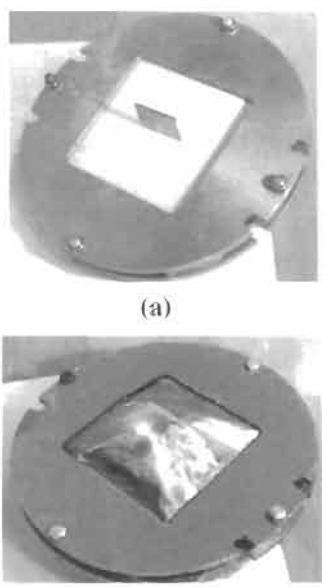

(a)

(b)

Fig. 7.39. Plate no. 2 (see Table 7.2) after the impact test: (a) front view; (b) back view.

Fig. 7.40. Back view of plate No. 3 (see Table 7.2) after the impact test

Table 7.2
Ballistic test of plates made of aramid fabric.

Plate no.	Projectile velocity (m/s)	Test results
1	315	No penetration
2	320	The projectile is "caught" by the containment
3	325	Penetration

further referred to as $0°/90°$ layers. All the plates listed in Table 7.2 have $n = 32$ of such couples.

To calculate the projectile velocity below which it fails to perforate the plate (the so-called ballistic limit) we use the energy conservation law according to which

$$\tfrac{1}{2}m_{\mathrm{p}}(V_{\mathrm{s}}^2 - V_{\mathrm{r}}^2) = n(W + T) \ , \tag{7.63}$$

where V_{s} is the projectile striking velocity, V_{r} is its residual velocity, $m_{\mathrm{p}} = 0.25$ kg is the projectile mass, $n = 32$ is the number of the $0°/90°$ layers, W is the fracture work for the $0°/90°$ layers, and T is the kinetic energy of the layer. All the other factors and the fiberglass cover of the plate are neglected.

Fracture work can be evaluated using the quasi-static test shown in Fig. 7.41. A couple of mutually orthogonal fabric layers is fixed along the plate contour and loaded with the projectile. The area under the force-deflection curve (solid line in Fig. 7.41) can be treated as the work of fracture which for the fabric under study has been found to be $W = 120$ Nm.

To calculate T, the deformed shape of the fabric membrane has been measured. Assuming that the velocities of the membrane points are proportional to deflections f and that $\mathrm{d}f_m/\mathrm{d}t = V_{\mathrm{s}}$ kinetic energy of the fabric under study (density of the layer unit surface is $0.2\,\mathrm{kg/m^2}$) turn out to be $T = 0.0006\,V_{\mathrm{s}}^2$.

To find the ballistic limit, we should take $V_{\mathrm{r}} = 0$ in Eq. (7.63). Substituting the foregoing results in this equation we get $V_b = 190.5$ m/s which is much lower than the experimental result ($V_b = 320$ m/s) following from Table 7.2.

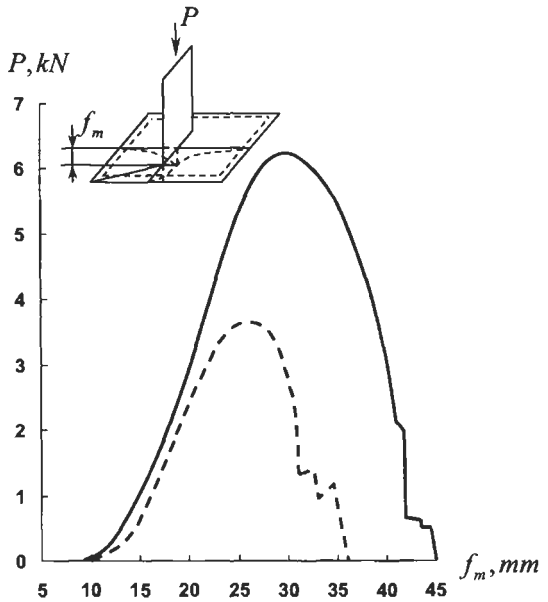

Fig. 7.41. Force–deflection diagrams for square aramid fabric membranes ——— couple of layers with orthogonal orientations, – – – – superposition of the diagrams for individually tested layers.

Let us change the model of the process and assume that the fabric layers fail one after another rather than all of them at once, as it is presented in Eq. (7.63). The result is expected to be different because the problem under study is not linear, and the principle of superposition is not valid for it. Bearing this in mind, we write Eq. (7.63) in the following incremental form:

$$\tfrac{1}{2}m_{\mathrm{p}}(V_{k-1}^2 - V_k^2) = W + T_{k-1} \ . \tag{7.64}$$

Here, V_{k-1} and V_k are the projectile velocities before and after the failure of the kth couple of fabric layers, W is, as earlier, the fracture work consumed by the kth couple of layers, $T_{k-1} = 0.0006\,V_{k-1}^2$ and the last term in the right-hand side of Eq. (7.64) means that we account for the kinetic energy of only those fabric layers that have been already penetrated by the projectile. Solving Eq. (7.64) for V_k we arrive at

$$V_k = \sqrt{[1 - 0.0048(k-1)]V_{k-1}^2 - \frac{2}{m_{\mathrm{p}}}W} \ . \tag{7.65}$$

For $k = 1$, we take $V_0 = 320$ m/s, in accordance with the experimental ballistic limit, and have $V_1 = 318.5$ m/s from Eq. (7.65). Taking $k = 2$ we repeat the calculation

and find that after the failure of the second couple of fabric layers $V_2 = 316.2$ m/s. This process is repeated until $V_k = 0$, and thus found number k determines the minimum number of 0°/90° layers that can stop the projectile with striking velocity $V_s = 320$ m/s. The result of calculation is presented in Fig. 7.42 from which it follows that $k = 32$. This is exactly the same number of layers that have been used to construct the experimental plates.

Thus, it can be concluded that the high impact resistance of aramid fabrics is determined by two main factors. First, by relatively high work of fracture which is governed not only by the high strength, but also by the interaction of the fabric layers. The broken line in Fig. 7.41 shows the fracture process constructed as a result of superposition of experimental diagrams for individual 0° and 90° layers. The solid line corresponds as was noted, to 0° and 90° layers tested together (the ratio of the fabric strength under tension in the warp and the fill direction is 1.3). As can be seen, the area under the solid line is much larger that under the broken one which indicates high contribution of the layers interaction to the work of fracture. If this conclusion is true, we can expect that for layers with higher anisotropy and for laminates in which the principal material axes of the adjacent layers are not orthogonal, the fracture work can be higher than for the orthotropic laminate under study. The second factor increasing the impact resistance of aramid fabrics is associated with a specific process of the failure during which the fabric layers fail one after another but not at once. Plates of the same number of layers but consisting of resin impregnated and co-cured layers that fail at once demonstrate much less impact resistance.

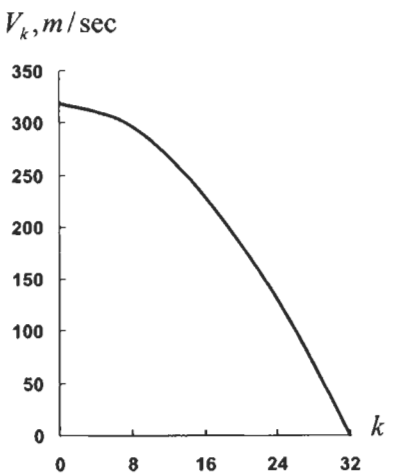

Fig. 7.42. Dependence of the residual velocity of the projectile on the number of penetrated layers.

7.4. Manufacturing effects

As was already noted, composite materials are formed in the process of fabrication of a composite structure, and their properties are strongly dependent on the type and parameters of processing. This means that material specimens that are used to determine mechanical properties should be fabricated with the same manufacturing method that is expected to be used to fabricate the structure under study.

To demonstrate direct correlation that can exist between processing and material properties, consider the process of circumferential winding on the cylindrical surface as in Fig. 7.43. As a rule, the tapes are wound with some overlap w_0 shown in Fig. 7.44(a). Introducing dimensionless parameter

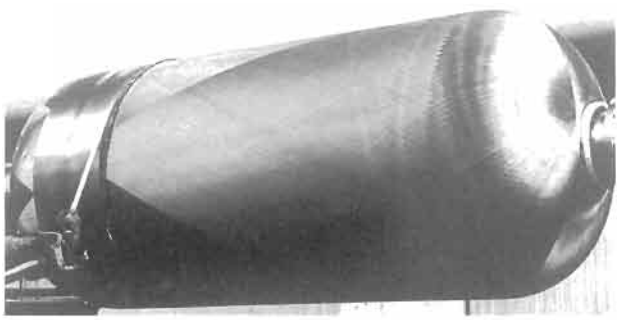

Fig. 7.43. Winding of a circumferential layer. Courtesy of CRISM.

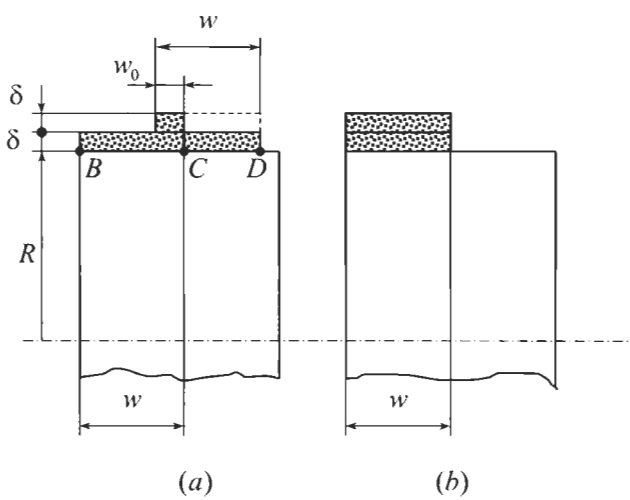

Fig. 7.44. Circumferential winding with (a) partial overlap $w_0 < w$ and (b) complete overlap $w_0 = w$.

$$\lambda = \frac{w_0}{w} \quad , \tag{7.66}$$

we can conclude that for the case of complete overlap (Fig. 7.44(b)) we have $\lambda = 1$. Initial position of the tape placed with overlap w_0 as in Fig. 7.44(a) is shown in this Figure with a broken line, while the final position of the tapes is shown with solid lines. Assume that after the winding and curing are over, the resulting structure is a unidirectionally reinforced ring which is removed from the mandrel and loaded with internal pressure, so that the ring radius being R before the loading becomes R_1. Decompose the resultant force acting in the ring cross-section into two components, i.e.

$$F = F' + F'' \tag{7.67}$$

and introduce the apparent stress acting along the fibers of the ring as

$$\sigma_1 = \frac{F}{A} \quad , \tag{7.68}$$

where $A = 2w\delta$ is the cross-sectional area of the ring made from two tapes as shown in Fig. 7.44. Force F'corresponds to part BC of the ring (Fig. 7.44(a)) and can be found as

$$F' = A' E_1 \frac{R_1 - R}{R} \quad ,$$

where $A' = (w + w_0)\delta$ is the cross-sectional area of this part of the ring and E_1 is the modulus of elasticity of the cured unidirectional composite. To calculate force F'' that corresponds to part CD of the ring (Fig. 7.44(a)), we should take into account that the fibers start to take the load only when this part of the tape reaches the position indicated with broken lines, i.e.

$$F'' = A'' E_1 \frac{R_1 - (R + \delta)}{R} \quad ,$$

where $A'' = (w - w_0)\delta$. With due regard to Eqs. (7.66), (7.67), and (7.68) we can write the result of the foregoing analysis in the following form:

$$\sigma_1 = E_1 \left[\varepsilon_1 - \frac{\delta}{2R}(1 - \lambda) \right] \quad . \tag{7.69}$$

Here, $\varepsilon_1 = (R_1 - R)/R$ is the apparent strain in the fiber direction. For complete overlap in Fig. 7.44(b), $\lambda = 1$, and $\sigma_1 = E_1 \varepsilon_1$. It should be noted that there exists also the so-called tape-to-tape winding for which $\lambda = 0$. This case cannot be described by Eq. (7.69) because of assumptions introduced in derivation, and the resulting equation for this case is $\sigma_1 = E_1 \varepsilon_1$.

As follows from Eq. (7.69), which is valid for winding without tension, overlap of the tape results in reduction of material stiffness. Because the levels of loading for the fibers of *BC* and *CD* parts of the ring (Fig. 7.44(a)) are different, reduction of material strength can also be expected.

Filament winding is usually performed with some initial tension of the tape. This tension improves material properties because it straightens the fibers and densifies the material. However, high tension may result in fiber damage and reduction of material strength. For glass and carbon fibers, preliminary tension usually does not exceed 5% of the tape strength, while for aramid fibers that are less sensitive to damage the level of initial tension can reach 20% of the tape strength. Preliminary tension reduces the effect of the tape overlap discussed above and described by Eq. (7.69). However, this effect can show itself in reduction of material strength, because the initial stresses which are induced by preliminary tension in the fibers can be different, and some fibers can be overloaded or underloaded under external forces acting on the structure in operational conditions. Strength reduction of aramid–epoxy unidirectional composites on the tape overlap observed in experiments of Rach and Ivanovskii (1986) for winding on a 200 mm diameter mandrel is demonstrated in Fig. 7.45.

The absence of the tape preliminary tension or low tension can cause the ply waviness shown in Fig. 7.46 which can occur in the filament wound laminates as a result of pressure exerted by the overwrapped plies on the underwrapped plies or in flat laminates due to material shrinkage in the process of curing.

The simplest for analysis is the regular waviness presented in Fig. 7.46(a). To determine the apparent modulus in the x-direction, we can use the expression similar to one presented in Eqs. (4.76), i.e.

$$\frac{1}{E_x} = \frac{\cos^4\alpha}{E_1} + \frac{\sin^4\alpha}{E_3} + \left(\frac{1}{G_{13}} - \frac{2\nu_{31}}{E_1}\right)\sin^2\alpha\cos^2\alpha \ . \tag{7.70}$$

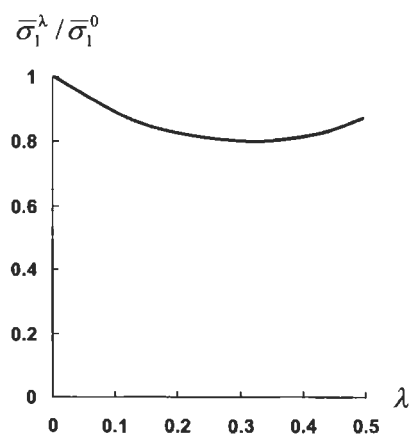

Fig. 7.45. Dependence of the normalized longitudinal strength of unidirectional aramid–epoxy composite on the tape overlap.

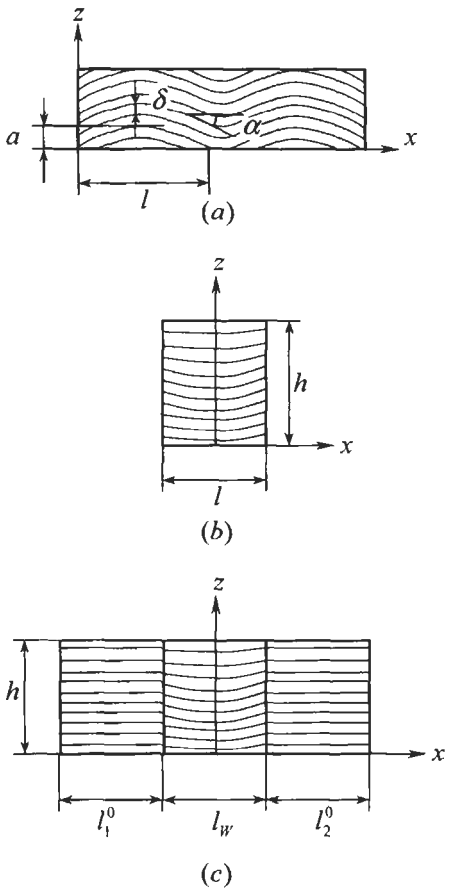

Fig. 7.46. Regular (a), through-the-thickness (b), and local (c) ply waviness.

Then, because the structure is periodic

$$\frac{1}{E_x^{(r)}} = \frac{1}{l}\int_0^l \frac{\mathrm{d}x}{E_x} \quad . \tag{7.71}$$

Approximating the ply wave as

$$z = a \sin \frac{\pi x}{l} \quad ,$$

where a is the amplitude, we get

$$\tan \alpha = \frac{\mathrm{d}z}{\mathrm{d}x} = f \cos \frac{\pi x}{l} \quad ,$$

where $f = \pi a/l$. Substitution into Eqs. (7.70) and (7.71) and integration yield (Tarnopol'skii and Roze, 1969)

$$\frac{1}{E_x^{(r)}} = \frac{1}{2\lambda}\left[\frac{2+f^2}{E_1} + \frac{1}{E_3}(2\lambda - 2 - 3f^2) + \left(\frac{1}{G_{13}} - \frac{2\nu_{31}}{E_1}\right)f^2\right] ,$$

where $\lambda = (1+f^2)^{3/2}$. Simplifying this result under the assumption that $f^2 \ll 1$ we arrive at

$$E_x^{(r)} = \frac{E_1}{1 + \frac{E_1 f^2}{2G_{13}}} . \tag{7.72}$$

For glass–, carbon–, and aramid–epoxy composites with properties listed in Table 3.5 dependencies corresponding to Eq. (7.72) are presented in comparison with experimental results of Tarnopol'skii and Roze (1969) in Fig. 7.47.

If the ply waviness varies through the laminate thickness as in Fig. 7.46(b), Eq. (7.72) can be generalized as

$$E_x^{(t)} = \frac{E_1}{h}\int_0^h \frac{dz}{1 + \frac{E_1}{2G_{13}} f^2(z)} \tag{7.73}$$

and finally, for the local waviness (see Fig. 7.46(c)) we get

$$\frac{1}{E_x^{(l)}} = \frac{\bar{l}_1^0}{E_1} + \frac{\bar{l}_w}{E_x^{(t)}} + \frac{\bar{l}_2^0}{E_1} ,$$

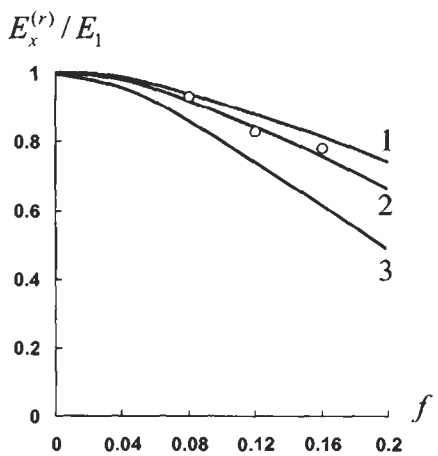

Fig. 7.47. Reduction of the normalized modulus with the ply waviness parameter, f, for (1) glass-, (2) carbon-, and (3) aramid–epoxy composites. ——— Eqs. (7.72), o experiment for glass–epoxy composite.

where

$$\bar{l}_{1,2}^0 = \frac{l_{1,2}^0}{l_1^0 + l_w + l_2^0}, \quad \bar{l}_w = \frac{l_w}{l_1^0 + l_w + l_2^0}$$

and $E_x^{(t)}$ is specified by Eq. (7.73).

Even moderate ply waviness dramatically reduces material strength under compression along the fibers, as can be seen in Fig. 7.48 demonstrating experimental results of V.F. Kutinov for unidirectional carbon–epoxy composite. The other strength characteristics of unidirectional composites are just slightly affected by the ply waviness.

There exist also some specific for composites manufacturing operations that cause stresses and strains appearing in composite structural elements in the process of their fabrication. As an example, consider the problem of bending and warping of unsymmetric laminates during the fabrication. Assume that some laminated polymeric composite panel is cured under temperature T_c and cooled to room temperature T_0. Under slow cooling, the temperature change, $\Delta T = T_0 - T_c$, is the same for all the layers. Because thus fabricated panel is free of loading (i.e., no loads are applied to its edges and surfaces) the forces and moments in the left-hand sides of Eqs. (7.23) and (7.24) are zero, and these equations form a linear algebraic system for generalized strains ε_T, γ_T and κ_T. Integration of strain–displacement equations, Eqs. (7.28), allows us to determine the shape of the fabricated panel.

Analysis of Eqs. (7.25) and (7.26) similar to that performed in Section 5.6 shows that for symmetric laminates $M_{mn}^T = 0$. Because $C_{mn} = 0$ for such laminates, the

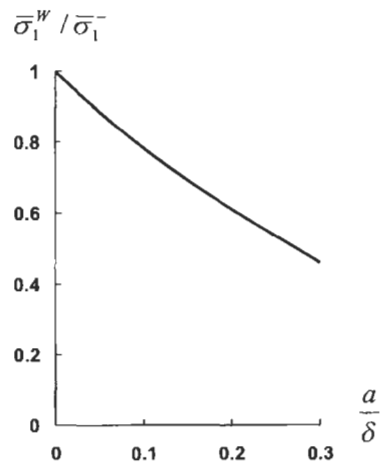

Fig. 7.48. Experimental dependence of carbon–epoxy composite longitudinal compression strength related to the corresponding strength of material without ply waviness on the ratio of the waviness amplitude to the ply thickness.

last three equations of Eqs. (7.23) in which $M_x = M_y = M_{xy} = 0$ form a set of homogeneous equations whose solution is $\kappa_{xT} = \kappa_{yT} = \kappa_{xyT} = 0$. This means that a flat symmetric panel does not acquire curvature in the process of cooling. Naturally, the in-plane dimensions of the panel become different from those that the panel had before cooling. The corresponding thermal strains $\varepsilon^0_{xT}, \varepsilon^0_{yT}$ and γ^0_{xyT} can be found from the first three equations of Eqs. (7.23) in which $N_x = N_y = N_{xy} = 0$, but N^T_{11}, N^T_{22} and N^T_{12} are not zero.

However, for unsymmetric laminates, in general, $M^T_{mn} \neq 0$, and these laminates experience bending and warping in the process of cooling. To demonstrate this, consider two antisymmetric laminates studied in Section 5.7.

The first is a two-layered orthotropic cross-ply laminate shown in Fig. 5.13. Using stiffness coefficients calculated in Section 5.7, taking into account that for a cross-ply laminate $N^T_{12} = M^T_{12} = 0$, and applying Eqs. (7.23) for N_{xy} and M_{xy} we get $\gamma^0_{xyT} = 0$ and $\kappa_{xyT} = 0$. Thus, cooling of the cross-ply laminated panel does not induce its in-plane shear and twisting. The other four of Eqs. (7.23) acquire the form:

$$\begin{aligned}
&a_{xx}\varepsilon^0_{xT} + a_{xy}\varepsilon^0_{yT} - c_{xx}\kappa_{xT} = n_x,\\
&a_{yx}\varepsilon^0_{xT} + a_{yy}\varepsilon^0_{yT} + c_{yy}\kappa_{yT} = n_y,\\
&-c_{xx}\varepsilon^0_{xT} + b_{xx}\kappa_{xT} + b_{xy}\kappa_{yT} = m_x,\\
&c_{yy}\varepsilon^0_{yT} + b_{xy}\kappa_{xT} + b_{yy}\kappa_{yT} = m_y\ ,
\end{aligned} \tag{7.74}$$

where

$$\begin{aligned}
&a_{xx} = a_{yy} = h\bar{E}, \quad a_{xy} = a_{yx} = \bar{E}_1 \nu_{12} h,\\
&c_{xx} = c_{yy} = \frac{h^2}{8}(\bar{E}_1 - \bar{E}_2), \quad b_{xx} = b_{yy} = \frac{h^3 \bar{E}}{12},\\
&b_{xy} = b_{yx} = \frac{h^3}{12}\bar{E}_1 \nu_{12}, \quad \bar{E} = \frac{1}{2}(\bar{E}_1 + \bar{E}_2),\\
&n_x = n_y = \frac{h}{2}[\bar{E}_1(\alpha_1 + \nu_{12}\alpha_2) + \bar{E}_2(\alpha_2 + \nu_{21}\alpha_1)]\Delta T,\\
&-m_x = m_y = \frac{h^2}{8}[\bar{E}_1(\alpha_1 + \nu_{12}\alpha_2) - \bar{E}_2(\alpha_2 + \nu_{21}\alpha_1)]\Delta T\ .
\end{aligned}$$

The solution of Eqs. (7.74) can be written as

$$\begin{aligned}
\varepsilon^0_{xT} &= \frac{n_x}{a_{xx} + a_{xy}} + \frac{c_{xx}}{a^2_{xx} - a^2_{xy}}(a_{xx}\kappa_{xT} + a_{xy}\kappa_{yT}),\\
\varepsilon^0_{yT} &= \frac{n_x}{a_{xx} + a_{xy}} - \frac{c_{xx}}{a^2_{xx} - a^2_{xy}}(a_{xx}\kappa_{yT} + a_{xy}\kappa_{xT})\ ,
\end{aligned} \tag{7.75}$$

$$\kappa_{xT} = \frac{\tilde{m}_x}{e_{xx} - e_{xy}}, \quad \kappa_{yT} = -\frac{\tilde{m}_x}{e_{xx} - e_{xy}}\ , \tag{7.76}$$

where

$$\tilde{m}_x = m_x + \frac{c_{xx}n_x}{a_{xx}+a_{xy}}, \quad e_{xx} = b_{xx} - \frac{a_{xx}c_{xx}^2}{a_{xx}^2 - a_{xy}^2}, \quad e_{xy} = b_{xy} - \frac{a_{xy}c_{xx}^2}{a_{xx}^2 - a_{xy}^2} \ .$$

As follows from Eqs. (7.75) and (7.76), ε and κ do not depend on x and y.

To find the in-plane displacements we should integrate Eqs. (7.28) which acquire the form

$$\frac{\partial u}{\partial x} = \varepsilon_{x\mathrm{T}}^0, \quad \frac{\partial v}{\partial y} = \varepsilon_{y\mathrm{T}}^0, \quad \frac{\partial u}{\partial y} + \frac{\partial v}{\partial x} = 0 \ .$$

Referring the panel to coordinates x and y shown in Fig. 7.49 and assuming that $u(x=0, y=0) = 0$ and $v(x=0, y=0) = 0$ we get

$$u = \varepsilon_{x\mathrm{T}}^0 x, \quad v = \varepsilon_{y\mathrm{T}}^0 y \ . \tag{7.77}$$

Now consider Eqs. (7.24) in which $V_x = V_y = 0$. Thus, $\gamma_{x\mathrm{T}} = \gamma_{y\mathrm{T}} = 0$, and Eqs. (7.30) yield $\theta_x = -\partial w/\partial x, \theta_y = -\partial w/\partial y$. The plate deflection can be found from Eqs. (7.29) which reduce to

$$\frac{\partial^2 w}{\partial x^2} = -\kappa_{x\mathrm{T}}, \quad \frac{\partial^2 w}{\partial y^2} = -\kappa_{y\mathrm{T}}, \quad \frac{\partial^2 w}{\partial x \partial y} = 0 \ .$$

Assuming that $w(x=0, y=0) = 0, \theta_x(x=0, y=0) = 0, \theta_y(x=0, y=0) = 0$ we can write the result of integration as

$$w = -\tfrac{1}{2}(\kappa_{x\mathrm{T}} x^2 + \kappa_{y\mathrm{T}} y^2) \ . \tag{7.78}$$

To present thus obtained solution in an explicit form, consider, for the sake of brevity, material with zero Poisson's ratios ($\nu_{12} = \nu_{21} = 0$). Then, Eqs. (7.75)–(7.78) yield

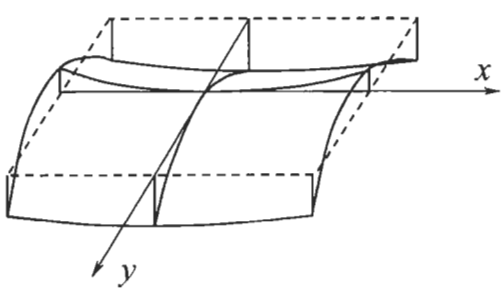

Fig. 7.49. Deformed shape of a cross-ply antisymmetric panel.

$$u = \frac{\Delta T x}{E_1 + E_2}\left[E_1\alpha_1 + E_2\alpha_2 + 6(E_1 - E_2)\frac{E_1E_2(\alpha_2 - \alpha_1)}{E_1^2 + 14E_1E_2 - E_2^2}\right],$$
$$v = \frac{\Delta T y}{E_1 + E_2}\left[E_1\alpha_1 + E_2\alpha_2 + 6(E_1 - E_2)\frac{E_1E_2(\alpha_2 - \alpha_1)}{E_1^2 + 14E_1E_2 - E_2^2}\right],$$
$$w = -\frac{12\Delta T}{h}\frac{E_1E_2(\alpha_2 - \alpha_1)}{E_1^2 + 14E_1E_2 - E_2^2}(x^2 - y^2) \ .$$

The deformed shape of the panel is shown in Fig. 7.49. Note that displacements u and v correspond to the panel reference plane which is the contact plane of 0 and 90 layers (see Fig. 5.13).

Another typical antisymmetric structure is the two-layered angle-ply laminate shown in Fig. 5.14. Using stiffness coefficients of this laminate found in Section 5.7 and Eqs. (7.25) and (7.27), we can write Eqs. (7.23) in the following form:

$$A_{11}\varepsilon^0_{x\mathrm{T}} + A_{12}\varepsilon^0_{y\mathrm{T}} - \frac{h}{4}A_{14}\kappa_{xy\mathrm{T}} = A^{\mathrm{T}}_{11},$$
$$A_{12}\varepsilon^0_{x\mathrm{T}} + A_{22}\varepsilon^0_{y\mathrm{T}} - \frac{h}{4}A_{24}\kappa_{xy\mathrm{T}} = A^{\mathrm{T}}_{22},$$
$$A_{44}\gamma^0_{xy\mathrm{T}} - \frac{h}{4}(A_{14}\kappa_{x\mathrm{T}} + A_{24}\kappa_{y\mathrm{T}}) = 0,$$
$$-A_{14}\gamma^0_{xy\mathrm{T}} + \frac{h}{3}(A_{11}\kappa_{x\mathrm{T}} + A_{12}\kappa_{y\mathrm{T}}) = 0,$$
$$-A_{24}\gamma^0_{xy\mathrm{T}} + \frac{h}{3}(A_{12}\kappa_{x\mathrm{T}} + A_{22}\kappa_{y\mathrm{T}}) = 0,$$
$$A_{14}\varepsilon^0_{x\mathrm{T}} + A_{24}\varepsilon^0_{y\mathrm{T}} - \frac{h}{3}A_{44}\kappa_{xy\mathrm{T}} = A^{\mathrm{T}}_{12} \ ,$$

where

$$A^{\mathrm{T}}_{11} = [\bar{E}_1(\alpha_1 + \nu_{12}\alpha_2)\cos^2\phi + \bar{E}_2(\alpha_2 + \nu_{21}\alpha_1)\sin^2\phi]\Delta T,$$
$$A^{\mathrm{T}}_{22} = [\bar{E}_1(\alpha_1 + \nu_{12}\alpha_2)\sin^2\phi + E_2(\alpha_2 + \nu_{21}\alpha_1)\cos^2\phi]\Delta T,$$
$$A^{\mathrm{T}}_{12} = [\bar{E}_1(\alpha_1 + \nu_{12}\alpha_2) - \bar{E}_2(\alpha_2 + \nu_{21}\alpha_1]\Delta T\sin\phi\cos\phi \ .$$

The solution is

$$\varepsilon^0_{x\mathrm{T}} = \frac{1}{A}\left[A^{\mathrm{T}}_{11}A_{22} - A^{\mathrm{T}}_{22}A_{12} + \frac{h}{4}(A_{14}A_{22} - A_{24}A_{12})\kappa_{xy\mathrm{T}}\right],$$
$$\varepsilon^0_{y\mathrm{T}} = \frac{1}{A}\left[A^{\mathrm{T}}_{22}A_{11} - A^{\mathrm{T}}_{11}A_{12} + \frac{h}{4}(A_{24}A_{11} - A_{14}A_{22})\kappa_{xy\mathrm{T}}\right],$$
$$\gamma^0_{xy\mathrm{T}} = 0, \quad \kappa_{x\mathrm{T}} = 0, \quad \kappa_{y\mathrm{T}} = 0,$$
$$\kappa_{xy\mathrm{T}} = \frac{A_{14}(A^{\mathrm{T}}_{11}A_{22} - A^{\mathrm{T}}_{22}A_{12}) + A_{24}(A^{\mathrm{T}}_{22}A_{11} - A^{\mathrm{T}}_{11}A_{12}) - A^{\mathrm{T}}_{12}}{h\left[\frac{4}{3}A_{44} + \frac{1}{4}(2A_{14}A_{24}A_{12} - A^2_{14}A_{22} - A^2_{24}A_{11})\right]} \ ,$$

where $A = A_{11}A_{22} - A_{12}^2$.

Thus, the panel under study experiences only in-plane deformation and twisting. Displacements u and v can be determined with Eqs. (7.34), while the following equations should be used to find w

$$\frac{\partial^2 w}{\partial x^2} = 0, \quad \frac{\partial^2 w}{\partial y^2} = 0, \quad \frac{\partial^2 w}{\partial x \partial y} = -\kappa_{xyT} \ .$$

The result is

$$w = -\kappa_{xyT} xy \ .$$

The deformed shape of the panel is shown in Fig. 7.50.

Depending on the laminates structures and dimensions there exist the whole class of stable and unstable laminate configurations studied by Hyer (1989).

Deformation and warping of laminates appearing after the manufacturing process is over can occur not only due to cooling of the cured composite but also as a result of material shrinkage due to release of fibers tension after the composite part is removed from the mandrel or chemical setting of the polymeric matrix.

To demonstrate these effects, consider a thin unidirectional layer formed with circumferential plies wound on a metal cylindrical mandrel (see Fig. 7.51) under some tension. Because the stiffness of the mandrel is much higher than that of the layer, we can assume that under cooling from the curing temperature T_c to room temperature T_0 the strains in the principal material coordinates of the layer are governed by the mandrel with which the cured layer is bonded, i.e.

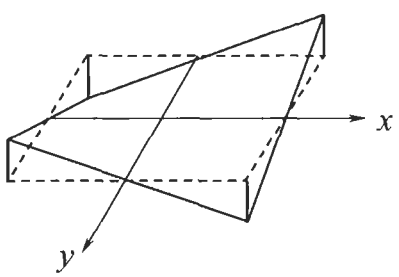

Fig. 7.50. Deformed shape of an angle-ply antisymmetric panel.

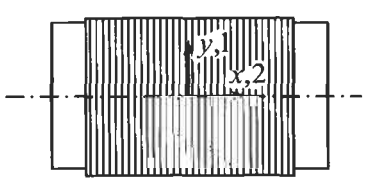

Fig. 7.51. A unidirectional circumferential layer on a cylindrical mandrel.

$$\varepsilon_1^T = \varepsilon_2^T = \alpha_0 \Delta T \ , \tag{7.79}$$

where α_0 is the CTE of the mandrel material and $\Delta T = T_0 - T_c$. On the other hand, if the layer is cooled being preliminary removed from the mandrel, its strains can be calculated as

$$\varepsilon_1 = \alpha_1 \Delta T + \varepsilon_1^0, \quad \varepsilon_2 = \alpha_2 \Delta T + \varepsilon_2^0 \ . \tag{7.80}$$

The first terms in the right-hand sides of these equations are free temperature strains along and across the fibers (see Fig. 7.51), while ε_1^0 and ε_2^0 correspond to the possible layer shrinkage in these directions.

Using Eqs. (7.79) and (7.80) we can determine the strains that appear in the layer when it is removed from the mandrel, i.e.

$$\begin{aligned} \bar{\varepsilon}_1 &= \varepsilon_1 - \varepsilon_1^T = \varepsilon_1^0 + (\alpha_1 - \alpha_0)\Delta T, \\ \bar{\varepsilon}_2 &= \varepsilon_2 - \varepsilon_2^T = \varepsilon_2^0 + (\alpha_2 - \alpha_0)\Delta T \ . \end{aligned} \tag{7.81}$$

These strains can be readily found if we measure the layer diameter and length before and after it is removed from the mandrel. Then, the shrinkage strains can be determined as

$$\begin{aligned} \varepsilon_1^0 &= \bar{\varepsilon}_1 - (\alpha_1 - \alpha_0)\Delta T, \\ \varepsilon_2^0 &= \bar{\varepsilon}_2 - (\alpha_2 - \alpha_0)\Delta T \ . \end{aligned}$$

For a glass–epoxy composite with the following thermo-mechanical properties:

$$\begin{aligned} &E_1 = 37.24 \text{ GPa}, \quad E_2 = 2.37 \text{ GPa}, \quad G_{12} = 1.2 \text{ GPa}, \\ &\nu_{12} = 0.26, \quad \alpha_1 = 3.1 \times 10^{-6} \text{ 1/°C}, \quad \alpha_2 = 25 \times 10^{-6} \text{ 1/°C} \ , \end{aligned}$$

Morozov and Popkova (1987) found $\varepsilon_1^0 = -93.6 \times 10^{-5}$, $\varepsilon_2^0 = -64 \cdot 10^{-5}$. Further experiments performed for different winding tensions and materials of the mandrel have shown that, while strain ε_1^0 strongly depends on these parameters, strain ε_2^0 – practically does not change. This supports the assumption that strain ε_2^0 is caused by the chemical shrinkage of the resin and depends only on its properties.

For a cylinder in which fibers make angle ϕ with the x-axis in Fig. 7.51, the strains induced by the removal of the mandrel can be found from Eqs. (4.70), i.e.

$$\begin{aligned} \bar{\varepsilon}_x &= \bar{\varepsilon}_1 \cos^2 \phi + \bar{\varepsilon}_2 \sin^2 \phi, \\ \bar{\varepsilon}_y &= \bar{\varepsilon}_1 \sin^2 \phi + \bar{\varepsilon}_2 \cos^2 \phi, \\ \bar{\gamma}_{xy} &= (\bar{\varepsilon}_1 - \bar{\varepsilon}_2) \sin 2\phi \ , \end{aligned} \tag{7.82}$$

where $\bar{\varepsilon}_1$ and $\bar{\varepsilon}_2$ are specified by Eqs. (7.81). Dependencies of $\bar{\varepsilon}_x$, $\bar{\varepsilon}_y$, and $\bar{\gamma}_{xy}$ on ϕ plotted with the aid of Eqs. (7.82) are shown in Fig. 7.52 together with experimental

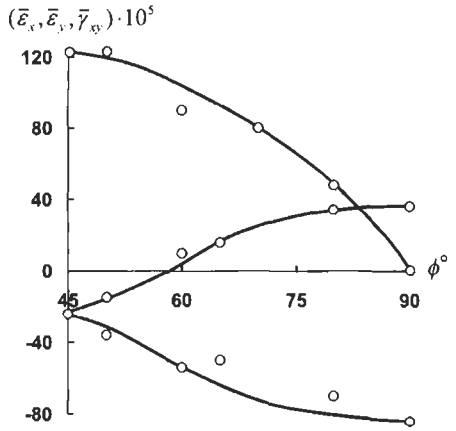

Fig. 7.52. Dependence of residual strains in a glass–epoxy filament wound cylinder on the winding angle ——— calculation, ○ experiment.

data of Morozov and Popkova (1987). As can be seen, the composite cylinder experiences in the general case not only the change in its length ($\bar{\varepsilon}_x$) and diameter ($\bar{\varepsilon}_y$), but also twist ($\bar{\gamma}_{xy}$).

To study the $\pm\phi$ angle-ply layer, we should attract the thermoelasticity constitutive equations, Eqs. (7.23). Neglecting bending and coupling stiffness coefficients we can write for the case under study

$$\begin{aligned} N_x &= B_{11}\bar{\varepsilon}_x + B_{12}\bar{\varepsilon}_y - N_{1T}, \\ N_y &= B_{21}\bar{\varepsilon}_x + B_{22}\bar{\varepsilon}_y - N_{2T} \ . \end{aligned} \tag{7.83}$$

Applying these equations to the angle-ply composite cylinder removed from the mandrel we should put $N_x = 0$, $N_y = 0$ because the cylinder is free of loads and take $\varepsilon_1^T = \bar{\varepsilon}_1$, $\varepsilon_2^T = \bar{\varepsilon}_2$ in Eqs. (7.18), (7.25) and (7.26) that specify N_{1T} and N_{2T}. Then, Eqs. (7.83) yield the following expressions for strains that appear in the angle-ply cylinder after it is removed from the mandrel:

$$\bar{\varepsilon}_x = \frac{1}{B}(N_{1T}B_{22} - N_{2T}B_{12}),$$

$$\bar{\varepsilon}_y = \frac{1}{B}(N_{2T}B_{11} - N_{1T}B_{12}) \ .$$

Here, $B = B_{11}B_{22} - B_{12}^2$

$$\begin{aligned} N_{1T} &= h\left[\bar{E}_1(\bar{\varepsilon}_1 + \nu_{12}\bar{\varepsilon}_2)\cos^2\phi + \bar{E}_2(\bar{\varepsilon}_2 + \nu_{21}\bar{\varepsilon}_1)\sin^2\phi\right], \\ N_{2T} &= h\left[\bar{E}_1(\bar{\varepsilon}_1 + \nu_{12}\bar{\varepsilon}_2)\sin^2\phi + \bar{E}_2(\bar{\varepsilon}_2 + \nu_{21}\bar{\varepsilon}_1)\cos^2\phi\right] \ , \end{aligned}$$

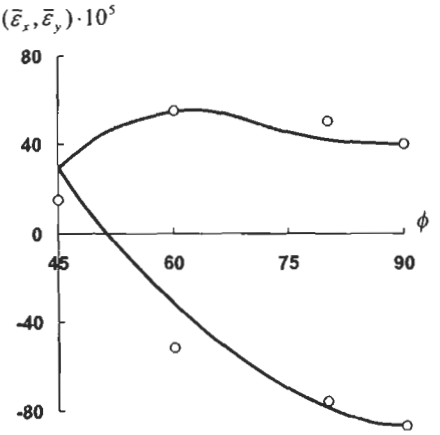

Fig. 7.53. Residual strains in a $\pm\phi$ angle-ply filament wound glass-epoxy cylinder, —— calculation, ○ experiment.

where $\bar{\varepsilon}_1$ and $\bar{\varepsilon}_2$ are given by Eqs. (7.81), $B_{mn} = A_{mn}h$, where A_{mn} are specified by Eqs. (4.72), and h is the cylinder thickness. Results of calculation for experimental cylinder studied by Morozov and Popkova (1987) are presented in Fig. 7.53.

As follows from Figs. 7.52 and 7.53, approach described above and based on constitutive equations for laminates, Eqs. (7.23), with shrinkage characteristics of a unidirectional ply or an elementary layer determined experimentally provides fair agreement of predicted results with experimental data.

7.5. References

Anderson, J.A., Mikelsons, M.Ya., Tamuzh, V.P. and Taraschuch, I.V. (1991). Fatigue failure of laminated carbon-fiber-reinforced plastic. *J. Mech. Composite Mater.* **27** (1), 74–78.

Apinis, R.P., Mikelsons, M.Ya. and Khonichev, V.I. (1991). Fatigue resistance of carbon material in symmetric tension-compression. *Mech. Composite Mater.* **5**, 928–930, (in Russian).

Barnes, J.A., Simms, I.J., Farrow, G.J., Jackson, D., Wostenholm, G. and Yates, B. (1989). Thermal expansion behavior of thermoplastic composite materials. In *Proc. Am. Soc. for Composite Mater.*, Fourth Tech. Conf., Blacksburg, Virginia. Technomic Publ. pp. 717–725.

Ha, S.K. and Springer, G.S. (1987). Mechanical properties of graphite epoxy composites at elevated temperatures. In *Proc. 6th Int. Conf. on Composite Materials (ICCM-6)*, July 1987, Vol. 4, (F.L. Matthews et al. eds.), Elsevier Applied Science, London, pp. 422–430.

Hamilton, J.G. and Patterson, J.M. (1993). Design and analysis of near-zero *CTE* laminates and application to spacecraft. In *Proc. 9th Int. Conf. on Composite Materials (ICCM/9)*, Madrid, 12–16 July, Vol. 6, Composite Properties and Applications, Univ. of Zaragoza, Woodhead Publ. Ltd., pp. 108–119.

Hyer, M.W. (1989). *Mechanics of Unsymmetric Laminates. Handbook of Composites*, Vol. 2, Structure and Design. (C.T. Herakovich and Yu.M. Tarnopol'skii eds.) Elsevier Applied Science, pp. 86–114.

Limonov, V.A. and Anderson, J.A. (1991). Effect of stress ratio on the strength of organic plastics. *J. Mech. Composite Mater.* **27** (3), 276–283.

Milyutin, G.I., Bulmanis, V.N., Grakova, T.S., Popov, N.S. and Zakrzhevskii, A.M. (1989). Study and prediction of the strength characteristics of a wound epoxy organic-fiber plastic under different environmental effects. *J. Mech. Composite Mater.* **25** (2), 183–189.

Morozov, E.V. and Popkova, L.K. (1987). Combined theoretical and experimental method of determining residual stresses in wound composite shells. *J. Mech. Composite Mater.* **23** (6), 802–807.

Murakami, S., Kanagawa, Y., Ishida, T. and Tsushima, E. (1991). Inelastic deformation and fatigue damage of composite under multiaxial loading. In Inelastic Defromation of Composite Materials (G.J. Dvorak ed.), Springer Verlag, New York, pp. 675–694.

Ni, R.G. and Adams, R.D. (1984). The damping and dynamic moduli of symmetric laminated composite beams – theoretical and experimental results. *J. Composite Mater.* **18** (2), 104–121.

Perov, Yu.Yu. and Kruzhkova, E. Yu. (1991). Influence of moisture on mechanical properties of carbon-reinforced plastics with various porosities. *J. Mech. Composite Mater.* **27** (2), 144–151.

Rabotnov, Yu. N. (1980). *Elements of Hereditary Solid Mechanics*, Mir Publishers, Moscow.

Rach, V.A. and Ivanovskii, V.S. (1986). On the effect of fiber length variation in filament wound structures. *Mech. Composite Mater.* 67–72 (in Russian).

Rogers, E.F., Phillips, L.M., Kingston-Lee, D.M. et al. (1997). The thermal expansion of carbon fiber-reinforced plastics. *J. Mater. Sci.* **1** (12), 718–734.

Schapery, R.A. (1974). Viscoelastic behavior and analysis of composite materials. In Composite Materials (L.J. Broutman and R.H. Krock eds.), Vol. 2 Mechanics of Composite Materials (G.P. Sendeckyj ed.), Academic Press, Inc., New York, pp. 85–168.

Schulte, K., Reese, E. and Chou, T.-W. (1987). Fatigue behavior and damage development in woven fabric and hybrid fabric composites. *Proc. 6th Int. Conf. on Composite Materials and 2nd European Conf. on Composite Materials (ICCM and ECCM)*, Vol. 4 (F.L. Matthews, N.C.R. Buskel, J.M. Hodgkinson and J. Morton eds.), Elsevier Science Ltd, London, pp. 89–99.

Shen, S.H. and Springer, G.S. (1976). Moisture absorption and desorption of composite materials. *J. Composite Mater.* **10**, 2–20.

Skudra, A.M., Bulavs, F.Ya., Gurvich, M.R. and Kruklinsh, A.A. (1989). *Elements of Structural Mechanics of Composite Truss Systems.* Riga, Zinatne (in Russian).

Soutis, C. and Turkmen, D. (1993). High-temperature effects on the compressive strength of glass fiber-reinforced composites. In *Proc. 9th Int. Conf. on Composite Materials (ICCM/9)*, Madrid, 12–16 July *Vol. 6, Composite Properties and Applications*, University of Zaragoza, Woodhead Publ. Ltd., pp. 581 588.

Strife, J.R. and Prevo, K.M. (1979). The thermal expansion behavior of unidirectional kevlar/epoxy composites. *J. Composite Mater.* **13**, 264–276.

Sukhanov, A.V., Lapotkin, V.A., Artemchuk, V.Ya. and Sobol', L.A. (1990). Thermal deformation of composites for dimensionally stable structures, *J. Mech. Composite Mater.* **26** (4), 432–436.

Tamuzh, V.P. and Protasov, V.D. (Editors) (1986). *Fracture of Composite Structures.* Riga, Zinatne (in Russian).

Tarnopol'skii, Yu.M. and Roze, A.V. (1969). *Specific Features of Analysis for Structural Elements of Reinforced Plastics.* Riga, Zinatne (in Russian).

Vasiliev, V.V. and Sibiryakov, A.V. (1985). Propagation of elastic waves in a laminated strip. *Mech. Solids* **1**, 104–109.

Verpoest, I., Li, L. and Doxsee, L. (1989) A combined micro- and macromechanical study of the impact behavior of carbon and glass fiber epoxy composites. In *Proc. 7th Int. Conf. on Composite Materials (ICCM-7)*, November 1989, Guangzhou, China, Vol. 2 (W. Yunshu, G. Zhenlong and W. Rrenjie eds.), Pergamon Press, Oxford, pp. 316–321.

Zinoviev, P.A. and Ermakov, Yu. N. (1994). *Energy Dissipation in Composite Materials*, Technomic Publ.

Chapter 8

OPTIMAL COMPOSITE STRUCTURES

Advanced composite materials are characterized with high specific strength and stiffness and, in combination with automatic manufacturing processes, make it possible to fabricate composite structures with high level of weight and cost efficiency. The substitution of metal alloys by composite materials, in general, reduces the structure mass by 20–30%. However, in some special cases the number of which progressively increases, the combination of material directional properties with design conception utilizing these properties being supported by the possibilities of modern composite technology gives a qualitative improvement of the structure performance. Such efficiency is demonstrated by composite structures of uniform strength in which the load is taken by uniformly stressed fibers.

To introduce composite structures of uniform strength, consider a laminated panel shown in Fig. 8.1 and loaded by in-plane forces N_x, N_y, and N_{xy} uniformly distributed along the panel edges. Let the laminate consist of k unidirectional composite layers characterized with thicknesses h_i and fiber orientation angles ϕ_i $(i = 1, 2, 3, \ldots, k)$. For the plane stress state, the stacking sequence of the layers is not important.

8.1. Optimal fibrous structures

To derive the optimality criterion specifying the best structure of the panel in Fig. 8.1, we first use the simplest monotropic model of the unidirectional composite (see Section 3.3) assuming that forces N_x, N_y and N_{xy} are taken by the fibers only. For the problem of design, this is a reasonable model because transverse and shear strength of a unidirectional composite ply (stresses $\bar{\sigma}_2$ and $\bar{\tau}_{12}$) are much lower than the ply strength in the longitudinal direction (stress $\bar{\sigma}_1$). Using Eqs. (4.68) in which we put $\sigma_2 = 0$ and $\tau_{12} = 0$ we can write the following equilibrium equations linking the acting forces with stresses $\sigma_1^{(i)}$ in the direction of the fibers of the ith layer:

$$N_x = \sum_{i=1}^{k} \sigma_x^{(i)} h_i = \sum_{i=1}^{k} \sigma_1^{(i)} h_i \cos^2 \phi_i,$$

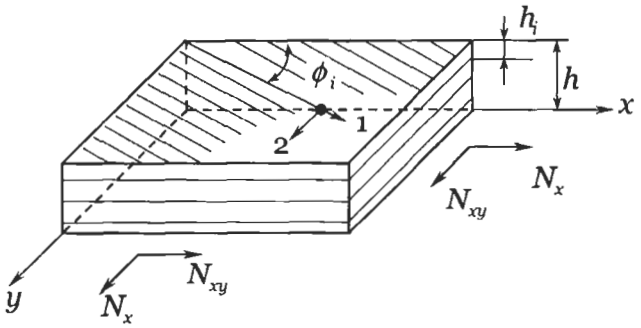

Fig. 8.1. A laminated plate in a plane state of stress.

$$N_y = \sum_{i=1}^{k} \sigma_y^{(i)} h_i = \sum_{i=1}^{k} \sigma_1^{(i)} h_i \sin^2 \phi_i,$$
$$N_{xy} = \sum_{i=1}^{k} \tau_{xy}^{(i)} h_i = \sum_{i=1}^{k} \sigma_1^{(i)} h_i \sin \phi_i \cos \phi_i \ . \tag{8.1}$$

Strain $\varepsilon_1^{(i)}$ in the fiber direction of the ith layer can be expressed in terms of strains in coordinates x, y with the aid of the first equation of Eqs. (4.69). Using constitutive equations for the monotropic model of the ply, Eqs. (3.61), we arrive at

$$\sigma_1^{(i)} = E_1 \varepsilon_1^{(i)} = E_1 (\varepsilon_x \cos^2 \phi_i + \varepsilon_y \sin^2 \phi_i + \gamma_{xy} \sin \phi_i \cos \phi_i) \ . \tag{8.2}$$

It is assumed that the layers are made of one and the same material.

Consider the design problem and assume that the best structure of the laminate is the one providing the minimum total thickness

$$h = \sum_{i=1}^{k} h_i \tag{8.3}$$

for the given combination of loads. Thus, we should minimize the laminate thickness in Eq. (8.3) under constraints imposed by Eqs. (8.1) and (8.2). To solve this problem we can use the method of Lagrange multipliers, according to which we should introduce multipliers λ and minimize the following augmented function:

$$L = \sum_{i=1}^{k} h_i + \lambda_x \left(N_x - \sum_{i=1}^{k} \sigma_1^{(i)} h_i \cos^2 \phi_i \right) + \lambda_y \left(N_y - \sum_{i=1}^{k} \sigma_1^{(i)} h_i \sin^2 \phi_i \right)$$
$$+ \lambda_{xy} \left(N_{xy} - \sum_{i=1}^{k} \sigma_1^{(i)} h_i \sin \phi_i \cos \phi_i \right)$$
$$+ \sum_{i=1}^{k} \lambda_i [\sigma_i - E_1 (\varepsilon_x \cos^2 \phi_i + \varepsilon_y \sin^2 \phi_i + \gamma_{xy} \sin \phi_i \cos \phi_i)]$$

with respect to design variables h_i, ϕ_i and multipliers λ, i.e.

$$\frac{\partial L}{\partial h_i} = 0, \quad \frac{\partial L}{\partial \phi_i} = 0, \quad \frac{\partial L}{\partial \lambda_x} = \frac{\partial L}{\partial \lambda_y} = \frac{\partial L}{\partial \lambda_{xy}} = \frac{\partial L}{\partial \lambda_i} = 0 \ . \tag{8.4}$$

Minimization with respect to λ gives, obviously, constraints in Eqs. (8.1) and (8.2), while the first two of Eqs. (8.4) yield

$$\sigma_1^{(i)}(\lambda_x \cos^2 \phi_i + \lambda_y \sin^2 \phi_i + \lambda_{xy} \sin \phi_i \cos \phi_i) = 1 \ , \tag{8.5}$$

$$h_i \sigma_1^{(i)}[(\lambda_y - \lambda_x) \sin 2\phi_i + \lambda_{xy} \cos 2\phi_i] = E_1 \lambda_i[(\varepsilon_y - \varepsilon_x) \sin 2\phi_i + \gamma_{xy} \cos 2\phi_i] \ . \tag{8.6}$$

The solution of Eq. (8.6) is

$$\lambda_x = E_1 \varepsilon_x \frac{\lambda_i}{h_i \sigma_1^{(i)}}, \quad \lambda_y = E_1 \varepsilon_y \frac{\lambda_i}{h_i \sigma_1^{(i)}}, \quad \lambda_{xy} = E_1 \gamma_{xy} \frac{\lambda_i}{h_i \sigma_1^{(i)}} \ .$$

These equations allow us to conclude that

$$\frac{\lambda_i}{h_i \sigma_1^{(i)}} = \frac{\lambda_x}{E_1 \varepsilon_x} = \frac{\lambda_y}{E_1 \varepsilon_y} = \frac{\lambda_{xy}}{E_1 \gamma_{xy}} = \frac{1}{c^2} \ ,$$

where c is a constant. Substituting λ_x, λ_y, and λ_{xy} from these equations into Eq. (8.5) and taking into account Eq. (8.2) we get

$$\left(\sigma_1^{(i)}\right)^2 = c^2 \ . \tag{8.7}$$

This equation has two solutions: $\sigma_1^{(i)} = \pm c$.

Consider the first case, i.e., $\sigma_1^{(i)} = c$. Adding up the first two equations of Eqs. (8.1) and taking into account Eq. (8.3) we have

$$h = \frac{1}{c}(N_x + N_y) \ .$$

Obviously, the minimum value of h corresponds to $c = \bar{\sigma}_1$, where $\bar{\sigma}_1$ is the ultimate stress. Thus, the total thickness of the optimal plate is

$$h = \frac{1}{\bar{\sigma}_1}(N_x + N_y) \ . \tag{8.8}$$

Taking now $\sigma_1^{(i)} = \bar{\sigma}_1$ in Eqs. (8.1) and eliminating $\bar{\sigma}_1$ with the aid of Eq. (8.8) we arrive at the following two optimality conditions in terms of design variables and acting forces:

$$\sum_{i=1}^{k} h_i(N_x \sin^2 \phi_i - N_y \cos^2 \phi_i) = 0 \ , \tag{8.9}$$

$$\sum_{i=1}^{k} h_i[(N_x + N_y) \sin \phi_i \cos \phi_i - N_{xy}] = 0 \ . \tag{8.10}$$

Thus, $2k$ design variables, i.e., k values of h_i and k values of ϕ_i, should satisfy three equations, Eqs. (8.8)–(8.10). All possible optimal laminates have the same total thickness in Eq. (8.8). As follows from Eq. (8.2), condition $\sigma_1^{(i)} = \bar{\sigma}_1$ is valid, in the general case, if $\varepsilon_x = \varepsilon_y = \varepsilon$ and $\gamma_{xy} = 0$. Applying Eqs. (4.69) to determine the strains in the principal material coordinates of the layers we arrive at the following result $\varepsilon_1 = \varepsilon_2 = \varepsilon$ and $\gamma_{12} = 0$. This means that the optimal laminate is the structure of uniform stress and strain in which the fibers of each layer coincide with the directions of principal strains. An important feature of the optimal laminate follows from the last equation of Eqs. (4.150) which yields $\phi_i' = \phi_i$. Thus, the optimal angles do not change under loading.

Introducing new variables

$$\bar{h}_i = \frac{h_i}{h}, \quad n_y = \frac{N_y}{N_x}, \quad n_{xy} = \frac{N_{xy}}{N_x}, \quad \lambda = \frac{1}{1 + n_y}$$

and taking into account that

$$\sum_{i=1}^{k} \bar{h}_i = 1 \tag{8.11}$$

we can transform Eqs. (8.8)–(8.10) that specify the structural parameters of the optimal laminate to the following final forms:

$$h = \frac{N_x}{\lambda \bar{\sigma}_1} \ , \tag{8.12}$$

$$\sum_{i=1}^{k} \bar{h}_i \cos^2 \phi_i = \lambda, \quad \sum_{i=1}^{k} \bar{h}_i \sin^2 \phi_i = \lambda n_y \ , \tag{8.13}$$

$$\sum_{i=1}^{k} \bar{h}_i \sin \phi_i \cos \phi_i = \lambda n_{xy} \ . \tag{8.14}$$

For uniaxial tension in the x-direction, we have $n_y = n_{xy} = 0, \lambda = 1$. Then, Eqs. (8.13) yield $\phi_i = 0$ $(i = 1, 2, 3, \ldots, k)$ and Eq. (8.12) gives the obvious result $h = N_x/\bar{\sigma}$.

To describe tension in two orthogonal directions x and y, we should put $n_{xy} = 0$. As follows from Eq. (8.14), the laminate structure in this case should be symmetric,

i.e., each layer with angle $+\phi_i$ should be accompanied with the layer of the same thickness but with angle $-\phi_i$.

Consider, for example, the uniform tension such that $N_x = N_y = N$, $N_{xy} = 0$, $n_y = 1$, $n_{xy} = 0$, $\lambda = 0.5$. For this case, Eqs. (8.12) and (8.13) yield

$$h = \frac{2N}{\bar{\sigma}_1}, \quad \sum_{i=1}^{k} \bar{h}_i \cos 2\phi_i = 0 \ . \tag{8.15}$$

The natural structure for this case corresponds to the cross-ply laminate for which $k = 2$, $\phi_1 = 0°$, $\phi_2 = 90°$ (Fig. 8.2(a)). Then, the second equation of Eqs. (8.15) gives the evident result $\bar{h}_1 = \bar{h}_2$.

Consider the first equation from which it follows that the total thickness of the optimal laminate is twice as high as the thickness of the metal plate under the same loading conditions. This result is quite natural because, in contrast to isotropic materials, the monotropic layer can work only in one direction – along the fibers. So, we need to have the 0°-layer to take $N_x = N$ and the same, but 90°-layer to take $N_y = N$. From this we can conclude that the directional character of a composite ply stiffness and strength is actually the material shortcoming rather than its advantage. Real advantages of composite materials are associated with their high specific strength provided by thin fibers (see Section 3.2.1), and if we had isotropic materials with such specific strength, no composites would be developed and implemented.

Return to the second equation of Eqs. (8.15) which shows that in addition to a cross-ply laminate there exists an infinite number of optimal structures. For example, this equation is satisfied for a symmetric ±45°angle-ply laminate (Fig. 8.2b). Moreover, all the quasi-isotropic laminates discussed in Section 5.5 and listed in Table 5.1 satisfy the optimality conditions for uniform tension.

A loading case, important for applications, corresponds to a cylindrical pressure vessel considered in Section 6.3. Winding of such a vessel is shown in Fig. 7.43. For this type of loading

$$N_x = \tfrac{1}{2} pR, \quad N_y = pR, \quad N_{xy} = 0 \ ,$$

where N_x and N_y are the circumferential and the axial stress resultants, respectively, p the internal pressure and R is the cylinder radius. Thus, we have $n_y = 2$ and

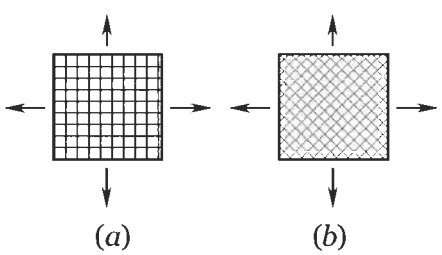

Fig. 8.2. Cross-ply (a) and ±45° angle-ply (b) optimal structures for uniform tension.

$\lambda = 1/3$. Because $N_{xy} = 0$, the structure of the laminate is symmetric with respect to the cylinder meridian, and Eqs. (8.12)–(8.14) can be reduced to

$$h = \frac{3pR}{2\bar{\sigma}_1} , \tag{8.16}$$

$$\sum_{i=1}^{k} \bar{h}_i(3\cos^2 \phi_i - 1) = 0 . \tag{8.17}$$

Comparing Eq. (8.16) with the corresponding expression for the thickness of the metal pressure vessel which is $h_m = pR/\bar{\sigma}$ we can see that the thickness of an optimal composite vessel is 1.5 times higher than h_m. Nevertheless, because of higher strength and lower density, composite pressure vessels are significantly lighter than metal ones. To show this, consider pressure vessels with radius $R = 100$ mm made of different materials and designed for the burst pressure $p = 20$ MPa. The results are listed in Table 8.1. As can be seen, the thickness of the glass–epoxy vessel is the same as that of the thickness of the steel vessel, because the factor 1.5 in Eq. (8.16) is compensated by the composite strength which is 1.5 times higher than the strength of steel. However, the density of a glass–epoxy composite is much lower than the density of steel, and as a result, the mass of the unit surface area of the composite vessel makes only 27% of the corresponding characteristic for a steel vessel. The most promising for pressure vessels are aramid composites having the highest tensile specific strength (see Table 8.1).

Consider Eq. (8.17) which shows that there can exist an infinite number of optimal laminates with one and the same thickness specified by Eq. (8.16).

The simplest is the cross-ply laminate having $k = 2$, $\phi_1 = 0°$, $h_1 = h_0$, and $\phi_2 = 90°$, $h_2 = h_{90}$. For this structure, Eq. (8.17) yields $h_{90} = 2h_0$. This result seems obvious because $N_y/N_x = 2$. For symmetric $\pm\phi$ angle-ply laminate, we should take $k = 2$, $h_1 = h_2 = h_\phi/2$, $\phi_1 = +\phi$, $\phi_2 = -\phi$. Then

$$\cos^2 \phi = \tfrac{1}{3}, \quad \phi = \phi_0 = 54°44' .$$

Table 8.1
Parameters of metal and composite pressure vessels.

Parameter	Material					
	Steel	Aluminum	Titanium	Glass–epoxy	Carbon–epoxy	Aramid–epoxy
Strength, $\bar{\sigma}, \bar{\sigma}_1$ (MPa)	1200	500	900	1800	2000	2500
Density, ρ (g/cm^3)	7.85	2.7	4.5	2.1	1.55	1.32
Thickness of the vessel, h_m, h (mm)	1.67	4.0	2.22	1.67	1.5	1.2
Mass of the unit surface area, ρh (kg/m^2)	13.11	10.8	10.0	3.51	2.32	1.58

As a rule, helical plies are combined with circumferential plies as in Fig. 7.43. For this case, $k = 3$, $h_1 = h_2 = h_\phi/2$, $\phi_1 = -\phi_2 = \phi$, $h_3 = h_{90}$, $\phi_3 = 90°$, and Eq. (8.17) gives

$$\frac{h_{90}}{h_\phi} = 3\cos^2\phi - 1 \ . \tag{8.18}$$

Because the thickness cannot be negative, this equation is valid for $0 \leqslant \phi \leqslant \phi_0$. For $\phi_0 \leqslant \phi \leqslant 90°$, the helical layer should be combined with the axial one, i.e., we should put $k = 3$, $h_1 = h_2 = h_\phi/2$, $\phi_1 = -\phi_2 = \phi$ and $h_3 = h_0$, $\phi_3 = 0°$. Then

$$\frac{h_0}{h_\phi} = \frac{1}{2}(1 - 3\cos^2\phi) \ . \tag{8.19}$$

Dependencies corresponding to Eqs. (8.18) and (8.19) are presented in Fig. 8.3. As an example, consider a filament wound pressure vessel whose parameters are listed in Table 6.1. Cylindrical part of the vessel shown in Figs. 4.14 and 6.23 consists of a $\pm 36°$ angle-ply helical layer and a circumferential layer whose thickness $h_1 = h_\phi$ and $h_2 = h_{90}$ are presented in Table 6.1. The ratio h_{90}/h_ϕ for two experimental vessels is 0.97 and 1.01, while Eq. (8.18) gives for this case $h_{90}/h_\phi = 0.96$ which shows that both vessels are close to optimal structures. Laminates reinforced with uniformly stressed fibers can exist under some restrictions imposed on the acting forces N_x, N_y, and N_{xy}. Such restrictions follow from Eqs. (8.13) and (8.14) under the conditions that $\bar{h}_i \geqslant 0$, $0 \leqslant \sin^2\phi_i, \cos^2\phi_i \leqslant 1$ and have the form

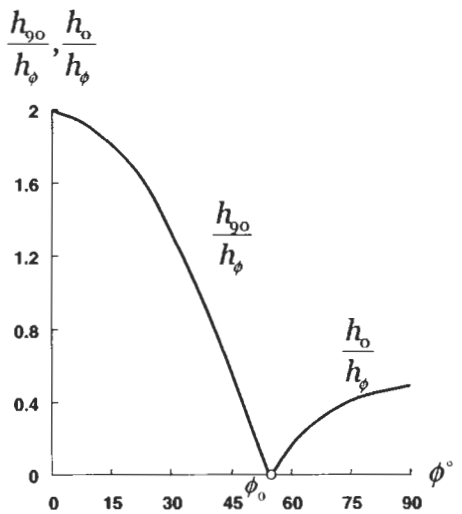

Fig. 8.3. Optimal thickness ratios for a cylindrical pressure vessel consisting of $\pm\phi$ helical plies combined with circumferential (90°) or axial (0°) plies.

$$0 \leqslant \lambda \leqslant 1, \quad -\tfrac{1}{2} \leqslant \lambda n_{xy} \leqslant \tfrac{1}{2} \ .$$

Particularly, Eqs. (8.13) and (8.14) do not describe the case of pure shear for which only shear stress resultant, N_{xy}, is not zero. This is quite natural because strength condition $\sigma_1^{(i)} = \bar{\sigma}_1$ under which Eqs. (8.12)–(8.14) were derived is not valid for shear inducing tension and compression in angle-ply layers.

To study in-plane shear of the laminate, we should use both solutions of Eq. (8.7) and assume that for some layers, e.g., with $i = 1, 2, 3, \ldots, n-1$, $\sigma_1^{(i)} = \bar{\sigma}_1$ while for the other layers ($i = n, n+1, n+2, \ldots, k$), $\sigma_1^{(i)} = -\bar{\sigma}_1$. Then, Eqs. (8.1) can be reduced to the following forms:

$$N_x + N_y = \bar{\sigma}_1 (h^+ - h^-) \ , \tag{8.20}$$

$$N_x - N_y = \bar{\sigma}_1 \left(\sum_{i=1}^{n-1} h_i^+ \cos 2\phi_i - \sum_{i=n}^{k} h_i^- \cos 2\phi_i \right) \ , \tag{8.21}$$

$$N_{xy} = \frac{1}{2} \sigma_1 \left(\sum_{i=1}^{n-1} h_i^+ \sin 2\phi_i - \sum_{i=n}^{k} h_i^- \sin 2\phi_i \right) \ , \tag{8.22}$$

where

$$h^+ = \sum_{i=1}^{n-1} h_i^+, \quad h^- = \sum_{i=n}^{k} h_i^-$$

are the total thicknesses of the plies with tensile and compressive stresses in the fibers, respectively.

For the case of pure shear ($N_x = N_y = 0$), Eqs. (8.20) and (8.21) yield $h^+ = h^-$ and $\phi_i = \pm 45°$. Then, assuming that $\phi_i = +45°$ for the layers with $h_i = h_i^+$, while $\phi_i = -45°$ for the layers with $h_i = h_i^-$ we get from Eq. (8.22)

$$h = h^+ + h^- = \frac{2N_{xy}}{\bar{\sigma}_1} \ .$$

The optimal laminate, as follows from the foregoing derivation, corresponds to $\pm 45°$ angle-ply structure shown in Fig. 8.2b.

8.2. Composite laminates of uniform strength

Consider again the panel in Fig. 8.1 and assume that unidirectional plies or fabric layers, that form the panel are orthotropic, i.e., in contrast to the previous section, we do not neglect now stresses σ_2 and τ_{12} in comparison with σ_1 (see Fig. 3.29). Then, constitutive equations for the panel in plane stress state are specified by the first three equations in Eqs. (5.35), i.e.

$$N_x = B_{11}\varepsilon_x + B_{12}\varepsilon_y + B_{14}\gamma_{xy},$$
$$N_y = B_{21}\varepsilon_x + B_{22}\varepsilon_y + B_{24}\gamma_{xy}, \tag{8.23}$$
$$N_{xy} = B_{41}\varepsilon_x + B_{42}\varepsilon_y + B_{44}\gamma_{xy} \ ,$$

where in accordance with Eqs. (4.72) and (5.28), (5.42)

$$B_{11} = \sum_{i=1}^{k} h_i\left(\bar{E}_1^{(i)}\cos^4\phi_i + \bar{E}_2^{(i)}\sin^4\phi_i + 2E_{12}^{(i)}\sin^2\phi_i\cos^2\phi_i\right),$$

$$B_{12} = B_{21} = \sum_{i=1}^{k} h_i\left[\bar{E}_1^{(i)}\nu_{12}^{(i)} + \left(\bar{E}_1^{(i)} + \bar{E}_2^{(i)} - 2E_{12}^{(i)}\right)\sin^2\phi_i\cos^2\phi_i\right],$$

$$B_{22} = \sum_{i=1}^{k} h_i\left(\bar{E}_1^{(i)}\sin^4\phi_i + \bar{E}_2^{(i)}\cos^4\phi_i + 2E_{12}^{(i)}\sin^2\phi_i\cos^2\phi_i\right),$$

$$B_{14} = B_{41} = \sum_{i=1}^{k} h_i\left(\bar{E}_1^{(i)}\cos^2\phi_i - \bar{E}_2^{(i)}\sin^2\phi_i - E_{12}^{(i)}\cos 2\phi_i\right)\sin\phi_i\cos\phi_i, \tag{8.24}$$

$$B_{24} = B_{42} = \sum_{i=1}^{k} h_i\left(\bar{E}_1^{(i)}\sin^2\phi_i - \bar{E}_2^{(i)}\cos^2\phi_i + E_{12}^{(i)}\cos 2\phi_i\right)\sin\phi_i\cos\phi_i,$$

$$B_{44} = \sum_{i=1}^{k} h_i\left[\left(\bar{E}_1^{(i)} + \bar{E}_2^{(i)} - 2\bar{E}_1^{(i)}\nu_{12}^{(i)}\right)\sin^2\phi_i\cos^2\phi_i + G_{12}^{(i)}\cos^2 2\phi_i\right] \ .$$

and

$$\bar{E}_{1,2}^{(i)} = \frac{E_{1,2}^{(i)}}{1 - \nu_{12}^{(i)}\nu_{21}^{(i)}}, \quad E_{12}^{(i)} = \bar{E}_1^{(i)}\nu_{12}^{(i)} + 2G_{12}^{(i)} \ .$$

In the general case, the panel can consist of layers made of different composite materials. Using the optimality criterion developed in the previous section for the fibrous structures we assume that the fibers in each layer are directed along the lines of principal strains, or principal stresses because $\tau_{12}^{(i)} = G_{12}\gamma_{12}^{(i)}$ for an orthotropic layer and condition $\gamma_{12}^{(i)} = 0$ is equivalent to condition $\tau_{12}^{(i)} = 0$ (see section 2.4). Using the third equation in Eqs. (4.69) we can write these conditions as

$$2(\varepsilon_y - \varepsilon_x)\sin\phi_i\cos\phi_i + \gamma_{xy}\cos 2\phi_i = 0 \ . \tag{8.25}$$

This equation can be satisfied for all the layers if we take

$$\varepsilon_x = \varepsilon_y - \varepsilon, \quad \gamma_{xy} = 0 \ . \tag{8.26}$$

Then, Eqs. (8.23) yield

$$N_x = (B_{11} + B_{12})\varepsilon, \quad N_y = (B_{21} + B_{22})\varepsilon, \quad N_{xy} = (B_{41} + B_{42})\varepsilon \ .$$

These equations allow us to find strain, i.e.

$$\varepsilon = \frac{N_x + N_y}{B_{11} + 2B_{12} + B_{22}} \quad . \tag{8.27}$$

and to write two relationships specifying the optimal structural parameters of the laminate

$$\begin{aligned}
&(B_{11} + B_{12})N_y - (B_{21} + B_{22})N_x = 0, \\
&(B_{41} + B_{42})(N_x + N_y) - (B_{11} + 2B_{12} + B_{22})N_{xy} = 0 \quad .
\end{aligned}$$

Substitution of B_{mn} from Eqs. (8.24) results in the following explicit form of these conditions:

$$\begin{aligned}
&\sum_{i=1}^{k} h_i \Big[\bar{E}_1^{(i)} \Big(1 + \nu_{12}^{(i)} \Big) (N_x \sin^2 \phi_i - N_y \cos^2 \phi_i) \\
&\qquad + \bar{E}_2^{(i)} \Big(1 + \nu_{21}^{(i)} \Big) (N_x \cos^2 \phi_i - N_y \sin^2 \phi_i) \Big] = 0, \\
&\sum_{i=1}^{k} h_i \Big\{ (N_x + N_y) \Big(\bar{E}_1^{(i)} - \bar{E}_2^{(i)} \Big) \sin \phi_i \cos \phi_i \\
&\qquad - N_{xy} \Big[\bar{E}_1^{(i)} \Big(1 + \nu_{12}^{(i)} \Big) + \bar{E}_2^{(i)} \Big(1 + \nu_{21}^{(i)} \Big) \Big] \Big\} = 0 \quad .
\end{aligned} \tag{8.28}$$

To determine the stresses that act in the optimal laminate, we use Eqs. (4.69) and (8.26) that specify the strains in the principal material coordinates of the layers as $\varepsilon_1 = \varepsilon_2 = \varepsilon$, $\gamma_{12} = 0$. Applying constitutive equations, Eqs. (4.56), substituting ε from Eq. (8.27) and writing the result in the explicit form with the aid of Eqs. (8.24) we arrive at:

$$\begin{aligned}
\sigma_1^{(i)} &= \frac{\bar{E}_1^{(i)}}{S_i} \Big(1 + \nu_{12}^{(i)} \Big) (N_x + N_y), \\
\sigma_2^{(i)} &= \frac{\bar{E}_2^{(i)}}{S_i} \Big(1 + \nu_{21}^{(i)} \Big) (N_x + N_y), \\
\tau_{12}^{(i)} &= 0 \quad ,
\end{aligned} \tag{8.29}$$

where

$$S_i = \sum_{i=1}^{k} h_i \Big[\bar{E}_1^{(i)} \Big(1 + \nu_{12}^{(i)} \Big) + \bar{E}_2^{(i)} \Big(1 + \nu_{21}^{(i)} \Big) \Big]$$

is the laminate stiffness coefficient.

If all the layers are made from one and the same material, Eqs. (8.28) and (8.29) are simplified as

$$\sum_{i=1}^{k} h_i[N_x \sin^2 \phi_i - N_y \cos^2 \phi_i + n(N_x \cos^2 \phi_i - N_y \sin^2 \phi_i)] = 0,$$
$$\sum_{i=1}^{k} h_i[m(N_x + N_y) \sin \phi_i \cos \phi_i - (1 + n)N_{xy}] = 0 \ , \tag{8.30}$$

$$\sigma_1^{(i)} = \sigma_1 = \frac{N_x + N_y}{h(1 + n)}, \quad \sigma_2^{(i)} = \sigma_2 = \frac{n(N_x + N_y)}{h(1 + n)}, \quad \tau_{12}^{(i)} = 0 \ , \tag{8.31}$$

where

$$n = \frac{E_2(1 + \nu_{21})}{E_1(1 + \nu_{12})}, \quad m = \frac{E_1 - E_2}{E_1(1 + \nu_{12})}, \quad h = \sum_{i=1}^{k} h_i \ .$$

Laminates of uniform strength exist under the following restrictions:

$$\frac{n}{1 + n} \leqslant \frac{N_x}{N_x + N_y} \leqslant \frac{1}{1 + n}, \quad \left|\frac{N_{xy}}{N_x + N_y}\right| \leqslant \frac{1 - n}{2(1 + n)} \ .$$

For monotropic model of the unidirectional ply considered in the previous section, $n = 0$, $m = 1$, and Eqs. (8.30) reduce to Eqs. (8.9) and (8.10).

To determine the thickness of the optimal laminate, we should use Eqs. (8.31) in conjunction with one of the strength criteria discussed in Chapter 6. For the simplest case, using the maximum stress criterion in Eqs. (6.2), the thickness of the laminate can be found from the following conditions $\sigma_1 = \bar{\sigma}_1$ or $\sigma_2 = \bar{\sigma}_2$, so that

$$h_1 = \frac{N_x + N_y}{(1 + n)\bar{\sigma}_1}, \quad h_2 = \frac{n(N_x + N_y)}{(1 + n)\bar{\sigma}_2} \ . \tag{8.32}$$

Obviously, for the optimal structure, we would like to have $h_1 = h_2$. However, this can happen only if material characteristics meet the following condition:

$$\frac{\bar{\sigma}_2}{\bar{\sigma}_1} = n = \frac{E_2(1 + \nu_{21})}{E_1(1 + \nu_{12})} \ . \tag{8.33}$$

The results of calculation for typical materials whose properties are listed in Tables 3.5 and 4.4 are presented in Table 8.2. As can be seen, Eq. (8.33) is approximately valid for fabric composites whose stiffness and strength in the warp and fill directions (see section 4.6) are controlled by the fibers of one and the same nature. However for unidirectional polymeric and metal matrix composites, whose longitudinal stiffness and strength are governed by the fibers and transverse characteristics are determined by the matrix properties, $\bar{\sigma}_2/\bar{\sigma}_1 \ll n$. In accordance

Table 8.2
Parameters of typical advanced composites.

Parameter	Fabric-epoxy composites			Unidirectional-epoxy composites				Boron–Al
	Glass	Carbon	Aramid	Glass	Carbon	Aramid	Boron	
$\bar{\sigma}_2/\bar{\sigma}_1$	0.99	0.99	0.83	0.022	0.025	0.012	0.054	0.108
n	0.85	1.0	1.0	0.28	0.1	0.072	0.11	0.7

with Eqs. (8.32), this means that $h_1 \ll h_2$, and the ratio h_2/h_1 varies from 12.7 for glass–epoxy to 2.04 for boron–epoxy composites. Now, return to the discussion presented in section 4.4.2 from which it follows that in laminated composites transverse stresses σ_2 reaching their ultimate value, $\bar{\sigma}_2$, cause cracks in the matrix which do not result in the failure of the laminate whose strength is controlled by fibers. To describe the laminate with cracks in the matrix (naturally, if the cracks are admitted for the structure under design), we can use the monotropic model of the ply and, hence, results of optimization presented in Section 8.1.

Consider again the optimality condition Eq. (8.25). As can be seen, this equation can be satisfied not only by strains in Eqs. (8.26), but also if we take

$$\tan 2\phi_i = \frac{\gamma_{xy}}{\varepsilon_x - \varepsilon_y} \ . \tag{8.34}$$

Because the left-hand side of this equation is a periodic function with period π, Eq. (8.34) determines two angles, i.e.

$$\phi_1 = \phi = \frac{1}{2}\tan^{-1}\frac{\gamma_{xy}}{\varepsilon_x - \varepsilon_y}, \quad \phi_2 = \frac{\pi}{2} + \phi \ . \tag{8.35}$$

Thus, the optimal laminate consists of two layers, and the fibers in both layers are directed along the lines of principal stresses. Assume that the layers are made of the same composite material and have the same thickness, i.e. $h_1 = h_2 = h/2$, where h is the thickness of the laminate. Then, using Eqs. (8.24) and (8.35) we can show that $B_{11} = B_{22}$ and $B_{24} = -B_{14}$ for this laminate. After some transformation involving elimination of γ^0_{xy} from the first two equations of Eqs. (8.23) with the aid of Eq. (8.34) and similar transformation of the third equation from which ε^0_x and ε^0_y are eliminated using again Eq. (8.34) we get

$$N_x = (B_{11} + B_{14}\tan 2\phi)\varepsilon^0_x + (B_{12} - B_{14}\tan 2\phi)\varepsilon^0_y,$$
$$N_y = (B_{12} - B_{14}\tan 2\phi)\varepsilon^0_x + (B_{11} + B_{14}\tan 2\phi)\varepsilon^0_y,$$
$$N_{xy} = (B_{44} + B_{14}\cot 2\phi)\gamma^0_{xy} \ .$$

Upon substitution of coefficients B_{mn} from Eqs. (8.24) we arrive at

$$N_x = \frac{h}{2}\left[(\bar{E}_1 + \bar{E}_2)\varepsilon_x^0 + (\bar{E}_1 \nu_{12} + \bar{E}_2 \nu_{21})\varepsilon_y^0\right],$$

$$N_y = \frac{h}{2}\left[(\bar{E}_1 \nu_{12} + \bar{E}_2 \nu_{21})\varepsilon_x^0 + (\bar{E}_1 + \bar{E}_2)\varepsilon_y^0\right],$$

$$N_{xy} = \frac{h}{4}[\bar{E}_1(1 - \nu_{12}) + \bar{E}_2(1 - \nu_{21})]\gamma_{xy}^0 \ .$$

Introducing average stresses $\sigma_x = N_x/h$, $\sigma_y = N_y/h$, and $\tau_{xy} = N_{xy}/h$ and solving these equations for strains we have

$$\varepsilon_x^0 = \frac{1}{E}(\sigma_x - \nu\sigma_y), \quad \varepsilon_y^0 = \frac{1}{E}(\sigma_y - \nu\sigma_x), \quad \gamma_{xy}^0 = \frac{\tau_{xy}}{G} \ . \tag{8.36}$$

where

$$E = \frac{1}{2(E_1 + E_2)}\left[2E_1E_2 + \frac{E_1^2(1 - \nu_{12}^2) + E_2^2(1 - \nu_{21}^2)}{1 - \nu_{12}\nu_{21}}\right],$$
$$\nu = \frac{E_1\nu_{12} + E_2\nu_{21}}{E_1 + E_2}, \quad G = \frac{E}{2(1 + \nu)} \ . \tag{8.37}$$

Changing strains for stresses in Eqs. (8.35) we can write the expression for the optimal orientation angle as

$$\phi = \frac{1}{2}\tan^{-1}\frac{\tau_{xy}}{\sigma_x - \sigma_y} \ . \tag{8.38}$$

As follows from Eqs. (8.36), the laminate consisting of two layers reinforced along the directions of principal stresses behaves like an isotropic layer, and Eqs. (8.37) specify elastic constants of the corresponding isotropic material. For typical advanced composites, these constants are listed in Table 8.3 (the properties of unidirectional plies are taken from Table 3.5). Comparing elastic moduli of the optimal laminates with those for quasi-isotropic materials (see Table 5.1) we can see that for polymeric composites the characteristics of the first group of materials are about 40% higher than those for the second group. However, it should be emphasized that while the properties of quasi-isotropic laminates are the universal

Table 8.3
Effective elastic constants of an optimal laminate.

Property	Glass epoxy	Carbon–epoxy	Aramid–epoxy	Boron–epoxy	Boron–Al	Carbon–carbon	Al_2O_3–Al
Elastic modulus, E (GPa)	36.9	75.9	50.3	114.8	201.1	95.2	205.4
Poisson's ratio, ν	0.053	0.039	0.035	0.035	0.21	0.06	0.176

material constants, the optimal laminates demonstrate characteristics shown in Table 8.3 only if the orientation angles of the fibers are found from Eqs. (8.35) or (8.38) and correspond to a particular distribution of stresses σ_x, σ_y, and τ_{xy}.

As follows from Table 8.3, the modulus of a carbon–epoxy laminate is close to the modulus of aluminum, while the density of the composite material is less by the factor of 1.7. This is the theoretical weight-saving factor that can be expected if we change aluminum for carbon–epoxy composite in a thin-walled structure. Because the stiffness of both materials is approximately the same, to find the optimal orientation angles of the structure elements, we can substitute in Eq. (8.38) the stresses acting in the aluminum prototype structure. Thus designed composite structure will have approximately the same stiffness as the prototype structure and, as a rule, higher strength because carbon composites are stronger than aluminum alloys.

To evaluate the strength of the optimal laminate, we should substitute strains from Eqs. (8.36) into Eqs. (4.69) and thus found strains in the principal material coordinates of the layers – into constitutive equations, Eqs. (4.56), that specify stresses σ_1 and σ_2 ($\tau_{12} = 0$)acting in the layers. Applying the proper failure criterion (see Chapter 6) we can evaluate the laminate strength.

Comparing Tables 1.1 and 8.3 we can see that boron–epoxy optimal laminates have approximately the same stiffness that titanium (but is lighter by the factor of about 2) and boron-aluminum can be used to substitute steel with a weight-saving factor of about 3.

For preliminary evaluation, we can use a monotropic model of unidirectional plies neglecting stiffness and load-carrying capacity of the matrix. Then, Eqs. (8.37) acquire the following simple forms:

$$E = \frac{E_1}{2}, \quad \nu = 0, \quad G = \frac{E_1}{4} \ . \tag{8.39}$$

As an example, consider an aluminum shear web with thickness $h = 2$ mm, elastic constants $E_a = 72$ GPa, $\nu_a = 0.3$ and density $\rho_a = 2.7$ g/cm^3. The panel is loaded with shear stress τ. Its shear stiffness is $B^a_{44} = 57.6$ GPa mm and the mass of a unit surface is $m_a = 5.4$ kg/m^2. For the composite panel, taking $\sigma_x = \sigma_y = 0$ in Eq. (8.38) we get $\phi = 45°$. Thus, the composite panel consists of $+45°$ and $-45°$ unidirectional layers of the same thickness. The total thickness of the laminate is $h = 2$ mm, i.e., the same as for an aluminum panel. Substituting $E_1 = 140$ GPa and taking into account that $\rho = 1.55$ g/cm^3 for a carbon-epoxy composite that is chosen to substitute aluminum we get $B^c_{44} = 70$ GPa mm and $m_c = 3.1$ kg/m^3. Stresses acting in the fiber directions of the composite plies are $\sigma^c_1 = \pm 2\tau$. Thus, the composite panel has 21.5% higher stiffness and its mass makes only 57.4% of the mass of a metal panel. Composite panel has also higher strength because the longitudinal strength of unidirectional carbon–epoxy composite under tension and compression is more than twice higher than the shear strength of aluminum.

Possibilities of the composite structure under discussion can be enhanced if we use different materials in the layers with angles ϕ_1 and ϕ_2 specified by Eqs. (8.35).

According to the derivation of Obraztsov and Vasiliev (1989), the ratio of the layers' thicknesses is

$$\frac{h_2}{h_1} = \frac{\bar{E}_1^{(1)} - \bar{E}_2^{(1)}}{\bar{E}_1^{(2)} - \bar{E}_2^{(2)}} ,$$

and elastic constants in Eqs. (8.37) are generalized as

$$\bar{E} = \frac{E}{1-\nu^2} = \frac{\bar{E}_1^{(1)}\bar{E}_1^{(2)} - \bar{E}_2^{(1)}\bar{E}_2^{(2)}}{\bar{E}_1^{(1)} + \bar{E}_1^{(2)} - \bar{E}_2^{(1)} - \bar{E}_2^{(2)}},$$

$$\nu = \frac{\bar{E}_1^{(1)}\bar{E}_1^{(2)}(\nu_{12}^{(1)} + \nu_{12}^{(2)}) - \bar{E}_2^{(1)}\bar{E}_2^{(2)}(\nu_{21}^{(1)} + \nu_{21}^{(2)})}{\bar{E}_1^{(1)}\bar{E}_1^{(2)} - \bar{E}_2^{(1)}\bar{E}_2^{(2)}} .$$

Superscripts 1 and 2 correspond to layers with orientation angles ϕ_1 and ϕ_2, respectively.

8.3. Application to pressure vessels

As an example of application of the foregoing results, consider filament wound membrane shells of revolution, that are widely used as pressure vessels, solid propellant rocket motor cases, tanks for gases and liquids, etc. (see Figs. 4.14 and 7.43). The shell is loaded with uniform internal pressure p and axial forces T uniformly distributed along the contour of the shell cross-section $r = r_0$ as in Fig. 8.4. Meridional, N_α, and circumferential, N_β, stress resultants acting in the shell

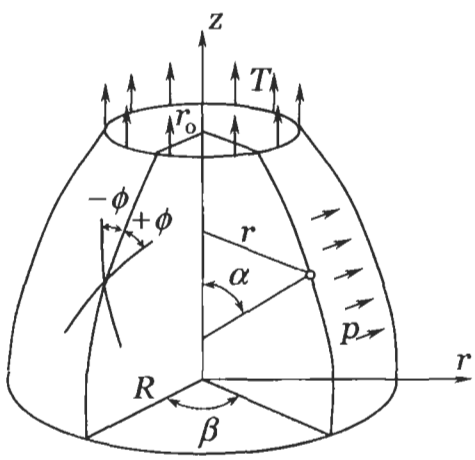

Fig. 8.4. Axisymmetrically loaded membrane shell of revolution.

follow from the corresponding free body diagrams of the shell element and can be written as (see, e.g., Vasiliev, 1993)

$$N_\alpha = -Q\frac{\left[1+(z')^2\right]^{1/2}}{rz'}, \quad N_\beta = -\frac{1}{z'}\left[1+(z')^2\right]^{1/2}\left\{pr - \frac{Qz''}{z'\left[1+(z')^2\right]}\right\}, \tag{8.40}$$

where $z(r)$specifies the form of the shell meridian, $z' = dz/dr$, and

$$Q = Tr_0 + \frac{p}{2}(r^2 - r_0^2) \tag{8.41}$$

Let the shell be made by winding an orthotropic tape at angles $+\phi$ and $-\phi$ with respect to the shell meridian as in Fig. 8.4. Then, N_α and N_β can be expressed in terms of stresses σ_1, σ_2 and τ_{12}, referred to the principal material coordinates of the tape with the aid of Eqs. (4.68), i.e.

$$\begin{aligned} N_\alpha &= h(\sigma_1 \cos^2\phi + \sigma_2 \sin^2\phi - \tau_{12}\sin 2\phi), \\ N_\beta &= h(\sigma_1 \sin^2\phi + \sigma_2 \cos^2\phi + \tau_{12}\sin 2\phi) \ , \end{aligned} \tag{8.42}$$

where h is the shell thickness. Stresses σ_1, σ_2, and τ_{12} are linked with the corresponding strains by Hooke's law, Eqs. (4.55), as

$$\varepsilon_1 = \frac{1}{E_1}(\sigma_1 - \nu_{21}\sigma_2), \quad \varepsilon_2 = \frac{1}{E_2}(\sigma_2 - \nu_{12}\sigma_1), \quad \gamma_{12} = \frac{\tau_{12}}{G_{12}} \ , \tag{8.43}$$

while strains $\varepsilon_1, \varepsilon_2$, and γ_{12} can be expressed in terms of the meridional, ε_α, and circumferential, ε_β, strains of the shell using Eqs. (4.69), i.e.

$$\varepsilon_1 = \varepsilon_\alpha \cos^2\phi + \varepsilon_\beta \sin^2\phi, \quad \varepsilon_2 = \varepsilon_\alpha \sin^2\phi + \varepsilon_\beta \cos^2\phi, \quad \gamma_{12} = (\varepsilon_\beta - \varepsilon_\alpha)\sin 2\phi \ . \tag{8.44}$$

Because the right-hand side parts of these three equations include only two strains, ε_α and ε_β, there exists a compatibility equation linking $\varepsilon_1, \varepsilon_2$ and γ_{12}. This equation is

$$(\varepsilon_1 - \varepsilon_2)\sin 2\phi + \gamma_{12}\cos 2\phi = 0 \ .$$

Writing this equation in terms of stresses with the aid of Eqs. (8.43) we get

$$\left[\frac{\sigma_1}{E_1}(1+\nu_{21}) - \frac{\sigma_2}{E_2}(1+\nu_{12})\right]\sin 2\phi + \frac{\tau_{12}}{G_{12}}\cos 2\phi = 0 \ .$$

In conjunction with Eqs. (8.42), this equation allows us to determine stresses as

$$\sigma_1 = \frac{1}{2hC}\left\{(N_\alpha + N_\beta)\left[1 + \frac{2G_{12}}{E_2}(1 + \nu_{12})\tan^2 2\phi\right] + \frac{N_\alpha - N_\beta}{\cos 2\phi}\right\},$$

$$\sigma_2 = \frac{1}{2hC}\left\{(N_\alpha + N_\beta)\left[1 + \frac{2G_{12}}{E_1}(1 + \nu_{21})\tan^2 2\phi\right] - \frac{N_\alpha - N_\beta}{\cos 2\phi}\right\},$$

$$\tau_{12} = \frac{G_{12}\tan 2\phi}{hC\cos 2\phi}\left[N_\beta\left(\frac{1 + \nu_{21}}{E_1}\sin^2\phi + \frac{1 + \nu_{12}}{E_2}\cos^2\phi\right)\right.$$

$$\left. - N_\alpha\left(\frac{1 + \nu_{21}}{E_1}\cos^2\phi + \frac{1 + \nu_{12}}{E_2}\sin^2\phi\right)\right], \tag{8.45}$$

where

$$C = 1 + G_{12}\left(\frac{1 + \nu_{21}}{E_1} + \frac{1 + \nu_{12}}{E_2}\right)\tan^2 2\phi \ .$$

Now, assume that in accordance with results presented in the previous section the optimal shell is reinforced along the lines of principal stresses, i.e., in such a way that $\tau_{12} = 0$. In accordance with the last equation of Eqs. (8.43), for such a shell $\gamma_{12} = 0$ and, as follows from Eqs. (8.44), $\varepsilon_\alpha = \varepsilon_\beta = \varepsilon_1 = \varepsilon_2$.

Putting $\tau_{12} = 0$ in the last equation of Eqs. (8.45) we can conclude that for the optimal shell

$$\frac{N_\beta}{N_\alpha} = \frac{1 - (1 - n)\cos^2\phi}{n + (1 - n)\cos^2 2\phi} \ , \tag{8.46}$$

where as earlier

$$n = \frac{E_2(1 + \nu_{21})}{E_1(1 + \nu_{12})} \ . \tag{8.47}$$

Substituting N_α and N_β from Eqs. (8.40) into Eq. (8.46) we arrive at the following equation for the meridian of the optimal shell:

$$\frac{rz''}{z'\left[1 + (z')^2\right]} = \frac{pr^2}{Q} - \frac{1 - (1 - n)\cos^2\phi}{n + (1 - n)\cos^2\phi} \ . \tag{8.48}$$

The first two equations of Eqs. (8.45) yield the following expressions for stresses acting in the tape of the optimal shell:

$$\sigma_1 = \frac{\sigma_2}{n} = \frac{N_\alpha}{h[n + (1 - n)\cos^2\phi]}, \quad \tau_{12} = 0 \ . \tag{8.49}$$

Taking into account that, in accordance with Eqs. (8.45)

$$\sigma_1 + \sigma_2 = \frac{1}{h}(N_\alpha + N_\beta) \ ,$$

we arrive at the following relationships:

$$\sigma_1 = \frac{N_\alpha + N_\beta}{h(1+n)}, \quad \sigma_2 = \frac{n(N_\alpha + N_\beta)}{h(1+n)}, \quad \tau_{12} = 0$$

which coincide with Eqs. (8.31).

Substituting N_α from the first equation of Eqs. (8.40) into Eq. (8.49) we get

$$\sigma_1 h = -\frac{Q\left[1 + (z')^2\right]^{1/2}}{rz'[n + (1-n)\cos^2\phi]} \ . \tag{8.50}$$

Assume that the optimal shell is the structure of uniform stress. Differentiating Eq. (8.50) with respect to r and taking into account that according to the foregoing assumption $\sigma_1 = constant$, we arrive at the following equation in which z'' is eliminated with the aid of Eq. (8.48):

$$\frac{\mathrm{d}}{\mathrm{d}r}\left\{rh\left[n + (1-n)\cos^2\phi\right]\right\} - h\left[1 - (1-n)\cos^2\phi\right] = 0 \ . \tag{8.51}$$

This equation specifies either the thickness or the orientation angle of the optimal shell.

Consider two particular cases. First, assume that a fabric tape of variable width $w(r)$ is laid up on the surface of the mandrel along the meridians of the shell of revolution to be fabricated. Then, $\phi = 0$ and Eq. (8.51) acquires the form

$$\frac{\mathrm{d}}{\mathrm{d}r}(rh) - nh = 0 \ .$$

The solution for this equation is

$$h = h_R\left(\frac{r}{R}\right)^{n-1} \ , \tag{8.52}$$

where $h_R = h(r = R)$ is the shell thickness at the equator $r = R$ (see Fig. 8.4). Assuming that there is no polar opening in the shell ($r_0 = 0$)or that it is closed ($T = pr_0/2$) we have from Eq. (8.41) $Q = pr^2/2$. Substituting this result in Eqs. (8.48) and (8.50) we obtain

$$\frac{rz''}{z'\left[1 + (z')^2\right]} = 2 - n \ , \tag{8.53}$$

$$\sigma_1 = -\frac{pr}{2z'h}\sqrt{1 + (z')^2} \ . \tag{8.54}$$

Integrating Eq. (8.53) under the condition $1/z' = 0$ for $r = R$ which means that the tangent line to the shell meridian is parallel to axis z at $r = R$ (see Fig. 8.4) we arrive at

$$z' = -\frac{r^{2-n}}{\sqrt{R^{2(2-n)} - r^{2(2-n)}}} \,. \tag{8.55}$$

Further integration results in the following parametric equation for the shell meridian:

$$\frac{r}{R} = (1-t)^{\lambda},$$

$$\frac{z}{R} = \lambda \int_0^t t^{-1/2}(1-t)^{-\lambda}\,\mathrm{d}t = \lambda B_x\left(\frac{1}{2}, 1-\lambda\right),$$

$$\lambda = \frac{1}{2(2-n)} \,.$$

Here, B_x is the β-function (or the Euler integral of the first type). Constant of integration is found from the condition $z(r = R) = 0$. Meridians corresponding to various n-numbers are presented in Fig. 8.5. For $n = 1$ the optimal shell is a sphere, while for $n = 2$ it is a cylinder. As follows from Eq. (8.52), the thickness of the spherical ($n = 1$) and cylindrical ($n = 2$, $r = R$) shells is constant. Substituting Eqs. (8.52) and (8.55) into Eq. (8.54) and taking into account Eqs. (8.49) we have

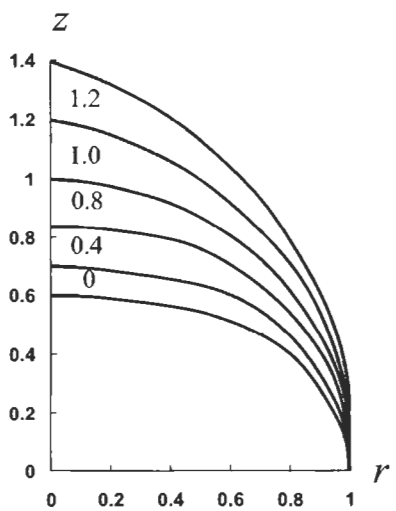

Fig. 8.5. Meridians of optimal composite shells.

$$\sigma_1 = \frac{\sigma_2}{n} = \frac{pR}{2h_R} \ .$$

This equation allows us to determine the shell thickness at the equator ($r = R$), h_R, matching σ_1 or σ_2 with material strength characteristics.

As was already noted, the shells under study can be made laying up fabric tapes of variable width, $w(r)$, along the shell meridians. The tape width can be linked with the shell thickness, $h(r)$, as

$$kw(r)\delta = 2\pi r h(r) \ , \tag{8.56}$$

where k is the number of tapes in the shell cross-section (evidently, k is the same for all the cross-sections) and δ is the tape thickness. Substituting $h(r)$ from Eq. (8.52) we get

$$w(r) = \frac{2\pi h_R r^n}{\kappa\delta R^{n-1}} \ .$$

Consider the second special case – a shell made by winding of unidirectional composite tapes at angles $\pm\phi$ with respect to the shell meridian. The tape width, w_0, does not depend on r, and its thickness is δ. Then, equation similar to Eq. (8.56) can be written as

$$\frac{kw_0\delta}{\cos\phi(r)} = 2\pi r h(r) \ ,$$

where k is the number of tapes with angles $+\phi$ and $-\phi$. Thus, the shell thickness is

$$h(r) = \frac{kw_0\delta}{2\pi r\cos\phi(r)} \ .$$

It can be expressed in terms of the thickness value at the shell equator $h_R = h(r = R)$ as

$$h(r) = h_R \frac{R\cos\phi_R}{r\cos\phi(r)} \ , \tag{8.57}$$

where $\phi_R = \phi(r = R)$. It should be noted that this equation is not valid for $r < r_0 + w_0$, i.e., in the shell area close to the polar opening where tapes are completely overlapped.

Substituting $h(r)$ from Eq. (8.57) into Eq. (8.51) we arrive at the following equation for the tape orientation angle:

$$r\frac{d\phi}{dr}\cdot\frac{\sin\phi[n-(1-n)\cos^2\phi]}{\cos\phi[1-(1-n)\cos^2\phi]} = 1 \ .$$

The solution of this equation that satisfies the boundary condition $\phi(r = R) = \phi_R$ is presented as follows:

$$r\left[1 - (1 - n)\cos^2 \phi(r)\right]^{(1-n)/2}\cos^n \phi(r) = R\left[1 - (1 - n)\cos^2 \phi_R\right]^{(1-n)/2}\cos^n \phi_R \ . \tag{8.58}$$

As has been already noted in the previous section, the simplest and rather adequate model of unidirectional fibrous composites for design problems is the monotropic model ignoring the stiffness of the matrix. For this model, we should take $n = 0$ in the foregoing equations. Particularly, Eq. (8.58) yields in this case

$$r \sin \phi(r) = R \sin \phi_R \ . \tag{8.59}$$

This is the equation of a geodesic line on the surface of revolution. Thus, in the optimal filament wound shell the fibers are directed along the geodesic lines. This substantially simplifies the winding process because the tape placed on the surface under tension automatically acquires the form of the geodesic line if there is no friction between the tape and the surface.

As follows from Eq. (8.59), for $\phi = 90°$, the tape touches the shell parallel of radius

$$r_0 = R \sin \phi_R \tag{8.60}$$

and the polar opening of this radius is formed in the shell (see Fig. 8.4).

Transforming Eq. (8.48) with the aid of Eqs. (8.59) and (8.60) and taking $n = 0$ we arrive at the following equation that specifies the meridian of the optimal filament wound shell:

$$\frac{z''}{z'\left[1 + (z')^2\right]} = \frac{2r}{r^2 - \eta^2} - \frac{r_0^2}{r(r^2 - r_0^2)} \ , \tag{8.61}$$

where

$$\eta^2 = r_0^2 - \frac{2T}{p} r_0 \ . \tag{8.62}$$

Integrating Eq. (8.61) with due regard for the condition $1/z'(R) = 0$ which, as earlier, requires that for $r = R$ the tangent to the meridian be parallel to z-axis, we get

$$z' = -\frac{r(r^2 - \eta^2)\sqrt{R^2 - r_0^2}}{\sqrt{R^2(r^2 - r_0^2)(R^2 - \eta^2)^2 - r^2(R^2 - r_0^2)(r^2 - \eta^2)^2}} \ . \tag{8.63}$$

Using this equation to transform Eq. (8.50) in which we take $n = 0$ and substituting h from Eq. (8.57) we get the following equation for the longitudinal stress in the tape:

$$\sigma_1 = \frac{p(R^2 - r_0^2) + 2r_0 T}{2Rh_R \cos^2 \phi_R} \tag{8.64}$$

As can be seen, σ_1 does not depend on r, and the optimal shell is a structure reinforced with uniformly stressed fibers.

Such fibrous structures are referred to as isotensoids. To study the types of isotensoids corresponding to loading shown in Fig. 8.4, factor the expression in the denominator of Eq. (8.63). The result can be presented as

$$z' = -\frac{r(r^2 - \eta^2)}{\sqrt{(R^2 - r^2)(r^2 - r_1^2)(r^2 + r_2^2)}}, \tag{8.65}$$

where

$$r_{1,2}^2 = \left(\frac{R^2}{2} - \eta^2\right)\left\{\sqrt{\frac{R^2}{R^2 - r_0^2}\left[1 + \frac{(3R^2 - 4\eta^2)r_0^2}{(R^2 - 2\eta^2)^2}\right]} \pm 1\right\}. \tag{8.66}$$

As follows from Eq. (8.65), quantities R and r_1 are the maximum and minimum distances from the meridian to the rotation axis. Meridians of isotensoids corresponding to various loading conditions are shown in Fig. 8.6. For $p = 0$,

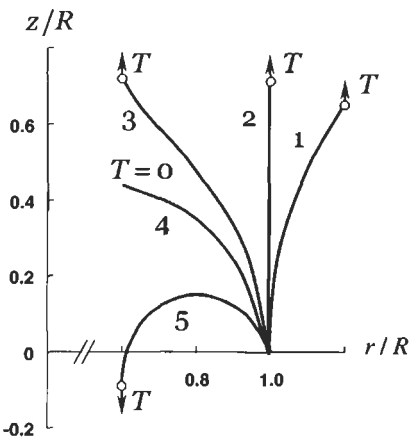

Fig. 8.6. Isotensoid corresponding to various loading conditions.

i.e., under axial tension, a hyperbolic shell is obtained with the meridian determined as

$$r^2 - z^2 \tan^2 \phi_R = R^2 \ .$$

This meridian corresponds to line 1 in Fig. 8.6. For $\phi_R = 0$, the hyperbolic shell degenerates into a cylinder (line 2). Curve 3 corresponds to $T = pr_0/2$, i.e., to a shell for which the polar opening of radius r_0 is closed. For the special angle $\phi_R = \phi_0 = 54°44'$, the shell degenerates into a circular cylindrical shell (line 2) discussed in section 8.1. For $T = 0$, i.e., in case of an open polar hole, the meridian has the form corresponding to curve 4. The change in the direction of axial forces T yields a toroidal shell (line 5). Performing integration of Eq. (8.65) and introducing dimensionless parameters

$$\bar{r} = \frac{r}{R}, \quad \bar{z} = \frac{z}{R}, \quad \bar{r}_0 = \frac{r_0}{R}, \quad \bar{\eta} = \frac{\eta}{R} \ ,$$

we finally arrive at

$$\bar{z} = \frac{k_2 - \bar{\eta}^2}{\sqrt{1 - k_2}} F(k, \theta) + \sqrt{1 - k_2}\, E(k, \theta) \ , \tag{8.67}$$

where

$$F(k, \theta) = \int_0^{\theta} \frac{\mathrm{d}\theta}{\sqrt{1 - k^2 \sin^2 \theta}}, \quad E(k, \theta) = \int_0^{\theta} \sqrt{1 - k^2 \sin^2 \theta}\, \mathrm{d}\theta$$

are the first-kind and the second-kind elliptic integrals and

$$k_{1,2} = \left(\frac{1}{2} - \bar{\eta}^2\right) \left\{ \pm \sqrt{\frac{1}{1 - \bar{r}_0^2} \left[1 + \frac{3 - 4\bar{\eta}^2}{(1 - 2\bar{\eta}^2)^2} \right]} - 1 \right\},$$

$$k^2 = \frac{1 - k_1}{1 - k_2}, \quad \sin \theta = \sqrt{\frac{1 - \bar{r}^2}{1 - k_1}} \ .$$

As an application of the foregoing equations, consider the optimal structure of the end closure of the pressure vessel shown in Fig. 4.14. The cylindrical part of the vessel consists of $\pm\phi_R$ angle-ply layer with thickness h_R, that can be found from Eq. (8.64) in which we should take $T = pr_0/2$, and a circumferential ($\phi = 90°$) layer whose thickness is specified by Eq. (8.18), i.e.

$$h_{90} = h_R(3 \cos^2 \phi_R - 1) \ .$$

The polar opening of the dome (see Fig. 4.14) is closed. So $T = pr_0/2$, $\bar{\eta} = 0$, and the dome meridian corresponds to curve 3 in Fig. 8.6. As has already been noted, upon

winding, an opening of radius r_0 is formed at the shell apex. However, the analysis of Eq. (8.65) for r_1 that determines the minimum distance from the meridian to the z-axis (see Fig. 8.7) shows that r_1 is equal to r_0 only if a shell has an open polar hole (curve 4 in Fig. 8.6). For a pressure vessel whose polar hole is closed, $r_1 \geqslant r_0$ and the equality takes place only for $\phi = 0$, i.e., when $r_1 = r_0 = 0$. In real vessels, polar holes are closed with rigid polar bosses shown in Fig. 8.8. The meridian of the shell under consideration can be divided into two segments. For $R \geqslant r \geqslant b$, the meridian corresponds to curve 3 in Fig. 8.6 for which $T = pr_0/2$ and $\eta = 0$. In Fig. 8.7 this segment of the meridian is shown with a solid line. The meridian segment $b \geqslant r \geqslant r_0$, where the shell touches the polar boss, corresponds to curve 4 in Fig. 8.6 for which $T = 0$. In Fig. 8.7, this segment of the meridian is indicated with the dashed line. Radius b in Figs. 8.7 and 8.8 can be set as the coordinate of an inflection point of this curve determined by the condition $z''(r = b) = 0$. Differentiating Eq. (8.65) and taking $\eta = 0$ for the closed polar opening we get

$$b = \sqrt{\frac{3}{2}} r_0 = 1.225 r_0 \ .$$

Because the segment $(b - r_0)$ is relatively small, we can assume that the contact pressure p_1 between the shell and the boss is uniform. Then, from the condition of boss equilibrium (the hole in the boss is closed), we have

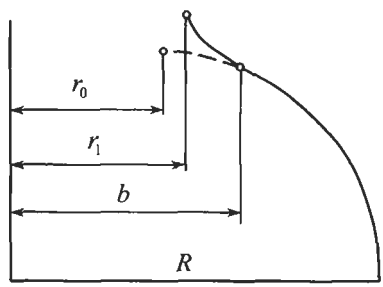

Fig. 8.7. Combined meridian of the pressure vessel dome.

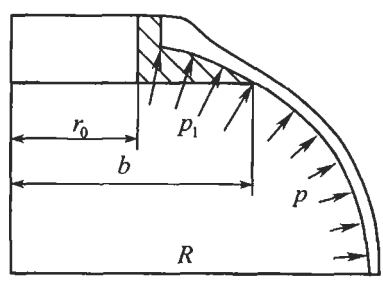

Fig. 8.8. Isotensoid dome with a polar boss.

$$p_1 = \frac{pb^2}{b^2 - r_0^2} \quad . \tag{8.68}$$

Constructing the combined meridian we should take into account that functions $z(r)$ and $z'(r)$ must be continuous for $r = b$. Finally, using Eqs. (8.65) and (8.67), we obtain:

For $R \geqslant r \geqslant b$ $(T = pr_0/2, \eta = 0)$

$$z' = -\frac{r^3\sqrt{R^2 - r_0^2}}{\sqrt{R^6(r^2 - r_0^2) - r^6(R^2 - r_0^2)}} \tag{8.69}$$

and

$$\bar{z} = \frac{k_2}{\sqrt{1 - k_2}} F(k, \theta_1) + \sqrt{1 - k_2} E(k, \theta_1) \quad ,$$

where

$$k_{1,2} = \frac{1}{2}\left(\pm\sqrt{\frac{1 + 3\bar{r}_0^2}{1 - \bar{r}_0^2}} - 1\right), \quad \sin\theta_1 = \sqrt{\frac{1 - \bar{r}^2}{1 - k_1}}, \quad k^2 = \frac{1 - k_1}{1 - k_2} \quad .$$

For $b \geqslant r \geqslant r_0$ $(T = 0, \eta = r_0)$

$$z' = -\frac{rb^2\sqrt{(r^2 - r_0^2)(R^2 - r_0^2)}}{\sqrt{R^6(b^2 - r_0^2)^2 - r^2b^4(r^2 - r_0^2)(R^2 - r_0^2)}} \tag{8.70}$$

and

$$\bar{z} = -\frac{m_1}{\sqrt{m_1 + m_2}}[F(m, \theta_2) - F(m, \theta_2^*)] + \sqrt{m_1 + m_2} \cdot [E(m, \theta_2) - E(m, \theta_2^*)]$$
$$+ \frac{k_2}{\sqrt{1 - k_2}} F(k, \theta_1^*) + \sqrt{1 - k_2} E(k, \theta_1^*) \quad ,$$

where

$$m_{1,2} = \frac{\bar{r}_0^2}{2}\left[\sqrt{1 - \frac{4(\bar{b}^2 - \bar{r}_0^2)^2}{\bar{b}^4\bar{r}_0^4(1 - \bar{r}_0^2)}} \pm 1\right], \quad m^2 = \frac{m_2}{m_1 + m_2}, \quad \cos\theta_2 = \sqrt{\frac{\bar{r}^2 - \bar{r}_0^2}{m_2}}$$

$$\sin\theta_1^* = \sqrt{\frac{1 - \bar{b}^2}{1 - k_1}}, \quad \cos\theta_2^* = \sqrt{\frac{\bar{b}^2 - \bar{r}_0^2}{m_2}}, \quad \bar{b} = \frac{b}{R} \quad ,$$

Meridians plotted in accordance with these equations and corresponding to various values of parameter $\bar{r}_0$ specifying the radius of polar opening (which is closed) are presented in Fig. 8.9. The curve $\bar{r}_0 = 0$ corresponds to the shell reinforced along the meridians and is the same as that of the curve $n = 0$ in Fig. 8.5. This isotensoid shape can be readily obtained experimentally if we load with internal pressure a balloon reinforced along the meridians as in Fig. 8.10.

Stresses acting along the fibers of the shells whose meridians are presented in Fig. 8.9 are determined by Eq. (8.50) in which we should take $n = 0$. Substituting h from Eq. (8.57), ϕ from Eqs. (8.59), (8.60) we should consider two segments of the meridian. For the first segment we take $T = pr_0/2$ and z' in accordance with

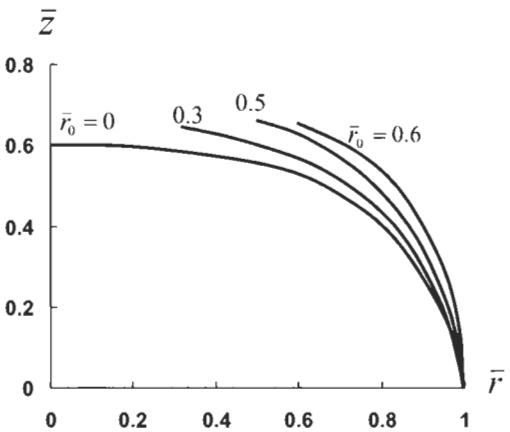

Fig. 8.9. Meridians of isotensoids.

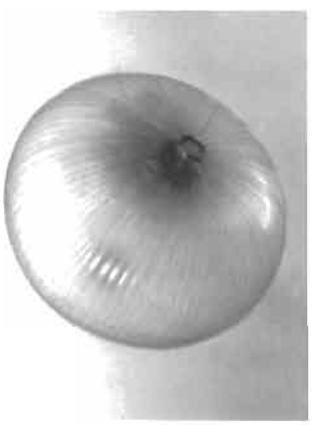

Fig. 8.10. A model isotensoid reinforced along the meridians.

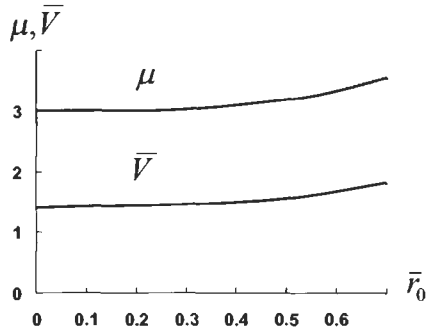

Fig. 8.11. Mass efficiency parameter μ and the normalized internal volume $\bar{V} = V/R^3$ of the isotensoid pressure vessel as functions of the polar opening radius.

Eq. (8.69), while for the second one we substitute z' from Eq. (8.70) and put $T = 0$, $p = p_1$, where p_1 is specified by Eq. (8.68). For both segments, we arrive at one and the same result, i.e.

$$\sigma_1 = \frac{pR}{2h_R \cos^2 \phi_R} \ .$$

The shell mass and internal volume can be found as

$$M = 2\pi\rho h_R \cos \phi_R \int_{r_0}^{R} \sqrt{1 + (z')^2}\, \frac{\mathrm{d}r}{\cos \phi},$$

$$V = \pi \int_{r_0}^{R} z' r^2 \, \mathrm{d}r \ ,$$

where ρ is the density of the material. The mass of a composite pressure vessel is often evaluated by using the parameter μ in the equation

$$M = \mu \frac{p_u V}{\bar{\sigma}_1 / \rho} \ .$$

Here, p_u is the ultimate pressure, and $\bar{\sigma}_1/\rho$ is the specific strength of the material. The variation of the parameter μ and the normalized internal volume $\bar{V} = V/R^3$ as function of the radius of the polar opening are shown in Fig. 8.11. Other applications of uniformly stressed composite structures can be found elsewhere (Obraztsov and Vasiliev, 1989).

8.4. References

Obraztsov, I.F. and Vasiliev, V.V. (1989). Optimal design of composite structures. In *Handbook of Composites*: *Vol. 2, Structure and Design* (C.T. Herakovich and Yu, M. Tarnopol'skii, eds.). Elsevier, Amsterdam, pp. 3–84.

Vasiliev, V.V. (1993). *Mechanics of Composite Structures*. Taylor & Francis, Washington.

AUTHOR INDEX

[Plain numbers refer to text pages on which the author (or his/her work) is cited. Boldface numbers refer to the pages where bibliographic references are listed.]

SUBJECT INDEX

ISBN 0 08 042702 2